ATMOSPHERIC GRAVITY WAVES: OBSERVATIONS AND THEORY

By

Stephen D. Eckermann, B.Sc. (Hons)

A THESIS

PRESENTED FOR THE DEGREE OF

DOCTOR OF PHILOSOPHY

AT THE

UNIVERSITY OF ADELAIDE

(DEPARTMENT OF PHYSICS AND MATHEMATICAL PHYSICS)

July 1990

Contents

Abstract

Theoretical and observational aspects of gravity wave motions within the lower and middle atmosphere are addressed in this thesis. The opening chapter provides a non–technical review of these waves in atmospheric settings, giving particular emphasis to the important role these waves play in a variety of fluid–dynamical processes in geophysics and astrophysics. Chapter 2 sets forth selected aspects of the theory of atmospheric gravity waves which are drawn from in later chapters.

Remaining chapters comprise the body of the research work. Arguments are developed in Chapter 3 which advise care in the analysis of small–scale atmospheric fluctuations. If one assumes that these perturbations are produced by gravity waves, in almost all cases a spectrum of many waves exists, and it is shown that analysis based on monochromatic premises can produce (and has produced) misleading results. Furthermore, there is currently debate as to whether atmospheric fluctuations are indeed due to gravity waves, or whether quasi two–dimensional turbulence (also known as vortical modes) produces most of the variance. Experimental assessment of these two theories has centred on comparing the power spectra of these fluctuating fields with the separate spectral predictions of gravity–wave and vortical–mode theory. However, observations also imply that these spectra must be nonstationary, and simulations reveal that experimental spectra can be distorted from the stationary theoretical predictions, making comparisons with theory ineffectual. A non–spectral statistic is developed to provide more stationary experimental evaluations of the competing theories.

In Chapter 4, this newly–developed theoretical test is applied to time series of atmospheric wind velocities measured in the lower atmosphere (2–12km height range) with a VHF radar system. The analysis reveals that these fluctuations are consistent with gravity waves, and inconsistent with quasi–two–dimensional turbulence. These observations were conducted during the passage of cold fronts, and strong correlations between these frontal passages and bursts in gravity–wave energy are presented and analyzed.

It was argued in the previous two chapters that distortion of gravity–wave frequency spectra at mesospheric heights (60–90km) should not be severe, and this is assessed experimentally in Chapter 5 by spectrally analyzing a large base of wind data from this region, as measured with an HF radar system. The observations confirm that distortions are not significant, and in the process some important characteristics of the wave field at these heights are brought to light.

Upper–stratospheric heights (20–60km) cannot be probed by radar, and so information on gravity

wave characteristics here is limited. However, rockets have probed this region for many years from a number of sites around the world, and these data are analyzed in Chapter 6 for evidence of gravity wave motions. New and important information on seasonal variations in the amplitudes and propagation directions of gravity waves are obtained, and the significance of some of these new findings is discussed.

These observations, together with others performed elsewhere, have now resolved some basic features of gravity waves in the middle atmosphere. Surprisingly, many of these characteristics have yet to be explained. In Chapter 7, simple ideas are developed which are used to explain observed seasonal variations of gravity wave amplitudes. However, these same arguments cannot explain the geographical variability evident in measurements. The theoretical investigation is therefore extended through the use of a more complex numerical model, which simulates gravity wave propagation through the zonally–averaged middle atmosphere. The model is used to help explain various observed features of middle–atmospheric gravity waves, and deliberately avoids including any initial amplitude or wave–propagation anisotropy, so that any such anisotropy which subsequently arises must be due to propagation effects. Results from model simulations support more rigorously the simple earlier arguments as to the origin of the seasonal variations in wave activity. However, the model also produces information on many other gravity–wave parameters, and these findings are compared with available measurements, with apparent agreement in some cases. The model also highlights, and enables investigation of, an important physical process by which horizontal wavelengths and ground–based phase speeds can change due to horizontal refraction of the wave.

In its entirety, this work provides not only observational information on the nature of gravity waves in a number of different regions of the atmosphere, but in all cases theoretical analysis of these data casts light on some of the processes which act to produce this observed structure.

Preface

To the best of my knowledge and belief, this thesis contains no material previously published or written by another person, except where due reference is made in the text of this thesis, and contains no material which has been accepted for the award of any other degree or diploma in any other University. I consent to this thesis being made available for photocopying and loan by the librarian of the University of Adelaide, subject to acceptance for the award of the degree.

Stephen D. Eckermann, B.Sc. (Hons)

Acknowledgements

An extended period of study, as summarized in this thesis, necessarily owes much to a great many people. I thank my supervisors Dr. R.A. Vincent and Dr. W.K. Hocking for their guidance and encouragement. I thank also the following colleagues of mine from The Atmospheric Physics Group, who have all helped me in no small part throughout my time with them; Dr. I.M. Reid, Dr. B.H. Briggs, Dr. Andre Phillips, Laurie Campbell, Damian Murphy, Bob Hurn, Shane Dillon, Drazen Lesicar, Lyn Birchby, Dallas Kirby, Trevor Harris, Brenton Vandepeer, Kong Mu, and David Low. Furthermore, I thank the following visitors to the group for helpful conversations; Dr. Mamoru Yamamoto, Prof. C.S. Gardner, Dr. K.S. Gage, Dan Senft, and Richard Collins. To anyone I've forgotten, I apologize, but thanks anyway!

In a more specific sense, many sections of the work contained in this thesis were aided by helpful input from a number of people, who I must now thank.

The work presented in section 3.2 was performed collaboratively with Wayne Hocking, and has been published elsewhere [*Eckermann and Hocking*, 1989; see Appendix *F*]. I thank Wayne particularly, as well as Bob Vincent, Basil Briggs, Prof. I. Hirota[1] and two anonymous referees for constructive comments on earlier versions of this work. A lot of the work in section 3.3 has also been submitted and accepted for publication [*Eckermann*, 1990; see Appendix *G*]. In this regard, I must particularly thank Wayne Hocking for stimulating discussions on vortical modes and turbulence. I also thank Wayne Hocking, Iain Reid, Basil Briggs, Dr. T.E. VanZandt[2] and Bob Vincent for their comments on various earlier drafts of the manuscript, and two anonymous referees for their helpful review comments on the submitted manuscript.

Much of the observational analysis in section 4.2 was performed collaboratively with Bob Vincent, and has been published elsewhere [*Vincent and Eckermann*, 1990; see Appendix *H*]. Critical reviews of early versions of this work by Basil Briggs, Wayne Hocking, Iain Reid, and Prof. K. C. Yeh[3] were much appreciated. In the subsequent work in section 4.3, I thank Warwick Grace, from The Bureau of Meteorology in Adelaide, for providing plots of the altitude variation of temperature derived from their routine balloon–borne radiosonde measurements at Adelaide Airport.

The work detailed in chapter 5 was undertaken collaboratively with Iain Reid, who I thank for his insights and assistance.

[1] Geophysical Institute, Kyoto University, Kyoto, Japan
[2] National Oceanic and Atmospheric Administration, Boulder, Colorado, U.S.A.
[3] Department of Electrical and Computing Engineering, University of Illinois, Urbana, U.S.A.

The analysis of rocket data in section 6.3 was performed in collaboration with Prof. Hirota and Wayne Hocking, for which I thank them. Dr. Masato Shiotani's assistance with the raw data, and useful discussions with Dr's Kevin Hamilton[4], Iain Reid, and Bob Vincent, were much appreciated.

Helpful correspondence with Dr. D.G. Andrews[5], Dr. M.R. Schoeberl[6], Dr. D.F. Strobel[7], and the late Prof. S.B. Fels[8] in connection with the modelling in section 7.3 is gratefully acknowledged.

Thanks to my friends in the Adelaide University Cricket Club and elsewhere for providing me with innumerable enjoyable times, which my time at University has made me appreciate. Being at the end of my Ph.D., my thoughts go out most especially to Stephen Pell, who was also on the way towards completing all those years of study towards a Ph.D., and to finally reap the rewards of all those years of hard yakka for little or no money, until the road accident last week which appears to have made him a quadraplegic. It has always been in the back of my mind that it would be terrible to study all this time, and then have "the full-time hooter blown" just as one was about to finally enjoy the benefits. Life can be bloody unfair!

Thanks to Mum and Dad for putting up with "the perennial student" for so long, to my brother and best mate Bronte for all the good times (and the many more to come), to Uncle Geoff and the rest of the family. Thanks also to H.G. Nelson and Rampaging Roy Slaven for being very very funny men. Lastly, I think of those from school who I still keep in touch with, many of whom are now on the dole, or in jobs they hate with long hours and poor pay, and I thank my lucky stars.

[4] Geophysical Dynamics Laboratory, Princeton University, U.S.A.
[5] Dept. Atmospheric, Oceanic and Planetary Physics, Oxford University, U.K.
[6] Goddard Space Flight Centre, Maryland, U.S.A.
[7] Dept. Physics and Astronomy, John Hopkins University, Baltimore, U.S.A.
[8] Geophysical Dynamics Laboratory, Princeton University, U.S.A.

Chapter 1

Background

1.1 Introduction

For some time, the theory and observation of atmospheric gravity waves appeared to be a rather esoteric, narrowly–defined study of a little-known fluid wave motion, which had little impact on our understanding of the large–scale structure and circulation of the atmosphere. Only recently has it been realized that many regions of the Earth's atmosphere, whose structure had previously been poorly understood, are now understood far better since the effects of gravity waves on these regions have been considered. Indeed, over the last thirty years, but particularly during the last decade, many of the most puzzling aspects of the neutral atmosphere's circulation and thermal structure have become better understood as a direct result of advances in our understanding of both planetary Rossby wave and internal gravity wave motions within the atmosphere [see, e.g., *Andrews*, 1987].

The purpose of this opening chapter is to give a general impression as to why the study of atmospheric wave motions, and most especially gravity waves, is important, and also to illustrate how the understanding gained in the atmospheric context can be applied elsewhere. We begin, however, with a simple general discussion of the mean structure of the lower and middle atmosphere.

1.2 The Lower and Middle Atmosphere

The work to follow focuses on the region of the Earth's atmosphere between the surface and an altitude of about $100km$. The atmospheric constituents at these heights are, for the most part, un–ionized and well–mixed by turbulence, and so density stratification arises from *hydrostatic balance* between gravitational

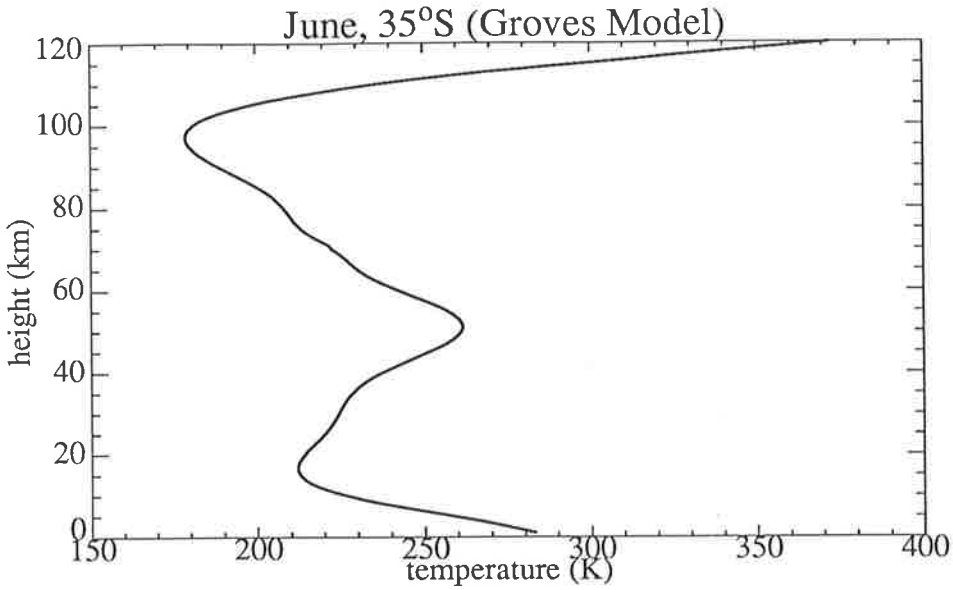

Figure 1: Typical vertical variation of atmospheric temperature with height. These data are taken from the zonal–mean reference temperatures of *Groves* [1985, 1987] at 35°S in June.

and buoyancy forces in the vertical, giving a vertical density e-folding length or *density scale height* H_ρ which is set principally by the air temperature T. The prevailing horizontal flow below $\sim 70km$ in height is predominately zonal[1], due to *geostrophic balance* in the horizontal between the Coriolis force of the revolving Earth and horizontal pressure–gradient forces within the atmospheric fluid. These geostrophic winds can be calculated from the vertical and latitudinal distribution of the air temperature T by using the so-called thermal wind equation [see, e.g., *Andrews et al.*, 1987]. Thus knowledge of the global distribution of atmospheric temperature also implies knowledge of the first order density and flow characterisitics of the neutral atmosphere, and so it is the most fundamental quantity to consider and to attempt to understand.

At any position on the Earth[2], the observed change in atmospheric temperature with height has the same qualitative variation as that depicted in Figure 1. On ascending from the surface, temperatures decrease rather uniformly up to around[3] $10km$, whereupon they increase gradually to a peak value of $\sim 270K$ at around $50km$. Above this peak, T decreases to a minimum near $90km$ before increasing once again. The reproducable thermal structure in each of these four height regimes has led to their individual naming, and they are known, in order of ascent, as the *troposphere*, *stratosphere*, *mesosphere*, and *thermosphere*.

[1] i.e. directed either east or west
[2] except at near–polar latitudes in perpetual darkness during winter
[3] This height varies with latitude, ranging from $\sim 18km$ at the tropics to $\sim 7km$ near the poles

1.3 Solar Irradiance

The trends in Figure 1 are caused principally by the surface warming and atmospheric photochemistry produced by solar electromagnetic radiation impinging upon the Earth. Different heating and cooling processes occur at different heights, and this produces in observed temperature variations with altitude.

The thermal structure of the troposphere is determined principally by the heating of the planet's surface due to absorption of solar radiation. Most (~70%) of the radiation reaching the surface is absorbed, and heats the surface to a temperature around $260K$. This heated surface then re–emits a $260K$ Planck (black body) spectrum of radiation, which peaks in intensity at infra-red wavelengths.

If the atmosphere was transparent to this predominately infra-red surface radiation, atmospheric temperatures would decrease with height at $\Gamma_a = 9.8K\ km^{-1}$ due to natural abiabatic cooling, where Γ_a is the so-called *dry adiabatic lapse rate*. However, atmospheric water vapour, carbon dioxide, and other "greenhouse gases" absorb some of these re-emitted infra-red wavelengths, and heat the atmosphere. All of these processes combine to give typical tropospheric lapse rates in the range $3–10K\ km^{-1}$.

These tropospheric lapse rates are both spatially and temporally variable. For example, local surface or chemical heating can often produce a temperature *increase* over a small height range (called an inversion), examples of which are shown in Figure 52 in chapter 4. At altitudes further away from this heating, however, a compensating lapse rate which is superadiabatic[4] can often result. The vertical position of an air parcel in a superadiabatic background temperature gradient is highly unstable: if the parcel is displaced slightly upwards, then it becomes warmer than the background and will rise further, or if displaced downwards, it becomes cooler than the background and will continue its descent. In both cases, the vertically displaced parcels attain temperatures which differ from the local background temperature, giving rise to vertical heat fluxes and a consequent alteration of the thermal structure. The resulting motion of all these parcels is termed *convection*, and is a complex, three dimensional process which subsides only when the atmosphere has equilibrated to a new and stable vertical temperature structure. Consequently, superabiabatic lapse rates are often referred to as a *convective instabilities*. Because typical tropospheric lapse rates are ~$3–10\ K\ km^{-1}$, convective instabilities freqeuntly arise, and it is because of this that the troposphere (literally "turning-sphere") is so named.

Indeed, because the radiative driving of the troposphere has appreciable geographical variability (e.g., land–sea–ice contrast, variable solar zenith angle) and temporal intermittency (e.g., isolated evaporation or condensation of water vapour), the troposphere is very dynamic. These dynamics are also rather

[4] a temperature decrease with height which exceeds Γ_a

nonlinear, and a variety of complex meteorological phenomena arise. These include large/synoptic–scale phenomena such as high and low pressure systems, fronts, and cyclones. These flows can interact with each other, or can be modified by surface friction, geostrophic and/or convective adjustment, orography, and further radiative driving, giving rise to smaller scale motions such as gravity waves and turbulence. The generation of gravity waves during the passage of tropospheric cold fronts is investigated observationally in section 4.3.

At a height around $10km$, the falloff in temperature abates and the atmosphere remains essentially isothermal[5] up to $\sim 20km$. This region is often termed the *lower stratosphere*. The accompanying increase in atmospheric stability that this temperature structure provides makes vertical motions far more difficult to produce and sustain, and so the atmosphere is highly stratified (hence "stratosphere"). The stability of lower stratosphere acts as a "lid" to the underlying tropospheric air, and so the interface between the two regions is known as the *tropopause*. Typical tropopause heights range from $18km$ near the equator to around $7km$ at the poles.

Above $20km$, temperatures increase gradually to a peak value at around $50km$, and so the *upper stratosphere* is very stable and highly stratified. This rise in temperature is caused by dissocation of ozone by solar ultra-violet radiation in the 200-300nm wavelength range, with absorption maximizing at a height of $\sim 40km$. The global distribution of ozone gives rise to a global temperature structure which drives strong zonal winds at these heights[6], with mid–latitude wind speeds approaching $100m\ s^{-1}$ during winter at a height of $\sim 50km$ (see, e.g., Figure 97 in chapter 6).

Above $50km$ the temperature decreases with height, due to rapidly decreasing ozone concentrations. By analogy to the tropospheric situation, the height of maximum temperature near $50km$ is called the *stratopause*. The subsequent atmosphere up to $\sim 90km$, where the temperature decrease abates, is called the *mesosphere* (literally "middle sphere"), and this upper level is called the *mesopause*. Around the mesopause, where the coldest atmospheric temperatures are encountered, the atmosphere assumes very different characterisitics.

Firstly, the air now becomes slightly ionized, mainly through photoionization of nitrous oxide (NO) by ultra-violet Lyman-α emission ($\sim 121nm$) from the Sun, and the resulting electrons form the *D–region* (50–$90km$). However, the total ionization is too small to produce significant distortion to the dynamics through electromagnetic effects, so that this ionized air is merely advected with the neutral air. Also, the background velocity of the neutral air becomes highly ageostrophic; that is, a strong and persistent

[5] constant temperature
[6] via the thermal wind equation

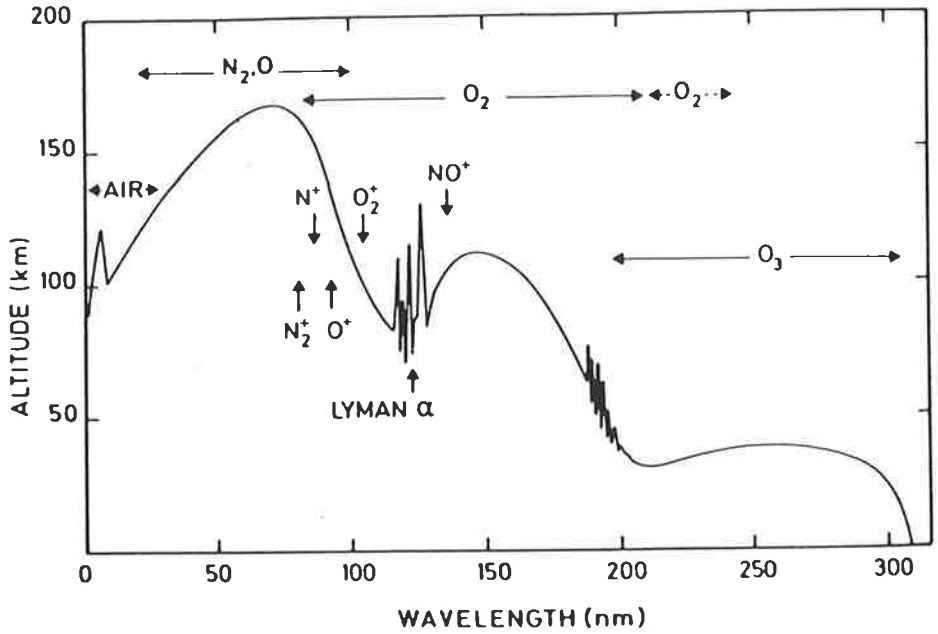

Figure 2: Plot of the altitude of maximum absorption as a function of solar radiation wavelength, for wavelengths less than $300nm$ [from *Brasseur and Solomon*, 1984].

persistent meridional[7] component to the background wind exists. These features are discussed in section 1.4.3

The remaining atmosphere above the mesopause is known as the thermosphere. As its name suggests, the temperatures here are large and increase monotonically with height, due to rapidly increasing photoionization of various chemical species. Above $100km$, ionization starts to affect the dynamics through interactions with earth's electic and magnetic fields, and kinematic viscosity increases to a point where turbulent eddies are damped out, so that the atmospheric constituents can no longer be continually mixed. Molecular diffusion dominates therefore, and so the concentrations of different ions vary with height according to their atomic weight.

Figure 2 shows the height of maximum absorption as a function of wavelength for solar radiation impinging vertically on the atmosphere. Note that, while stratospheric ozone filters $200–300nm$ UV light, hard UV and X–radiation are absorbed by chemicals in the mesosphere and thermosphere. Therefore, any depletion in the ambient concentrations of the indicated chemicals within the stratosphere, mesosphere, and thermosphere may result in increased levels at the ground of these energetic and biologically harmful electromagnetic wavelengths. Therefore, understanding and continuous monitoring of the entire middle and upper atmosphere is clearly warranted.

[7] directed north or south

1.4 Effects of Atmospheric Wave Motions

In the previous discussion, it was shown that much of the actual temperature structure of the lower and middle atmosphere can be understood in terms of radiative equilibrium between solar-driven heating and natural abiabatic cooling. However, collation of measurements of atmospheric temperature and wind speed over the entire globe, starting around 1960, revealed progressively more puzzling features of the atmosphere which could not be reproduced by even the most sophisticated numerical models of atmospheric composition and photochemistry.

Since background wind speeds could be broadly reproduced from temperatures, and temperatures appeared to be set by radiative eqilibrium amongst photochemistry and abiabatic cooling, there was an implicit belief that all of the large–scale circulation was merely a coupled response to photochemisity. In other words, chemistry affected the dynamics, but dynamics did not significantly affect the chemistry. This belief meant that wave motions within the atmospheric fluid, for example, were regarded as "noise" superimposed on the photochemically determined mean circulation, producing no lasting effects on this background state. Hence these waves were thought of as dynamical "noise", the effects of which would disappear after long–term averaging. Therefore, although atmospheric waves were being observed and their theory developed, these studies were considered of little more than academic interest, and their influence was largely ignored [see., e.g., *Fritts*, 1984; *Hines*, 1989].

Despite this, observations and theoretical development in the field of atmospheric waves continued. Then, in the late 1960's, atmospheric waves were demonstrated to drive the dynamics of the equatorial lower stratosphere by *Lindzen and Holton* [1968]. They developed a theory involving atmospheric waves alone to explain the anomalous quasi–biennial oscillation[8] (QBO) of wind and temperature in this region. Since then, more and more regions of the atmosphere have been identified where inclusion of wave motions and wave dissipation has greatly aided understanding of the structure of that region. Yet only very recently (during the 1980's) has there been general acceptance that the deposition of momentum and energy by dissipating atmospheric wave motions drives many of the anomalous atmospheric circulations that cannot be explained by radiative arguments.

It happens that the atmosphere can support many different types of wave motions, A well–known example is the acoustic (sound) wave. However, more energetic, larger–scale waves occur too. So–called *internal gravity wave motions* with horizontal scales in the range $\sim$10–1000km arise from the restoring forces of gravity acting downwards and buoyancy acting upwards on vertically displaced air parcels. On

[8] i.e. an oscillation of about, but not exactly, two years: the mean equatorial QBO period in the lower stratosphere is $\sim$27 months

planetary scales[9], *Rossby waves* arise from a quasi–linear variation in potential vorticity with meridional displacement. Detailed descriptions of the origin and nature of these waves are given in a number of texts [see, e.g., *Gossard and Hooke*, 1975; *Gill*, 1982; *Andrews et al.*, 1987], and some further details of gravity waves and other closely related motions considered important for this thesis are given in Chapter 2.

A qualitative discussion of wave–driven atmospheric features that have been identified in the lower and middle atmosphere will now be given, starting from the ground and moving up. As this thesis focuses on gravity waves, by far the greatest emphasis will be given to the gravity–wave–driven circulations of the lower and middle atmosphere. This is not to say that the effects of other types of waves, such as planetary Rossby waves, are unimportant in this regard. Indeed, in many regions of the atmosphere they have far greater impact than gravity waves, and so where necessary their effects will also be mentioned briefly.

1.4.1 Gravity Waves in the Troposphere (1–10km)

Production and propagation of internal gravity waves within the troposphere has been known of for some time. Gravity waves produced by flow over mountains, referred to assortedly as "lee waves", "mountain waves", and "stationary waves", were first studied experimentally [*Kuettner*, 1939*a*,*b*] and mathemetically [*Queney*, 1948; *Scorer*, 1949] some time ago, and since then have been observed and studied over many mountainous areas [see reviews by *Smith*, 1979, 1989]. *Brunk* [1949] was amongst the first to study ground–level pressure pulsations produced by gravity waves[10] which were not forced by undular terrain, but instead were associated with the onset of intense convective storms. Gravity waves have since been found to arise from a range of meteorological phenomena [see, e.g., *Uccellini and Koch*, 1987; *Einaudi et al.*, 1987]. Yet only now are meteorological modellers beginning to appreciate the importance that gravity waves might play in many aspects of tropospheric dynamics, and in understanding and forecasting weather. At the same time, there is increasing interest from the middle atmosphere community in tropospheric gravity waves, as it now appears that most of the wave energy in the middle atmosphere originates from tropospheric sources.

Perhaps the first indication of the importance that gravity waves can have on weather came from the study of the severe downslope winds that often occur near mountain ranges. Well documented examples are the "Helm wind" on the west side of the Pennines in England [e.g., *Brunskill*, 1884; *Manley*, 1945], and the strong downslope winds near The Rocky Mountains in Colorado, which can sometimes exceed

[9] i.e. horizontal scales of the order of the distance around the earth
[10] then known as "waves of depression"

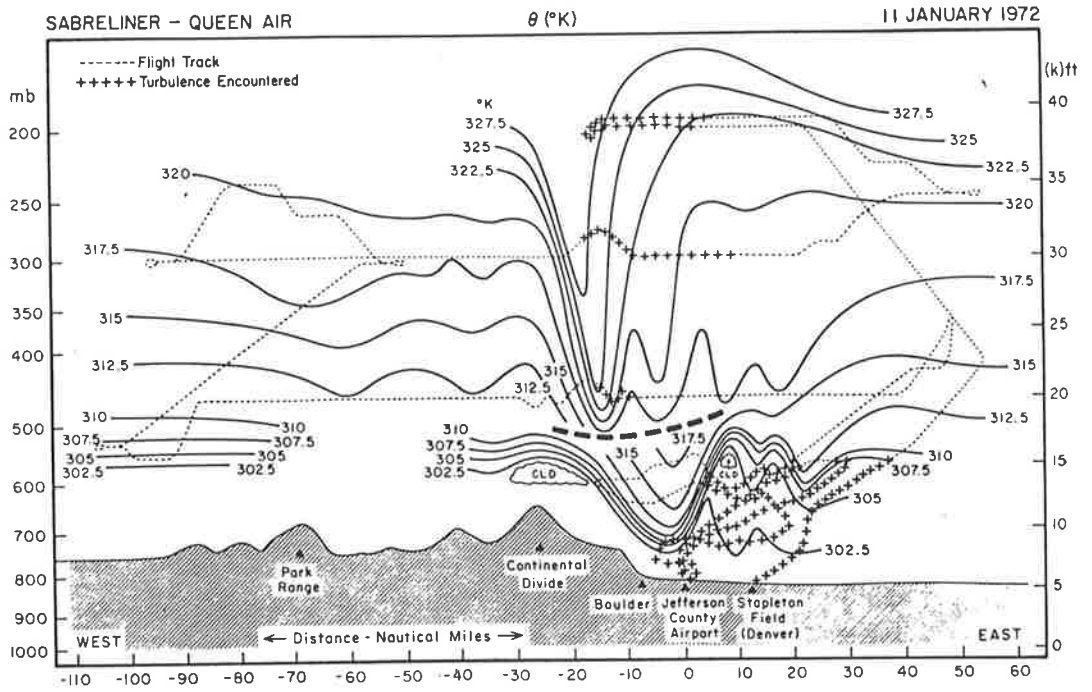

Figure 3: Plot of the strong gravity wave motion over the Rocky Mountains in Colorado which occurred on 11th. January 1972, in which winds gusted up to $150km\ hr^{-1}$. Solid lines connect regions of constant potential temperature. This diagram is after *Lilly* [1978].

$150km\ hr^{-1}$ and pose an enormous hazard to property and aircraft [see, e.g., *Lilly and Zipser*, 1972; *Lilly*, 1978]. Milder local versions of this phenomenon are the well–known "gully winds" that occur in the Adelaide Hills during the late afternoon [see, e.g., *Baines*, 1990]. Downslope winds are caused by strong lee wave motions arising from flow over orography [see, e.g., *Lilly*, 1978], and a good summary of current understanding of the processes involved is provided by *Scinocca and Peltier* [1989]. One of the more spectacular (and damaging) examples occurred over Colorado in 1972, and is profiled in Figure 3. The intense high-frequency wind gusts which cause most of the damage during such severe events have only been modelled recently, and arise secondarily through a highly nonlinear "breaking" of the original wave motion [*Scinocca and Peltier*, 1989].

Another well–known meteorological phenomenon which occurs over north–eastern Australia is the so–called "morning glory". During a "morning glory", an observer experiences one, sometimes several, intense wind surges, often accompanied by the rapid passage overhead of a spectacular rolling cloud formation. This cloud has very limited extent both vertically, and horizontally along its direction of motion, but can extend as a "wavefront" over hundreds of kilometres transverse to its horizontal propagation direction. The "morning glory" forms on a low–level temperature inversion produced at night by the land re–radiating heat. Sea breezes from the east and west coast of the Cape York Peninsula flow inland and

collide, producing intense upwelling and a large propagating pressure "step", called a *bore*, which propagates away on the inversion as the "morning glory". In time, the bore becomes more sinuous, as solitary gravity wave packets arise at the leading edge of the bore, and, if there is sufficient moisture, clouds form with the ascent and erode with the subsidence caused by the wave motion, producing the "rolling cloud" effect. Normally these waves would propagate vertically, but in this case the waves are vertically trapped[11] and propagate within a horizontal waveguide, and so the event persists [*Crook*, 1988]. Dawn produces solar heating and convection which rapidly dissipates the inversion, and so too the "morning glory" [*Clarke*, 1989]. While numerical modelling seems to support the concept of the "morning glory" as a bore with associated gravity wave oscillations [see, e.g., *Clarke*, 1989], *Christie* [1989] has argued that the entire phenomenon is a complex nonlinear gravity wave motion. It appears that "morning glory" processes occur quite commonly elsewhere, but are unaccompanied by cloud lines [see the review of *Smith*, 1988], and the strong vertical motions they give rise to can endanger low–flying aircraft [*Christie and Muirhead*, 1983] and can trigger deep convective thunderstorm activity [*Smith*, 1988]. For example, the possibility that bore waves might propagate ahead of cold fronts, which are common weather phenomena over southern Australia, was reviewed *inter alia* by *Smith and Reeder* [1988]. Gravity wave motions produced by cold fronts are studied observationally in section 4.3.

Indeed, very strong associations have been found between tropospheric gravity waves and convective activity generally [see, e.g., *Einaudi et al.*, 1987; *Kuettner et al.*, 1987]. Convection is usually believed to produce gravity waves [see, e.g., *Ferguson*, 1967; *Bosart and Cussen*, 1973; *Curry and Murty*, 1974; *Balachandran*, 1980; *Larsen et al.*, 1982*b*], although sometimes pre–existing gravity waves actually trigger convective storm activity [see, e.g., *Matsumoto and Akiyama*, 1969; *Uccellini*, 1975; *Koch and McCarthy*, 1982; *Stobie et al.*, 1983]. Gravity wave motions also appear to be important in the development of some tornadoes [see, e.g., *Miller and Sanders*, 1980], in altering the nature and distribution of cloud and precipitation events [e.g., *Testud et al.*, 1980; *Ley and Peltier*, 1981; *Pecnick and Young*, 1984; *Balaji and Clark*, 1988], and even in triggering condensation and latent heat release [see, e.g., *Einaudi and Lalas*, 1975; *Chimonas et al.*, 1980].

The momentum flux associated with gravity wave motions was appreciated quite early in tropospheric studies [see, e.g., *Long*, 1955; *Sawyer*, 1959; *Eliassen and Palm*, 1961], and the theory of drag on the mean flow due to the momentum flux convergence produced by a dissipating gravity wave was developed in depth by *Bretherton* [1969*a*,*b*]. *Lilly* [1972] suggested that the omission from models of such wave drag could be a significant source of the errors encountered in long–range tropospheric forecasts. Mountain

[11] They cannot propagate very far up or down before they are reflected due to special atmospheric conditions which occur

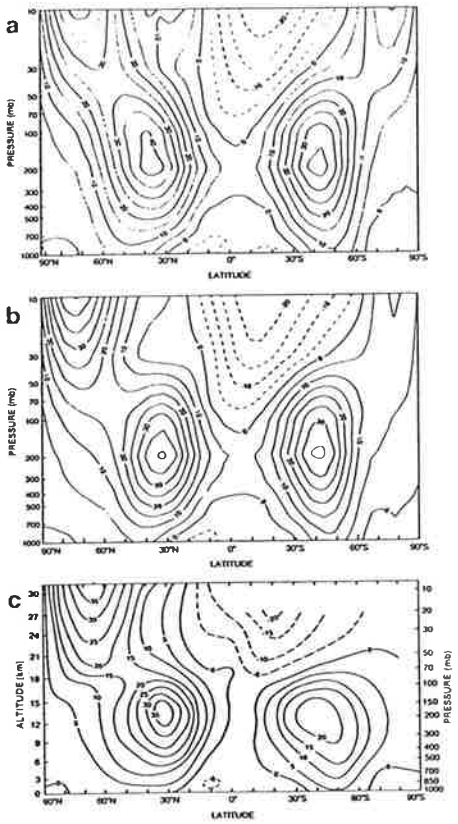

Figure 4: Plots of the latitude–height structure of the zonal wind in the lower atmosphere showing; (*a*) the structure produced by a general circulation model without gravity wave drag; (*b*) the simulated structure after inclusion of an orographic gravity wave drag parameterization, and; (*c*) the actual structure. The diagram is from *McFarlane* [1987].

wave drag in the troposphere was measured in subsequent airborne experiments [see, e.g., *Lilly and Kennedy*, 1973; *Lilly*, 1978; *Smith*, 1978; *Brown*, 1983], and was shown to be episodically large.

Despite this, wave drag was largely ignored or discounted by meteorologists [see e.g., *Hines*, 1989] until very recently, and was only reconsidered after it was proved important in middle atmospheric dynamics. Indeed, it was *Lindzen* [1985] who used the same wave drag parameterization that he had applied to the mesosphere [*Lindzen*, 1981] to quantitatively demonstrate that stationary gravity waves should dissipate and induce significant mean flow accelerations at altitudes of near–zero mean wind in the lower stratosphere. This latest indication of the importance of gravity wave drag has finally been taken up and incorporated into general circulation models of the lower atmosphere by *Boer et al.* [1984], *Palmer et al.* [1986], *Tanaka* [1986], and *McFarlane* [1987], with consequent improvement of the model results as anticipated (see Figure 4). Indeed, simulations with a general circulation model (GCM) by *Boer* [1990] have indicated that atmospheric torques due to gravity–wave drag and turbulent momentum–flux convergence in the boundary layer produce much of the angular–momentum exchange between the Earth and the atmosphere, which causes variations in the Earth's rotation, and hence in the length of a day [see

the review of *Wahr*, 1988]. Yet the broader effects on tropospheric regions of a spectrum of gravity waves with varying phase speeds has still to be considered by modellers, despite strong theoretical evidence that it is likely to be very important, for example, at the tropopause [see, e.g., *VanZandt and Fritts*, 1989].

1.4.2 Gravity Waves in the Stratosphere (15–50km)

Observations

Observations of mesoscale[12] motions within the stratosphere have been limited by instrumental effects, since balloons can only ascend to lower stratospheric heights, and the most powerful ST[13] radars still cannot obtain acceptable signal–to–noise ratios from altitudes much above 30km.

Those studies between ~15–30km, however, have frequently revealed large amplitude, quasi–coherent gravity wave oscillations with vertical scales around 2–5km, elliptical polarization in the horizontal, and upward propagation of wave energy [see, e.g., *Sawyer*, 1961; *Weinstein et al.*, 1966; *Newell et al.*, 1966; *Lilly and Lester*, 1974; *Thompson*, 1978; *Cadet and Teitelbaum*, 1979; *Maekawa et al.*, 1984; *Hirota and Niki*, 1986; *Cot and Barat*, 1986; *Sato*, 1989; *Kitamura and Hirota*, 1989; *Yamanaka et al.*, 1989]. At equatorial latitudes, a range of equatorially–ducted gravity wave modes of planetary scale arise [*Matsuno*, 1966]. The principal modes are the eastward propagating Kelvin wave, which was first observed by *Maruyama* [1967] and *Wallace and Kousky* [1968], and the westward propagating mixed Rossby–gravity wave, which was first observed by *Yanai and Maruyama* [1966] (and so is occasionally called a Yanai wave). Further lower stratospheric observations of equatorial waves have been performed by *Maruyama* [1969], *Lindzen and Tsay* [1975], and *Cadet and Teitelbaum* [1979].

In the stratosphere above 30km, meteorological rocket salvoes and isolated lidar[14] measurements have been the only source of data on such motions, and so knowledge of the wave characteristics at these heights is presently sparse. Small observed increases in wave amplitudes with height suggest that wave energy is dissipating at these heights [*Hirota and Niki*, 1985; *Hass and Meyer*, 1987; *Eckermann and Vincent*, 1989]. Distinct seasonal cycles in wave amplitudes are also evident [e.g., *Hirota*, 1984; *Shibata et al.*, 1986], and the waves propagate their energy upwards [e.g., *Hirota and Niki*, 1985; *Hass and Meyer*, 1987; *Eckermann and Vincent*, 1989] within a narrow range of azimuths [*Eckermann and Vincent*, 1989; *Eckermann and Hocking*, 1989]. At equatorial latitudes, high phase speed Kelvin waves are also prevalent [e.g., *Hirota*, 1978, 1979; *Salby*, 1984; *Devarajan et al.*, 1985]. Rapid advancement in Rayleigh lidar probing of this region [see e.g., *Chanin and Hauchercorne*, 1981; *Shibata et al.*, 1986;

[12] small–scale motions which are of larger scale than turbulent (microscale) motions
[13] Stratosphere–Troposphere
[14] the optical equivalent of a radar, using visible or UV light from a pulsed laser

Shibata et al., 1988; *Gardner et al.*, 1989; *Wilson et al.*, 1989] and plans for an extremely powerful VHF radar at the equator [*Fukao et al.*, 1989*b*] offer the promise of more comprehensive measurements from this region in the future. Chapter 6 details the results of analyzing a large base of meteorological rocket data from the upper stratosphere for gravity waves, revealing many new characteristics, and goes some way towards redressing the observational dearth of information on waves from this region.

Effects

Planetary Rossby waves, forced by orography and land–sea temperature contrast, can propagate into the winter stratosphere, and when of unusually large amplitude they can produce increases in the temperature of the high–latitude stratosphere of the Northern Hemispheric of $\sim 30K$ in a few weeks; so–called *sudden statospheric warmings* [see, e.g., Chapter 6 of *Andrews et al.*, 1987]. The breaking of these Rossby waves produces significant effects on the mean structure of the high–latitude winter stratosphere [see, e.g., *Geller et al.*, 1983]. At the stratopause, however, residual accelerations of $\sim 5m\ s^{-1}\ day^{-1}$ have been inferred from satellite data, which cannot be accounted for by either radiative arguments or Rossby wave dissipation [see, e.g., *Geller et al.*, 1983; *Smith and Lyjak*, 1985], although some values may be overestimated due to calculation approximations [*Robinson*, 1986]. *Smith and Lyjak* [1985] suggested that gravity wave drag may be the source of this unaccounted driving. *Eckermann and Vincent* [1989] calculated mean flow accelerations of $\sim 0.1\text{–}1m\ s^{-1}\ day^{-1}$ at the stratopause from rocket obervations of gravity wave motions over Woomera (31°S), which are of the order of satellite estimates. *Hitchmann et al.* [1989] invoked a numerical model to investigate these issues, and they concluded that gravity wave drag is responsible for the separated temperature structure of the stratopause at high latitudes during winter.

At the equator the zonal wind and temperature of the lower stratosphere exhibits a quasi-biennial oscillation (QBO) of $\sim 27 \pm 6$ months [see, e.g., *Reed et al.*, 1961; *Veryard and Ebdon*, 1961; *Wallace*, 1973; *Dunkerton and Delisi*, 1985; *Naujokat*, 1986; see also Figure 90 in chapter 6]. Neither radiative arguments nor Rossby wave dissipation can explain this remarkable phenomenon [see, e.g., *Wallace and Holton*, 1968; *Wallace*, 1973; *Plumb*, 1984]. *Lindzen and Holton* [1968] argued that alternating dissipation and transmission of an eastward–propagating Kelvin wave and a westward–propagating mixed Rossby–gravity wave might drive this feature. *Holton and Lindzen* [1972] later used a numerical model to demonstrate that the observed height-time structure of the QBO was well reproduced using this hypothesis. This theory has since been verified and refined in a number of subsequent studies [see, e.g., *Lindzen and Tsay*, 1975; *Plumb*, 1977; *Plumb and McEwan*, 1978; *Hamilton*, 1981, 1984; *Dunkerton*, 1981, 1982*a*; *Plumb and*

Bell, 1982; *Tanaka and Yoshizawa*, 1987]. The QBO may well turn out to be *the* most important gravity–wave–driven atmospheric feature, since non–equatorial quasi–biennial oscillations have been observed in lower stratospheric temperature, geopotential height [e.g., *Holton and Tan*, 1980, 1982], stratospheric warmings [*Dunkerton et al.*, 1988] and ozone column abundances [e.g., *Ramanathan*, 1963; *Angell and Korshover*, 1973; *Oltmans and London*, 1982; *Hasebe*, 1983; *Hamilton*, 1989; *Bowman*, 1989], all of which appear to arise from QBO–driven changes in chemistry and dynamics [*Ling and London*, 1986; *Gray and Pyle*, 1989]. The effects of gravity waves on ozone are discussed more fully in section 1.4.4. Similarly, the response of the entire atmosphere to the 11–year solar cycle appears to be strongly modulated according to the phase of the QBO [see the review of *Labitzke and van Loon*, 1989].

It should be noted that a low–altitude QBO has apparently been detected in tropospheric dynamics [e.g., *Landsberg*, 1962], in rainfall [e.g., *Fleer*, 1981; *Tyson*, 1986], and in sea surface temperatures [e.g., *Trenberth*, 1975]. Surprisingly, this near–surface QBO appears to be unrelated to the stratospheric QBO [*Trenberth*, 1980], and instead is believed to arise from complex atmosphere–ocean circulation processes [see, e.g., *Currie and Hameed*, 1988]. For example, biennial oscillations are often observed in temperature/pressure/precipitation patterns driven by the El Niño/Southern Oscillation (ENSO) [see, e.g., *Wright*, 1985].

In the equatorial upper stratosphere, the zonal wind exhibits a semiannual oscillation (SAO) [see, e.g., *Reed*, 1965, 1966; *Belmont and Dartt*, 1973; *Hirota*, 1978, 1980; *Delisi and Dunkerton*, 1988; see also Figure 90 in chapter 6], which again defies a radiative explanation [*Meyer*, 1970]. Although all of the mixed Rossby–gravity wave modes and the lower phase–speed Kelvin waves are damped out in driving the underlying QBO, *Holton* [1975] suggested that higher phase–speed Kelvin waves should propagate to these heights and drive the eastward phase of the SAO. Such waves were later observed in rocket data by analyzed by *Hirota* [1978]. The westward forcing of the SAO is more complex, and results from a combination of planetary Rossby wave forcing in the winter hemisphere [*Hopkins*, 1975] and accelerations due to the mean meridional flow across the equator, which itself arises from extratropical wave forcing [*Holton and Wehrbein*, 1980].

The SAO was very accurately reproduced by the G.F.D.L.[15] "SKYHI" general circulation model (GCM) [*Mahlman and Umscheid*, 1984], where it arose in their model "naturally" through the aforementioned forcing mechanisms. However, a subsequent higher resolution simulation with this GCM by *Hamilton and Mahlman* [1988] indicated that only ~20% of the eastward forcing was due to Kelvin waves,

[15] Geophysical Fluid Dynamics Laboratory, at Princeton University, U.S.A.

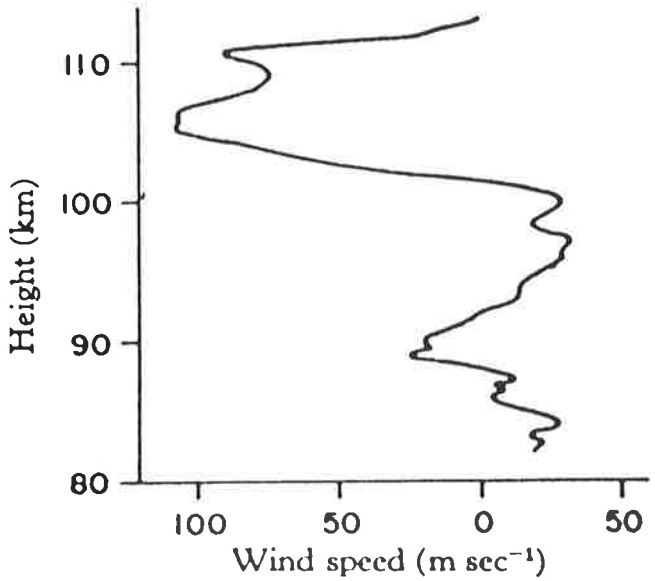

Figure 5: One of the earliest measurements of mesospheric wind speed versus height, derived from photographs of meteor trails by *Liller and Whipple* [1954].

and the remainder was produced by higher–frequency gravity waves. *Hitchman and Leovy* [1988] presented indirect observational estimates of a Kelvin–wave eastward forcing which was smaller than that required to drive the SAO, and they too concluded that gravity waves may provide a significant fraction of the residual forcing which is required. Further observational evidence in this matter is provided in chapter 6.

1.4.3 Gravity Waves in the Mesosphere and Lower Thermosphere (60–100km)

With hindsight, it is fortuitous that the region of the atmosphere between ~60 and 100km in height has come to be called the *mesosphere* (literally "middle sphere"), because it is in this region of the atmosphere that mesoscale dynamics are most active in the formation of the mean circulation, composition, and thermal structure.

The earliest observations of this region soon revealed that the wind at these heights had a seemingly irregular appearance (see Figure 5). A period of intense debate ensued thereafter as to the dynamical cause of these peculiar winds, most of it seeking to invoke turbulence as the cause of the observed fluctuations [see the historical review of *Hines*, 1989]. *Hines* [1960], in a seminal paper, argued instead that the observed wind variability was produced by a superposition of gravity wave motions. In this study, *Hines* provided both a mathematical and conceptual description of these waves, and anticipated many of their important upper atmospheric effects. As observations of this region improved and increased during the 60's and 70's, *Hines'* explanation of the wind variability in terms of gravity waves was strengthened

by repeated experimental corroboration [see, e.g., *Witt*, 1962; *Gossard*, 1962; *Kochanski*, 1964; *Theon et al.*, 1967; *Woodrum and Justus*, 1968; *Manson et al.*, 1973, 1974, 1975; *Rastogi and Bowhill*, 1976; *Vincent and Stubbs*, 1977; *Vincent and Ball*, 1977; *Miller et al.*, 1978; *Fukao et al.*, 1979].

About this time too, modellers became aware that the mean state of the mesosphere departed significantly from radiative equilibrium, and reasonable simulations of its structure were only possible by artificially parameterizing some as–yet–unidentified dynamics through the use of a so–called Rayleigh drag coefficient [*Leovy*, 1964; *Schoeberl and Strobel*, 1978; *Holton and Wehrbein*, 1980]. *Houghton* [1978] attempted to identify the actual process(es) involved, and concluded that the dissipation of gravity wave motions at these heights was the most likely candidate. *Holton and Wehrbein* [1980] demonstrated that the use of Rayleigh drag coefficients indeed approximated some aspects of the gravity–wave drag process.

The big step forward in testing this idea was supplied by *Lindzen* [1981], who developed mathematical relations which encapsulated the essential physics of gravity propagation and dissipation within the middle atmosphere, yet were simple enough to be easily incorporated into numerical models. *Lindzen's* preliminary calculations suggested that gravity waves could indeed provide the required drag on the mean flow. The scheme was quickly utilized by modellers to evaluate the gravity wave idea more accurately, and they found that inclusion of gravity wave drag produced far better agreement with observations than had previously been obtained [see, e.g., *Matsuno*, 1982; *Holton*, 1982, 1983; *Dunkerton*, 1982*b*; *Schoeberl et al.*, 1983; *Holton and Zhu*, 1984]. Direct measurement of momentum fluxes and mean–flow accelerations associated with gravity waves in the mesosphere were later provided by *Vincent and Reid* [1983] and *Reid* [1984], who found that they were indeed of the order of the values required to maintain observed mean wind speeds. This provided some of the observational verification needed to vindicate *Houghton's* original gravity–wave postulate.

Thus gravity waves are responsible not only for the irregular fluctuating structure of mesospheric winds, but also for the mean wind structure upon which these fluctuations are superimposed. The extent to which mesospheric winds are dominated by gravity wave motions can be seen in the following collection of diagrams.

Figure 6 presents a time–height plot of horizontal wind vectors in the mesosphere above northern Norway (69°N), as measured by the SOUSY[16] radar [*Czechowsky et al.*, 1989]. Note the time and altitude variability of the winds, which are produced by gravity waves. Figure 7 shows a temporal power spectrum of the horizontal wind fluctuations observed by radar in the mesosphere over Australia.

[16] Sounding System: This VHF radar is operated by The Max Planck Institut für Aeronomie

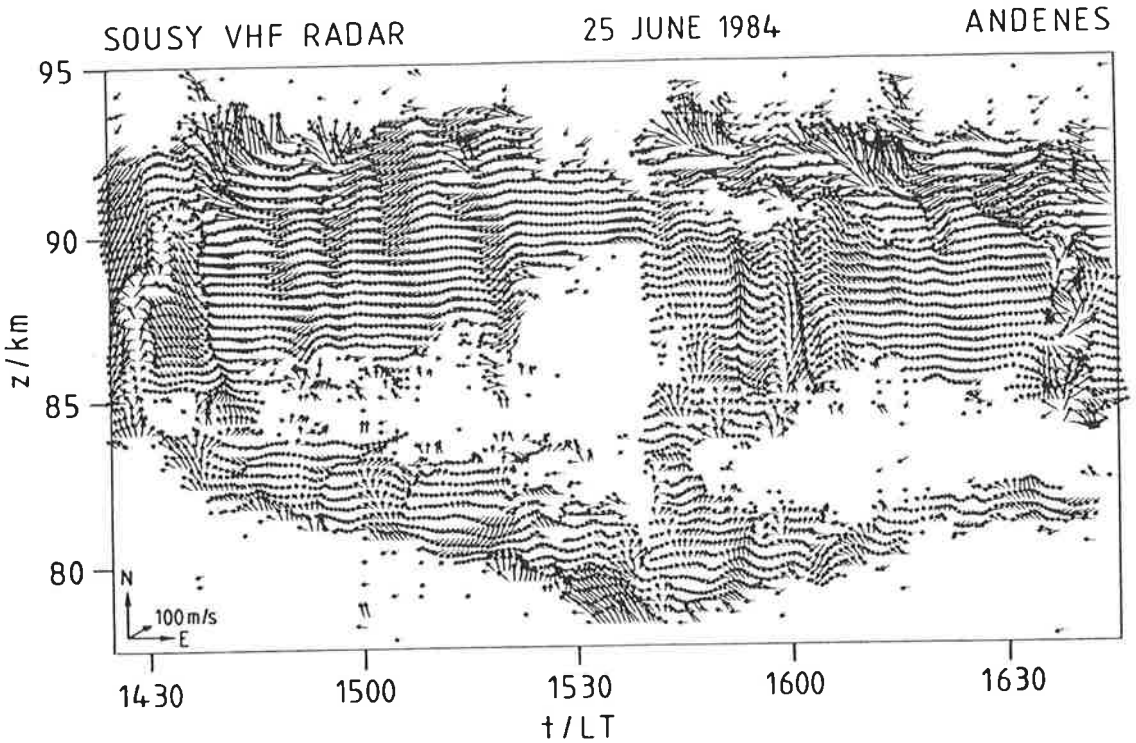

Figure 6: Horizontal wind vectors in the mesosphere above Andenes (69°N, 16°E) measured by the mobile SOUSY VHF radar on June 25th, 1984 [after *Czechowsky et al.*, 1989].

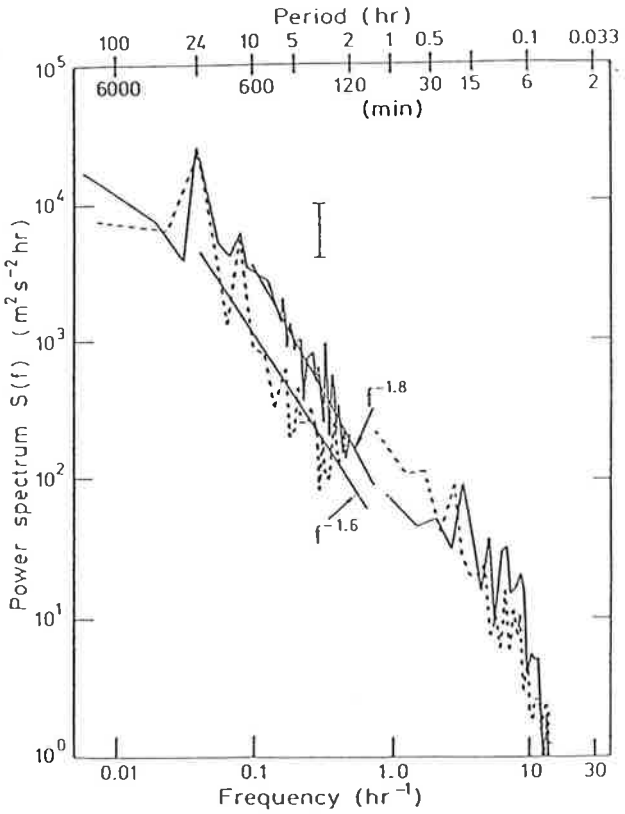

Figure 7: Power spectra of the horizontal winds measured by radar at Adelaide (35°S, 138°E) and Townsville (19°S, 147°E) in March 1979 [after *Ball*, 1981]. The Adelaide spectra are plotted with solid lines, and the Townsville results are the dashed curves.

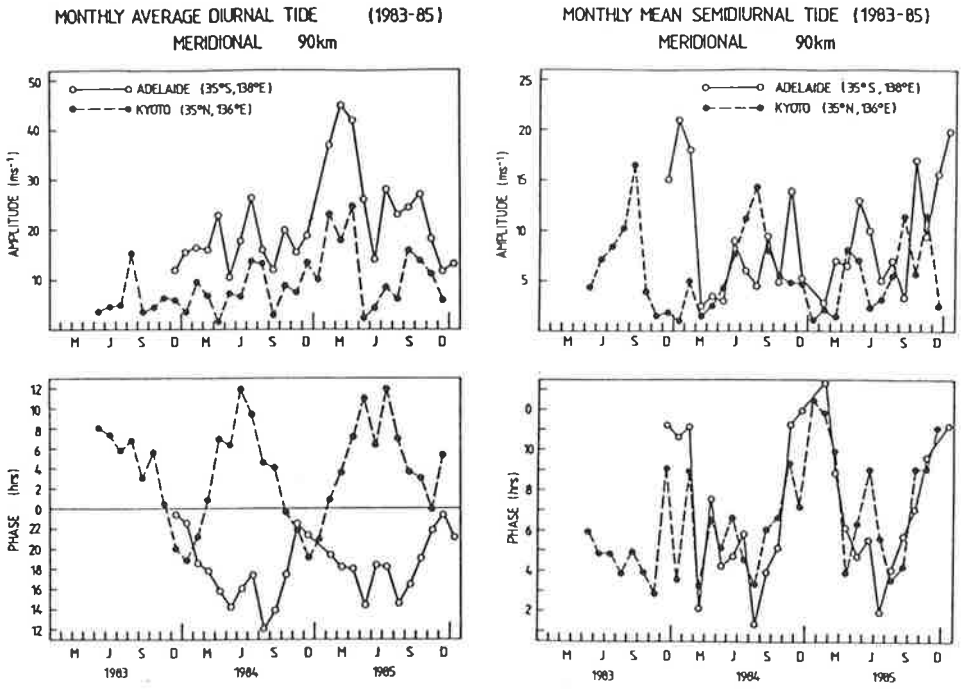

Figure 8: Seasonal variation in amplitude and phase of the meridional wind component of the diurnal and semidiurnal solar tides at Adelaide and Kyoto [after *Vincent et al.*, 1988].

Note the large peaks at 24 and 12 hours, which correspond to the diurnal[17] and semidiurnal[18] solar tides[19] respectively. These tidal gravity waves attain large amplitudes, and show distinct seasonal and geographical variability in amplitude and phase, as shown in Figure 8. Figure 9 shows height–time contours of gravity wave variance, with the tides removed, in the 1–24 hour observed period range in the mesosphere over Adelaide.

Figures 7–9 serve to indicate that while most attention is usually focused on the role of gravity wave drag in producing mean mesospheric structure, the wave fluctuations themselves produce standard deviations about the mean winds which are often larger than these means (see chapter 5). Large wave–induced variability also exists in temperatures [see, e.g., *Theon et al.*, 1967]. Reviews by *Fritts* [1984, 1989], *Reid* [1986, 1989], and *Vincent* [1987] give more extensive details of current knowledge of the characteristics of mesospheric gravity waves.

Nevertheless, mean winds and temperatures are fundamental to the global circulation and composition of the mesosphere. Figure 10 combines three latitude–height contours of zonal wind. Plot *A* shows the mesospheric wind structure that arises in a detailed numerical simulation of this region's photochemistry in the absence of dissipating gravity waves, while plot *B* shows the observed wind structure. Clearly the comparison is poor. However, inclusion of gravity wave drag into a model dramatically improves

[17] daily
[18] half-daily
[19] Large amplitude, planetary scale gravity waves, forced by the passage and atmospheric heating of the Sun

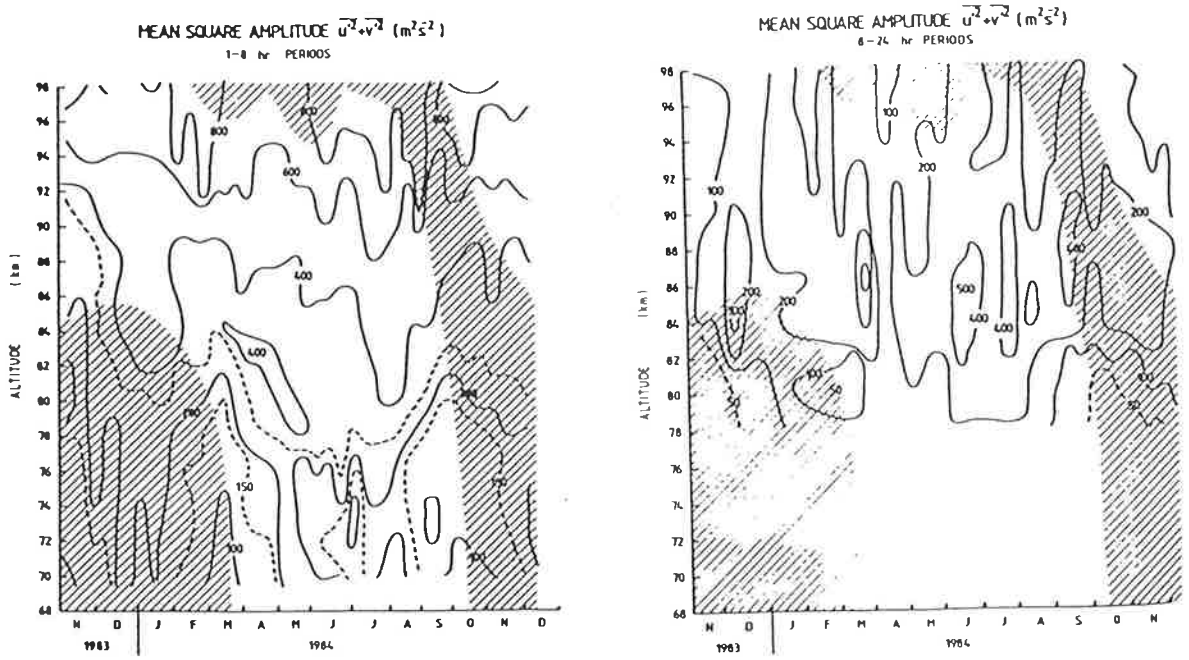

Figure 9: Time–height contours of gravity wave horizontal velocity variance in the 1–8 hr and 8–24 hr observed–period range, derived from radar observations over Adelaide (35°S, 138°E) during 1984 [after *Vincent and Fritts*, 1987]. Tidal oscillations have been removed.

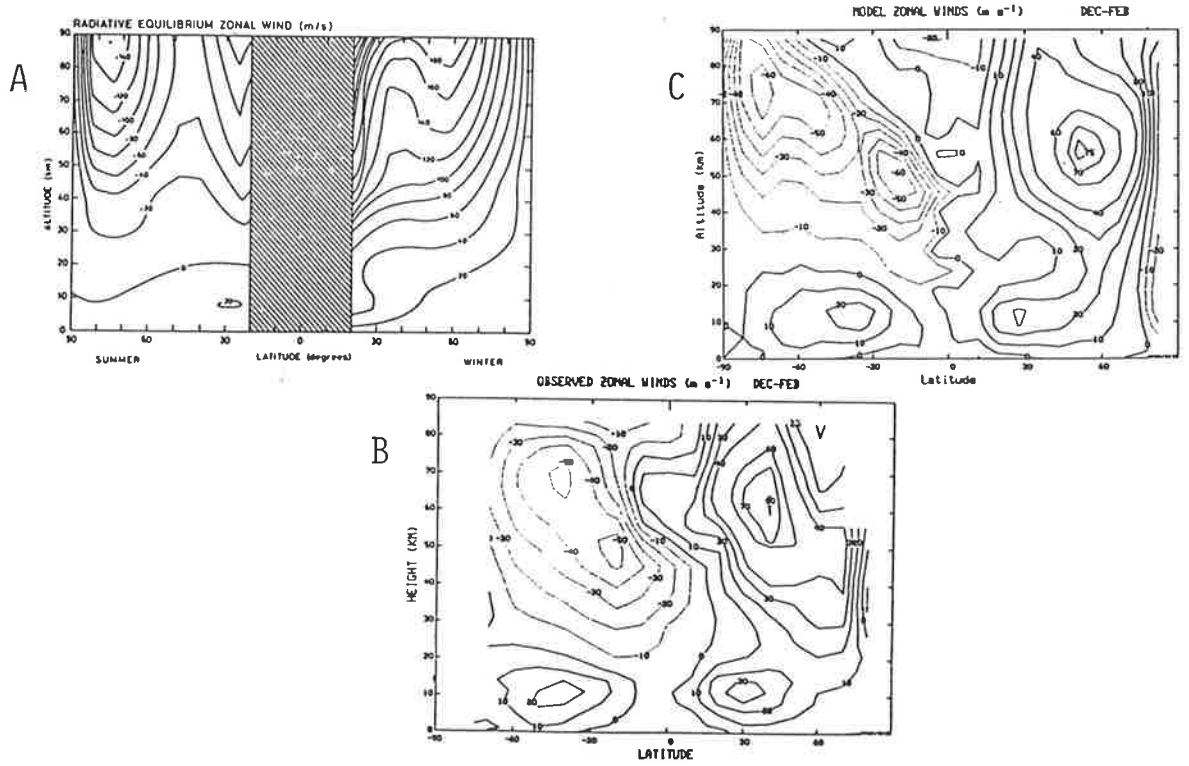

Figure 10: Plot *A* shows simulated geostrophic winds in the absence of gravity–wave drag [from *Brasseur and Solomon*, 1984]. Plot *B* shows the observed geostrophic winds, and plot *C* shows the simulated geostrophic winds after inclusion of a gravity–wave drag parameterization [after *Rind et al.*, 1988].

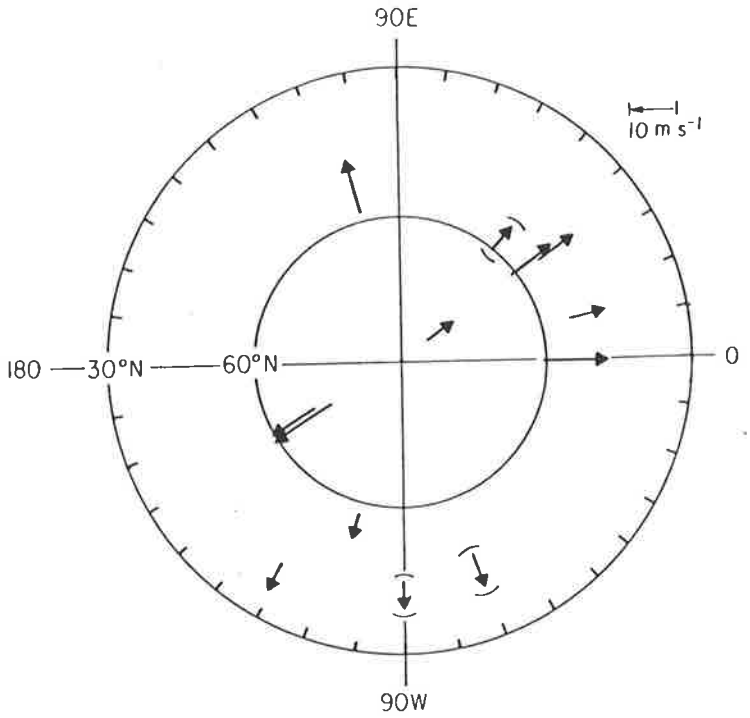

Figure 11: Mean meridional wind vectors observed in the mesosphere (~90 km) over various sites in the Northern Hemisphere [after *Nastrom et al.*, 1982].

the simulated structure, as seen in the plot C, from *Rind et al.* [1988]. Intercomparison of these plots indicates just how far gravity waves drive the mean state away from radiative equilibrium, by rapidly decelerating the mean zonal winds at mesospheric heights.

To conserve momentum, this quasi–continuous deceleration of the zonal wind away from its radiatively determined state must be accompanied by a mean meridional wind, so that a balancing Coriolis torque exists. Figure 62 in chapter 5 plots mean zonal and meridional winds in the mesosphere over Adelaide [see also *Phillips and Vincent*, 1989], and reveals that mean meridional winds do indeed arise. Below $90km$, the meridional flow is predominately poleward, peaking in strength during winter, but is equatorward in the summer, qualitatively as predicted. Figure 11 shows monthly averaged values of the meridional wind near $90km$ as measured over various sites in the Northern Hemisphere during June (summer). A global equatorward flow, in response to eastward deceleration of zonal winds through gravity–wave drag, is clearly evident.

As the meridional flow is oppositely directed in the Southern (winter) Hemisphere, this implies a net poleward flow from the summer hemisphere toward the winter hemisphere, and thus a schematic circulation of the form shown in Figure 12. Figure 12 also indicates that there should be upwelling in the high–latitude summer hemisphere mesosphere, and downward motion in the high–latitude winter hemisphere. This ascent and subsidence should lead to cooling of the summer hemisphere, and heating

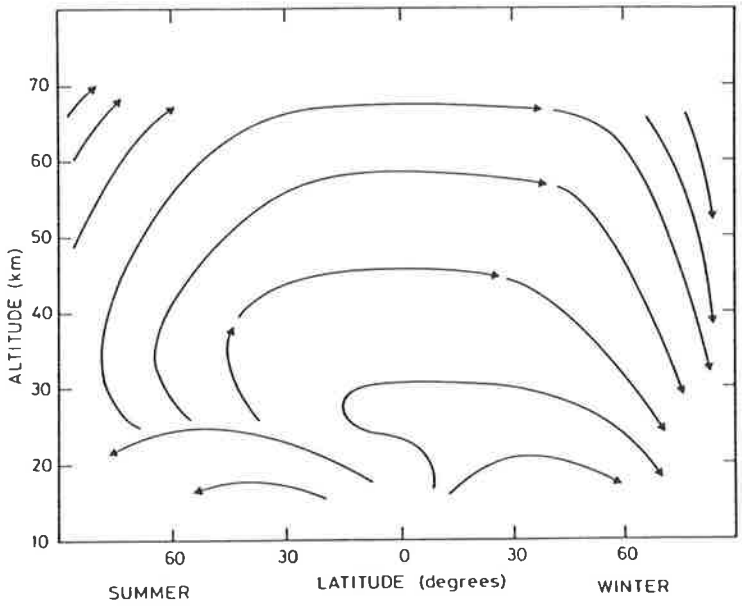

Figure 12: A schematic representation of the latitude–height flow which occurs globally in the upper middle atmosphere. Note the strong flow from the summer into the winter mesosphere [after *Dunkerton*, 1978].

of the winter hemisphere[20].

The anticipated heating effects are indeed observed. Consideration of solar irradiance alone leads one to predict a warm summer mesopause and a cold winter mesopause, much like the conventional seasons we experience at ground level [see, e.g., chapter 2 of *Andrews et al.*, 1987]. However, observations reveal that the *opposite* occurs in the mesosphere. Measurements of the temperature structure, shown in Figure 13, reveal a cold summer mesopause and a warm winter mesopause. It should be stressed again that this reversal of the radiatively anticipated temperature gradient results from gravity–wave drag acting globally.

Recent higher resolution measurements have revealed important additional features of the temperature structure of the mesosphere. Mid–latitude measurements by *Schmidlin* [1976], *Hauchecorne et al.* [1987], and *Clancy and Rusch* [1989] have revealed that gravity wave breaking often produces mesospheric temperature inversions and thus a "double mesopause" structure, most noticeably during winter (see Figures 14 and 15). High–latitude measurements by *vonZahn and Meyer* [1989], shown in Figure 16, have also revealed a much colder summer mesosphere ($129 \pm 6K$) than previously evident in data from satellites (compare with Figure 13).

From the temperature measurements, one can then predict that mean upward (summer) and downward (winter) motions of $\sim 1 cm\ s^{-1}$ are required to maintain these mesospheric temperatures. Accurate

[20] this can also be predicted using the thermal wind equation on the observed vertical profiles of zonal wind.

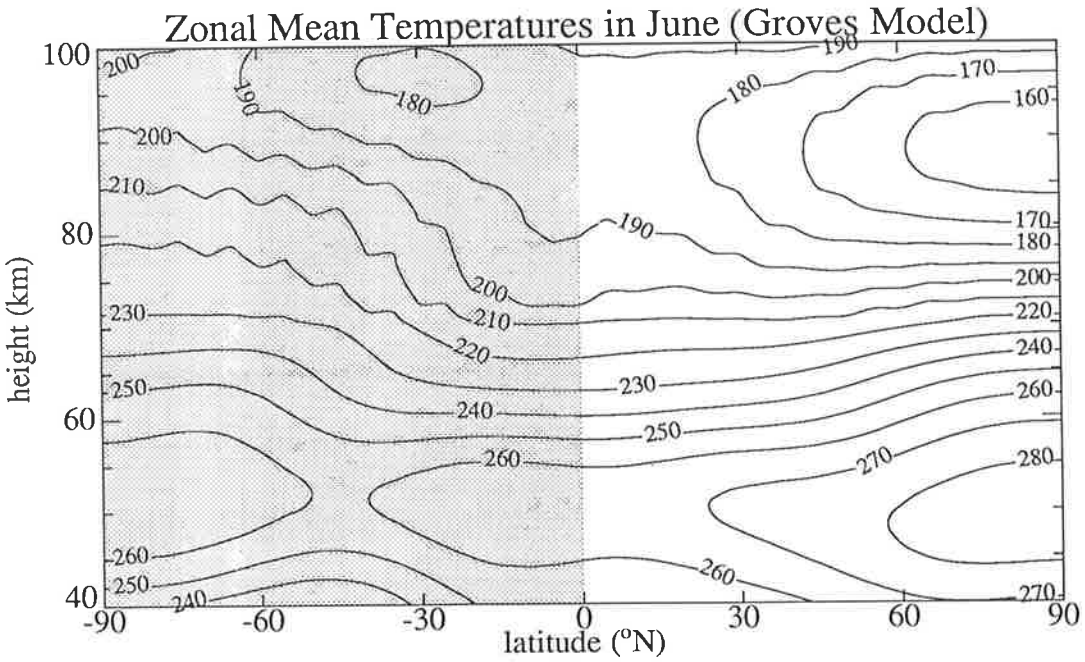

Figure 13: Latitude–height contours of monthly– and zonally–averaged temperatures from 40–100km in June, using the reference temperatures of *Groves* [1985, 1987]. These data are derived mainly from quasi–continuous measurements from 1973–1978 aboard the *Nimbus* 5 and 6 satellites [see, e.g., *Barnett and Corney*, 1985]. The winter (southern) hemisphere is shaded.

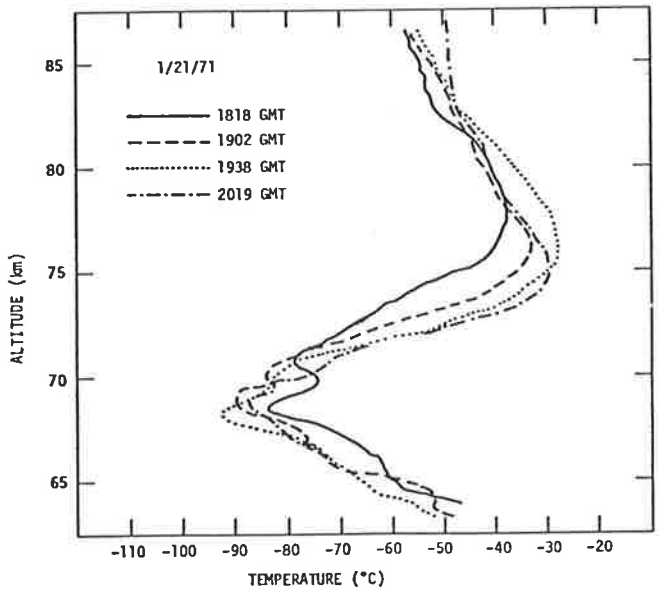

Figure 14: Temperatures measured at ~30–40min intervals by falling–sphere experiments over Wallops Island (38°N, 75°W) on 21st January 1971 [after *Schmidlin*, 1976].

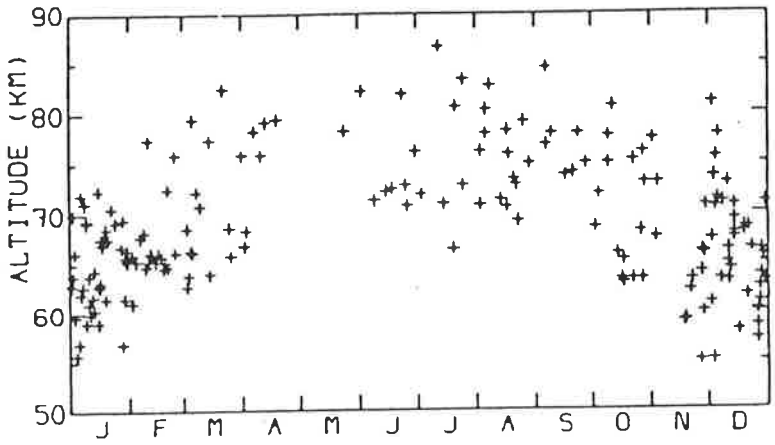

Figure 15: Seasonal variation of the secondary temperature minimum in lidar temperature profiles (June 1981 to September 1986) over France (44°N, 6°E) [after *Hauchecorne et al.*, 1987].

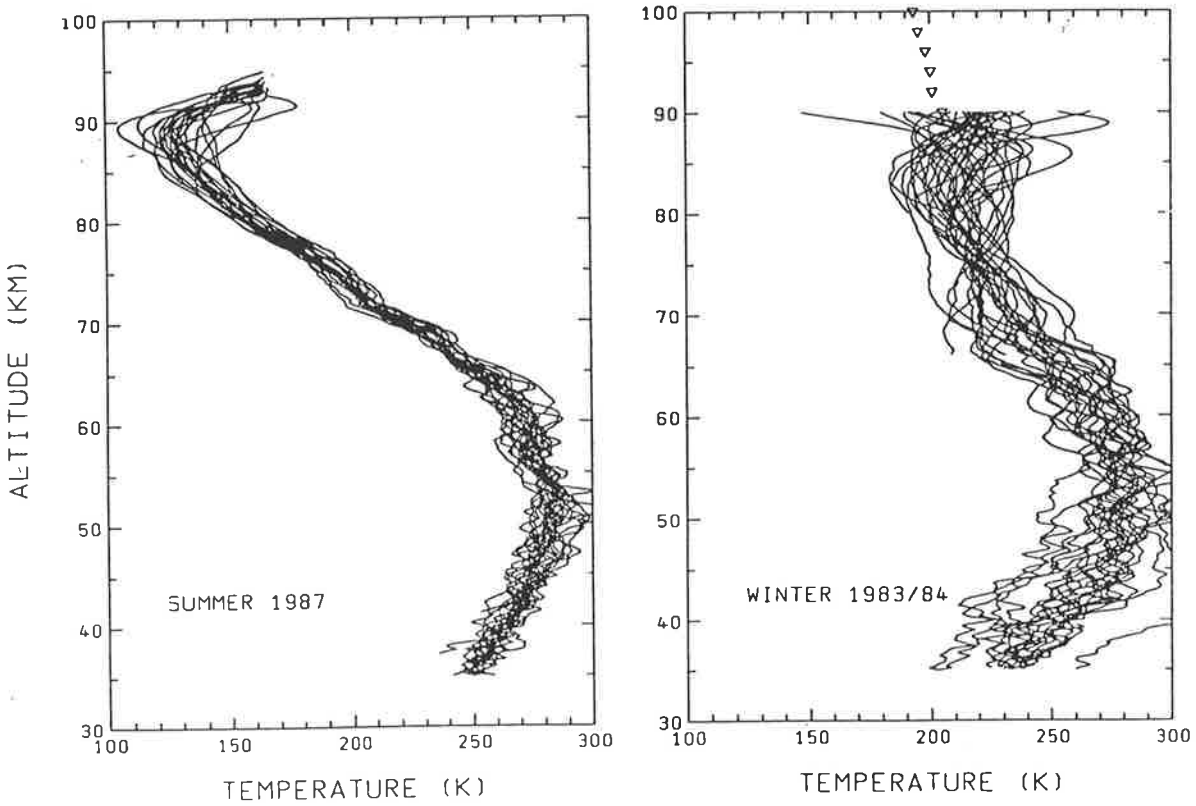

Figure 16: 26 summer and 41 winter temperature profiles obtained by falling–sphere experiments over Andøya (69°N, 16°E) [after *vonZahn and Meyer*, 1989]. Open triangles show mean temperatures measured by a co–located lidar.

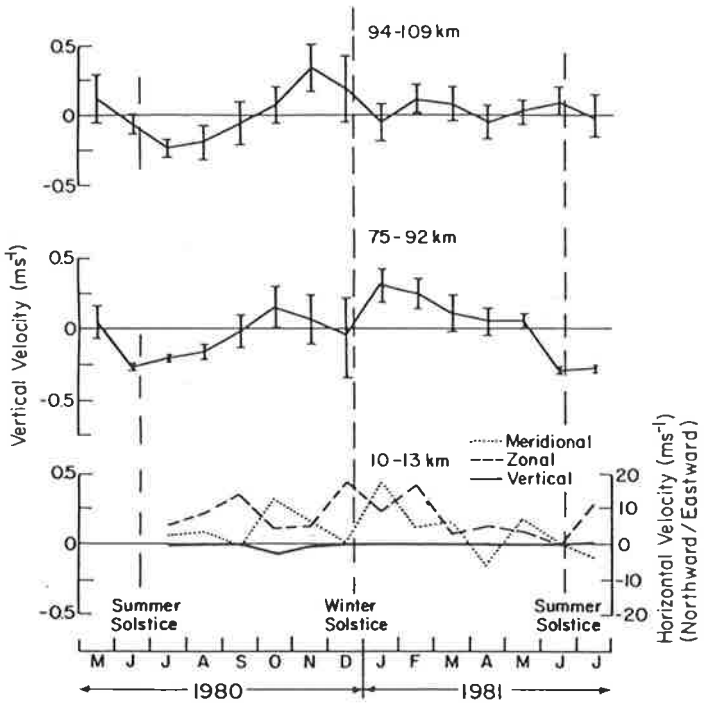

Figure 17: Monthly averaged vertical wind velocities from May 1980–July 1981, as measured by radar methods at Poker Flat [65°N, 147°W] within the indicated height ranges [after *Balsley and Riddle*, 1984].

measurements of such small vertical velocities are made difficult by a number of instrumental and geophysical effects [see, e.g., *Balsley and Riddle*, 1984; *Meek and Manson*, 1989], but observational evidence is emerging which suggests that observed vertical velocities are much larger ($\sim 10 cm\ s^{-1}$), and often of different sign to the anticipated vertical velocity values. Figure 17 shows the seasonal variation of monthly mean vertical velocities within two height regimes of the high latitude mesosphere, as measured with a vertically–pointed Doppler radar system [*Balsley and Riddle*, 1984]. Note the quasi–annual variations, peaking at the soltices, with upward velocities in winter and downward velocities in summer, which is and order of magnitude larger and in the opposite sense to the mean vertical motion anticipated in Figure 12.

Part of the difference here seems to result again from the motions associated with gravity waves in a compressible[21] atmosphere. Radars measure velocities from a fixed point on the ground and look at a fixed point in the sky (a so–called *Eulerian* frame). The ascent and subsidence depicted in Figure 12, however, occurs in a frame following the natural displacement of fluid parcels (a so–called *Lagrangian* frame). *Coy et al.* [1986] argued that mean vertical velocities in each of these reference frames can differ appreciably in the mesosphere due to the natural air parcel displacements associated with upward propagating gravity waves. This difference is known as the Stokes drift[22], and arises due to a small component of the gravity wave oscillation being in the direction of the vertical phase velocity of the wave.

[21] Essentially, an atmosphere where the speed of sound is finite, and thus the compression associated with sound waves is possible

[22] since Stokes first appreciated the effect in water waves

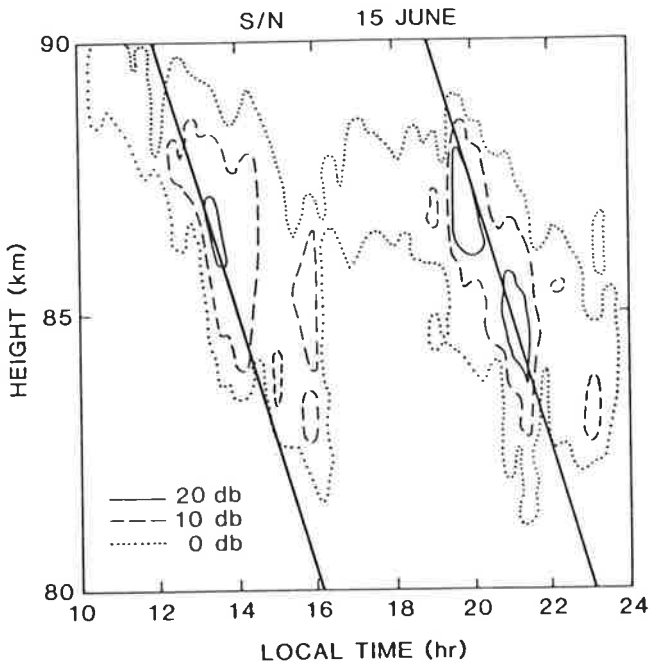

Figure 18: Time–height contours of radar signal to noise, which qualitatively indicates changes in the turbulence intensity. The line shows the phase path of the most unstable region of a coexisting gravity wave motion [after *Fritts et al.*, 1988].

Coy et al. [1986] calculated a vertical Stokes drift due to gravity waves of $\sim 10 cm\ s^{-1}$ upwards in the mesosphere. Since the Lagrangian vertical velocity is only $\sim 1 cm\ s^{-1}$ upwards, as estimated from the observed temperature structure, this forces a compensating downward Eulerian mean flow of around $-10 cm\ s^{-1}$, as measured in Figure 17 during summer. However, this phenomenon cannot currently explain the wintertime results. Indeed, subsequent measurements by *Meek and Manson* [1989] over Saskatoon (52°N, 107°W) have revealed a complex structure, consisting of upward velocities below 90 km, as observed at Poker Flat in Figure 17, and downward velocities above 90 km.

Walterscheid and Hocking [1990] conducted extensive numerical simulations of the Stokes drift of fluid parcels in the presence of a more realistic spectrum of mesospheric gravity waves. Due to the random nature of the wave superposition, they found, in addition to the mean vertical Stokes drift, that random parcel diplacements occur about this mean which are diffusive[23], in a similar way to which turbulence produces diffusion. Photochemical models of the mesosphere, which consider dynamical transport, have only modelled the turbulent diffusion produced by gravity wave dissipation, whereas this *Stokes diffusion* will occur even for non–dissipating waves.

This is not to say that mesospheric turbulence is not important, because the mesosphere *is* very turbulent due to the energy deposition produced by breaking gravity waves. There is much observational verification that dissipating gravity waves in the mesosphere do indeed produce large bursts of turbulence

[23] i.e. the separation amongst parcels from their centre of mass increases with time

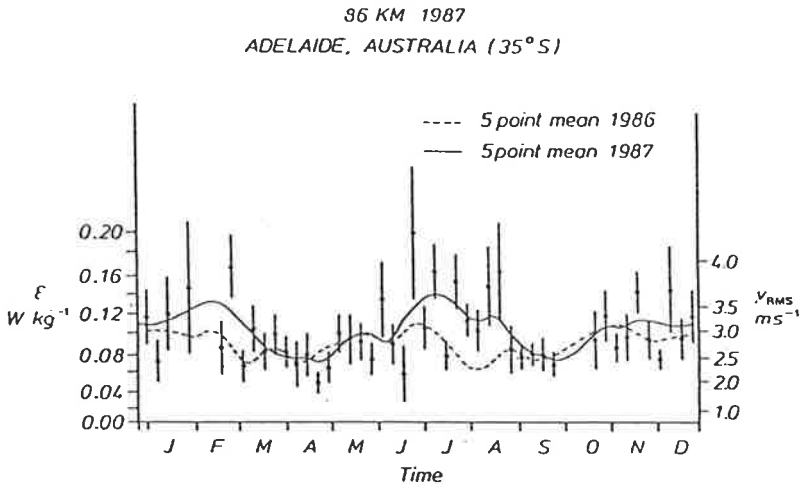

Figure 19: Weekly averages of various radar–inferred statistical measures of turbulence activity over Adelaide (ε is energy dissipation rate, K is the turbulent diffusion coefficient, and V_{RMS} are the root mean square fluctuating horizontal velocities [after *Hocking*, 1989].

[see, e.g., *Fritts et al.*, 1988; *Yamamoto et al.*, 1989], an example of which is depicted in Figure 18. These types of observations show that the turbulent bursts are confined to rather thin layers in the vertical [see the review of *Hocking*, 1987*b*]. A few direct measurements of mesospheric turbulence statistics have been attempted on a long–term basis, of which the radar measurements of *Hocking* [1988, 1989] are the most complete to date. The seasonal variations in various statistical measures which indicate the level of turbulent activity measured by *Hocking* [1989] during 1986–1987 are shown in Figure 19. Note the large interannual variability and the semiannual cycle in 1987. Larger values in 1985 (not presented) arose due to an unusually large–amplitude diurnal tide that year (see Figure 8), which is known to produce large modulations in gravity–wave breaking [*Fritts and Vincent*, 1987; *Bjarnason et al.*, 1987]. *Hocking* [1988] also presented evidence of a semiannual variation in turbulent activity below $80km$, with equinoctial minima, which again correlates well with measurements of gravity–wave activity in Figure 9.

The relative roles of Stokes diffusion and turbulent diffusion (both produced by gravity waves) in the large scale vertical diffusion of the mesosphere is a question that has only just been raised. The relevance of this question can be seen in the following two sections, which highlight the vital role that gravity wave–induced diffusion is believed to play in the chemical composition of the mesosphere.

1.4.4 Effects of Gravity Waves on Ozone

Previous sections stressed the important role that gravity waves play in the formation of the mean and fluctuating dynamics of the atmosphere. Of further importance, however, is the way in which gravity waves influence the distribution of biologically important atmospheric chemicals, such as ozone.

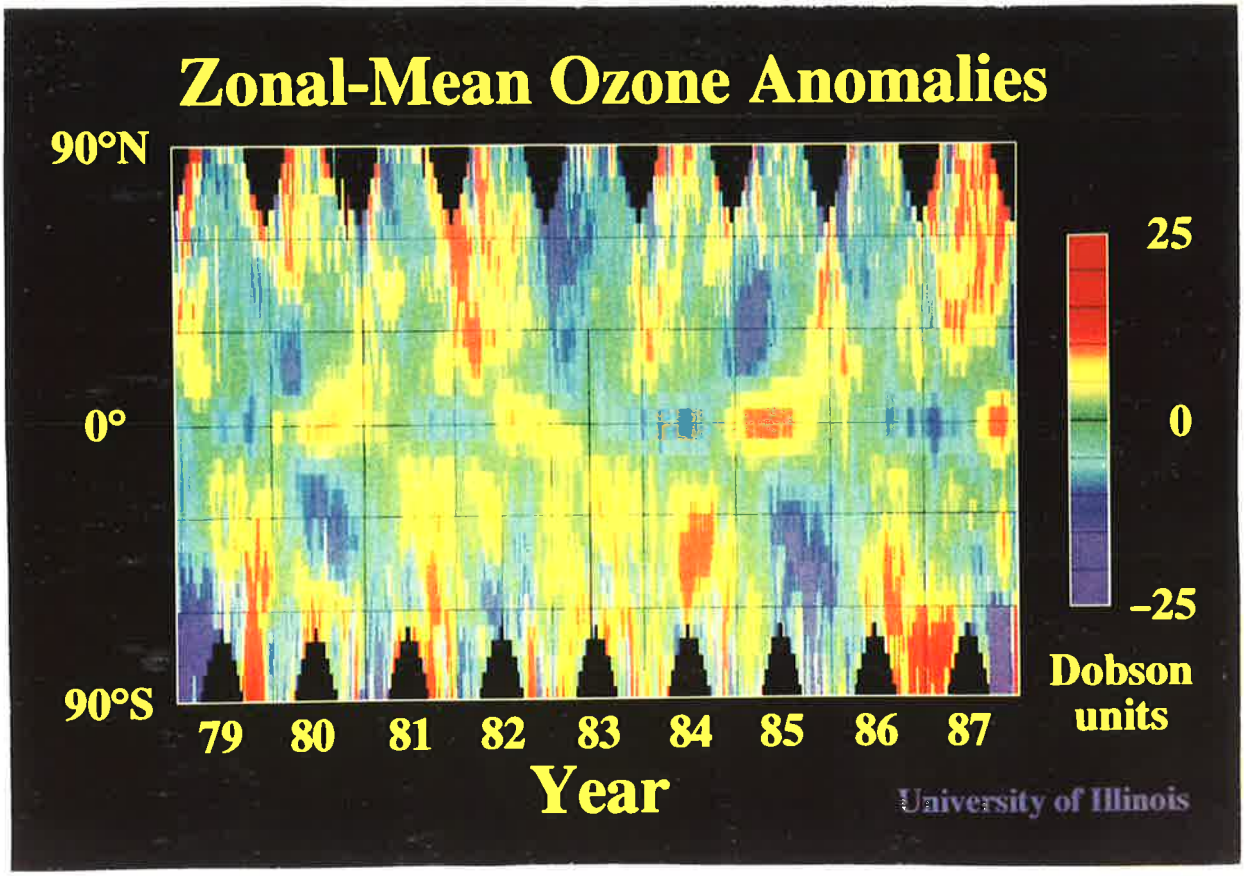

Figure 20: Latitude–year departures of the zonally averaged total ozone (measured in Dobson Units) from the mean values calculated over the 9 year observation period (1979–1987). The data are taken from the Total Ozone Mapping Spectrometer (TOMS) aboard the *Nimbus 7* satellite [after *Bowman*, 1989].

Certainly the influence of gravity waves on mean dynamics affects the way such chemicals are advected about the globe, and gravity wave–modified mean temperatures must modify reaction rates, and thus local concentrations. However, it turns out that gravity waves have more direct influences on ozone abundances than these alone.

It was mentioned earlier that there is, in addition to the QBO in wind and temperature, a QBO in the total column abundances of ozone [see, e.g., *Angell and Korshover*, 1973; *Bowman*, 1989]. However, as opposed to the dynamical QBO, the ozone QBO is not confined to the equator, but is global in extent, as shown in Figure 20. It was initially believed that the equatorial features of this oscillation, which clearly differ from the extra–tropical structure, might simply be explained in terms of alterations to the chemical rate coefficients produced by the presence of the background temperature QBO. When tested, however, this turned out to be roughly valid only above $\sim 25km$ in altitude. Below this height, it is vertical transport forced by the temperature QBO that drives the ozone QBO [*Ling and London*, 1986; *Gray and Pyle*, 1989; *Bowman*, 1989]. One should again note that these two ozone QBO mechanisms are both

driven by the temperature QBO, which itself is driven by alternating Kelvin–wave and mixed–Rossby–gravity–wave drag. These waves are, to all intents and purposed, just equatorially–ducted gravity wave motions. Hence there is a clear causal relation between these waves and equatorial ozone concentrations.

The extratropical ozone QBO is more problematical, but it would appear likely that it is dynamically coupled to the equatorial QBO in some manner. *Holton* [1989] proposed that an annual cycle in the mean meridional circulation (the well–known Hadley circulation) may be important, whereas *Hamilton* [1989] suggested that planetary Rossby waves may transport equatorial ozone structure to higher latitudes. Observations do not appear to have borne out either theory [*Bowman*, 1989]. Resolution of this feature may come from explanation of a similar, recently observed QBO–modulation of the atmosphere's response to the 11–year solar cycle [*Labitzke and vanLoon*, 1989], which has stirred considerable interest.

In the upper stratosphere and lower mesosphere, ozone abundances also exhibit clear but different seasonal variations, as shown in Figure 21. Variations are especially large at middle and high latitudes, the equinoctial concentrations being about three times larger than those at the soltices. Local photochemistry alone cannot account for this structure, since the temperature–dependent rate coefficients predict largest concentrations during summer, when the mesopause is at is coldest (due to gravity wave drag). However, one should note that this variability is concentrated within a narrow height band of $\sim 10km$, centred at about the $80km$ region; below and above this region, the variability is quasi–annual, with a winter maximum below and summer maximum above [see, e.g., *Thomas et al.*, 1984*b*].

Thomas et al. [1984*a*] suggested that seasonal variations in gravity–wave induced vertical transport may drive these semiannual variations. By considering the wave breaking scheme of *Lindzen* [1981] in the presence of representative solticial and equinoctial temperature and wind profiles, *Thomas et al.* [1984*a*] argued that the turbulent vertical diffusion produced by breaking gravity waves should be considerably smaller at equinox than at the soltices. This smaller equinoctial diffusion, it was argued, should reduce water vapour abundances[24] by reducing its vertical transport from the stratosphere, and should also reduce the downward flux of odd oxygen from the thermosphere (see next section), also reducing ozone destruction. These two processes should act together to increase the ozone abundance.

Detailed modelling along these lines by *Garcia and Solomon* [1985] simulated both the observed ozone variability and the suggested variations in turbulent diffusion very well. A further modelling study by *Bjarnason et al.* [1987] found that the diurnal variation in the background flow produced by solar tides produced time–varying wave breaking, time–varying vertical turbulent diffusion, and thus a diurnal variation in mesospheric ozone abundances which again agreed very well with SME observations.

[24] water vapour gives rise to hydrogen radicals which destroy ozone

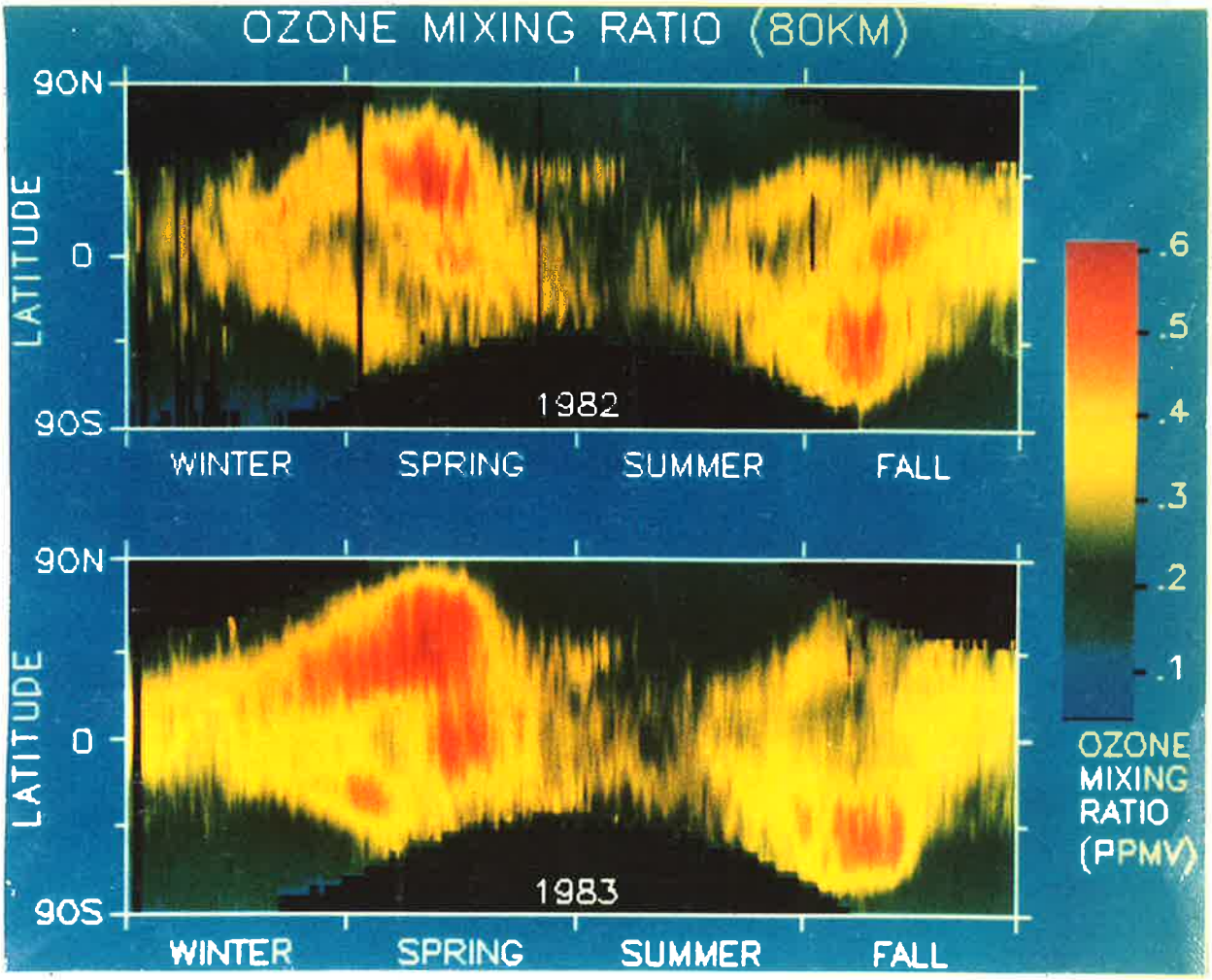

Figure 21: Season–Latitude plot of the ozone mixing ratio at $80km$ during 1982–83, using data from The Solar Mesosphere Explorer (SME) Satellite [after *Thomas et al.*, 1984*a*].

This agreement between observations and modelling studies, which used the simplified wave breaking parameterization of *Lindzen* [1981], is a little puzzling, however, since subsequent work has revealed that application of Lindzen's scheme to this problem may have several important shortcomings. These include the interrelated and unresolved problems of wave–induced turbulent Prandtl numbers greater than unity [e.g., *Chao and Schoeberl*, 1984; *Strobel et al.*, 1987; *Strobel*, 1989], wave "supersaturation" [e.g., *McIntyre*, 1987, 1989; *Lindzen*, 1988; *Weinstock*, 1989], and whether wave–induced advection or diffusion is the more important transport process [e.g., *Holton and Schoeberl*, 1988]. The relative roles of Stokes and turbulent diffusion, as discussed in the previous section, are also unclear.

This uncertainty has been heightened by recent reports of long–term ground–based measurements of mesospheric water vapour by *Bevilacqua et al.* [1989, 1990]. While early studies suggested a semiannual variation in H_2O concentrations, as predicted by the diffusive ozone model calculations, *Bevilacqua et*

al. [1989] analyzed a more extensize data base to show that the semiannual variation was very small compared to a strong annual variation, with a winter minimum and summer maximum. The mean water–vapour abundances are also much lower than model predictions [see, e.g., *Strobel et al.*, 1987]. More sophisticated subsequent modelling by *Garcia* [1989] has improved these abundance comparisons, but it still cannot reproduce these observed seasonal variations. *Bevilacqua et al.* [1990] have argued that advective[25] rather than diffusive vertical transport is more important in producing the observed H_2O variability. Furthermore, they used both observations and modelling to argue that the observed seasonal variability of mesospheric water vapour cannot produce the observed semiannual ozone variations in Figure 21, at least as the chemistry and dynamics are presently understood. Identifying additional photochemical or dynamical factors which might resolve these anomalies is the subject of current research. While gravity–wave transport still seems likely to play a major role, the exact mechanisms responsible for these variations in ozone and water–vapour abundances are still to be determined.

On smaller time scales again, *Froidevaux et al.* [1989] investigated the effect of wave–induced temperature perturbations on ozone abundances in the upper stratosphere and mesosphere. They found that planetary waves produced little effect, because their periods were longer than typical chemical lifetimes. Shorter–period gravity–wave motions, however, produced quite significant variations in ozone concentrations in the lower mesosphere, consistent with observations. In the upper stratosphere, *Froidevaux et al.* argued that observed ozone variability was best explained by the perturbing effects of waves with ground–based periods in the range 1–5 days, which should include the low frequency inertia gravity wave activity which is commonly observed at these heights [see, e.g., *Hirota and Niki*, 1985].

In light of the perceived importance of gravity waves on the ozone distribution of the upper middle atmosphere, it is worth asking whether similar effects might occur in the lower stratosphere. *Holton* [1987] has analyzed some high–resolution aircraft data from this region, and has argued that inertia gravity waves are indeed responsible for much of the small–scale variability in ozone abundances evident in these limited observations. However, the general effects of gravity waves on lower stratospheric ozone are still to be properly addressed, despite their possible significance [see, e.g., *Plumb et al.*, 1986].

The advent of the "Ozone Hole" during Spring over Antarctica has heightened interest in understanding all mechanisms which influence the ozone abundances here. Several wave–driven aspects of the problem have already emerged. *Garcia and Solomon* [1987] and *Lait et al.* [1989] have demonstrated that much of the interannual variability in the severity of Antarctic ozone depletion may be coupled to

[25] one should note that meridional and vertical advective transport in the mesosphere is driven by gravity waves (see previous section)

the equatorial (wave–driven) QBO. This could be entirely due to the aforementioned QBO in ozone that occurs globally, although QBO modulation of the depletion chemistry may also contribute.

On this point, *Poole et al.* [1989] have detected a strong QBO in the occurrence of polar stratospheric clouds (PSC) over Antarctica. These PSCs are crucial to ozone depletion chemistry. They denitrify and dehydrify the atmosphere, and then also act as catalyzing sites for reactions which convert chlorine and bromine from their inert forms into reactive radicals, forms in which they very efficiently and rapidly destroy ozone in a photochemical reaction [see, e.g., *Salawitch et al.*, 1988]. This QBO in PSC occurrence strongly suggests, therefore, that ozone depletion will be more severe in years when the QBO phase is eastward [*Poole et al.*, 1989].

Yet local gravity waves also appear to play a very direct role in the formation of PSCs, and hence in ozone depletion. PSCs, of which there are several types, require very cold temperatures and a given rate of cooling in order to form initially [*Toon et al.*, 1989]. *Gary* [1989] observed that gravity waves, produced by flow over Antarctic orography, are abundant in the troposphere and lower stratosphere over Antarctica during spring, when ozone depletion occurs within the polar vortex. *Cariolle et al.* [1989] observed that rapid air cooling produced by vertical air motions associated with these mountain gravity waves triggered the formation of many PSCs over the Antarctic continent during spring. Modelling of Antarctic mountain waves has now commenced [*Bacmeister et al.*, 1990].

One should also note that planetary Rossby waves have important effects on the global distrubution of ozone, and actually prevent formation on an ozone hole over the Arctic. *Salby and Garcia* [1990] give an illustrative non–technical discussion of these effects.

From an Australian perspective, it is important to know how ozone–depleted air is transported and mixed when the entraining polar vortex breaks up during November. Clearly an understanding of both large– and small–scale dynamics is required to achieve this. In the long–term, one must understand how the global QBO in ozone and Antarctic ozone depletion relates to the wave–driven equatorial QBO, and how this impacts on ozone abundances over Australia. It is also important to know how ozone concentrations can vary locally on small time scales (~1 day), particularly as UV "forecasts" are now being attempted in weather reports in the media. It is clear that gravity waves are a prime candidate for producing such temporal variability [see, e.g., *Holton*, 1987; *Froidevaux et al.*, 1989]. Therefore, a knowledge of gravity–wave characteristics in the Australian region may aid in the understanding of gravity–wave modulation of local ozone concentrations, and thus the degree of temporal intermittency in ground–level UV radiation intensities.

1.4.5 Effects of Gravity Waves on Airglow Emission from Atomic Oxygen

Excited atomic oxygen emits a wavelength ($557.7nm$) whose intensity depends principally on the number density of the chemical. It occurs at a height $\sim 100km$ in the atmosphere, and emits an "airglow" which can be observed at the ground; the so–called "green light of the night sky". This emission was first reported by *Rayleigh* [1924], and is one of the most thoroughly studied atmospheric airglow phenomena [see the review of *Bates*, 1981].

Even the early studies of Lord Rayleigh revealed a strong vernal maximum in the intensity of this emission [*Rayleigh*, 1935; *Hernandez and Silverman*, 1964]. Subsequent ground–based [*Fukuyama*, 1977] and satellite–based observations [*Cogger et al.*, 1981] revealed strong seasonal variations in the emission intensity, particularly at middle and high latitudes, with equinoctial maxima and solticial minima.

Because lifetimes are large in the thermosphere and very small in the mesosphere, atomic oxygen concentrations at this level are set principally by downward transport of the chemical from a thermospheric reservoir to a mesospheric "sink". *Garcia and Solomon* [1985] argued that the seasonal variability in gravity wave–induced vertical turbulent diffusion may be responsible for the seasonal behaviour of the airglow intensity. Extending arguments originally set forth by *Colegrove et al.* [1965], they argued that if vertical diffusion is large, atomic oxygen is rapidly transported downward to $\sim 80km$ where it is destroyed, thus preventing significant buildup of the chemical at $\sim 100km$ where it luminesces. When diffusion is small however, the buildup of the chemical at $\sim 100km$ should increase, leading to more intense airglow emission. The predicted equinoctial minima and solsticial maxima in gravity wave–driven vertical turbulent diffusion coefficients (see previous section) qualitatively support this idea.

Garcia and Solomon [1985] used a detailed numerical model to evaluate this hypothesis. Figure 22 compares their simulated results of the green light emission intensities with the satellite observations presented by *Cogger et al.* [1981]. Once again, the similarity of the model results and observations is impressive, despite the problems of oversimplification discussed in the previous section. *Bjarnason et al.* [1987] have also shown that the diurnal variability in this emission [see, e.g., *Fukuyama*, 1976] is well reproduced by a model which incorporates the diurnal variability in gravity wave breaking produced by tides.

1.4.6 Gravity Waves in the Ocean

Due to the ease with which data can be obtained from the ocean, internal gravity waves[26] were measured and studied within the ocean much earlier than in the atmosphere. They exist because oceanic densities

[26] not to be confused with surface/surfers' waves, internal gravity waves exist below the ocean surface

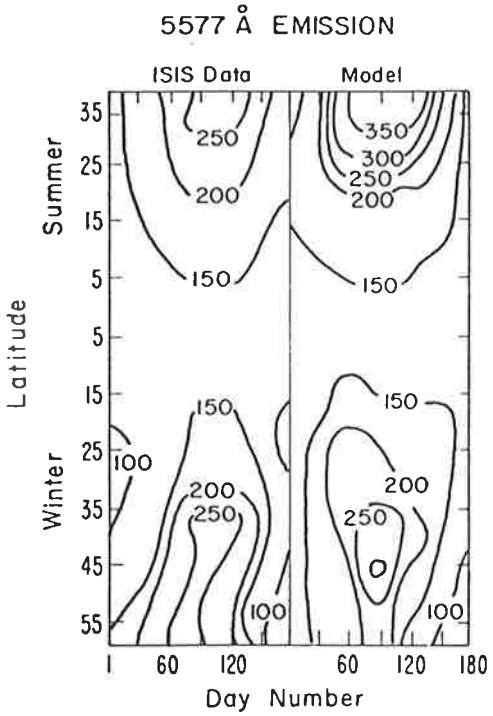

Figure 22: Season–latitude intensity in atmomic oxygen 557.7 *nm* emission measured by satellite (left), and as reproduced by a model incorporating the relevant chemistry and vertical turbulent diffusion induced by gravity–wave breaking [after *Garcia and Solomon*, 1985].

also vary vertically due to changes in salinity. The observational and theoretical literature on oceanic gravity waves is considerable [see, e.g., reviews by *Defant*, 1961; *Briscoe*, 1975; *Roberts*, 1975; *Phillips*, 1977; *Garrett and Munk*, 1979; *Munk*, 1981; *Müller et al.*, 1986], and only a brief description will be attempted here.

Gravity waves motions are ubiquitous within the ocean, with typical horizontal scales $\sim$1–10000m, vertical wavelengths $\sim$1-1000m, and a total vertically integrated energies per unit area $\sim$4 x 10^3 Jm^{-2} [see, e.g., *Garrett and Munk*, 1975]. These waves give rise to spatio–temporal power spectra which are suprisingly invariant to changes in season and location [*Garrett and Munk*, 1975, 1979], and in this respect appear to behave rather like the similarly–shaped atmospheric gravity wave spectrum [see, e.g., *VanZandt*, 1982].

In fact, the atmospheric and oceanic gravity–wave fields are considerably different in nature. In the atmosphere, there is intense and sporadic production of waves, which, as they propagate upwards, grow rapidly in amplitude due to the exponentially–decreasing air density, and eventually dissipate as the wave motions produce superabiabatic temperature gradients. Thus the wave spectrum here is transient, selectively filtered by dissipation, and often so energetic that the spectrum becomes "saturated". It is this saturation that is believed to produce the observed spectral shapes [see, e.g., *Fritts*, 1984; *Smith et*

al., 1987]. The transience also makes the spectrum rather variable in time and space (see section 3.3 and references therein).

Mean flows and vertical density variations are nowhere near as large within the ocean, and so the two aforementioned wave dissipation mechanisms occur much less frequently. Oceanic gravity waves are therefore much longer lived, so that the characteristics of the wave field vary much less in time and space. Indeed, the long lifetimes of these waves allow them time to interact with one another, giving rise to a number of processes known collectively as *wave–wave interactions*, where an interaction between two preexisting waves produces a third wave [see, e.g., *Hasselmann*, 1966]. It is believed that natural equilibration of these various wave–wave interactions leads to observed shapes of oceanic gravity wave spectra [see the review of *Müller et al.*, 1986]. However, occasional large–amplitude solitary waves are observed, which are well modelled by nonlinear soliton theory [see the review of *Ostrovsky and Stepanyants*, 1989].

Because of their different characteristics, oceanic gravity waves produce different effects to atmospheric gravity waves. Oceanic wave–induced drag and mean–flow acceleration are not significant [see, e.g., *Holloway and Müller*, 1990], and the primary concern is the role of the wave spectrum in the mixing of chemical tracers, heat and salinity. This can occur through sporadic instabilities caused by a superposition of waves [*Desaubies and Smith*, 1982], or by a (speculated) horizontal Stokes diffusion induced by the wave spectrum [*Sanderson and Okubo*, 1988]. Gravity waves are important also because they give rise to local variations in the speed of sound, which produce distortions to acoustic signals [*Flatté et al.*, 1979] that can hamper, for example, sonar detection of submarines. In fact, moving submarines radiate gravity waves, and it is rumoured that considerable military research has been directed towards reliably detecting this wave stream. The vertical motions associated with oceanic gravity waves also impact on the productivity and distibution of microorganisms within the ocean [see, e.g., *Kamykowski*, 1974].

1.4.7 Gravity Waves within other Planetary Atmospheres

Venus

The surface of Venus is obscured by a thick cloud layer which extends up to $\sim 50km$ from the surface of the planet. These clouds sweep longitudinally around the planet once every 4 (Earth) days, yet the planet itself rotates much more slowly in comparison (1 Venusian day $\sim$ 243 Earth days). This implies an atmospheric wind speed near the equator of around $100m\ s^{-1}$. How, then, is this so-called "superrotation" of the Venusian atmosphere driven and maintained?

Schubert and Whitehead [1969] investigated the problem using a so–called "moving flame" laboratory apparatus, similar to the one originally used by *Stern* [1959] to simulate the Earth's atmosphere. In this particular experiment, the planetary atmosphere was simulated by a annulus containing liquid mercury, and the Sun by a flame. Movement of this flame around the stationary annulus induced a persistent flow within the fluid near the surface, which must result from the stress produced by a spatial gradient in momentum flux. To produce such a gradient, however, a momentum flux "sink" must exist within the fluid, and following Stern's original suggestion, *Schubert and Whitehead* [1969] speculated that the sink in their experiments, and in the superrotating atmosphere of Venus, was viscous dissipation.

Within any stratified fluid like a planetary atmosphere, however, there are, in addition to these simple heating and viscosity effects, many purely dynamical processes which of themselves can produce momentum flux gradients and give rise to persistent mean flows. Internal gravity waves, which radiate away from source regions and then propagate into other regions where they dissipate, are one such dynamical process. *Lindzen* [1973] suggested that gravity–wave drag may in fact be the primary cause of this "superrotation".

Since then, probes have been sent to Venus, and have revealed wave structure within its atmosphere [see, e.g., *Brace et al.*, 1983; *Gierasch*, 1987; *Ingersoll et al.*, 1987; *Kasprzak et al.*, 1988]. The VEGA balloon mission even located a region of intense wave activity in the atmosphere above the Aphrodite mountains (around 7° "south" of the equator), suggesting intense orographic forcing of waves in this region [*Blamont et al.*, 1986]. Theoretical efforts are now being concentrated towards computational models of the atmosphere of Venus which incorporate its chemistry, surface topography, and the solar radiation it receives. Most importantly, these models are endeavouring to simulate the production, propagation, and dissipation of gravity–wave motions, so that their effect on the mean atmospheric structure can be ascertained [see, e.g., *Schubert and Walterscheid*, 1984; *Young et al.*, 1987; *Mayr et al.*, 1988]. The models, however, are still developmental at present, and better understanding of gravity–wave dynamics within the Earth's atmosphere will undoubtedly aid modelling of the Venusian atmosphere as well.

Mars

One of the most spectacular phenomena on Mars is the global dust storm. During such events the entire surface of the planet becomes shrouded in a blanket of airborne dust, transforming the "Red Planet" into a dullish brown colour [see, e.g., *Leovy*, 1985].

Leovy and Zurek [1981] observed strong diurnal and semidiurnal tides which were closely associated with these dust storms, due to direct atmospheric heating produced by this dust, which forced the tides.

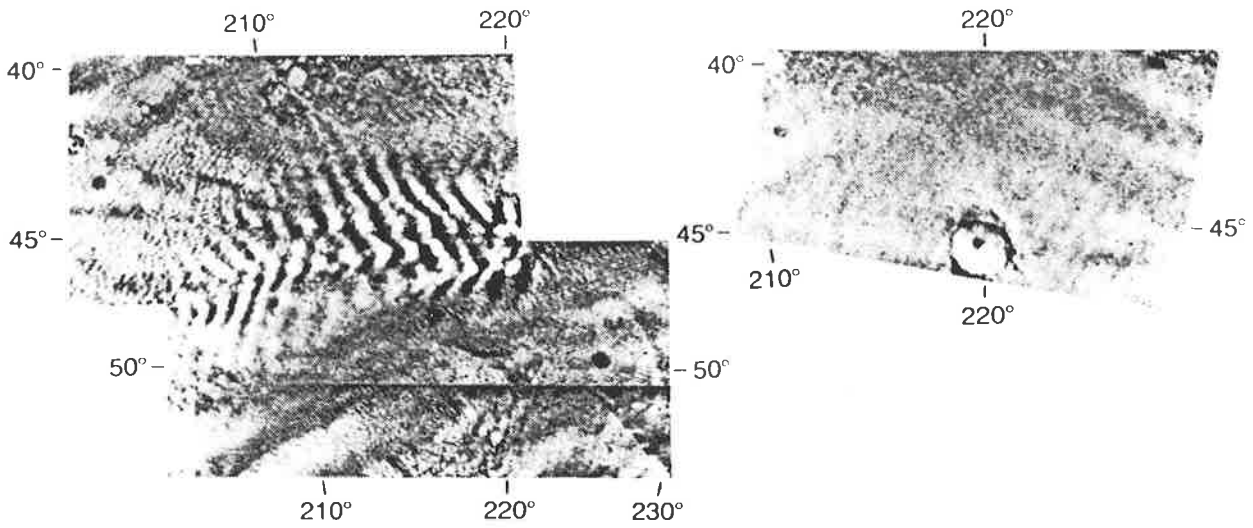

Figure 23: On the left is a photograph from the *Mariner 9* spacecraft of banded cloud structure in the Martian atmosphere, indicating a gravity wave motion. The photograph on the right shows the same area a day earlier. There is a surface crater, which is obscured in the other picture, and which probably orographically forced this wave motion [after *Leovy*, 1977].

Recent analysis of surface meteorological data from The Viking Landers revealed additional oscillations, which *Tillman* [1988] and *Zurek* [1988] identified as planetary–scale Kelvin wave motions with frequencies that are quasi–diurnal and quasi–semidiurnal. More importantly, it appears that these oscillations are greatly enhanced at the onset of global dust storms. *Tillman* [1988] studied these oscillations in depth, and tentatively concluded that the enhancement of the oscillations occured *prior* to global dust storms, and actually initiated the event. *Zurek* [1988] attempted a theoretical appraisal, and was equivocal in his interpretation, arguing that because these oscillations are quasi–diurnal and quasi–semidiurnal, solar heating of airborne dust may actually force these waves. *Zurek* [1988] also considered another theory where the Kelvin waves arise initially, slightly enhancing the atmospheric dustiness, whereupon solar heating of this dust drives a resonant increase in the amplitude of these nearly diurnal and semidiurnal Kelvin wave oscillations, producing a runaway dust storm.

Television pictures from the Mariner 9 satellite (see Figure 23), which orbited Mars, have also revealed lee wave patterns in clouds which were produced by flow over surface craters and volcanoes [see, e.g., *Briggs and Leovy*, 1974; *Leovy*, 1977]. These waves have been analyzed by *Pirraglia* [1976] and *Pickersgill and Hunt* [1979], but it is unclear whether they are trapped in the lower atmosphere, or can propagate into the upper atmosphere.

Titan

Gravity waves have been detected in the equatorial neutral atmosphere (its "stratosphere") of Titan by a radio occultation experiment aboard the Voyager spacecraft [*Hinson et al.*, 1983]. By estimating wave parameters from the data and using the wave–drag parameterization scheme of *Lindzen* [1981], *Hinson et al.* [1983] estimated the gravity–wave drag and concluded that it is likely to be important in driving the mean atmospheric circulation.

Neptune

The atmosphere of Neptune, as revealed recently by Voyager 2, exhibits a differential atmospheric super-rotation, similar to that on Venus. The Great Dark Spot, at around 22°S, is advected in the opposite direction to the planetary rotation by winds of $\sim 300 m\ s^{-1}$ [see, e.g., *Kinoshita*, 1989]. While uninvestigated at present, a gravity–wave drag process, similar to that on Venus, must be a prime candidate in explaining this feature.

1.4.8 Wave Effects in the Solar Atmosphere

Historically, one of the great unexplainable features of the Sun was the extreme temperature ($\sim 10^6 K$) of tenuous outer reaches of the solar atmosphere known as the *corona*. Such temperatures cannot be explained by radiative arguments, as the corona is too far removed from the active core of the Sun to be heated much above $10^4 K$.

Whitaker [1963][27] demonstrated that internal gravity waves are efficiently launched from convective regions of the Sun. The waves can then propagate freely out into the solar corona, where they are eventually dissipated by thermal conduction. This process mechanically heats the corona to a temperature $\sim 10^6 K$, a value 10–100 times larger than that due to radiative heating alone, and broadly consistent with observed coronal temperatures [*Whitaker*, 1963].

Presently, a modified wave–driven coronal heating process is believed to occur which involves Alfvén waves, rather than gravity waves. Alfvén waves arise within an ionized fluid in the presence of electric and magnetic fields through the constaining effects of Maxwell's equations on the fluid motion, and propagate along magnetic field lines [*Alfvén*, 1950]. It should be stressed that, while these wave solutions arise from Maxwell's equations, they are *not* electromagnetic waves, but are magneto–hydrodynamic (MHD) wave motions of the fluid plasma. It is believed Alfvén waves are produced by photospheric fluid motions

[27] note that Colin Hines, who first pioneered the study of gravity waves in the middle atmosphere, is credited with first suggesting this mechanism.

induced by underlying solar convection [*Ionson*, 1978], then propagate along field lines into the solar corona where they become heavily damped by resisitivity and viscosity [*Einaudi and Mok*, 1987]. The resulting turbulent deposition of this wave energy is now generally accepted to be a major source of the required coronal heating [see, e.g., *Strauss*, 1989; *VanHoven*, 1989].

MHD waves and higher frequency electrostatic plasma waves have also been detected in cometary streams [see, e.g., *Tsurutani and Smith*, 1986; *Grard et al.*, 1986]. These waves propagate away and are later absorbed, producing rapid heating of solar wind protons [*Sharma et al.*, 1988].

1.4.9 Concluding Comments

In conclusion, it can be seen that atmospheric gravity waves play an important role in the dynamics and chemistry of planetary atmospheres, and in particular the Earth's atmosphere. The work presented hereafter provides observational and theoretical data on gravity–wave characteristics in the troposphere, stratosphere, and mesosphere.

Chapter 2

Theory

2.1 Introduction

While the opening chapter was fairly non–technical and rather general in its scope, this short chapter will focus on some specific theoretical aspects of atmospheric gravity waves relevant to this thesis. The first section gives a basic mechanistic description of the atmospheric gravity wave. The remaining sections discuss theoretical apsects of gravity–wave motions which are poorly documented in texts at present and so are not widely appreciated, thus necessitating some introductory discussion of these topics before their more–detailed application in later chapters. Some working knowledge of basic fluid mechanics will be assumed throughout.

2.2 Physical Nature of the Gravity Wave

There are many mathematical methods of deriving the gravity–wave solution from the Navier–Stokes momentum equations, the mass continuity equation, and the adiabatic energy equation, modified to the atmospheric situation with appropriate simplification. The essential feature which supports internal gravity waves is the exponential decrease of atmospheric density with height due to hydrostatic balance in the vertical; that is, balance between gravity acting downwards and buoyancy acting upwards on fluid parcels, which is why these gravity waves are alternatively referred to as buoyancy waves[1]. As these are the only external forces *required* to drive the gravity wave motion, other force terms in the Navier–Stokes equations are usually dropped to simplify the derivation. Indeed, when some of the other force terms

[1] This term is often used to avoid confusion with the gravity waves (gravitational radiation) predicted by Einstein's General Theory of Relativity.

are included (e.g. Coriolis force), they produce only secondary changes to the wave motion. It serves no purpose to replicate such derivations here, and we shall merely quote the important results, appropriately referenced where necessary.

The method of solution is as follows;

(1) express all variables as the sum of a mean and a perturbation (e.g., the vertical velocity $w = \bar{w} + w'$, the mean and perturbation velocities, respectively). One hereafter assumes that both the mean and perturbation terms satisfy the equation sets, which affords considerable simplification. This is known as *linearization.*

(2) assume sinusoidal solutions for the perturbation terms of the form $e^{i(kx+ly+mz-\sigma t)}$, where (x, y, z) is the conventional displacement in Cartesian coordinates, $\mathbf{K} = (k, l, m)$ is a corresponding wavenumber vector, t is time, and σ is a ground–based/Eulerian wave frequency.

In this thesis, all observations are confined to the lower and middle atmosphere. Here, to first–order, the important forces controlling gravity–wave physics are the gravitational force, pressure–gradient forces, and the Coriolis force of the rotating earth. Many other appropriate simplifications are also used frequently (e.g., the assumption that the mean–wind vector $\bar{\mathbf{U}} = (\bar{U}(z), 0, 0)$). Mathematical manipulation leads to a dispersion relation for gravity waves of the following form [see, e.g., *Gossard and Hooke*, 1975; *Gill*, 1982];

$$m^2 = k_h^2 \left(\frac{N^2 - \omega^2}{\omega^2 - f^2} \right) - \frac{1}{4H_\rho^2} + \frac{\omega^2}{C_s^2}, \tag{1}$$

such that

$$k_h^2 = k^2 + l^2, \tag{2}$$

$$N^2 = \frac{g}{T} \left(\frac{dT}{dz} + \frac{g}{C_p} \right), \tag{3}$$

$$f \approx \frac{4\pi}{24\text{hrs}} \sin\theta, \tag{4}$$

$$\omega = \sigma - k\bar{U} - l\bar{V}, \tag{5}$$

and where g is the gravitational acceleration, T is the background temperature, H_ρ is the density scale–height, C_s is the speed of sound, C_p is the atmospheric specific heat at constant pressure, and θ is latitude. N is called the Brunt-Väisälä frequency, f the Coriolis or inertial frequency, and ω the intrinsic/Lagrangian wave frequency.

If one uses (1) to plot m against k_h, and assuming the last term is small, hyperbolae result for constant ω (see Figure 24). The last term in (1) is indeed negligibly small in the middle atmosphere, and the scale–height term is only significant for waves with vertical wavelengths $2\pi m^{-1}$ larger than $\approx 40km$.

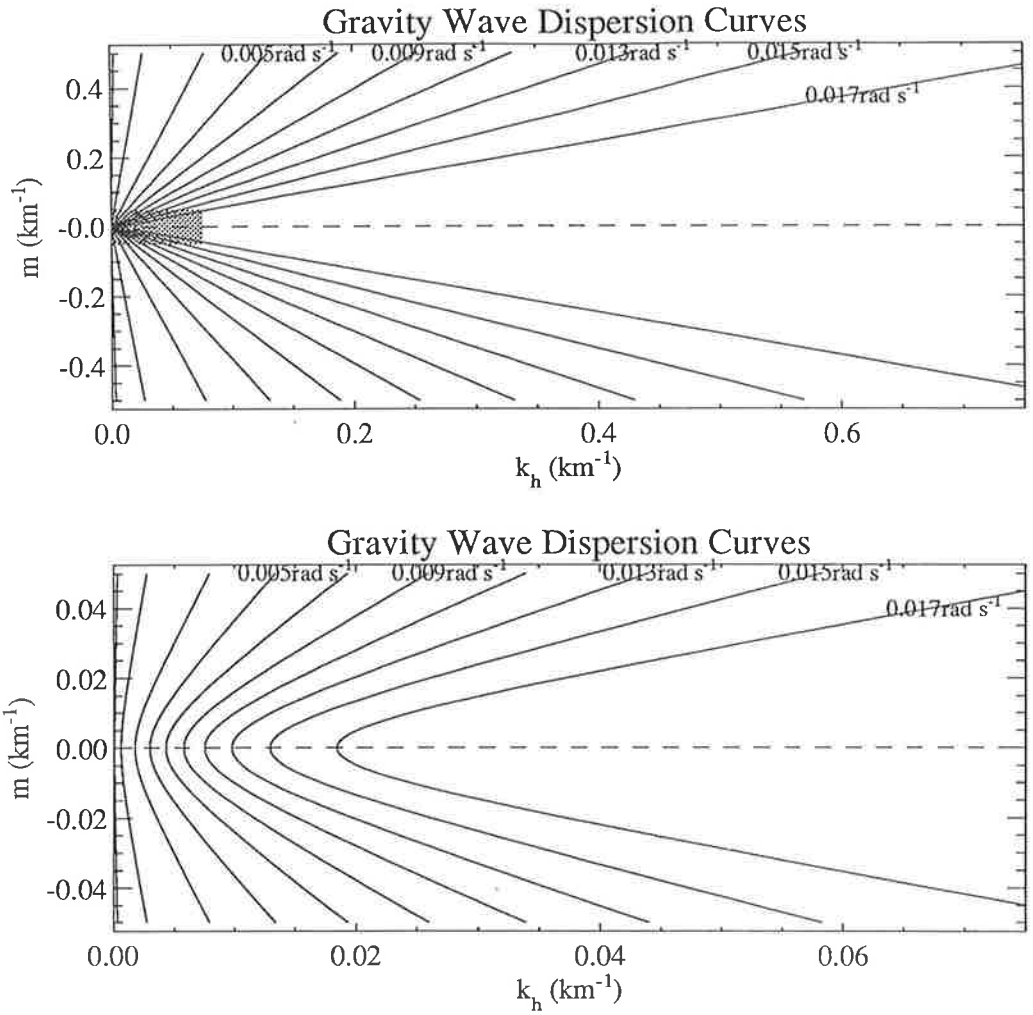

Figure 24: Plots of m versus k_h for various constant values of ω as indicated on the solid curves, which form hyperbolae. The shaded area in the top plot is enlarged in the lower plot.

Therefore, the first term on the right–hand side of (1) is adequate for most purposes, and gives real solutions when $f <\mid \omega \mid< N$, so that f and N define upper and lower bounds, respectively, on the intrinsic wave frequency ω.

A number of *polarization relations* also result, which relate wave–induced fluctuations of various fluid parameters. Hereafter we shall assume zonal propagation (i.e. along the x–direction, so that $l = 0$), which is equivalent to rotating the coordinates so that the x–axis lies along the horizontal wave vector direction $\mathbf{k_h} = (k, l)$. The 3–component velocity fluctuations (u', v', w') then are related as follows;

$$v' = i\frac{f}{\omega}u', \tag{6}$$

$$w' = -\frac{k}{m}u'. \tag{7}$$

This describes the velocity polarization of the wave. Horizontal–velocity fluctuations are longitudinal (i.e. parallel with $\mathbf{k_h}$), but aquire a transverse component and thus become circularly polarized as ω

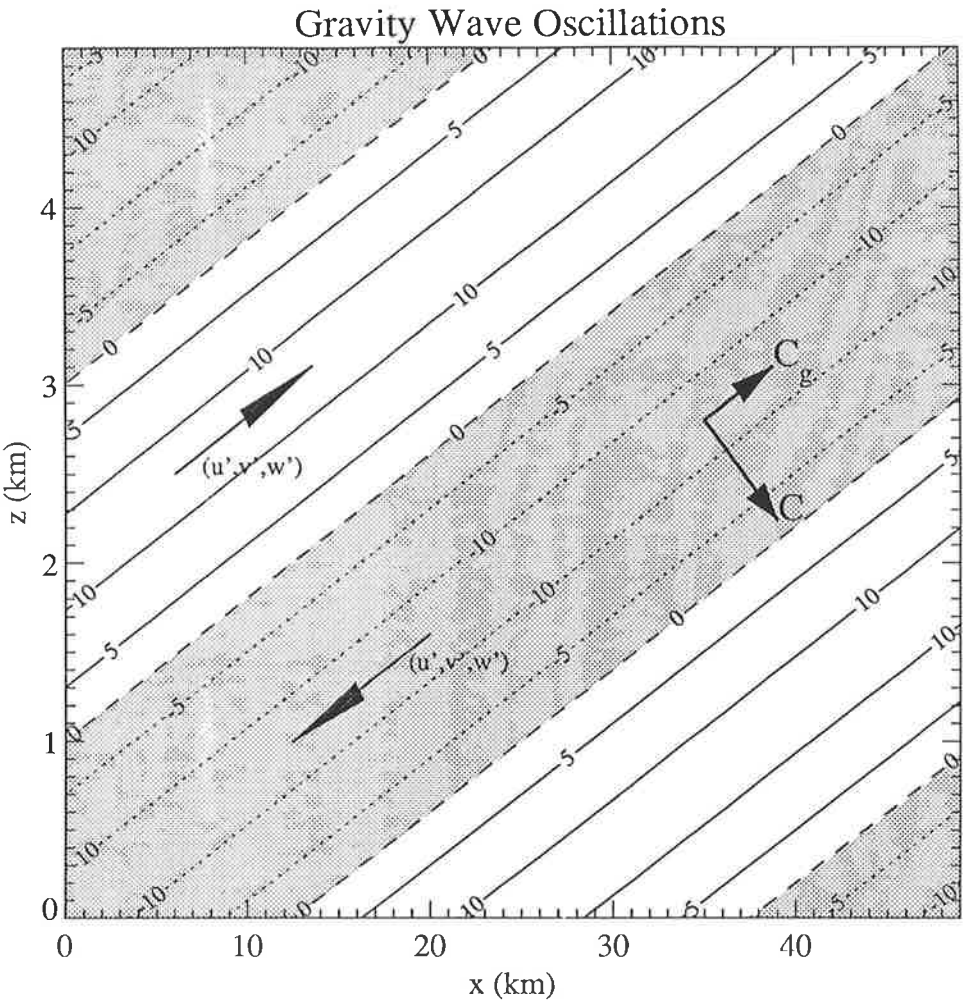

Figure 25: Gravity–wave velocity oscillations corresponding to a given wave vector **K**. For this k/m ratio, $\omega \gg f$, so that $v' \approx 0$ and the elliptical polarization is small. Shaded areas show negative velocities with respect to the positive x and z indicated on the plot axes, as indicated by sample (u', v', w') vectors. Phase–velocity (**C**) and group–velocity ($\mathbf{C_g}$) vectors are also shown. The diagonal lines are velocity contours, labelled in $m\ s^{-1}$. The peak wave amplitude is $11m\ s^{-1}$.

approaches f. Vertical–velocity fluctuations are in antiphase with the longitudinal horizontal velocity fluctuations.

However, one must incorporate m to understand the full three–dimensional structure of the gravity wave. Figure 25 gives a three–dimensional representation of the velocity fluctuations (u', v', w'), for a given **K** vector. Note that the gravity wave is a fully transverse wave motion, even though horizontal–plane projections of the wave motion produce longitudinal behaviour.

Note from Figure 25 that when wave energy propagates upwards (i.e. the vertical component of the group velocity, $\partial\omega/\partial m$, is upward), wave phase fronts move downwards (i.e. the vertical component of the phase velocity ω/m is directed downwards), and vice versa. This follows directly from the dispersion relation (1), and can be inferred from inspection of the curves in Figure 24. Thus, for upward–propagating

wave energy, while the wave–amplitude envelope will ascend vertically with time, the wavefronts actually descend with time, and vice versa for downward–propagating wave energy.

These simple relations are really all that is needed to give a picture of the physical nature of the gravity wave. There are many more polarization that relate other perturbation quantities, such as temperature T', pressure p', and density ρ' [see, e.g., *Gossard and Hooke*, 1975], yet these variations result from the vertical adiabatic displacement of air parcels by the wave, and so can be understood by appreciating the w' fluctuations. Further discussion of wave polarization and dispersion is given by *Hines* [1960], *Gossard and Hooke* [1975], *Lighthill* [1978], *Gill* [1982], and *Andrews et al.* [1987], yet one should remember that most of the sometimes complex discussion in some of these texts almost always revolves around equations (1)–(7).

2.3 Five–Dimensional "F–System" Wave Solutions

The aforementioned linearization process focused only on gravity waves, yet more careful analysis reveals that other mesoscale wave solutions exist. The linearized, inviscid, adiabatic air motion over a rotating earth is governed by five equations in five unknowns, which *Dong and Yeh* [1988] expressed in terms of the following five–dimensional state vector $\tilde{F} = F_i$, where i=1,2,3,4,5, $\rho + \rho'$ is the density, and $p + p'$ is pressure;

$$\tilde{F} = \begin{bmatrix} \frac{p' - C_s^2 \rho'}{C_s(\rho(\gamma-1))^{1/2}} \\ \frac{p'}{C_s \rho^{1/2}} \\ \rho^{1/2} u' \\ \rho^{1/2} v' \\ \rho^{1/2} w' \end{bmatrix}. \tag{8}$$

With this definition, the problem can be formulated as a matrix eigenvalue problem assuming sinusoidal solutions for the perturbation quantities, and is known as the "5–D F–system" [*Yeh and Liu*, 1981; *Dong and Yeh*, 1988]. The eigenvalues correspond to the intrinsic frequency ω, and so the five eigenvalue solutions ω_j, where j=1,2,3,4,5, are referred to as the eigenfrequencies. Re–expressing $\mathbf{K} = (k, l, m)$ in polar coordinates (k, θ, φ), the eigenfrequencies are [*Yeh and Dong*, 1989]

$$\omega_1 = 0, \tag{9}$$

$$\omega_2 = \left(N^2 \sin^2\theta + f^2\right)^{1/2} = \left(N^2 \frac{k^2}{k^2 + m^2} + f^2\right)^{1/2}, \tag{10}$$

$$\omega_3 = -\omega_2, \tag{11}$$

$$\omega_4 = kC_s, \tag{12}$$

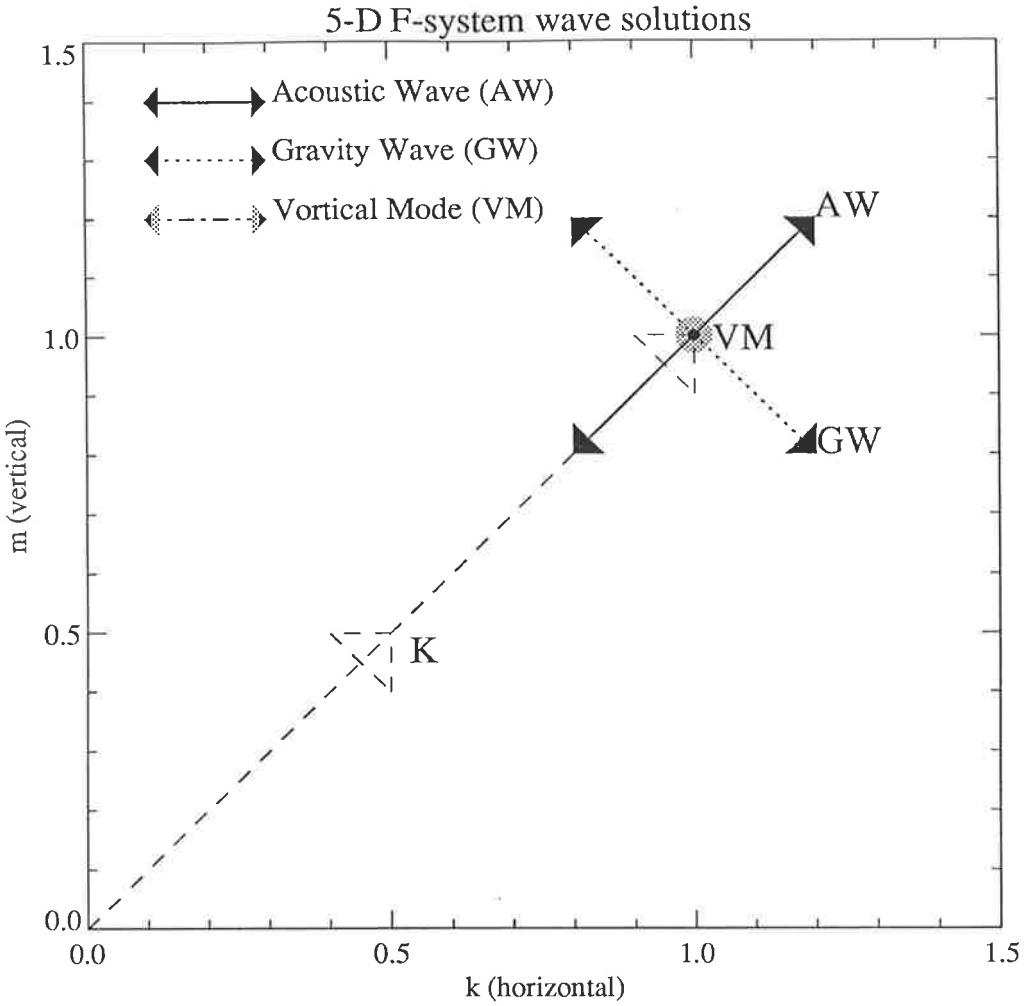

Figure 26: Schematic representation of the three mesoscale wave solutions given by the "5–D F–system" solution of the linearized fluid equations; the gravity wave (GW), the acoustic wave (AW), and the vortical mode (VM). The dotted vector shows the wavenumber **K**, given by $(k, 0, m)$ in this diagram. The vortical–mode vector points perpendicularly into and out of the page, so that all three wave vector schemes are mutually orthogonal.

$$\omega_5 \;=\; -\omega_4. \tag{13}$$

The components ω_2 and ω_3 are the gravity–wave solutions, and components ω_4 and ω_5 are the acoustic–wave (sound–wave) solutions. The identically–zero ω_1 component is a solution known as the vortical mode. The corresponding eigenvectors $\tilde{F}_j = (F_i)_j$ for each eigenvalue ω_j detail the wave–vector fluctuations of these solutions, and are plotted in Figure 26. The transverse nature of the gravity wave again becomes apparent, as does the well–known longitudinal nature of the acoustic wave. The vortical–mode arrow points straight into and out of the page, so that its fluctuations are constrained to the horizontal. Notice that the fluctuations of these three different waves are mutually orthogonal.

The geophysical significance of the vortical–mode solution will be highlighted and investigated in section 3.3 and chapter 4.

2.4 Gravity–Wave "Activity" Conservation

Many analyses of gravity–wave amplitudes assume that the total gravity–wave energy E is conserved. For a high–frequency wave (i.e. $\omega \gg f$) there is equipartition between kinetic and potential energy in the wave [see, e.g., *Dunkerton*, 1984], and so one can assume that wave kinetic energy E_k is also conserved as follows (assuming a zonally propagating wave)

$$E_k = \frac{1}{2}\rho u'^2. \tag{14}$$

Since atmospheric density ρ varies vertically as e^{-z/H_ρ}, conservation of kinetic energy therefore implies

$$u'(z) = u'(z_0)e^{(z-z_0)/2H_\rho}, \tag{15}$$

so that the vertical velocity perturbation grow exponentially with altitude.

However, gravity–wave energy is not conserved, but is continously exchanged with the background flow. It is the *total wave action* which is conserved, such that the wave–action density $A = E/\omega$ obeys the following continuity equation

$$\frac{\partial A}{\partial t} + \nabla.\left(\hat{\mathbf{c}}_\mathbf{g} A\right) = 0, \tag{16}$$

where $\hat{\mathbf{c}}_\mathbf{g}$ is the ground–based group velocity, equal to the wave group velocity plus any mean–wind velocity which advects the wave packet (see also section 7.3). This formula was first derived for slowly–varying waves by *Bretherton and Garrett* [1968], but was shown to hold generally by *Andrews and McIntyre* [1978]. Equation (16) is the fundamental conservation equation governing the amplitude of wave disturbances in fluids, and other better–known conservation relations are all just special cases of this general relation.

For example, it is perhaps better known that the so–called Eliassen–Palm (EP) flux is conserved for waves in zonal–mean flows. Indeed *Eliassen and Palm* [1961] first derived this conserved quantity for stationary gravity waves propagating above a non–rotating earth, and in this case it equals the upward flux of zonal momentum $\rho\overline{u'w'}$ for a zonally–propagating wave. The EP–flux was generalized by *Andrews and McIntyre* [1976] so that, to second order in wave amplitude, the following equation was applicable generally;

$$\frac{\partial \tilde{A}}{\partial t} + \nabla.\mathbf{G} = 0. \tag{17}$$

For a non–rotating earth, the gravity–wave EP flux vector $\mathbf{G}$ is given by [*Andrews et al.*, 1987]

$$\mathbf{G} = \begin{pmatrix} 0 \\ -\rho\overline{u'v'} \\ -\rho\overline{u'w'} \end{pmatrix}. \tag{18}$$

Note that, for non–transient conservative wave motions, $\nabla.\mathbf{G} = 0$. For a zonally–propagating wave, $\mathbf{G} = (0, 0, -\rho\overline{u'w'})$, so that $\rho\overline{u'w'}$ is conserved, which is the Eliassen–Palm result, and the oft–quoted conservation relation for gravity wave activity.

However, similarity between (17) and (16) is quite apparent. Indeed, for these slowly–varying plane–wave solutions, $\mathbf{G} = \mathbf{c_g}\tilde{A}$, where $\mathbf{c_g} = (c_{gx}, c_{gy}, c_{gz})$ is the intrinsic group–velocity vector of the wave, $\tilde{A} = -kA$, and k is the zonal component of the horizontal wavenumber [*Andrews et al.*, 1987]. Note, however, that this equality does not hold zonally, since G_x is defined to be zero in the EP–flux formulation. G_x is set zero because in such zonal–mean problems $\partial/\partial x$ is always zero, and it is the EP–flux divergence which is dynamically important. However, by inspection of (18), one might guess that $G_x = -\rho\overline{u'^2}$ is a more appropriate definition in three dimensions. Indeed, for slowly–varying waves in a non–rotating atmosphere, the following Reynolds–stress terms can be simply expressed in terms of the wave–action density, as follows [*Bretherton*, 1969*b*]

$$\begin{pmatrix} \rho\overline{u'^2} & \rho\overline{u'v'} & \rho\overline{u'w'} \\ \rho\overline{u'v'} & \rho\overline{v'^2} & \rho\overline{v'w'} \end{pmatrix} = \begin{pmatrix} k \\ l \end{pmatrix} A\mathbf{c_g}. \tag{19}$$

Now note that for a non–transient zonally–propagating wave in a zonal–mean atmosphere, the wave action equation (16) reduces to $\partial/\partial z(\hat{c}_{gz}A) = 0$, so that $c_{gz}A$ is a constant (since $\bar{w}$ equals zero), which, according to (19) also implies $\rho\overline{u'w'}$ is a constant, since k is stays constant on a zonal–mean flow (see section 7.3). Thus, the well–known result for gravity waves, that the upward flux of horizontal momentum (EP–flux) is conserved, is merely a special case of wave action conservation to situations where no time variability and only limited spatial variability of wave amplitudes arise.

Gravity–waves eventually become unstable and dissipate, giving rise to non–zero EP–flux divergences which exert a drag upon the middle atmosphere, inducing appreciable mean–flow accelerations as discussed qualitatively in the opening chapter. The relevant effects are well–documented, and similar discussion will not be reproduced here; review articles by *Fritts* [1984, 1989] and section 4.6 of *Andrews et al.* [1987] give excellent descriptions of the basic mechanics of the gravity–wave drag process. For some discussion on current uncertainities in parameterizing the wave drag, see *Chao and Schoeberl* [1984], *Lindzen* [1988], *Dunkerton* [1989], *Strobel* [1989], and *McIntyre* [1987, 1989].

Chapter 3

Interpreting Gravity Wave Measurements

3.1 Chapter Theme

The atmosphere can support gravity waves with any intrinsic period between the inertial period τ_i ($\approx 12hrs/\sin\theta$), and the Brunt–Väisälä period τ_{BV} (typically about $5min$ in the middle atmosphere and about $10min$ in the troposphere). Virtually any combination of vertical and horizontal wavelengths which satisfy the dispersion relation is also permitted. The only important exception is that a small vertical–wavelength cutoff λ_z^c arises, after which smaller vertical wavelengths are "quenched" by eddy diffusion [*Hines*, 1964], and the motion enters the regime of buoyancy–modified turbulence [see, e.g., *Weinstock*, 1978; *Sidi and Dalaudier*, 1989]. This small wavelength cutoff is about $1km$ at an altitude of $100km$ [*Hines*, 1964], but is smaller at middle atmospheric heights due to smaller eddy diffusivities (see Figure 1.9*c* of *Hocking* [1981]).

There is, therefore, a broad range of both spatial and temporal scales (often termed the mesoscale) over which atmospheric gravity wave motions can occur. Many measurements of atmospheric fluctuations over these ranges have been made, yet their interpretation as gravity waves has been, and still remains, difficult and sometimes controversial.

The principal reason for this difficulty is that observed fluctuations are rarely sinusoidal[1]. On the few occasions that a monochromatic gravity wave has been identified, the wave persisted for little more than an oscillation or two [see, e.g., *Fritts et al.*, 1984; *Muraoka et al.*, 1987; *Yamamoto et al.*, 1987].

[1] this excludes tides

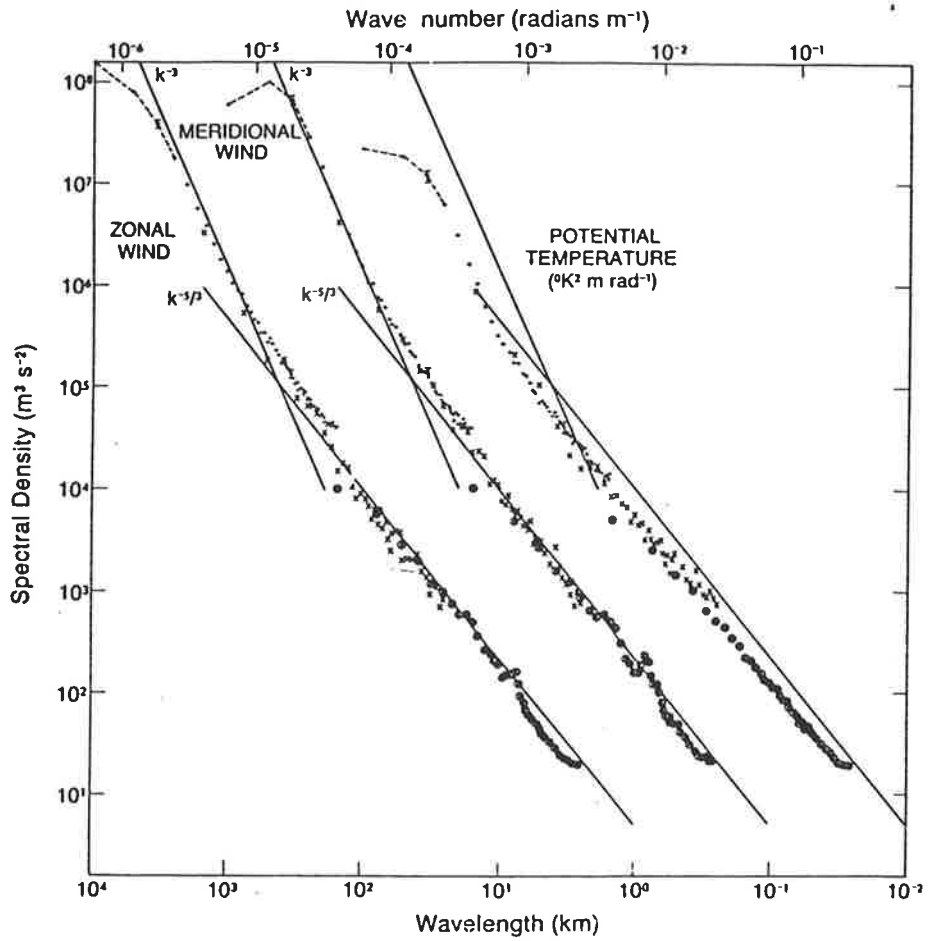

Figure 27: Horizontal wavenumber spectra of zonal wind, meridional wind, and potential temperature, as measured by sensors attached to commercial aircraft. The k^{-3} shape at large wavelengths appears to be due to enstrophy–cascading geostrophic turbulence [*Charney*, 1971]. The remaining $k^{-5/3}$ spectrum is thought to be produced by either gravity waves or quasi two–dimensional turbulence. The diagram is after *Nastrom and Gage* [1985].

Computation of the ground–based frequency spectra $S(\Omega)$ of these fluctuations has revealed that, while spectral peaks due to solar tides are often evident, the remainder of the spectrum has the appearance of "red noise", which is well–fitted by a power law relation Ω^{-p}, where p $\approx$ 1–2 (see Figure 7). A similar situation arises when vertical wavenumber spectra (see Figure 33) and horizontal wavenumber spectra (see Figure 27) are computed. Therefore if these fluctuations are produced by gravity waves, a superposition of many waves exists in general, and the single wave polarization relations cannot be applied to the data directly to test the gravity wave hypothesis.

Nevertheless, atmospheric perturbations evident in measurements are often inspected for oscillations which appear monochromatic, and single–wave theory is often used in subsequent analyses. The potential and realized misinterpretations that can result unless care is exercised in such studies are discussed in section 3.2.

As monochromatic gravity wave theory cannot be applied directly to analyze these fluctuations, much effort has been devoted to the development of a spectral theory of atmospheric gravity waves, which can then be applied to experimentally calculated spectra. An alternative theory has also been proposed which attributes these fluctuations to quasi two–dimensional turbulence (vortical modes), and a spectral theory for this hypothesis has also been developed for testing. Yet there are wide disparities in the conclusions of different experimental evaluations of these two hypotheses using spectral computation and inspection; some studies have supported the gravity wave model, others have supported a vortical mode interpretation, while still others have produced equivocal conclusions. Consequently, this problem is still an area of active research and debate. Its ultimate resolution is very important, as spatial and temporal power spectra are being used to draw conclusions from mesoscale measurements not only of winds, but also of temperature [see, e.g., *Shibata et al.*, 1988; *Gardner et al.*, 1989; *Manney and Stanford*, 1990], passive scalars [*Nastrom et al.*, 1986], and rainfall rates [*Crane*, 1990]. Subsequent analysis and inferred implications of these spectra are usually based on only one of the proposed models; the gravity wave model is currently preferred in the middle atmosphere [see, e.g., *Shibata et al.*, 1988; *Fritts et al.*, 1989; *Wu and Widdel*, 1989, 1990], whereas two–dimensional turbulence is often the only model considered when analyzing tropospheric spectra [see, e.g., *Gifford*, 1989; *Crane*, 1990], despite the uncertainties which have arisen when the predictions of both models have been compared with measurements [see, e.g., *Nastrom et al.*, 1987].

In section 3.3, we find that observations reveal, and the theories predict, that these spectra often vary in shape and intensity during the course of the measurements. When this occurs, simulations detailed in this section demonstrate that a significantly distorted final spectrum can result. This effect may provide at least a partial explanation as to why experimental evaluations of the motion field using spectra have not yet provided reproducible conclusions. To provide an independent alternative to spectral analysis of the motion field, a new fractional quantity, which should be less affected by sporadic changes in the spectral form during the measurement, is derived and presented as a further aid in evaluating the gravity wave/vortical mode question, .

3.2 Effect of Superposition on Measurements of Atmospheric Gravity Waves

3.2.1 Introduction

Present knowledge of the characteristics of atmospheric gravity waves in the height interval between 30 and $60km$ is fragmentary, with rockets and lidars being the only significant sources of information. Despite this, studies have revealed distinct local, seasonal, and latitudinal features in the wave field [e.g., *Hirota*, 1984; *Hirota and Niki*, 1985; *Shibata et al.*, 1986; *Hass and Meyer*, 1987; *Eckermann and Vincent*, 1989]. However, few explanations of these important observations have been put forward.

We shall focus here on some puzzling findings of gravity wave intrinsic frequency estimates made at these heights [*Hirota and Niki*, 1985]. The results indicated that quasi-monochromatic inertia gravity waves dominate in this region. Distributions of intrinsic frequencies peaked sharply at around 3 times the inertial frequency, essentially independent of latitude or season. This is at odds with recent theories of a broad spectrum of atmospheric gravity waves [e.g., *VanZandt*, 1982]. Other studies in the lower stratosphere have revealed that apparently monochromatic inertia gravity waves can often be observed [e.g., *Cadet and Teitelbaum*, 1979; *Maekawa et al.*, 1984; *Cot and Barat*, 1986]. Yet, if the spectrum of waves does indeed have a peak at 3 times the inertial frequency in the lower stratosphere, it seems difficult to imagine how this could be maintained into the upper stratosphere, where strong mean wind shears should substantially alter wave intrinsic frequencies and hence the position of this peak. If the peak found by *Hirota and Niki* [1985] is real, then the results seem to indicate that some "in situ" wave generation or enhancement process acts on a global scale, which selectively produces this peak in intrinsic frequency; alternatively, there may be shortcomings in the analysis technique advanced by *Hirota and Niki* [1985]. It is important that this observation becomes better understood, as it has recently been incorporated by *Yamanaka* [1990] into a global parameterization of gravity–wave effects in the middle atmosphere as a universal constant, which he has termed the "Hirota number".

The measurement technique used to infer these results is reexamined in this study. After careful inspection, one must conclude that the results are biased by wave superposition and do not reflect the true situation. Furthermore, it is argued that the results are rather an indicator of the azimuthal directionality in wave propagation. These assertions are supported by both computer simulations and derived analytical formulae. Finally, these new interpretations of the physical significance of the measurements are compared with a recent general circulation model simulation of wave production and propagation in the middle

atmosphere. To begin, however, it will be illustrated how analysis of individual wave events can be potentially hazardous and the results misleading, assuming that a broad spectrum of superposed gravity waves exists in the atmosphere.

3.2.2 "Monochromatic" Wave Events

Extended atmospheric observations have revealed a spectrum of waves in the atmosphere [e.g., *VanZandt*, 1982; *Dewan et al.*, 1984]. How, then, can one reconcile this with frequent "observations" of, and indeed analysis of, quasi-monochromatic waves [e.g., *Hirota and Niki*, 1985; *Devarajan et al.*, 1985; *Cot and Barat*, 1986; *Yamamoto et al.*, 1987; *Muraoka et al.*, 1987]?

A simulation was performed to investigate this. An analytical vertical wave number power spectral density $A(m) = E(1 + [m/m_*]^3)^{-1}$, which best models observed spectra [*VanZandt*, 1985; *Smith et al.*, 1987; see also section 3.3.2], was adopted, where E is a constant. Wave fields were then synthesized digitally from $A(m)$, using a simple Fourier–transform technique described by *Owens* [1978] and *Hocking* [1987*a*]. However, in this example a random phase was introduced between the real and imaginary components of each harmonic in Fourier space, and the transformed amplitude spectrum was Hermitian, in order to ensure a real wave field, with all the waves coaligned. In this way a series of differently superposed single-wave profiles were produced, while the energy distribution as a function of wave number in every profile was the same.

On inspecting these profiles, occasionally "monochromatic" wavelike oscillations arise merely by fortuitous superposition amongst a wave ensemble (Figure 28*a*). Indeed, even a flat spectrum with equal power spectral density over a range of wave numbers produces similar "monochromatic" events (Figure 28*b*), indicating that the occurrence of such events is independent of the spectral form. Typical wave profiles, which show no "monochromatic" events, are shown in Figures 28*c* and 28*d*.

Interpretation of oscillations in single atmospheric profiles as "monochromatic waves" must be considered dangerous in light of these findings. It is not clear whether it is valid to analyze a wave of this type by treating it as a monochromatic wave. It is possible that the oscillation arises because all the other Fourier components fortuitously sum to zero over this range, leaving one true wave, but caution should certainly be exercised in analysis. The dangers in subjective analysis of wind data have previously been illustrated by *Hines* [1966]. For example, it is well known that two superposing waves of wave numbers m_1 and m_2 and constant amplitude will produce a "beating" wave of wave number $(m_1 + m_2)/2$ and an amplitude envelope of wave number $(m_1 - m_2)/2$. Analysis of this beating pattern as a monochromatic

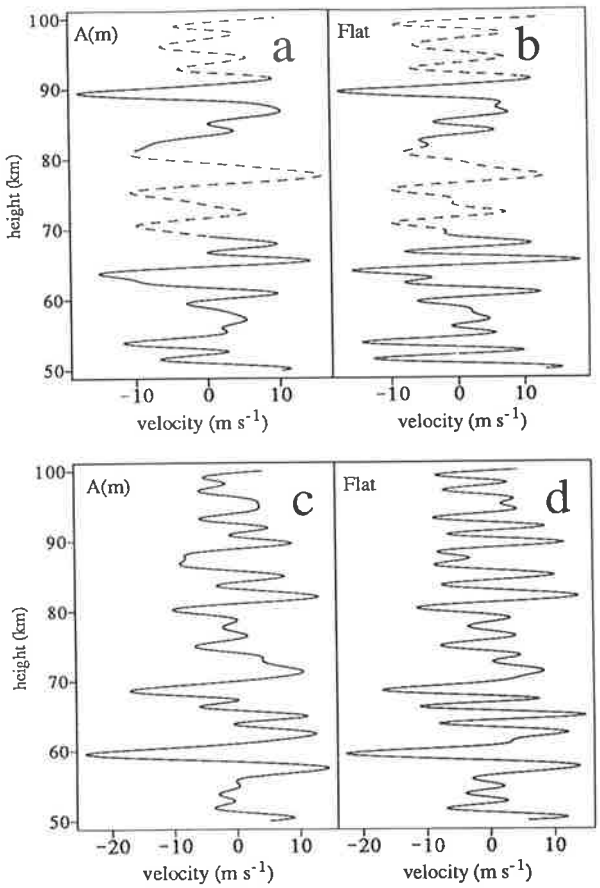

Figure 28: Horizontal velocity oscillations produced by waves with random phases and governed in amplitude by a power spectral density $P(m)$ in the 2- to 10-km vertical wavelength interval (containing 20 waves), and zero power spectral density outside this band. This models experimental rocket profiles [e.g., *Hirota*, 1984]. $P(\mathrm{m}) = A(m) = E\ (1 + [m/m_*]^3)^{-1}$ ($m_* = 2\pi/(5$ km)) was used in Figures 28*a* and 28*c*, and $P(m) = E'$ (flat) was used in Figures 28*b* and 28*d*, with E and E' scaled so that the variance was 100 m^2 s^{-2} in each case. The same phases were used in Figures 28*a* and 28*b* and in Figures 28*c* and 28*d*. "Monochromatic" oscillations are highlighted by dashed curves. The height scale is arbitrary.

event would clearly give erroneous wave number and amplitude information. Notice that the "monochromatic" oscillation between 70 and 80km in Figure 28*a* seems to grow with height somewhat, even though no growth with height is incorporated in the simulation, and so it must be, to some extent, a "beating" or coherence length effect. Superposition effects like this might explain why gravity waves often only appear to exist over one or two time cycles and only retain coherence over a few kilometers in the vertical [e.g., *Harper and Woodman*, 1977; *Miller et al.*, 1978].

One should not interpret these arguments as a refutation of all observations of monochromatic waves. The atmospheric gravity wave spectrum has enormous variability over small time scales, and individual large-amplitude waves certainly arise [e.g., *Balsley et al.* 1983, *Cot and Barat*, 1986; *Yamamoto et al.*, 1987; *Muraoka et al.*, 1987]. Instead, these results should encourage efforts to verify the coherence of such waves before subjecting them to an in-depth analysis. If this is not done, superposition effects

may lead one to infer individual wave amplitudes and wavelengths which are incorrect. Since measured wave parameters are often used to trace waves back through the atmosphere to their source and wave amplitude variation with height is used to investigate wave saturation effects, then clearly a potential for erroneous inferences exists. An example of the dangers in analyzing generally polychromatic wave motions will now be presented.

3.2.3 Inferences about f/ω

The horizontal wind velocity perturbations of a small amplitude gravity wave of intrinsic frequency ω, propagating in an unsheared, inviscid atmosphere with Coriolis parameter f, are governed by the following polarization relation [*Gossard and Hooke*, 1975]

$$V' = -i\frac{f}{\omega}U' \tag{20}$$

where U' and V' are the velocity components parallel with, and transverse to, the direction of horizontal propagation, respectively.

The formula implies an elliptically polarized wave motion in the horizontal with a frequency dependent ellipse axial ratio. *Hirota and Niki* [1985] (hereafter referred to as HN) realized that by measuring $|V'/U'|$, it was possible to determine f/ω and hence the intrinsic wave frequency ω. This is a potentially powerful way of measuring this important wave parameter, since ground-based measurements of wave frequencies (e.g., radars, lidars) are contaminated by the Doppler-shifting effects of the background winds.

Since in an experiment it is usual to measure the zonal (u') and meridional (v') oscillations, (20) must be expressed with respect to these coordinate axes, and so depends on u', v', and the wave propagation azimuth direction θ. Rather than infer θ, HN computed the ellipse vector length $r = (u'^2+v'^2)^{1/2}$, reasoning that the ratio of the maximum and minimum ellipse vectors defines the ellipse axial ratio and hence f/ω. Local maxima and minima of the wave motion were located from this quantity, and inner and outer "r" envelopes of the wave motion determined by interpolation. The ratio of the inner to outer envelope at each height was then taken to be a measure of f/ω.

Results from many meteorological rocket stations were collated into histograms and are reproduced in Figure 29. HN found that, virtually regardless of season or location, a most probable value of $f/\omega \approx 0.3$ results, and there is little probability of finding values of f/ω near 0 or 1. Only a slight but distinct decrease in peak value with decreasing latitude is evident. This result is despite the fact that changes in latitude alter the inertial frequency f and that the strong variation of the upper stratospheric background wind with altitude, latitude, and season must also change ω. *Yamanaka* [1990] proposed that

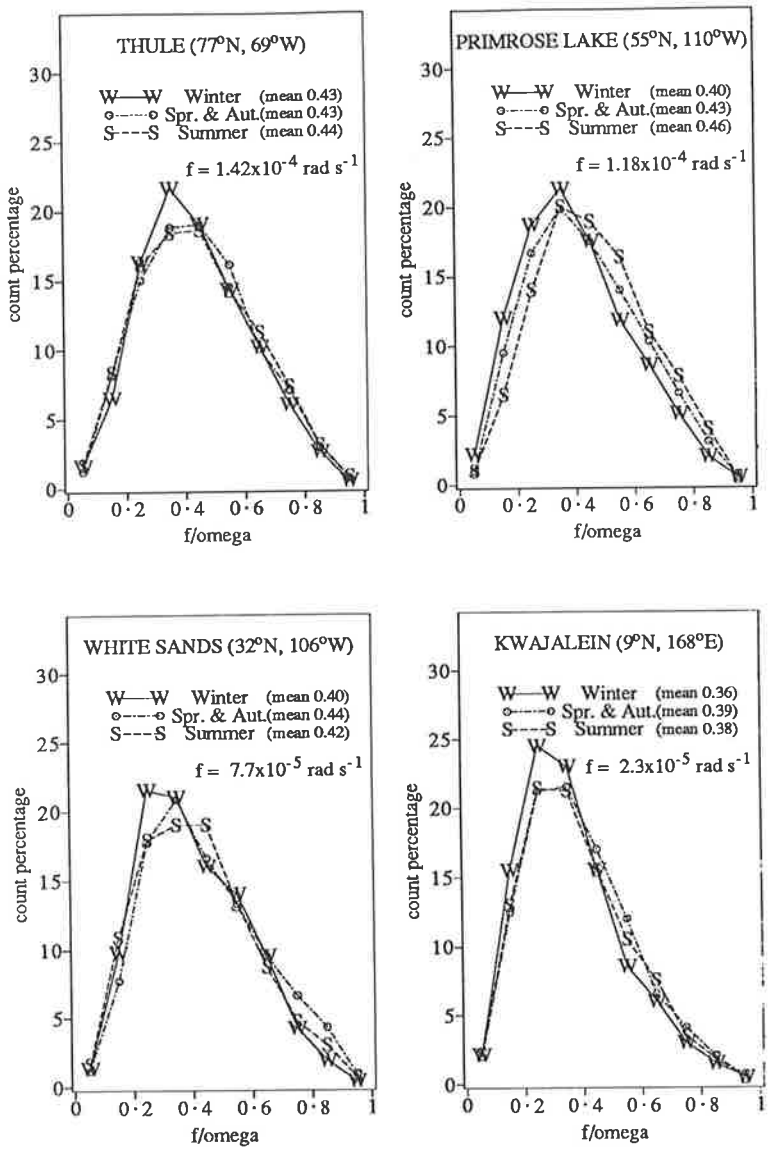

Figure 29: Histograms of f/ω for gravity waves between 30 and $60km$ from four different rocket stations, using all available data [after *Hirota and Niki*, 1985].

this indicated that f/ω was a global constant, which he labelled the "Hirota number", and *Yamanaka* incorporated this constant ratio of ~0.3 into a numerical parameterization of the gravity–wave field in the middle atmosphere.

It is proposed in the next section that these f/ω distributions are, in fact, an artifact of the method of analysis.

3.2.4 Explanation of Observations

Clearly, the HN analysis is perfectly valid for a single wave (assuming background wind shears are not significant). However, a spectrum of gravity waves exists in the atmosphere which, as has already been

shown, will produce important superposition effects. Therefore a random superposition of waves exists generally, and individual wave ellipses will be severely distorted by the remaining oscillations (e.g., Figure 1 of HN). As r_{min}/r_{max} must, by definition, lie between 0 and 1, one must ask whether the observed ratio of ~0.3 might result rather from the data's distribution. For example, even if the wave spectrum were composed entirely of high-frequency waves, there is no reason why wave superposition could not produce r_{min}/r_{max} ratios anywhere in the range 0–1.

To examine this possibility, a simple simulation was performed. Independent zonal and meridional real oscillations due to many linearly polarized waves with random phase and amplitude were synthesized, as in Figure 28. This independence means that the vector length $(u'^2+v'^2)^{1/2}$ has two degrees of freedom. These data are statistically equivalent to an azimuthally isotropic wave field, which has two degrees of freedom in vector length as a result of the independence of the polar coordinates (r,ϕ). These simulated profiles were then analyzed using the HN technique. The dashed curves in Figure 30 are the distributions of r, r_{min}, r_{max} and r_{min}/r_{max} produced in a typical simulation. Notice especially the similarity in form of the simulated r_{min}/r_{max} distribution (Figure 30*e*) and the experimental f/ω distributions in Figure 29. The peak at $f/\omega \sim 0.3$ should be particularly noted.

One can also demonstrate analytically that the peak near 0.3 is spurious. It is well known that a random superposition of phasors produces a resultant phasor whose vector length is Rayleigh distributed [e.g., *Beckmann*, 1962]. So, for a random superposition of gravity waves, u' and v' will have a Normal distribution, $r^2 = (u'^2+v'^2)$ will have a χ^2 distribution with ν equal to two degrees of freedom, denoted $p^{\nu}_{\chi}(r'^2)$, and r will have a corresponding Rayleigh distribution, denoted $p^{\nu}_{R}(r')$ (Figure 30*a*).

$$p^{\nu}_{R}(r') = \frac{2r'}{2^{\nu/2}\Gamma(\nu/2)} r'^{(\nu-2)} e^{-r'^2/2} = 2r'\, p^{\nu}_{\chi}(r'^2) \tag{21}$$

where $r' = r/\sigma$, and $\Gamma(x)$ is the gamma function.

Since f/ω is inferred from r_{min}/r_{max}, it is the latter quantity one must consider. Let us initially assume that like r, r_{min} and r_{max} are Rayleigh distributed with mean square values σ^2_{min} and σ^2_{max}. The ratio $(r_{min}/r_{max})^2$ will then have an F distribution, with (ν_1=2,ν_2=2) degrees of freedom [*Johnson and Kotz*, 1970], denoted $p^{\nu_1,\nu_2}_{F}(t)$.

$$p^{\nu_1,\nu_2}_{F}(t) = \frac{1}{B(\nu_1/2,\nu_2/2)} \frac{t^{(\nu_1-2)/2}}{(1+t)^{(\nu_1+\nu_2)/2}} \tag{22}$$

where $t = (r_{min}/r_{max})^2(\sigma_{max}/\sigma_{min})^2$, and $B(x,y)$ is the beta function.

Figures 30*b* and 30*c* overlay simulated distributions of r_{min} and r_{max}, respectively, with Rayleigh distributions (using σ^2 values evaluated in the simulation). The simulated and analytical curves agree

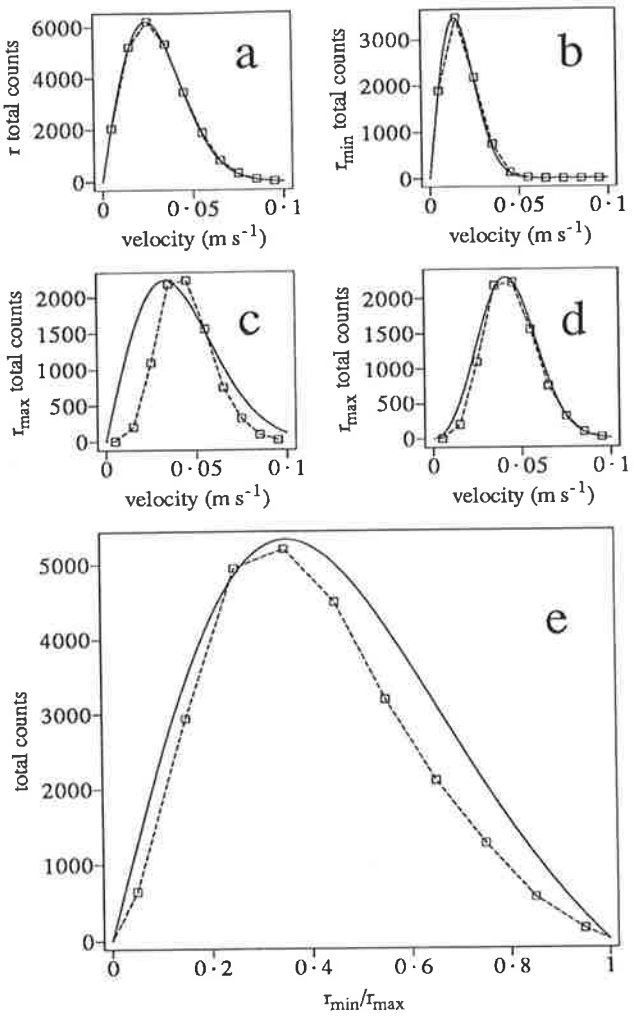

Figure 30: Simulated (dashed curve) and analytical (solid curve) distributions of (*a*) r; (*b*) r_{min}; (*c*) and (*d*) r_{max}; and (*e*) r_{min}/r_{max}, where $r = (u'^2 + v'^2)^{1/2}$. See text for further details.

well for r_{min} but poorly for r_{max}. This poor agreement for r_{max} is not surprising, because one must expect this distribution to be offset to the right somewhat. Indeed, apart from an x axis shift, the simulated r_{min} and r_{max} distributions are similar in form and so the r_{max} distribution is better described by a noncentral Rayleigh distribution, denoted $p_R^{\nu,\lambda}(r)$, where λ is the square of some (constant) offset from zero along the x axis [*Johnson and Kotz*, 1970].

$$p_R^{\nu,\lambda}(r') = 2r' \sum_{j=0}^{\infty} \left(\frac{(\lambda/2)^j}{j!} \right) e^{-(\lambda/2)} \left[p_\chi^{\nu+2j}(r'^2) \right] \tag{23}$$

This formula holds for a constant offset λ, whereas in this application the offset itself has a probability distribution (Figure 30*b*). Despite this, on fitting (23) to the simulated r_{max} distributions, one obtains close agreement (Figure 30*d*). Consequently, the ratio $(r_{min}/r_{max})^2$ should then have a noncentral F

distribution, with (ν_1=2,ν_2=2) degrees of freedom [*Johnson and Kotz*, 1970], denoted $p_F^{\nu_1,\nu_2,\lambda}(t)$.

$$p_F^{\nu_1,\nu_2,\lambda}(t) = \sum_{j=0}^{\infty} \left(\frac{(\lambda/2)^j}{j!} \right) e^{-(\lambda/2)} \left[p_F^{\nu_1,\nu_2+2j}(t) \right] \tag{24}$$

Using conservation of probability (i.e., $P(A^2)\ d(A^2) = P(A)\ dA$), one then finds that the ratio $\epsilon = r_{min}/r_{max}$ is distributed as $Q(\epsilon)$, where

$$Q(\epsilon) = 2\epsilon\ p_F^{\nu_1,\nu_2,\lambda}\left[\epsilon^2\ (\sigma_{max}^2/\sigma_{min}^2)\right] \tag{25}$$

Calculations of r_{min}/r_{max} necessarily lie between 0 and 1. So the distribution value produced at ϵ = ϵ^* will be proportional to $Q(\epsilon^*)$ + $Q(1/\epsilon^*)$, since a value of ϵ greater than 1 will be treated as its reciprocal in the analysis. Since $P(1/A)$ = -A^2[$P(A)$], we finally derive the form of the f/ω distribution, $P(f/\omega)$, where K is a normalization constant.

$$P(f/\omega) = K\ (1 - (f/\omega)^2)\ Q(f/\omega) \tag{26}$$

Figure 30*e* overlays both the simulated f/ω distribution (from analysis of simulated data) and the analytical distribution (26), using λ, σ_{min}^2, and σ_{max}^2 values from the distributions in Figures 30*b* and 30*d*. Notice the similarity in shape amongst the simulated, analytical, and experimental (Figure 29) distributions.

Thus it is clear that the shape of the curves derived by HN and the peak at $f/\omega \sim 0.3$ are not necessarily indicative of the major gravity waves. Indeed, the same shape would even arise if the atmospheric gravity wave spectrum comprised only linearly polarized waves, and waves with $f/\omega \sim 0.3$ did not exist! While it may be that some of the profiles analyzed by HN provided information on monochromatic oscillations, it seems clear that the combined results in Figure 29 are a statistical manifestation of a generally superposed wave field.

3.2.5 Mathematical Implications

The illustrated sole dependence of these f/ω distributions on the statistical parameters λ, σ_{min}^2, and σ_{max}^2 has important implications. In particular, any horizontal anisotropy in wave propagation directions would effectively reduce the degrees of freedom ν_1 and ν_2, which in turn alters σ_{min}^2 and σ_{max}^2 and produces a change in shape of the distributions.

To investigate this possibility, two simulations were performed. In the first, independent zonal and meridional oscillations were produced in the manner previously outlined. A variable attenuation factor α was applied to the meridional components of oscillation, so that the degrees of freedom were effectively

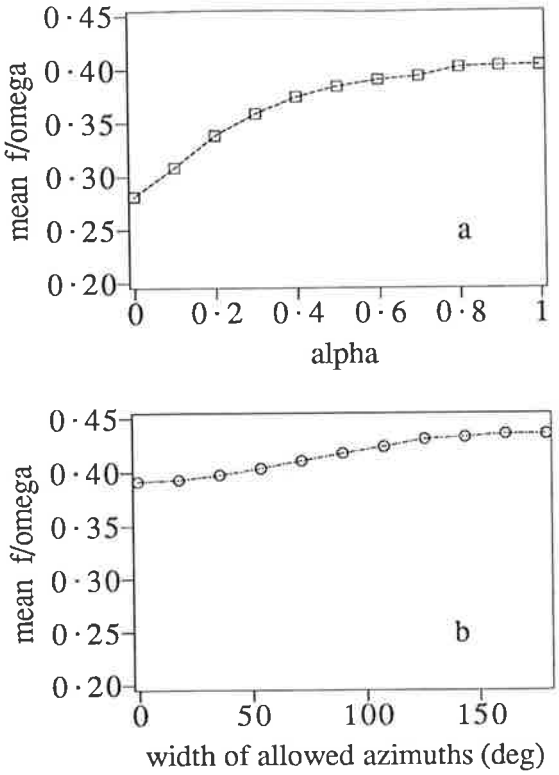

Figure 31: Graphs of the change in the mean ratio $<f/\omega> = <r_{min}/r_{max}>$ with increased horizontal directionality, (a) using attenuation α of random meridional oscillations and (b) a numerical model in which gravity waves have a restricted width of allowed azimuths equal to $\beta(180°)$. See text for details of the model used in Figure 31b.

reduced, and the HN analysis was then performed. Since the unattenuated profiles are statistically equivalent to an azimuthally isotropic wave field, this process is equivalent to making the wave azimuth distribution progressively more anisotropic. From the resulting distributions, a mean value $<f/\omega> = \int(f/\omega)P(f/\omega)\ d(f/\omega)$ was evaluated. A mean value rather than the peak value was used to allow more accurate comparison with the distributions in Figure 29. Figure 31a plots the change in $<f/\omega>$ with attenuation α.

This simulation assumes that all the waves are linearly polarized along the direction of propagation. In fact, a secondary oscillation orthogonal to the direction of propagation is predicted by (20). Consequently, a more physically realistic simulation was performed using a gravity wave computer model. In this model a grid was set up in vertical wave number and intrinsic frequency space, and each point on the grid was defined an individual wave, except that the wave azimuth was, at this stage, undefined. Wave amplitudes were assigned by analytically integrating the two-dimensional wave spectrum [*VanZandt*, 1985; *Smith et al.*, 1987] over a rectangle centered on the relevant grid point and with dimensions equal to the grid spacing. Each wave was given a random starting phase and was allowed to propagate in time and space. All of the waves propagated energy upwards ($m < 0$), consistent with observations [e.g., HN; *Eckermann*

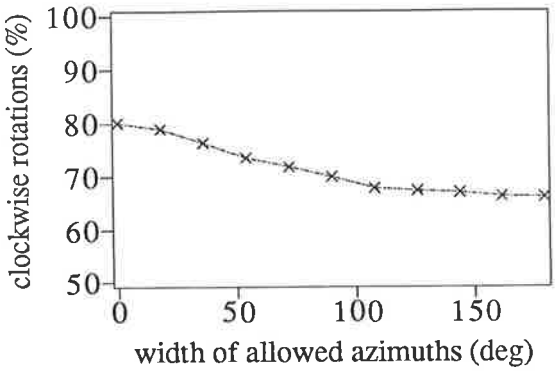

Figure 32: Variation in the percentage of clockwise wave vector rotations (northern hemisphere) with azimuthal directionality for an ensemble of 128 waves produced by a numerical gravity wave model, as used to produce Figure 31*b*.

and Vincent, 1989]. An isothermal 250 K atmosphere with no mean wind was used in this study. To investigate isotropy effects, each wave was also assigned a random azimuth direction between 0° and $\beta(180°)$, where β was between 0 and 1. In this way, azimuthal wave propagation had a "box car" polar diagram of width $\beta(180°)$. Resulting wave fields were analyzed using the HN method and $<f/\omega>$ values obtained as in the first simulation. The change in $<f/\omega>$ as a function of $\beta(180°)$ is shown in Figure 31*b* and may be compared with the mean f/ω values in Figure 29.

Using this gravity wave model, each simulated profile was also stored and analyzed for its direction of wave vector rotation, using the change in the ellipse vector phase angle with height, as described by HN. Using this technique, HN found appreciable anisotropy in the direction of wave vector rotation, consistent with the majority of the wave energy propagating from lower altitudes. Despite extensive superposition, we find, using the gravity wave model, that 65–70% of the rotations are clockwise in the mid-latitude northern hemisphere for a azimuthally isotropic field of 128 waves, consistent with the HN results. If one either decreases the number of waves (i.e., if one reduces the superposition) or if one introduces some azimuthal directionality, this clockwise percentage increases further. An example of the variation with azimuthal directionality is shown in Figure 32.

3.2.6 Physical Implications

Inspection of (23)–(26) reveals that the distributions depend only on the parameters λ, σ^2_{min}, and σ^2_{max}. Hence inferences of dominant wave frequencies from such results are not sustainable. Rather, the values are a measure of the horizontal localization in direction of the oscillations (Figure 31). With this new perspective, Figure 29 implies greater directionality in azimuthal wave propagation with decreasing northern latitude. It also reveals more alignment during winter than in the other seasons, which is consistent with

increased critical level filtering by the strong wintertime zonal wind jets.

Some tentative corroboration for these inferences of wave directionality comes from a global gravity wave simulation using the Geophysical Fluid Dynamics Laboratory (GFDL) "SKYHI" general circulation model [*Miyahara et al.*, 1986]. All of the rocket stations in the HN study lie within a relatively narrow longitude interval, with eight of the 12 lying between 60° and 120°W. In this longitude zone, *Miyahara et al.* [1986] found a strong stratospheric $\overline{u'\Omega'}$ flux, with Ω' equal to vertical pressure velocity, a pressure weighted vertical velocity expressed in log-pressure coordinates [*Miyahara et al.*, 1986], peaking at -2 x 10^{-5} m s^{-1} mbar s^{-1} at latitudes around 50°-60°N. At the equatorial locations of the HN study (Kwajalein and Ascension Island), a strongly positive $\overline{u'\Omega'}$ flux of 4 x 10^{-5} m s^{-1} mbar s^{-1} was produced in the stratosphere, twice as large as the peak at 50°N. However, an earlier study by *Hirota* [1984] revealed that wave amplitudes around 50°N greatly exceed those at either Kwajalein or Ascension Island. This can only mean one of two things. Either the wave field at the tropical stations is far more directional than at the mid-latitude stations, which is precisely the result that we inferred earlier, or a much larger $\overline{v'\Omega'}$ flux occurs at 50°N than at the equatorial sites. Unfortunately, meridional stress terms are not presented by *Miyahara et al.* [1986], nor in a more recent simulation with the Goddard Institute for Space Studies (GISS) model by *Rind et al.* [1988]. Mesospheric measurements from Saskatoon (52°N, 107°W) do suggest some preference for a north-south alignment during winter [*Manson and Meek*, 1988]. However, Figure 17 of *Miyahara et al.* [1986] shows more sign of meridional wave propagation at the equatorial stations than at the mid-latitude stations. Similarly, the wintertime scatter plots of *Hirota* [1984] show more indication of a preferred meridional alignment at Kwajalein (9°N, 168°E) than at Thule (77°N, 69°W). This tends to favor our interpretation of greater equatorial directionality, though clearly only direct measurement can confirm this.

Furthermore, we note from Figure 29 that the oscillations at Kwajalein exhibit even more directional localization than is allowed for in Figure 31*b*. So not only is the wave field here very directional, but there is less energy in the V' oscillations than theoretically predicted for a representative model spectrum of gravity waves. This means from (20) that, rather than a predominance, there is a relative dearth of inertia gravity waves at this location. This means that there is a low-frequency dip in the equatorial gravity wave intrinsic frequency spectrum, so that, in the end, the HN results have told us something about the intrinsic frequency of gravity waves. This result seems to be consistent with other observations that Kelvin wave and mixed Rossby-gravity wave motions are prevalent in the equatorial stratosphere [e.g., *Wallace*, 1973; *Hirota*, 1978; *Devarajan et al.*, 1985], since these fundamentally different types of waves are physically constrained to discrete horizontal directions, as opposed to simple gravity waves, giving

rise to a very directional wave field. However, there is strong theoretical and observational evidence to suggest that mixed Rossby-gravity waves only occur in the lower stratosphere, due to radiative damping [e.g., *Hirota*, 1980], which favors an interpretation in terms of Kelvin waves alone.

Some experimental support for these assertions comes from the fact that the clockwise energy percentages calculated by HN at the equatorial stations (~65%) are significantly less than those at more northward latitudes (~80–90%). This implies either an azimuthally isotropic equatorial wave field (Figure 32), which contradicts our earlier inferences, or a lack of equatorial inertia gravity wave energy compared to that at more northward latitudes. Notice also that the 80–90% clockwise rotation found by HN at the nonequatorial sites indicates that superposition in the real atmosphere is less severe than in the 128-wave simulation used to produce Figure 32, as one might reasonably expect.

Reanalysis of f/ω distributions can tell us nothing about directions of propagation, only the degree of directionality. At the tropical locations, *Miyahara et al.* [1986] found distinct indications of meridional gravity wave propagation from the low-latitude southern troposphere into the low to mid-latitude northern stratosphere, produced by the filtering action of easterly planetary wave winds. The study of *Miyahara et al.* [1986] simulated only short time intervals in December, January, and February. The invariance with season of the f/ω distributions at Kwajalein suggests that similarly directional gravity wave propagation may occur all the year round, although Kelvin wave and mixed Rossby-gravity wave motions must also be considered.

Further investigations into the horizontal propagation directions of stratospheric gravity waves are clearly needed, in order to compare with the three-dimensional wave propagation being found in global simulations. *Eckermann and Vincent* [1989] inferred highly directional south–eastward wave propagation during summer. General circulation model simulations during the southern summer [*Miyahara et al.*, 1986] also produce distinct south-eastward wave propagation from the equatorial troposphere into the middle atmosphere above Australia. Since these simulations have so far only produced climatologies of the $\overline{u'\Omega'}$ stress term (a partially cancelling quantity), more detailed knowledge of horizontal wave directionality will also be needed in order to make more meaningful comparisons amongst these results and the mean u'^2 and T'^2 values that are most easily calculated in observational studies. These and other issues raised in this study are addressed by observational analysis in chapter 6.

3.2.7 Conclusions

Wave superposition can lead to, and has led to, erroneous inferences concerning the occurrence of seemingly "monochromatic" gravity waves in the middle atmosphere. The need for caution in analyzing such

events has been noted. In particular, we have addressed some recent measurements of wind structure made by rocket-borne techniques, which were analyzed in order to determine gravity wave intrinsic frequencies. We have shown that the analysis method, based on single wave assumptions, does not in fact supply information about intrinsic frequencies because of superposition effects, but it can, however, be reinterpreted to give information about the azimuthal directionality in wave propagation. A reanalysis reveals more wave directionality in winter than in other seasons at all latitudes and a highly directional wave field at the tropics. The equatorial directionality exceeds theoretical predictions for gravity waves and suggests a dearth of inertia gravity waves at the tropics, with Kelvin wave and/or mixed Rossby-gravity wave motions being more prevalent.

3.3 Effects of Nonstationarity on Spectral Analysis of Mesoscale Motions in the Atmosphere

3.3.1 Introduction

Computation of power spectra has become standard in the analysis of mesoscale motions within the atmosphere and ocean. In the atmosphere, advances in ground-based remote sensing techniques have facilitated spectral investigations of velocity, temperature and density fluctuations over a wide spatial and temporal range. Many such measurements have been made at different times of the year and at different locations, and they have revealed reproducible shapes and similar intensities [see, e.g., *Balsley and Carter*, 1982; *Vincent*, 1984; *Meek et al.*, 1985*b*; *Fritts and Chou*, 1987; *Fritts et al.*, 1988*a*; *Shibata et al.*, 1988; *Fritts et al.*, 1990; *Kwon et al.*, 1990]. Much theoretical effort has been directed towards understanding the dynamics which give rise to these observed spectra, and two different processes have been proposed.

VanZandt [1982] suggested that the spectra are produced by internal gravity wave motions. Following the successful analysis of similar oceanic spectra by *Garrett and Munk* [1972, 1975], *VanZandt* [1982] presented empirical analytical relations which best modelled the observed spectra, while ensuring consistency with the dispersion relation for gravity waves. This approach has been continued and updated by *Sidi et al.* [1988]. On the other hand, *Gage and Nastrom* [1985, 1986] have argued that quasi two-dimensional turbulence, or the vortical mode of motion as it is now often interpreted [see, e.g., *Müller et al.*, 1988; *Gage and Nastrom*, 1988], is responsible for these spectra and the associated mesoscale variance.

Both theories predicts the spectral shapes which should be observed if either process is the more

dominant in energy [see, e.g., *Gage*, 1979; *VanZandt*, 1982; *Scheffler and Liu*, 1986; *Dewan and Good*, 1986; *Fritts and VanZandt*, 1987; *Smith et al.*, 1987; *Gage and Nastrom*, 1988]. Despite this, comparisons of spectral measurements with the predictions of each theory have been equivocal. While it now seems generally accepted that gravity wave motions are responsible for the vertical velocity frequency spectra measured in light wind conditions [see, e.g., *Ecklund et al.*, 1986], in stronger wind conditions and in the horizontal there is enough ambiguity in the comparisons that neither process can yet be accepted as dominant or dismissed as inconsistent with observations This superficially suggests that both types of motion coexist, as postulated by *Lilly* [1983], but that the relative and absolute contributions to the total mesoscale variance are variable, or *nonstationary*.

Analysis of the spectra in terms of gravity waves has generally been more successful, and so this interpretation has gained wider acceptance. However, the physical processes that act on the gravity wave field to produce the observed spectral shape and intensity have yet to be agreed upon. The ability of non-linear interactions amongst a wave ensemble to produce and maintain the oceanic spectrum has been extensively investigated (see the review of *Müller et al.* [1986]). In the atmosphere, however, wave amplitude saturation due to convective instability is now thought to be responsible for much of the spectral structure, although other mechanisms have also been considered (see reviews by *Fritts* [1984], *Fritts* [1989] and *Dunkerton* [1989]). *Dewan and Good* [1986] and *Smith et al.* [1987] have used a linear gravity wave saturation hypothesis to derive a theoretical vertical wavenumber spectrum for horizontal velocity fluctuations in the atmosphere. This theory, if correct, could have important applications in parameterizing the effects on the background flow of a full spectrum of dissipating gravity waves [see, e.g., *Fritts*, 1989; *VanZandt and Fritts*, 1989].

Spectra computed from measurements have been used to test this idea too, and again the degree of correspondence with the theory has been variable. While the model spectrum agrees very well with some measurements [*Dewan et al.*, 1984; *Fritts and Chou*, 1987; *Fritts et al.*, 1988*a*; *Wu and Widdel*, 1989, 1990], there are other experimentally determined vertical wavenumber spectra where the agreement is less marked, and so these spectra appear to deviate somewhat from the model [see, e.g., *Vincent*, 1984; *Hass and Meyer*, 1987; *Maekawa et al.*, 1987; *Shibata et al.*, 1988; *Eckermann and Vincent*, 1989].

While dynamical theories which can explain the observed atmospheric spectra have been actively pursued, possible sources of contamination that might affect such spectral measurements have not been investigated in depth. Nevertheless many such sources have been identified in measurements, such as the sampling and digitization used in recording the data [see e.g., *Kristensen and Kirkegaard*, 1987; *Moore et al.*, 1988; *Kaimal et al.*, 1989], and many different instrumental effects [see, e.g., *Miller*, 1969; *Fukao et*

al., 1988*a*, *b*; *May et al.*, 1988; *Sidi et al.*, 1988; *Eckermann and Vincent*, 1989]. In addition, the motion spectra themselves vary in response to environmental factors, such as background wind speed [see, e.g., *Ecklund et al.*, 1986; *Scheffler and Liu*, 1986; *Fritts and VanZandt*, 1987] and atmospheric stability [see, e.g., *Smith et al.*, 1987; *VanZandt and Fritts*, 1989].

Whatever the actual dynamics are, it is clear from observations that the resulting mesoscale variance often changes appreciably on both short and long time scales [see, e.g., *Hirota*, 1984; *Meek et al.*, 1985*b*; *Vincent and Fritts*, 1987; *Fritts and Chou*, 1987; *Cornish*, 1988; *Fukao et al.*, 1989*a*; *Fritts*, 1989]. The variance also increases systematically with altitude [see, e.g., *Balsley and Carter*, 1982; *Hirota and Niki*, 1985; *Balsley and Garello*, 1985] and exhibits appreciable geographic variability [see, e.g., *Hirota*, 1984; *Gage and Nastrom*, 1986; *Nastrom et al.*, 1987; *Fritts et al.*, 1989; *Jasperson et al.*, 1990]. This means that spatial and temporal series of experimentally sampled data, from which spectra are computed, must indeed be *nonstationary*; that is, the variance, and hence the spectral form, is not the same at all points in the data series. Although "nonstationarity" is usually associated with time series analysis, it will be used hereafter to describe the variability evident in both spatial and temporal data series.

It is well known that nonstationarity can change the spectral shape when data are Fourier transformed, yet the possible effects on spectral computations of nonstationary characteristics evident in mesoscale motion data have not been adequately addressed. Since the shape and intensity of measured spectra are now being used to evaluate theories about the nature of these fluctuating dynamics, investigation of possible nonstationary distortion of computed spectra is warranted.

To address these issues, the specific problem of nonstationarity with altitude of the model vertical wavenumber spectrum of *Smith et al.* [1987] is first considered in section 3.3.2. The insights gained here are then applied in section 3.3.3 to the general problem of spectral analysis of mesoscale motions in the frequency and horizontal wavenumber domain. In section 3.3.4 a fractional measure, which remains stationary even when the variance is nonstationary, is developed and presented as being potentially useful in experimentally evaluating whether gravity waves or vortical modes are the more energetic fluctuations in generally nonstationary data.

3.3.2 Altitude Nonstationarity of the Vertical Wavenumber Spectrum

To investigate the general problem of spectral nonstationarity, we shall first consider a specific one; the change of form with altitude of the model vertical wavenumber spectrum proposed by *Smith et al.* [1987]. This is done for two main reasons. The first is that height variation of this spectrum has a regular exponential form, and so is amenable to analysis. Secondly, the wave saturation theory

used to derive the model spectrum of *Smith et al.* [1987] is important in its own right, and requires experimental corroboration. Therefore, any contamination of the spectral measurements which might affect the comparisons needs to be investigated.

Background Theory

Consider a gravity wave, produced at ground level with a peak horizontal velocity amplitude u'_0 and vertical wavenumber m_0, which propagates upwards and zonally into the middle atmosphere. Assuming the wave has neither a very low nor very high intrinsic frequency, then on propagating to some altitude z, the peak wave amplitude $u'_{peak}(z)$ is given approximately by the expression [*Lindzen*, 1981; *Schoeberl*, 1985]

$$u'_{peak}(z) = u'_0 \left(\frac{m}{m_0}\right)^{1/2} e^{z/2H_\rho}, \tag{27}$$

where

m = vertical wavenumber, and

H_ρ = density scale height.

A wave therefore grows in amplitude exponentially as it propagates vertically into the less–dense upper atmosphere. The wave amplitude may eventually become so large that it produces a vertical temperature gradient which exceeds the adiabatic lapse rate of the background atmosphere, and so the wave becomes convectively unstable. This occurs when [see, e.g., *Fritts*, 1984]

$$u'_{peak}(z) \geq \mid \bar{U} - c \mid \approx N/m, \tag{28}$$

where

$\bar{U}$ = background horizontal wind speed,

c = ground-based horizontal phase speed, and

N = Brunt-Väisälä frequency.

Saturation theory, in its simplest form [see, e.g., *Lindzen*, 1981; *Fritts*, 1984, 1989; *Dunkerton*, 1989], predicts that the wave does not overturn and dissipate completely at this altitude. Instead, only sufficient turbulent diffusion is generated to maintain the wave amplitude $u'_{peak}(z)$ at the instability threshold N/m. *Dewan and Good* [1986] argued that this implies a saturated vertical wavenumber power spectrum of u' fluctuations, designated hereafter F_u(m), proportional to N^2/m^3. *Smith et al.* [1987] extended this single wave theory to include a general superposition of both saturated and unsaturated waves. They arrived at the following quasi-empirical expression for the power spectrum.

$$F_u(m) = \frac{N^2}{6m_*^3} \frac{1}{[1 + (m/m_*)^3]}. \tag{29}$$

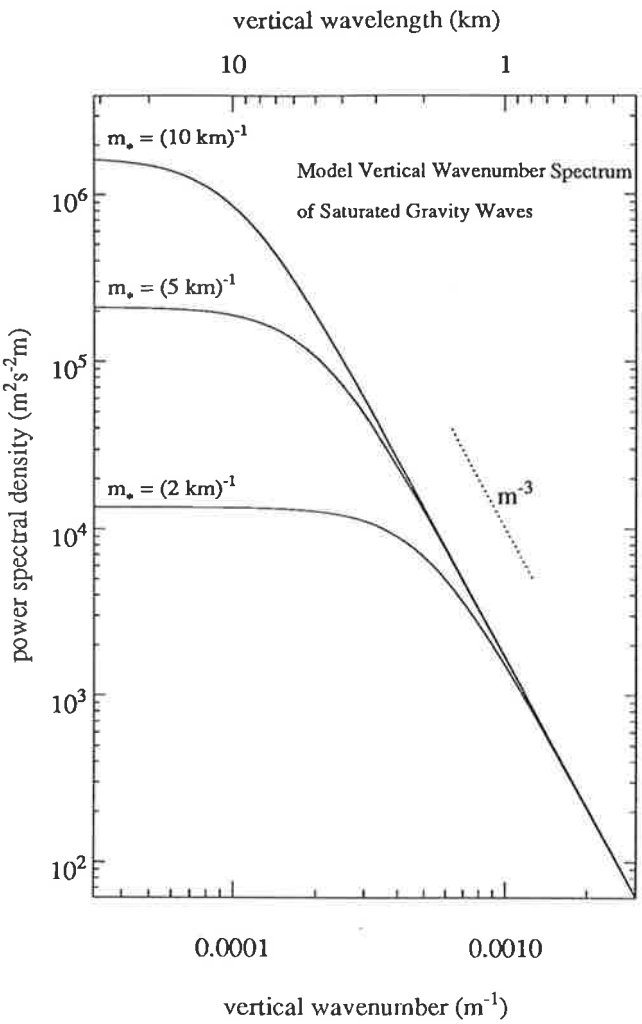

Figure 33: The model vertical wavenumber power spectrum of horizontal velocity fluctuations produced by gravity waves, due to *Smith et al.* [1987], evaluated using $m_* = (2km)^{-1}$, $(5km)^{-1}$, and $(10km)^{-1}$. These values of m_* are typical of the lower, middle, and upper stratosphere respectively. Note the variation of the spectrum with $m_*(z)$.

This model spectrum is illustrated in Figure 33. The waves which have wavenumbers greater than m_* are saturated and produce an m^{-3} spectrum, whereas waves with wavenumbers less than m_* are unsaturated, produce a flat spectrum, and grow in amplitude approximately as $e^{z/2H_\rho}$. Hence there is a convenient partitioning of the saturated and unsaturated waves in the vertical wavenumber domain. The analytical function (29), however, is to some extent arbitrary. The formula itself was originally used by *Desaubies* [1976] to model the oceanic wave spectrum. It was later adopted by *VanZandt* [1985] and *Smith et al.* [1987] for the atmospheric spectrum because it most closely represents the observed spectral shape of the transition region between the saturated and unsaturated spectrum, which theory currently makes no prediction about. Nevertheless, different analytical formulae can be, and have been, used [see, e.g., *VanZandt*, 1982; *Sidi et al.*, 1988; *VanZandt and Fritts*, 1989].

The flat nature of the unsaturated spectrum is also somewhat arbitrary, and is chosen again because it corresponds with the observations. *Fukao et al.* [1989a] showed that the wave amplitude variation (27) implies a flat unsaturated spectrum for a constant u_0', just as (28) implies an m^{-3} spectrum. However, *VanZandt and Fritts* [1989] argued that the unsaturated portion of the spectrum should have a positive spectral index, so that the vertical flux of wave action remains finite. In any case, in the real atmosphere source transience will always make this part of the spectrum rather variable in form, and so any functional fit of the unsaturated spectrum can never be adequate for every measurement.

The variance of the wave field $\overline{u'^2}$ is found, according to Rayleigh's theorem [*Bracewell*, 1978], by integrating this spectrum.

$$\begin{aligned}\overline{u'^2(z)} &= \int_{m_1}^{m_2} \frac{N^2}{6m_*^3(z)} \frac{1}{1+[m/m_*(z)]^3} dm \\ &= \frac{N^2}{6m_*^2(z)} \left[\frac{1}{6} \ln \left(\frac{(\mu+1)^2}{\mu^2-\mu+1} \right) + \frac{1}{\sqrt{3}} \arctan \left(\frac{2\mu-1}{\sqrt{3}} \right) \right]_{m_1}^{m_2}, \end{aligned} \tag{30}$$

where $\mu = m/m_*(z)$, and where m_1 and m_2 define the wavenumber range. On integrating over all wavenumbers ($m_1 = 0$ to $m_2 = \infty$), one finds $\overline{u'^2} \approx N^2/5{m_*}^2$. This total wave variance is assumed to grow with height as e^{z/H_E}, where $H_E > H_\rho$ due to the non-growth with height of the saturated waves. This in turn implies

$$m_*(z) \approx m_*(z_0) e^{-(z-z_0)/2H_E}, \tag{31}$$

indicating that, with increasing altitude, a greater fraction of the wave field ($m > m_*$) becomes saturated. As most of the variance is concentrated around m_* [see, e.g., *Smith et al.*, 1987], this also implies that the vertical wavelength of the most energetic waves in the spectrum increases with height.

This model spectrum, however, is unusual, in so far as it holds only at a given height, since m_* is height dependent. Yet the very process of obtaining a vertical wavenumber spectrum involves transforming data over a prescribed height range. Clearly then, if one were to compute a vertical wavenumber spectrum from data over a large altitude range, one would expect this change in spectral form with height (see Figure 33) to produce a resultant spectrum somewhat different to (29). The effect has been considered for a single wave propagating in the sodium layer by *Gardner and Voelz* [1985, 1987] and within the neutral atmosphere by *Gardner et al.* [1989]. A detailed consideration of the problem in a general sense will be attempted here for a full spectrum of waves. Before introducing a model used to accurately simulate the full effects, however, a brief outline of the problem will be given.

Formulation of the Problem

Let $v'(z)$ be a height profile of wave fluctuations which are governed by the model spectrum (29) as evaluated at one height z_1 (so that $v'(z)$ is stationary), and let $V(m)$ be its Fourier transform, where $V(m)$ is generally complex. Now we define a more realistic wave profile $p'(z)$ which grows in amplitude with height as $a(z)$, such that $p'(z) = a(z)v'(z)$. If the Fourier Transform of $a(z)$ is $A(m)$, then it is well known that the Fourier Transform of $p'(z)$, designated $P(m)$, is given by the *convolution* of $A(m)$ with $V(m)$ [see, e.g., *Bracewell*, 1978], here denoted $A(m) \otimes V(m)$. Thus the measured spectrum $|P(m)|^2$ will generally be different to the model spectrum $|V(m)|^2$ given by (29).

Consider first a case where $m_* \to \infty$, so that all the constituent waves are unsaturated and grow in amplitude with height as $a(z) = e^{z/2H_\rho}$. The Fourier transform $A(m)$ of this exponential growth over an altitude range $z_s = z_2 - z_1$ (where z_2 and z_1 are the upper and lower height limits of the measurement, respectively) is

$$\begin{aligned} A(m) &= \frac{2}{(1/2H_\rho)^2 + m^2}\left[\left(\frac{1}{2H_\rho}\sinh(z_s/4H_\rho)\cos(mz_s/2) + m\cosh(z_s/4H_\rho)\sin(mz_s/2)\right)\right. \\ &\quad \left. +i\left(m\sinh(z_s/4H_\rho)\cos(mz_s/2) - \frac{1}{2H_\rho}\cosh(z_s/4H_\rho)\sin(mz_s/2)\right)\right] \qquad (32) \\ &= A_R(m) + iA_I(m). \end{aligned}$$

Figure 34*a* plots $A_R(m)$ and $A_I(m)$ as dotted and dashed lines, respectively, using representative values of $z_s = 40km$ [*Hass and Meyer*, 1987; *Eckermann and Vincent*, 1989] and $H_\rho = 7km$. $|A(m)|$ is overlayed with a solid curve.

Since $A_R(m)$ and $A_I(m)$ have a modulated sinusoidal nature, the convolved spectrum $P(m) = A(m) \otimes V(m)$ must depend on the instantaneous phases amongst the constituent waves in the spectrum $V(m)$. Such phases are indeterminate, and so for one spectral measurement, the exact form of the measured power spectrum $|P(m)|^2$ cannot be predicted. However, since no preferred phase scheme for the wave spectrum $V(m)$ should occur, the averaged effect of this convolution will be dictated largely by the forms of $|A(m)|$ and $|V(m)|$. The intrinsic spectral amplitude at a wavenumber m_i, $|V(m_i)|$, should therefore be spread on average through wavenumber space according to $|A(m - m_i)|$. Figure 34*b* illustrates how $|A(m)|$ evolves as the scale height H_ρ changes. When $H_\rho \gg z_s$, the wave growth $a(z)$ is negligible, the profile is stationary, and $|A(m)|$ produces the $\sin(m)/m$ spectral spreading which characterizes truncated data [see, e.g., *Kaimal et al.*, 1989]. Dashed lines in Figur 34*b* mark the points which are sampled using a Fast Fourier Transform algorithm. This $\sin(m)/m$ shape appears as a delta function using digital Fourier techniques, and so no further spreading occurs, as one would expect for a stationary process. As the scale

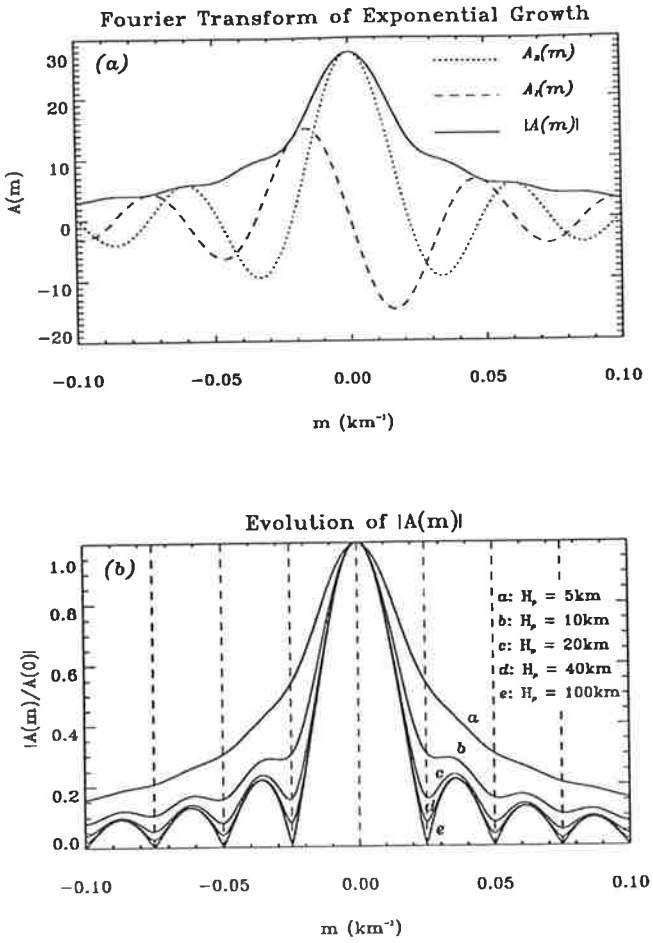

Figure 34: The top panel shows the Fourier Transform $A(m) = A_R(m) + iA_I(m)$ of the exponential wave amplitude growth with height $e^{z/2H_\rho}$, using representative values of $z_s = 40km$ and $H_\rho = 7km$. The bottom panel details the change in $|A(m)/A(0)|$ with H_ρ. The dashed lines show the points where these curves are sampled when using a Fast Fourier Transform algorithm.

height H_ρ decreases and exponential growth over the height range z_s becomes more pronounced, however, these $|A(m)|$ curves assume a broad Lorentzian shape, which will produce spreading of the stationary spectral power $|V(m)|^2$.

Since $|A(m - m_i)|$ spreads energy equally either side of m_i, the flat unsaturated part of the spectrum should ideally be unaltered in shape after convolution with $|A(m)|$. However, as the computational realization of this convolution is incomplete at the end points of the spectrum (the amplitude can be spread in one direction but cannot be spread in the other direction), then this must in practice result in some reduction of spectral power at the smallest wavenumbers.

The effect on the saturated part of the spectrum, however, should be more pronounced. Even though $|A(m)|$ produces a symmetrical spreading of spectral power, the "red" m^{-3} nature of $|V(m)|^2$ at saturated wavenumbers must result in more spectral power being spread to higher wavenumbers than that spread to lower wavenumbers, and will produce an actual fall-off in spectral power more gradual than m^{-3}.

The effects on the spectrum of the exponential growth of a single wave have been considered by *Gardner and Voelz* [1985, 1987] and *Gardner et al.* [1989], and similar convolution effects to those anticipated here do indeed arise. In the sodium layer due to a highly nonlinear response, a single wave is characterized by a "notch" in the spectrum between two peaks [*Gardner and Voelz*, 1985]. Any exponential wave growth with height results in spectral power being spread from the peaks to fill in this "notch" region. Indeed, *Gardner and Voelz* [1985, 1987] have used the observed difference in height between the "notch" and peaks (i.e., how much the "notch" has been "filled in") to measure the amplitude growth with height of individual waves. Within the neutral atmosphere, the relative density response of a monochromatic wave gives rise to a main peak with side lobes in the density fluctuation spectrum [*Gardner et al.*, 1989]. Here again, wave growth with height causes spreading which fills in the gaps between successive peaks.

Numerical Simulation of the Problem

If $a(z)$ indeed had a well defined functional form of the type $e^{z/2H_\rho}$ for all wavenumbers m, the growth could be mathematically incorporated into the model spectrum, as in the single wave derivations of *Gardner and Voelz* [1985, 1987] and *Gardner et al.* [1989]. However, in most measurements the growth profile of the gravity waves is a function of both height and wave number, designated $\hat{a}(z,m)$. This arises because some wavenumbers in the profile are saturated at all heights, others are unsaturated but grow with height to eventually saturate at some altitude, while still others are unsaturated at all heights. This makes mathematical analysis of the problem infeasible, and so the best way to gauge the effect of the growth $\hat{a}(z,m)$ on the spectrum is by numerical simulation. A model used to carry this out will now be described.

At a starting height z_1, $K/2$ individual waves of wavenumber m_i were defined. Their initial wave variances $\overline{u'^2(z_1,m_i)} = u'^2_{peak}(z_1,m_i)/2$ $(i = 1,...,K/2)$ were calculated by integrating under the model spectrum (29) over a wavenumber interval which was centred on $m_i = i(\Delta m)$ and had a width $\Delta m = 2\pi/(K\delta z)$, where δz was the height resolution. This integral was evaluated using the exact analytical expression (30). The fully superposed wave field $p'(z)$ of K sampled points was then synthesized up to a height z_K using the superposition relation

$$p'(z) = \sum_{j=1}^{K} \sum_{i=1}^{K/2} u'_{peak}(z_j, m_i) \sin(m_i z_j + \varphi_i), \tag{33}$$

where the peak amplitude $u'_{peak}(z_j, m_i)$ was recalculated at each height z_j using (30). This must be done because the spectrum, and hence the wave variance, changes with height according to its m_* dependence

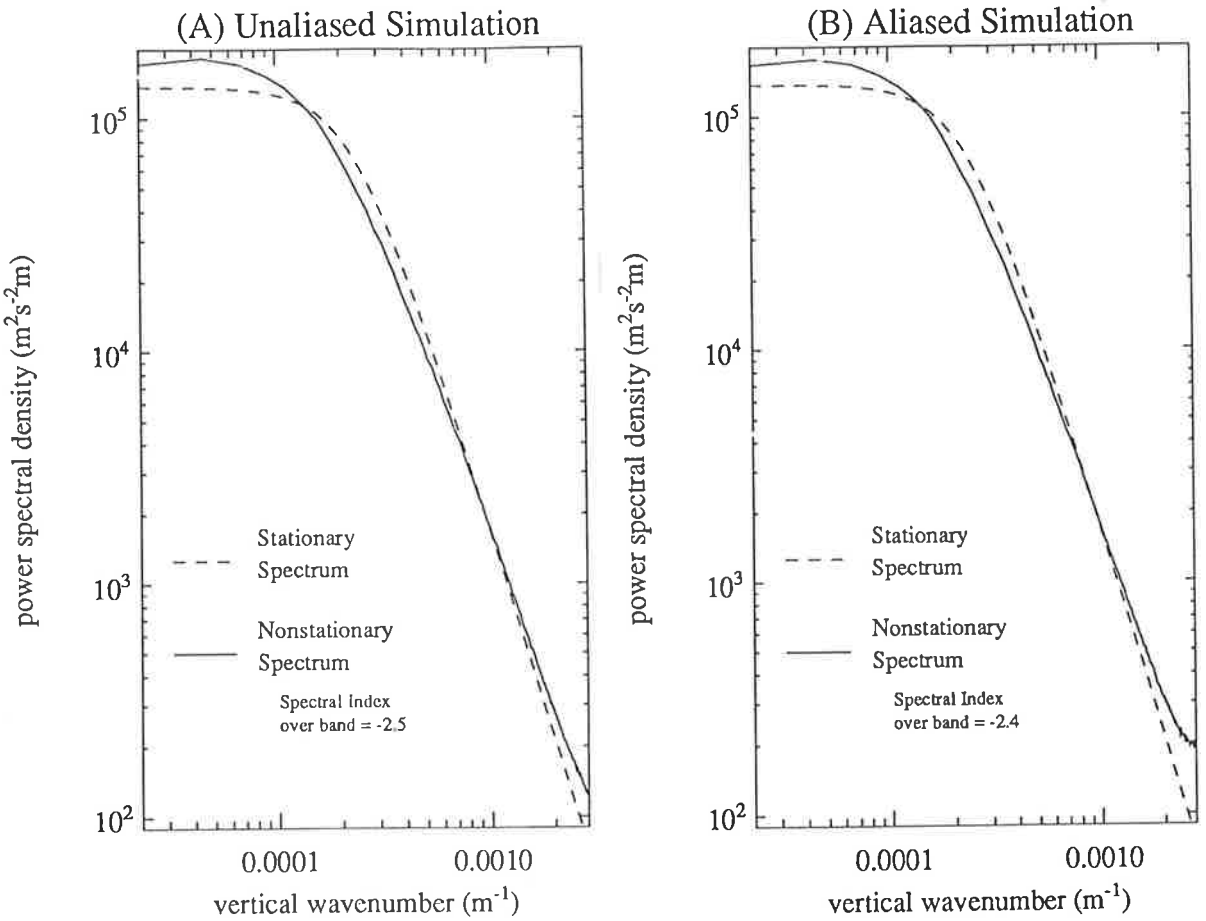

Figure 35: Phase–averaged nonstationary spectra resulting from unaliased (a) and aliased (b) numerical simulations performed 2000 times in each case and averaged. The stationary model spectrum is also plotted for comparison. The simulation used a total height range $z_K - z_1 = 44.8km$, $K = 256$, $N = 0.02$ $rad\ s^{-1}$, $H_E = 10km$, and $m_*(z_1) = (1km)^{-1}$. See text for details about the numerical model used here. A least–squares determination of the nonstationary spectral index in the 0.0002–$0.0028m^{-1}$ wavenumber range is also provided.

in (31). This results in the same wave growth with height and wavenumber $\hat{a}(z, m)$ that is incorporated in the model spectrum (29). The wave phases φ_i were set randomly between 0° and 360°. The data were then Fourier transformed using an FFT algorithm, and the power spectrum calculated.

This entire process was carried out 2000 times in the example presented here to produce one phase–averaged mean power spectrum. It is plotted as the solid curve in Figure 35*a*, and will be referred to as the nonstationary spectrum. In this simulation, values of $z_K - z_1 = 44.8$ km, $K = 256$, $N = 0.02$ $rad\ s^{-1}$, $H_E = 10km$, and $m_*(z_1) = (1km)^{-1}$ were used. The original model spectrum (29), evaluated using a value of m_* which gives a near fit to the nonstationary spectrum, is also plotted for comparison with a dashed line.

Clearly the nonstationary spectrum exhibits a more gradual transition in slope than the model spectrum (29). The addition of power at the largest wavenumbers, as anticipated earlier, is particularly

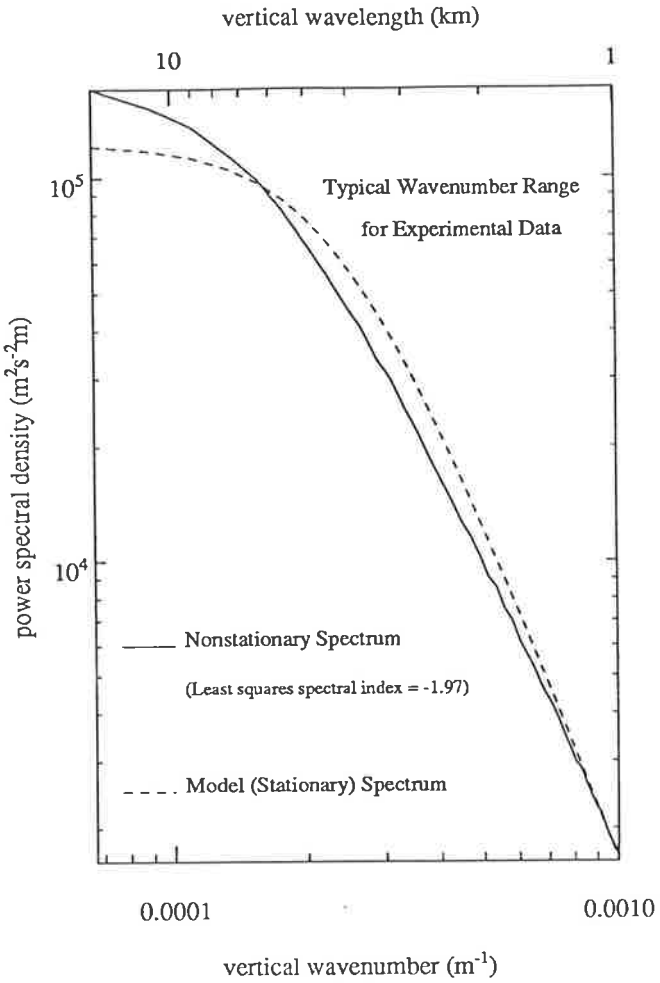

Figure 36: An enlargement of the vertical wavelength region ~ 1–$15km$ from Figure 35. Such a wavelength range is typical of many spectra computed from experimental data from the middle atmosphere. Aliasing at the largest wavenumbers is not included.

significant, and in this example gives rise to a constant power law form of $m^{-2.5}$ at the saturated wavenumbers, as opposed to the stationary m^{-3} shape. Figure 36 enlarges the region between $1km$ and $15km$, which approximates the smallest and largest resolvable vertical wavelengths, respectively, of various rocket [see, e.g., *Hirota*, 1984; *Eckermann and Vincent*, 1989], lidar [see, e.g., *Shibata et al.*, 1988; *Gardner et al.*, 1989], and radar [see, e.g., *Vincent*, 1984; *Maekawa et al.*, 1987] observations of the middle atmosphere. Note the more gradual transition in slope of the nonstationary spectrum as compared to the model spectrum.

One should be a little wary in comparing the results in Figure 35 too closely with actual spectral measurements. As mentioned earlier, the model spectrum (29) is a quasi-empirical relation, and may not depict the true local spectrum. In fact, being based to some extent on observations, (29) must really be a nonstationary version of the local spectrum, arising from the effects that nonstationarity with height must have on even the most high resolution spectral measurements. Since a principal effect of

the altitude nonstationarity is to make the transition from the saturated to unsaturated spectral regimes more gradual (see Figure 36), it suggests that the break point in the local spectrum may be sharper than in the present model. As (29) is therefore already somewhat broadened, these simulations probably overestimates the spreading effects a little. If a better form of the local spectrum is found, similar nonstationarity simulations should be more correctly applied to it rather than the current model.

There are other experimental effects in addition to nonstationarity with height that must be considered. For example, spectral aliasing may be important. To investigate this, the same simulation was repeated with the original $K/2$ unaliased waves, plus a further $K/2$ aliased waves, all of which are governed by the model spectrum (29). The results are shown in Figure 35*b*. Comparing Figures 35*a* and 35*b*, one can see that aliasing produces further enhancement of spectral power at the largest saturated wavenumbers.

There are many other experimental and environmental factors that may also produce spectral contamination. However, while one can sometimes eliminate the effects of these processes with judicious correction techniques, distortion due to the inherent nonstationarity of the spectrum with height is an experimentally intractable problem.

Comparison with Observations

Figures 35 and 36 show that a major effect of nonstationarity in height is the production of a somewhat constant power law form of m^{-t} over a significant wavenumber range, where $0 < t < 3$. Many measured wavenumber spectra that do not correspond very well with the model spectrum of *Smith et al.* [1987] have such a shape, and are also taken over a large altitude and moderate wavenumber range, similar to Figure 36 [see, e.g., *Vincent*, 1984; *Maekawa et al.*, 1987; *Hass and Meyer*, 1987; *Shibata et al.*, 1988; *Eckermann and Vincent*, 1989]. Furthermore, intercomparisons of various spectral studies in the upper stratosphere [e.g., *Hass and Meyer*, 1987; *Eckermann and Vincent*, 1989] and mesosphere [e.g. *Vincent*, 1984; *Maekawa et al.*, 1987] measured over similar wavenumber ranges revealed a spectral index $t \approx 1$–2 in the stratosphere, but $t \approx 2$–3 at mesospheric altitudes. *Eckermann and Vincent* [1989] demonstrated explicitly that t grows with height by comparing spectral calculations at an upper and lower height range. This is consistent with the findings presented here, since a greater fraction of the waves at higher altitudes are saturated/stationary, according to (31), and so the shift in the spectral index away from the saturated value of t=3 toward the unsaturated t=0 should be less severe in the mesosphere than in the stratosphere.

One must now ask why some other measured spectra do indeed agree very well with the original model

spectrum [*Dewan et al.*, 1984; *Fritts and Chou*, 1987; *Fritts et al.*, 1988*a*; *Wu and Widdel*, 1989, 1990]. The study of *Dewan et al.* [1984] used stratospheric smoke-trail data over a small height range, with a vertical resolution of $10m$. *Wu and Widdel* [1989, 1990] analyzed high–resolution radar measurements of the motion of foil–clouds released by rockets, which provided data with a vertical resolution of $25m$ over about a $10km$ height range. *Fritts and Chou* [1987] analyzed ST radar data between 9 and $19km$ with a resolution of $300m$, and *Fritts et al.* [1988*a*] analyzed high resolution balloon and radar data over several small altitude ranges. In all cases, the spectra were taken over short time spans. Therefore in each study any effects of nonstationarity in both height and time were minimized. The high vertical resolution in each data set also means that a significant fraction of the resolved wave field at large wavenumbers was always saturated, and therefore stationary, as can be seen in Figure 33.

"Universal" Spectra

This spectral nonstationarity impacts on the so-called "universal spectrum" of gravity waves. The idea of spectral universality first arose from long-term averaging of observed oceanic and atmospheric spectra [e.g., *Garrett and Munk*, 1972, 1975; *VanZandt*, 1982], and so the "universal spectrum" was a relation that was only applicable to long-term spectral averages. With the ensuing theoretical development of the gravity wave vertical wavenumber spectrum [e.g., *Dewan and Good*, 1986; *Smith et al.*, 1987], and appreciation of the nonstationarity of this spectrum, comparisons with the new model are now best done in the atmosphere using data with good height and time resolution, but taken over a restricted height range.

With this new perspective, the initial "universal" vertical wavenumber spectrum put forward by *VanZandt* [1982] can be viewed as the mean result of altitude (and possibly temporal) nonstationarity of the local wave spectrum. The "universal" spectral index of t=2.4, initially found by *VanZandt* [1982] to best fit the measured spectra from the lower atmosphere, is likely the long-term end result of the distortion of a largely saturated spectrum of gravity waves by spectral nonstationarity. The $m^{-2.5}$ shape of the simulated nonstationary spectrum in Figure 35*a* should be especially noted. Other theoretical studies addressing Doppler shifting of gravity wave energy [*Scheffler and Liu*, 1986; *Fritts and VanZandt*, 1987] have also altered the perspective on spectral "universality" in the frequency domain. The atmospheric gravity wave spectrum in fact can be rather variable, and ideas of long-term "universality" of gravity wave spectra, which initially motivated their study, have now been superseded by the resulting advances in theoretical understanding of these spectra.

The analytical spectral formula $F'(m)$ adopted by *VanZandt* [1982] is the same relation that *Garrett*

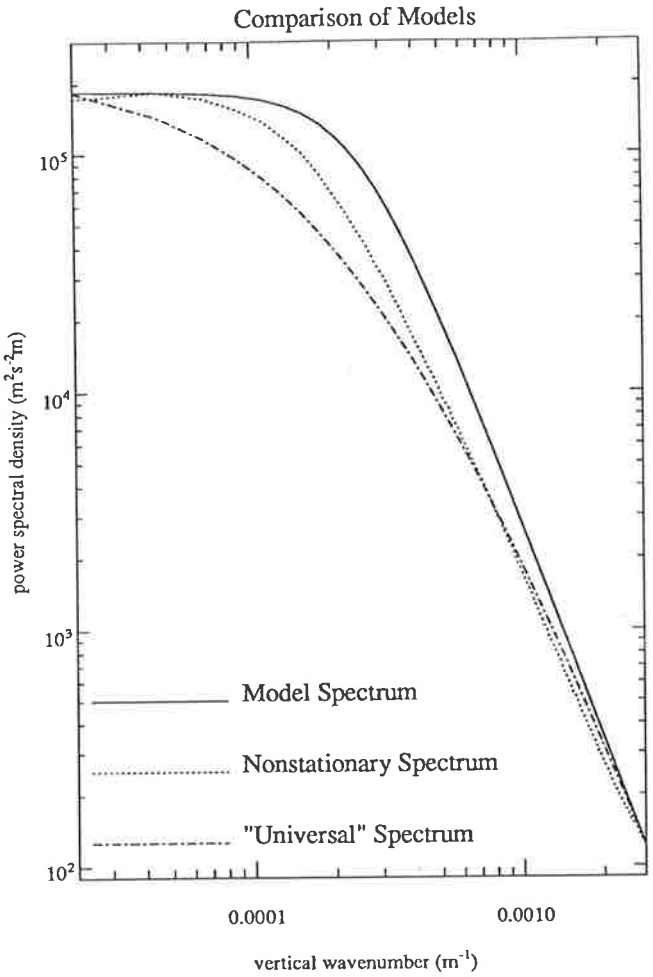

Figure 37: Plot of the model saturated spectrum of *Smith et al.* [1987], the nonstationary realization of this spectrum from Figure 4*a*, and the "universal" spectral formula adopted by *VanZandt* [1982].

and Munk [1975] used in their spectral parameterization of the oceanic wave field, and has the form

$$F'(m) = \frac{E}{m_*} \frac{t-1}{(1+m/m_*)^t} \tag{34}$$

where E is the total energy. Although *VanZandt* [1982] used $t = 2.4$, the spectrum is plotted in Figure 37 using $t = 3$ for ease of comparison with the model of *Smith et al.* [1987]. The model saturated spectrum (29) and the nonstationary spectrum from Figure 35*a* are replotted in Figure 37 as well. Notice in Figure 37 that (34) incorporates a more gradual transition between saturated and unsaturated spectral shapes than the transition region of the model spectrum of *Smith et al.* [1987]. The nonstationary spectrum also exhibits a more gradual transition than the model spectrum, and any temporal nonstationarity may produce further broadening. Thus spectral nonstationarity drives the spectrum towards a shape more like that of the Garrett-Munk relation (34) used by *VanZandt* [1982]. This adds weight to the assertion that the original "universal" spectral parameterizations may be viewed as the long-term results of nonstationarity in both height and time of the local gravity wave spectrum.

3.3.3 Nonstationarity of Other Spectra

In addition to vertical wavenumber spectra, one can also compute horizontal wavenumber spectra and ground–based frequency spectra of mesoscale motions in the atmosphere. However, there are several factors which make the analysis of these spectra less straightforward than vertical wavenumber spectral analysis.

Firstly, the altitude variability of the vertical wavenumber spectrum has a well–defined form. No such systematic nonstationarity arises in the study of horizontal wavenumber or frequency spectra. Quasi–random changes occur in these cases, and so an all–encompassing simulation of the problem is impossible. Consequently, only representative simulations of some observed examples of nonstationarity will be attempted here.

Secondly, the exact dynamics and the intrinsic spectral shapes are not well–known for these spectra. While a gravity wave interpretation of mesoscale motion spectra was assumed in section 3.3.2, *Gage* [1979], *Lilly* [1983] and *Gage and Nastrom* [1985, 1986] have argued instead that quasi two–dimensional turbulence is responsible for the fluctuation spectra. More recently, *Gage and Nastrom* [1988] and *Müller et al.* [1988] have associated this quasi two–dimensional turbulence with the vortical mode of motion. Quasi two–dimensional turbulence currently makes no predictions about the vertical wavenumber spectrum, and so only the gravity wave model can be tested in this case, although *Weinstock* [1985] argued that the m^{-3} spectrum is also consistent with an extended buoyancy subrange of three–dimensional turbulence. For horizontal wavenumber and frequency spectra, however, the gravity wave and vortical mode theories both make predictions, and to date, spectral measurements have been unable to conclusively verify or disprove either theory. As a result, consideration of both theories is required when studying these spectra.

Theory

A third wave solution to the fluid equations arises in a three–dimensional formulation, in addition to to the gravity wave and acoustic wave solutions [see, e.g., *Dong and Yeh*, 1988; see also chapter 2]. It has only recently been considered in the atmospheric context, and has come to be known as the "vortical mode". It is termed "vortical" because it possesses a vertical component of potential vorticity, unlike gravity waves [*Müller et al.*, 1988]. The vortical mode has no intrinsic frequency, and its velocity oscillations are constrained to the horizontal plane. As a result, this "wave" does not propagate, unlike gravity and acoustic waves, hence the preferred nomenclature "mode."

The horizontal velocity oscillations produced by a single high–frequency gravity wave and a single

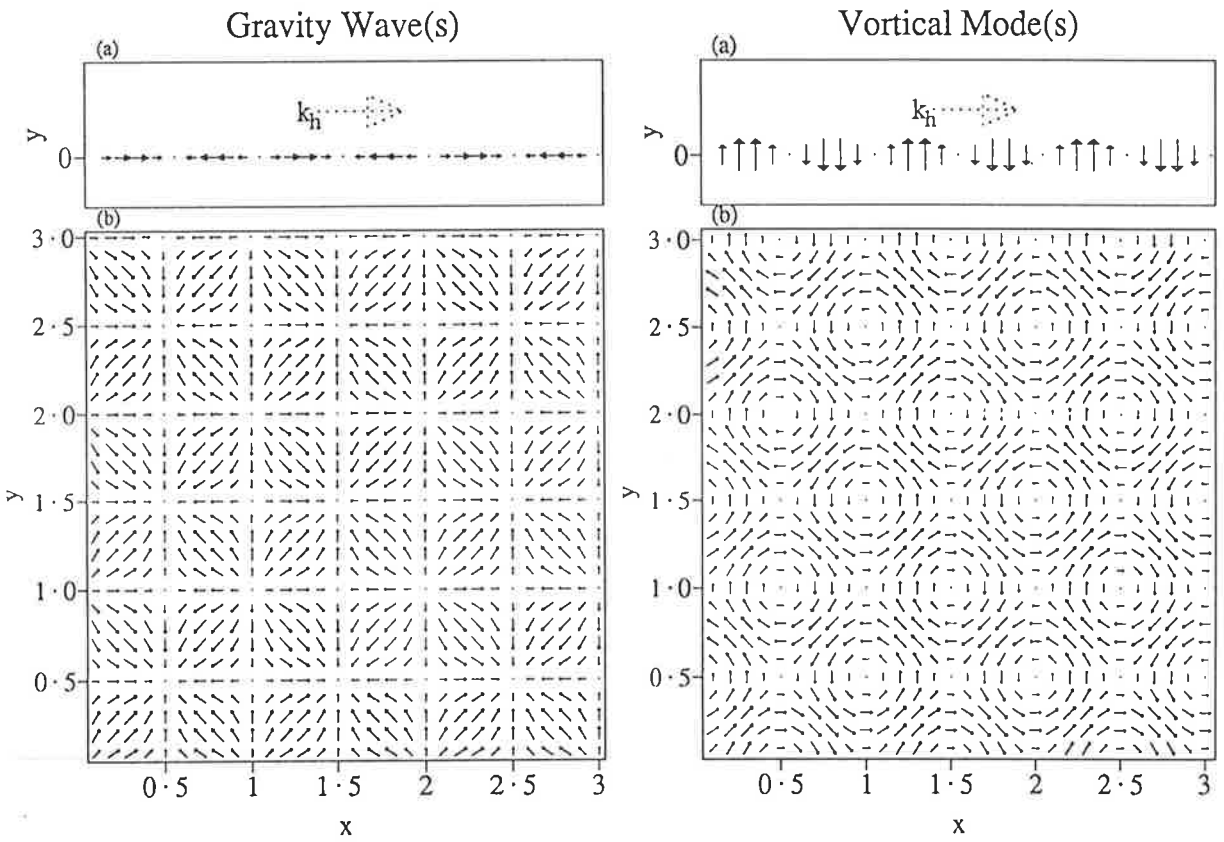

Figure 38: The horizontal velocity oscillations of a single gravity wave and vortical mode are shown in Figure 38*a*. The dotted vector represents the horizontal wavevector k_h. Figure 38*b* shows the instantaneous horizontal velocity vectors produced by the superposition of two orthogonally aligned gravity waves and vortical modes. x and y are displacements normalized by the wavelengths λ_x and λ_y, respectively, and $\lambda_x = \lambda_y$ in these examples.

vortical mode are depicted in Figure 38*a*. Notice that with respect to the horizontal wave vector k_h, the horizontal velocity fluctuations are longitudinal for gravity waves, and transverse for the vortical mode (the absolute k_h direction of the vortical mode is really $\pm 180°$ uncertain, since it is non-propagating). When two orthogonally aligned vortical modes superpose, they produce rotational structure in the horizontal [*Dong and Yeh*, 1988], whereas similarly superposed gravity waves produce irrotational, divergent structure (see Figure 38*b*). Whereas this vortical mode structure is "frozen" in the background flow, the gravity wave structure will vary continously due to wave propagation.

Quasi two-dimensional turbulence, on the other hand, has been known of since the theoretical study of *Kraichnan* [1967]. A review of the theory is given by *Kraichnan and Montgomery* [1980], and more recent numerical and experimental investigations have been reviewed in an oceanic context by *Hopfinger* [1987]. The theory predicts that production occurs at small scales and that progressively larger stratified motions arise from strong nonlinear interactions amongst the horizontally stratified eddies. Such interactions have

been observed and studied in the laboratory [see, e.g., *Hopfinger*, 1987] and the entire process is known as "reverse cascading", since conventional three dimensional turbulence cascades to smaller scales. A resulting $k^{-5/3}$ horizontal wavenumber energy spectrum is predicted, and *Gage* [1979] argued that the same $k^{-5/3}$ turbulence spectrum exists in the atmosphere at horizontal scales between $\sim$10–500km. This argument has been further developed by *Lilly* [1983] and *Gage and Nastrom* [1985, 1986, 1988].

While usually assumed, the equivalence between vortical modes and quasi two-dimensional turbulence is not clearly established at present. Although both theories predict a horizontally stratified, eddylike structure, an important interpretative difference is that the vortical mode solution is wavelike. While the eddylike structure that a superposition of vortical modes produces may appear rather random, it is certainly not turbulent in the strict sense. A likely explanation is that vortical mode non–linearities have been omitted, such as the coupling of vortical modes with each other or with other waves. For example, *Dong and Yeh* [1988] and *Yeh and Dong* [1989] have shown that vortical modes grow in amplitude through nonresonant wave–wave interactions with large amplitude gravity waves. Yet *Yeh and Dong* [1989] proposed that the resultantly excited vortical modes cascade not into larger scale structures, but into *smaller* scale structures which are eventually dissipated by viscosity. This cascade process clearly differs from the "reverse cascade" that occurs for two–dimensional turbulence. Nevertheless, in the subsequent discussion equivalence between vortical modes and quasi two-dimensional turbulence will be assumed.

Spectral Theory and Observations

Both the gravity wave and two-dimensional turbulence theories make definite spectral predictions. The spectral theory of gravity waves is most clearly developed through the saturated vertical wavenumber spectrum (29) of *Smith et al.* [1987]. Quasi two–dimensional turbulence, however, currently makes no predictions as to the form of the vertical wavenumber spectrum.

The most direct spectral prediction that quasi two-dimensional turbulence theory provides is a horizontal wavenumber spectrum of horizontal velocities, $\mathcal{F}_u(k)$, proportional to $k^{-5/3}$ [*Gage*, 1979]. Using the vertical wavenumber spectrum (29), a simplified dispersion relation, and assuming spectral separability, gravity wave theory predicts that $\mathcal{F}_u(k)$ should have the same shape as the vertical wavenumber spectrum (29), giving a k^{-3} spectrum for $k > k_*$, and a flat spectrum for $k < k_*$, where k_* performs the same function as m_* in (29) [see, e.g., *VanZandt*, 1985]. Thus, it would appear that measurements of horizontal wavenumber spectra should enable discrimination between the two theories.

Nastrom and Gage [1985] calculated mean horizontal wavenumber spectra of horizontal velocities,

using data from a large number of commercial aircraft flights. They found that the final mean spectrum had a $k^{-5/3}$ shape at wavenumbers less than $\sim 500km$, which *Gage and Nastrom* [1986] interpreted as direct evidence of quasi two-dimensional turbulence at atmospheric mesoscales. Subsequent measurements by *Nastrom et al.* [1987], *Fritts et al.* [1989], *Kwon et al* [1990], and *Jasperson et al.* [1990] also found spectral shapes of the form k^{-p}, with $p \sim 1$–2. However all of these latter studies found some spectral behaviour which agreed with gravity wave theory, and *Fritts et al.* [1989] argued that nonseparability of the gravity wave spectra may result in a gravity wave horizontal wavenumber spectrum different from the predicted k^{-3}, and more like the shape observed. Evidence for such spectral nonseparability was presented by *Fritts and Chou* [1987]. Hence the dynamics responsible for these spectra are still under debate.

The spectral measurement that is predicted best by both theories is the frequency spectrum of horizontal velocities measured by a ground-based sensor, hereafter denoted $E_u(\Omega)$. For gravity waves, all the constituent waves of the spectrum have their own intrinsic wave frequency ω, and so, in a frame moving with the mean atmospheric motion $\bar{U}$, an *intrinsic frequency spectrum* exists, which is believed to have the form $\omega^{-5/3}$. However, at the ground these intrinsic frequencies are Doppler shifted by the mean motion of the atmosphere $\bar{U}$, producing a ground–based frequency Ω given by

$$\Omega = \omega + k\bar{U}\cos\phi \tag{35}$$

where ϕ is the angular difference between the wave propagation direction and the wind speed direction [see, e.g., *Scheffler and Liu*, 1986; *Fritts and VanZandt*, 1987]. Thus, the ground–based frequency spectrum for gravity waves, $E_u^{GW}(\Omega)$, can differ considerably from its intrinsic frequency spectrum. *Scheffler and Liu* [1986] and *Fritts and VanZandt* [1987] modelled how $E_u^{GW}(\Omega)$ evolved as background wind speeds varied, and the results of the latter study are shown in Figure 39*a* for equal amounts of up– and down–shifting of wave frequencies, and where $\beta = \bar{U}m_*/N$ conveniently quantifies the degree of Doppler shifting by the mean wind $\bar{U}$. Note that an ω^{-2} rather than an $\omega^{-5/3}$ intrinsic frequency spectrum was used by *Fritts and VanZandt* [1987] for analytical convenience.

For quasi two-dimensional turbulence, a simple Taylor transformation is used to predict the frequency spectrum $E_u^{VM}(\Omega)$ measured at the ground as the "frozen–in" turbulence structure is advected by the mean wind over the ground–based field of view, producing an $\Omega^{-5/3}$ spectrum [see, e.g., *Gage*, 1979; *Gage and Nastrom*, 1988]. Using a vortical mode interpretation, this transformation is better understood in terms of a Doppler shifting of the zero intrinsic frequency of the vortical modes to non-zero ground-based values, according to (35). The variation of $E_u^{VM}(\Omega)$ with wind speed, as calculated by *Gage*

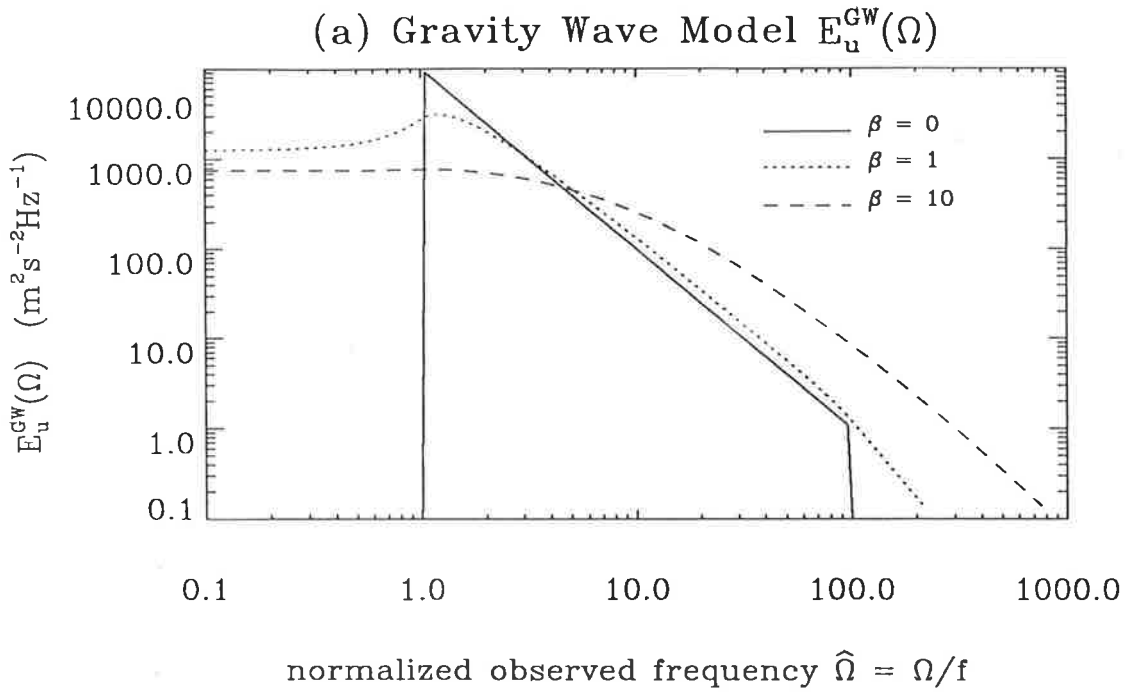

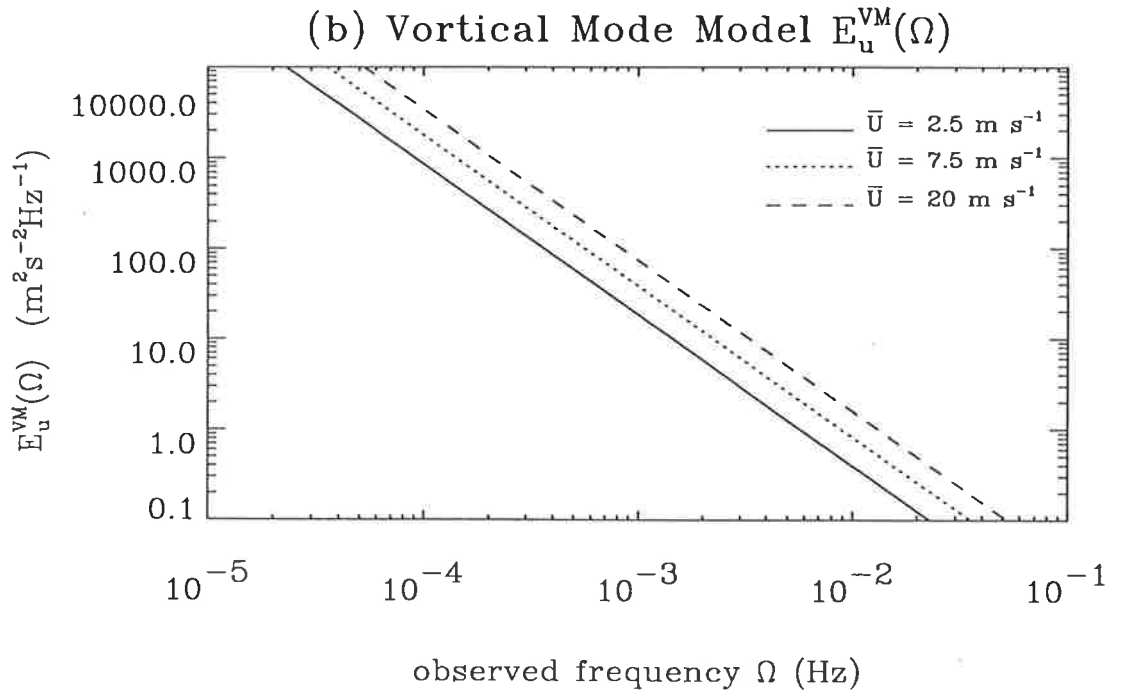

Figure 39: Theoretical ground-based frequency spectra for gravity waves (a) and vortical modes (b) in different background wind conditions. The gravity wave model parameter $\beta = \bar{U} m_* / N$ parameterizes the degree of Doppler shifting, and at a given height is proportional to the mean wind $\bar{U}$. These gravity wave spectra are computed for equal amounts up- and down-shifting of frequencies [see *Fritts and VanZandt*, 1987], and plotted frequency labels $\hat{\Omega}$ are normalized by the inertial frequency f. The vortical mode spectrum here is based on a Taylor-transformed $k^{-5/3}$ horizontal wavenumber spectrum. One should also note that the vortical mode frequency spectrum for $\bar{U} = 0$ is a delta function at zero frequency (since vortical modes have no intrinsic frequency).

and Nastrom [1988], is shown in Figure 39*b*. The vortical mode spectrum preserves its $\Omega^{-5/3}$ shape in all wind conditions, whereas the gravity wave spectrum becomes "flatter" as the wind speed increases. Consequently, investigating the behaviour of measured ground-based frequency spectra with wind speed should indicate which theory, if either, fits the observations better, thus providing information on the nature of these fluctuating dynamics.

Early experimental studies averaged spectral calculations from all heights and times to produce a mean spectrum. While some such studies revealed an $\Omega^{-5/3}$ shape [see, e.g., *Balsley and Carter*, 1982; *Larsen et al.*, 1982*a*], other studies revealed more variable shapes and spectral indices [see, e.g., *Vincent*, 1984; *Meek et al.*, 1985*b*; *Balsley and Garello*, 1985; *Fukao et al.*, 1985; *Fritts and Chou*, 1987; *Fritts et al.*, 1990]. *Gage and Nastrom* [1988] compared the spectral models in Figure 39 with computed frequency spectra from ground-based radar data. They found that neither theory fitted the observations very closely, but that the two-dimensional turbulence model gave a better fit. On the other hand, while *Fritts et al.* [1990] also found variable agreement with the models, they concluded that their observations were more consistent with gravity waves. Therefore, here too the comparisons give equivocal findings as to whether the gravity wave or vortical mode theory is more consistent with observations.

Spectral Nonstationarity due to Doppler Shifting

It can be seen from Figure 39 that *both* the gravity wave and vortical mode theories *predict* that the ground–based frequency spectrum $E_u(\Omega)$ is nonstationary when the background wind $\bar{U}$ changes. Significant mean wind variability often occurs in the lower atmosphere due to meteorological phenomena [see, e.g., *Fukao et al.*, 1989*a*; see also chapter 4], and in the middle atmosphere due to large amplitude planetary waves and tides [see, e.g., *Andrews et al.*, 1987], which must give rise to nonstationary spectral shapes.

In the case of the vortical mode spectrum, this mean wind variability gives rise to *nonstationary frequencies*, according to (35), rather than nonstationary variance. Put another way, the variations in spectral shape detailed in Figure 39*b* are due to nonstationarity of the horizontal axis variable (frequency), as opposed to the variations in the vertical axis variable that occurred in the studies of nonstationary variance in section 3.3.2. Indeed, the gravity wave vertical wavenumber spectrum $F_u(m)$ of *Smith et al.* [1987] should also suffer from *nonstationary wavenumbers* because the vertical wavenumber m varies with $\bar{U}$, but as their model was presented as being applicable in all wind conditions, such effects must be implicitly incorporated into their spectrum.

At first glance, one might expect that the variability of the gravity wave spectrum due to Doppler

shifting in Figure 39*a* must also arise from nonstationary frequencies according to (35). In fact, this is not the case. While for vortical modes, ω is a constant (zero) and Ω varies with the mean wind $\bar{U}$, for gravity waves the opposite is true; the intrinsic frequency ω varies with $\bar{U}$, and the ground–based frequency Ω is a constant. So for gravity waves, the frequency Ω is stationary, and the variability of $E_u^{GW}(\Omega)$ is a problem of nonstationary variance within a given frequency band.

Therefore two rather different simulations were performed to investigate the effects of mean wind variability on computation of the frequency spectra $E_u^{GW}(\Omega)$ and $E_u^{VM}(\Omega)$. In the gravity wave case, simulations very similar to those detailed in section 3.3.2 were undertaken. Temporal fluctuations $q'(t)$ were synthesized using the superposition relation (33) adapted for time series analysis as follows

$$q'(t) = \sum_{j=1}^{K} \sum_{i=1}^{K/2} u'_{peak}(t_j, \Omega_i) \sin(\Omega_i t_j + \varphi_i), \tag{36}$$

where again peak amplitudes $u'_{peak}(t_j, \Omega_i)$ had to be recalculated at each time t_j, because variations in $\beta = \bar{U} m_* / N$ change the spectral shape according to analytical relations derived by *Fritts and VanZandt* [1987] (see Figure 39*a*). Phases φ_i were chosen randomly, and 600 profiles were Fourier transformed in every simulation to obtain a final phase–averaged mean spectrum.

Results for three different time variations in β, which is proportional to $\bar{U}$, are shown in Figure 40. The Gaussian β profile roughly models strong, transient intensifications of the mean wind which have been observed in the lower atmosphere [see, e.g., *Fukao et al.*, 1989*a*; see also chapter 4]. The sinusoidal profile crudely models the effects of a planetary wave or tide, which are important in the middle atmosphere [see, e.g., *Andrews et al.*, 1987]. Although these large variations in β imply a highly nonstationary spectral shape (see Figure 39), the results of these simulations reveal that the final nonstationary spectrum is well–fitted in each case by the stationary Doppler–shifted spectrum of *Fritts and VanZandt* [1987] evaluated using the mean value of β over the time interval, denoted $\overline{\beta}$. Thus the "Doppler nonstationarity" of $E_u^{GW}(\Omega)$ appears to have limited impact on comparisons of this model spectrum with observed spectra. Aliasing also produces only small distortions to the spectral shape in these examples.

More complex modelling was required to simulate the variability of the vortical mode spectrum $E_u^{VM}(\Omega)$, as frequency variability must be incorporated here. To achieve this, 1024 "waves" were defined by integrating the $k^{-5/3}$ horizontal wavenumber spectrum proposed by *Gage* [1979] in 1024 successive harmonic wavenumber steps. The largest wavelength was chosen to be $\lambda_x^{max} = 1024km$, so that the smallest resulting wavelength was $\lambda_x^{min} = \lambda_x^{max}/1024 = 1km$. The mean wind $\bar{U}$ was allowed to vary only between $\bar{U}_{min} = 5ms^{-1}$ and $\bar{U}_{max} = 40ms^{-1}$. Since the period $\tau = \lambda_x/\bar{U}$, then as the wind varies between $\bar{U}_{min}$ and $\bar{U}_{max}$, the smallest fluctuating period $\tau_{min} = \lambda_x^{min}/\bar{U}$ ranges from $\lambda_x^{min}/\bar{U}_{max} = 25s$

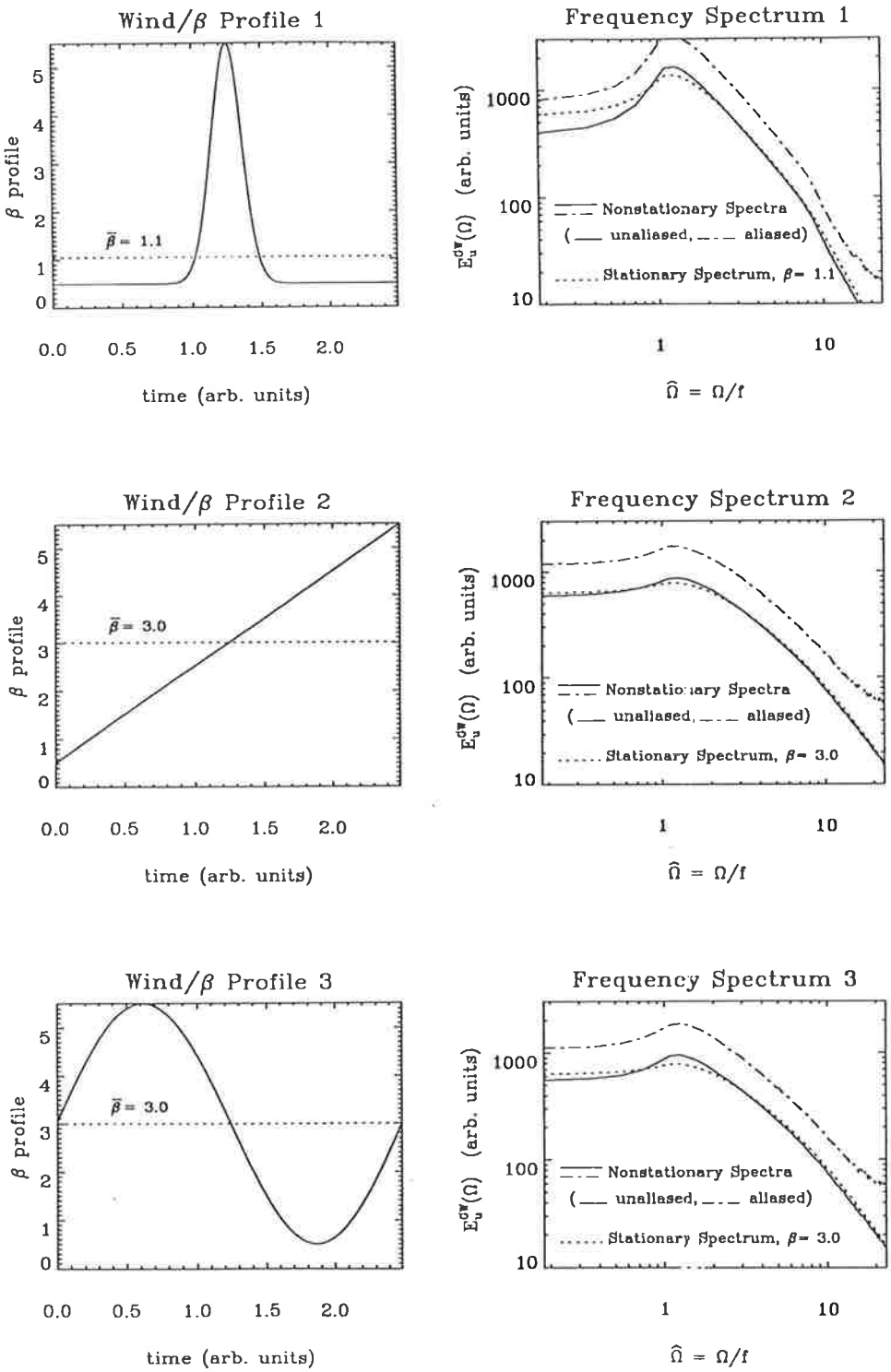

Figure 40: The three panels on the left show various time variations in the gravity wave Doppler–shifting parameter $\beta = \bar{U}m_*/N$. The dotted line shows the mean value $\overline{\beta}$ over the time interval. The corresponding plots on the right show the resulting nonstationary gravity wave frequency spectra that these variations in Doppler shifting produce. The aliased spectrum has been displaced vertically by 0.3 of a decade. These spectra are also compared to the stationary Doppler–shifted spectrum evaluated for $\beta = \overline{\beta}$ (dotted line), as one would usually do when comparing computed and model spectra. Equal up– and down–shifting of energy, and a value of $\hat{N} = N/f = 9.18$, were used in each example.

to $\lambda_x^{min}/\bar{U}_{min} = 200s$. Similarly the maximum wave period $\tau_{max} = \lambda_x^{max}/\bar{U}$ varies between ~7.11 and 56.89 hours. Thus, the period interval between $200s$ and 7.11 hours is always "full" of wave frequencies, and so temporal fluctuations were digitally synthesized from the wavenumber data using a Nyquist frequency of $100s$ and a total data length of ~7.11 hours, which corresponds to 256 data points. Since periods greater and smaller than these values also arise, the data were somewhat aliased, and mean values arose which had to be removed before Fourier transformation. A total of 2000 randomly–phased profiles were analyzed to give one phase–averaged mean nonstationary spectrum.

Figure 41 shows the temporal variations in $\bar{U}$ used in the simulations, which are similar to those used in the gravity wave simulations in Figure 40. The graphs on the right show three spectra in each case; a simulated nonstationary spectrum, a simulated spectrum evaluated using a constant value of $\bar{U} = 20m\ s^{-1}$ (i.e., an aliased stationary spectrum), and the theoretical $\Omega^{-5/3}$ spectral shape.

Several spectral features in Figure 41 bear highlighting. Firstly, the simulated stationary and nonstationary spectra decrease more gradually with frequency than $\Omega^{-5/3}$, which is in part due to the addition of spectral power at the highest frequencies by aliased fluctuations. The nonstationary spectra have a least–squares power law form around $\Omega^{-1.4}$ in each case When one computes the spectral indices over the frequency band $\Omega = 0.00004$–$0.002Hz$, which excludes the highest frequencies which are contaminated by aliased fluctuations, the simulated stationary spectrum assumes an $\Omega^{-5/3}$ shape, whereas the nonstationary spectrum still has a "bluer" shape around $\Omega^{-1.6}$ This implies that the gradual spectral roll–off with frequency of the nonstationary spectrum is due in part to aliasing, but also in part to frequency nonstationarity.

Another feature is a flattening of the nonstationary spectrum in examples 1 and 3 at the lowest frequencies, yet this does not arise in the simulated stationary spectrum in either case. Therefore, this must be a product of the nonstationarity. This flattening makes the computed spectra in these cases appear more like the model gravity wave spectral shapes at low frequencies in Figure 39*a*. The finding of absolute values of the nonstationary spectral index $< 5/3$ (i.e., ~1.4) is also superficially more consistent with the behaviour of the Doppler–shifted gravity wave spectra in Figure 39*a* rather than the vortical mode model spectra in Figure 39*b*, despite this being a nonstationary vortical mode spectrum.

Figure 42 shows results from further simulations where the wind was allowed to vary between 3 and $48m\ s^{-1}$. This gives rise to a period range between $333s$ and 5.93 hours which is always "full" of wave frequencies, and so fluctuations were synthesized from the previous horizontal wavenumber data, using a Nyquist frequency of $167s$ and a total data length of ~5.93 hours, which produced 128 data points. The frequency nonstationarity is greater in these examples due to the larger temporal excursions in $\bar{U}$. The

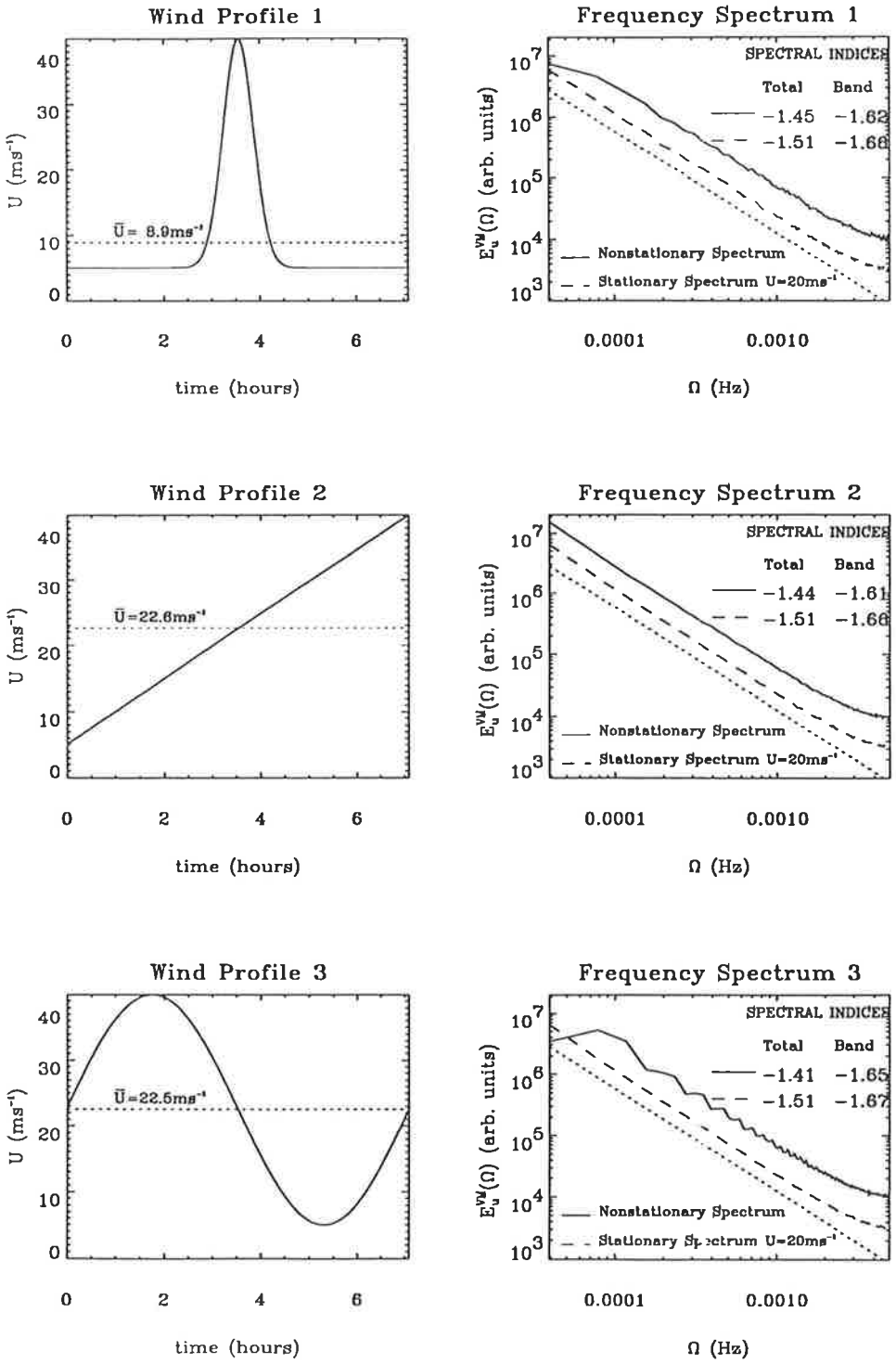

Figure 41: The three panels on the left show various time variations in the background wind speed $\bar{U}$, and the dotted line shows the mean value evaluated over the whole time interval. The solid curves on the right show the resulting nonstationary vortical mode frequency spectra that these variations in wind speed give rise to. The dashed line shows the simulated results for a stationary wind speed of $20m\ s^{-1}$. Both of these spectra are aliased. The theoretical $\Omega^{-5/3}$ is also plotted as a dotted curve for reference. Least–squares determinations of the spectral indices of the simulated spectra are given in each case over the whole spectrum, and over the band $\Omega = 0.00004$–$0.002Hz$, which excludes the highest frequencies.

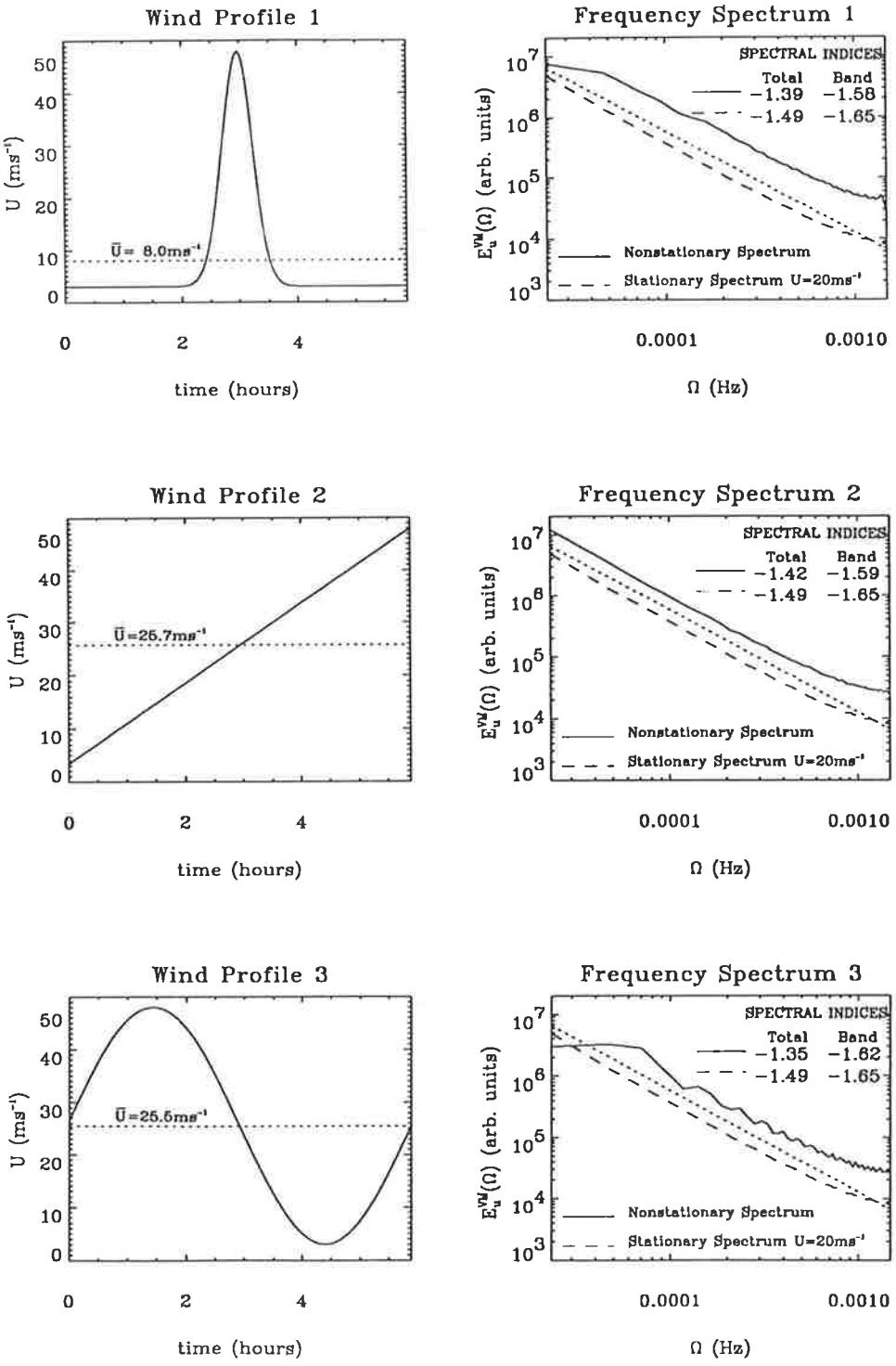

Figure 42: As for Figure 41, but for mean wind variability between 3 and $48m\ s^{-1}$ rather than between 5 and $40ms^{-1}$. There are 128 points in the time series in these examples rather than 256 in the examples in Figure 41. The band over which spectral indices were fitted was $\Omega = 0.000025$–$0.00065Hz$.

results show that the computed absolute values of the spectral indices of the nonstationary spectra are smaller than in Figure 41, and that the spectral flattening at the lowest frequencies persists.

Nonstationary Variance

Notwithstanding the nonstationarity of frequency spectra due to Doppler shifting, observed time series of mesoscale motions also exhibit large, transient bursts in variance above the ambient level. Examples from the lower atmosphere are strong increases in wave/turbulence activity associated with meteorological events [see, e.g., *Fritts and Chou*, 1987; *Fukao et al.*, 1989*a*; see also section 4.3.3]. Transient bursts in the fluctuating variance are recorded commonly in the middle atmosphere as well [see, e.g., *Vincent and Reid*, 1983; *Vincent and Fritts*, 1987].

To investigate the effect such nonstationarity might have on computed frequency spectra, Monte Carlo simulations similar to those described in section 3.3.2 and earlier in this section were performed for a stationary spectrum of the form $\Omega^{-5/3}$, which closely fits the two spectral models $E_u^{GW}(\Omega)$ and $E_u^{VM}(\Omega)$. Fluctuations were synthesized from this spectrum as in (33) and (36), and were then modulated by a Gaussian "burst" function, which approximates some observed increases in variance [see, e.g., *Fritts and Chou*, 1987]. Various modulation profiles, and the modified spectra they produce, are shown in Figure 43. The results show that the computed spectral indices are reasonably robust to the applied nonstationarity in these examples, differing by no more than 3% from the stationary value of -5/3.

Horizontal Wavenumber Spectra

The simulations detailed in this section also have some impact on computations of horizontal wavenumber spectra. For example, Figure 43 can be quite validly applied to horizontal wavenumber spectra, as a similarly shaped $k^{-5/3}$ spectrum occurs [*Nastrom and Gage*, 1985]. Furthermore, large bursts in variance with horizontal flight distance are also encountered in such measurements. For instance, *Nastrom et al.* [1987] found that the mesoscale velocity variance for flight segments over rough terrain was ~2–5 times greater than that over flat terrain or oceans, and they showed explicitly that the horizontal wavenumber spectra over each type of terrain differed significantly. These trends were confirmed in a subsequent study by *Jasperson et al.* [1990], who utilized a greater amount of flight data in a more quantitative statistical study of terrain roughness and atmospheric variance. Similar variability with flight distance was reported by *Fritts et al.* [1989].

Problems involving nonstationary horizontal wavenumbers arise too, similar to the frequency nonstationarity which arises in the vortical mode frequency spectrum. An airborne sensor moving horizontally

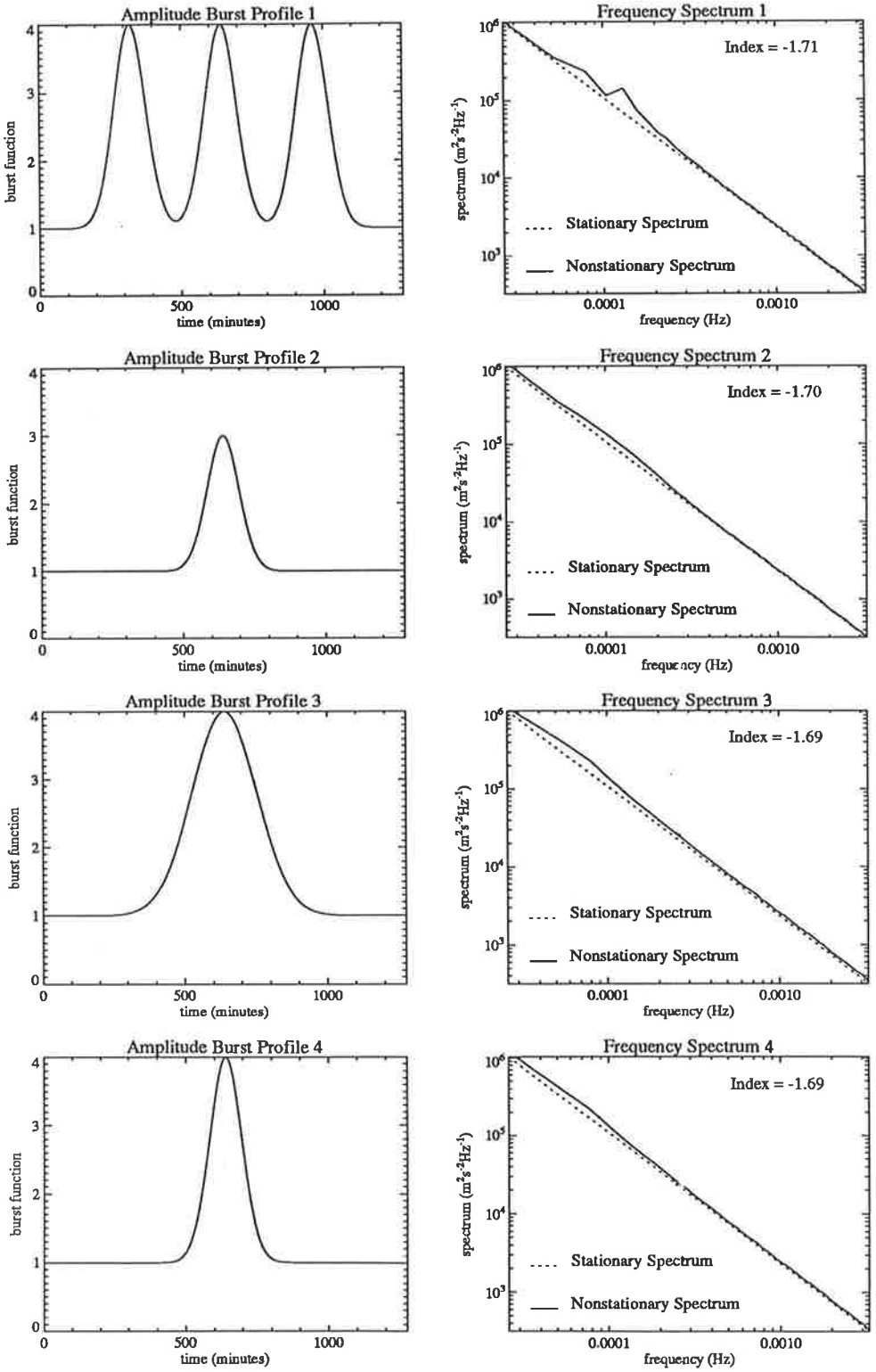

Figure 43: The panels on the left show various time variations in the fluctuating variance. The corresponding plots on the right show the stationary $\Omega^{-5/3}$ spectrum (dotted curve) and the simulated nonstationary spectrum (solid curve). Each simulated spectrum is an average of 2000 individual spectra from randomly-phased time series. A least–squares determination of the nonstationary spectral index is given in each case.

with velocity V, and measuring a fluctuation moving with respect to the ground with a speed C, will record the horizontal wavelength of this fluctuation to be λ_x', which differs from its intrinsic horizontal scale, λ_x, according to the Doppler–shifting formula

$$\lambda_x' = \lambda_x \left(1 + \frac{C}{V}\right). \tag{37}$$

For gravity waves, C is the ground–based horizontal phase speed of the wave, and for vortical modes $C = \bar{U}$, as vortical modes are merely advected by the background flow. *Kwon et al.* [1990] investigated how the horizontal motion of airborne sensors can produce artificial Doppler shifts in the horizontal wavelengths of measured fluctuations, and presented experimental examples of varying spectral shapes produced by such effects.

3.3.4 "Stationary" Analysis of Mesoscale Motions

Simulations in the previous section have indicated how observed variability of mesoscale variance can complicate spectral analysis of these fluctuating motions. While nonstationary variances appear to produce limited distortion, nonstationary frequencies arising in the ground–based frequency spectrum of vortical modes produce a spectral change with frequency more gradual than $\Omega^{-5/3}$, and in some cases producing rather flat shapes at the lowest frequencies, both of which are more consistent with a *gravity wave* interpretation (see Figure 39).

Comparison of experimental spectra with model spectra is currently used widely to provide information about the fundamental dynamics (gravity waves or vortical modes), yet a number of such studies have produced equivocal findings to date. While this may indicate that both gravity waves and vortical modes usually coexist with approximately equal variance, the aforementioned spectral distortions due to nonstationarity can also produce similar uncertainty. There is no easy way to compensate for nonstationary distortion. One can circumvent the problem by spectrally analyzing only those data segments where the spectra should theoretically be quasi–stationary [*Fritts and Chou*, 1987], but the amount of available data may then be very small, whereupon the uncertainties in the computed spectral shape will be large. For nonstationary data, it would be better to be able to calculate a more stationary quantity, which produces distinctly different results in the presence of either gravity waves or vortical modes.

The Polarization Ratio

In time series analysis of horizontal velocity data from ground-based sensors, we define the ratio R of the fluctuating horizontal velocity variance parallel ($\overline{u_p'^2}$) and transverse ($\overline{u_t'^2}$) to the direction of the mean

wind.

$$R = \frac{\overline{u_p'^2}}{\overline{u_t'^2}}. \tag{38}$$

Being a ratio of horizontal variance components, nonstationarity of the total variance does not affect its value (i.e., it is stationary to variance changes). Furthermore, at middle to high ground-based frequencies, we shall show that the ground–based spectral theories of gravity waves and vortical modes (Figure 39) can still be used to predict distinctly different R values if one or the other dynamical process is the more energetic.

The gravity wave model spectra depicted in Figure 39*a* show that, at mid to high ground–based frequencies, the Doppler–shifted frequency spectrum is more intense than the intrinsic (unshifted) frequency spectrum [*Scheffler and Liu*, 1986; *Fritts and VanZandt*, 1987]. Since waves with k_h parallel to the mean wind direction are strongly Doppler shifted, whereas waves with k_h orthogonal to the wind direction experience no such shift, according to (35), it implies an enhancement in the observed high frequency variance of those waves aligned with the mean wind direction relative to those aligned transverse to it. The effect becomes more pronounced as background wind speeds increase (see Figure 39*a*).

The observed frequency Ω induced by a vortical mode is also given by the Doppler–shift formula (35), which, since $\omega = 0$ in this case, takes the form $k\bar{U}\cos\phi$, where ϕ is the difference in azimuth between the vortical mode alignment and the mean wind direction. For any given value of Ω and $\bar{U}$, $k\cos\phi$ will be the same for all the modes which contribute to the variance at this observed frequency. However, those modes where k is smallest produce the greatest contribution to this variance, due to the $k^{-5/3}$ wavenumber spectrum [*Gage*, 1979]. Therefore, since $k\cos\phi$ is constant, these smallest wavenumber modes must also have $\phi \sim 0°$, which implies that they are aligned with the background wind direction.

Thus both theories predict enhancements in the measured variance of those motions with k_h coaligned with the background wind direction. However, the different horizontal polarization of the gravity wave and the vortical mode results in distinctly different trends in the ratio R in each case. Since the horizontal fluctuations of a gravity wave oscillate parallel with k_h (Figure 38*a*), the enhanced gravity waves should therefore produce values of $R > 1$ on average (i.e., $\overline{u_p'^2} > \overline{u_t'^2}$). The value of R should increase as the mean wind speed increases, because the enhancement in variance of the Doppler–shifted wave spectrum increases with $\bar{U}$ (see Figure 39a). It should be noted, however, that the model Doppler–shifted spectra in Figure 39a assume equal amounts of up– and down–shifting of wave frequencies. While this variance enhancement persists for a wide variety of different up– and down–shifting amounts, in extreme cases where almost every wave in the spectrum is down–shifted in frequency, these enhancements in variance may not occur [*Fritts and VanZandt*, 1987].

One other complicating factor is that, at the very lowest frequencies, a gravity wave become elliptically polarized, aquiring a transverse component v'_{peak} of f/ω times its longitudinal component u'_{peak}, where f is the inertial frequency. Note, however, that v'_{peak} is always smaller than u'_{peak}, and that v'_{peak} attenuates rapidly with frequency. The individual variances u'^2 and v'^2 over the entire intrinsic frequency spectrum are given by

$$u'^2 = \int_f^N W\omega^{-5/3}d\omega = \frac{3W}{2f^{2/3}}\left[1-(f/N)^{2/3}\right], \tag{39}$$

$$v'^2 = \int_f^N \left(\frac{f}{\omega}\right)^2 u'^2 = \int_f^N Wf^2\omega^{-11/3}d\omega = \frac{3W}{8f^{2/3}}\left[1-(f/N)^{8/3}\right], \tag{40}$$

where

W is a constant.

For a realistic value of $N \sim 100f$, the terms in square parentheses in (39) and (40) are both near one, so that equating (39) and (40) gives

$$\frac{u'^2}{v'^2} \approx \frac{3/2}{3/8} = 4 \tag{41}$$

This illustrates that, over the entire spectrum, the longitudinal fluctuations produce 80% of the variance. Within high observed frequency bands, this percentage will be even higher. Therefore these transverse gravity wave fluctuations are of insufficient amplitude to alter the general trends in R produced by the longitudinal gravity wave fluctuations (i.e., $R > 1$).

The vortical mode, unlike a gravity wave, oscillates at right angles to its wavevector k_h (Figure 38*a*). Therefore, even though those fluctuations with k_h in the direction of $\bar{U}$ are enhanced in variance, just as for gravity waves, the transverse polarization of the vortical mode means that values of $R < 1$ must arise in the presence of such a spectrum (i.e. $\overline{u'^2_t} > \overline{u'^2_p}$).

These trends in R can be qualitatively visualized by inspecting the simple superposition structure in Figure 38b. On moving in either the x or y direction in these diagrams and observing the variation of the wind vectors, one can see that the gravity wave structure produces fluctuations in the direction of movement ($R > 1$), whereas the vortical mode structure fluctuates transverse to the movement ($R < 1$). Therefore, notwithstanding the strong enhancement in the variance within high frequency bands of those gravity waves aligned with the mean wind direction predicted in Figure 39*a*, values of $R > 1$ still arise due to the horizontal polarization of the wave.

Equivalence between vortical modes and quasi two–dimensional turbulence has been assumed to now. However, some discrepansies between the two theories were highlighted earlier, and one or the other process may be the more relevant to consider. Therefore it is worth determining whether two–dimensional

turbulence theory can also be used to predict a trend in R, and whether it is comparable with the vortical mode prediction of $R < 1$.

Gage [1979] has adapted the well–developed theory of inertial range three–dimensional turbulence to this postulated two–dimensional inertial range turbulence. Longitudinal and transverse Eulerian (ground–based) structure functions were defined by *Gage* [1979] as follows

$$D_{long}(r) = A_{long}\epsilon^{2/3}r^{2/3}, \tag{42}$$

$$D_{tran}(r) = A_{tran}\epsilon^{2/3}r^{2/3}, \tag{43}$$

where

A_{long}, A_{tran} are constants,

ϵ is the eddy dissipation rate per unit mass, and

r is the spatial separation.

Using analogous derivations to those advanced in the three–dimensional theory, *Gage* [1979] then argued that $A_{long} \sim 1.75$, and

$$A_{tran} = \frac{5}{3}A_{long}. \tag{44}$$

In the same way, longitudinal and transverse horizontal wavenumber spectra can also be defined, using the $k^{-5/3}$ two–dimensional turbulence spectrum proposed by *Gage* [1979], as follows

$$E_{long}(k) = B_{long}\epsilon^{2/3}k^{-5/3}, \tag{45}$$

$$E_{tran}(k) = B_{tran}\epsilon^{2/3}k^{-5/3}, \tag{46}$$

The structure function constants (A_{long}, A_{tran}) are related to the spectral constants (B_{long}, B_{tran}) by a multiplicative constant [see, e.g., *Tatarski*, 1961], so that (44) also implies

$$B_{tran} = \frac{5}{3}B_{long} \tag{47}$$

Assuming now that a mean wind $\bar{U}$ advects this "frozen–in" two–dimensional turbulence spectrum over a ground–based observer, then ground–based frequency spectra are given by a simple Taylor transformation ($\Omega = k\bar{U}$) of the horizontal wavenumber spectra (45) and (46) [see, e.g., *Gage and Nastrom*, 1988], producing

$$F_{long}(\Omega) = \frac{B_{long}\epsilon^{2/3}(\Omega/\bar{U})^{-5/3}}{\bar{U}} \tag{48}$$

$$F_{tran}(\Omega) = \frac{B_{tran}\epsilon^{2/3}(\Omega/\bar{U})^{-5/3}}{\bar{U}} \tag{49}$$

One can now see that u'_p fluctuations are governed by the $F_{long}(\Omega)$ spectrum, and u'_t fluctuations are governed by $F_{tran}(\Omega)$, so that, using (47)–(49), one can theoretically evaluate R as follows

$$\begin{aligned} R &= \frac{\overline{u_p'^2}}{\overline{u_t'^2}}, \\ &= \frac{\int_{\Omega_1}^{\Omega_2} F_{long}(\Omega)d\Omega}{\int_{\Omega_1}^{\Omega_2} F_{tran}(\Omega)d\Omega}, \\ &= \frac{\int_{\Omega_1}^{\Omega_2} B_{long}\epsilon^{2/3}\Omega^{-5/3}\bar{U}^{2/3}d\Omega}{\int_{\Omega_1}^{\Omega_2} 5/3 B_{long}\epsilon^{2/3}\Omega^{-5/3}\bar{U}^{2/3}d\Omega}, \\ &= 3/5. \end{aligned} \tag{50}$$

Hence the vortical mode and quasi two–dimensional turbulence theories both predict R values less than unity. The two–dimensional turbulence theory suggests that the measured R value is a constant, and does not vary in value as mean wind speeds increase.

To investigate whether similar results might apply to a spectrum of vortical modes, some simple modelling was performed. A horizontal field of vortical modes governed by a $k^{-5/3}$ spectrum was synthesized using similar techniques to those described by equations (33) and (36), with each mode vector having a random azimuth direction. This "frozen" non–interacting spectrum was then advected by a mean flow of velocity $\bar{U}$, and time–series of fluctuating horizontal velocities were recorded at a fixed point on the ground. The variances $\overline{u_p'^2}$ and $\overline{u_t'^2}$ were evaluated for a series of simulations in which $\bar{U}$ was varied, and R values computed. In this simulation, 20 horizontal wavenumber harmonics were used, with the largest equalling $400km$. Based on these choices, an intersampling period of $200s$ was adopted in order to avoid aliasing, and 2500 points recorded in each time series. Due to the random azimuths used, mean values arise due to long–wavelength vortical modes which produce very small frequencies, and must be removed, as would be the case in any experimental study. The results of a number of such simulations are plotted in Figure 44. Each curve is the mean of 60 independently generated time series.

The model produces R values less than unity as predicted. There is a clear tendency for the R values to increase a little as $\bar{U}$ increases, but it is unclear whether this effect is an artifact of the low resolution of the model. Further higher resolution simulations are now in progress.

The final results are summarized below:

Gravity waves	R > 1 (R increases with $\bar{U}$) ,
Vortical modes	R < 1 (R $\approx$ 3/5) .
Quasi two-dimensional turbulence	R < 1 (R = 3/5) .

This ratio R affords several practical advantages over spectral analysis in evaluation of the gravity

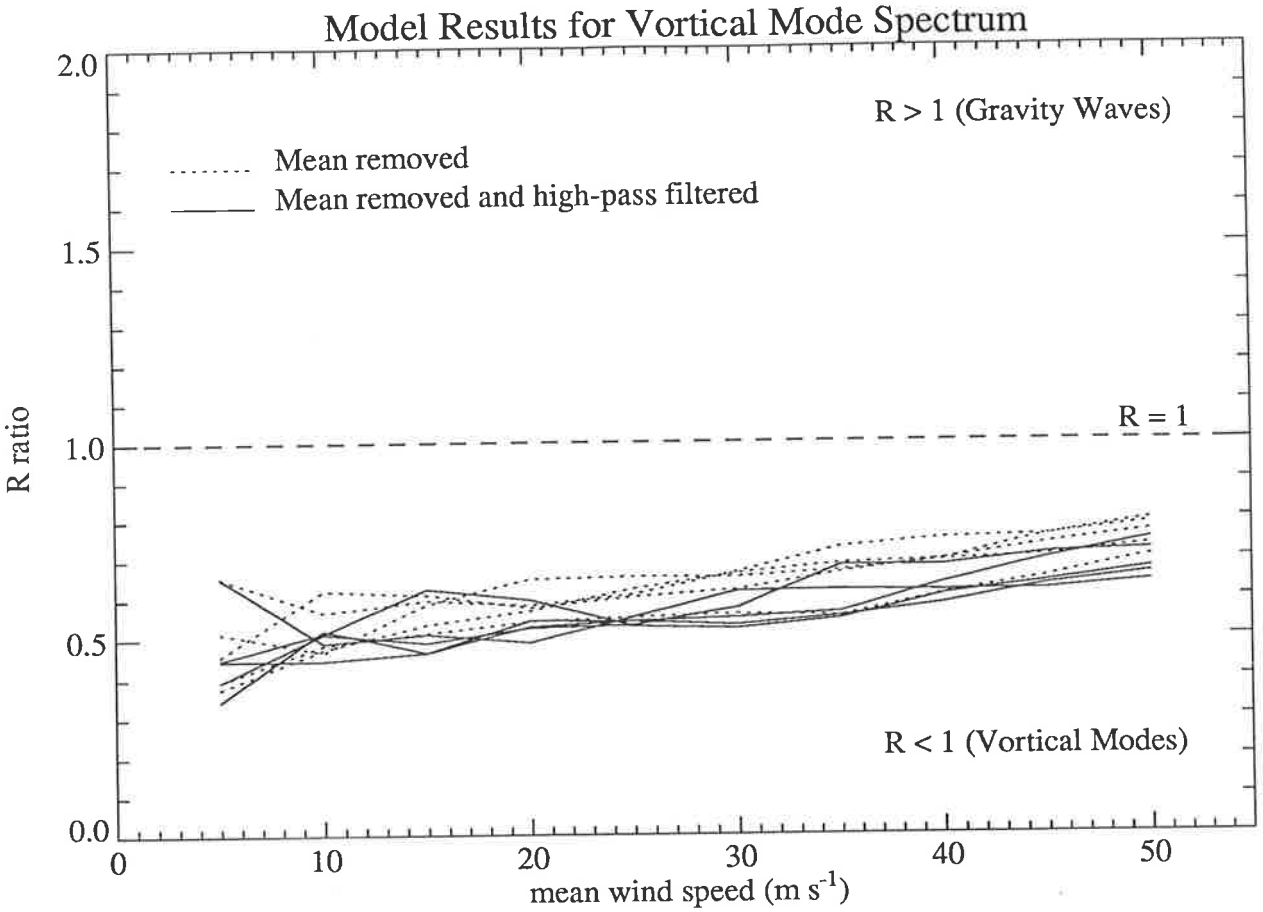

Figure 44: Simulated results of the variation of R with wind speed $\bar{U}$ for a non–interacting $k^{-5/3}$ velocity spectrum of vortical modes. Solid curves are the results obtained when the simulated time series was high–pass filtered such that observed periods greater than $4000min$ were removed. See text for model details.

wave/vortical mode question. Firstly, R remains stationary even when the fluctuating variance is nonstationary, unlike spectra. R can vary, however, when "Doppler nonstationarity" occurs due to mean wind variability, yet these varying values are always > 1 for gravity waves and < 1 for vortical modes, thus still enabling differentiation between each dynamical process. Simulations in the previous section indicated that such differentiation may not always be possible when spectrally analyzing the motion field. R is also a less-derived computation, using the measured fluctuations of horizontal wind velocities directly, whereas spectra must be numerically computed after aquiring the wind data, introducing possible distortion of the spectra during such computations. Yet the well–developed gravity wave and vortical mode spectral theories can still be used to derive theoretical R ratios. Finally, this additional method of evaluating the mesoscale motion field is useful because it provides an independent check of inferences provided by other means (e.g., spectral analysis).

In section 4.2, we apply this polarization ratio R to time series of radar-derived horizontal wind

velocities from the troposphere, and compare the experimental findings with the above predictions of the gravity wave and vortical mode theories. Further theoretical and experimental studies are needed to better quantify the principally qualitative trends in R initially derived in this study.

3.3.5 Conclusions

The nonstationarity nature of mesoscale atmospheric motions can distort the computed spectra of these motions, thus complicating interpretation based upon such spectra. The inherent nonstationarity with altitude of the saturated vertical wavenumber spectrum of gravity waves proposed by *Smith et al.* [1987] gives rise to experimentally calculated spectra which differ significantly in shape from the model spectrum. The principal changes are a broadening of the transition region from saturated to unsaturated spectral shapes, and an enhancement of spectral power at saturated wavenumbers. Both effects combine to give a horizontal velocity power spectrum of the form m^{-t} over a broad range of wavenumbers, where t lies between the nominal unsaturated value of $t = 0$ and the saturated value of $t = 3$. These effects can explain the apparently anomalous nature of many spectral measurements, while not precluding the close agreement to the model spectrum found in other measurements.

More random nonstationarity is encountered in the computation of horizontal wavenumber spectra and ground–based frequency spectra of mesoscale atmospheric fluctuations, While nonstationary variance appears to produce small changes to the stationary spectral shapes, the frequency nonstationarity arising from the advection of a field of vortical modes over a ground–based sensor by a time–varying mean flow can produce distortions to computed ground–based frequency spectra which drive the shape away from the stationary $\Omega^{-5/3}$ shape, and, in some cases, more towards the shape predicted by the competing gravity wave model! Such modifications to spectral shapes due to nonstationarity may well explain, at least in part, the widely varying conclusions of various experimental spectral evaluations of the gravity wave and vortical mode descriptions of these fluctuating motions.

In light of this possibility, the more stationary "polarization ratio" R was developed for time series analysis of ground-based atmospheric measurements of horizontal velocity. This ratio is stationary even when the mesoscale variance is nonstationary, and assumes a distinctly different value if the either gravity waves or vortical modes dominate the variance. This statistic may provide a useful independent means of checking conclusions about the fundamental nature of these mesoscale dynamics made using conventional spectral inspection or other means.

Chapter 4

Gravity Waves in the Troposphere

4.1 Theme

The previous chapter highlighted some of the difficulties involved in objectively analyzing mesoscale atmospheric motions, and offered some possible solutions. In particular, the polarization ratio R was formulated in section 3.3.4 and was presented as being potentially useful in analyzing whether gravity waves or vortical modes/quasi two-dimensional turbulence are responsible for the bulk of the fluctuating variance of the horizontal wind. These ideas are employed in section 4.2 in analyzing horizontal velocity fluctuations in the lower atmosphere as recorded by a VHF radar during the passage of cold fronts over the Adelaide area. In–depth analysis reveals that the fluctuations are consistent with gravity waves, and inconsistent with quasi two-dimensional turbulence.

Having argued that this fluctuating variance is produced mainly by gravity waves, the time–height nature of this tropospheric gravity–wave energy, and its relationship with the frontal activity, is analyzed in section 4.3.

4.2 Evidence for gravity waves

4.2.1 Introduction

Ground–based radars have been used widely to measure mesoscale wind motions in the lower and middle atmosphere, in particular the motions of atmospheric gravity waves. Radar observations have provided information from many sites about various gravity–wave parameters [see, e.g., *Meek et al.*, 1985*a*; *Reid and Vincent*, 1987*b*] and also the spectral characteristics of the wave field in both the wavenumber

and frequency domains [see, e.g., *Frezal et al.*, 1981; *Balsley and Carter*, 1982; *Larsen et al.*, 1982*a*; *Vincent*, 1984; *Balsley and Garello*, 1985; *Fukao et al.*, 1985; *Fritts and Chou*, 1987; *Fritts et al.*, 1988*a*; *Franke et al.*, 1988; *Fritts et al.*, 1990]. These observations revealed that spectra recorded at different locations and at different times of the year often show great similarity in shape and, to a lesser extent, in magnitude. These observations stimulated considerable theoretical effort towards explaining these spectral characteristics. It now appears that the shape of the vertical wavenumber spectrum is determined by gravity wave saturation processes, as discussed in section 3.3.2. Furthermore, *Scheffler and Liu* [1986] and *Fritts and VanZandt* [1987] (hereinafter FV87) have also modelled how the frequency spectrum of gravity waves measured by these ground–based devices varies as a function of background wind speed.

Nevertheless, in the lower atmosphere there is still active debate as to whether the mesoscale horizontal–velocity variance is produced by gravity waves, vortical modes/quasi two–dimensional turbulence, or both (see section 3.3 and references therein). Quasi two–dimensional turbulence also provides spectral predictions, yet, as discussed and demonstrated in section 3.3.3, discrimination between gravity waves and quasi two-dimensional turbulence by direct spectral computation and inspection has some difficulties, most noteably the inherent nonstationarity of these motion spectra, and experimental studies have yet to produce conclusive results. However, these spectral predictions were used in section 3.3.4 to formulate predicted variations in a new term which is more insensitive to the inherent nonstationarity of the mesoscale variance. This relation R, which was termed the "polarization ratio", is computed from ground–based measurements of horizontal-velocity variance according to equation (38), and so can be applied to ground–based radar measurements of atmospheric winds.

An ST[1] radar operating at VHF (54.1 MHz) at a site near Adelaide was operated for extended periods during late–1988, and resolved high–frequency fluctuations superimposed on the background flow. These particular observations were part of a larger study of the mesoscale dynamics associated with the passage of cold fronts, and were directed toward investigating possible gravity wave generation by frontal activity. However, before such analysis can be performed, one must determine whether the observed mesoscale variability is due to gravity waves or quasi two-dimensional turbulence. The wind fluctuations with periods of a few hours or less exhibited a high degree of azimuthal anisotropy, such that they were aligned preferentially along the direction of the background wind, an effect which became more noticeable as background wind speeds increased. Although both gravity waves and two–dimensional turbulence may contribute to the mesoscale wind field, theory and observation, based primarily around trends in the "polarization ratio" R computed from these data, reveal that the observed behaviour is

[1] stratosphere–troposphere

more consistent with the anticipated effects of Doppler shifting of gravity wave energy, as described by FV87.

The experimental situation and data analysis techniques are described in section 4.2.2. The morphology of the mean winds and the mesoscale fluctuations about these means is discussed in sections 4.2.3 and 4.2.4, respectively. The results are evaluated in terms of the gravity wave and turbulence models in section 4.2.5, and their implications for these and other ground–based wind studies in the middle atmosphere are discussed in section 4.2.6.

4.2.2 Data Analysis

The data analyzed hereafter were acquired during the passage of cold fronts across southern Australia. The wind measurements were made using The PHARLAP[2] System, which is an ST radar wind profiler located on a coastal plain some $40km$ north of Adelaide (35°S, 138°E). The site is flat, and the nearest hills are situated about 40–$50km$ to the east. The radar operates at a frequency of 54.1 MHz, and is designed to use either spaced antenna or Doppler beam–swinging methods to measure winds. The data used in this study were obtained exclusively by the spaced–antenna method.

Full details of the configuration and operation of The PHARLAP System are given by *Vincent et al.* [1987], but salient features are briefly described here. The transmitting antenna array is of the coaxial–colinear (CoCo) type, is 16λ square, and has a theoretical half–power half–width of about 1.6° [see, e.g., *Eckermann*, 1986]. In these experiments, it was phased to transmit vertically. Three smaller Yagi arrays were arranged to form an equilateral triangle with a basic spacing of $\sim 50m$ and were used for reception. A solid–state transmitter with a pulse repetition frequency (PRF) of $8192Hz$ was used, and 4096 received pulses were coherently integrated, so that the sampling interval was $0.5s$. Using a pulse length of $7ms$, the mean power was about $300W$, and with this relatively low power, echoes were received from the troposphere and the lowest part of the stratosphere only. These echoes were sampled every $500m$ in a height range between 2 and $12km$.

In this experiment, The PHARLAP System transmitted for about $2min$, and the returns were then analyzed in real time before the next set of measurements were made. Since the analysis took a total of about $2min$ for the full 20 heights sampled, this meant that winds were recorded every $4min$. Horizontal wind velocities were computed by applying so–called Full Correlation Analysis to the complex echo amplitudes, after correction for noise [*Briggs*, 1984; *Vincent et al.*, 1987; *May*, 1988]. There is close

[2] Phased Array Radar for Lower Atmosphere Profiling: This system is owned and operated by The Department of Physics and Mathematical Physics, University of Adelaide.

START TIME	FINISH TIME	TOTAL DURATION
10 a.m., 19th. August	7.30 a.m., 30th. August	10 days, 21.5 hours
2 p.m., 10th. November	7.30 a.m., 18th. November	7 days, 15.5 hours
12 noon, 18th. November	9.30 a.m., 24th. November	5 days, 21.5 hours
10 a.m., 28th. November	10.45 a.m., 11th. December	13 days, 0.75 hours

Table 1: Starting times, finishing times, and total durations of 4 extended observational campaigns conducted during 1988 using The PHARLAP System at Buckland Park, the data from which were analyzed in this study.

agreement between the resulting radar wind velocities, and winds measured by balloon–borne radiosondes launched from nearby Adelaide Airport [*Vincent et al.*, 1987]. Vertical wind velocities were deduced from the Doppler shifts of the echoes, using the phase of the complex autocorrelation functions. The resulting wind data were then stored on disc for subsequent off–line analysis.

Post–analysis commenced with an editing procedure designed to remove spurious points (outliers) from the data. Various editing techniques have been proposed [see, e.g., *Bemra et al.*, 1986] and, after some testing, a procedure which progressively removed outliers in a series of repeated steps at each height of observation was adopted. The algorithm operated as follows: (1) The mean wind velocity vector was computed within a given time window of 2–hour duration. (2) The individual wind value in that block which showed the largest deviation in vector magnitude from the mean was discarded. (3) Steps (1) and (2) were repeated four times before moving on to the next 2–hour block.

This method typically removed about 10% of the data, and while it probably removed some good data points, it also succeeded in removing most outliers. To increase the reliability, and to reduce aliasing by high–frequency motions, 15–*min*-average values were formed for the zonal (u), meridional (v), and vertical (w) velocity components at each height. Due to the horizontal displacement between the transmitting and receiving antennae, it was necessary to correct the vertical velocities for possible contamination by the horizontal winds [see, e.g., *Vincent et al.*, 1987]. Any short gaps in the 15–*min* averages were interpolated using a cubic spline which was fitted over the good data in the time series. This was done to ensure that sharp transitions due to missing data did not contaminate the spectrum during numerical filtering of the data into different period bands using an FFT[3] routine. However, these interpolated values were "labelled" so that they were not used in any subsequent calculations using the data.

4.2.3 Mean Winds

Winds were measured continuously for periods extending up to a month in duration, with passages of cold fronts usually occurring every 5 to 10 days. In this study, data from 4 long–term observations in 1988

[3]Fast Fourier Transform

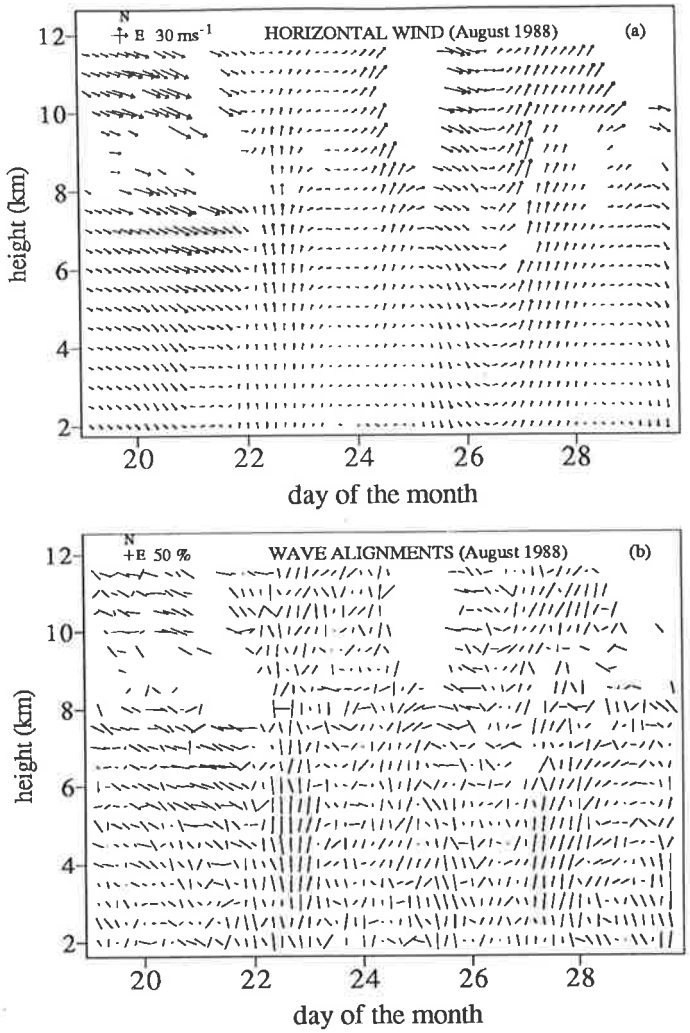

Figure 45: (a) Height–time cross sections of the horizontal winds observed in the troposphere at Adelaide from 19th.–30th. August, 1988. Mean wind vectors are plotted every 4 hours. (b) Height–time cross sections of the alignment of mesoscale motions in the period August 19 to 30, 1988. Each line represents the degree of polarization and alignment (see text) of motions in the period range 0.5–2 hours averaged over a 4-hour interval. The x–axis ticks occur at midday on the indicated day of the month.

were used, which totalled about 35 days of tropospheric wind data (see Table 1). Figures 45*a*, 46*a*, and 47*a* all show the morphology of the mean horizontal wind variations which occurred during the passage of frontal systems during August and November 1988. The plots are of 4–hourly averaged wind vectors which show the magnitude and direction toward which the wind is directed. An upward–pointing vector indicates northward flow, and a vector pointing to the right indicates eastward flow (see the key in the top–left corner of the plots). The time evolution of the wind field during the passage of the fronts on August 22, August 26, November 14, and November 20/21 is typical of that observed during the passage of moist wintertime and early–summer fronts [*May*, 1986; *Vincent et al.*, 1987; *May et al.*, 1990]. Ahead of the front the winds are strong ($\sim$20–40$m\ s^{-1}$) and are directed toward the southeast. After the frontal boundary has passed overhead, the winds swing round or "back", and become essentially northward.

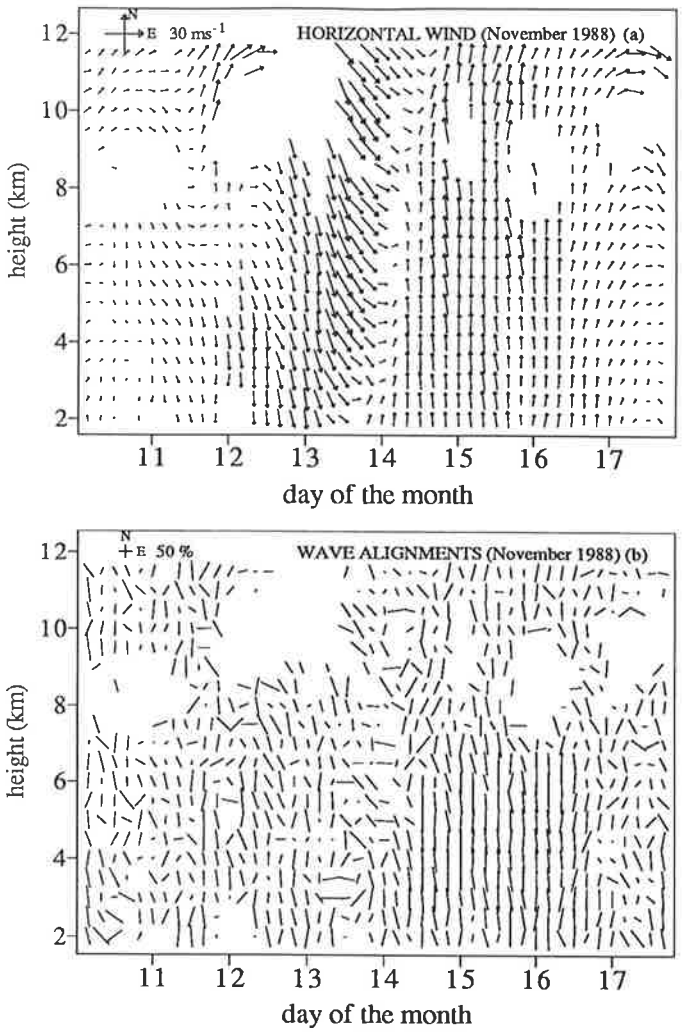

Figure 46: As for Figure 45, but for the period November 10 to 18, 1988.

Mean winds, and other quantities computed later, were rejected as unreliable if >50% of the expected number of data points were missing in any given calculation. One can see in Figures 45*a*, 46*a*, and 47*a* that data gaps result for lengthy periods at altitudes above 7–8km. There are two reasons for these breaks in the data. The principal reason is that temperature lapse rates at heights immediately below the tropopause, which varied during frontal passages but was usually at an altitude near 10km during these measurements, were often very close to the dry adiabatic lapse rate. This is particularly so just prior to a frontal passage. Even in the presence of strong turbulence there can be only small fluctuations in the radio refractive index, and hence weak radar backscatter from these regions. This process is investigated in greater depth in section 4.3. Secondly, the galactic centre, which is a strong source of noise at VHF, passes close to the zenith for several hours each day [see. e.g., *Eckermann*, 1986]. The strong increase in background noise coupled with weak scatter often resulted in poor signal–to–noise ratios for echoes just below the tropopause, and the data were frequently rejected.

4.2.4 Mesoscale Wind Motions

The temporal variations of motions associated with mesoscale phenomena were studied by numerically filtering time series of zonal, meridional, and vertical wind components. The time series of 15–*min.*–average wind values were bandpass filtered to produce perturbation wind components, u', v', and w', in three different bands which covered the period ranges 8 to 24 hours, 2 to 8 hours and 30 *min* to 2 hours, respectively. Hereafter these ranges are referred to as the "long–", "medium–", and "short–" period bands. The variances of the wind components were computed for each band. Examination of the sum of the horizontal variances $\overline{u'^2_{TOT}} = (\overline{u'^2} + \overline{v'^2})$, which is proportional to kinetic energy per unit mass, indicated that these energies varied strongly with time, and this variation was strongly coupled to the fronts. Section 4.3 is devoted to the study of these features. Here, however, the anisotropy which was evident in the horizontal motions is investigated.

An objective way of determining the polarization of wave energy in a statistical sense is to compute the so–called Stokes parameters, a method which has been applied to studies of wave motions in the mesosphere [*Vincent and Fritts*, 1987] and stratosphere [*Eckermann and Vincent*, 1989] (see also chapter 6). The method makes use of the following quantities, calculated for a suitable frequency band:

$$I = \overline{u'^2} + \overline{v'^2}, \tag{51}$$

$$D = \overline{u'^2} - \overline{v'^2}, \tag{52}$$

$$P = 2\overline{u'v'\cos\delta}, \tag{53}$$

$$Q = 2\overline{u'v'\sin\delta}. \tag{54}$$

I is the sum of the zonal and meridional velocity variances, D their difference, P and Q the in–phase and quadrature covariances, and δ is the phase difference between the u' and v' components. For high frequency motions ($\omega \gg f$), the u' and v' motions are essentially in–phase ($\delta \approx 0°$), so that Q (which is difficult to compute) should be negligible. The inertial frequency, f, is $8.34\text{x}10^{-5} rad\ s^{-1}$ at Adelaide, which corresponds to a period of 20.9 hours, so that Q is probably small for intrinsic wave periods less than ~2 hours, since these periods are much smaller than the inertial period, although the effects of Doppler shifting of frequencies must be borne in mind.

Using these Stokes parameters, it is possible to calculate the degree of polarization, defined as

$$d = \frac{(D^2 + P^2 + Q^2)^{1/2}}{I}, \tag{55}$$

which reduces to

$$d = \frac{(D^2 + P^2)^{1/2}}{I} \tag{56}$$

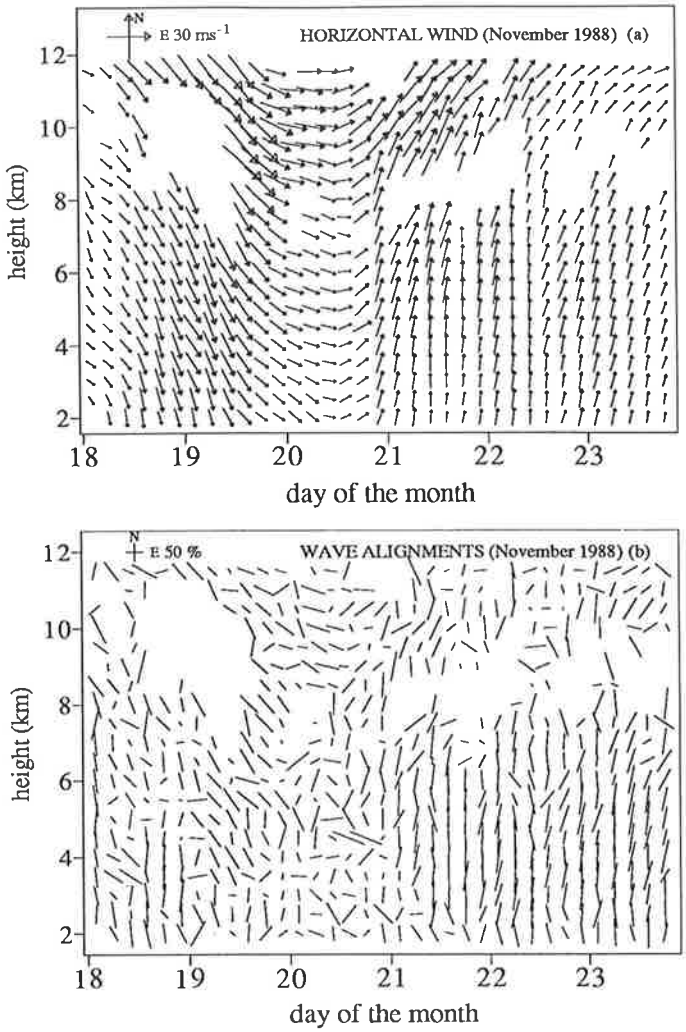

Figure 47: As for Figure 45, but for the period November 18 to 25, 1988.

in the high–frequency limit. This factor d gives the ratio of the polarized to unpolarized motions, so that $d = 1$ signifies a totally polarized field, whereas $d = 0$ denotes an random wave field. The mean azimuthal alignment of the polarized motions, $\bar{\phi}$, is given by

$$\bar{\phi} = \frac{1}{2} \arctan\left(\frac{P}{D}\right). \tag{57}$$

Figures 45*b*, 46*b*, and 47*b* show plots of the time–height polarization characteristics of the fluctuating wind motions in the 30–*min* to 2–hour period range. Results have been averaged over the same 4–hour intervals as were used for the mean wind vectors shown in Figures 45*a*, 46*a*, and 47*a*. The polarization is represented by a line whose length is proportional to the degree of polarization d, and whose rotation anticlockwise from east denotes the alignment $\bar{\phi}$. The d values were calculated using the high–frequency formula (56), and so must be considered lower–bounds on this value. Yet despite this, high degrees of polarization d are frequently observed (note the length scale in the top–left corner of the plots). These lines are, of course, not vectors since the Stokes–parameters technique does not provide information

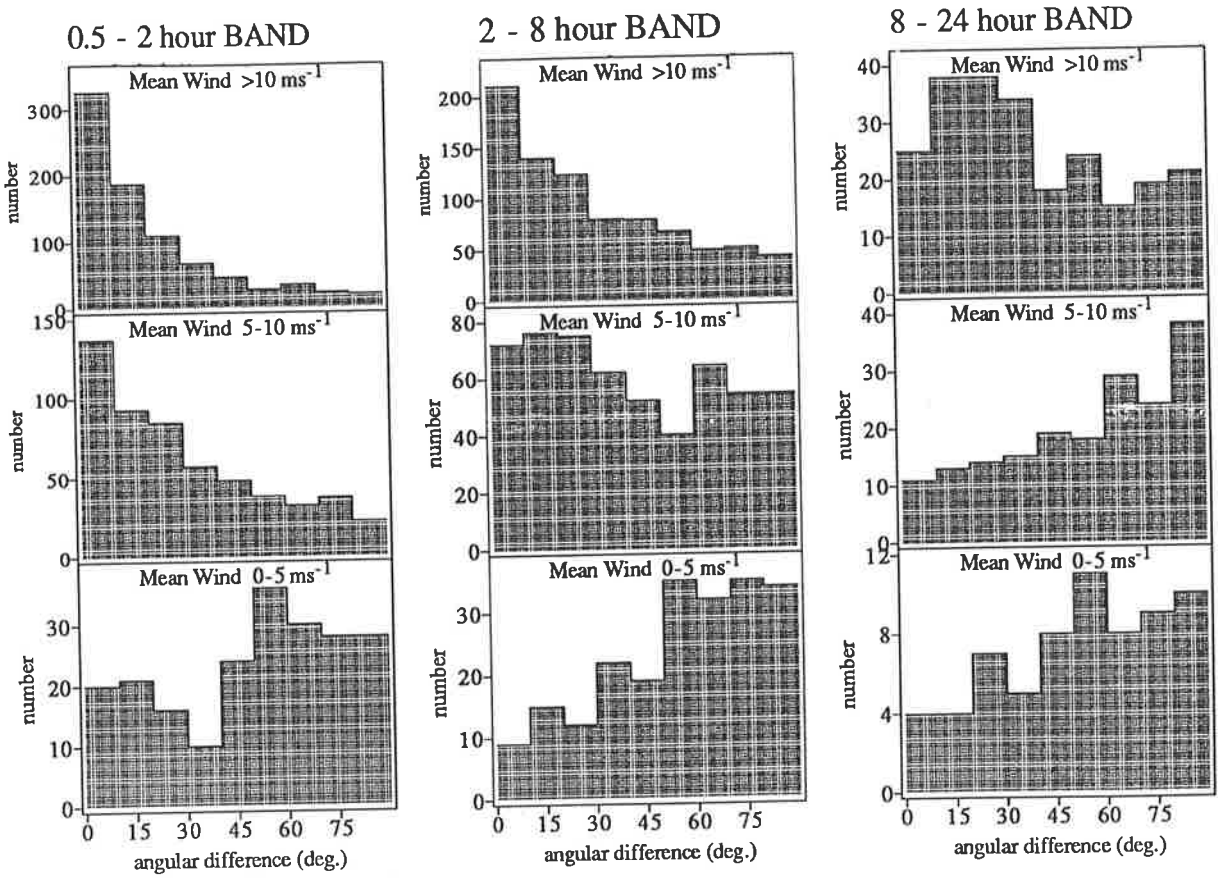

Figure 48: Histograms of the difference between the direction of the mean wind ($\bar{U}$) and the alignment of mesoscale motions plotted for mean wind speeds of 0–5, 5–10, and $>10m\ s^{-1}$. 0° implies parallel alignment, and 90° means transverse alignment. For motions in the 0.5–2 hour and 2–8 hour period bands, the data are for all heights of observation averaged over 8–hour intervals. For the 8–24 hour period band, the data are averaged over 24-hour intervals.

about the absolute directions of propagation of any waves which may cause the perturbation wind field to be polarized. Close inspection of these wind vector and polarization–plot pairs reveals that there is a strong correlation between the alignments and the direction of the mean wind vectors, such that the perturbations are aligned along the direction of the mean wind. This tendency is especially strong during periods of high wind speed, particularly when the wind is steady in strength and direction over a long duration.

To quantify this apparent relation between alignment and wind, the alignment data were classified into three background wind speed ranges of 0–$5m\ s^{-1}$, 5–$10m\ s^{-1}$, and greater than $10m\ s^{-1}$, corresponding to (arbitrary) low–, medium–, and high–wind conditions respectively. For each wind range, the angular differences between the alignments and wind vectors were computed, and grouped in 10° intervals in the range 0–90°. Figure 48 shows histograms of the number of observations in each interval as a function of mean wind speed, for all three period bands, and using all the radar wind observations detailed in Table 1. To simplify the comparisons, the data for both the short– and medium–period bands were both

averaged over 8–hour segments, and the long–period band data were averaged over 24–hour segments.

For motions in the short-period band at low wind speeds ($\bar{U}$ = 0–5m s^{-1}), the angular differences are reasonably evenly spread, although there is some preference for perturbation wind motions to be aligned within a range of angles at 45–90° to the mean wind (i.e., approximately transverse to the wind direction). As the wind speed increases, however, the histograms become more strongly clustered in the range 0–20° (i.e., there is a strong polarization parallel to the mean wind).

Results for motions in the medium– and long–period bands are also shown in Figure 48. Similar trends are evident in the medium–period motions, although the clustering evolves more gradually with $\bar{U}$ than it does for the high–period data. There are fewer intervals for analysis in the long–period (8–24 hour) range, as the results are averaged over 24–hour intervals. The long–period histograms contrast the higher frequency results by exhibiting a stronger tendency for these perturbations to become aligned transverse (~90°) to the wind for speeds between 5–10m s^{-1}. Even in high–wind conditions, the histogram shows that the angular differences are rather evenly spread, with a slight tendency to group in ranges near 30°, as opposed to the strong clustering near 0° evident for the higher frequency motions.

Care must be taken in attributing all of the motion in the low–frequency range to phenomena such as waves or turbulence because, particularly during the passage of fronts, the mean wind itself changes systematically in magnitude and direction on time scales of about a day (see Figures 45a, 46a, and 47a). During the filtering process, these systematic changes themselves will produce Fourier components which will contribute to the variance at long periods.

4.2.5 Interpretation of the Data

Computation of the Stokes parameters of the horizontal wind fluctuations has revealed high degrees of polarization and strong azimuthal anisotropy. For motions with periods of 8 hours or less, there is an increasing tendency for the motions to be aligned along the mean wind direction as the wind velocity increases. This tendency is particularly marked in the short–period fluctuations. An immediate question is whether this effect is an artifact of the spaced antenna wind measuring technique used to make the measurements.

There are several reasons that indicate that the effect is not consistent with some sort of measurement bias. Firstly, the receiving antennae were carefully arranged at the vertices of an equilateral triangle so as to alleviate any possible biases in the measurement of wind direction [*Vincent et al.*, 1987]. Secondly, estimates of the random errors which arise during spaced antenna wind measurements, based on the theory of *May* [1988], show that the errors are equally distributed between the wind components parallel and

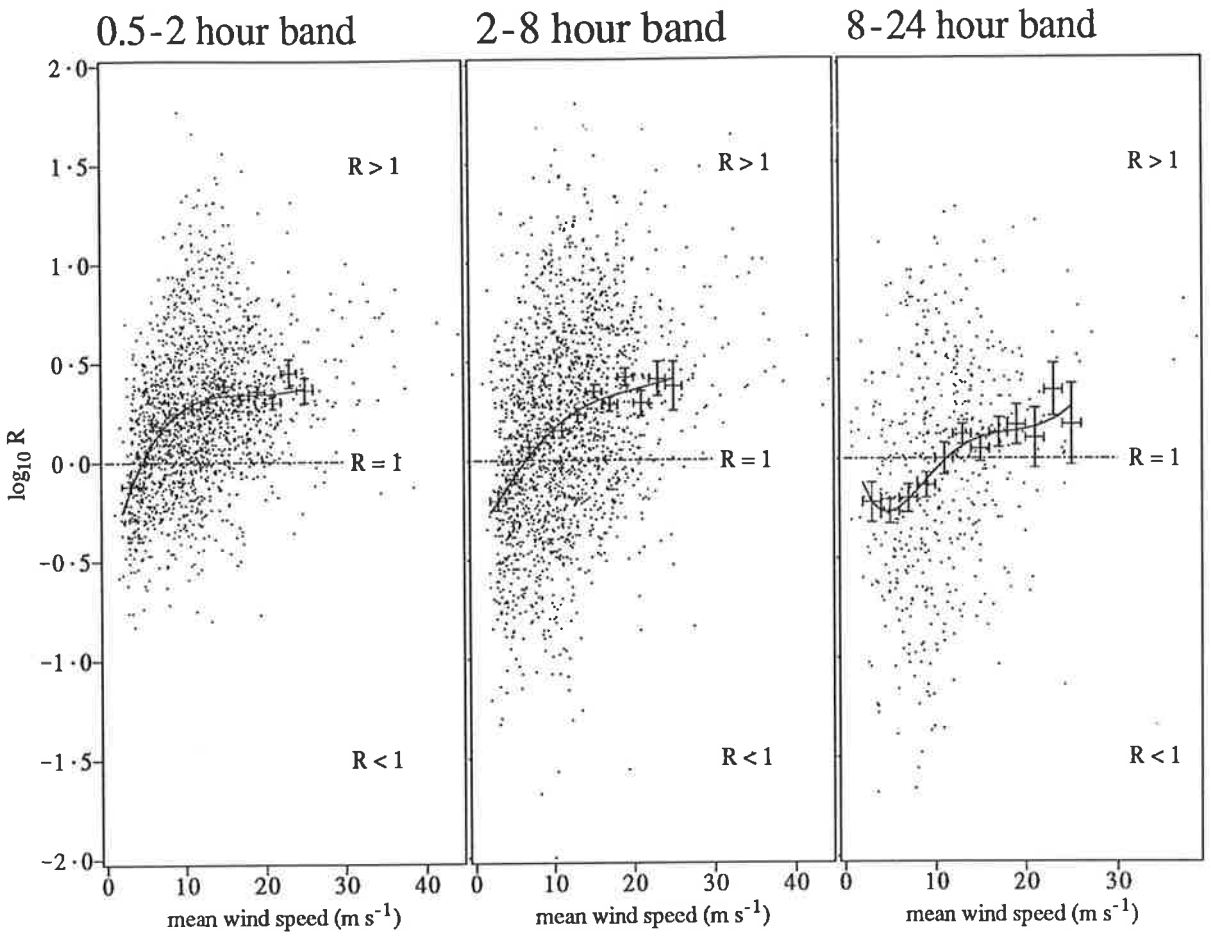

Figure 49: Plots of the $\log_{10}(R)$ versus $\bar{U}$, where R is the ratio of the variances of mesoscale motions parallel to and transverse to the mean wind direction. Each point represents an 8–hour average for the 0.5–2 hour and 2–8 hour period bands, and 24–hour averages for the 8–24 hour band. The solid line is a least–squares sixth–order polynomial fit to the data, and the bars show the associated standard errors within the indicated x–axis ranges.

transverse to the mean wind vector. Thirdly, any effects of random errors are also considerably reduced by the extensive averaging that was carried out, firstly into 15–*min* means, and then by averaging the band–passed data in 4–, 8–, and 24–hour time blocks. Finally, if these fluctuations were due to random errors of some kind, the degrees of polarization, d, should be near–zero after such extensive averaging. It is clear from Figures 45*b*, 46*b*, and 47*b* that most values of d lie between 50 and 100%.

On these bases, one must conclude that the observed anisotropies are manifestations of atmospheric mesoscale phenomena which are strongly influenced by the strength of the prevailing wind. We must now determine whether gravity waves and/or quasi two-dimensional turbulence are responsible for the mesoscale variance, and can account for the systematic behaviour of the azimuthal alignment of these fluctuations as a function of mean–wind speed.

In order to determine which process(es) produce this measured variance, the "polarization ratio" R was calculated, and its behaviour investigated as a function of background wind within the various frequency

intervals. Figure 49 plots $\log_{10}(R)$ versus the mean wind speed $\bar{U}$, using all the available data. For the short– and medium–period bands, each point represents an 8-hour average, while for the long–period data each point represents a 24–hour mean. The solid curve is the least–squares fit of a sixth–degree polynomial to $\log_{10}(R)$; this unbiased fit more clearly and quantitatively illustrates the trends which are evident in the scattered data points. The y–axis bars are the computed standard errors within the mean wind ranges indicated by the x–axis bars. These plots show more quantitatively what was evident from inspection of Figure 48. Except at low wind speeds ($\bar{U} < 5m\ s^{-1}$), R is always greater than unity for the shorter period bands, and increases steadily as $\bar{U}$ increases, to values of R ~2–10. For the long-period motions, however, R is less than unity for $\bar{U}$ less than about $15m\ s^{-1}$, indicating that transverse motions appear to predominate. Only at the largest wind speeds does u'_p exceed u'_t.

According to the theory developed in section 3.3.4, the qualitative trends in Figure 49 support a gravity–wave interpretation. While the spectral theories were discussed in some depth in section 3.3.3, the discussion is extended here to enable more quantitative application of the spectral theories of FV87 and *Gage and Nastrom* [1988] to the polarization ratio R.

The Gravity Wave Model

The effects of Doppler shifting on gravity–wave frequency spectrum $E_u^{GW}(\Omega)$ are best demonstrated by using the relations derived by FV87. They considered the case of a two–dimensional model where waves could propagate either with or against the mean–flow direction. As (35) shows, those waves which propagate perpendicular to the mean flow are not Doppler shifted in frequency. Figure 39*a*, which follows Figure 4*a* of FV87, shows the model ground–based frequency spectra of horizontal wind motions for three values of β, where β is the wind speed, $\bar{U}$, divided by the so–called characteristic intrinsic horizontal phase speed of the wave field, c_*. This characteristic phase speed is, in turn, more conveniently expressed in terms of the characteristic vertical wavenumber, m_* (see (29) and (31) in section 3.3.2), so that $\beta = \bar{U}/(N/m_*)$, where N is the Brunt-Väisälä frequency [FV87]. As we are interested here in the change in variance of the horizontal motions, a better impression of this change is given by replotting the frequency spectra in energy content form, $\Omega E_u^{GW}(\Omega)$ [*VanZandt*, 1985], as shown in Figure 50. The vertical lines indicate approximately the boundaries of the frequency intervals used in this study. The horizontal velocity variance in any given interval for a particular value of $\bar{U}$ is directly proportional to the area under the appropriate curve in Figure 50. The shifting of variance to higher frequencies as β (proportional to $\bar{U}$) increases is especially apparent in these energy–content spectra; indeed, for $\beta = 5$, the spectral peak has shifted to observed periods of about 6–7 hours, and at $\beta = 10$, the curve peaks at

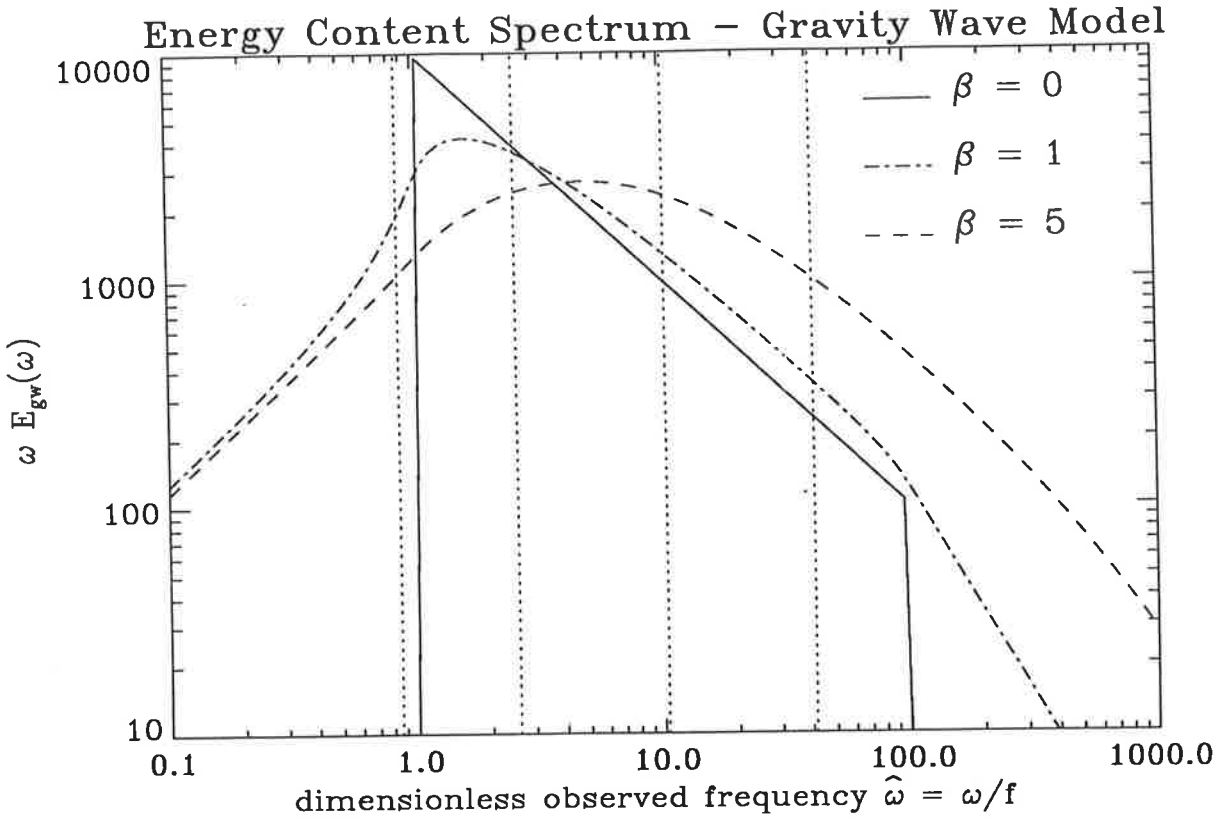

Figure 50: Model ground–based frequency spectra of gravity wave horizontal velocity motions, re–plotted in energy–content form, $\Omega E_u^{GW}(\Omega)$.

about a 2–hour observed period.

Under high–wind conditions (β ~5–10), one can estimate that for the short–period band, the variance due to gravity waves with a significant component of their motion parallel to the mean flow will be a factor ~2–3 times greater than that for the zero–wind situation. Since the variance due to waves propagating at right angles to the horizontal flow is unaffected by Doppler shifting (i.e., $\beta = 0$), we know from section 3.3.4 that this should make R significantly greater than unity for large $\bar{U}$.

Some caution must be exercised before applying the theoretical results shown in Figures 39*a* and 50 to the results in Figures 45–49. Firstly, for ease of calculation, one should note that FV87 used a model of the intrinsic frequency spectrum in which the spectral density varied as ω^{-2}, rather than the usually accepted $\omega^{-5/3}$. However, use of a more realistic spectral slope is unlikely to change the overall conclusions presented here. Secondly, we do not know the appropriate value for $c_* = N/m_*$, the characteristic horizontal phase speed. Estimates of m_* can be made from inspecting the computed vertical wavenumber spectra [see, e.g., *Smith et al.*, 1987; see also section 3.3.2], but there is insufficient height resolution to enable such a computation with these data. Observations in the Northern Hemisphere give values in the range $(m_*)^{-1}$ ~1–3km in the troposphere and lower stratosphere [*Smith et al.*, 1987;

Fritts and Chou, 1987; *Fritts et al.*, 1988], which suggests that $c_* = N/m_* \sim 1.5\text{–}5m\ s^{-1}$, using a value of $N \sim 0.01\ rad\ s^{-1}$ appropriate to the troposphere. Characteristic phase speeds of this magnitude imply that values of β greater than about 10 are quite feasible during the passage of fronts, when wind speeds up to and exceeding $30m\ s^{-1}$ are maintained for many hours (see Figures 45*a*, 46*a*, and 47*a*). Such values of β, therefore, could easily produce the observed changes in R seen in Figure 49 for the high– and medium–period bands.

For the long–period band, it is more difficult to predict how R should change as $\bar{U}$ increases. Figure 50 shows that there is a net decrease in the parallel wind component as β increases, which initially suggest that R should be less than unity here, as observed in light–wind conditions in Figure 49. However, as discussed in section 3.3.4, the horizontal motions of gravity wave oscillations where ω is near f are elliptically polarized, which means that there will be a decrease in the contribution to u'_t from parallel propagating waves. Waves propagating transverse to $\bar{U}$ will also contribute to u'_p. For reasons outlined in section 3.3.4, this effect should not be serious over the whole spectrum, but it may be serious within this low–frequency band. Yet another complicating factor is the probable contamination caused by systematic changes in the mean wind during by frontal passages, which contributes to these low–frequency variances, as mentioned earlier.

Doppler shifting of the gravity–wave spectra also redistributes the energy of the vertical fluctuating motions. The net effect is to produce a decrease in energy at observed frequencies less than the Brunt-Väisälä frequency, N, and an increase for frequencies greater than N [see FV87]. At the frequencies we are dealing with here, the predicted effect is to increase the ratio of horizontal to vertical fluctuating variances as $\bar{U}$ increases [see FV87, Figure 5], especially in the short– to medium–period bands. Figure 51 shows scatter plots of $\log_{10}(\overline{u'^2_{TOT}}/\overline{w'^2})$ against $\bar{U}$ for the three period bands, where $\overline{u'^2_{TOT}} = (\overline{u'^2} + \overline{v'^2})$ is the total variance of the horizontal motions. It is clear that the ratio increases in the manner predicted, with the ratio for the short–period band increasing by greater than an order of magnitude as the wind speed increases from near zero to over $30m\ s^{-1}$. Inspection of Figure 6 in FV87 suggests that one would expect an increase of about a factor of 10 as β increases from 0 to 10. Considering the approximations inherent in the calculations of FV87, there is extremely good agreement between the results in Figure 51 and their predictions.

Vortical Mode Model

The mesoscale fluctuations produced by vortical modes in the short wavelength limit are transverse to the wave normal, and are constrained to the horizontal plane (see Figure 38 in section 3.3.3). As

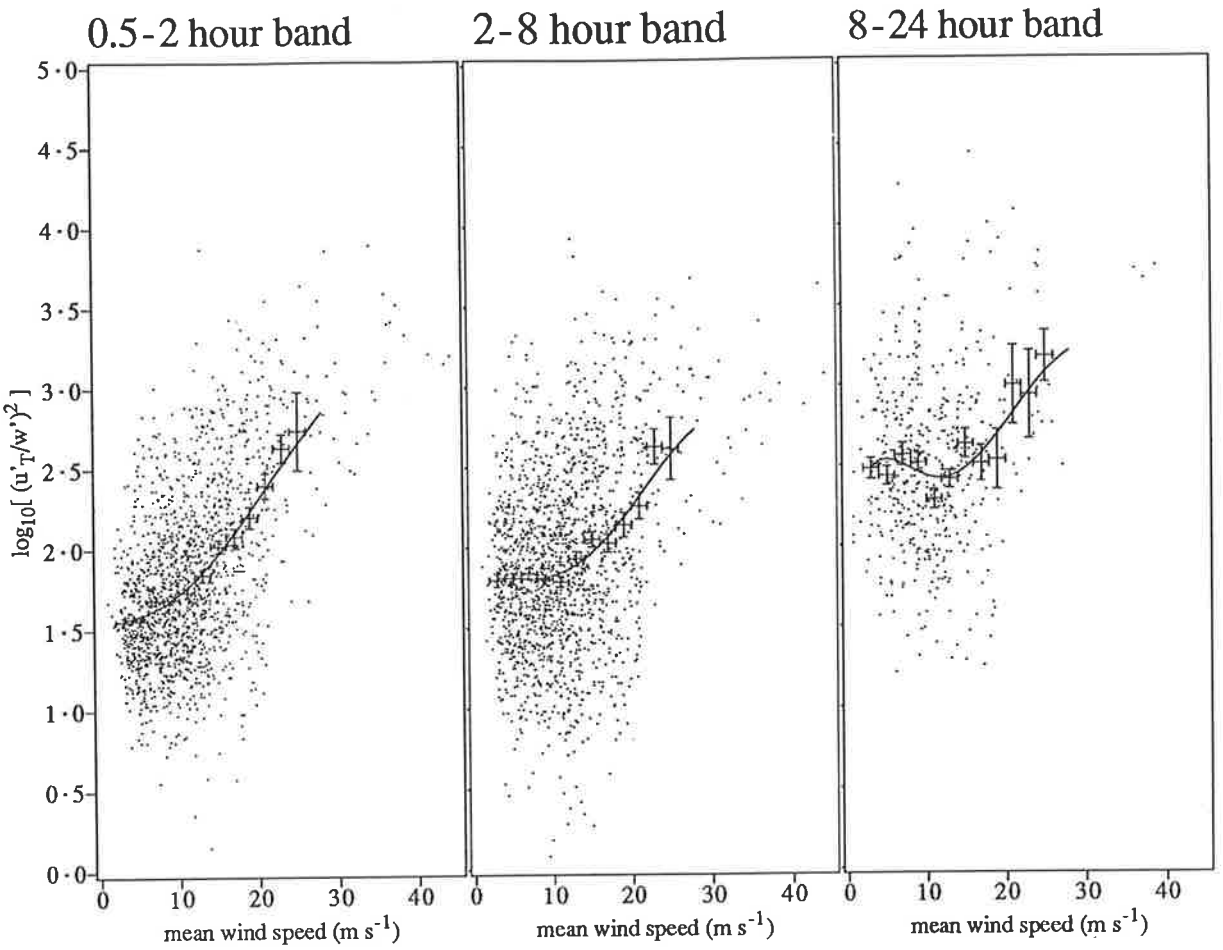

Figure 51: Scatterplots of $\log_{10}(\overline{u'^2_{TOT}}/\overline{w'^2})$ as a function of wind speed. Each point in the 0.5–2 hour and 2–8 hour bands represents an 8–hour average, and the points in the 8–24 hour band are 24–hour averages. The solid line is a least–squares sixth–degree polynomial fit to the data, and the y–axis bars show the standard errors within the indicated x–axis ranges.

discussed in section 3.3.3, vortical modes have no intrinsic frequency ($\omega = 0$), but a prevailing wind of velocity $\bar{U}$ produces a Doppler shift which gives rise to an associated vortical mode frequency measured at the ground of $\Omega = \mathbf{k_h}.\bar{\mathbf{U}}$. *Gage and Nastrom* [1988] used this relation (which took the form of a Taylor transformation in their analysis because they adopted a quasi two–dimensional turbulence interpretation) to determine the frequency spectrum, $E_u^{VM}(\Omega)$, of vortical modes as a known horizontal wavenumber spectrum $\mathcal{F}_u^{VM}(k_h)$ is advected over a vertically–pointed ground–based remote sensor. The resulting frequency spectrum is

$$E_u^{VM}(\Omega) = \mathcal{F}_u^{VM}(k_h)/\bar{U} = \mathcal{F}_{vm}(\Omega/\bar{U})/\bar{U}, \tag{58}$$

where of spectral analysis of winds measured by instrumented aircraft (The Global Atmospheric Sampling Program) were used to provide a model form for $\mathcal{F}_u^{VM}(k_h)$ proportional to $k_h^{-5/3}$, as shown earlier in Figure 27 [*Nastrom and Gage*, 1985].

It should be noted that (58) is incomplete in the strict mathematical sense, in that a more extensive

analysis shows that a better spectrum would have the functional form $\mathcal{F}_{vm}(\Omega/\bar{U}\cos\phi)$ / $(\bar{U}\cos\phi)$, if the k_h spectrum is isotropic, and assumes different forms again if the k_h spectrum is anisotropic [*K. C. Yeh*, private communication, 1989]. All theory to date has assumed an isotropic k_h spectrum of vortical modes. For gravity waves, critical level interactions and (possibly) directional sources can produce an anisotropic k_h spectrum, but there is no obvious physical process evident in the literature which might give rise to an anisotropic k_h spectrum of vortical modes/two–dimensional turbulence. We therefore take (58) as the being appropriate for our purposes.

Figure 39*b* illustrates the Doppler–shifted spectrum predicted by *Gage and Nastrom* [1988], plotted for different background wind conditions. Comparison with Figure 39*a* shows that the shape of the vortical mode spectrum is preserved as $\bar{U}$ increases, unlike the Doppler–shifted gravity wave spectrum, and that the spectral density at a given observed frequency increases as $\bar{U}$ increases. Using this theory, it was demonstrated in section 3.3.4 that such a spectrum of vortical modes advected over a ground–based observing site will give rise to R values less than unity, notwithstanding an alternative interpretation in terms of quasi two–dimensional turbulence, which clearly disagrees with the results presented in Figure 49. Due to the divergence between theoretical predictions and observational results, one must conclude therefore that vortical modes do not contribute significantly to the motion field in these tropospheric observations.

4.2.6 Discussion

Wind measurements made with the Adelaide VHF ST radar (The PHARLAP System) show that time–fluctuating horizontal winds, which are associated with mesoscale phenomena in the troposphere, exhibit strong azimuthal anisotropy. The anisotropy manifests itself as a tendency for the motions to become increasingly aligned along the direction of the background wind as its strength increases, and the fluctuations have high degrees of polarization d. The effect is most strongly observed in motions with observed periods in the 30–*min* to 2–hour range.

The results were interpreted in terms of the effects of Doppler shifting by a non–zero mean wind, $\bar{\mathbf{U}}$, on model spectra of atmospheric gravity waves and vortical modes/quasi two–dimensional turbulence. In both of these models, Doppler shifting produces an increased variance at middle– to high–observed frequencies for "waves" which have a component of their horizontal wavenumber parallel or antiparallel to $\bar{\mathbf{U}}$. Oscillations which are aligned at right angles to $\bar{\mathbf{U}}$ are unaffected by Doppler shifting. However, the resulting ratio, R, of the recorded variance parallel to and perpendicular to $\bar{\mathbf{U}}$ is different for the two models, a disparity which arises because of the different polarization of the perturbation motions

associated with gravity waves and vortical modes, as developed in section 3.3.4. Gravity wave theory predicts an enhancement of R greater than unity as $\bar{U}$ increases, as observed in Figure 49, whereas the vortical mode model predicts R less than unity as $\bar{U}$ increases, in complete contrast to the observations.

On this basis, one must conclude that these mesoscale fluctuations are consistent with the hypothesis that, in the lower atmosphere, gravity waves are responsible for the bulk of the variance in the mesoscale wind field, and that vortical modes or quasi two–dimensional turbulence are not significant in terms of energy. The contribution that vortical modes might make to shear and potential vorticity in the atmosphere has yet to be explored, although it appears they may play a significant role in this regard within the ocean [*Müller et al.*, 1988]. The gravity–wave interpretation here is in accord with that of *Fritts and Chou* [1987] and *Fritts et al.* [1988*a*], who spectrally analyzed ST radar winds measured at Poker Flat (65°N, 147°W) in Alaska and Kyoto (35°N, 136°E) in Japan. Additional support for the gravity–wave model comes from the computation of the ratio of the horizontal to vertical velocity variances, which increase in value as $\bar{U}$ increases in value, in line with the predictions of FV87.

Further support of the gravity wave hypothesis came from the fact that the fluctuations had large degrees of polarization d, which weighs against a two–dimensional turbulence interpretation. However, a small degree of polarization does not necessarily preclude a gravity wave interpretation, as it might rather indicate that a superposition of many gravity waves exists. Indeed, the mesospheric gravity wave field over Adelaide has typical degrees of polarization of only 10–20% [*Vincent and Fritts*, 1987]. Yet it is a little difficult to reconcile small degrees of polarization at mesospheric heights, where the upwardly–propagating wave spectrum is believed to be extensively filtered so that fewer waves exist, with the large d values observed here in the troposphere, from where many waves are believed to originate.

The redistribution of wave energy by Doppler shifting can also account for the large degrees of polarization observed here. In general, the intrinsic wave spectrum will be made up of many waves with a range of propagation azimuths ϕ. However, within a given observed–frequency band, Doppler shifting enhances the variance of those waves propagating parallel to the mean flow relative to those propagating orthogonal to it. Therefore, while the intrinsic wave spectrum may contain many waves of comparable amplitude, suggesting ($d \sim 0$), only those few waves propagating nearly parallel to the mean–flow direction contribute most to the variance when observed within mid– to high–frequency bands by ground–based remote sounders. These waves "stand out" from the rest, and produce (artificially) larger d values.

These findings have some implications for studies which use ground–based radar wind measurements to investigate azimuthal anisotropies of gravity wave motions in the middle atmosphere, especially if the observations are confined to a narrow observed–frequency range. For example, *VanZandt et al.* [1990]

have noted and studied azimuthal changes in the variance of radial velocity fluctuations measured in the troposphere and lower stratosphere using a multi–beam Doppler radar. *Vincent and Fritts* [1987] and *Ebel et al.* [1987] have reported significant anisotropies in wave fluctuations within given observed frequency bands in the mesosphere, and have interpreted their results in terms of the directional filtering effects produced by critical level interactions and/or source effects acting on a spectrum of waves propagating upwards through the middle atmosphere. However, Doppler shifting acting on a spectrum of gravity waves whose horizontal phase speed distribution is azimuthally isotropic, can produce differences in the observed frequency spectra, so that similar biasing of wave alignments as observed in Figures 45*a*, 46*a*, and 47*a* may also occur, an effect not anticipated in these earlier studies. The situation is particularly acute at high observed frequencies, and, as demonstrated earlier, will be more pronounced if c_* is small compared with $\bar{U}$ (or equivalently if m_*^{-1} is small compared with $\bar{U}/N$).

Although measurements of m_*^{-1} are not numerous, *Smith et al.* [1987] suggest that values ~5 and $20km$ are typical for the middle stratosphere and mesosphere, respectively. Using $N \sim 0.02\ rad\ s^{-1}$, these values then give c_* values $\sim 16m\ s^{-1}$ in the stratosphere and ~60–70 $m\ s^{-1}$ in the mesosphere. Doppler–shifting effects are likely to be very important, therefore, in the stratosphere where, at the solstices, mean wind speeds of up to $100m\ s^{-1}$ are possible. The higher values of c_* and smaller mean winds in the mesosphere combine to suggest that "Doppler biasing" of wave variance and wave alignments is probably less severe at these heights. Mean winds $\sim 70m\ s^{-1}$ correspond to values of $\beta \sim 1$, which will produce only small changes in the spectrum of horizontal motions (see, e.g., Figure 50), and so the findings of *Vincent and Fritts* [1987] and *Ebel et al.* [1987] are probably not appreciably contaminated by Doppler shifting effects. The small d values observed by *Vincent and Fritts* [1987] appears to bear this out. Nevertheless, it is conceivable that the semiannual variation in the magnitude of the mean zonal wind in the lower mesosphere could accentuate the semi–annual variation of gravity wave horizontal velocity variances which has been observed in this region [see, e.g., *Vincent and Fritts*, 1987; *Ebel et al.*, 1987]. The fact, however, that the semiannual variation in gravity wave activity is still apparent in the mesosphere at Adelaide after the variances have been integrated over most of the frequency spectrum [*Vincent and Fritts*, 1987] strongly suggests that this semiannual variation must be intrinsic to the wave spectrum, and not produced by an interchange of wave energy amongst frequency bands due to Doppler shifting. The effect of Doppler shifting on time–fluctuating horizontal–velocity variances measured by a ground–based radar at mesospheric heights is observationally assessed in the next chapter.

On the other hand, the observations of *VanZandt et al.* [1990] from the lower atmosphere should, in principle, suffer from similar azimuthal biasing at middle to high observed frequencies as evident in

the lower atmospheric measurements presented here. *VanZandt et al.* [1990] noted a strong azimuthal anisotropy in the high–frequency fluctuating variance, and analyzed it by comparing these azimuthal changes with the predictions provided by a gravity wave spectral model. However, this model did not incorporate the effects of Doppler shifting on the wave frequency spectrum, a limitation they appreciated. For this reason they did not attempt to fit their model curves to the observed variations, but nevertheless concluded that the azimuthal changes were broadly consistent with the predictions of their gravity wave model. However, the results presented here indicate that Doppler shifting is the dominant factor in determining the azimuthal distribution of the time–fluctuating variance, particularly in high–wind conditions. Inferences based on their model curves would likely provide erroneous information on wave propagation directions. *VanZandt et al.* [1990] also noted that the theory of quasi two–dimensional turbulence was not yet sufficiently developed to allow them to compare its predictions with their observed azimuthal distribution of the fluctuating variance. A first step towards rectifying this has now been made through the development of the polarization relation in section 3.3.4, and application of this theory here has shown that the markedly different predictions that the gravity wave and two–dimensional turbulence theories provide can facilitate objective analysis of the nature of these motions.

Perhaps of greater concern is the effect that Doppler shifting might have on gravity wave momentum flux measurements. Such measurements are important, as any divergence of the momentum flux indicates that a drag is being exerted on the mean flow, which can have significant impact on the structure of that region of the atmosphere. A multi–beam radar technique for directly measuring momentum fluxes was developed by *Vincent and Reid* [1983], and measurements of mesospheric momentum fluxes [*Vincent and Reid*, 1983; *Reid and Vincent*, 1987*a*; *Fritts and Vincent*, 1987; *Reid et al.*, 1988; *Fritts and Yuan*, 1989] have revealed that large fluxes and flux divergences arise at these heights. For the reasons previously outlined, one does not anticipate that Doppler–shifting effects will significantly bias these results.

However, similar measurements have also been made in the lower atmosphere [*Fukao et al.*, 1988*c*; *McAfee et al.*, 1989; *Avery and Balsley*, 1990; *Fritts et al.*, 1990]. The shape of the intrinsic frequency spectrum of momentum flux terms such as $\overline{u'w'}$ (the vertical flux of zonal momentum) is not well–known, and is complicated by the fact that these are partially–cancelling covariance terms. Nevertheless, following *Reid* [1984] and *Reid and Vincent* [1987*a*] (see also *Fritts* [1984]), for a zonally propagating wave w' and u' are related, to within a sign, by the simplified relation

$$w' = \frac{\omega}{N} u', \tag{59}$$

and so

$$u'w' = \frac{\omega}{N}u'^2, \tag{60}$$

so that, over a given intrinsic frequency band between ω_1 and ω_2, and based on the $\omega^{-5/3}$ spectrum proposed for u', then

$$\overline{u'w'} = \frac{1}{N}\int_{\omega_1}^{\omega_2} \omega^{-2/3} d\omega. \tag{61}$$

Hence using this crude derivation, the $\overline{u'w'}$ spectrum has a shape $\sim \omega^{-2/3}$, the energy content spectrum is then $\sim \omega^{1/3}$, and so more energy is concentrated at high intrinsic frequencies. Because $\overline{u'w'}$ is a partially cancelling quantity, azimuthal integration needs to be performed in more realistic derivations. Despite these limitations, mesospheric measurements have supported the result that most of the flux is contained at the highest frequencies [see, e.g., *Reid and Vincent*, 1987*a*; *Fritts and Vincent*, 1987]. This suggests that Doppler shifting will tend to shift energy away from these high frequencies and will enhance the energy at higher (greater than N) and lower frequency ranges, much in the manner of the modelled effects of Doppler shifting of the vertical velocity spectrum [*Fritts and VanZandt*, 1987]. Such Doppler shifting may explain, at least in part, the nature of the observed frequency distribution of momentum flux recorded in the lower atmosphere, which has revealed more flux at low frequencies than at high frequencies [*Fukao et al.*, 1988*c*; *McAfee et al.*, 1989; *Fritts et al.*, 1990]. *Fritts et al.* [1990] advanced a similar hypothesis. These ideas raise the disconcerting possibility that observed vertical variations of the density–weighted momentum flux within narrow observed–frequency bands at these heights may have less to do with actual wave drag and mean flow accelerations, but more to do with vertical variations in the degree of Doppler shifting due to changes with altitude in the strength and direction of the background wind!

It is often necessary to examine the gravity wave motions in a number of frequency bands in order, for example, to determine the influence of possible wave sources. The results from this paper suggest, however, that considerable caution must be exercised when variations of gravity wave amplitudes are investigated with ground–based sensors, in order that the possible influence of Doppler shifting is taken into account. The observations support the conclusions of *Fritts and VanZandt* [1987] that particular care should be taken at high observed frequencies, where Doppler–shifting effects can be significant.

To minimize these effects, computation of velocity variances or momentum fluxes over the whole observed–frequency range should be used wherever possible. Alternatively, studies which use the vertical spatial structure of the wave motions to investigate azimuthal anisotropies [see, e.g., *Eckermann and Vincent*, 1989; see also Chapter 6] will not be affected by these Doppler–shifting effects, because the

vertical wave number is itself an intrinsic wave parameter.

4.2.7 Summary and Conclusions

Observations of mesoscale horizontal wind motions in the lower atmosphere over Adelaide, Australia, show that the fluctuating motions are often closely aligned to the background wind direction. This alignment becomes more pronounced as the strength of the background wind speed increases, especially at high observed frequencies. In order to explain this phenomenon, the manner in which the gravity wave and vortical mode (quasi two–dimensional turbulence) models of atmospheric mesoscale motions respond to changes in the background flow. Both models predict that Doppler–shifting effects will cause increased energy to be measured at high observed frequencies as the magnitude of the background wind increases. However, because the horizontal wind components of gravity waves and vortical modes are polarized differently relative to their horizontal wave number vector, the partitioning of variance parallel and transverse to the mean wind direction is different. For gravity waves, Doppler shifting causes the fluctuations parallel with the mean wind to be enhanced in variance relative to the transverse oscillations, whereas for vortical modes the opposite is the case. Doppler shifting of gravity wave energy would therefore result in an apparent alignment of the fluctuations with the mean flow, as is observed. Similarly, the polarization ratio, which was developed in section 3.3.4, was computed and became distinctly greater than one as mean–wind speeds increased, again consistent with a field of gravity waves. One must therefore conclude that the observations are in better accord with the predictions of Doppler shifting of gravity wave energy, and that gravity wave motions dominate the mesoscale energetics of these lower atmospheric measurements. The ramifications for other ground-based radar measurements of the enhancements in high–frequency variance by Doppler shifting of gravity waves were discussed, and it was pointed out that Doppler shifting may significantly bias the results unless the effects are carefully accounted for.

4.3 Gravity Wave Production by Cold Fronts

4.3.1 Introduction

Common synoptic–scale features of weather systems over southern Australia are cold fronts. During summer, the passage of these events frequently produces a local "cool change" in southern coastal areas, where temperatures can drop $10°C$ in only $20–30min$, as southward winds from the heated Australian land mass are replaced by cooler north–eastward winds from the sea. The impact of these fronts on

Australian weather and its forecasting is therefore obvious, yet their structure, formation, evolution, and dissipation were poorly understood up to 1979, when the Cold Fronts Research Programme (CFRP) was initiated [*Smith et al.*, 1982; *Ryan et al.*, 1985]. This concentrated observational campaign provided a detailed picture of the morphology of summertime fronts over southern Australia [see, e.g., *Wilson and Stern*, 1985; *Garratt et al.*, 1985], and stimulated the development of models which attempted to explain their mesoscale structure [see, e.g., *Wilson and Stern*, 1985; *Ryan and Wilson*, 1985; *Reeder and Smith*, 1987, 1988; *Physick*, 1988]. Development of and subsequent improvements to these models will be aided by more detailed measurements of frontal dynamics.

In this regard, a VHF radar at Adelaide (The PHARLAP System) was incorporated into the final observational phase of the CFRP during November and December, 1984 [*Ryan et al.*, 1985], and analysis of the observed wind velocity structure associated with fronts which passed over the radar during this time was provided by *May* [1986] and *Vincent et al.* [1987]. Further frontal observations were performed with the radar during August, 1985, and the results were analyzed by *May et al.* [1990], who compared their observations with various model predictions. These radar measurements proved particularly valuable in verifying the existence of vertical circulation patterns across the frontal surface, which arose in model simulations of *Reeder and Smith* [1987, 1988].

Determining when a front arrives is difficult, as the frontal boundary is complex. It is characterized by a frontal transition zone (FTZ), which contains an evolving wind structure which separates the regular (but different) wind structures both behind of and ahead of the front (see, e.g., Figures 45–47). The FTZ is usually characterized by a series of sudden jumps or "change lines", which are routinely observed in surface pressure records [see, e.g., *Garratt et al.*, 1985]. The FTZ is defined by the spatial/temporal interval between the first and last such change line, and the arrival of the last line is usually taken as the arrival time of the front. Hence, according to these definitions, these change lines occur ahead of the front. Change lines associated with Australian cold fronts have been attributed to density/gravity currents, produced by the interaction of two air masses of different densities [see, e.g., *Garratt and Physick*, 1983, 1986; *Garratt et al.*, 1985]. However, a recent review of gravity–current theory and frontogenesis by *Smith and Reeder* [1988] has cast doubt as to whether such gravity currents arise in summertime cold fronts over southern Australia. *Smith and Reeder* raised the possibility that a bore–like disturbance, with one or more large–amplitude solitary internal gravity waves at its leading edge, may instead produce change lines in the presence of a low–level stable layer. Bore–like disturbances, such as "morning glory" events in far north–eastern Australia [*Smith*, 1988; *Clarke*, 1989], produce similar–looking change lines in surface pressure records. Unless special atmospheric conditions prevail to trap and maintain such

disturbances, however, vertically propagating internal gravity waves will radiate this energy away [see, e.g., *Crook*, 1988; *Fulton et al.*, 1990].

Some recent high–resolution modelling of the general process of frontal development has revealed that gravity wave motions closely associated with the front arise [see, e.g., *Orlanski and Ross*, 1984; *Keyser and Pecnick*, 1985; *Gall et al.*, 1987, 1988; *Garner*, 1989*a*]. *Gall et al.* [1988] investigated the characteristics of the waves which arose in their model. They identified classes of waves which were stationary with respect to the front both above and below the frontal surface, and also a set of waves propagating ahead of the front. They also postulated that these frontal gravity waves produce the cloud banding evident in satellite observations of some frontal regions [see, e.g., *Erickson and Whitney*, 1973]. These ideas were originally developed by *Ley and Peltier* [1978], who argued that large vertical temperature gradients which occur during frontogenesis will radiate gravity waves ahead of the moving front. Indeed, it has been postulated that frontal gravity waves could impose a limiting scale on a developing front [*Ley and Peltier*, 1978; *Levy and Bretherton*, 1987], although recent debate suggests that such gravity waves may not be energetic enough to achieve this [see, e.g., *Garner*, 1989*a*, 1989*b*; *Levy and Bretherton*, 1989]. Nevertheless, gravity–wave generation appears to be common feature of most frontal models which can resolve such small–scale structure. Similar high resolution measurements are needed to determine whether such frontal wave activity does indeed occur, and if so, whether its characteristics are similar to the model results.

There is increasing observational evidence of gravity waves which are closely associated with frontal regions over the United States. Here, correlations have repeatedly been found between observations of single, large–amplitude gravity waves and convection (see section 1.4.1), and this convection is often associated with frontal activity. *Uccellini and Koch* [1987] collated and analyzed a number of such observations over North America, and found that similar synoptic conditions existed in all cases, including the presence of a front. However, they argued that the gravity waves were not produced by the fronts, but instead were radiated during geostrophic adjustment of upper–level jet streams ahead of the frontal boundary. Subsequent analyses of large–amplitude gravity wave events over North America appear to support this production scenario [*Bosart and Seimon*, 1988; *Koch and Dorian*, 1988]. Other studies of possibly smaller–scale gravity waves have suggested that convection is the source of observed gravity wave activity [see, e.g., *Einaudi et al.*, 1987; *Lin and Goff*, 1988], whereas *Bosart and Sanders* [1986] concluded that frontogenetical forcing produced an observed onset of gravity wave activity in their case study.

As pointed out by *Einaudi et al.* [1987], the lack of height information in many of the observations to date has severely limited the answers they can provide. For example, *Uccellini and Koch* [1987] argued

that the gravity waves evident in the observations they reanalyzed persisted over many oscillations because their vertical propagation was inhibited by the background structure (i.e. the waves were ducted), yet the observations provided no information on the vertical variation of wave energy. Subsequent data with better height resolution now appear to support their ducting mechanism [*Bosart and Seimon*, 1988; *Koch and Dorian*, 1988]. Similarly, explanations of frontal change lines as gravity currents or bore–wave complexes rely on similar ducting of the disturbance. If, however, ducts are not maintained or are "leaky", internal gravity waves will radiate this energy vertically, and may constitute an important source of gravity wave energy for upper regions of the atmosphere, where the dissipation of gravity waves originating from underlying regions has major impact (see section 1.4.3).

The excellent time–height resolution afforded by VHF radar measurements of tropospheric winds enables one to resolve and study oscillations that might result from frontal activity. Earlier radar studies of cold fronts over Adelaide detected vertical velocity fluctuations during frontal passages [*May*, 1986; *Vincent et al.*, 1987; *May et al.*, 1990], which *May et al.* [1990] speculated might be gravity wave motions associated with the front. The purpose of this study is to analyze such fluctuations in tropospheric wind velocities observed with The PHARLAP System during the passage of cold fronts. Analysis of these data in the previous section has indicated that the horizontal wind fluctuations are consistent with a gravity wave interpretation, and inconsistent with quasi two–dimensional turbulence (vortical modes). Here the time–height structure of these gravity waves and their relationship with the background wind and temperature structure produced by quasi–periodic passages of cold fronts is addressed.

4.3.2 Data

The data analyzed here are the same radar wind measurements described in section 4.2.2, the time coverages of which were given earlier in Table 1. These data were analyzed for fluctuating motions, and consisted of zonal (u), meridional (v), and vertical (w) velocity measurements made every $15min$ at $0.5km$ height intervals between 2 and $11.5km$. Radiosonde profiles of atmospheric temperature, made every 12 hours at Adelaide Airport (approximately $36km$ south of the radar site), were also available during the November observations. The data, which came manually plotted on aerological diagrams, were transcribed into digital data values and stored on computer, so that other quantities, such as potential temperature, could be computed. The method used to calculate potential temperatures from unequally–spaced radiosonde temperatures is described in Appendix C.

This temperature information facilitated an investigation of the relationship between background temperature gradients and gaps in the radar wind data. Ignoring humidity terms, the radar refractive

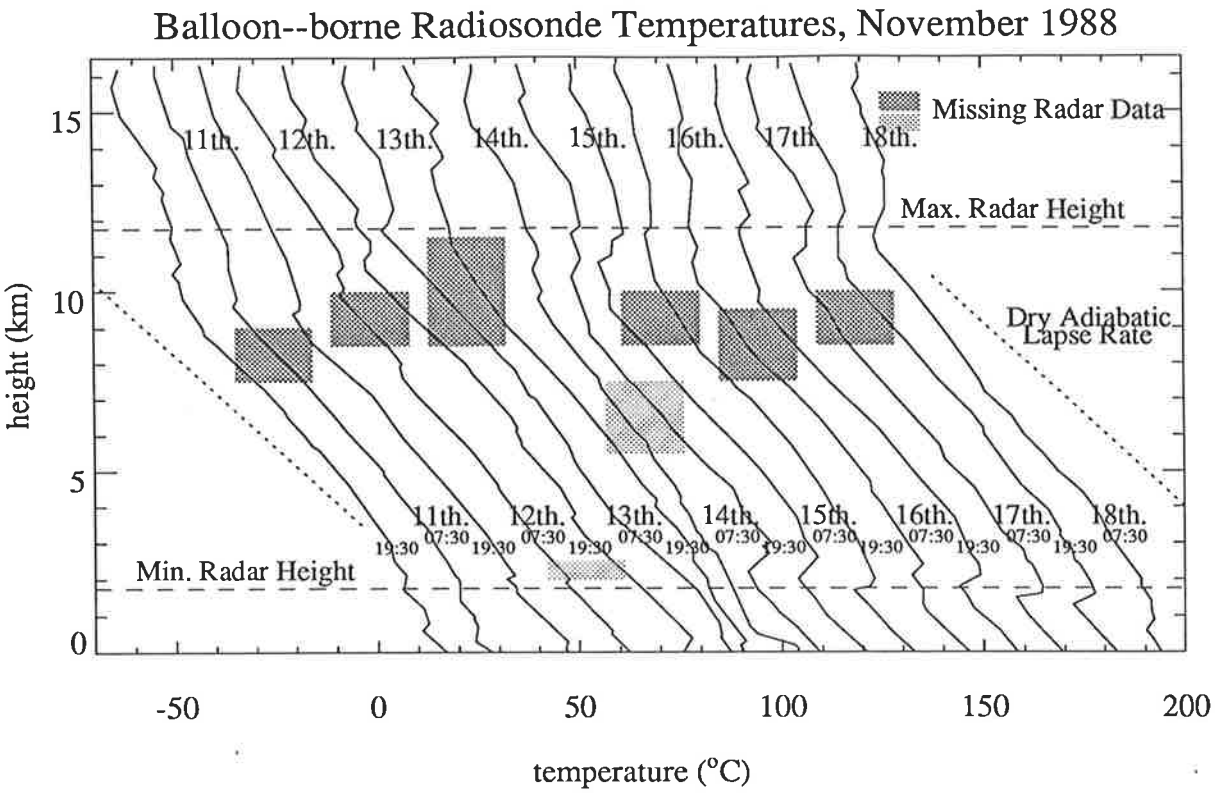

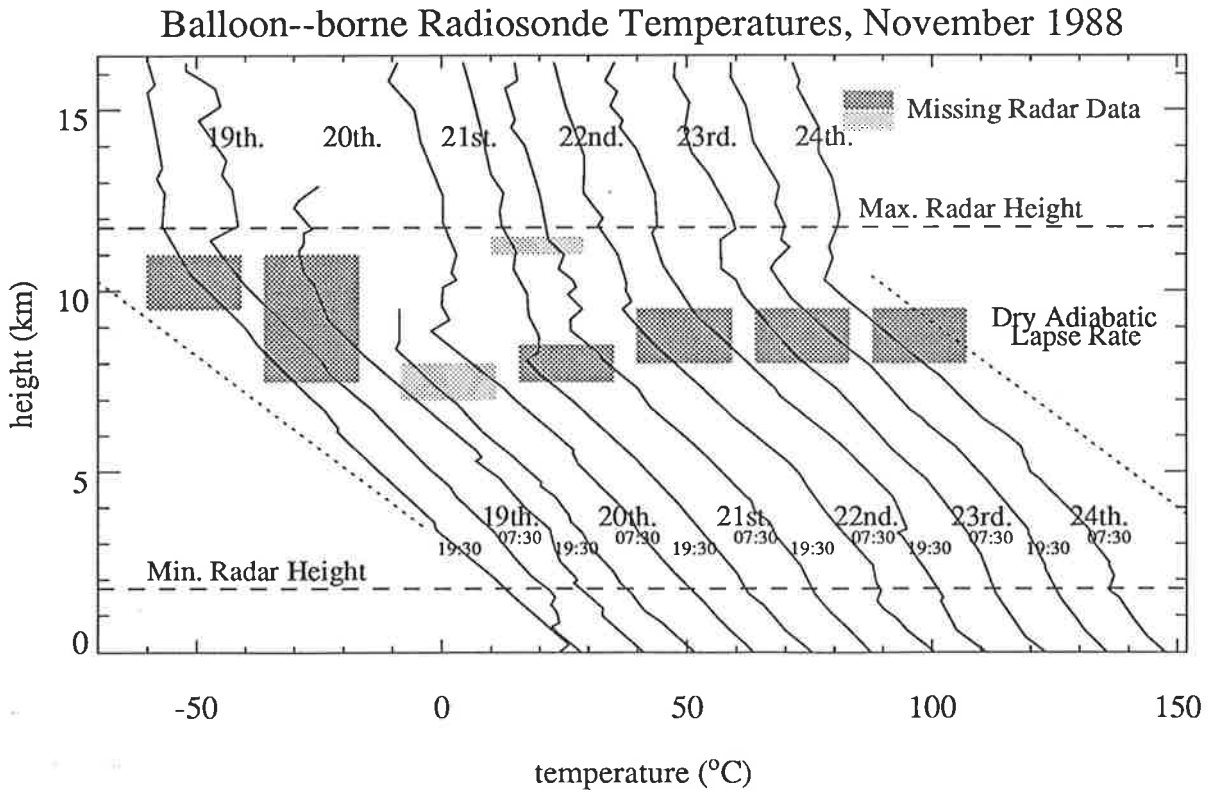

Figure 52: Solid lines show altitude profiles of atmospheric temperatures during November 1988. Temperatures are recorded at 07:30 and 19:30 Central Standard Time (local time) each day. Successive 12–hourly profiles are displaced $12°C$ to the right. Shaded areas indicate regions of missing wind data evident in Figures 46 and 47. Dark shading indicates extended gaps, and lighter shading indicates a more restricted gap. Dotted curves indicate the dry adiabatic lapse rate.

index n in the troposphere is given approximately by the following formula [see, e.g., *Balsley and Gage*, 1980]

$$n = 1 + 77.6\ 10^{-6}\frac{p}{T}, \tag{62}$$

where p is pressure and T is temperature. Turbulent fluctuations in these quantities can increase n, and thus the backscattered power, effects which are vital to the ST radar technique. If we now differentiate expression (62) with respect to z, we find that the change in radio–refractive index Δn over a height interval Δz is given by

$$\Delta n \approx 0.0224\frac{\rho N^2}{g}\Delta z, \tag{63}$$

where N is the local Brunt–Väisälä frequency, ρ is the local density, and g is the gravitational acceleration. In the presence of a background temperature profile which is near convective instability, $N \sim 0$, so that Δn is small according to (63). Furthermore, turbulence can only give rise to small perturbation gradients, as it takes only small fluctuations upon this background temperature profile to produce local superabiatic lapse rates, and thus convective overturning. These regions are soon mixed and returned to stable gradients, and so any fluctuations in n are severely limited in magnitude. Notwithstanding strong turbulent mixing which may occur in these regions, the fluctuations in radio refractive index that occur are small, and thus returned signal powers should be similarly small, and often unacceptably small compared to the background noise power.

Background temperatures and areas of missing radar wind data are combined in Figure 52. Areas of dark shading indicate extended regions of missing wind data ("biteout"), whereas lighter shading depicts more restricted data gaps. In virtually every case, these areas of missing wind data correspond to vertical temperature gradients at or near the dry adiabatic lapse rate. However, the converse is not always true; that is, near adiabatic lapse rates are not always accompanied by gaps in the wind data. Note also that most of the gaps occur at high altitudes just below the tropopause.

These findings indicate that there is a limit on the extent to which the radar–derived wind velocities can be used to investigate interrelationships between regions of convective instabilities and increases in gravity wave energy. The problem is most severe at the uppermost heights. This limitation will be alleviated somewhat in future studies, however, as the power transmitted by the radar will soon be increased significantly.

4.3.3 Analysis

In section 4.2, application of a theoretical test to the radar–derived horizontal wind data revealed that temporal fluctuations about the mean winds were on the whole consistent with the predicted behaviour of a spectrum of gravity waves, but inconsistent with the expected behaviour of a field of vortical modes. This test was applied to the entire data set, whereas here we focus mostly on bursts in the time–varying horizontal velocity variance, which are closely associated with frontal passages. Figures 53–60 detail this structure. The "burst" regions are characterized by large horizontal velocity flucuations which appear rather incoherent but are very energetic, yet are unaccompanied by similar bursts in vertical velocity.

Since these isolated portions of the fluctuating data have much greater variance than the rest, it is conceivable that these regions have a fundamentally different character than more typical regions, so that conclusions drawn from considering the entire data set may not be appropriate here. For this reason, we shall analyze these "bursty" regions separately as to their fundamental nature, considering in turn a number of possible explanations.

Errors

The possibility of radar measurement errors was discussed in some depth in the previous section, and discounted. Some additional questions arise in these "burst" portions of the data, however.

Firstly, these regions are located in the vicinity of data gaps associated with near–adiabatic lapse rates, which suggest that the signal–to–noise ratios of these data were not high. This raises the possibility that measurements errors may be responsible for these large amplitude fluctuations. Additionally, it is also possible that, despite the use of cubic splines in the analysis to smooth gaps in the data, sharp transitions due to missing data may artificially produce or enhance fluctuations at the edge of these gaps when the raw profiles were numerically filtered into period bands.

There are several reasons for rejecting this hypothesis. Note firstly that the vertical velocity data, which should suffer equally from both of the aforementioned effects, show little or no evidence of enhanced fluctuating energy in these regions. Indeed, data gaps are not always accompanied by increases in the amplitude of the horizontal velocity fluctuations (see, e.g., November 10–12, November 23–24). These points are likely to be reliable, since the spaced antenna technique imposes a number of rigorous rejection criteria and internal consistency checks on the radar returns that it processes, including rejection of returns with "unacceptably small" signal to noise ratios, so that points with large errors are usually rejected in real time by the aquisition algorithm. Furthermore, if these fluctuations were due to large,

random measurement errors, then one would expect the mean–wind vectors to reflect these errors by showing large deviations in magnitude and direction at adjacent heights and times. However, the mean wind vectors in all cases exhibit strong height–time regularity in these regions. One must therefore conclude that these wind fluctuations and not spurious, but instead depict actual wind variability.

Vortical Modes/2–D Turbulence

As this mesoscale wind variability is geophysical, theory currently offers two explanations; gravity waves or quasi two–dimensional turbulence (vortical modes). The possibility of quasi–horizontal mesoscale turbulence was addressed in depth in the previous section, and discounted. Nevertheless, the possibility is raised again here because the data are superficially consistent with such an interpretation; horizontal velocity fluctuations are large and somewhat incoherent, yet the vertical velocity fluctuations are minimal, just as one would expect for horizontally–stratified turbulent motions. Even though a gravity wave interpretation prevails when all the data are analyzed, it is conceivable that vortical modes/quasi two–dimensional turbulence may be more energetic in these isolated segments of the data, especially when one considers that fronts are known to have strong vertical vorticity associated with them (gravity waves have no vertical vorticity component, unlike vortical modes [*Müller et al.*, 1988]). Therefore, some of the frontal vorticity could manifest itself in a mesoscale spectrum of quasi two–dimensional turbulence. Efforts at modelling frontal energy spectra have not addressed this possibility, but have concentrated more on reconciling the larger–scale structure with the geostrophic turbulence theory of *Charney* [1971] [see, e.g., *Andrews and Hoskins*, 1978].

Despite some initial promise, a gravity wave explanation appears more plausible here too, for the following reasons. Firstly, the analysis of the previous section demonstrated that, especially in high–wind conditions which accompany these bursts in fluctuating activity, the behaviour of these fluctuations is consistent with gravity waves and inconsistent with vortical modes. Additionally, these bursts in variance persist at a number of heights. Two–dimensional turbulence theory predicts that energy is injected at small horizontal scales, and cascades into larger scale structure which produces time–fluctuating variance when this structure is advected over the radar. An intense small-scale source, such as strong turbulence associated with the front, could very well exist in the troposphere, which gives rise to the observed intense mesoscale activity by a reverse–cascade process. However, these bursts of variance also persist into the lower stratosphere. As 2–D turbulent motions are quasi–horizontal, an intense small–scale energy source must exist at all heights where the activity is identified. It is very difficult to identify a similarly intense source in the lower stratosphere, where the isentropic structure is much stabler and more regular. The

observations are much more consistent with a vertical propagation of energy from upper–tropospheric source regions into the lower stratosphere, again consistent with gravity waves. Finally, stratified turbulence is actually constrained to isentropic surfaces, which are usually horizontal but occasionally slant somewhat. Such tilting occurs during the passage of cold fronts as the tropopause level drops. This means that a vertically–pointing radar will measure a component of this usually–horizontal motion along the slanting isentropic surface at this time. Therefore, during frontal passage, one might reasonably expect some observed correlation between horizontal and vertical bursts of fluctuating activity. Little if any of such a correlation is observed. Indeed, near–abiabatic temperatures in these regions mean that horizontal stratification is weakly forced, so that quasi–horizontal motions may not arise.

The weight of the evidence strongly points to these bursts of fluctuating activity being gravity wave motions. We shall commence the analysis by first considering the mean horizontal and vertical winds, and the mean horizontal velocity variance. The characteristics evident in each of the four sets of data (see Table 1) will be treated separately.

10th.–18th. November 1988

The mean horizontal velocities, horizontal velocity variance, and vertical velocities over this period of observation are shown in Figure 53. The rapid variation in the horizontal wind vectors during 13th.–14th. November is produced by a cold front passing over the radar. Dotted curves on the vector plots show lines of constant potential temperature Θ, derived from the radiosonde temperature data (see Appendix *C*). As the front moves in, these isentropes evolve in a similar fashion to the mean results presented by *Ryan and Wilson* [1985] (see also *May et al.* [1990]). Low–level isentropes subside, and a region of warm air of low static stability ($d\Theta/dz$ small) persists for some hours before the arrival of the front. After the front passes, a low–level region of cold air is entrained beneath a highly–stable inversion region. This feature, which mostly lies beneath the minimum radar range, can be seen clearly in the relevant temperature profiles in Figure 52. The evolving horizontal and vertical velocity patterns evident in Figure 53 can be identified with synoptic–scale isentropic flow of various air masses (so–called "conveyer belts" of air), as discussed in depth by *May et al.* [1990] in the context of radar–derived winds. Here too the winds evolve characteristically as the front moves in. On the 12th. November, the flow is weakly northward below $7km$ and weakly southward above. Hereafter the upper level winds "back", the flow becomes south–eastward at all heights, and the wind speeds intensify. Warm masses of air move in, and produce strong upwelling throughout the troposphere early on the 13th., and subsidence later up to noon on the 14th. Horizontal winds weaken, and the flow backs again to produce a very uniform northward flow from 15th.–17th.

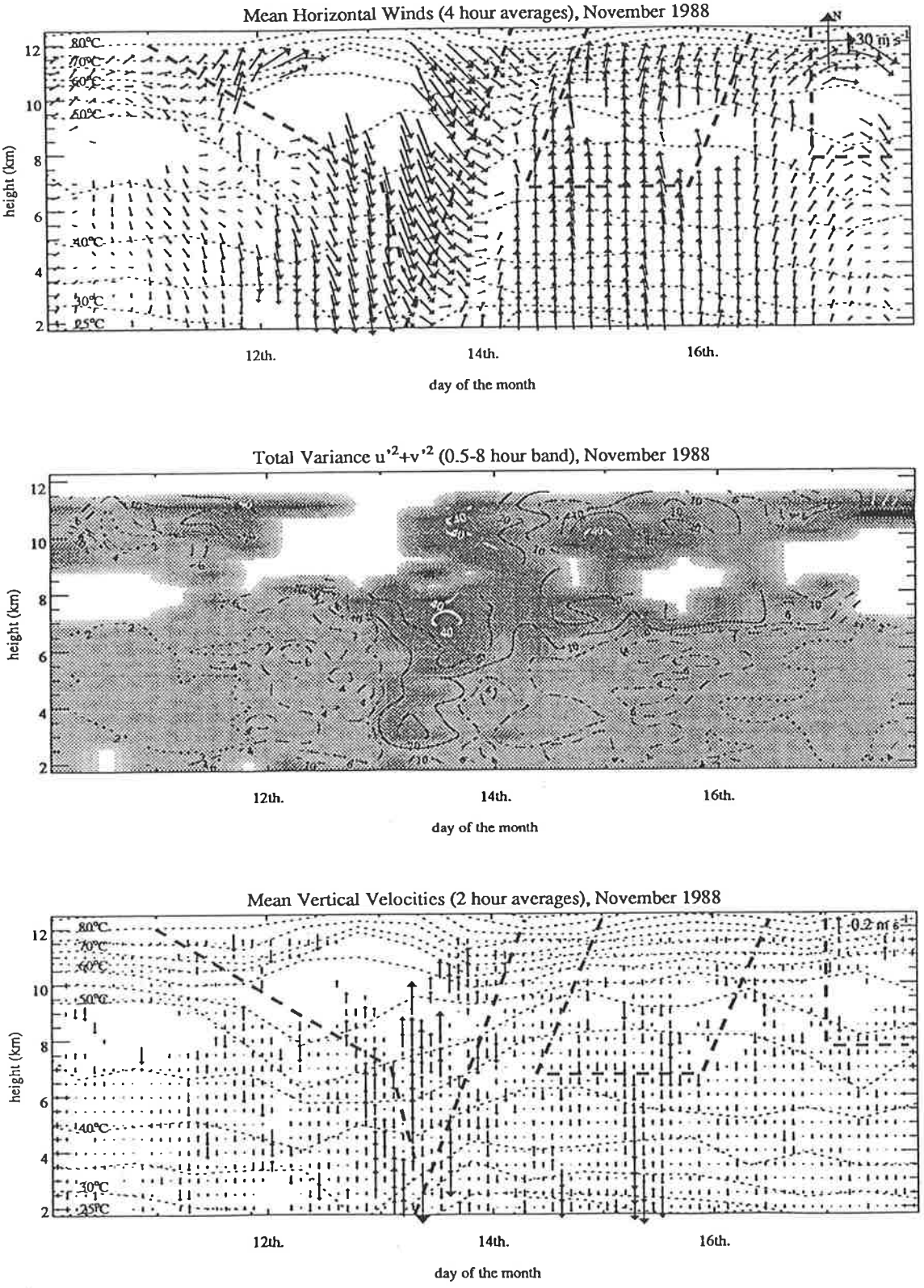

Figure 53: The top plot shows mean horizontal wind vectors (4 hour averages). Note the vector key in the top–right corner. Dotted lines show isentropes (lines of constant potential temperature) separated by 5°C, as calculated from the radiosonde data, and are labelled on the left side of the diagram. Thick dashed lines indicate boundaries between regions of high and low fluctuating activity. The middle plot shows time–height contours of the horizontal velocity variance (8 hour average) in the 0.5–8 hour observed period range. Contour labels are in $m^2 s^{-2}$. Dark areas indicate regions of large variance. The bottom diagram shows mean vertical velocities (2 hour averages). X–axis tick marks occur at noon on the indicated day.

November, after which the winds begin to back again, indicating that another front is moving in.

The region of low stability just prior to the arrival of the front is thought to extend into the middle troposphere, where the isentropes ascend somewhat and produce a "cold dome". No such structure is evident here, although the 12–hourly radiosonde data may not resolve it. However, the isentropes do show systematic variations in the height of the tropopause as the front moves through. Here the tropopause level first rises, producing near–adiabatic lapse rates just below, then appears to return to its former height at the onset of frontal wind activity. There also seems to be stratosphere–troposphere exchange of isentropic surfaces (e.g., the $55°C$ isentrope), which is known to be possible during frontogenesis and may be important in the vertical transport of tropospheric consituents[4] into the stratosphere, and vice versa [see, e.g., Chapter 9 of *Andrews et al.*, 1987]. Notice again the clear correspondence between weakly–stable temperature structure[5] and gaps in the radar wind data.

Contours of the total fluctuating variance $\overline{u'^2_{TOT}} = (\overline{u'^2} + \overline{v'^2})$, averaged over 8–hour blocks in the 0.5–8 hour observed period range, are plotted with time–height contours in Figure 53. Density shading is overlayed to highlight the structure. The variance was averaged over this broad period range to minimize the effects of variance changes due to Doppler shifting of the gravity wave energy spectrum, as discussed in the previous section. Periods greater than 8 hours were not incorporated, however, because systematic mean–wind changes of ~1 day occur during frontal passages (e.g. 14th. November), which will contribute harmonics that may bias the results. These issues were also discussed in the previous section.

Before and after the frontal passage, ambient variances are around 1–5 m^2s^{-2} in the lower and middle troposphere. The small increases/decreases in $\overline{u'^2_{TOT}}$ that do occur at these times correlate well with increases/decreases in the horizontal wind speed, indicating that these variations have more to do with Doppler shifting of wave energy into these observed–period bands than any wave or source transience. However, as the front moves through, a large burst of variance occurs throughout most of the troposphere. Despite the large mean wind speeds that occur at this time, the magnitude of the variance burst is too great to be accounted for by Doppler–shifting arguments. For example, northward flow of similar magnitude occurs after the front has passed, but this produces enhancements in the variance which are far smaller than the increases associated with the frontal activity.

While this burst is somewhat extended in time in the upper troposphere and lower stratosphere, in the lower–middle troposphere it is transient and is strongly correlated with the onset of frontal activity. Note also that this activity slopes forward with altitude, so that the onset of the burst occurs first at

[4] e.g., chlorofluorocarbons
[5] i.e. wide separation of isentropes in the vertical.

lower heights, and later at the upper heights. This also correlates with the sloping cold–frontal boundary, which arrives first at the low altitudes and later at upper heights.

While this plot gives an initial indication of the burst profile, computation of 8–hourly averages of the variance necessarily removes much of the inherent time resolution of the data. To better examine the relationship between bursts of wave activity and frontal activity, time series of zonal, meridional, and vertical velocity fluctuations are plotted at all heights in Figure 54. Vertical velocities are plotted in the 0.5–2 hour period band for two reasons. Firstly, according to gravity wave spectral theory, most of the gravity wave energy is concentrated at high frequencies, notwithstanding the effects of Doppler shifting [see, e.g., *Fritts and VanZandt*, 1987]. Secondly, mean vertical circulations are much more variable in time, so that the inclusion of the longer period bands can introduce harmonics which are due to variations in the background vertical velocities rather than wave activity (see Figure 53).

Regions of fluctuating horizontal–velocity bursts have a different height–time distribution than the bursts of vertical velocity. In general this is to be expected; the variance of time–fluctuating horizontal velocities is dominated by inertia gravity waves (waves with low intrinsic frequencies ω), whereas temporal vertical–velocity fluctuations are dominated by waves with high intrinsic frequencies [see, e.g., *Scheffler and Liu*, 1986; *Fritts and VanZandt*, 1987]. The horizontal–velocity bursts also exhibit a somewhat disorganized fluctuating structure, indicating an incoherent spectrum of many waves is present. While strong bursts of horizontal velocity variance do occur at lower heights as the front moves in, the activity is far more widespread in the upper troposphere and stratosphere, On the other hand, the vertical–velocity bursts are characterized by their quasi–sinusoidal appearance, and large amplitudes appear to be confined to the troposphere. Hence the horizontal and vertical velocity data resolve wave bursts of fundamentally different character (i.e. different intrinsic frequency regimes), and so they will be considered separately.

The sloping time–height structure of the bursts in $\overline{u'^2_{TOT}}$ is better defined in Figure 54. A prominent feature is a forward–sloping boundary from 13–14th. November, overplotted with a dashed line, which marks an abrupt lull in the fluctuating activity. These boundaries are also overplotted on the mean wind vectors in Figure 53. Two features are apparent. Firstly, the forward sloping boundary correlates strongly with the onset of weakening of the intense south–eastward winds ahead of the front. Secondly, active regions are associated with strong mean wind speeds. Finally, the isolated lower–level activity is also strongly correlated with the intense vertical circulations associated with the front. It is interesting to note that the forward–sloping boundary marking a lull in activity happens to separate upward velocites (to the left) and downward velocities (to the right) in Figure 53. The classical picture of these front involves upwelling ahead of the frontal boundary, and subsidence behind the frontal boundary [see, e.g.,

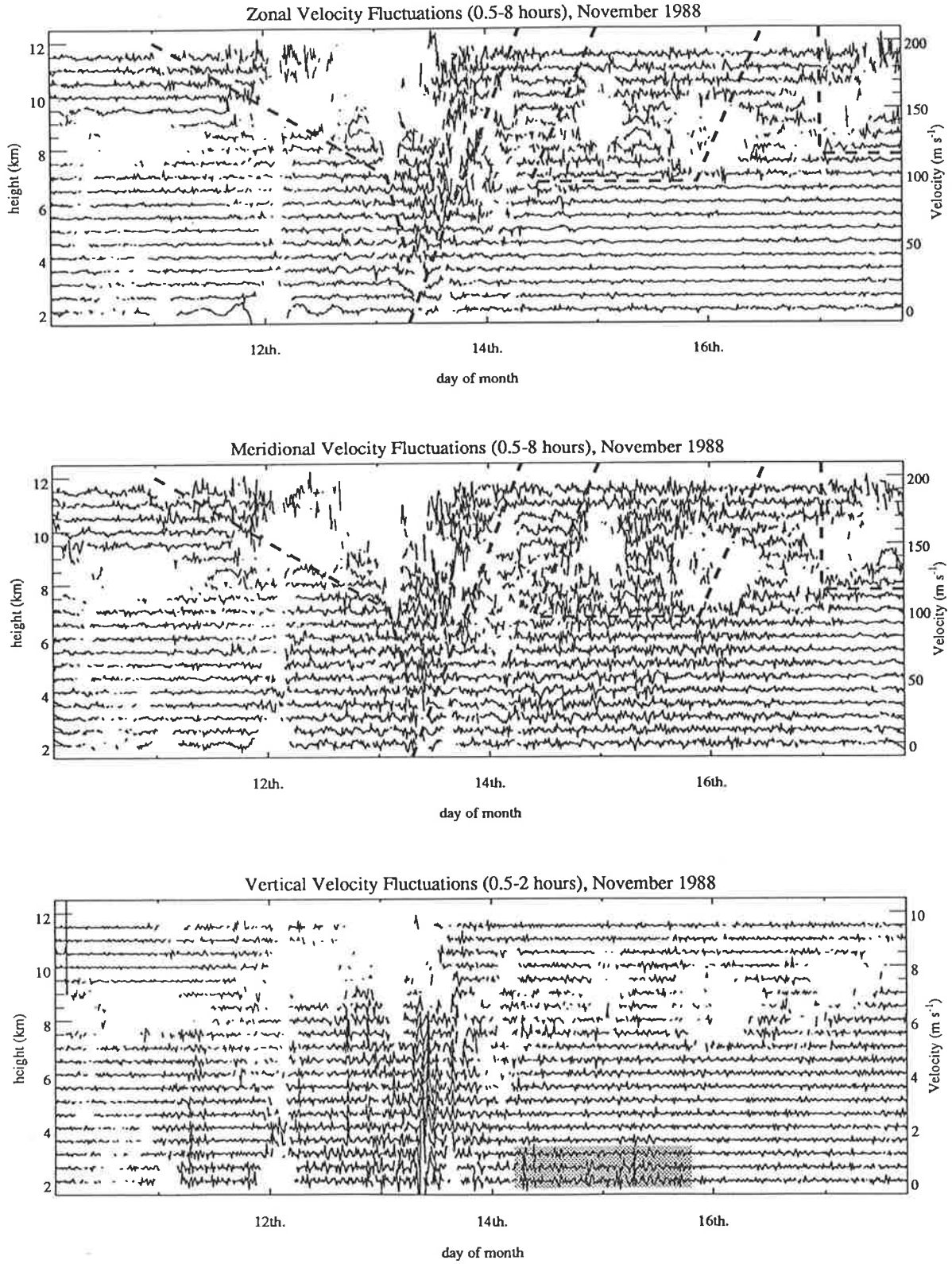

Figure 54: Plots of the zonal and meridional velocity time series of fluctuations in the 0.5–8 hour observed period range, and vertical velocities in the 0.5–2 hour band. X–axis tick marks occur at noon on the indicated day. Y–axis ticks on the left of the plot show the height at which these temporal fluctuations were recorded. Time series at each successive height are displaced vertically by $10m\ s^{-1}$ for the zonal and meridional velocity fluctuations, and by $0.5m\ s^{-1}$ for the vertical velocity, giving an incremented velocity scale on the right side of each plot. Thick dashed lines separate low and high activity regions of the horizontal velocity fluctuations.

Ryan and Wilson, 1985], so that, according to these definitions, these waves propagate *ahead of the front*, and the activity rapidly attenuates as the frontal boundary arrives. However, there is another smaller burst of activity at upper levels about a day after the front has passed. The final onset in activity (around 17th. November) is associated with further wind intensification as another front approaches.

The vertical velocity activity in Figure 54 exhibits large bursts as the frontal boundary moves in, and appears to be forced by the strong mean vertical circulations that occur at this time. Such mean motion can stimulate high–frequency air parcel oscillations as the atmosphere restores hydrostatic balance in the vertical, and such oscillations can radiate gravity waves. Activity here seems to occur both ahead of and behind the front, and some regions during 13th.–14th. November show quasi–monochromatic oscillations. The most intense region of activity, occurring at around $4p.m.$ on the 13th. November[6], produces vertical oscillation amplitudes of $\sim 1m\ s^{-1}$ from the lowest resolvable height right up the tropopause in an almost vertical column. Such fast vertical propagation is typical of high–frequency gravity waves, although it is unclear from the gappy data whether the propagation penetrates into the stratosphere. If these large vertical velocity oscillations persist near the ground, they may produce some of the "change line" structure associated with fronts. Alternatively, this activity may result from the leaking of trapped low–level density–current or bore–wave disturbances, which are believed to produce frontal change lines [*Garratt and Physick*, 1983, 1986; *Smith and Reeder*, 1988].

A region of low–level vertical velocity activity that is markedly different to the rest, in so far as it does not appear to correspond as strongly with mean vertical velocities as the other regions, is shaded in Figure 54. Note from Figure 52 that it is confined within a low–level temperature inversion. This region will be studied in more depth in later sections.

18th.–24th. November 1988

It was mentioned in the analysis of the previous data set that both the mean and fluctuating horizontal velocities appeared to indicate that another front was approaching. That indeed this was the case can be seen in Figure 55, where the first point occurs around 4 hours after the last point in Figure 53. The frontal structure is again quite similar to before, with strong intensification of south–eastward winds, followed by a "backing" to southward flow after the front has passed. The isentropes also evolve in the predicted manner, and the rise and fall of the tropopause as the front passes, as noted in the previous case, occurs even more strongly here, with clear indications of stratosphere–troposphere exchange of isentropic surfaces. Vertical velocities also intensify as the front moves in, although the circulations are a little

[6] remember that the tick marks occur at noon on the indicated day.

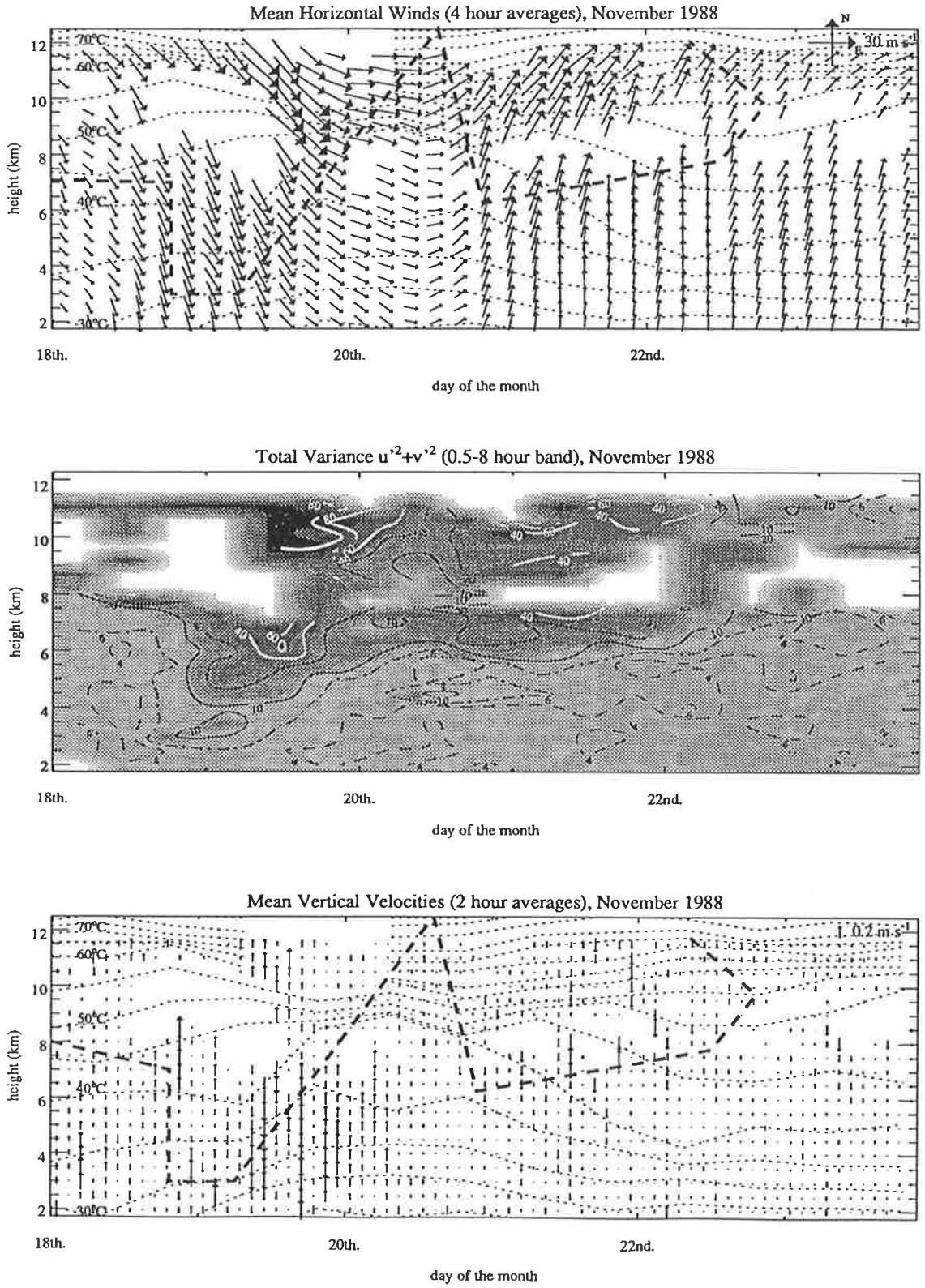

Figure 55: As for Figure 53, but for the period 18th.–24th. November 1988.

weaker in this example.

The fluctuating horizontal velocities show very similar time–height structure to that noted during 10th.–18th. November. Upper level activity occurs well before the front arrives, and then a forward–sloping region of activity extends low into the troposphere. Thereafter the activity decreases somewhat before increasing again at upper levels about a day later. As before, the precise nature of the activity is better revealed by plotting time series of the fluctuations at the various heights in Figure 56. Again there is a distinct forward–sloping boundary from 19th.–20th. November which marks a sudden abatement in the activity. Subjective boundaries which separate regions of high and low activity have again been overlayed with thick dashed curves, and these curves have also been overlayed on the mean wind vectors in Figure 55.

Referring back to Figure 55, the forward sloping boundary correlates well with the onset of a weakening of the strong south–eastward flow. This boundary also separates regions of weak ascent before the front arrives, and subsidence after it has passed, although shortly thereafter there is fairly strong ascent which persists for ~1 day. There is a lull in activity, then another smaller upper level bursts during November 21–22. Here the upper level winds are more south–eastward, rather than southward in the earlier example around the 15th. November.

Again too, the vertical velocity fluctuations have similar characteristics to the previous measurements. There is limited correlation between the horizontal and vertical velocity fluctuations. There are vertical velocity bursts ahead of the front, for almost a day beforehand in this case, and residual activity after the front has passed. At around $6p.m.$ on 20th. November, there are large vertical oscillations of around $1m\ s^{-1}$ through large regions of the troposphere, which appear quasi–monochromatic in height and time. Penetration of this structure into the stratosphere is difficult to detect.

28th. November–11th. December 1988

The remaining data sets have no digitized temperature data available from which to compute the background isentropic structure. Figure 57 shows that in these data there is no fully resolved frontal structure, although good portions of two fronts are measured in the first and last few days of these data. Again there is strong correlation between regions of high horizontal wind speeds and enhancements in the horizontal velocity variance. Boundaries are not drawn in here, as the variations are now clearly established, and can be observed directly. Notice that the active regions extend to low levels as the frontal boundary approaches at each end of the data series. Strong vertical velocity oscillations can be seen ahead of the front during 10th. December in Figure 58, which appear quasi–monochromatic in places. Any strato-

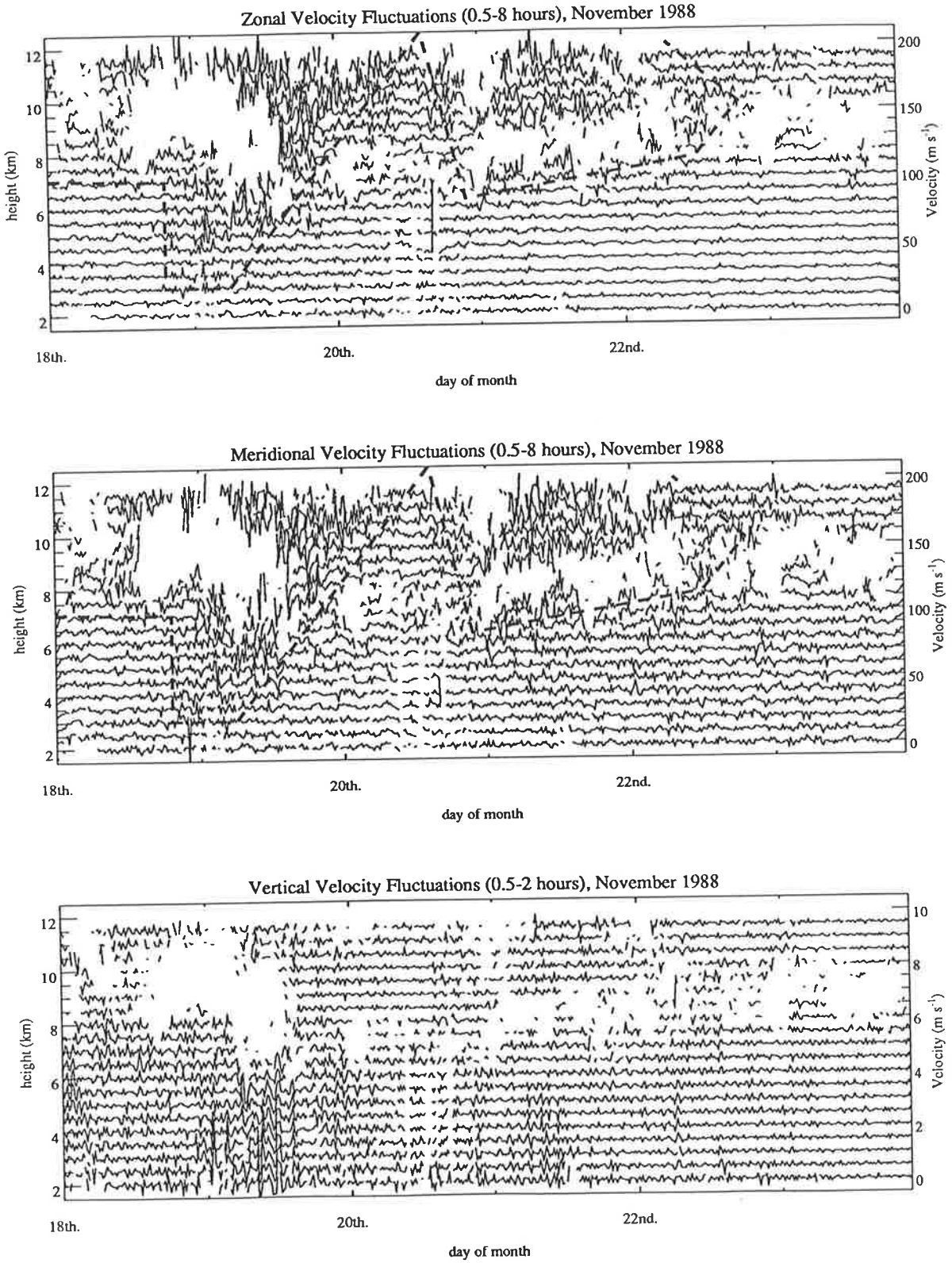

Figure 56: As for Figure 54, but for the period 18–24th. November 1988.

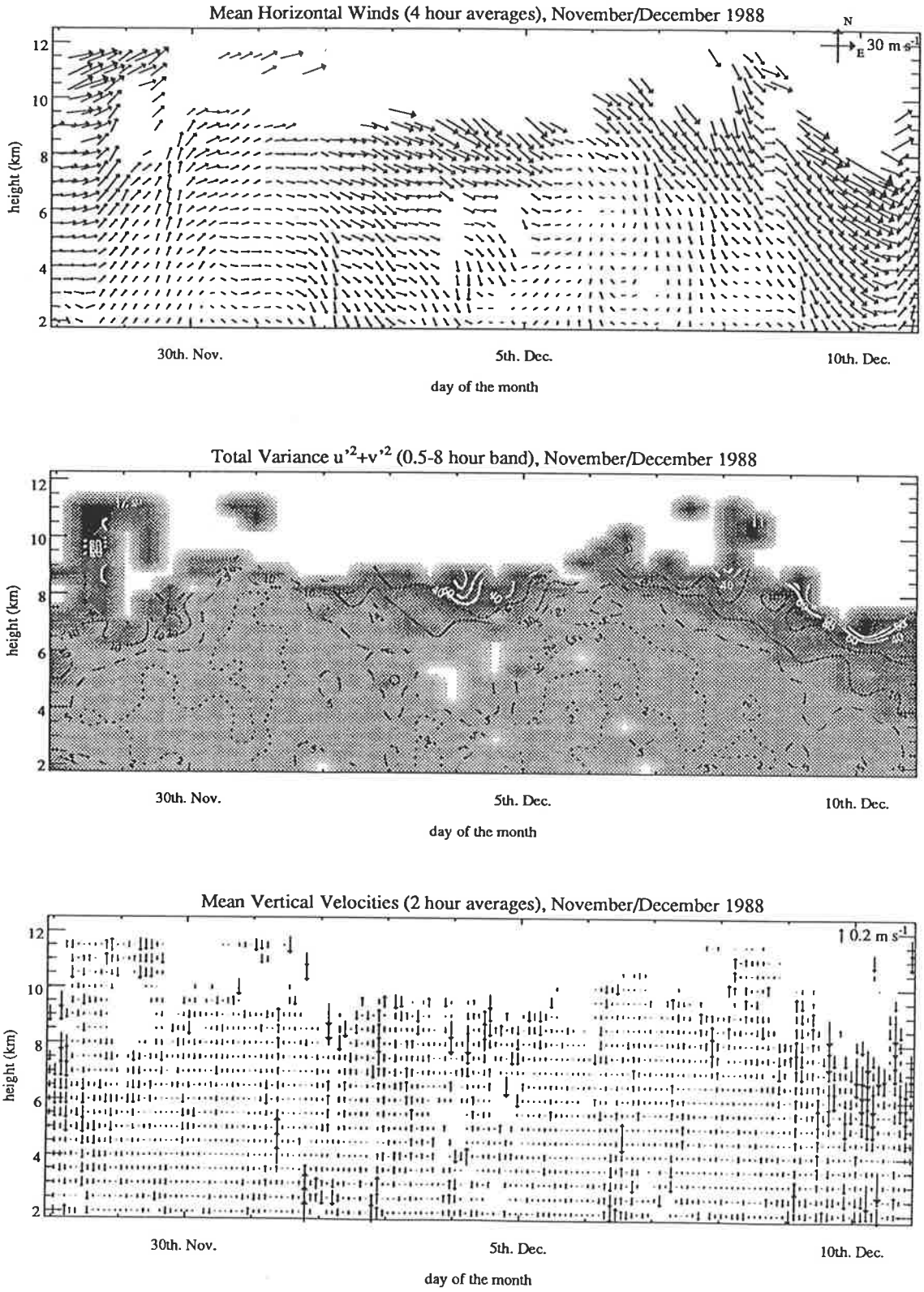

Figure 57: As for Figure 53, but for the period 18th.–24th. November 1988. No temperature data is provided here, nor are boundaries separating low and high activity regions overlayed.

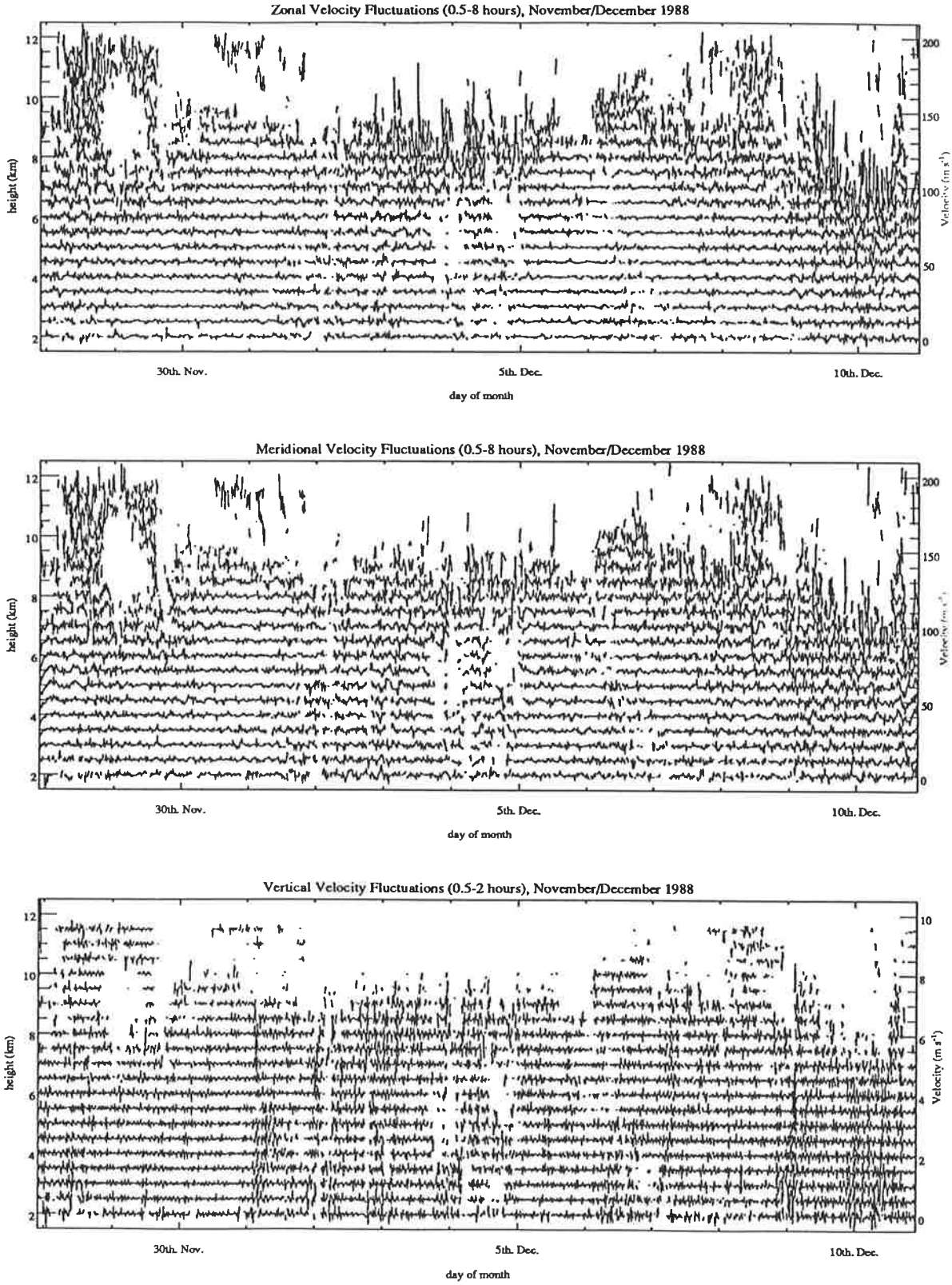

Figure 58: As for Figure 54, but for the period 28th. November–11th. December 1988.

spheric persistence of these oscillatory bursts is very difficult to gauge due to limited data acceptance at the uppermost heights.

19th.–30th. August 1988

These final measurements differ from the other data in so far as they occur late in winter. Two fronts are resolved, the first of which is very strong, producing upper–level mean winds as high as ~ 40–$50 m\ s^{-1}$ ahead of the front, yet it evolves in a very similar fashion to those detected in the aforementioned measurements (see Figure 59). A much weaker front also occurs around August 26. Nevertheless, the horizontal velocity activity associated with both fronts is intense, and of similar nature to that observed in the previous examples. Strong upper–level activity occurs before the front arrives, and progressively moves lower into the atmosphere as the front approaches. As the frontal boundary arrives, the activity abruptly abates in a forward sloping boundary, and then there is weaker upper level activity some time after the front has passed (see also Figure 60). The vertical velocity fluctuations are a little different in this case. For the first front, there are strong vertical velocity fluctuations both ahead of and behind the front, which appear quasi–sinusoidal in places, but a strong burst in activity as the frontal boundary arrives is not observed. In the case of the second weaker front, this burst does seem to be present, and there seems to be residual vertical velocity fluctuations after the front has passed, but there appears to be limited activity ahead of the front (except, perhaps, at the lowest heights). There seems to be some evidence for stratospheric penetration of the vertical velocity activity in the first case, but less evidence in the latter example.

4.3.4 Discussion

Horizontal Velocity Activity

The process(es) which act to produce the observed bursts of horizontal velocity are difficult to identify unambiguously, as the motion in these regions is rather complex. The active upper–level regions are characterized by strong, intensifying upper–tropospheric wind jets, and near–adiabatic lapse rates. As was discussed in the introduction, *Uccellini and Koch* [1987] have argued that geostrophic adjustment of upper–tropospheric winds produces large–amplitude quasi–monochromatic tropospheric gravity waves observed near the ground over various regions of the United States, whereas many earlier studies and some later studies have argued that convection is a strong wave source. Here, both proceses appear to be present simultaneously due to near–adiabatic lapse rates and strong zonal wind jets. Therefore,

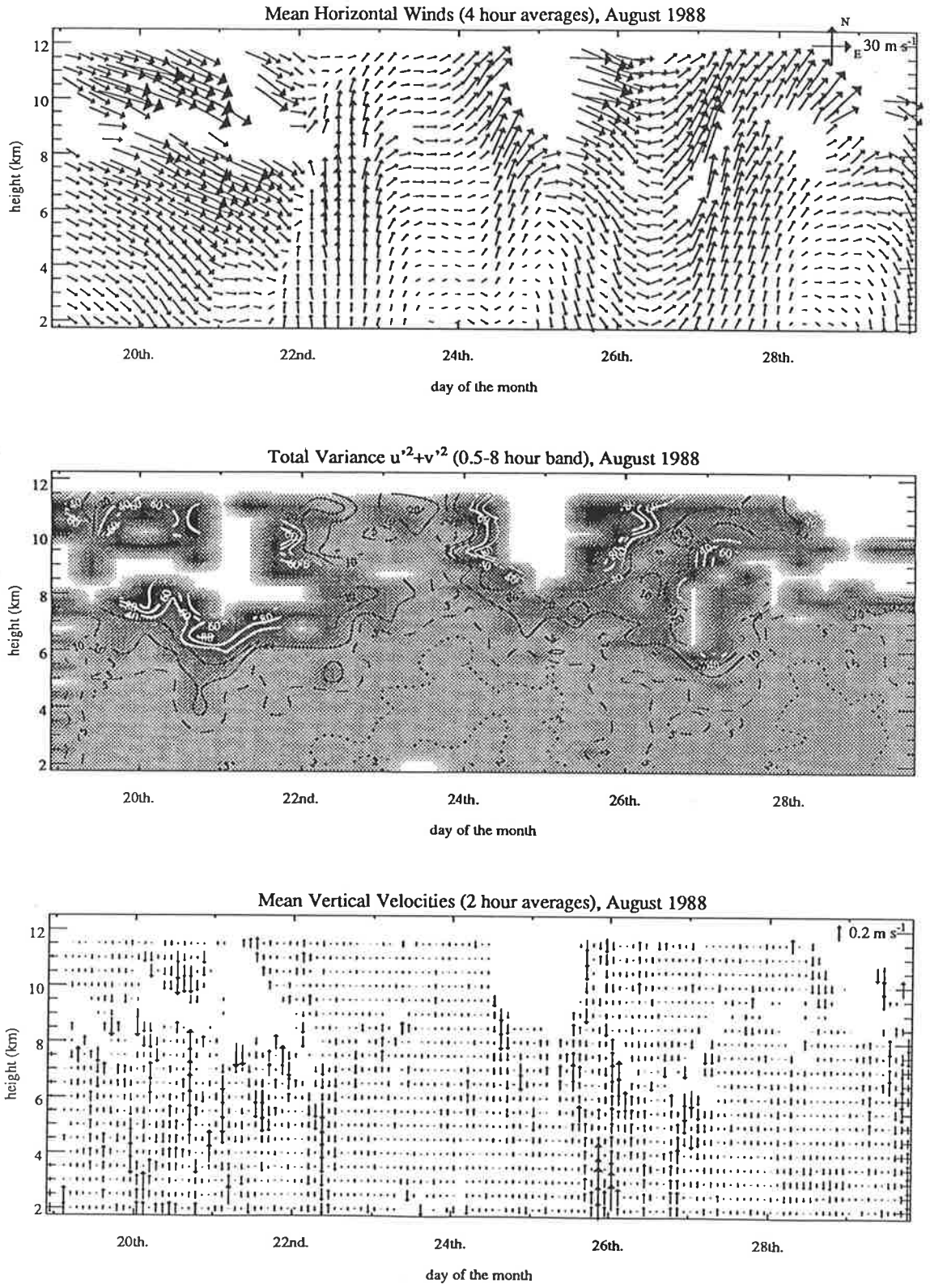

Figure 59: As for Figure 53, but for the period 19th.–30th. August 1988. No temperature data is provided here, nor are boundaries separating low and high activity regions overlayed.

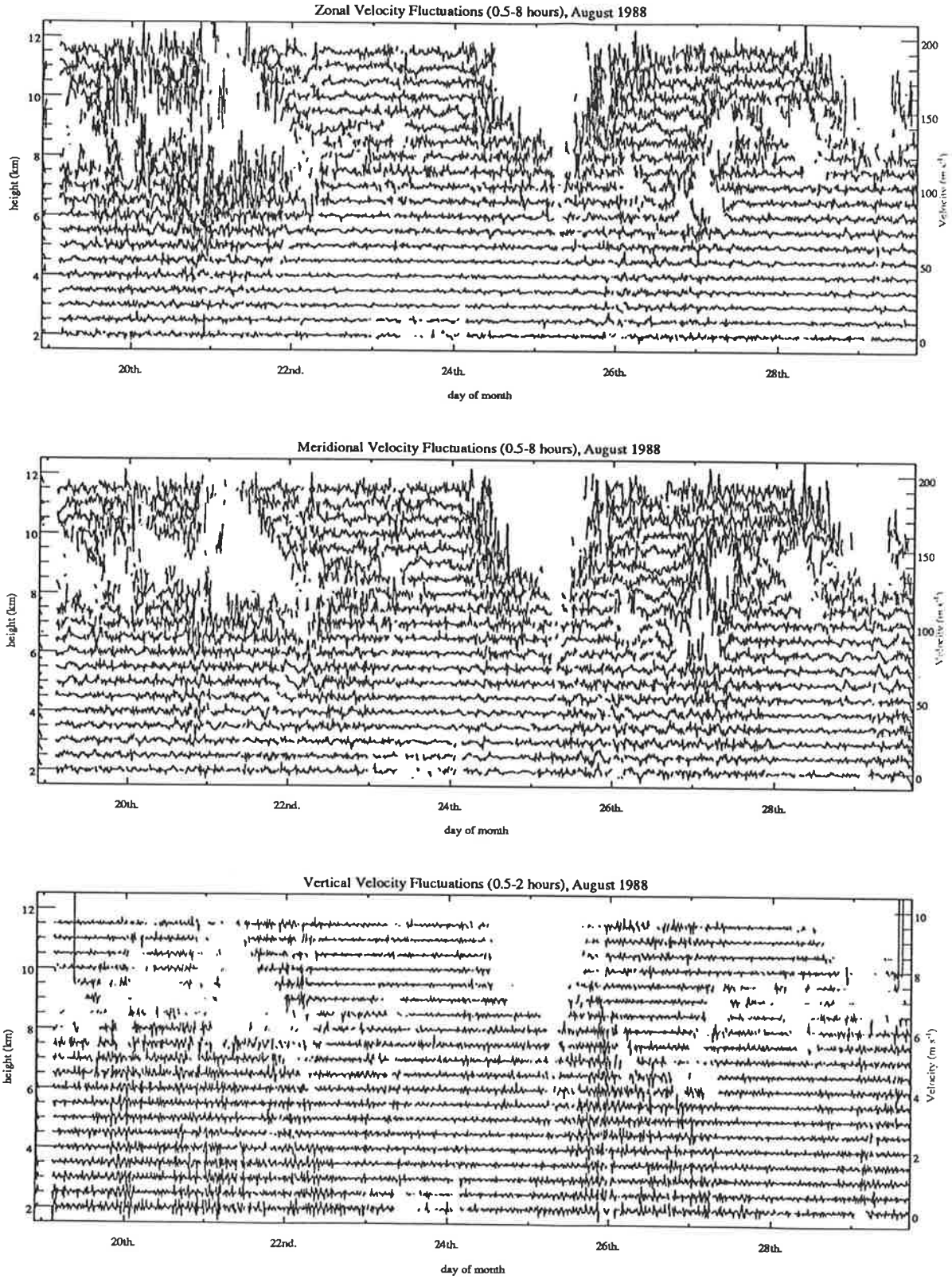

Figure 60: As for Figure 54, but for the period 19–30th. August 1988.

on the basis of correlations, it is impossible to say whether the source of this intense wave activity is convection or geostrophic adjustment. Additionally, the strong wind shears at these heights could also produce dynamic instabilities which can radiate gravity waves [see, e.g., *Gossard and Hooke*, 1975; *Fritts and Rastogi*, 1985].

However, by analyzing the environment where this wave activity occurs, one can make progress. Firstly, we note that geostrophic adjustment of wind velocities is believed to radiate inertia–gravity waves [see, e.g., *Blumen*, 1972; *Duffy*, 1990]; that is, waves which have intrinsic frequencies ω close to the inertial frequency f, the low–frequency cutoff. The highest frequency ω that a wave can attain is the Brunt–Väisälä frequency N, which is essentially a measure of the background atmospheric stability. But these active regions are characterized by near–adiabatic lapse rates, which give small values of the Brunt–Väisälä frequency, possibly values very close to f in near–unstable regions, such as in and around gaps in the radar wind data. Hence within these regions there is an narrow range of permitted wave frequencies ($N > \omega > f$), so that *geostrophic adjustment, convection, or indeed any other wave source will produce low–frequency gravity waves in these regions.* This measurements appear to resolve inertia gravity waves, since the fluctuations are characterized by large horizontal velocity fluctuations and smaller vertical velocity fluctuations, as evident in Figures 54, 56, 58, and 60.

One can now go further. Firstly, recall that the intrinsic wave frequency $\omega = \mathbf{k_h}.(\mathbf{c} - \bar{\mathbf{U}})$, where $\mathbf{k_h}$ is the horizontal wavenumber vector, $\mathbf{c}$ is the ground–based horizontal phase–speed vector, and $\bar{\mathbf{U}}$ is the mean wind vector, so that ω changes as it propagates into regions of different mean wind speed and direction. However, even small changes in $\bar{\mathbf{U}}$ will shift ω to values either less than f (whereupon the wave has essentially reached a critical level) or greater than N (whereupon the wave is totally reflected). Strong height variations in the mean wind speed $\bar{U}$ are observed in these high–wind regions, and one would therefore anticipate that both critical–level absorption and reflection of gravity wave energy will occur.

Now consider the wave amplitudes. It is well–known that the maximum horizontal velocity amplitude u'_{max} that a given gravity wave can attain, before it becomes unstable and begins shedding energy, is given by [see, e.g., *Fritts and Rastogi*, 1985],

$$u'_{max} = a \mid c - \bar{U}\cos\phi \mid = a\frac{\omega}{k_h} \approx a\frac{N}{m}, \tag{64}$$

where m is the vertical wavenumber, $k_h = \mid \mathbf{k_h} \mid$, $c = \mid \mathbf{c} \mid$, $\bar{U} = \mid \bar{\mathbf{U}} \mid$, ϕ is the azimuthal difference between the horizontal wave vector $\mathbf{k_h}$ and the mean wind vector $\bar{\mathbf{U}}$, and a is a constant, which is unity for high frequency waves, and less than one for inertia gravity waves [*Fritts and Rastogi*, 1985; see also section

7.3]. While (64) is derived using simple linear saturation theory, a number of theoretical studies have demonstrated that this saturation limit is fairly robust to the addition of superposition and nonlinear effects [see, e.g., *Fritts and Dunkerton*, 1984; *Fritts*, 1985; *Walterscheid and Schubert*, 1990], and it also appears to agree well with observations [see, e.g., *Fritts*, 1984, 1989; *Smith et al.*, 1987].

Equation (64) provides further information on the nature of these active regions. Firstly, the waves in these active regions have low frequencies ω, yet have large horizontal velocity amplitudes. Inspection of (64) indicates that low frequency waves have low saturation amplitudes u'_{max}. Since ω has a restricted low–frequency range in these active regions, the largest saturated amplitudes are attained by those waves with small k_h (i.e. long horizontal wavelengths) according to (64). As a sample calculation, if we take $a \sim 1$, and $\omega = 5f$ ($f = 8.34\ 10^{-5}\ rad\ s^{-1}$ at $35°S$), (64) gives u'_{max} ~6–7$m\ s^{-1}$ for $2\pi(k_h)^{-1} = 100km$. Lower frequencies and shorter horizontal wavelengths give smaller values of u'_{max}, but this simple calculation gives values of similar order to the observations, using values of ω and k_h which are not unrealistic. Note, however, that this calculation also means that waves are saturating in this region, and thus producing mean–flow drag.

This maximum amplitude u'_{max} equals the local intrinsic phase speed $\mid c - \bar{U}\cos\phi \mid$ of these waves. Its variation is closely coupled to the aforementioned intrinsic frequency variations, since $\omega = k_h(c - \bar{U}\cos\phi)$, and it was pointed out that these variations could not be large or else frequencies would exceed N or become less than f, so that

$$\frac{\mid f \mid}{k_h} < \mid (c - \bar{U}\cos\phi) \mid < \frac{N}{k_h}. \tag{65}$$

For a value in these active quasi–unstable regions of $2\pi/N = 1$ hour and $2\pi/k_h = 50km$, the upper bound on the intrinsic phase speed N/k_h is around $14m\ s^{-1}$, and smaller horizontal wavelengths or longer Brunt-Väisälä periods will decrease this value further.

With this in mind, we now consider the two limiting cases of ϕ. The first is where the wave vector is closely aligned with the mean wind (i.e. ϕ is around 0° or 180°). Since $\mid c - \bar{U}\cos\phi \mid$ ($= \mid c \pm \bar{U} \mid$ in this case) must lie within the bounds in (65), this means that the ground–based horizontal phase speeds of most of these waves must be non–zero and of the order of the mean wind speeds at these heights, which are typically 20–40$m\ s^{-1}$. However, since $\bar{U}(z)$ is observed to vary by as much as $20m\ s^{-1}$ with height in these regions, intrinsic phase speeds are likely to be shifted to values either less than f/k_h or exceeding N/k_h, so that further vertical propagation is inhibited

If one considers the other extreme, however, where ϕ equals either 90° or 270°, this gives rise to intrinsic phase speeds $\mid c - \bar{U}\cos\phi \mid$ equal to the ground–based phase speed c, so that variations in $\bar{U}(z)$ with height produce no shifting of $\mid c - \bar{U}\cos\phi \mid$, and thus vertical wave propagation is uninhibited.

We note that although $\bar{U}(z)$ varies in strength with altitude in the identifiably active regions, its direction varies little, so that ϕ does not change significantly with altitude. Hence the above arguments indicate that the background atmospheric conditions should strongly favour the upward transmission of gravity waves propagating *perpendicular* to the mean flow direction, and that waves propagating along the mean flow direction will experience frequency shifts that cause them to evanesce at some altitude. Unfortunately, this is difficult to assess experimentally, since analysis in section 4.2 revealed that calculations of azimuthal alignments of the fluctuations were biased by the effects of Doppler shifting, although this biasing does not occur if waves are propagating at right angles to the mean flow. Inspection of Figures 45–47 in section 4.2 show that the alignment biasing is often less distinct in the strong wind regimes associated with active regions than in the strong wind regimes which are unaccompanied by bursts in the variance, which is consistent with an excess of waves propagating orthogonal to the mean flow in active regions. While suggestive, this observation is not, however, conclusive.

Hence, from these simple considerations, one can propose a simple picture of the wave dynamics in these regions. The activity consists of low–frequency gravity waves which can have only a narrow range of permitted frequencies ω, due to the background environment. Waves propagating along the mean–flow direction are shifted in frequency, and so many are absorbed at critical levels or reflected vertically, whereas waves propagating orthogonally to the mean flow propagate freely in the vertical due to limited shifting of their intrinsic frequencies. Many of these waves have also attained their maximum saturation amplitudes, and so are dissipating energy and exerting a drag on the mean flow.

The wave drag may be very important; not only can it arise due to saturation of the waves, but the sudden jump in Brunt–Väisälä frequency at the tropopause produces "supersaturation" of already saturated waves, and further mean–flow drag results [*VanZandt and Fritts*, 1989]. This gravity–wave drag accelerates the mean winds locally, so that the mean winds become ageostrophic, which is often a characteristic of upper–level jet streams. If the forcing abates, geostrophic adjustment of these mean winds will occur, yet one process by which this can occur efficiently is by the radiation of inertia gravity waves from the ageostrophic region [*Blumen*, 1972; *Duffy*, 1990]! Hence one can envisage a process where a burst of waves is produced by some process (e.g., convection, geostrophic adjustment, wind shear, etc.), whereupon this wave energy propagates upwards, some of the waves saturate, and upper–level winds are accelerated. Geostrophic adjustment of these accelerated winds radiates secondary inertia gravity waves, which themselves may dissipate at some other altitude. Consequently, there may be a constant "feedback" or "cascade" process, whereby energy is constantly being exchanged between inertia gravity waves and the mean flow, producing a "diffusion" rather than a free propagation of inertia

gravity wave activity vertically and horizontally, particularly for waves propagating along the mean flow direction. Such continual production and absorption of waves would be consistent with the observed lack of monochromaticity of these regions of fluctuating activity. If this process is occurring, then although other processes may produce the original activity, this secondary geostrophic adjustment mechanism would be the important process in defining the final nature of the emerging gravity wave spectrum.

Zhu and Holton [1987] have performed some numerical modelling of the process of geostrophic adjustment to local gravity wave forcing of the upper troposphere and lower stratosphere. They noted that when gravity wave forcing of a region stopped, geostrophic adjustment re–radiated gravity waves of different wavelength and period and smaller momentum flux compared to the incident wave, and these secondary waves propagated obliquely in an azimuthal cone to cover a much larger horizontal area than the original forcing region. Such a process may explain the extended height–time structure of the wave activity both behind and ahead of the frontal activity, as observed in Figures 53–60. *Zhu and Holton*'s results also suggest that the wave–induced mean–flow accelerations can be significant, so that similar accelerations in these identified regions of strong wave activity could well be important in the mean dynamics of these fronts. Direct measurement of east–west wave momentum fluxes is possible with The PHARLAP System using Doppler–beam methods developed by *Vincent and Reid* [1983], and could be used to provide direct measurements of any wave–induced mean–flow accelerations in these regions[7].

Vertical Velocity Activity

Ground–based measurements of temporal vertical–velocity fluctuations due to gravity waves are dominated by waves with high intrinsic frequencies ω [see, e.g., *Scheffler and Liu*, 1986; *Fritts and VanZandt*, 1987]. Bursts in this activity are observed in the data within regions where strong mean vertical circulations are occurring (see Figures 53–60). Such mean vertical motion must arise because there is local hydrostatic disequilibrium in the vertical, and so air parcel ascent/descent can be thought of as hydrostatic adjustment process. When a parcel reaches a height where its density and the background density are equal, ascent will stop, but there will likely be some "overshoot", so that the parcel oscillates up and down a little before settling at its equilibrium height. Such parcel oscillations would occur at or near the Brunt–Väisälä frequency, and while this motion damps as the parcel settles at that height, the damped energy may be radiated as high–frequency gravity waves.

Large–scale mean vertical motions often have a cellular structure, and so they are usually referred to as convection. Many tropospheric studies have identified strong associations between gravity waves and

[7] bear in mind, however, the caveat due to Doppler shifting of wave energy discussed in section 4.2.6.

convection, yet there has been debate as to whether convection produces the gravity waves or whether the converse is true (see section 1.4.1). Here too we observe such correlations during the passage of frontal activity, but we note here that the convection (or, at least, vertical circulation associated with the front) almost certainly produces these high–frequency gravity waves. We can make this statement because it is known that the mean vertical motions associated with the front are not produced by gravity waves, since they are well–modelled without the inclusion of gravity wave dynamics [see, e.g., *Smith and Reeder*, 1987, 1988; *May et al.*, 1990].

An interesting feature of the vertical velocity fluctuations is that, while bursts in activity occur throughout the troposphere at certain times, similarly large amplitudes are infrequently observed in the stratosphere. This superficially suggests that these waves are not propagating beyond the tropopause. The variation with increasing altitude of the Brunt–Väisälä frequency may explain this feature. We notice from Figures 53–56 that active regions in the vertical velocity fluctuations are mostly characterized by gaps in the data above these regions, which in turn are caused by near–adiabatic lapse rates (see Figure 52). Since the bulk of the time–fluctuating vertical velocity variance is produced by waves of high intrinsic frequency, the decrease in N at these higher altitudes may mean that the frequencies ω of these waves exceed N at these upper heights, so that they are reflected back downwards, and thus confined to the troposphere. This may well explain why there is long duration activity in the vertical velocity fluctuations before and after frontal passage; normally such high–frequency wave energy propagates upwards very rapidly from its source region, and so the wave might only be observed for an oscillation or two. However, if these high–frequency waves are "ducted" or "trapped" between the ground and upper level quasi–unstable regions, the wave energy, since it cannot propagate away vertically, persists much longer, as observed.

Even if such upper–level wave ducting does not occur, the variation of the Brunt–Väisälä frequency as waves propagate upwards into the stratosphere can account for the small vertical velocity fluctuation amplitudes here. This is because, typically, N is observed to increase by a factor of 2–3 when one moves from the upper troposphere into the lower stratosphere in these regions (see Figure 52). Therefore, although a wave's frequency may be near the local value of N in the upper troposphere, in the stratosphere this same frequency is nearer to f than N, because of the two– to three–fold increase in the Brunt–Väisälä frequency. In such a case, the wave energy propagates upwards much more obliquely, as opposed to its almost vertical tropospheric propagation, and this also implies that the vertical velocity fluctuations produced by the wave are much smaller, as dictated by the simplified polarization relation for a zonally

propagating wave where $\omega \gg f$ [see, e.g., *Gossard and Hooke*, 1975]

$$w' \approx \frac{-k_h}{m} u' \approx \frac{-\omega}{\sqrt{(N^2 - \omega^2)}} u', \tag{66}$$

Thus this reduction in fluctuating vertical–velocity amplitudes at stratospheric heights may be evidence that high–frequency tropospheric waves are forced to propagate, and therefore oscillate, much more obliquely on penetrating into the stabler temperature structure of the stratosphere.

In Figure 54, a region of vertical fluctuations at the lowest measured heights (2–3km) from around November 14–16 was identified for further study. It was pointed out that these vertical velocity fluctuations occurred within a temperature inversion (see Figure 52), where the Brunt–Väisälä frequency N is much larger than elsewhere due to the increase in temperature with height. Above and below this height interval, N is much smaller, so that gravity waves between 2–3km which have frequencies ω near N cannot propagate far vertically because they encounter an environment where N decreases such that ω exceeds N, and thus the waves are reflected vertically. The temperature structure then acts as a waveguide, and waves are thermally ducted in the vertical.

The standard analysis of gravity wave structure within such ducts involves finding eigensolutions of the Taylor–Goldstein equation appropriately adapted to the background atmospheric environment [see, e.g., texts by *Gossard and Hooke*, 1975; *Gill*, 1982]. The thermal ducting situation here, consisting of a very stable layer between 2–3km capped above and below by weakly stable temperature structure, is a good approximation to the so–called three–layer model which has been solved by *Gossard and Hooke* [1975] (pages 150–156). Eigenmode solutions within the duct produce one–to–one frequency and vertical wavenumber pairs for each mode.

Because of Doppler shifting of intrinsic frequencies and the limited height resolution of the velocity data within this hypothesized duct region, the ducting relations derived by *Gossard and Hooke* [1975] cannot be definitively applied to these data. Nevertheless, the isolated region of active vertical velocity fluctuations, shaded in Figure 54, and the observation that a temperature inversion occurs in this region, are consistent with high–frequency ducted gravity wave modes. While the shaded vertical velocity structure in Figure 54 is only sporadically monochromatic, the amplitude structure appears similar from height to height, which suggests that the gravest eigenmode solutions produce most of the ducted wave activity. The wave phase also appears to vary little with height, suggesting long vertical wavelengths.

Such ducted waves are totally reflected due to wave frequencies exceeding N. However, waves of any frequency can also be partially reflected at altitudes where there is a sudden jump in the Brunt–Väisälä

frequency, according to the reflection coefficient [see, e.g., *Blumen*, 1985]

$$r_{AB} = \frac{N_B - N_A}{N_B + N_A}, \tag{67}$$

where N_A and N_B are the Brunt–Väisälä frequencies above and below the vertical interface upon which a gravity wave impinges. The duct region is characterized by large N values within the inversion between 2–3km, and small N values above and below this region, so that relection coefficients may be significant. If we define three layers from 1–2km (layer 1), 2–3km (layer 2), and 3–5km (layer 3), then approximate calculations from the temperature data in Figure 52 give values of $N_1 \sim 0.009 rad\, s^{-1}$, $N_2 \sim 0.027 rad\, s^{-1}$, and $N_3 \sim 0.013 rad\, s^{-1}$, suggesting $\mid r_{12} \mid \sim 1/2$, and $\mid r_{23} \mid \sim 1/3$.

Crook [1988] has derived a formula for the decay rate t_d of the total energy of intermediate frequency waves in layer A due to their propagation into layer B, such that

$$\frac{t_d}{T} \approx \frac{1}{8}\frac{N_A}{N_B}, \tag{68}$$

where T is the period of the wave. Equation (68) reveals that, despite Brunt–Väisälä frequency ratios around 2–3 at the layer interfaces for layers 1,2, and 3, these stability jumps are nonetheless insufficient to maintain significantly unattenuated wave energy over one period of the wave. For this reason, and also because the bulk of the vertical velocity fluctuations are produced by the highest frequency waves rather than lower frequency waves, the high–frequency ducting mechanism appears more consistent with the observations. Similar arguments also apply to earlier discussions of possible tropospheric ducting of fluctuating vertical velocity bursts during frontal passages.

Comparison with Models and Other Observations

The possibility of gravity wave launching from fronts was first theoretically investigated by *Ley and Peltier* [1978] as a means of correcting for ageostrophic and nonhydrostatic flow associated with a front. Their analysis produced high–frequency gravity waves which propagated ahead of and normal to the frontal boundary. More recently, gravity waves have arisen "naturally" in a number of high–resolution numerical models of frontogenesis [see, e.g., *Orlanski and Ross*, 1984; *Keyser and Pecnick*, 1985; *Gall et al.*, 1987, 1988; *Garner*, 1989*a*], but to date only *Gall et al.* [1988] have studied these simulated frontal gravity waves in any depth. *Gall et al.* [1988] noted strong fluctuating activity about the mean prefrontal ascent and postfrontal subsidence, much as in the observations presented here. They identified three classes of waves; the first were freely propagating waves above the frontal surface which were stationary with respect to the front. These waves were believed to result from approximately equal nonhydrostatic and ageostrophic

accelerations, which occur behind strong temperature gradients near the ground associated with the front. These waves could then propagate vertically above the frontal surface. A second class of stationary waves were trapped below the frontal boundary and the ground, and had quasi–monochromatic nature due to resonant forcing of a standing wave pattern. The associated temperature corrugations also induced similar monochromaticity in the first class of wave structure above the front, and in their simulations selectively produced waves with horizontal wavelengths around $50km$. The sub–frontal gravity waves also broke/saturated, and in the process forced further small–scale wave activity. A third class of waves were also visible well ahead of the surface front, which appeared to be of fundamentally different character to the stationary waves above and below the frontal surface, but these waves were not analyzed by *Gall et al.* [1988][8].

Quasi–monochromatic waves associated with the vertical motions either side of the frontal boundary, as modelled by *Gall et al.* [1988], were clearly observed in the vertical velocity fluctuations (see Figures 53–60). Waves stationary with respect to the ground cannot be resolved in ground–based time series of atmospheric wind measurements, since they produce no time variations, but since the front itself moves, the frontal–stationary waves of *Gall et al.* [1988] should be resolved. Assuming a representative frontal speed of $10m\ s^{-1}$ [*May et al.*, 1990] and a horizontal wavelength of $50km$ from *Gall et al.* [1988], this produces a ground–based period of $\sim 80min$, which is within the $30min$–2 hour period band of the fluctuating vertical velocities presented in Figures 54, 56, 58, and 60. The strong quasi–coherent vertical velocity oscillations which were observed during intense vertical frontal circulations may, then, well be related to the strong monochromatic frontal–stationary waves produced by the modelling of *Gall et al.* [1988]. The persistence of less intense, but nontheless significant fluctuating vertical velocity amplitudes both before and after frontal passages indicates that high–frequency waves which are not stationary with respect to the front must also be produced at, or in the vicinity of, the front.

Observations of frontal gravity waves are limited. *Bosart and Cussen* [1973] and *Bosart and Sanders* [1986] observed single large–amplitude gravity waves, which they believed originated from frontal forcing, but subsequent synoptic analysis has indicated that these waves might result instead from geostrophic adjustment of upper–level jet streams, and are tropospherically ducted [see, e.g., *Uccellini and Koch*, 1987; *Bosart and Seimon*, 1988]. These and other observations [see, e.g., *Uccellini and Koch*, 1987] have involved the analysis of data from widely–spaced surface microbarographs, which detect large–scale energetic single–wave disturbances. Finer–scale local measurements within frontal systems, much like

[8] it was noted in *Gall et al.* [1988] that this third class of waves were to form the subject of another paper. This paper has not appeared in the literature as yet.

the data presented here, were undertaken using an instrumented aircraft by *Shapiro and Kennedy* [1975]. They detected a large–amplitude quasi–monochromatic wave over undular terrain in a region just above a frontal boundary, and there was some evidence that the wave may have been ducted. However, these data were too limited to allow useful comparison with the frontal fluctuations observed here. *Testud et al.* [1980] identitifed quasi–coherent gravity waves in 12 hours of wind measurements with an obliquely–pointed[9] Doppler radar beam which was scanned azimuthally, enabling characterization of the wave motion parameters. Preliminary observations of frontal gravity waves have been made with the MU[10] radar in Japan [*Fukao et al.*, 1989*a*, *c*; *Yamanaka et al.*, 1989]. *Yamanaka et al.* [1989] identified quasi–monochromatic inertia gravity waves in 3 days of such data, and noted different wave characteristics at upper and lower levels.

In the Australian region, *Clarke* [1962] analyzed some surface–pressure fluctuations which occurred behind a cold front during mid–summer in southern Australia. These perturbations were associated with a gravity wave which was trapped within a temperature inversion at around 1–2km altitude. This observation has much in common with the low–level ducted wave activity identified in the shaded portion of Figure 54, which also occurred at low levels within a temperature inversion behind a cold front in southern Australia. Similar waves within inversions near these cold fronts were also observed indirectly by *Berson and Lamond* [1970].

4.3.5 Summary and Conclusions

A VHF radar in southern Australia was used to undertake extended measurements of 3–component wind velocities between 2–12km during the passage of cold fronts over the system. Time variations of the wind velocities were examined within this height range, and strong wave activity was detected in and around the fronts. The vertical and horizontal velocity variances, however, had fundamentally different time–height characteristics.

Bursts in the horizontal velocity variance were mostly confined to extended upper–level regions, when the mean flow was strong. However, this activity penetrated further into the lower troposphere as the frontal boundary neared. These fluctuations were identified with a relatively incoherent spectrum of energetic inertia gravity waves. A process was proposed by which wave–induced acceleration and geostrophic re–adjustment of strong upper–level winds might continually be dissipating and reradiating this inertia gravity wave energy. It was also argued that those waves propagating orthogonal to the mean

[9] the beam was directed almost horizontally
[10] Middle and Upper Atmosphere

flow should propogate upwards through this environment more easily.

Vertical velocity bursts, which are produced mainly by waves with high intrinsic frequencies, were most prominent below the tropopause. This could be due to reflection of waves just below the troposphere due to the small stability of these regions, but it also indicates that any emergent wave activity, while propagating almost vertically up through the troposphere, must propagate more obliquely in the stratosphere due to the greater stability here. Tropospheric bursts occurred both behind and ahead of the front, where strong mean vertical circulations arise, just like the simulated frontal wave activity in some models. In particular, strong coherent oscillations which are observed around the arrival time of the surface front have properties very much in common with a similarly–located large–amplitude frontal gravity wave arising from the model of *Gall et al.* [1988]. Less intense vertical velocity fluctuations are also observed before the front arrives, and persists after it has passed, indicating that high frequency waves may also propagate away from the frontal boundary. In one example, a region of vertical velocity fluctuations occurred within a low–level temperature inversion, which is consistent with thermally–ducted gravity–wave activity.

These observations provide compelling evidence that strong gravity wave motions occur throughout the troposphere with the passage of cold fronts over southern Australia. Furthermore, these observations comprise perhaps the most extensive and detailed measurements yet of the characteristics of small-scale wind motions in and around tropospheric frontal zones. Further observations are warranted which can better study the surface pressure variations and the finer-scale temperature structure, so that conjectures arising from this work, such as wave propagation directions, wave source mechanisms, wave stability, wave drag on the mean flow, and wave reflection, can all better be assessed.

Chapter 5

Gravity Waves in the Mesosphere

5.1 Introduction

In the previous chapter, it was shown that the Doppler shifting of gravity–wave energy into and out of narrow observed–frequency bands by non–zero mean winds induced large changes in the measured tropospheric variance at mesoscales. This process produced characteristic variations in the energy and azimuthal alignment of fluctuations within these frequency bands which, without due consideration of the effects, could be incorrectly ascribed to variations in the intrinsic characteristics of the wave field. In section 4.2.6 the possible effects on measurements of the mesospheric gravity–wave field were anticipated, and it was concluded that the effects at these altitudes should be small compared to the intrinsic variations in the wave field. Nevertheless, this conclusion was arrived at from a purely theoretical standpoint, and was based on a number of premises and choices of parameter values for which there is no explicit experimental verification.

It is important that this conclusion is assessed experimentally, because ground–based measurements currently provide the majority of information on mesospheric gravity waves. The height–time structure of the wave variance measured within various observed–period bands is presently viewed as evidence of changes in the intrinsic nature of the wave field [see, e.g., *Fritts*, 1989], yet if Doppler shifting *is* significant, some of the detected features could be spurious. For example, semiannual changes in the horizontal velocity variance at around $80km$ coincide with a semiannual variation in the background wind speed [*Meek et al.*, 1985*b*; *Vincent and Fritts*, 1987], which is superficially consistent with a Doppler–shifting hypothesis. On shorter time scales, high–frequency wave variance and momentum flux are modulated by strong diurnal and semidiurnal tidal motions at these heights [*Fritts and Vincent*, 1987; *Reid et al.*,

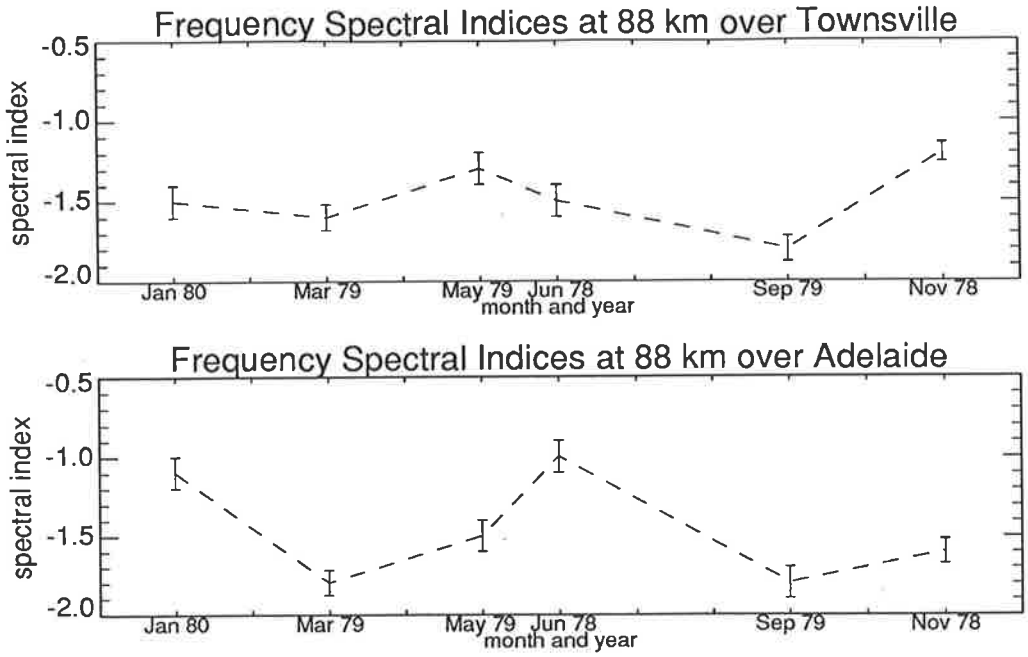

Figure 61: Seasonal variations of the least–squares frequency spectral indices of the horizontal winds at a height of $88km$ at Townsville (19°S, 147°E) and Adelaide (35°S, 138°E) over the 2–$8hr$ observed–period range. The data were taken from Table 7.1 of *Ball* [1981].

1988; *Fritts and Yuan*, 1989; *Wang and Fritts*, 1990; *D.J. Murphy*, private communication, 1990], yet these tidal winds could also cause significant Doppler shifting. Azimuthal wave alignments within various period bands have also been studied intensively [*Ebel et al.*, 1987; *Vincent and Fritts*, 1987], yet similar measurements at tropospheric heights are biased by Doppler shifting, as demonstrated in section 4.2.

Mesospheric variances have been analyzed quite successfully in terms of the adjustment of saturated horizontal–velocity amplitudes $\mid c - \bar{U}\cos\phi \mid$ as the mean wind speed $\mid \bar{U} \mid$ varies with time and/or height [*Vincent and Fritts*, 1987; *Fritts and Vincent*, 1987]. However, computed frequency spectra of the motions at these heights reveal a shape $\sim \Omega^p$, where the frequency spectral index p falls between –1 and –2 (see section 3.3.3 and references therein), which indicates that the Doppler–shifting theory of *Scheffler and Liu* [1986] and *Fritts and VanZandt* [1987] is applicable to these motions. The model, discussed in depth in section 3.3.3, predicts enhanced high–frequency variance and a consequent increase in p as the mean wind speed increases (see Figure 39). Earlier frequency spectral analysis of mesospheric winds over Adelaide (35°S, 138°E) and Townsville (19°S, 147°E) by *Ball* [1981] revealed a semiannual cycle at both sites, with minima at the equinoxes and maxima at the soltices (Figure 61). This feature correlates well with a semiannual oscillation of the zonal wind at this height (see, e.g., Figure 62), such that the results in Figure 61 are consistent with the predicted effects of Doppler shifting by these winds on the frequency spectrum.

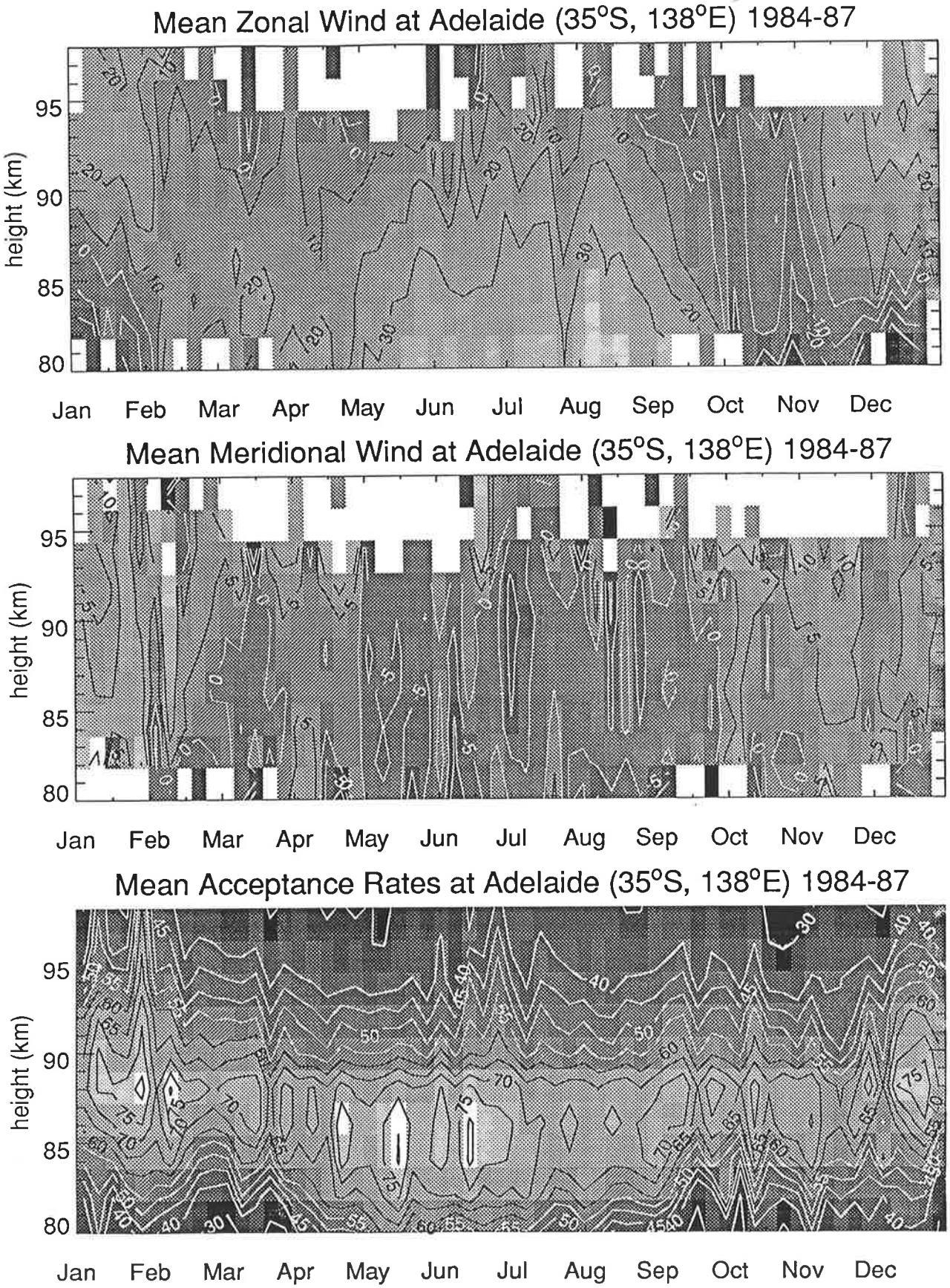

Figure 62: Mean zonal winds, meridional winds, and data acceptance rates calculated from routine MF–radar measurements of mesospheric winds. The results are 4–year averages from 1984–1987 in the 80–98km altitude range. Contour labels are in $m\ s^{-1}$ for the winds, and percentages for the acceptance data.

The preliminary data of *Ball* [1981] superficially suggest some discernable Doppler–shifting effect, whereas theory predicts limited effects. If the former is true, interpretation of earlier measurements of mesospheric gravity waves might need altering. If the latter is true, the data provide information on the shape of the intrinsic frequency spectrum, about which very little is known; it is presently believed to have a "universal" $\omega^{-5/3}$ shape, but if mesospheric Doppler shifting is small, Figure 61 indicates a rather variable intrinsic shape. This intrinsic spectral index is an important dynamical parameter, which determines the ratio of kinetic to potential energy over the entire wave spectrum [see, e.g., *Smith et al.*, 1987]. Hence, if Doppler shifting is significant or not, in either case the consequences are important. More generally, the evolution of the ground–based frequency spectrum due to Doppler shifting by the background wind, as predicted by *Scheffler and Liu* [1986] and *Fritts and VanZandt* [1987], has yet to be experimentally assessed in any detail at these heights.

The findings of an experimental study of the frequency spectra of horizontal winds in the mesosphere between $80km$ and $98km$ over Adelaide are set forth in this short chapter, and are analyzed to address some of these aforementioned uncertainties in theory and data interpretation.

5.2 Data Analysis

Essentially continuous measurements of winds in the altitude range 60–$100km$ commenced in 1983, using an MF radar facility at Buckland Park, near Adelaide. These winds are obtained by analyzing radar returns from this region using the Spaced Antenna (SA) technique. An extensive base of climatological wind data with a time resolution of $\sim 4min$ and height resolution[1] $\sim 2km$ now exists, which is ideal for studying the time–height morphology of mesospheric gravity waves [*Vincent and Fritts*, 1987].

The high temporal resolution of the data make them amenable to frequency spectral analysis, and four years of these data (1984–1987) were prepared for such calculations. This involved first averaging the raw data into $20min$ blocks to improve the acceptance rates. The mean time–height acceptance rates of these $20min$–averages are plotted in the bottom diagram in Figure 62. The most frequently recorded winds occur around 85–$90km$, although this height interval varies in a noteably annual fashion (for a discussion of this feature, see *Hocking* [1988]).

A suitable length of time over which individual spectral computations should be performed is a difficult and somewhat arbitrary choice to make; the time series needs to be of sufficient duration to produce acceptable spectral resolution, yet should not be too long lest temporal nonstationarity of the

[1] this is oversampled. The radar pulse width gives a true height resolution nearer $4km$.

spectrum becomes significant (see section 3.3.3). Data segments of two–day duration were spectrally analyzed here; two days appears to be a small–enough time scale to avoid the quasi–weekly variability of the variance observed by *Vincent and Fritts* [1987], yet it does not avoid the nonstationarity induced by tides and the summertime two–day wave. In this preliminary study, we shall concern ourselves only with possible spectral modification by the mean winds, and we leave investigation of the effects of long–period waves to subsequent studies.

Data rates at upper and lower levels are poor (see Figure 62), and such gappy data will produce unreliable spectra. Consequently, a minimum 70% data–acceptance criterion was imposed upon the two–day time series. The limited missing data within these accepted profiles were interpolated using a cubic spline, which was fitted over the good data. However, despite the high data rates in these accepted profiles, closer investigation revealed that if extended gaps in the data occurred, some spectral distortion could also arise from the smoothly–interpolated stucture over this region. Therefore, an additional constraint was imposed, such that if smaller segments of missing data within the time series arose which exceeded 10% of the total length of the time series, the spectra were also rejected, notwithstanding total acceptance rates >70%. Such discrimination resulted in rejection of the majority of raw data, with most of the accepted profiles concentrated at heights around 84–88km. After removal of mean winds, spectra were numerically computed using an FFT algorithm.

One must also choose a suitable band of frequencies over which the spectral characteristics should be studied. Long–period spectral peaks arise at 48hr, due to the two–day wave, and at 24, 12, and 8hr due to tidal harmonics [see, e.g., *Ball*, 1981; e.g., Figure 7]. Near the Nyquist period (40min), artificial enhancement of spectral power arises due to aliasing of shorter period waves (see Figures 35 and 40 in section 3.3.3). Therefore, we focus hereafter on the spectral characteristics over the intermediate 1–6hr band, which should ideally be free from the aforementioned distortions at low– and high–frequencies.

5.3 Results

To begin, we shall examine the seasonal variability of spectra of zonal and meridional winds in the 1–6hr range as a function of height and season. Results from 80–88km only are presented, since data at greater heights are too seasonally sparse to reveal trends. Figures 63 and 64 show the seasonal variation of the least–squares spectral indices over the 1–6hr band for the zonal and meridional velocities, respectively. We note here that the zonal indices are somewhat acyclic with season, whereas a semiannual variation occurs for meridional velocities, with solsticial minima and equinoctial maxima, which are are in complete

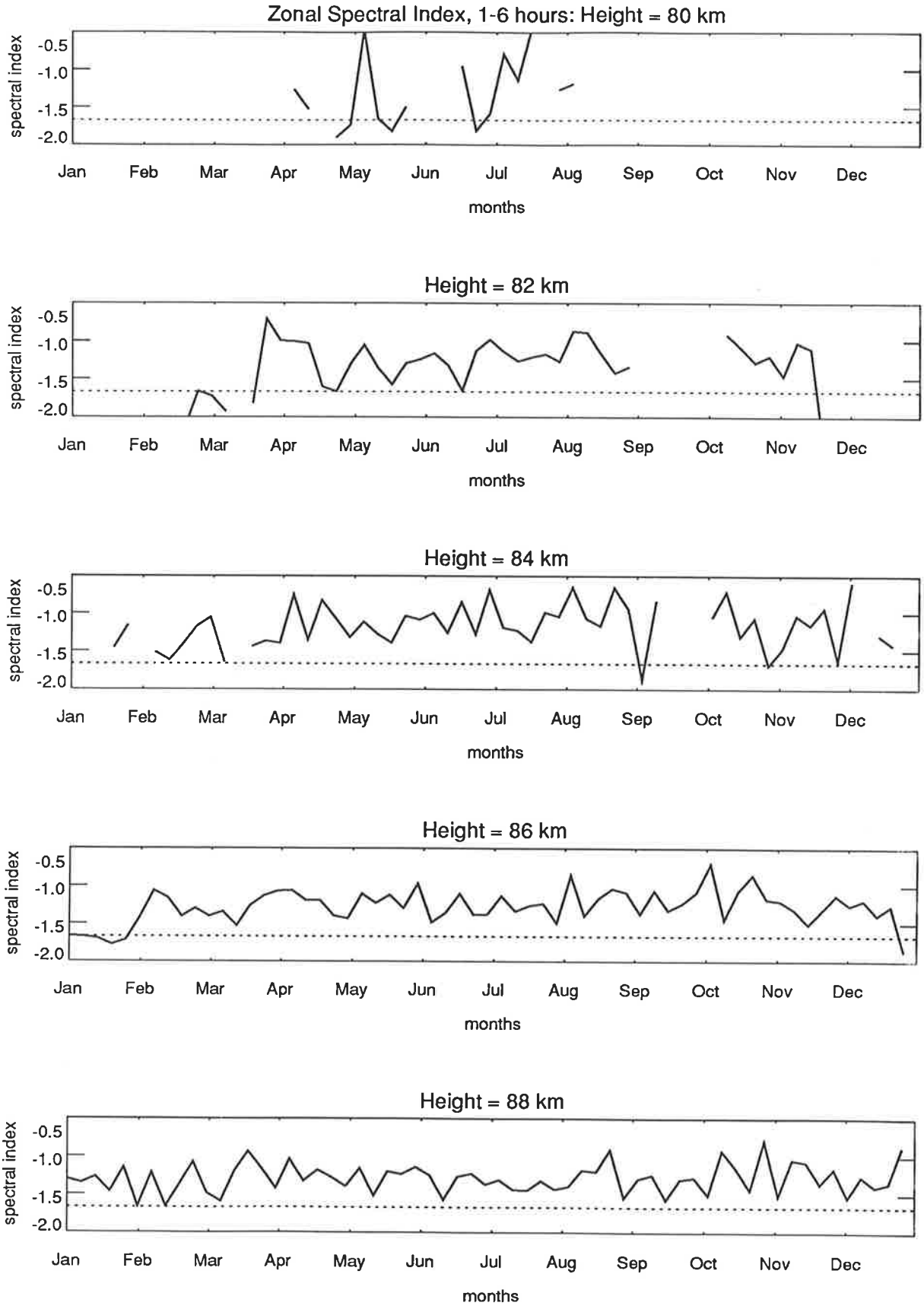

Figure 63: Seasonal variation of the mean least–squares spectral indices of the zonal velocity spectrum over the 1–6hr period band at 80–88km in height from 1984–87. Each point is a mean over a 6–day interval. The dotted line shows the theoretical intrinsic spectral index of –5/3.

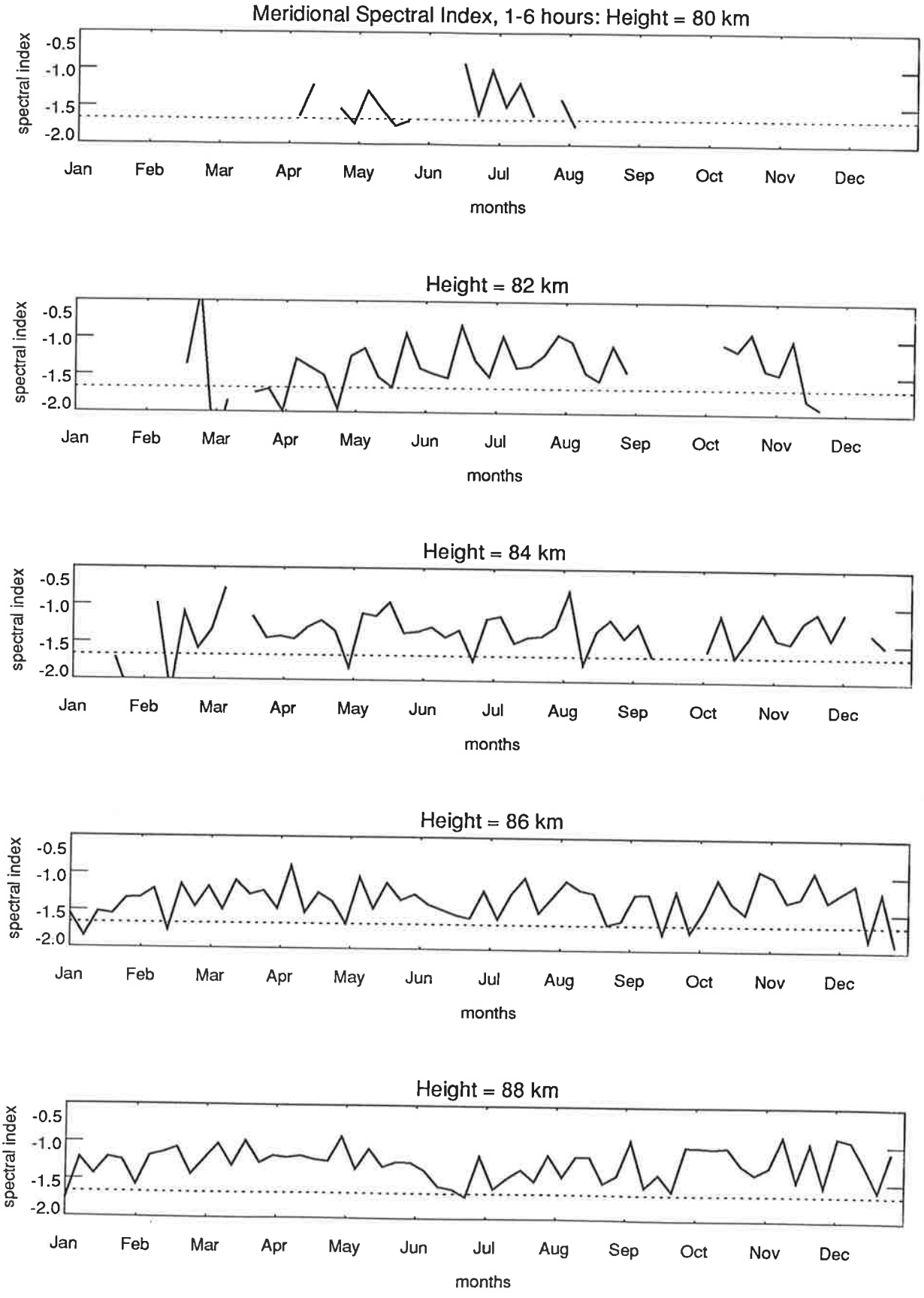

Figure 64: As for Figure 63, but for meridional velocities.

contrast to the results of *Ball* [1981] in Figure 61. We note, however, that there is large point–to–point variability in the indices, so that the isolated observations of *Ball* [1981] are proabably insufficient to reliably highlight seasonal trends. Note also that the spectral indices almost always exceed -5/3, with mean values around –1.4.

Integrating the 1–6hr spectra revealed that the zonal–velocity variance was also rather acyclic with season, although a small dip was observed during summer. The meridional–velocity variance, however, exhibited more seasonal variation, with a peak ($\sim 300 m^2\ s^{-2}$) in August and a noteable minimum in early summer ($\sim 150 m^2\ s^{-2}$), characteristics which compare well with earlier studies of the the 1–8hr variance of the 1984 data by *Vincent and Fritts* [1987]. *Vincent and Fritts* [1987] observed a weaker secondary peak in January–February, whereas here it is observed later (around March).

Phillips and Vincent [1989] have computed mean winds at these altitudes from 1985–1987, which agree with similar computations performed here (Figure 62). Zonal winds are eastward for most of the year, peaking at around 20–40$m\ s^{-1}$ during winter, whereas in the late–spring and summer months the flow is weakly westward. The mean meridional winds vary annually, with weak winds at the equinoxes, southward flow peaking around $10m\ s^{-1}$ in winter, and similarly intense northward flow during the summer months.

We now seek to relate these variations with Doppler -shifting predictions. Such relationships are made difficult because the wave–azimuth distribution becomes anisotropic at these altitudes due to critical–level filtering as the wave field propagates up through the underlying stratospheric winds. The model spectra in Figure 39a are valid for equal amounts of up– and down–shifting, and while the shallowing of the spectral rolloff with frequency in Figure 39 is relatively insensitive to moderate anisotropy in wave propagation directions, if either up— or down–shifting of frequencies occurs exclusively, the changes to the spectral shape are different in each case [*Fritts and VanZandt*, 1987]. From these data it is impossible to quantify the precise wave–azimuth distribution, although earlier computations of wave alignments by *Vincent and Fritts* [1987] showed that most of the fluctuations (and hence wave propagation) were directed meridionally rather than zonally. This suggests that Doppler–shifting effects on the spectrum should be more evident meridionally, but this assumes that the wave alignments computed by *Vincent and Fritts* [1987] have not been biased by Doppler shifting, which was not the case for the tropospheric measurements in section 4.2.

Because of these interrelated difficulties, we shall endeavour to answer only the following questions: (a) Is there evidence of regular changes in the spectral shape as mean wind speeds increase, which might then indicate Doppler shifting of the frequency spectrum? (b) Does the variance within the 1–6hr band

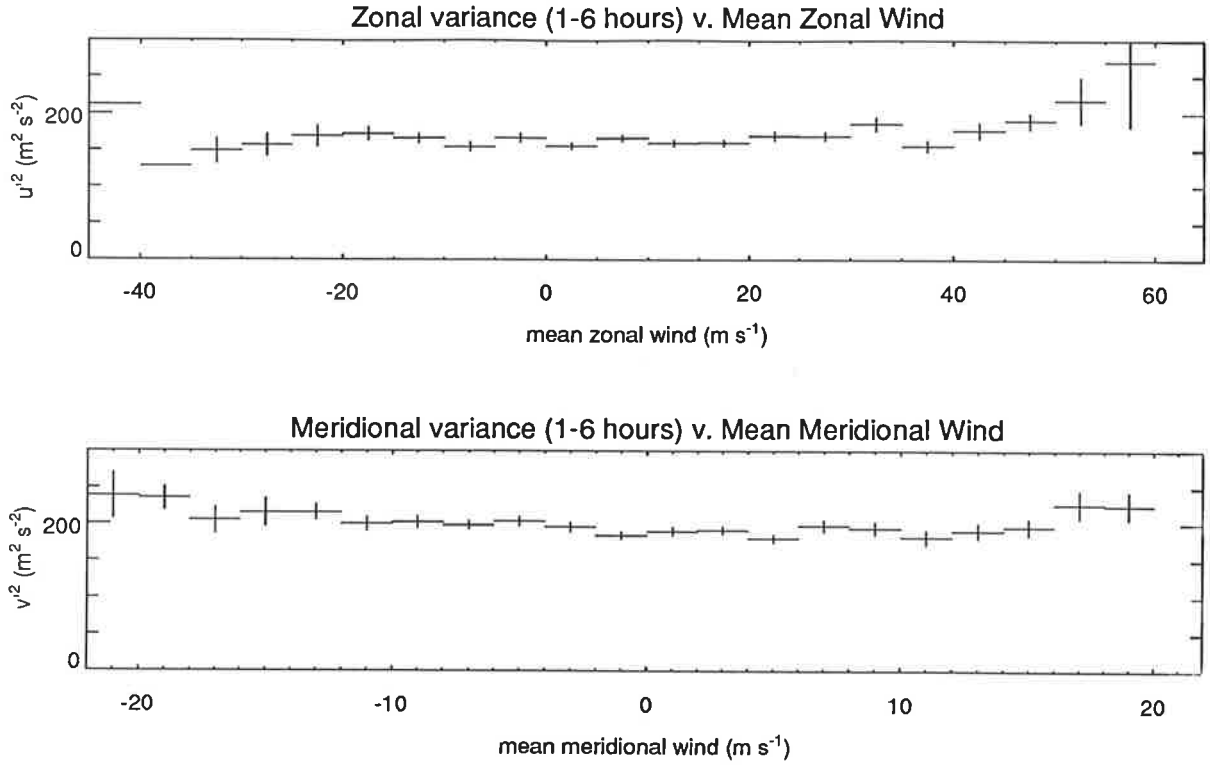

Figure 65: Mean variance in the 1–6hr period band at 80–88km plotted versus mean wind speed, for the zonal and meridional data. Y–axis error bars are standard errors of the mean, and no error range is plotted when only one point was available. In excess of 1000 accepted spectra were used to compose these results.

change systematically as the mean winds intensify, as observed in the troposphere (see section 4.2) where it arises due to Doppler–shifting of variance into and out of different frequency bands?

The seasonally–invariant zonal data cannot be analyzed conclusively, whereas meridional data produce trends which are more amenable to analysis. The smaller spectral indices in June–July and December–January occur when the mean meridional wind is strongest, whereas the least–negative values occur when the the mean meridional flow is near–zero; however, this is completely opposite to the effect predicted by the Doppler–shifting model in Figure 39. If wave–propagation was highly anisotropic such that down–shifting of wave frequencies occurred almost exclusively, then the model could explain this feature. However, such anisotropy is not anticipated meridionally, since lower–level meridional winds are weak and therefore produce less critical–level filtering. Furthermore, the seasonal variation in the strength of the meridional variance (i.e. peaks in August and March, and a summer minimum) does not correlate well with seasonal variations of the mean meridional wind. This suggests that the Doppler–shifting effects are not significant.

Figure 65 plots the mean variance in the 1–6hr band, as a function of mean wind speed, for both the zonal and meridional data. There is no significant change in the variance as mean wind speeds increase,

providing more direct evidence that these results are not significantly influenced by the injection of low–period wave energy into shorter ground–based period bands as the mean wind speeds increase. Small increases are weakly evident at the largest mean wind speeds, but these variations are insignificant when compared to the 200–1000% increases due to Doppler–shifting in the lower atmosphere (see section 4.2), and the natural time–height variability of the variance [*Vincent and Fritts*, 1987]. This adds observational weight to the theoretical conjecture in section 4.2.6 as to the lessening of Doppler–shifting effects at these heights, and implies that earlier mesospheric gravity–wave measurements do not require major reinterpretation.

Having broadly verified that "Doppler biasing" of these temporal gravity–wave fluctuations is not appreciable, we now use these spectral data to provide further information on the wave characteristics at these heights. Figure 66 plots the mean azimuthal alignment $\bar{\phi}$ of the horizontal velocity fluctuations in the 1–6hr band, which were computed according to (57) using the spectral form of the Stokes parameters, detailed in Appendix A. The data show a surprisingly regular seasonal variation; the alignments are strongly clustered north–south in all months, especially at the equinoxes, but become more NE/SW in winter (most noticeably at 88km) and SE/NW during summer, producing a noteable annual cycle in wave alignment. Differences between mean winter and summer alignments at this site during 1984 were noted by *Vincent and Fritts* [1987] in the 1–8hr band. The results in Figure 66, which have a six–day resolution rather than than the six–month resolution in the results of *Vincent and Fritts* [1987], indicate a smooth annual transition between these summer and winter alignment phases.

Mean winds are directed south–eastward (SE) in winter and north–eastward (NE) in summer [*Phillips and Vincent*, 1989], directions which are anticorrelated with the azimuthal alignments in Figure 66. Recall from section 4.2 that the two become strongly correlated when "Doppler–biasing" occurs; thus, the anti-correlation provides further compelling evidence that the effect is not significant here. This anticorrelation could be cited as evidence that vortical modes produce most of the variance. However, the invariance of the fluctuating energy with wind speed in Figure 65 invalidates a vortical–mode interpretation, since its model spectrum in Figure 39b dictates that the vortical–mode variance increases considerably with wind–speed in the same manner at all altitudes (as opposed to the gravity–wave spectrum). Moreover, in zero–wind conditions, vortical modes produce no time–fluctuating variance, yet similar variance is observed in Figure 65 in all wind conditions. It is clear from this and numerous other studies [see, e.g., *Fritts and Vincent*, 1987; *Fritts*, 1989] that the mesospheric variance is produced by an azimuthally anisotropic spectrum of gravity waves, whose energy distribution as a function of frequency is only weakly affected by Doppler shifting.

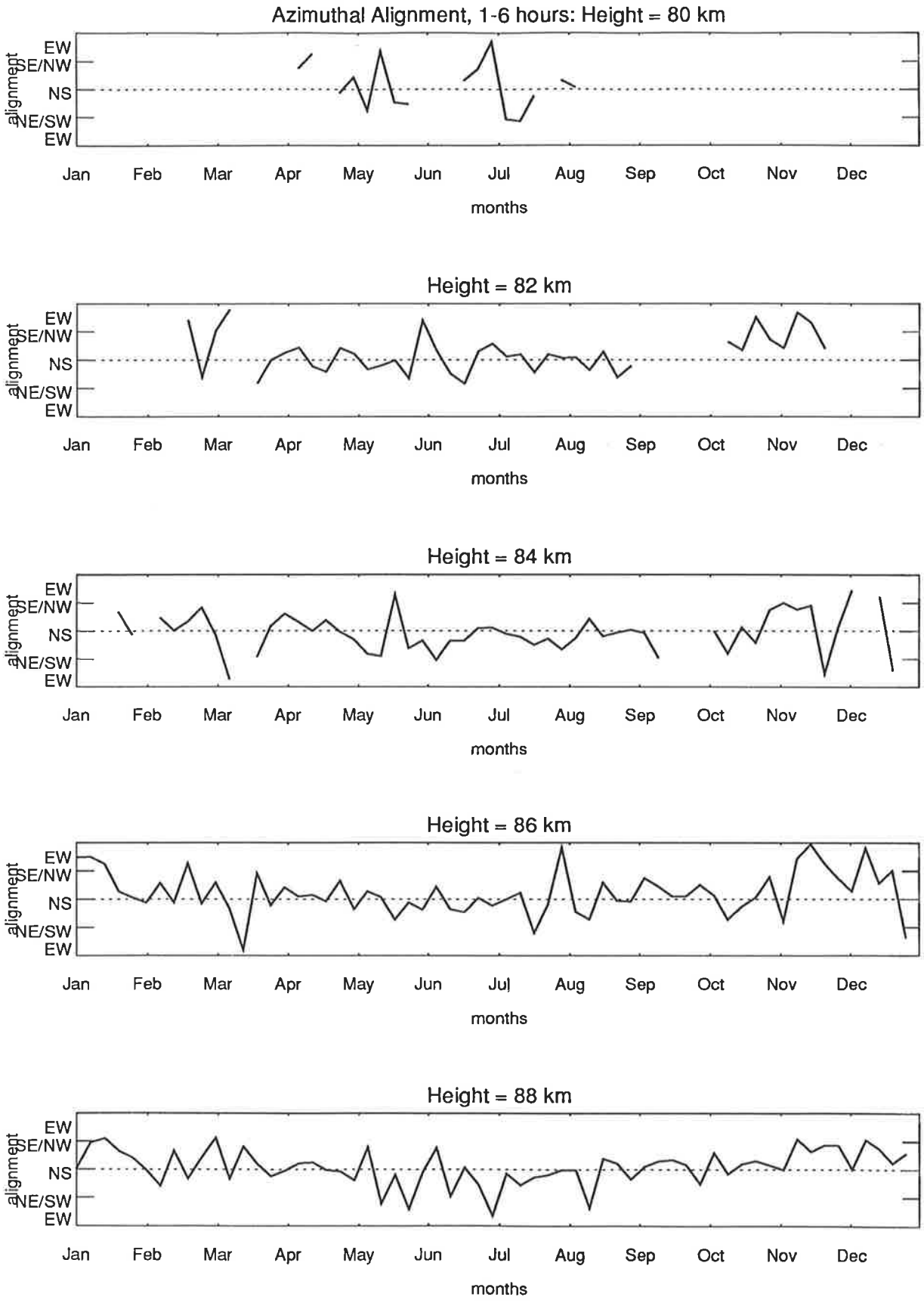

Figure 66: As for Figure 63, but for the mean azimuthal alignment $\bar{\phi}$. Separate $\bar{\phi}$ determinations were combined into multi–value means using the circular statistical techniques of *Mardia* [1972]. The dotted line indicates north–south alignment.

Rotary spectral components of the motion can also be calculated from the spectra. Such computations prove useful as an aid to determining the vertical sense of wave propagation when the vertical spatial structure of the wave is studied [*Vincent*, 1984; *Hirota and Niki*, 1985; *Eckermann and Vincent*, 1989; see also chapter 6]. However, interpretation of the temporal analogue of this calculation is unclear.

Following *Andrews et al.* [1987], we denote the instantaneous azimuth of the horizontal–wind phasor by ψ. When measured by a vertically–pointed, stationary ground–based radar, ψ is given by

$$\tan\psi = \frac{v'}{u'} = \frac{f}{\omega}\tan\left(mz - \Omega t\right), \tag{69}$$

where we assume for simplicity a zonally propagating wave, and $\Omega = \omega + k\bar{U} = kc$ is the ground–based wave frequency. Differentiating in time produces

$$\frac{d\psi}{dt}\sec^2\psi = \frac{-\Omega f}{\omega}\sec^2\left(mz - \Omega t\right). \tag{70}$$

Since the squared secants are always positive, then $d\psi/dt$ (the sense of phasor rotation with time) has the same sign as $-\Omega f/\omega$, a term which can be reexpressed as follows;

$$\frac{-\Omega f}{\omega} = \frac{-f}{1-\bar{U}/c}. \tag{71}$$

At first glance it appears that, in a given hemisphere, the terms Ω, f and ω have the same sign for all the waves, and thus no effect will occur. However, ω in fact becomes negative when the intrinsic phase speed $c-\bar{U}$ and ground–based phase speed c of a gravity wave are in the opposite direction. This in turn occurs when $\bar{U}/c > 1$, as shown in (71), which implies c is in the same direction as $\bar{U}$ but has a smaller value. Figure 67 shades those regions where $\omega < 0$, using a typical wintertime zonal wind profile at these heights [*Phillips and Vincent*, 1989]. Thus the temporal sense of rotation of the horizontal wind phasor is determined by the sign of the wave's intrinsic frequency, which in turn provides useful information on the ground–based phase–speed distribution of the wave spectrum. Note the similarity of this interpretation in terms of differently signed intrinsic frequencies, with similar phasor analysis of the vertical spatial structure of the wave, where positive and negative vertical wavenumbers rotate in the opposite sense [*Hirota and Niki*, 1985].

Figure 68 plots the seasonal variations of the percentage of wind–velocity variance contained in the anticlockwise–rotating rotary spectrum from 1–6hr, as computed from the spectral Stokes parameters using formulae in Appendix A. For anisotropy to arise (i.e. values $\neq$ 50%), two features need to occur. Firstly, the wave field obviously needs to be elliptically polarized to some extent, which implies f/ω is non–zero, and thus waves with small intrinsic frequencies must be present. For the 1–6hr data here, Doppler shifting of low intrinsic frequencies into this band would enhance the ellipticity, although 6hr

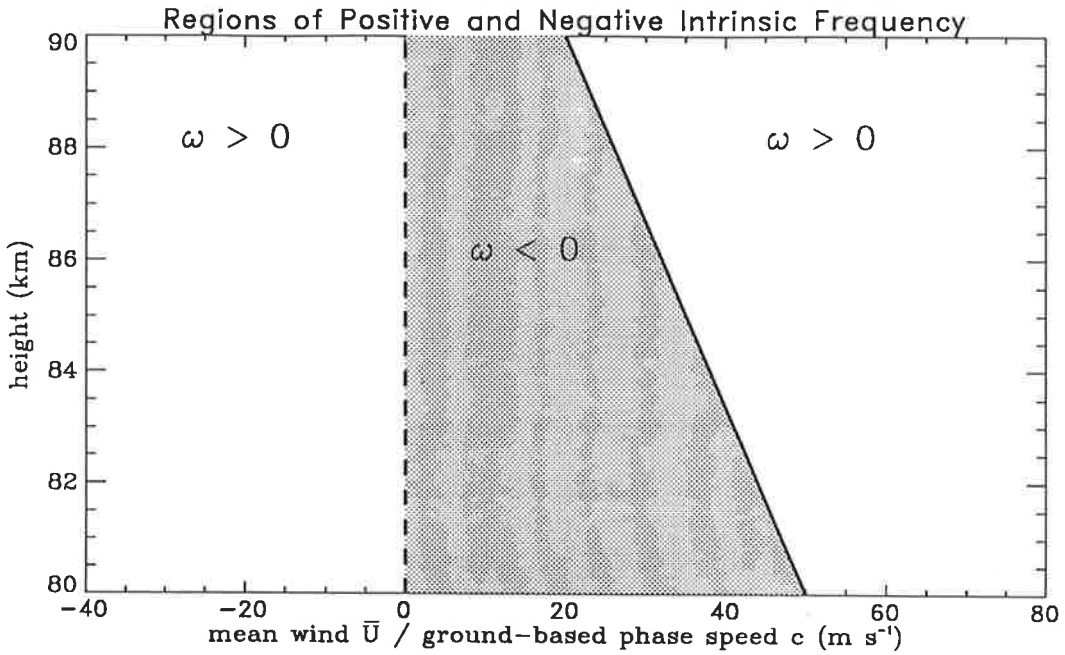

Figure 67: Schematic diagram which illustrates regions of positive and negative intrinsic frequencies. The solid line shows a representative wintertime mean zonal–wind profile, and the dotted line indicates $\bar{U} = 0$. The shaded region shows those ground–based phase speeds c which produce $\omega < 0$. Unshaded regions elsewhere indicate where $\omega > 0$.

intrinsic periods produce $f/\omega \sim 0.3$. Secondly, there must also be anisotropy in the relative contributions of the positive and negative intrinsic–frequency waves to the total variance. Due to critical–level filtering by the mean stratospheric winds, one would anticipate that waves for which $\omega > 0$ should be far more prevalent than negative–frequency waves. Since f is negative in the summer hemisphere, waves for which $\omega > 0$ will produce anticlockwise rotation.

The results in Figure 68 reveal anticlockwise percentages are indeed larger, but not significantly so (~55%), and these values exhibit no discernable seasonal variability. Rather than indicating that ~45% of the variance is produced by negative–frequency waves, however, one must argue instead that the limited Doppler shifting of low–frequency energy into this higher frequency band produces little elliptical polarization of the wave field, and thus the rotary partitioning is not complete [see, e.g., *Eckermann and Vincent*, 1989].

5.4 Discussion

Having argued that Doppler shifting of wave variance into and out of different frequency bands by the mean winds is limited, the seasonal variability of the spectral indices now require explanation.

Figure 69 shows a scatter plot of the computed spectral indices over a wind–speed range, centered

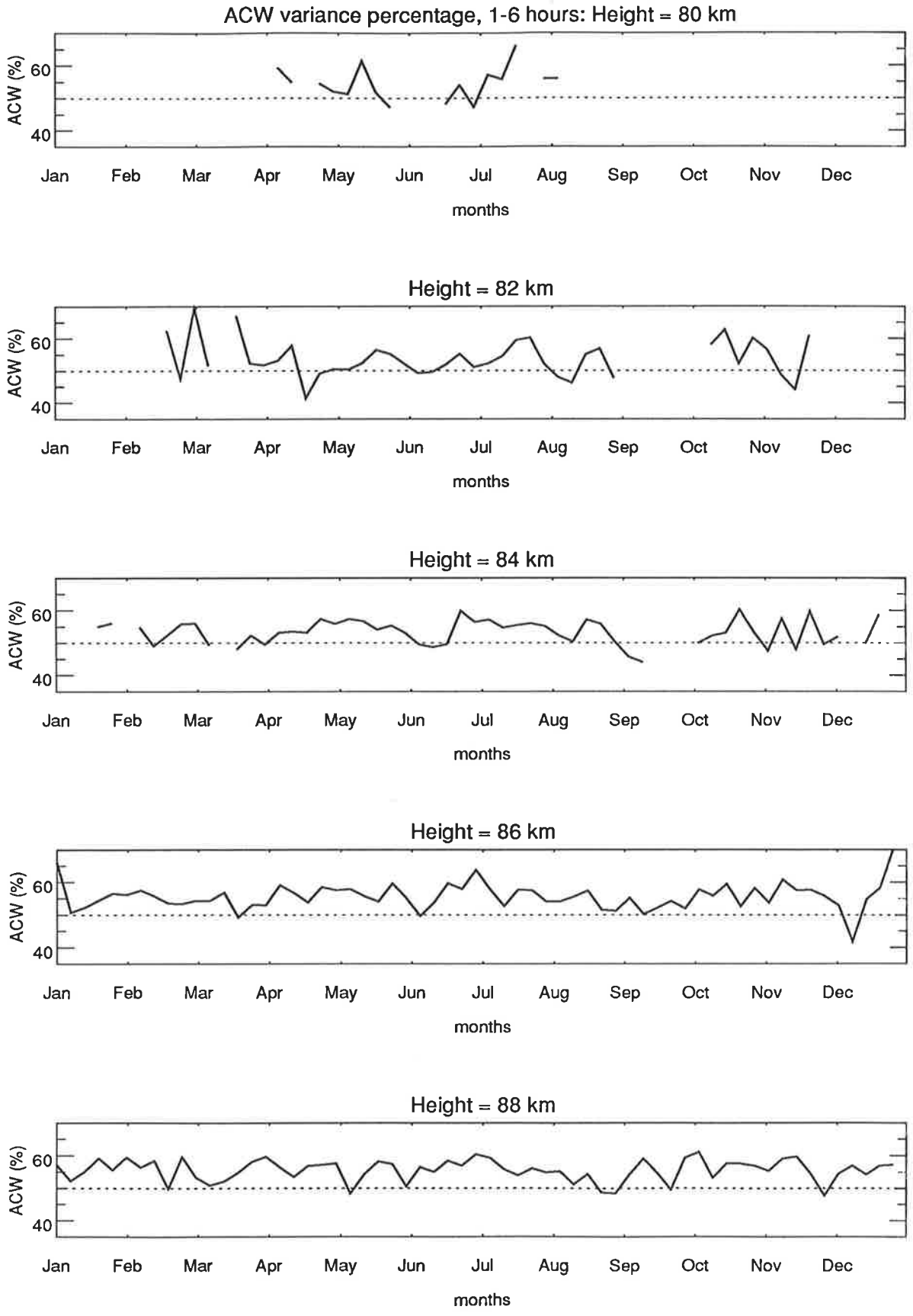

Figure 68: As for Figure 63, but for the mean percentage of anticlockwise wind-vector rotations using rotary spectral techniques. The dotted line indicates shows the 50% (equipartitioning) level.

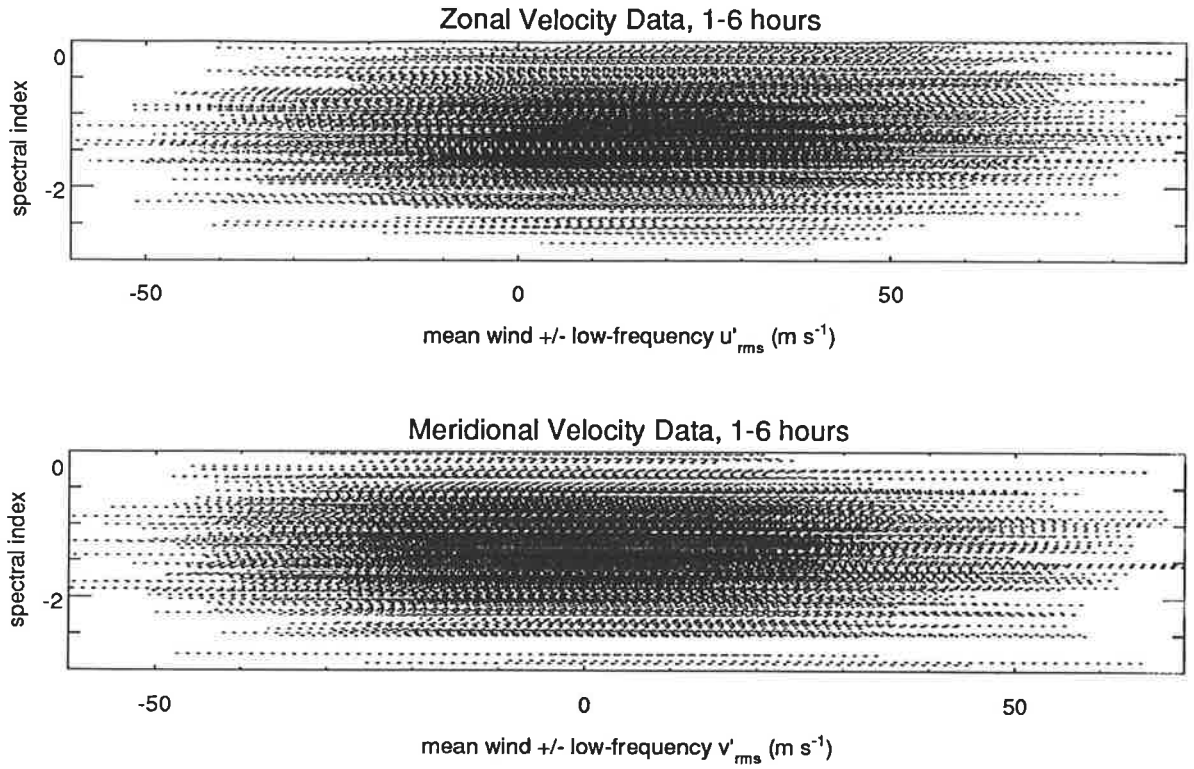

Figure 69: Scatter plots of the spectral index over the 1–6hr band versus a wind range, which is centered on the mean–wind velocity and extends over the r.m.s. amplitude of the spectrum over the 6–48hr range. These ranges are plotted as error–bars using dotted curves.

at the mean–wind speed and covering the r.m.s. fluctuating amplitude over the 6–48hr observed–period range. This figure serves to indicate that, especially in the meridional, the low–frequency wind variability is usually larger than the mean wind, and may cause nonstationarity of these time series due to the Doppler shifting produced by these time–varying winds, much like that modelled in Figure 40. The simulations in section 3.3.3 suggested that the Doppler–shifted spectra are reasonably well–modelled by using the r.m.s. amplitude of wind variability, and again predicts more positive spectral indices when Doppler shifting occurs. Inspection of the seasonal variation of the 6–48hr r.m.s. meridional–velocity amplitude around 88km revealed smallest values in May–July, larger values at the equinoxes of ~25–30$m\ s^{-1}$ due to tides [*Vincent et al.*, 1988], and a large peak (~30–40$m\ s^{-1}$) in January–February due to the 2–day wave [*Craig and Elford*, 1981]. Yet, as for the mean–wind variations, these seasonal variations do not correlate well with the seasonal characteristics of the 1–6hr meridional–velocity spectral indices in Figure 64.

Therefore, the variations of the spectral indices are not consistent with the predicted effects of Doppler shifting by either the mean or low–frequency winds. While questions still remain as to the effects that azimuthal anisotropy in wave propagation and tidal–wave and/or two–day–wave modulation might play in Doppler–shifting of the frequency spectrum, the current theory and these observations suggest that

distortion of the intrinsic frequency spectrum by these processes is limited. Consequently, these variations may well be indicative of seasonal variations in the shape of the intrinsic frequency spectrum.

While current theory assumes a "universal" $\omega^{-5/3}$ shape, these 1–6hr spectra reveal spectral indices which are more positive than –5/3, and which also vary greatly on both short and long time scales (Figures 63 and 64). The processes which combine to form the intrinsic frequency spectrum have yet to be investigated; it is likely that wave saturation plays a major role, since it is this mechanism that controls the vertical wavenumber spectrum [*Smith et al.*, 1987; see also section 3.3.2]. Indeed, this vertical wavenumber spectrum varies in shape within different wavenumber bands, and the entire spectral shape can vary with height and time (as discussed in section 3.3.2). Thus, variability in the shape of the intrinsic frequency spectrum is not an unprecedented idea.

5.5 Summary

The following results followed from spectral analysis of four years of upper–mesospheric horizontal–wind data:

(1) the redistribution of wave energy in the horizontal velocity frequency spectrum through Doppler shifting of wave frequencies by the mean winds appears to be small;

(2) meridional spectral indices in the 1–6hr band have a weak semiannual variation, with solsticial minima and equinoctial maxima, contrasting earlier findings of *Ball* [1981]. Mean zonal indices are seasonally acyclic, although their point–to–point variability increases at the equinoxes;

(3) mean wave alignments have a regular annual variation which is centered about a north–south mean;

(4) waves with $\omega > 0$ are more prevalent than waves for which $\omega < 0$.

Although this study has achieved its stated objective of assessing the impact of Doppler shifting of energy by the mean flow on ground–based measurements of mesospheric gravity wave energy, the analysis has also raised as many questions as it has answered. Consequently, further study would appear justified, particularly to assess whether these spectral indices characterize the intrinsic spectral shape. The modulated Doppler shifting of the frequency spectrum by large–amplitude low–frequency motions (e.g., tides, two–day wave) should be studied explicitly. This is probably best achieved by obtaining data with higher time resolution in a dedicated observational campaign. Seasonal variations in the spectral indices and band variances should also be studied within other frequency bands, so that a better picture of the spectral evolution emerges.

Chapter 6

Gravity Waves in the Stratosphere

6.1 Chapter Theme

This chapter details the results of analyzing atmospheric data obtained from rocket–borne sampling of the middle atmosphere for gravity waves. Section 6.2 briefly summarizes the wave features evident in data from falling–sphere experiments performed at Woomera, Australia, which provide the first information on upper–stratospheric gravity waves in the Southern Hemisphere. The study was designed to complement similar studies of rocket data from a number of Northern Hemispheric sites by *Hirota* [1984] and *Hirota and Niki* [1985]. Subsequent to these earlier studies, however, some questions about the original analysis, a better developed theory of these waves, and some as–yet uninvestigated wave properties, have all been identified, and these require further analysis of the Northern Hemispheric rocket data. The results of such an undertaking are given in section 6.3. This chapter provides a detailed morphology of stratospheric gravity waves on a global and climatological scale.

6.2 Falling Sphere Observations of Anisotropic Gravity Wave Motions in the Upper Stratosphere over Woomera

Only a brief summary of this work is provided here, as a full description of the analysis and results has already been published [*Eckermann and Vincent*, 1989], and can be found in Appendix *E*. Furthermore, much the same analysis techniques are applied in the next section to a more extensive base of meteorological rocket data from fifteen different sites, so that these single–site results can be viewed as complementary to the results to follow.

The data from Woomera (31°S, 136°E) consisted of vertical profiles of temperature and horizontal wind in the height interval 30–60km at approximately monthly intervals between 1962 and 1976. The vertical spatial structure of the waves were isolated by numerical filtering of these profiles to produce fluctuations in the 2–10km vertical–wavelength range. The gross features of the wave field compared favorably with those found in earlier studies from the Northern Hemisphere. Wave propagation was found to be both vertically and horizontally anisotropic. A rotary spectral analysis indicated predominately upgoing wave energy, suggesting that the majority of sources of these waves lie below 30km. A detailed statistical investigation of the waves, made using the Stokes parameters technique (see Appendix A), revealed that wave propagation was also highly localized azimuthally, with a significant zonal component in summer, and a strong meridional component in winter. Propagation towards the southeast was inferred in summer, indicating that the waves may emanate from tropospheric sources in equatorial regions to the north of Australia. The technique also showed that, on average, the waves appear to have mean ellipse eccentricities ($=f/\omega$) around 0.4–0.45, yet these values must be interpreted with considerable caution in light of the reanalysis of these ratios provided earlier in section 3.2. Indirect estimates of a number of important wave parameters were also attempted. In particular, $\overline{u'w'}$ and $\overline{v'w'}$ flux estimates are made over several height intervals. The vertical gradient of the density–weighted flux was estimated, and provided wave–induced mean–flow accelerations of the order 0.1–1 $m\ s^{-1}\ day^{-1}$. This suggests that dissipating gravity waves are a significant source of the momentum residuals that are encountered in studies of satellite data from this region.

6.3 Gravity Waves in Upper–Stratospheric Rocket Data

6.3.1 Introduction

The atmosphere between about 20 and 60km in altitude historically has been a difficult region to probe in detail. While satellites now provide excellent data on the background structure and planetary–scale wave disturbances around the globe, smaller–scale structure such as gravity waves are poorly resolved, if at all. Ground–based radar systems can probe the height intervals 0–30km and 60–100km with good time–height resolution, but they receive insufficient radiowave backscatter from 30–60km to enable atmospheric winds to be measured in the intervening heights.

Until quite recently, the only recourse was to rocket soundings of this region. The data provided by these experiments consist of horizontal winds and temperatures with good height resolution, and measurements have been performed over many years and from a number of sites around the world.

However, there are large, irregular time intervals between successive launches, so that gravity waves can only be resolved in the vertical using such data. Ground–based lidars can also remotely sound this region now, giving temperature and wind data with good height and time resolution. While it seems clear that this technique will supersede rockets as the primary source of information on gravity wave characteristics at these heights in the future, at present these observations are being performed at only a few sites, and the data base to date is limited in its seasonal and climatological coverage [see, e.g., *Shibata et al.*, 1986, 1988; *Gardner et al.*, 1989]. Therefore the rocket data is still the best data source as regards geographical and climatological coverage.

A basic climatology of upper stratospheric gravity waves evident in rocket data from around the world was first provided by *Hirota* [1984] and *Hirota and Niki* [1985]. Since these initial studies, the theory of atmospheric gravity waves has developed considerably. There is some uncertainty as to the interpretation of some quantities calculated by *Hirota* [1984] and *Hirota and Niki* [1985] in light of these theoretical developments. Furthermore, new questions and additional doubts concerning these results now exist, some of which were discussed in section 3.2 and others which were tackled in analysis of rocket data from single sites by *Hass and Meyer* [1987] and *Eckermann and Vincent* [1989].

These issues are all best addressed by further analyses of these rocket data, and form the subject of this work. The data and the manner in which they were analyzed for gravity waves are described in section 6.3.2. Mean seasonal variations in wave–induced wind and temperature variances are reinvestigated in section 6.3.3, spectra are analyzed in section 6.3.4, wave propagation directions are inferred by Stokes–parameter analysis in section 6.3.5, and the interannual variability is investigated in section 6.3.6. In section 6.3.7 these new results are brought together, and the new information they provide on the characteristics of gravity waves in this region is discussed. The major findings are succintly summarized in section 6.3.8.

6.3.2 Data

The data used hereafter were obtained from meteorological rocketsonde experiments [see, e.g., *Kays and Olsen*, 1967], and comprise a slightly extended version of the data base used in earlier studies by *Hirota* [1984] and *Hirota and Niki* [1985]. These data provide *in situ* measurements of atmospheric zonal wind U, meridional wind V, and temperature T, at $1km$ intervals between $20km$ and $60km$ in altitude. A decade of data from 1977 to 1987 was available from 15 different sites, most of which were concentrated in and around North America (see Figure 70). The number of launches in each month of every year is plotted in Figure 71. The characteristics vary greatly from site to site, but generally the greatest number occurred

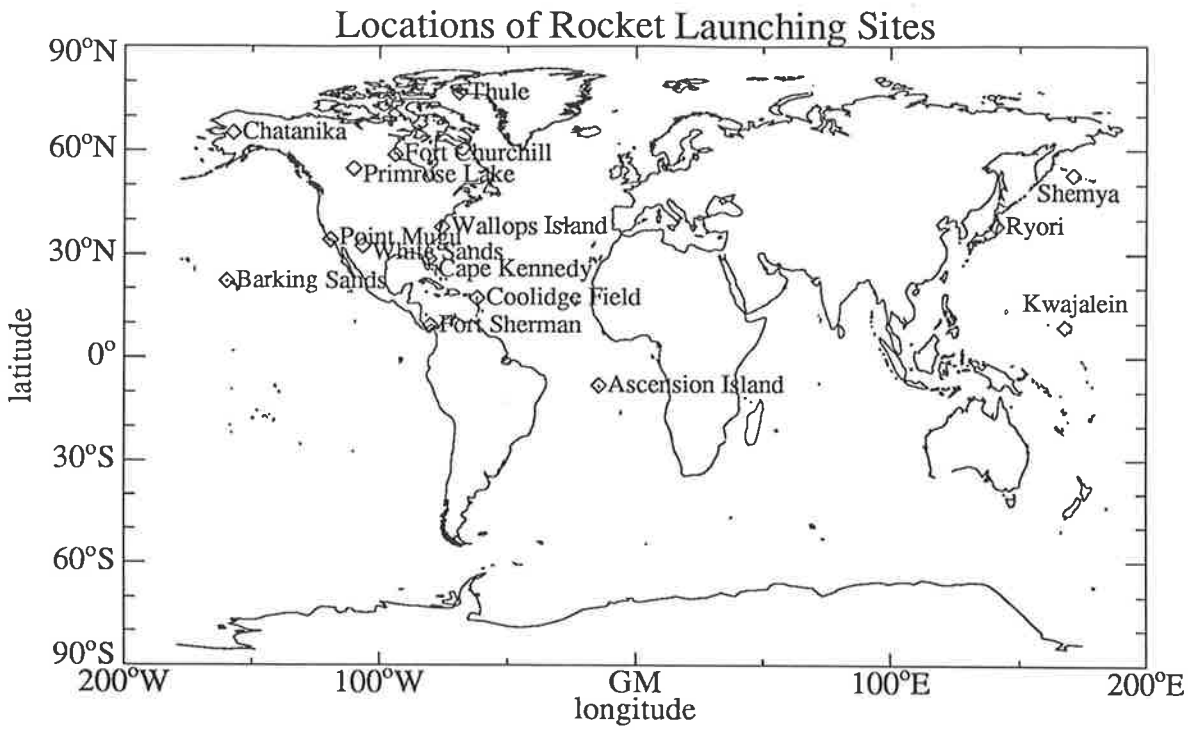

Figure 70: Geographical distribution of the rocket launching sites from where the data used hereafter were obtained.

between 1977 and 1981, with very few occurring after 1985. Apart from several of the high–latitude sites, the mean seasonal coverage of these data, shown in Figure 72, is fairly uniform. The observations, however, are heavily weighted towards certain times of the day, as shown in Figure 73.

Wavelike oscillations superimposed on the background flow are frequently observed in the data obtained from rocket soundings at these heights [*Newell et al.*, 1966; *Miller et al.*, 1968; *Hirota*, 1984; *Hirota and Niki*, 1985; *Hass and Meyer*, 1987; *Eckermann and Vincent*, 1989]. A typical example is shown in Figure 74. To isolate these fluctuations, the following scheme was adopted.

Firstly, if more than 20% of the data in any given profile was missing, it was rejected. The percentage of the original data which remained after such discrimination is given in Table 2. After any limited missing data in an accepted profile were interpolated using a cubic spline fit, a least–squares cubic polynomial was fitted to the profile, which accurately defined the instantaneous background structure (see Figure 74). The prevailing wind and temperatures were fitted in this manner, rather than calculating and subtracting climatological means, because there can be considerable interannual variability in this background structure due to varying planetary–wave amplitudes and sudden stratospheric warmings [*Labitzke*, 1981]. The fitted prevailing structure was then subtracted from the original profile, leaving only the fluctuations. After removing any small residual means that might exist, the data were numerically Fourier transformed, and stored for later analysis.

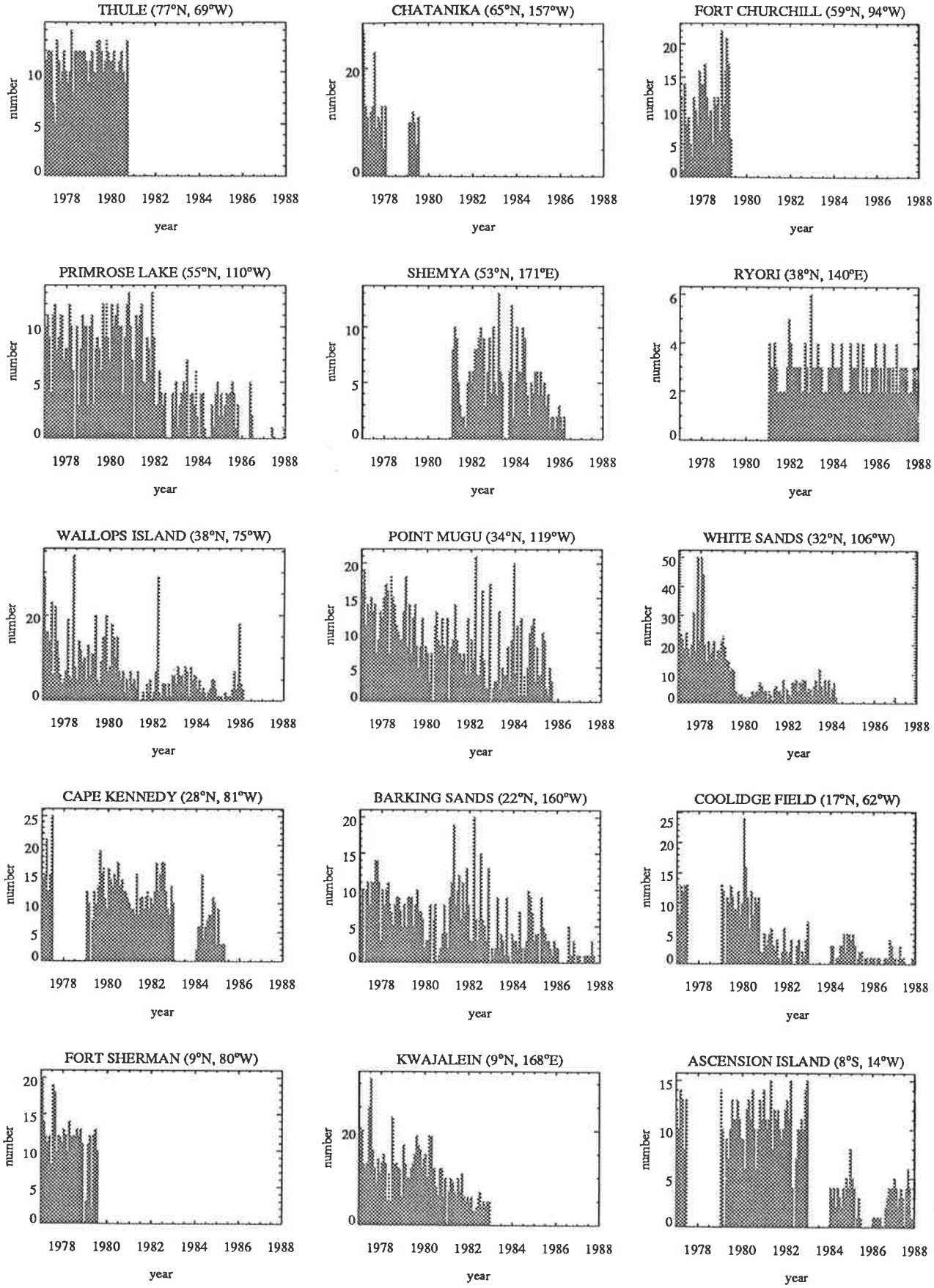

Figure 71: Histograms of the number of rocket launches in each month from 1977 to 1987 at all 15 sites.

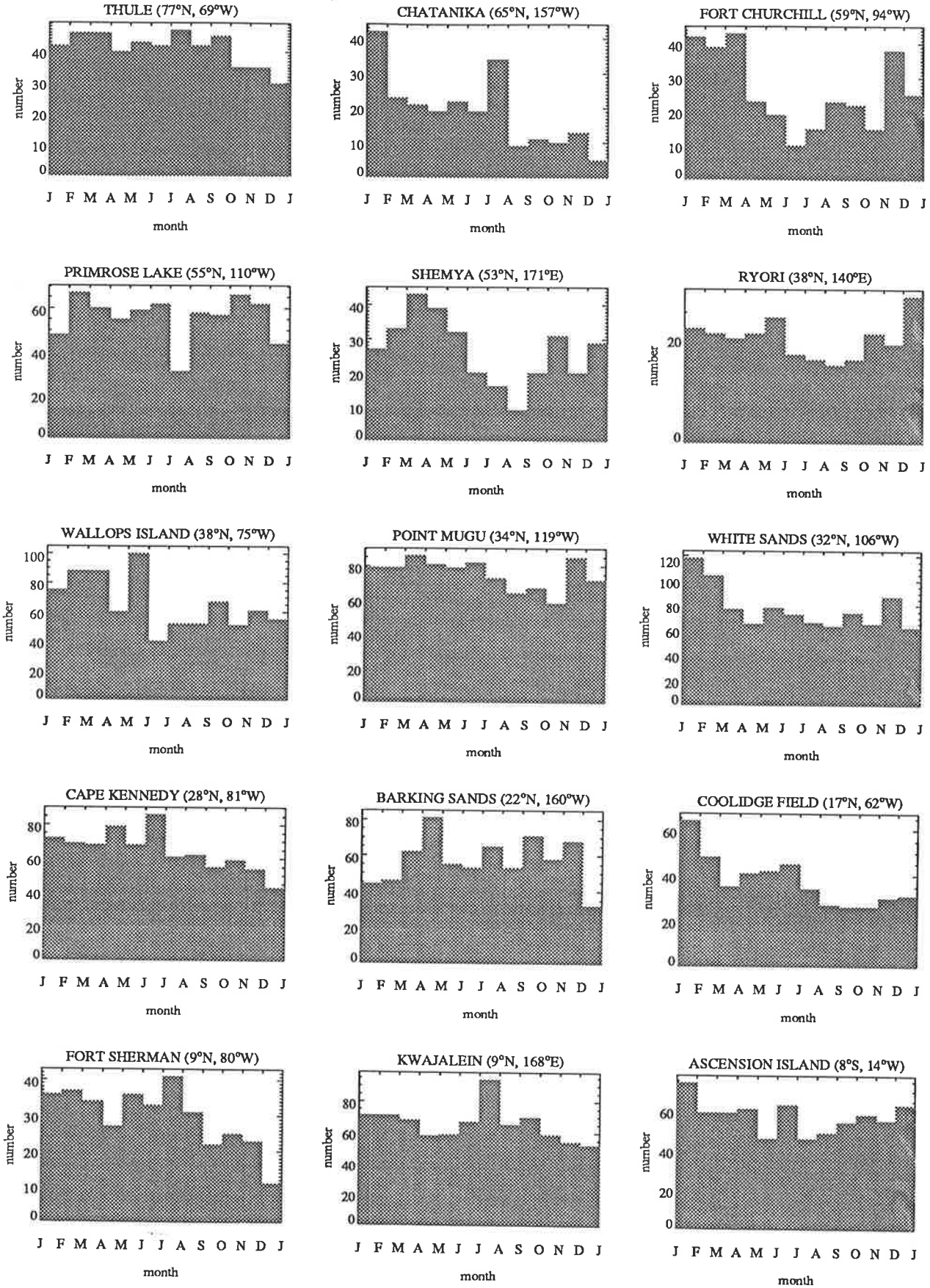

Figure 72: Histograms of the total number of rocket launches within each month at all 15 sites.

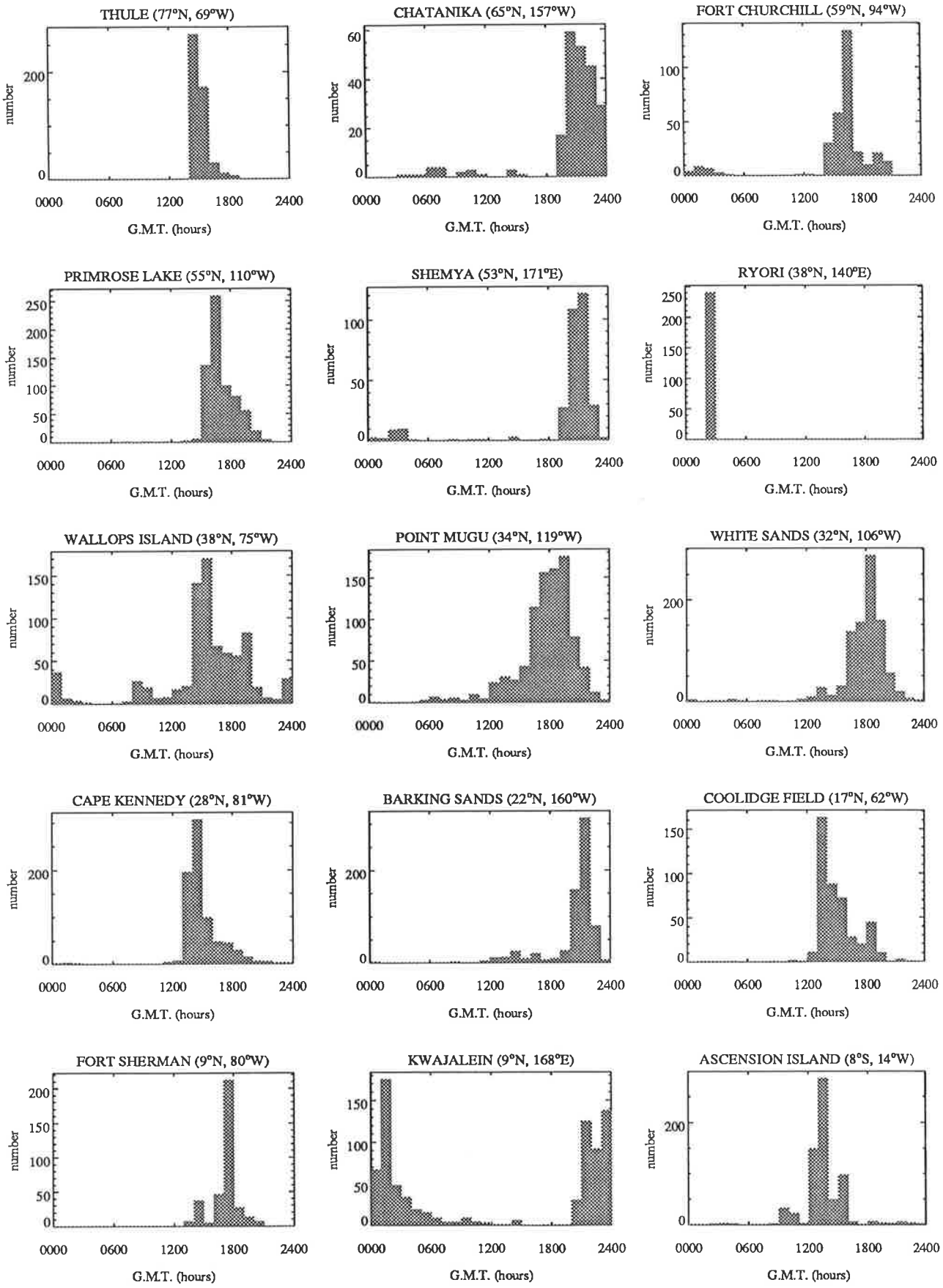

Figure 73: Histograms of the total number of rocket launches as a function of the time of day. The local time has been converted to Greenwich Mean Time (G.M.T.) at all 15 sites.

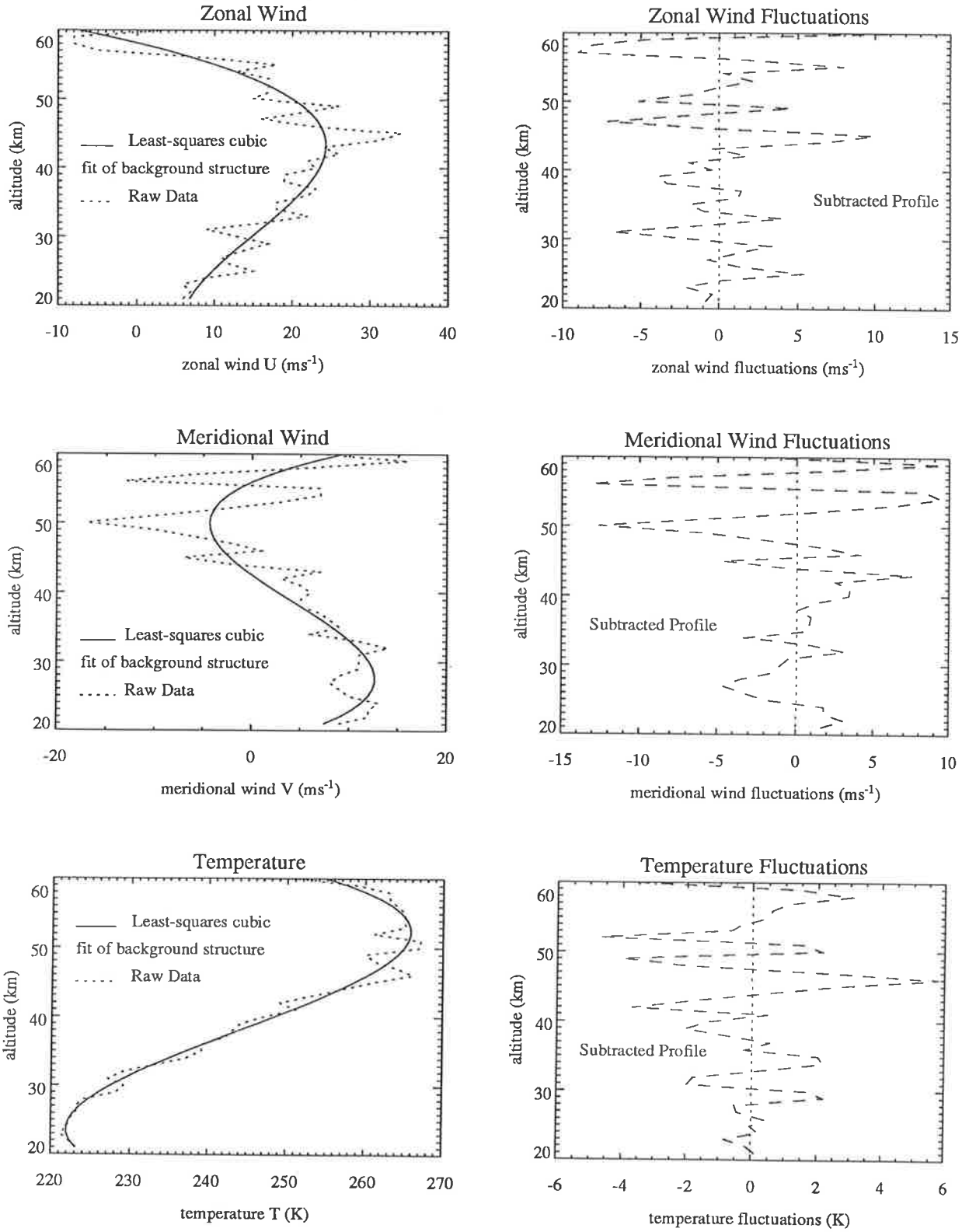

Figure 74: Dotted curves on the left show raw data taken over Thule (77°N, 69°W) on 16th. September 1977, at 14:47 GMT. The solid curves are least–squares cubic polynomial fits to the data, which were used to subtract out the background structure. The fluctuations remaining after such subtraction, followed by removal of the lowest two wavenumber harmonics, are shown in the corresponding plots on the right.

SITE	Horizontal Velocity	Temperature
Thule	87.0% (430 out of 494)	82.2% (406 out of 494)
Chatanika	90.3% (205 out of 227)	77.5% (176 out of 227)
Fort Churchill	88.6% (279 out of 315)	74.6% (235 out of 315)
Primrose Lake	90.2% (604 out of 670)	80.7% (541 out of 670)
Shemya	35.9% (115 out of 320)	27.8% (89 out of 320)
Ryori	92.5% (223 out of 241)	91.7% (221 out of 241)
Wallops Island	71.4% (564 out of 790)	61.3% (484 out of 790)
Point Mugu	73.4% (665 out of 906)	63.5% (575 out of 906)
White Sands	70.4% (626 out of 889)	55.2% (491 out of 889)
Cape Kennedy	80.1% (622 out of 777)	70.7% (549 out of 777)
Barking Sands	68.8% (474 out of 689)	57.8% (398 out of 689)
Coolidge Field	87.1% (392 out of 450)	79.3% (357 out of 450)
Fort Sherman	97.5% (348 out of 357)	79.0% (282 out of 357)
Kwajalein	99.2% (783 out of 789)	93.0% (734 out of 789)
Ascension Island	90.4% (622 out of 688)	88.4% (608 out of 688)

Table 2: The amount of the original raw data accepted at each site after rejection of profiles with more than 20% of the points missing.

The Fourier representation of the data was stored because one can then study various vertical wavelength bands by simply retransforming these data, after suitable band–pass filtering, in each case. In particular, large vertical–wavelength fluctuations due to planetary waves and tides need to removed to isolate the gravity wave contribution [*Hirota*, 1984], yet it is not immediately clear what range of wavelengths needs to be filtered out to achieve this. Storing the Fourier transform enables one to conveniently test various high–pass filters. After some experimentation, it was decided to remove the three largest harmonics, leaving a high–passed vertical wavelength band of $\sim$2–10km, as used by *Hirota* [1984]. This better ensured that tides and planetary waves were removed from the data, and allowed results within two height ranges (20–40km and 40–60km) to be averaged over at least two wavenumber cycles, thus improving the reliability of the averages.

6.3.3 Mean Seasonal Variations in Wave Activity

Hirota [1984] investigated seasonal variations of the gravity wave activity evident in rocket data by calculating the intensity of the fluctuations in various atmospheric variables X over the height range $z_1 < z < z_2$ using the following height–integrated formula

$$\bar{X}^2_{z_1 z_2} = \frac{1}{z_2 - z_1} \int_{z_1}^{z_2} \left(\frac{d^2 X}{dz^2} \right)^2 dz \qquad (72)$$

Results are reproduced in Figure 75 for the horizontal velocity fluctuations $(u_{zz})_{rms}$. A pronounced annual cycle at high latitudes is evident, with a winter maximum, confirming earlier tentative findings

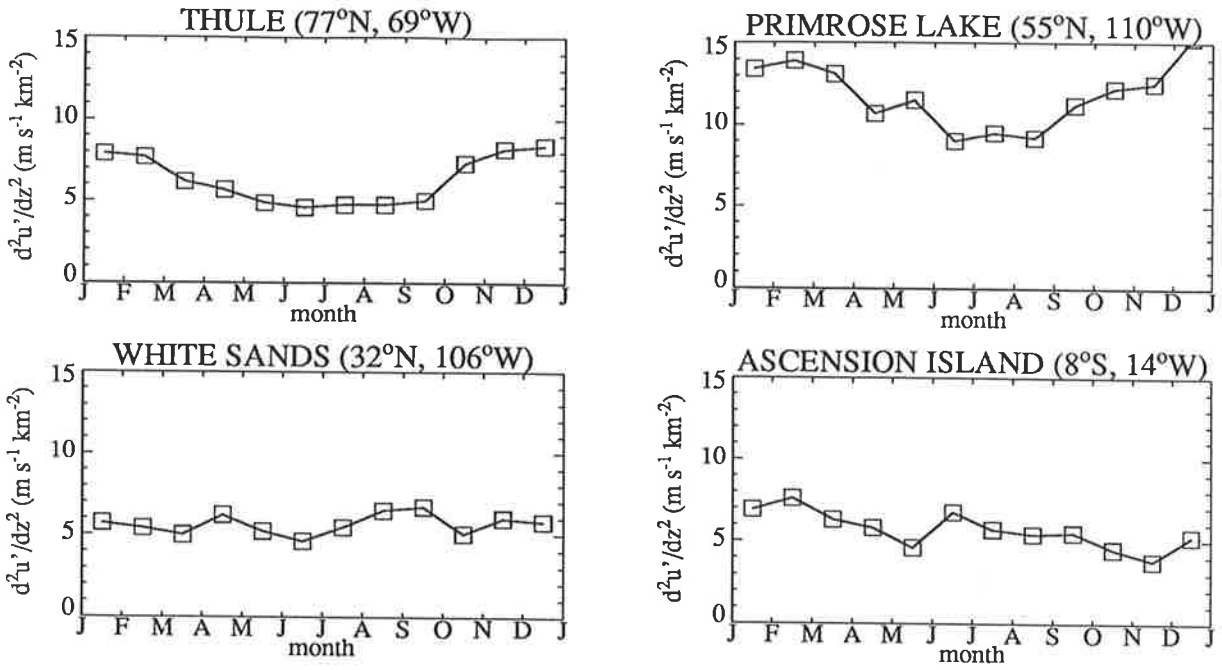

Figure 75: Seasonal variations of r.m.s. gravity wave activity $(u_{zz})_{rms}$ between 20 and $65km$ altitude at four selected launch sites (after *Hirota* [1984]).

[see, e.g., *Theon et al.*, 1967]. On progressing equatorward, the annual cycle attenuates, and a weak semiannual cycle becomes apparent.

Since *Hirota's* study, however, the theory of atmospheric gravity waves has advanced significantly. It is now clear that gravity wave amplitudes are limited by saturation processes in the middle atmosphere [see, e.g., *Fritts*, 1984, 1989], and this has led to the development of model vertical wavenumber spectra produced by both saturated and unsaturated gravity waves, as discussed in some depth in section 3.3.2. The model vertical wavenumber power spectra of horizontal winds and temperature are, respectively [*Smith et al.*, 1987; *Fritts et al.*, 1988],

$$F_u(m) = \frac{N^2}{6m_*^3} \frac{1}{[1+(m/m_*)^3]}, \tag{73}$$

$$F_{\hat{T}}(m) = \frac{N^4}{10g^2m_*^3} \frac{1}{[1+(m/m_*)^3]}, \tag{74}$$

where

m is the vertical wavenumber,

m_* is the "turnover wavenumber", which varies with height according to (31),

$\hat{T}' = T'/T_0$ is the relative temperature fluctuation,

T_0 is the background temperature,

$F_u(m)$ is the spectrum of horizontal velocities, and

$F_{\hat{T}}(m)$ is the spectrum of relative temperature.

$F_u(m)$ is plotted in Figure 33 in section 3.3.2. Recall from this section that waves which have wavenumbers greater than m_* are saturated and produce an m^{-3} spectrum, whereas waves with wavenumbers less than m_* are unsaturated, produce a flat spectrum, and grow in amplitude approximately as $e^{z/2H_\rho}$, where H_ρ is the density scale height.

Considering the horizontal velocity fluctuations u', we see that *Hirota's* measure of gravity wave activity (72) gives

$$\begin{aligned} u_{zz}^2 &= \frac{1}{z_2 - z_1} \int_{z_1=20km}^{z_2=65km} \left(\frac{d^2u'}{dz^2}\right)^2 dz \\ &= \frac{1}{z_2 - z_1} \int_{z_1}^{z_2} \left(m^2 u'(z)\right)^2 dz \\ &= \frac{1}{z_2 - z_1} \int_{z_1}^{z_2} \left(\int_{m_1}^{m_2} m^4 F_u(m,z) dm\right) dz \end{aligned} \tag{75}$$

Expression (75) results from the fact that the gravity–wave horizontal velocity variance is given by integrating the model power spectrum $F_u(m,z)$. The ranges m_1 and m_2 correspond to the limits of the observational wavenumber window, which, in *Hirota's* observations, were $2\pi(10km)^{-1}$ and $2\pi(2km)^{-1}$ respectively [*Hirota*, 1984].

To proceed, we shall assume that the vertical wavenumber m is independent of z. For a given wave this is incorrect, since m depends on the height variation of the background wind $\bar{U}(z)$, which can be considerable at these altitudes. However, the spectrum (73) was presented by *Smith et al.* [1987] as being insensitive to background wind variations, and no height variation in m was incorporated. Therefore, m is certainly independent of z in the mathematical sense as it is defined in equation (73), so that the integration order in (75) can be interchanged, thus giving

$$\begin{aligned} u_{zz}^2 &= \int_{m_1}^{m_2} m^4 \left(\int_{z_1}^{z_2} F_u(m,z) dz\right) dm, \\ &= \int_{m_1}^{m_2} m^4 \mathcal{F}_u(m) dm, \end{aligned} \tag{76}$$

where the "height–averaged" spectrum $\mathcal{F}_u(m)$ is given by the expression

$$\mathcal{F}_u(m) = \frac{N^2 H_E}{9(z_2 - z_1)m^3} \ln\left(\frac{1 + G(z_2)\mu^3}{1 + G(z_1)\mu^3}\right), \tag{77}$$

where

$G(z) = e^{3(z-z_1)/2H_E}$, and $\mu = m/m_*(z_1)$.

Therefore we obtain the useful result that u_{zz}^2, the measure of wave activity used by *Hirota* [1984], is given by the area beneath its height–averaged spectrum $\mathcal{F}_{u_{zz}}(m) = m^4 \mathcal{F}_u(m)$.

To plot this height-averaged spectrum (77), the parameters $m_*(z_1)$ and H_E must be determined. A technique for doing this is outlined in Appendix D, and a representative calculation therein, based on

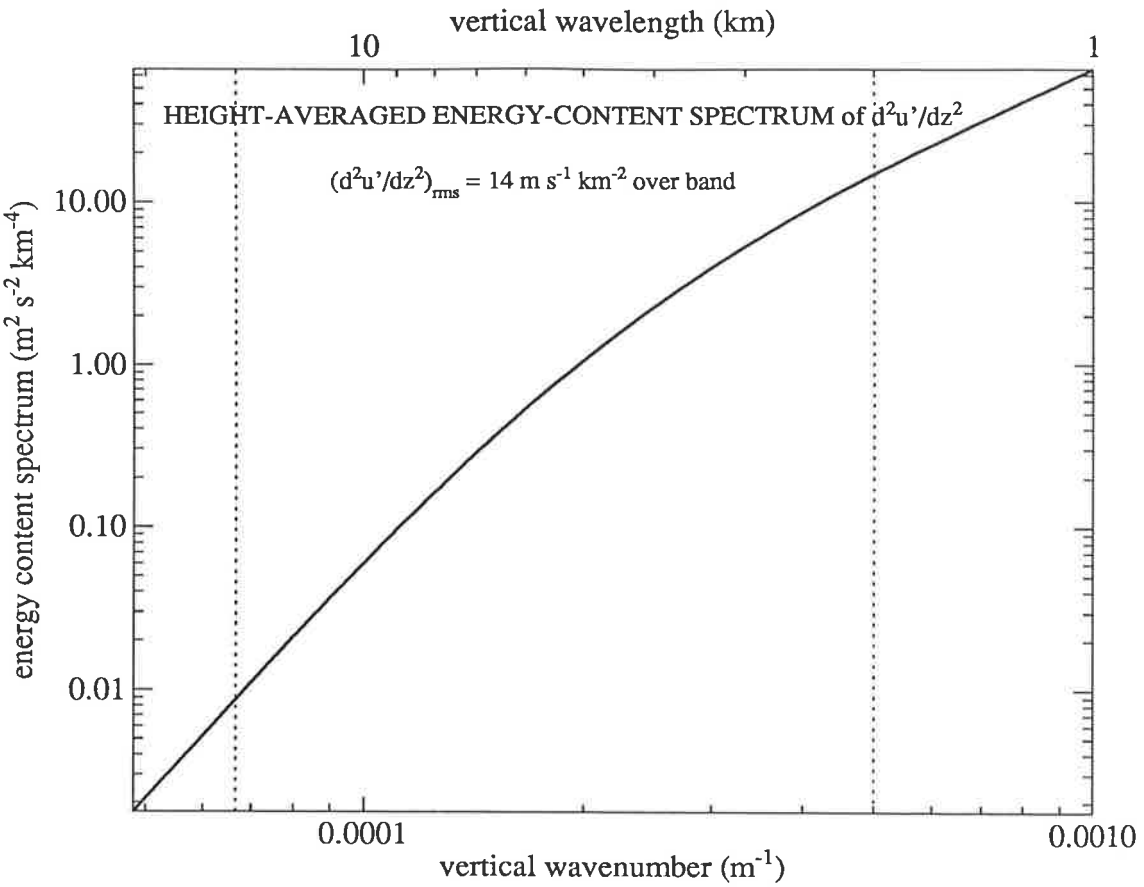

Figure 76: A plot of the "height–averaged" gravity wave vertical wavenumber spectrum of d^2u'/dz^2, based on previous measurements by *Hirota and Niki* [1985] in the 30–60km height range. Dotted lines indicate the wavenumber band covered in this study and the study of *Hirota and Niki* [1985], and the indicated r.m.s. value of d^2u'/dz^2 was obtained by integrating over this band, and agrees well with measured values in Figure 75, even though the wavenumber band in Figure 75 is narrower.

previous calculations of gravity wave amplitudes in the 30–60km altitude range by *Hirota and Niki* [1985], gives values of $m_*(z_1 = 30km) \approx 2\pi(2.7km)^{-1}$ and $H_E \approx 17km$. The resulting spectrum is plotted in its energy–content form $m\mathcal{F}_{u_{zz}}(m)$ in Figure 76. Since u_{zz}^2 is given by the area beneath this curve, one can see from Figure 76 that the majority of this variance is produced by the largest wavenumbers (smallest vertical wavelengths), which are *saturated* (i.e. $m > m_*$). Therefore the variations in Figure 75 are probably more indicative of seasonal changes in the local wave–saturation environment rather than changes in unsaturated gravity wave activity.

In light of this possibility, seasonal variations in $\overline{u'^2} + \overline{v'^2}$ and $\overline{\hat{T}'^2}$ were computed, as these variances should be less affected by saturated wave motions, according to (73) and (74) (see Figure 33).

Horizontal Velocities

The seasonal variations in $\overline{u'^2} + \overline{v'^2}$ at all 15 sites are plotted in Figure 77. The first 3 wavenumber harmonics over the 20–60km height range were removed, leaving fluctuations within about a 2–10km

vertical–wavelength band. Dashed curves show the results in the 20–40km height range and solid curves show results in the 40–60km range. Successive plots decrease in station latitude down the page and from left to right.

It is immediately clear that $\overline{u'^2} + \overline{v'^2}$ increases with altitude, in line with theoretical expectations that the unsaturated wave variance should increase approximately as e^{z/H_ρ}. The form of these height variations in the wave amplitudes have been investigated by *Hirota and Niki* [1985], and will not be repeated here.

For convenience, we now define four arbitrary latitude bands into which we shall classify the results; "high latitudes" ($\theta = 50°N$–$80°N$), "mid–latitudes" ($\theta = 25°N$–$50°N$), "low latitudes" ($\theta = 10°N$–$25°N$), and "equatorial latitudes" ($10°N$–$10°S$).

At the five "high–latitude" sites, a strong annual variation in $\overline{u'^2} + \overline{v'^2}$ is evident in both altitude ranges and at all sites, producing peaks in winter and a summer minimum. While the normalized trends at all five sites are similar, the variances at Primrose Lake are almost twice those at either Thule or Fort Churchill. Variations at Chatanika and Shemya are more variable and less reliable, due to low amounts of data from these sites.

Mean seasonal cycles at the four North American stations at "mid–latitudes" (25°–50°N) all show similar variations. In the 20–40km range, the variations are quasi–annual, with a winter maximum. However, a weak secondary maximum occurs at each station around August; indeed, the two peaks are of similar magnitude at Cape Kennedy, producing a more semiannual variation at low levels. Another small equinoctial peak around April arises at three of the four stations (Cape Kennedy is the exception). At the upper heights (40–60km), however, these variations differ. The wintertime peak is supressed somewhat, and a large burst in variance, which peaks during August, dominates the variations. The small peak in April observed at lower levels also occurs at 40–60km at White Sands and Point Mugu, whereas at Cape Kennedy and Wallops Island it is more of a plateau. At all four sites, there is also a deep minimum in wave activity around October, and a June minimum also occurs, most noticeably at Wallops Island. Note once again that while the normalized trends at Cape Kennedy, White Sands, and Point Mugu are all very similar, the absolute variances differ markedly from site to site. At Wallops Island, however, the normalized variations also differ somewhat to those at the other three sites, in that the August maximum is not as large, and the winter maximum is less supressed. These results contrast with the $(u_{zz})_{rms}$ variations from White Sands calculated by *Hirota* [1984], and reproduced in Figure 75, where one finds small maxima in April and September; here that former maximum is very weak, whereas the latter maximum is a very prominent feature and peaks earlier (around August).

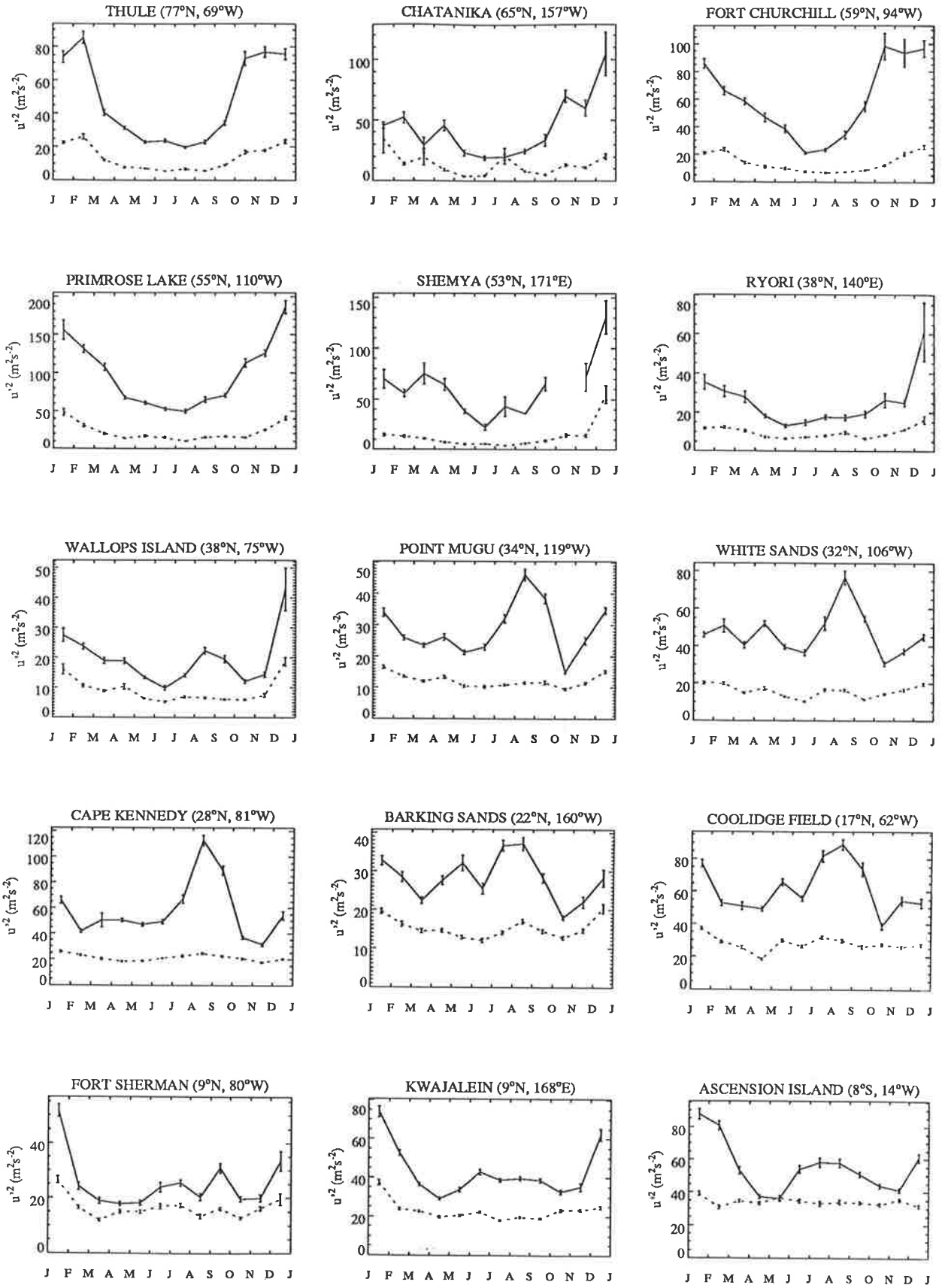

Figure 77: Mean seasonal variations in the fluctuating horizontal velocity variance within two altitude ranges of 20–40km (dashed curve) and 40–60km (solid curve). Error bars indicate standard errors of the mean. Note that the y–axis scales vary from plot to plot.

At Ryori, the only non–American "mid–latitude" station, the variations from 20–40km at this displaced longitude are similar to those at the North–American stations, but in the 40–60km range the cycle is strongly annual, peaking in winter, and no maxima occur at the equinoxes.

The two stations within the low–latitude interval (Barking Sands and Coolidge Field) are separated by $\sim 100°$ longitude, yet the mean seasonal variations of the gravity wave variances over these two sites are very similar at 40–60km. Here the variations are terannual, with peaks occurring around July–August, May, and January. Minima in activity in October (a deep minimum) and June are also observed at both sites, and are similar to the mid–latitude results. The high–altitude peak in May is the main difference in the low– and mid–latitude variations from 40–60km. In the 20–40km range, the two stations exhibit different character. The variations at Barking Sands are seminannual and similar to those at Cape Kennedy and White Sands, whereas the Coolidge Field data are somewhat acyclic, except for a minimum in April and a small maximum in January. Finally, note again the large discrepansies in the mean variances at each site.

The three stations within the "equatorial" latitude band are widely spaced in longitude, yet much of the upper level structure amongst the three is similar. Firstly, at the upper heights, there is a strong peak during January, and a broader secondary peak is centered around August (this is distorted somewhat at Fort Sherman). There is also strong dimunition of wave variance at upper levels during April–May and October–November, especially at Ascension Island. From 20–40km, the variations over each site differ. At Fort Sherman, the lower–level variations are similar to those at upper heights, whereas at Kwajalein the variation is weakly annual, with a January maximum. At Ascension Island, the amplitudes from 20–40km are acyclic with season.

Temperature Fluctuations

The seasonal variations in the variance of the relative temperature fluctuations $\overline{\hat{T}'^2} = \overline{(T'/T_0)^2}$ at all 15 sites are plotted in Figure 78. Again, the first 3 wavenumber harmonics over the 20–60km height range were removed, producing a 2–10km vertical–wavelength band in the data.

Is is immediately apparent that $\overline{\hat{T}'^2}$ does not increase with altitude as was observed for $\overline{u'^2} + \overline{v'^2}$ in Figure 77. Additionally, seasonal variations of $\overline{\hat{T}'^2}$ often differ from the same site variations in the horizontal velocity variance in Figure 77. These results are not anticipated theoretically, as the model vertical wavenumber spectra $F_u(m)$ and $F_{\hat{T}}(m)$ have the same shape and height dependence, and thus their variances should be strongly coupled. These findings therefore require some evaluation.

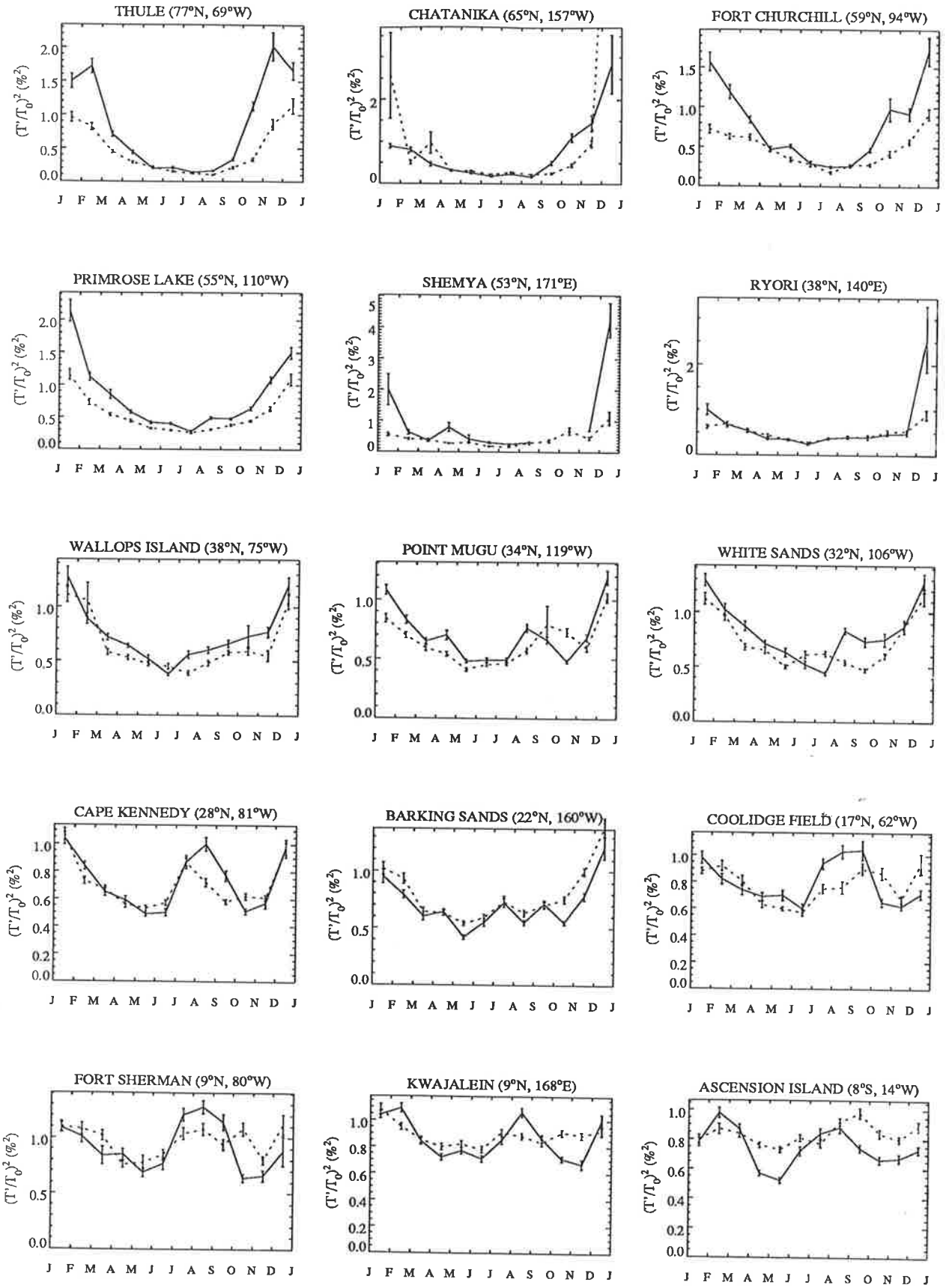

Figure 78: Mean seasonal variations in the relative temperature variance within two altitude ranges of 20–40km (dashed curve) and 40–60km (solid curve). Error bars indicate standard errors of the mean. The y–axis scales vary from plot to plot.

HEIGHT	σ_T^2 (K^2)	T_0	$\sigma_T^2/(T_0)^2$ $(\%)^2$
$35km$	0.70	$240K$	0.04
$40km$	1.00	$250K$	0.16
$45km$	1.34	$260K$	0.20
$50km$	1.73	$270K$	0.24
$55km$	1.65	$260K$	0.24
$60km$	5.55	$250K$	0.89

Table 3: Table of the measurement errors σ_T^2 in rocketsonde temperatures, as inferred by *Schmidlin* [1981]. Background temperatures T_0 were computed from the Wallops Island rocket measurements analyzed here, and are annual means (to the nearest $10K$).

Observe from Figure 78 that typical $\hat{T}'_{rms}$ values are ~1%. Assuming a typical background temperature of $250K$, this translates into an r.m.s. absolute temperature perturbation of ~$2.5K$. The raw temperature data were digitized to the nearest degree Kelvin, so that these perturbations are only marginally larger than the digitized increments in the temperature data. The horizontal winds were digitized to the nearest $m\ s^{-1}$, yet the typical r.m.s. wind perturbation amplitudes of ~5–$10m\ s^{-1}$ seen in Figure 77 are much larger than the digitization increment in this case. This raises the possibility that these small measured temperature perturbations may be unreliable.

Digitizing the temperature data to $1K$ introduces a noise variance $\overline{T'^2_{dig}}$ of $1/12K^2$ [*Kristensen and Kirkegaard*, 1987] (see also Appendix B), which is too small to significantly affect the $\overline{\hat{T}'^2}$ variations evident in Figure 78. However, if the intrinsic accuracy of the original temperature measurements is only around 1%, the variations in Figure 78 may be due to random measurement errors. *Schmidlin* [1981] assessed the accuracy of temperatures measured by rocketsondes at Wallops Island by observing the repeatability of temperatures obtained from successive launches separated by less than one hour. He found that the discrepansies increased as the time between successive launches increased, due to natural atmospheric variability. He then used regression techniques to extrapolate the measured deviations for various inter–measurement times back to an error value for a zero time difference, σ_T^2, which he took to be a measure of the intrinsic accuracy of rocketsonde temperature measurements. Using *Schmidlin's* results and mean temperatures computed from the Wallops Island data, measurement error noise variances at various heights are estimated in Table 3. These values are typically around 10–30% of the values in Figure 78, and so, while not an insignificant contribution, they nevertheless appear unable to account for these fluctuations. Spectral analysis of these fluctuations in the next section confirms that neither measurement errors nor digitization noise are consistent with this variance.

The final possibility is that this variance may result from processes other than gravity waves. For example, analysis of winter temperature perturbations at Chatanika, Shemya, and Ryori revealed some anomolously large values which strongly bias the results, as seen in Figure 78. Inspection of the raw data

revealed that these values were produced by isolated profiles where large impulsive temperature bursts occurred, and which were of small enough vertical scale to survive high–pass filtering. Such sudden stratospheric warmings are known to occur commonly during winter, and may enhance the observed winter variability. However, such impulses should approximate a delta–function, which produce flat spectra, yet later spectral analysis does not reveal a white, noiselike spectrum.

Hence, one is drawn to the conclusion that these temperature fluctuations are indeed produced mostly by gravity waves. For a wave of of intrinsic frequency ω (such that $\omega \ll N$), the following polarization relation holds approximately for a zonally propagating wave

$$\hat{T}' \approx \frac{N}{g} \left(1 - (f/\omega)^2\right)^{1/2} u'. \tag{78}$$

For $N \approx 0.02 rad\ s^{-1}$, $f/\omega \sim 0$, and $g \approx 10 m\ s^{-2}$, then a value of $u' \approx 5 m\ s^{-1}$, which is quite commonly observed in Figure 77, produces a $\hat{T}'$ amplitude of 1%. Therefore, the values in Figure 78 are certainly of the order of those anticipated for gravity waves based on the earlier measurements of the horizontal velocity amplitudes.

There is a clear lack of growth with altitude in the gravity wave temperature perturbations in the mid–, low–, and equatorial latitude belts, which is a surprising finding. Only at high altitudes is an increase in $\overline{\hat{T}'^2}$ with altitude evident. Here there are strong annual variations which peak in winter, as previously observed for $\overline{u'^2} + \overline{v'^2}$ in Figure 77. Summer values are very small at very high latitudes, and appear to approach the predicted values of the noise variance due to measurement errors as listed in Table 3.

At the mid–latitude sites the annual cycle in $\overline{\hat{T}'^2}$ persists more strongly than it did in the $\overline{u'^2} + \overline{v'^2}$ results, where a prominent peak also occurred in August. Such a peak is weakly evident at Point Mugu and White Sands, but is quite apparent at Cape Kennedy.

The two low–latitude sites of Barking Sands and Coolidge Field both exhibit annual variations, but at Coolidge Field the August peak occurs much more strongly. There is only a suggestion of the subsidiary peak in May observed in $\overline{u'^2} + \overline{v'^2}$ at both sites.

At the equatorial sites, the variations are qualitatively similar to those detected in the horizontal velocities. There is a peak in January and a broad peak in August, with sharp minima occurring around April and October. At Ascension Island, the mean $\overline{\hat{T}'^2}$ values in the 20–40km height interval actually exceed those between 40 and 60km.

Interpretation of these findings is attempted in subsequent sections.

6.3.4 Vertical Wavenumber Spectra

Some insight into the processes which produce these fluctations can be gained from analyzing the spectra of the fluctuations. However, it is important to realize that the spectral characteristics of the data are appreciably distorted during the measurement process.

There are a number of effects which alter the spectral characteristics of the horizontal wind measurements. Due to the exponential decrease in density with altitude, the response of the falling sensor to wind fluctuations is determined by the amplitude and vertical wavelength of the fluctuation, and this response also varies with height [*Hyson*, 1968; *Hass and Meyer*, 1987; *Eckermann and Vincent*, 1989]; the general effect is to attenuate the smaller wavelengths relative to the larger wavelengths (i.e. the spectrum is made artificially "redder") [*Hass and Meyer*, 1987; *Eckermann and Vincent*, 1989]. Techniques employed in some measurements to reduce the raw data also produce "reddening" of the spectrum [*Miller*, 1969]. Furthermore, white noise is added to the spectrum by digitizing the wind data, although this noise has negligible variance and can be removed because it's spectral characterisitics are easily quantified (see Appendix *B*). Random measurement errors also occur in radar tracking of the sensor motion; these values increase with altitude and vary from system to system, but are generally small [*Hyson*, 1968]. In addition to all these various instrumental effects, the gravity wave spectrum itself varies in shape and intensity with height, so that vertical wavenumber spectra computed over a large altitude range, such as the $40km$ height range employed here, are distorted by the inherent nonstationarity of the motion spectrum itself, and this produces a "bluer" calculated spectrum (see section 3.3.2).

All these effects make in–depth comparisons with the theoretical spectral shapes (73) and (74) impractical. With this in mind, the mean vertical wavenumber spectra of horizontal velocities from four selected stations are shown in Figure 79. The anticlockwise– and clockwise–rotating components of this spectrum are also shown; rather than computing these rotary components directly by Fourier transforming the velocity phasor [see, e.g., *Vincent*, 1984], these components were derived from the so–called Stokes parameters evaluated from the individual u' and v' raw spectra, using formulae developed in Appendix *A*.

In the Northern Hemisphere, clockwise–rotating variance is produced predominately by waves propagating their energy upwards, and the anticlockwise–rotating variance is produced mostly by downward propagating waves, whereas in the Southern Hemisphere the converse is true [*Hirota and Niki*, 1985]. Therefore Figure 79 reveals a nett preference towards upward propagation of wave energy, as has been inferred in a number of other studies [*Thompson*, 1978; *Vincent*, 1984; *Hirota and Niki*, 1985; *Fukao et*

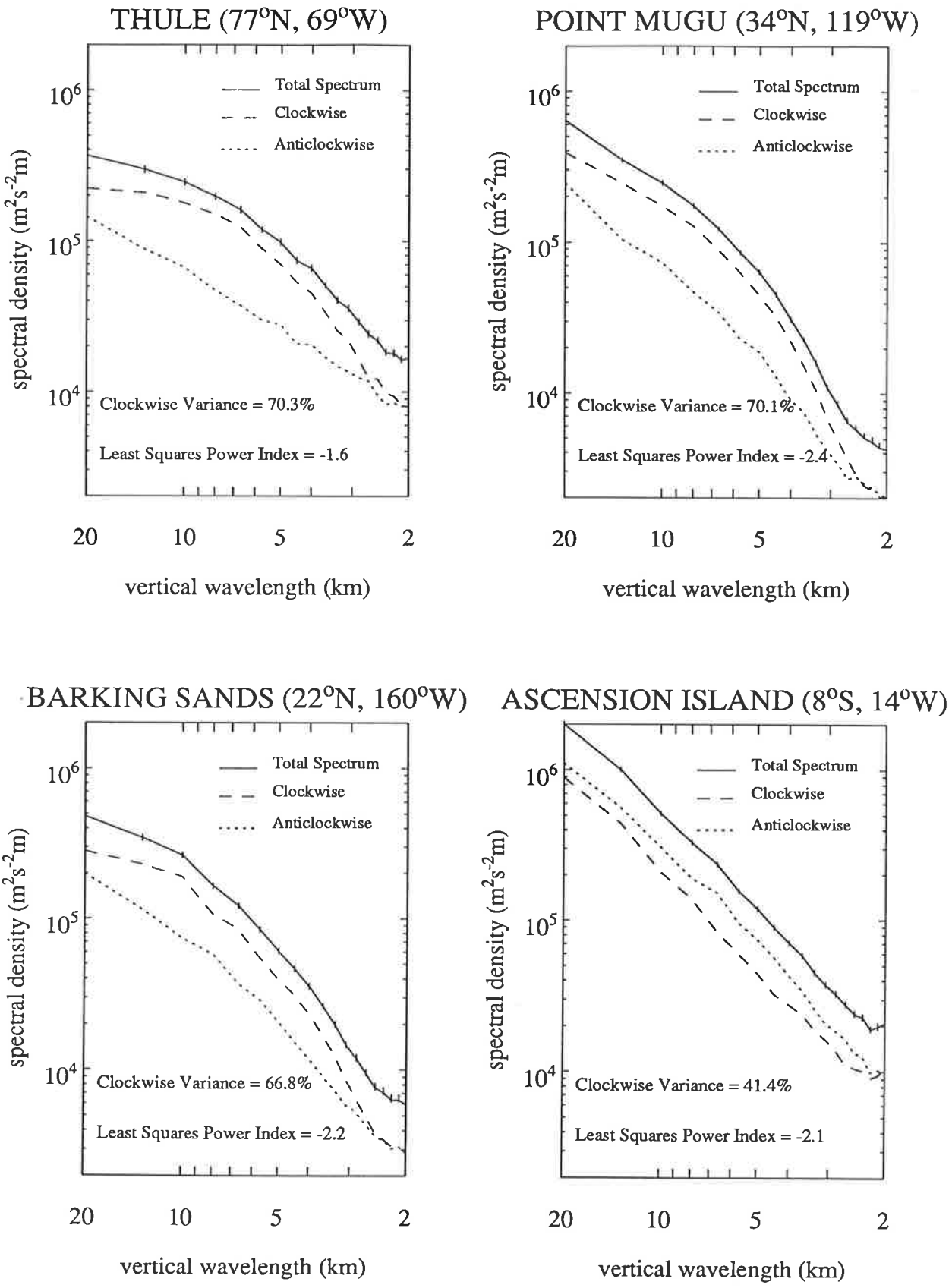

Figure 79: Mean rotary vertical–wavenumber spectra of horizontal velocities computed at four stations over the 20–60km height range. Error bars are standard errors of the mean spectral density at each given wavenumber. The variance under this clockwise–rotating spectrum, expressed as a percentage of the total variance, and a least–squares estimate of the spectral index of the total spectrum, are indicated on each plot.

al., 1985; *Hass and Meyer*, 1987; *Fritts and Chou*, 1987; *Eckermann and Vincent*, 1989].

To investigate these features in greater depth, mean seasonal variations in the ratio of the clockwise–rotating variance (the area beneath the clockwise–rotating spectrum) to the total variance $\overline{u'^2} + \overline{v'^2}$ are plotted as percentages in Figure 80. Complete separation of up– and down–going wave energy into the clockwise and anticlockwise spectra is only possible for a circularly–polarized wave, whereas most of the waves here are elliptically polarized [see, e.g., Figure 1 of *Hirota and Niki*, 1985] and so the partitioning is "blurred" somewhat [*Eckermann and Vincent*, 1989]. Therefore similar ratios were also computed using another independent technique developed by *Hirota and Niki* [1985], where the change in the wind phasor angle at adjacent heights is computed, and the wind profile rotation is classified according to whichever angular change (i.e. clockwise or anticlockwise) is the more common over the 20–60km range.

These two calculation schemes produce different absolute values of the clockwise rotation percentage, but give very similar seasonal variations. At virtually every site, the following features are evident; the values peak at the equinoxes (i.e. around April and September), and attain their minimum values at the soltices, of which the winter minimum is almost always the deeper. This suggests systematic seasonal variations in the percentage of upwardly–propagating wave energy, although ta different interpretation is provided in section 6.3.7. Note that anticlockwise percentages were plotted at Ascension Island because it is in the Southern Hemisphere.

Seasonal variations in least–squares estimates of the power indicies of these spectra are shown in Figure 81. Even though the absolute spectral indices are not directly comparable with (73) and (74), the aforementioned processes which distort the spectral shape do not vary appreciably with season, so that any variations about the mean should be geophysical in origin.

Firstly, we note that the mean spectral indices vary greatly from site to site. The high–latitude data, however, show an annual variation, with winter minima and summer maxima, a trend which is anticorrelated with the annual $\overline{u'^2} + \overline{v'^2}$ cycles in Figure 77. From the theoretical viewpoint, such anticorrelation is expected; in winter when $\overline{u'^2} + \overline{v'^2}$ is large, m_* must be small to accomodate this large variance, which in turn implies that more of the spectrum is saturated, thus producing spectral shapes nearer an m^{-3} shape. In summer, however, when the variances are much smaller, m_* is larger, so that more of the wave field now is unsaturated, and so the spectrum moves more towards the unsaturated flat spectral shape. At the other sites, however, the spectral index variations about the mean are, on the whole, too small to allow identification of systematic trends without there being doubts as to their statistical significance.

Corresponding mean absolute–temperature spectra from the same sites used in Figure 79 are plotted

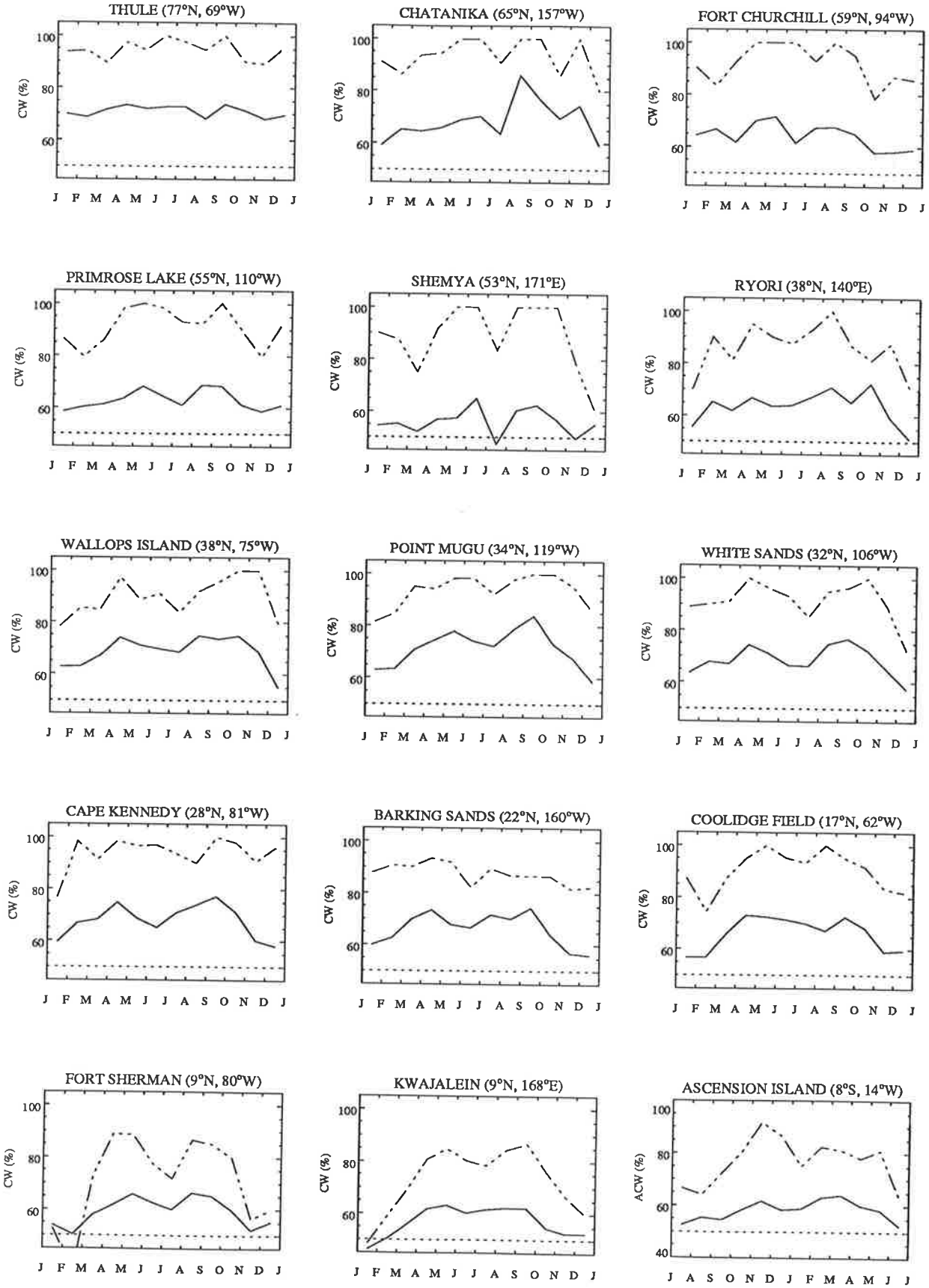

Figure 80: Mean seasonal variations in the percentage of clockwise wind rotations, as computed from the rotary component variances (solid curve) and from direct analysis of wind phasor rotations (broken curve). The Ascension Island results have a different ordering of months, so that seasonal ordering is the same in all plots. Anticlockwise rather than clockwise percentages are plotted at Ascension Island. The dashed lines mark the 50% level.

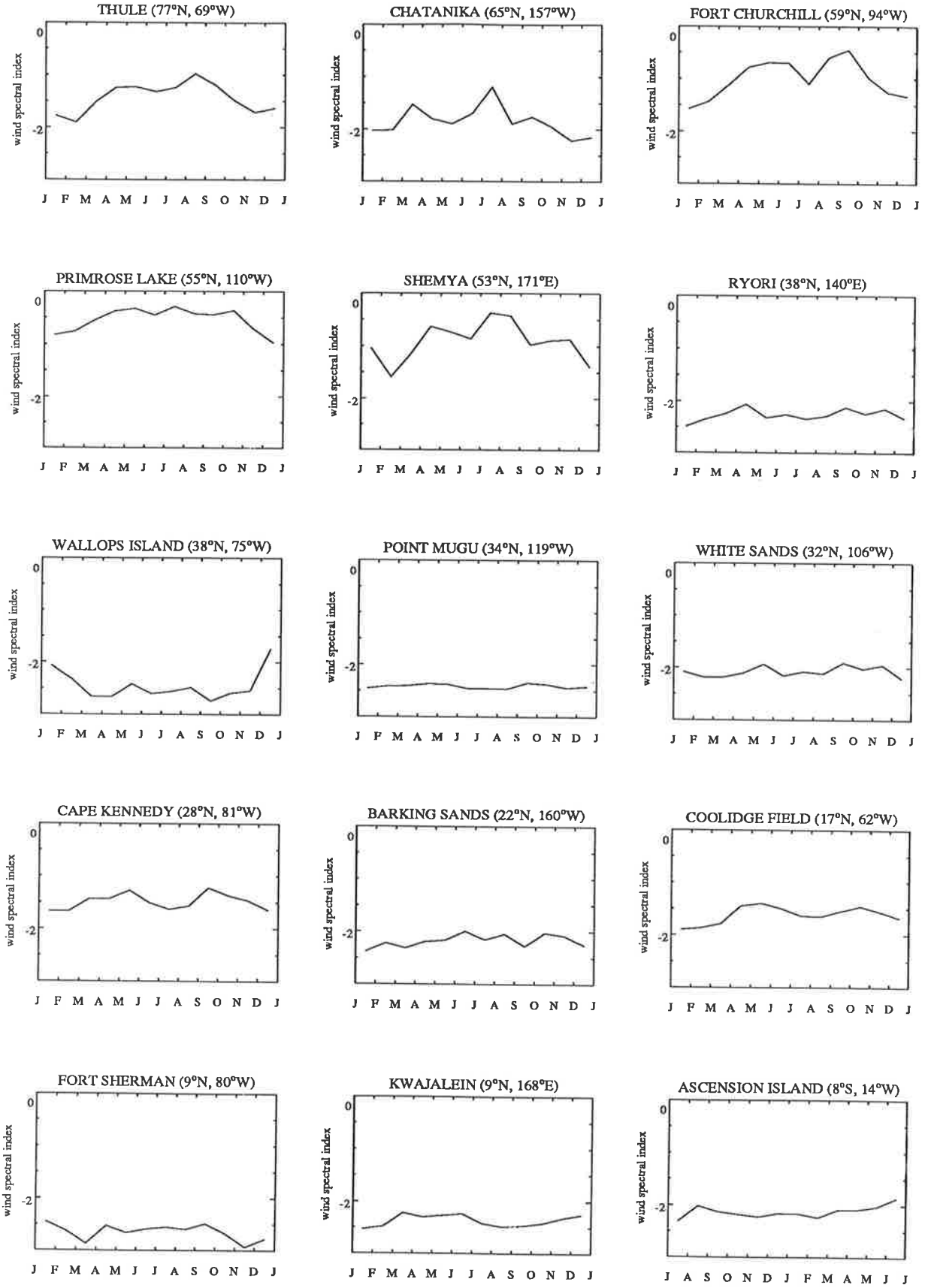

Figure 81: Mean seasonal variations in the spectral indices of the mean vertical wavenumber spectrum of horizontal velocities, as computed from least–squares fitting. Note again that the Ascension Island results have been ordered such that the seasons are similarly located in all plots.

in Figure 82. It seems clear that the temperature fluctuations cannot be due to random measurement errors, as such processes give rise to a white–noise (i.e. flat) spectrum. While some as–yet–unidentified "red noise" contamination cannot be entirely discounted, there is similarity amongst the shapes of these spectra, the horizontal velocity spectra in Figure 79, and the theoretical gravity–wave spectra (73) and (74). When combined with the earlier arguments that the best experimental error estimates appear to be too small to account for these fluctuations (see Table 3), yet the anticipated gravity wave temperature perturbations are of the order of those observed, it again indicates that the gravity–wave hypothesis is more consistent with the observations than other possible explanations.

As gravity waves appear to produce these fluctuating temperatures, the spectrum of relative temperature fluctuations $\hat{T}'$ is the more appropriate spectrum to compare with theory (see equation (74)). Seasonal variations in the spectral indices of these computed spectra are shown in Figure 83. The spectra have less–negative spectral indices than the absolute temperature spectra, whose values were mostly around -2 (see Figure 82). Although the absolute spectral indices here are less–negative on average than the spectral indices of the horizontal velocity spectra, there are similarities amongst the seasonal variations, in particular an annual cycle at high latitudes with winter minima. This was also observed in Figure 81 in the horizontal velocity fluctuations, and, like there, here too it is consistent with an observed annual cycles in $\overline{\hat{T}'^2}$ as governed by the model temperature spectrum (74).

6.3.5 Azimuthal Alignment

Using the horizontal velocity fluctuations, the mean azimuthal alignment of these fluctuations $\bar{\phi}$ over a given height range is given by the formula

$$\bar{\phi} = \frac{1}{2} \arctan \frac{\bar{P}}{\bar{D}} \tag{79}$$

where $\bar{P}$ and $\bar{D}$ are two of the so–called Stokes parameters of the fluctuating horizontal velocity motions over this height range, and can be computed from the horizontal velocity wavenumber spectra [*Eckermann and Vincent*, 1989; see also Appendix *A*]. Because gravity waves oscillate longitudinally in the horizontal plane, this alignment also gives the mean propagation direction of the waves. However, $\bar{\phi}$ gives an azimuth direction that is $\pm 180°$ uncertain, and therefore does not give the absolute sense of wave propagation, hence the nomenclature "alignment".

Performing this analysis on the vertical spatial wave structure is important. The vertical wavelength is a wave parameter which has the same magnitude when measured from the ground or from a frame moving with the background atmosphere, and therefore the distribution of wave energy as a function of

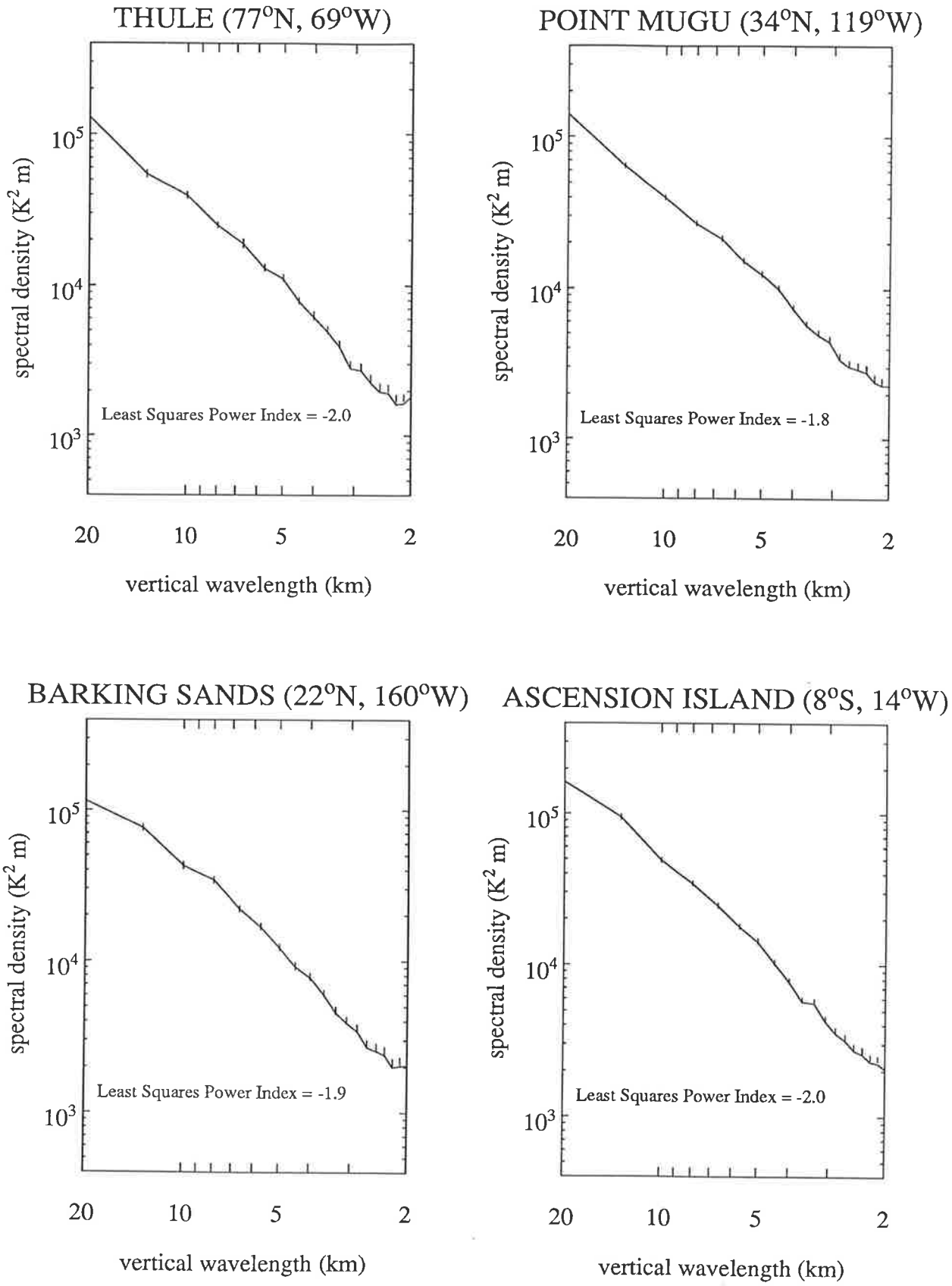

Figure 82: Mean vertical–wavenumber spectra of temperatures, computed at four stations over the 20–60km height range. Error bars are standard errors of the mean spectral density at each given wavenumber. A least–squares estimate of the spectral index is provided with each plot.

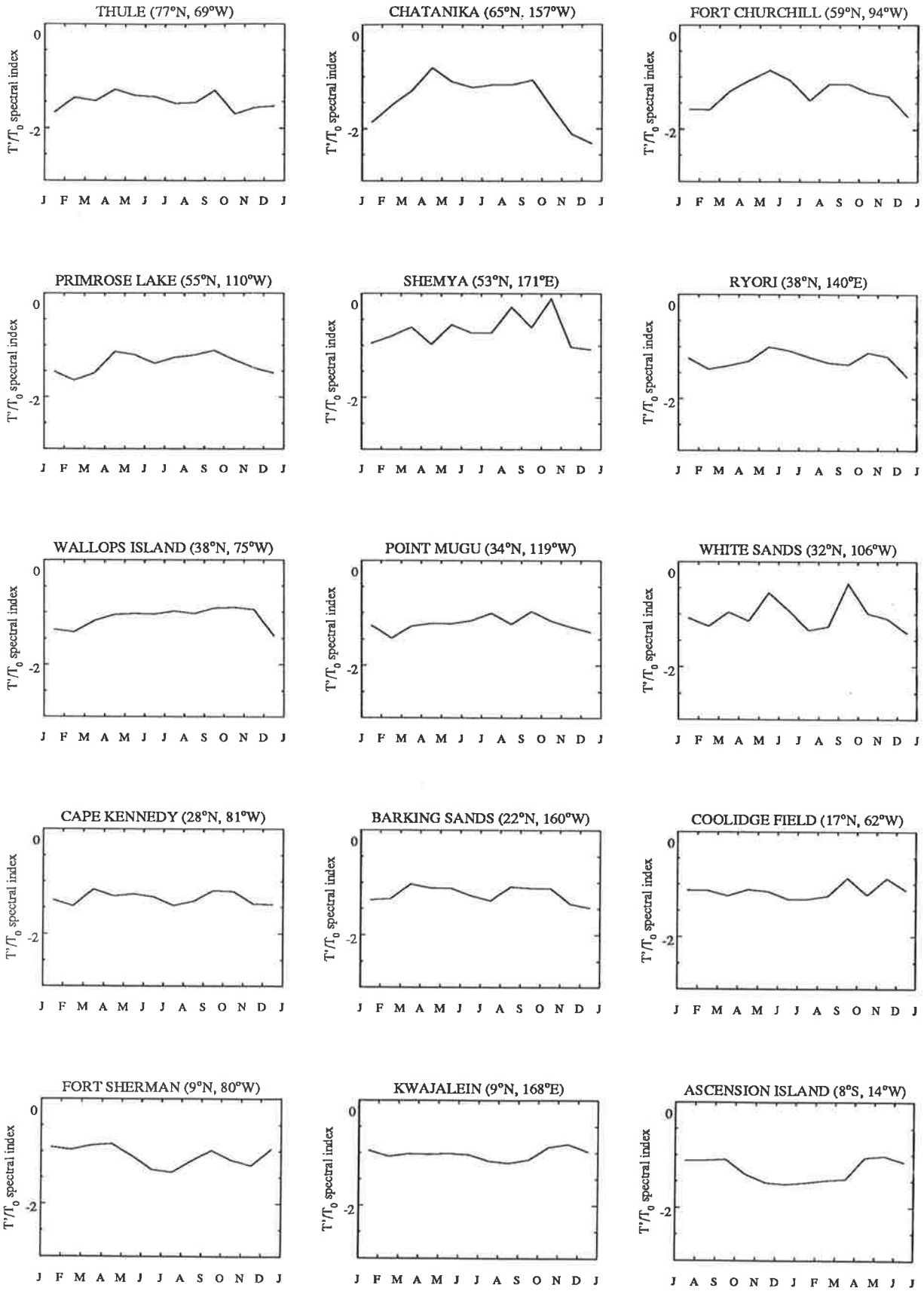

Figure 83: Seasonal variations in the spectral indices of the mean vertical wavenumber spectrum of relative temperature fluctuations, as computed from least–squares fitting. Note again that reordering of months for the Ascension Island results.

wavenumber is the same when measured from either frame. However, the wave frequency measured from these frames differs due to Doppler shifting by the horizontal flow, and it was demonstrated in section 4.2 that, because of this Doppler shifting, a similar analysis performed on time–fluctuating gravity wave motions as measured at the ground produces alignments which cannot in general be interpreted in terms of mean wave–propagation azimuths.

Computed azimuthal alignments from the high–latitude rocket data are displayed in Figure 84. The data are divided into conventional quarterly seasonal groupings, and the number of counts within 6 azimuth bins between 0° and 180° are plotted as histograms. Histograms for the various seasons are shaded differently to better highlight the seasonal divisions. Histogram error bars are 90% confidence intervals as given by the Poisson distribution, which is the appropriate counting statistic. The results from two height intervals (20–40km and 40–60km) are presented at each site. Note that the results from Shemya are not included due to insufficient data.

At Thule there is little if any alignment anisotropy at lower heights, whereas at upper heights there is a tendency for the fluctuations to align preferentially more east–west rather than north–south. At Chatanika the results are more evenly distributed, whereas at Fort Churchill east–west anisotropy is also observed at upper heights, except between September and November, when there is strong NW/SE[1] alignment at lower heights which persists more weakly at upper heights. A similar low–altitude preference for NW/SE alignment is observed at the nearby site of Primrose Lake, and again this alignment occurs less distinctly at upper heights. However, elsewhere at this site the $\bar{\phi}$ distributions are more isotropic, although some broad NS anisotropy is evident in the December–February interval, particularly at upper heights.

Similar results for the mid–latitude data are plotted in Figure 85. At Ryori, the alignments are very uniformly spread at lower heights, whereas in the upper height range the data are more sparse, although preferred NS orientation is apparent between December and May. This feature is also observed at the four remaining stations in the United States. At Wallops Island, a weak upper–level preference for meridional rather than zonal alignment is observed all–the–year round, whereas more isotropic orientations occur lower down; in fact, during March–May there is preferred zonal orientation from 20–40km. The closely–located sites of Point Mugu and White Sands exhibit similar alignment trends, where at lower heights the distributions are quite isotropic. At 40–60km, however, there is very strong anisotropy in the orientations during December–February, with the counts peaking around NNW/SSE at both sites. This upper level anisotropy persists into March–May, albeit less strongly, and meridional alignments are more prevalent

[1] either north–west or south–east

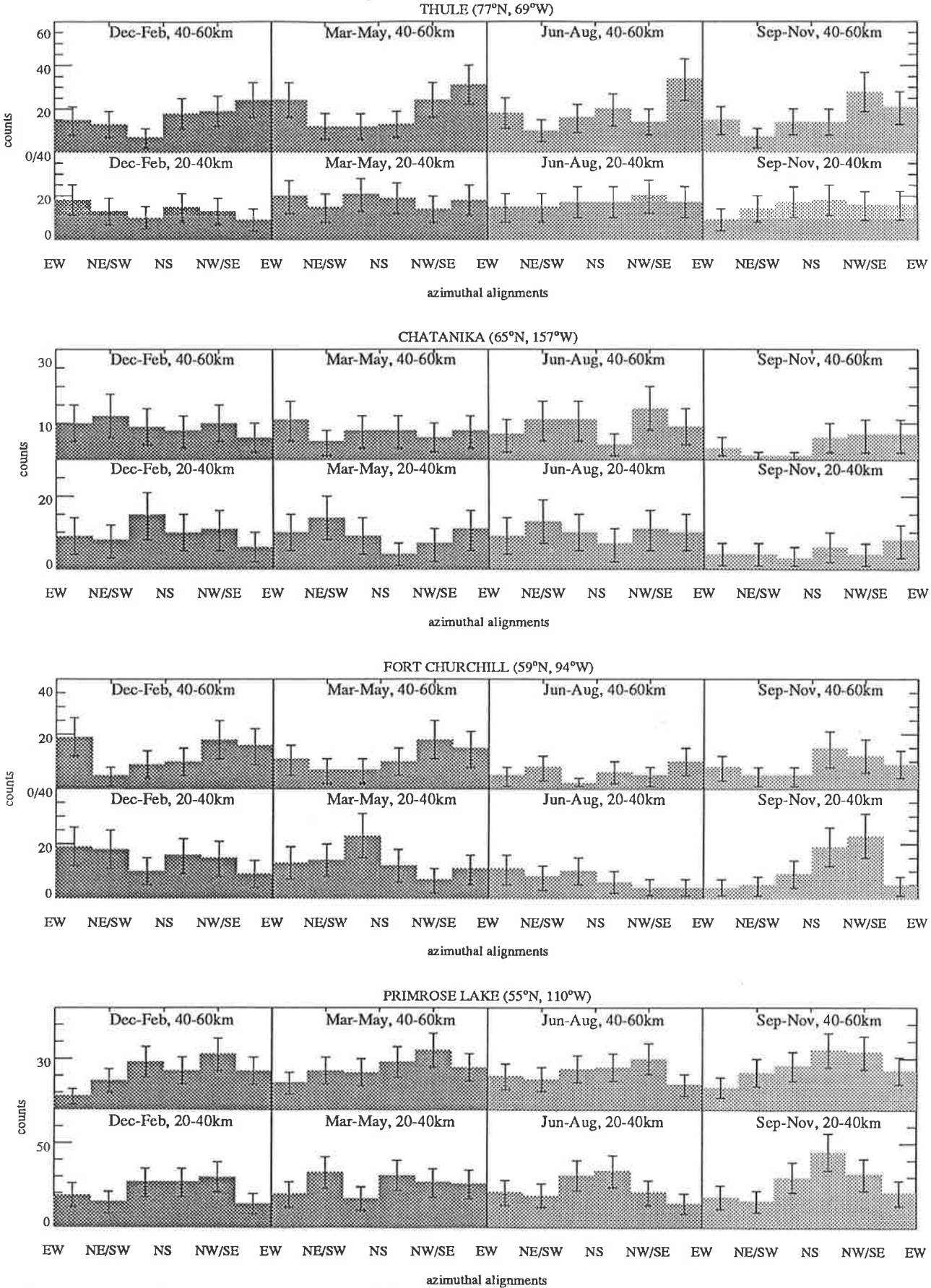

Figure 84: Histograms of the number of $\bar{\phi}$ occurrences within 6 azimuth bins as calculated from rocket data at four high–latitude sites. The data are split into summer, spring, winter and autumn groupings, and the histograms within each seasonal grouping are shaded differently. The lower and upper plot sequences at each site are results from a lower (20–40km) and upper (40–60km) height range. Error bars are 90% confidence intervals of the count as given by the Poisson distribution.

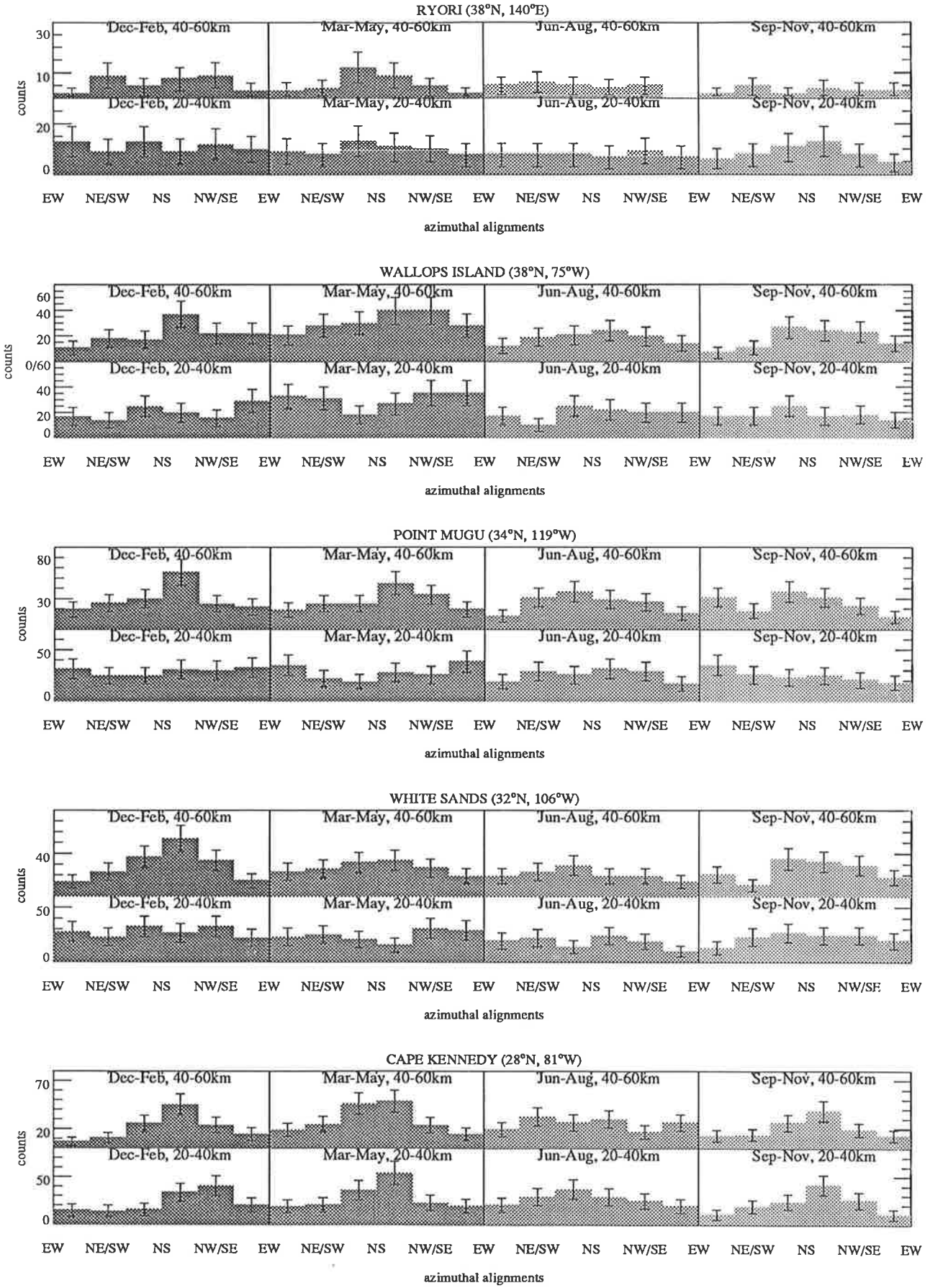

Figure 85: As for Figure 84, but for 5 mid–latitude sites.

than zonal alignments in the remaining seasons as well. The clearest trends occur at Cape Kennedy, where the upper–level NNW/SSE peak during December–February is very strong, but it differs from the other sites because similar anistropy is also observed in the lower height range. Indeed, near–meridional peaks in $\bar{\phi}$ counts are observed in the 20–40km in all seasons, with similarly shaped features evident at 40–60km everywhere except in June–August, when the upper–level anisotropy is small.

Figure 86 shows the results for the 5 remaining launching sites. The top two plots show the results from the "low–latitude" sites, which are closely spaced in latitude but widely spaced in longitude (see Figure 70). During December–February, a NNW/SSE anisotropy like that observed in Figure 85 is evident at both sites at 40–60km. Elsewhere the results differ at each site and little anisotropy is observed, except a near-meridional anisotropy in the 40–60km range at Coolidge Field during September–November.

The final three plots in Figure 86 show the equatorial alignments. In the 20—40km region, the alignments at all three sites and in all seasons are very strongly biased east–west. Strong east–west alignments also occur at 40–60km, but there is noticeable seasonal variability in the sharpness of the anisotropy. The zonal anisotropy is always strong during December–February, but weaker during March–May and September–November. From June through August, the upper–level zonal anisotropy is clear at Fort Sherman, a little weaker at Kwajalein, and much weaker at Ascension Island.

6.3.6 Interannual Variability

To date, the analyses have produced annual mean results using a number of years of data. Now we investigate how reproducible these mean seasonal variations in $\overline{u'^2} + \overline{v'^2}$ and $\overline{\hat{T}'^2}$ are from year to year, using data from selected sites where good month–to–month data rates are maintained for several years.

Figure 87 shows the variations in $\overline{u'^2} + \overline{v'^2}$ and $\overline{\hat{T}'^2}$ at a representative high–latitude site of Thule from 20km to 60km over four years from 1977 through 1980. We note that the mean annual cycles in $\overline{u'^2} + \overline{v'^2}$ and $\overline{\hat{T}'^2}$ observed in Figures 77 and 78 are clearly reproduced with similar characteristics from year to year in both height ranges Similar reproducibility is also found at Primrose Lake (55°N), although these results are not presented.

The mid–latitude variations at Point Mugu from 1977–1980 are shown in Figure 88. The mean $\overline{u'^2}+\overline{v'^2}$ variations in Figure 77 exhibited a terannual variation at this site from 40–60km, and these three peaks seem to occur every year, but the relative strengths of these peaks do show some interannual variability. From 20–40km, the small variations are similar in all years. The relative temperatures also show the same qualitative variations from year to year, although again the strength of these cycles can differ amongst the various years. The results from Cape Kennedy from 1979–1982 are also shown in Figure 89. The

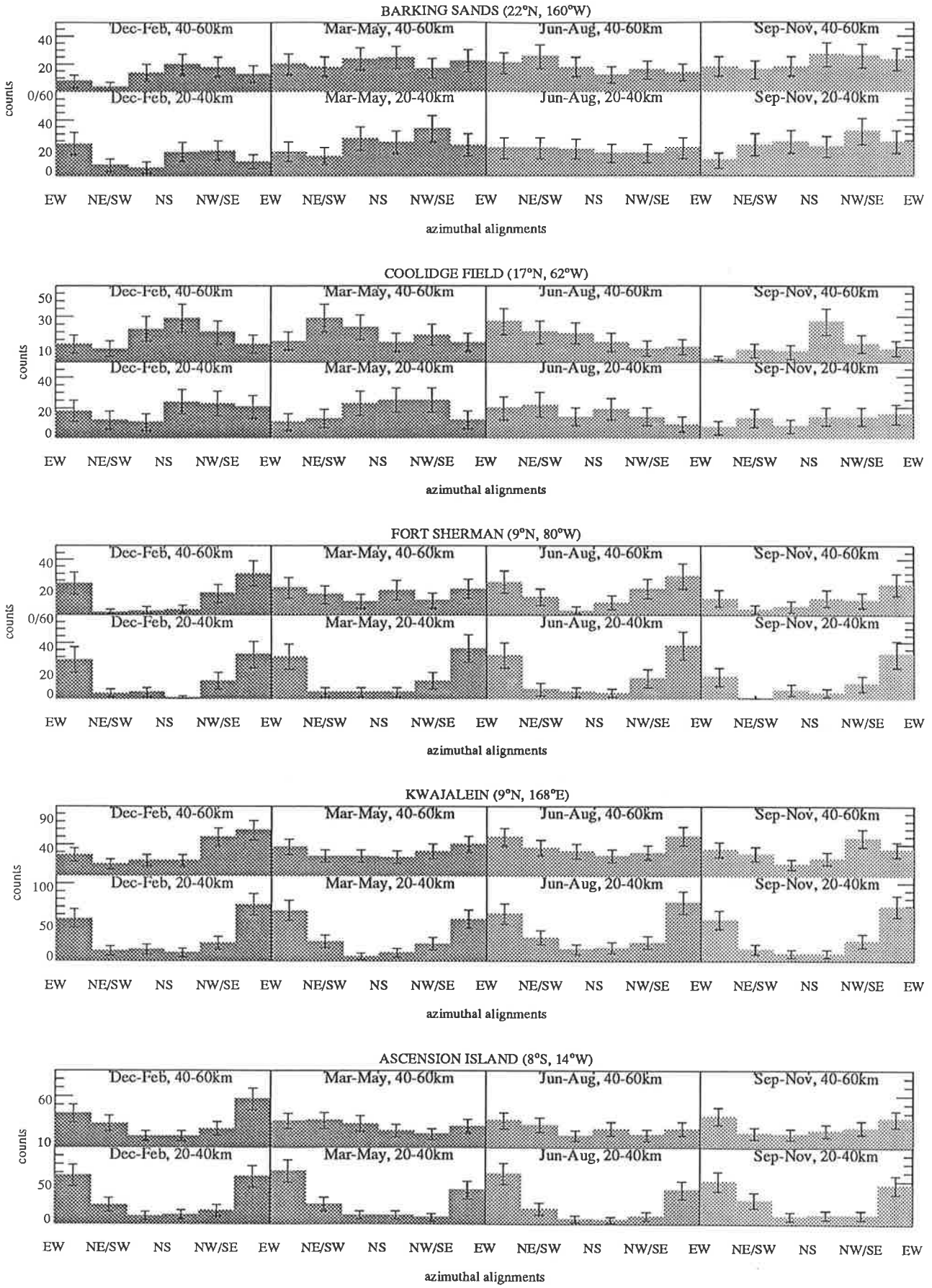

Figure 86: As for Figure 84, but for low–latitude and equatorial sites.

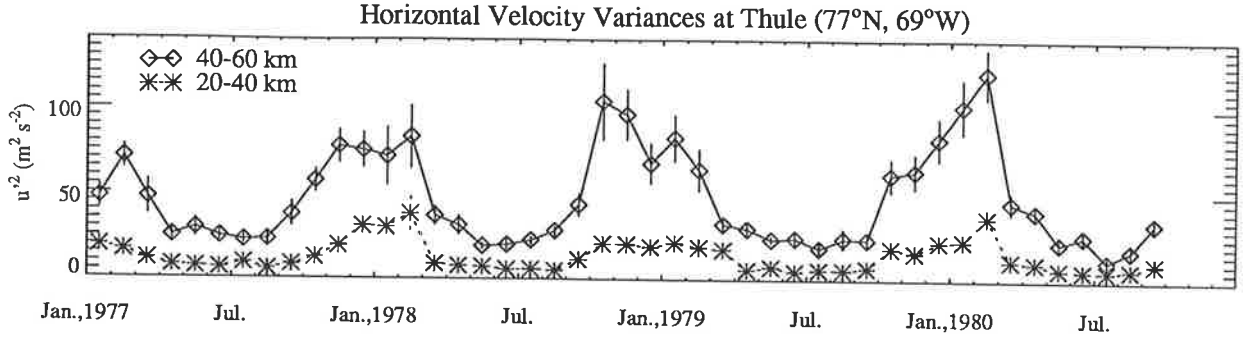

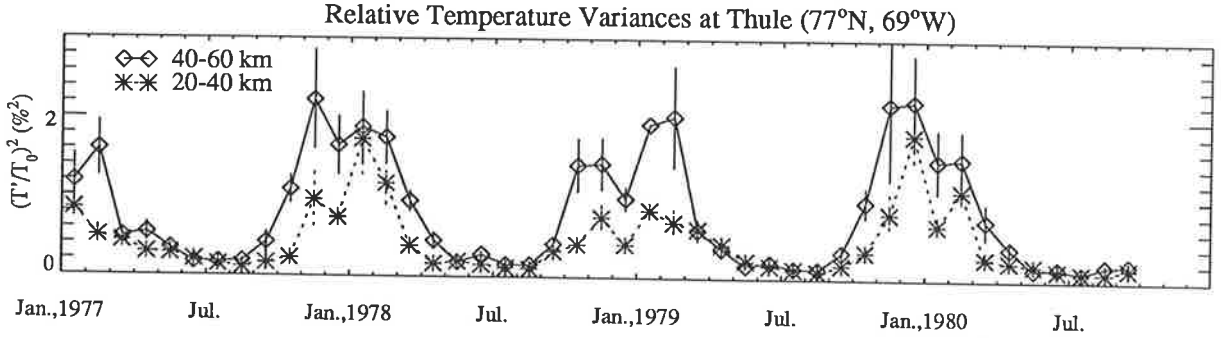

Figure 87: Monthly–mean horizontal velocity and relative temperature fluctuations from 1977–1980 over Thule. Bars indicate the standard errors of these means.

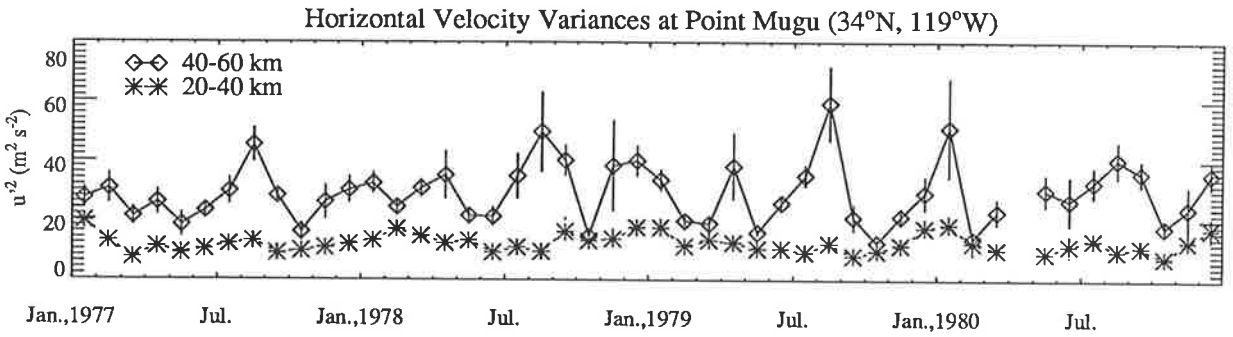

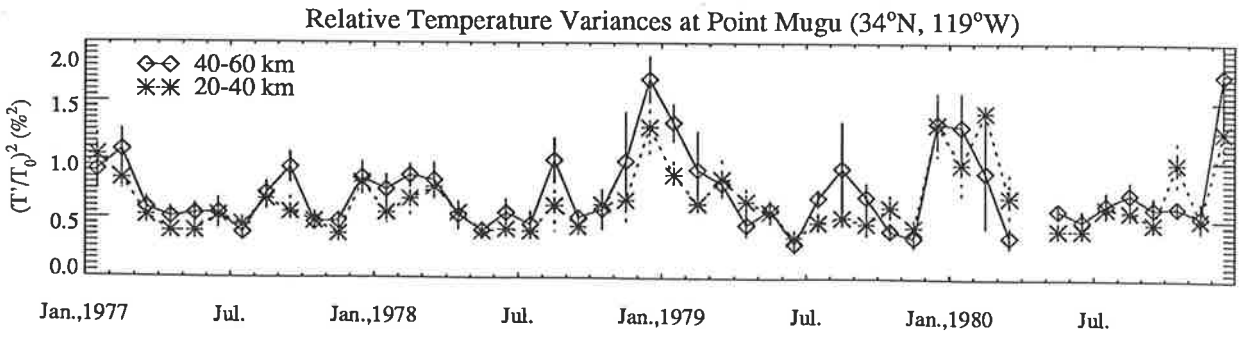

Figure 88: As for Figure 87, but at Point Mugu.

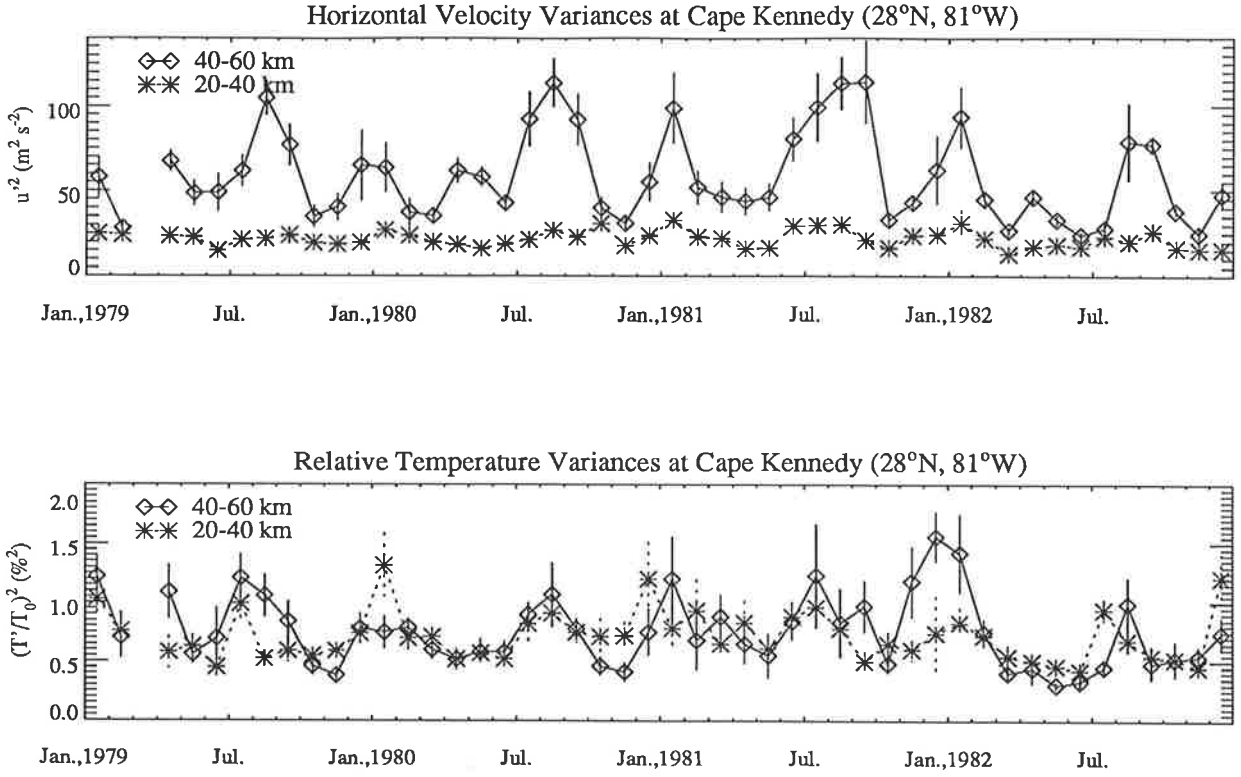

Figure 89: As for Figure 87, but at Cape Kennedy from 1979–1982.

large peaks in August and smaller maxima around January seen in Figure 77 repeat from year to year, but a small subsidiary equinoctial peak is observed during 1980 and 1982, but not during 1981, perhaps explaining the "plateau" structure around April alluded to earlier when analyzing the mean results at this site. Peaks in the relative temperature perturbation in August and January occur each year, but with somewhat variable intensity.

One location where one might anticipate some interannual variability is at the equatorial latitudes, where the lower stratosphere exhibits a quasi–biennial oscillation (QBO) in background wind and temperature. This structure can be seen clearly in the zonal wind structure in Figure 90, which shows monthly–mean winds and temperatures from 1977–1980 over Kwajalein. Above this region, one can also observe the well–known semiannual oscillation (SAO) of the equatorial upper stratosphere [see, e.g., *Hirota*, 1980]. The wind and temperature variances at Kwajalein over these years are shown in Figure 91.

While four years of data is probably insufficient to enable one to rigourously investigate QBO–modulation in wave activity, the results from 40–60km suggest that there is no major effect. A wintertime peak in $\overline{u'^2} + \overline{v'^2}$ occurs every year, albeit with non–constant intensity, as do a weak peak around August and minima around April and October. In the 20–40km height range, however, there appears to be a QBO–coupled interannual effect; from February, 1977 until March, 1978, the horizontal velocity variance

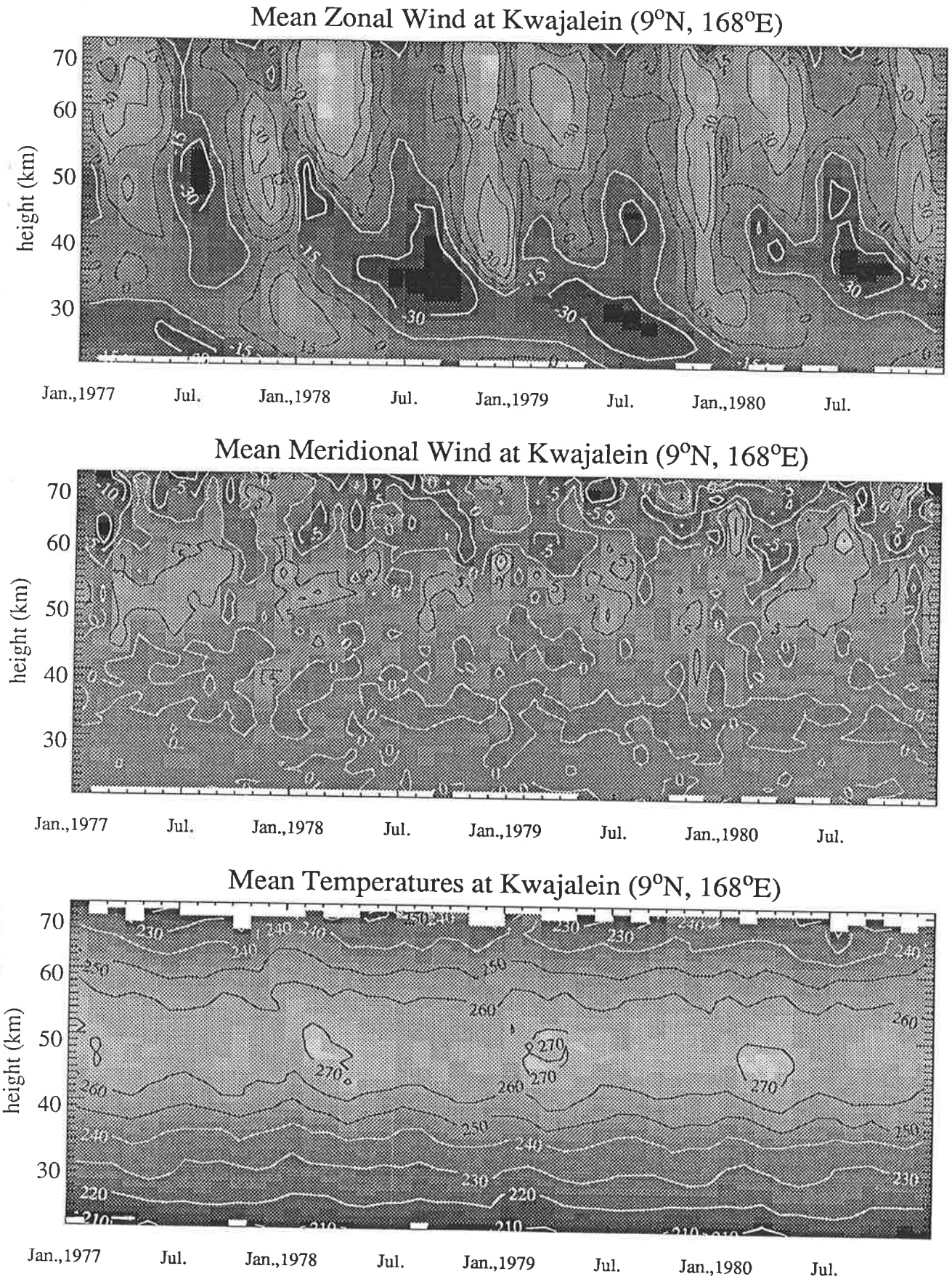

Figure 90: Monthly mean zonal winds, meridional winds, and temperatures from 1977 through 1980 over Kwajalein. Unshaded areas represent missing data, and the contour labels are in $m\ s^{-1}$ for wind and K for temperature. Positive zonal and meridional wind values are eastward and northward, respectively, and have light shading. Similarly, the warmest temperatures have lightest shading.

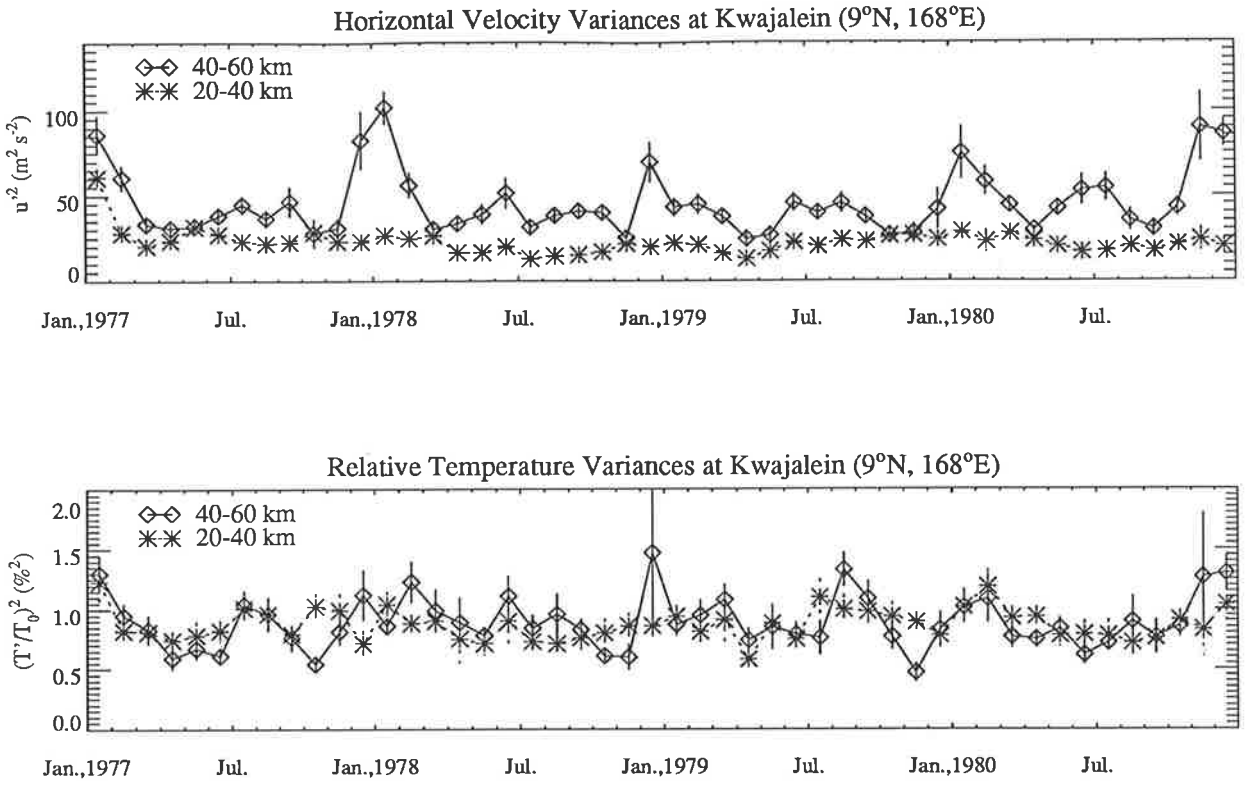

Figure 91: As for Figure 87, but at Kwajalein.

had a somewhat constant value around $25m^2\ s^{-2}$. For about six months centered around July 1978, however, the variances from 20–40km drop to values around $15m^2\ s^{-2}$. Similarly, from approximately August, 1979, until April, 1980, the low–level variance is larger, then drops again around June.

Similar low–level variability on scales greater than one year is also observed at Ascension Island (Figure 92). Although there is virtually no mean seasonal variations here at 20–40km (see Figure 77), one may observe in Figure 92 qualitatively similar low–level maxima and minima to those noted at Kwajalein on time scales greater than a year. Indeed, the variations during 1979–1981 appear correlated with the same variations at Kwajalein. As opposed to Kwajalein, however, similar variability can also be discerned in $\hat{T}'^2$.

These low–level amplitudes are enlarged in Figure 93, and a least–squares polynomial fit to the data is overlayed. The quasi–two year periodicity alluded to earlier is clearly apparent in this diagram. Note also that during the years when the data from each site overlap (1979–1981), the variations at each site are similar.

The variability in monthly–mean azimuthal alignments at 8 sites with acceptable monthly data rates over a four–year period are shown in Figure 94. The mean angles and standard errors were computed using circular Gaussian statistics [*Mardia*, 1972]. The clearest features here are the uniform east–west

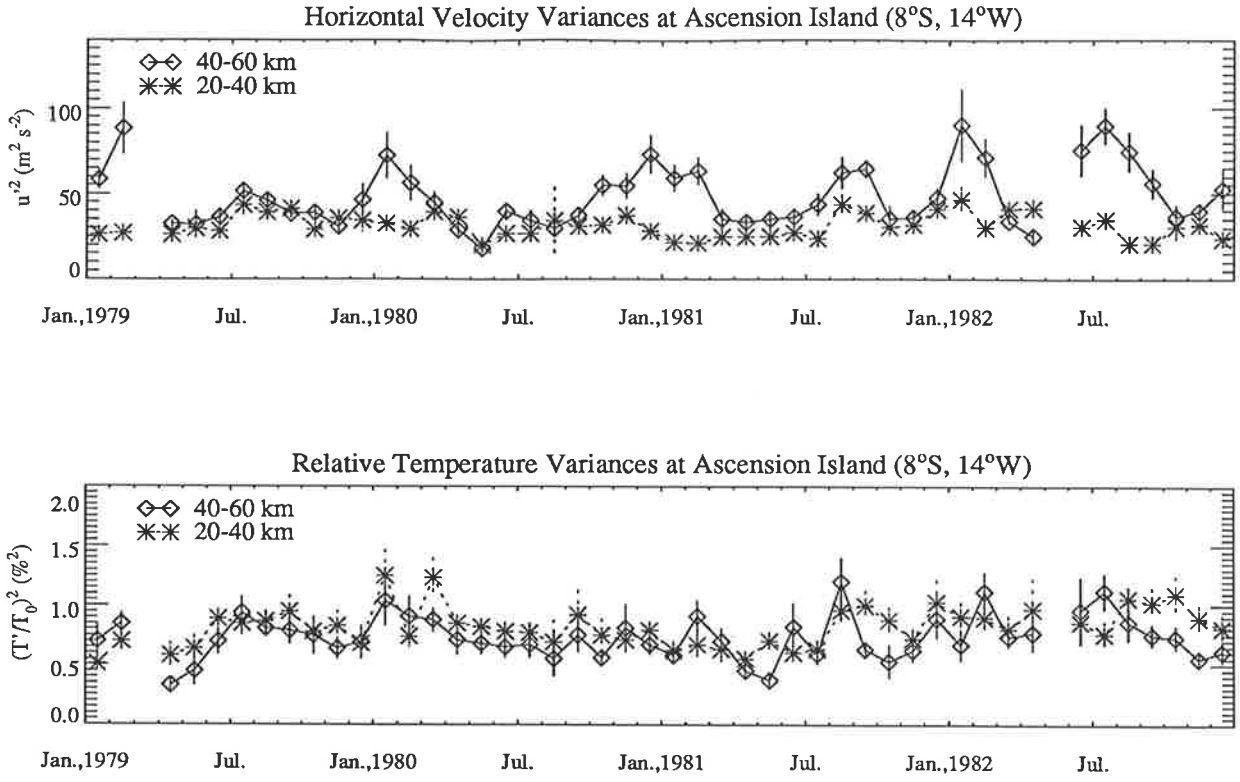

Figure 92· As for Figure 87, but at Ascension Island during 1979–1982.

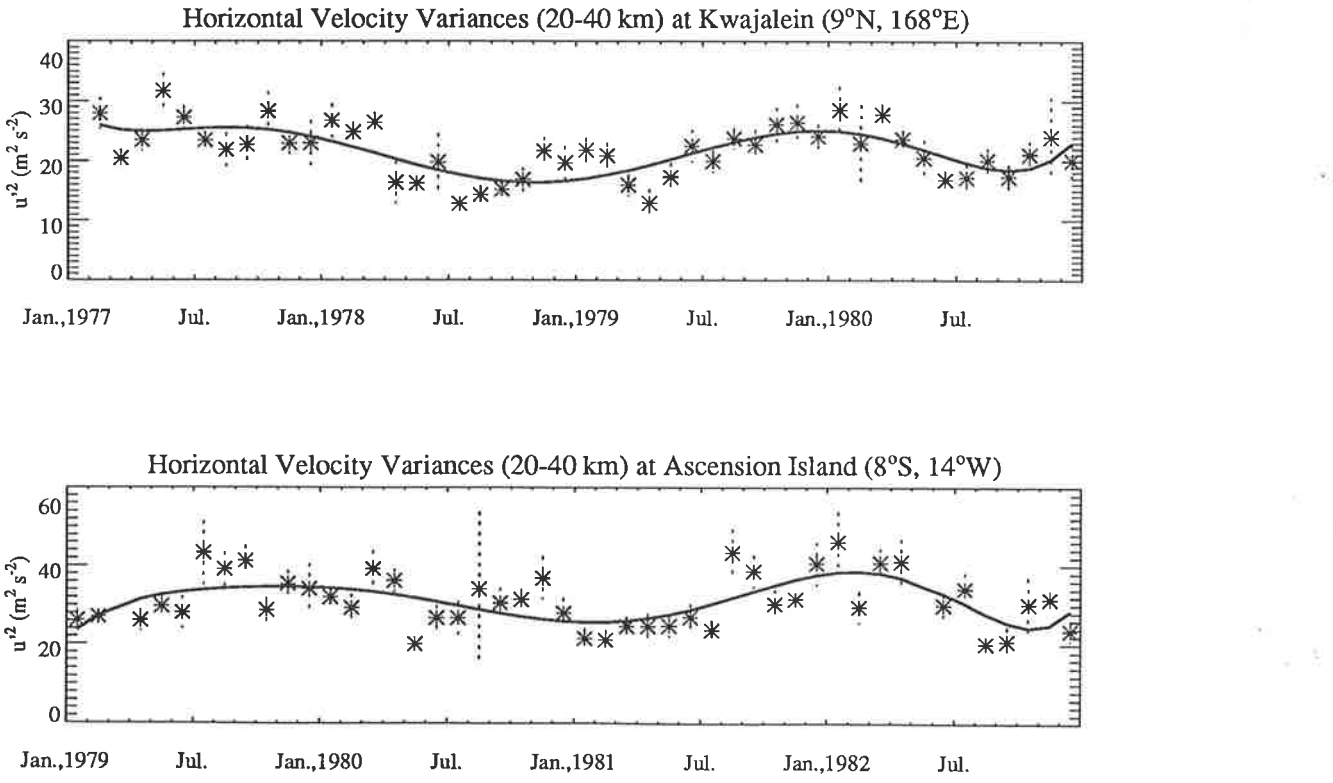

Figure 93: Expanded plots of $\overline{u'^2} + \overline{v'^2}$ at 20–40km from Figures 91. The solid line is a least–squares fit to the data of a seventh–degree polynomial, illustrating variation over a quasi–two year period. Note that the starting years of each plot differ.

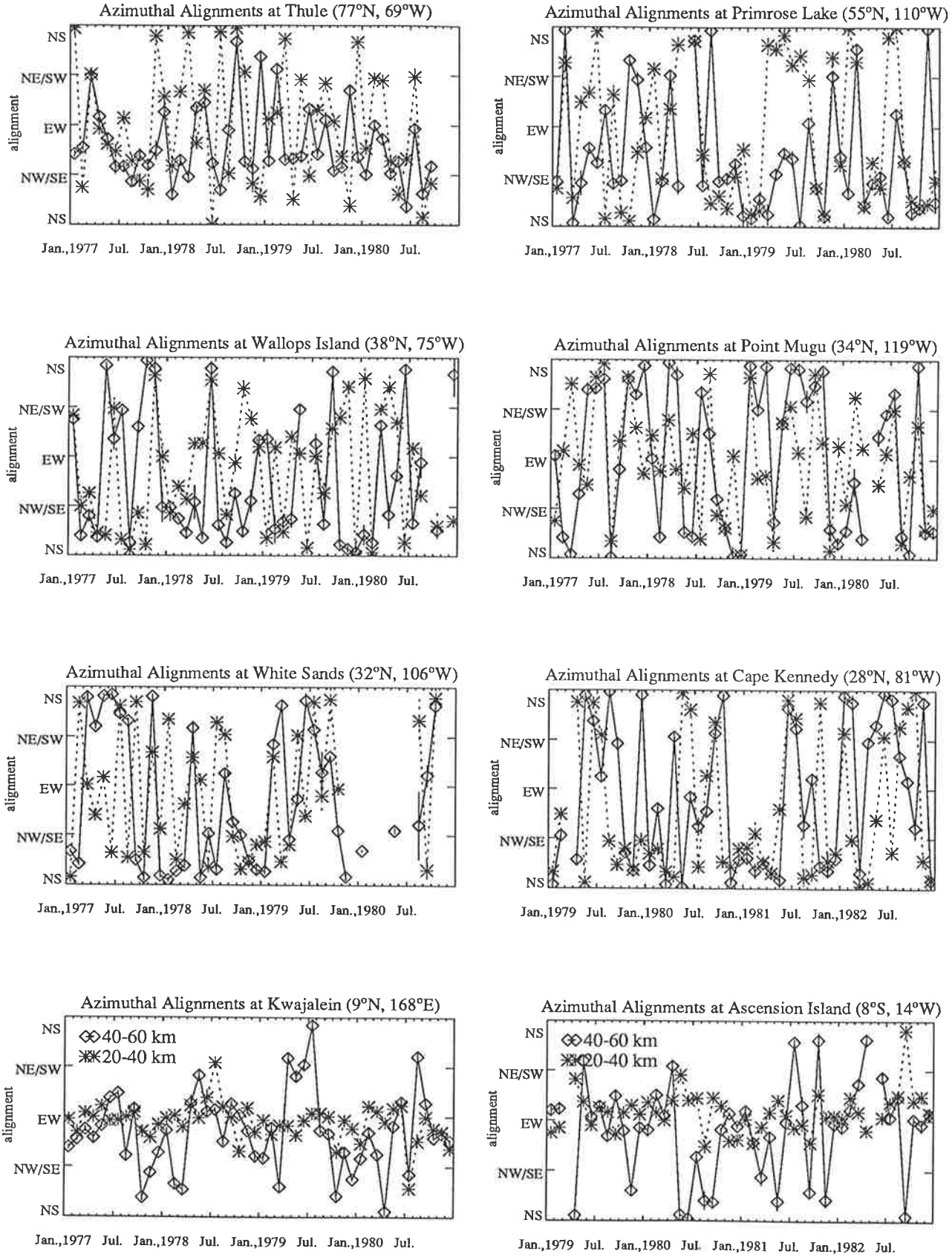

Figure 94: Plots of monthly–mean azimuthal alignments and their standard errors at eight selected sites. Results from 20 to 40km in altitude are plotted with asterisks and connected with dotted lines, whereas from 40–60km the data are plotted with diamonds and connected with solid lines.

alignments from 20–40km at the equatorial sites, whereas from 40–60km the alignments, while predominately east–west, exhibit much more variability. Possible QBO–modulation of alignment directions is difficult to gauge, since only ~2 QBO periods are spanned in these results, but any effect appears to be small. Most of the trends at other sites noted in Figures 84–86 are broadly reproduced from year to year, but with significant interannual variability, although the limited data within each month is also likely to accentuate any such variability.

6.3.7 Discussion

Analysis of the vertical spatial fluctuations produced by gravity waves, as evident in rocket–borne measurements between 20km and 60km in height, has resulted in a number of findings which will be discussed below. Characteristics which are common to the data at every site will first be addressed, then all the results will be collated to provide a basic picture of the gravity wave field in the atmosphere over different areas of the earth. The discussion will highlight many features, but no attempt will be made to develop complex theoretical ideas which might account for these features. Instead, only the most–easily explained features will be discussed in depth, and the following chapter will set forth and test some more–complex hypotheses about the physical processes which produce these observed characteristics.

Altitude Variation of $\hat{T}'^2$

It was noted in Figure 78 that the relative temperature variance $\overline{\hat{T}'^2}$ did not increase with altitude (except at high latitudes during winter), but that instead the variances were generally similar in the 20–40km and 40–60km height ranges. This result is quite unexpected theoretically, and contrasts with the altitude increases in the horizontal velocity variance observed in Figure 77 [see also *Hirota and Niki*, 1985].

While their small amplitudes and non–growth with height appear noise–like, analysis in section 6.3.3 indicated that the general characteristics of this variance were inconsistent with random errors. Indeed, it will now be shown that this non–growth probably results from the strong dependence that the $\overline{\hat{T}'^2}$ has on the background Brunt–Väisälä frequency N.

On combining (30), (74) and (78), $\overline{\hat{T}'^2}$ over the full wavenumber range is given by

$$\overline{\hat{T}'^2} \approx \frac{N^2}{g^2}\left(1-(f/\omega)^2\right)\left(\overline{u'^2}+\overline{v'^2}\right) \approx \frac{N^4}{8g^2m_*^2}, \tag{80}$$

since

$$\overline{u'^2}+\overline{v'^2} \approx \frac{N^2}{5m_*^2} = \frac{N^2}{5m_*(z_0)^2}e^{(z-z_0)/H_E}, \tag{81}$$

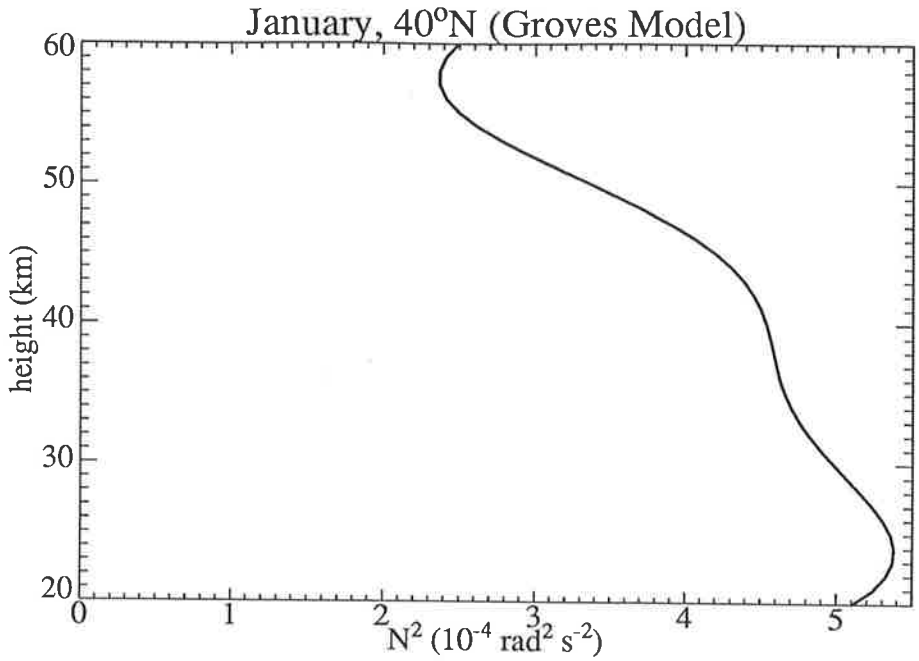

Figure 95: Plots of the height variation in N^2 with altitude, evaluated using the zonal–mean model atmosphere of *Groves* [1987] at 40°N in January.

according to (30). The exponential decrease with height in m_* in (31) gives an expected exponential increase in $\overline{\hat{T}'^2}$ with height, yet this assumes that N is a constant. In fact N decreases significantly with altitude on ascending from $20km$ to $60km$. Figure 95 shows the decrease in N^2 at 40°N in January using the model atmosphere of *Groves* [1987]. Note from this plot that N^2 values at lower heights are about twice those at the upper heights. By observing from Figure 77 that $\overline{u'^2} + \overline{v'^2}$ increases by a factor of ~2 from 20–40km to 40–60km, then since N^2 decreases by a similar amount over this range, (80) implies that $\overline{\hat{T}'^2}$ should not increase in variance over this range, as observed. Moreover, when the altitude increase in $\overline{u'^2} + \overline{v'^2}$ is larger than a factor of 2 (e.g., during winter at Thule, during August at Cape Kennedy), then some increase in $\overline{\hat{T}'^2}$ with height is also observed. Similarly, when $\overline{u'^2} + \overline{v'^2}$ grows little with height (e.g., April and October at Ascension Island), then $\overline{\hat{T}'^2}$ actually *decreases* with altitude. Note also that this N^2 scaling between $\overline{\hat{T}'^2}$ and $\overline{u'^2} + \overline{v'^2}$ holds rigourously for both saturated and unsaturated wave motions, since it follows from the wave polarization relations.

This explanation, if valid, has some impact. Simulations are conducted in the next chapter which further demonstrate that this scaling with N can explain much of the structure of these measured variances. A major consequence of this idea is that caution must be exercised when using height variations of wave amplitudes to investigate possible saturation of wave amplitudes. For example, this explanation implies that the non–growth with height of $\overline{\hat{T}'^2}$ in Figure 78 does not imply that the waves producing this variance are saturated. Similar sorts of problems in interpretation also arise when analyzing altitude

changes in the variance of time–varying fluctuations measured at the ground, due to Doppler–shifting, as discussed in section 4.2.6. To ascertain whether the constituent waves are saturated, the modulating effect of the change in N with height should ideally be corrected for. This modulating effect is particularly severe for $\overline{\hat{T}'^2}$, but also affects $\overline{u'^2} + \overline{v'^2}$ (see equations (27), (28) and (81)).

Spectral Indices

It was noted earlier that the high–latitude annual variation in the spectral indices of these fluctuations (see, e.g., Figure 81) is broadly consistent with the spectral models (73) and (74). Apart from this structure, the spectral indices vary little with seasonal, but exhibit large differences between sites. This is almost certainly due to different experimental distortions of the intrinsic spectral shapes due to varying instrumental effects amongst the sites, as discussed in section 6.3.4.

However, the following gross features are apparent in Figures 81 and 83; (1) the spectral indices are always more positive than the expected saturation value of –3; (2) the relative temperature spectral indices are more postive than those for the horizontal velocities. The latter of these features is consistent with instrumental processes which make the horizontal velocity spectrum artificially redder (see section 6.3.4). The other point, however, does not appear to be instrumental, but is consistent with the spectral shapes which arise when such spectra are computed over a large altitude range. This was discussed at length in section 3.3.2, and arises due to the inherent nonstationarity with height of the vertical wavenumber spectrum.

Seasonal Behaviour of Clockwise Rotation Percentages

Analysis of the rotation with height of the fluctuating wind vector revealed seasonal features that were common to all the sites (see Figure 80. Firstly, clockwise percentages exceeded 50% at all but the equatorial sites in every month, indicating that most of the wave energy propagates upwards from $20km$. Additional features were: (1) a deep minimum in the percentage of clockwise rotations during winter, and a smaller subsidiary minimum in summer; (2) maxima around March–May and August–October. While the effects are clear, their cause is more difficult to identify. The most obvious interpretation is that it is caused by seasonal variations in the ratio of upward–propagating to downward–propagating wave energy. However, these ratios are also influenced by seasonal variations in the intrinsic frequency distribution or degree of superposition of the wave field (see section 3.2), and other factors such as wave–packet localization [*Dong and Yeh*, 1989], and the effects of background wind shear.

The trends correlate well with the seasonal variations in the mean zonal wind $\bar{U}$; when the flow is

weak, the ratios are high, whereas when the stratospheric jets occur during the soltices, the ratios are small, with the smallest ratios generally occurring during winter when the zonal flow is most intense. Furthermore, at Thule were the flow is quite weak most of the year, the variations in Figure 80 are similarly small with season. At the soltices, upper stratospheric wind speeds increase with height to become strongly westward in summer and strongly eastward in winter, and this zonal wind structure filters the gravity–wave field such that the zonal–components of the ground–based wave phase speeds are largely antidirected to this mean–flow direction (i.e. eastward in summer, westward in winter). This gives rise to large intrinsic phase speeds $\hat{c} = \mid \bar{c} - \bar{U}\cos\phi \mid$, so long as the wave is not propagating essentially north–south ($\phi \approx 90°$ or $270°$). For $\phi \sim 0°$ or $180°$ (zonal propagation), intrinsic phase speeds can quite feasibly exceed $100m\ s^{-1}$ in the upper stratosphere, so that the intrinsic frequency $\omega = k_h\hat{c}$ will also be large unless horizontal wavelengths $2\pi k_h^{-1}$ are very large. For example, at 30°N and a value of $\hat{c} \approx 100m\ s^{-1}$, a horizontal wavelength of $\sim 4000km$ is required to produce an f/ω ratio of 0.5. Most of the gravity–wave horizontal wavelengths are likely to be much smaller than these values, implying less waves with small intrinsic frequencies, less elliptical polarization of the horizontal velocity oscillations (see (20)), and so less distinction between anticlockwise and clockwise rotations. During the equinoxes, however, the weak zonal winds permit small intrinsic phase speeds, and thus low ω values can be attained by waves with moderately–sized horizontal wavelengths. Hence, rather than indicating seasonal variations in the relative amount of upwardly–propagating wave energy, these results are consistent with seasonal changes in the intrinsic frequencies of the dominant waves. The much smaller clockwise percentages at the equator, previously detected by *Hirota and Niki* [1985], were addressed in section 3.2 and it was argued that a preponderance of Kelvin wave motions, which are not elliptically polarized in the horizontal, produced these smaller clockwise–rotating percentages. The consistence of this hypothesis with the data is investigated later.

Wave Directionality

After reinterpretating some previous measurements made by *Hirota and Niki* [1985] of f/ω from four rocket stations (Thule, Primrose Lake, White Sands, and Kwajalein), assertions were made in section 3.2 about the degree of directionality of the wave field in the upper stratosphere at several rocket sites. The major conclusion was that the wave field at equatorial locations appeared to suffer from "overdirectionality"; that is, the wave field appeared to be exhibit more directionality in the horizontal than theoretically expected for a spectrum of gravity waves. It was therefore speculated that other types of waves may contribute to the fluctuations here, of which the Kelvin wave was identified as the most likely

candidate. It was also noted that the wave field at most sites was more directional during the winter months, and that annual–mean directionalities appeared to decrease as one moved progressively more poleward. These results were published before the commencement of this work [*Eckermann and Hocking*, 1989], and indeed provided much of the motivation for the present study.

The alignment data presented in Figures 84–86 bear out most of these indirect conclusions. Alignment distributions during winter are usually more anisotropic than at other times. However, the lack of inertia gravity waves during winter, as inferred in the previous discussion on clockwise–rotation percentages, can also reduce the mean f/ω values and thus lead to an overestimate of the degree of directionality (see Figures 31 and the accompanying discussion in section 3.2.5). The speculated decrease in the mean directionality on progressing poleward is also quite evident in Figures 84–86 at Thule, Primrose Lake, White Sands, and Kwajalein. Most particularly, the strong east–west alignments of the equatorial fluctuations (Figure 86 and 94) provide strong support for the equatorial directionality assertions, and, as revealed in the discussion to follow, for the postulate that an apparent "overdirectionality" exists which suggests that Kelvin wave motions might be more prevalent than gravity waves at these latitudes.

Equatorial Wave Characteristics

The dynamics of the equatorial upper stratosphere is based around a semiannual oscillation (SAO) of winds and temperatures in this region [*Reed*, 1966; see also Figure 90], which is believed to result from wave driving. The conventional explanation is that the eastward phase of this oscillation is driven by the dissipation of short–period (long vertical wavelength) Kelvin waves, and the westward winds are driven by critical level absorption of Rossby waves [see the review of *Hirota*, 1980]. Furthermore, it is generally believed that longer period (short vertical wavelength) Kelvin waves are dissipated in the lower stratosphere in driving the QBO, and so do not occur at these heights.

The results from the height range 20–40km in Figures 86 and 94 strongly suggest that short–vertical–wavelength Kelvin waves penetrate the lowest levels of the QBO (i.e. below 20km) to dominate the horizontal velocity variance here in all seasons. These Kelvin–wave amplitudes are, however, clearly modulated by the phase of the QBO (Figure 93). By inspecting computed mean zonal winds between 20–30km at these sites (e.g., Figure 90), peaks in $\overline{u'^2} + \overline{v'^2}$ seem to develop during times when the QBO winds are changing from westward to eastward at 20–30km, which is consistent with the larger–amplitude Kelvin waves dissipating around 20–30km and exerting a drag which forces the westward flow to become more eastward, as in the conventional picture of QBO dynamics [see, e.g., *Andrews et al.*, 1987]. Minima in activity usually arise at times when eastward winds are becoming progressively more westward. This

is also consistent with reduced Kelvin wave transmission and reduced eastward wave drag, during times when mixed Rossby–gravity waves accelerate the wind westward. Note that these types of waves are not observed at 20–40km since the alignments are east–west, which is consistent with the expected strong dissipation and thermal damping of such waves in the lower stratosphere [see, e.g., *Hirota*, 1980].

The question now arises as to whether similar small-scale Kelvin waves persist above QBO heights (>30km). The results in Figure 86 indicate that short–wavelength Kelvin waves dominate at 40–60km during winter, whereas in the other months the preferred east–west alignments, while usually detectable, are not as distinct. The seasonal variation of the clockwise–rotation percentages at the tropics in Figure 80 provides independent support for this conclusion, since values near 50% occur in winter, which are consistent with the presence of linearly–polarized Kelvin waves. Reasonably clear but weaker east–west alignments occur during June–August at Fort Sherman and Kwajalein, which again is reinforced by a second weaker summertime dip in the rotation percentages near the equator in Figure 80. The wintertime upper–level Kelvin waves give rise to large $\overline{u'^2} + \overline{v'^2}$ values at these times (see Figure 77), and a smaller secondary peak occurs around August, when the smaller secondary zonal–alignment phase arises. During April and October when the alignments are more isotropic, however, $\overline{u'^2} + \overline{v'^2}$ at 40–60km is strongly attenuated. Gravity waves appear to be the more prevalent at these times.

These upper–level maxima in $\overline{u'^2} + \overline{v'^2}$ arise when the zonal winds of the SAO are westward, so that eastward–propagating Kelvin waves can propagate vertically through the stratosphere, whereas the activity minima occur when the SAO is in its eastward phase. When combined with fact that alignments are biased east–west when the peaks in $\overline{u'^2} + \overline{v'^2}$ occur, but are more isotropic when the activity is strongly attenuated, it indicates that short–wavelength Kelvin waves are again determining the seasonal nature of the small–scale horizontal–velocity variance at these heights.

These results suggest that Kelvin waves in the 2–10km vertical–wavelength range do indeed occur in the upper stratosphere. Earlier analysis by *Hirota* [1978] concentrated on long–wavelength (~15km) Kelvin waves in the data from this region at Ascension Island, but his results also showed evidence of a wintertime oscillation in the zonal wind with a wavelength ~9km. *Salby et al.* [1984] found evidence of a number of short–vertical–wavelength Kelvin modes in analysis of satellite data taken during October 1978 and January–February 1979. In particular, a strong horizontal–wavenumber–2 mode with a vertical wavelength of 7–13km was identified. *Devarajan et al.* [1985] studied oscillations of the zonal wind from two–years of equatorial rocket data at two sites (13.7°N and 21.5°N). They found that most of the waves here had rather small vertical scales (~6–12km), which they also interpreted as being wavenumber–2 Kelvin waves. Figure 96 shows the seasonal variations in Kelvin–wave zonal–velocity amplitudes found

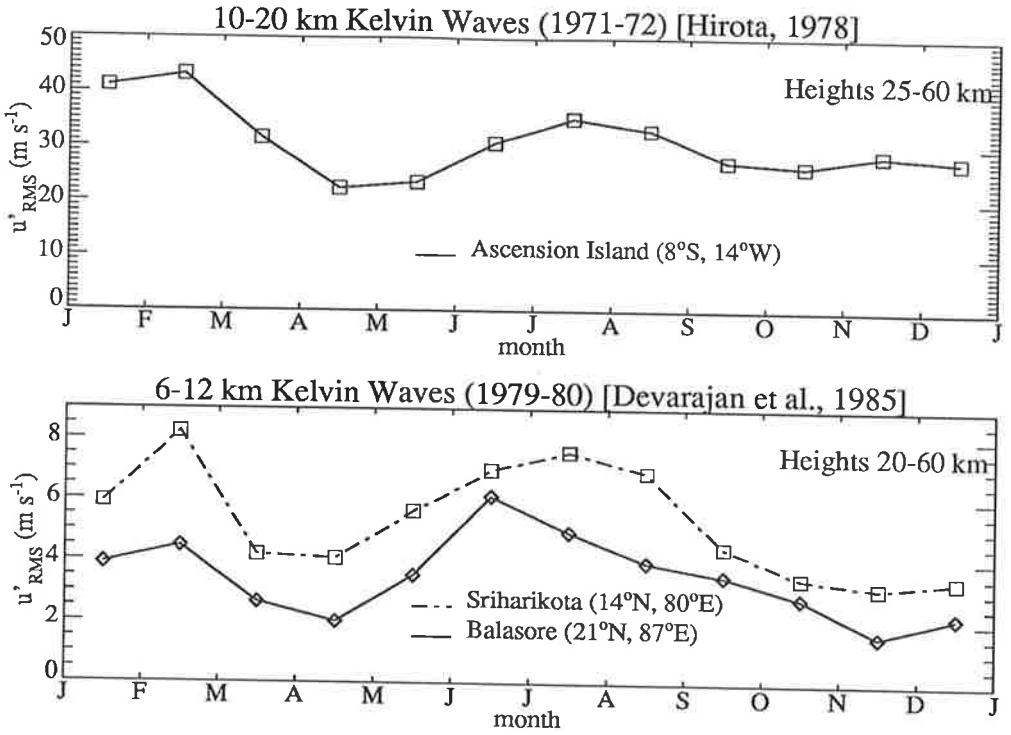

Figure 96: Seasonal variations of upper–stratospheric Kelvin–wave activity in the 10–20km vertical–wavelength band [after *Hirota*, 1978] and in the 6–12km range [after *Devarajan et al.*, 1985].

by *Hirota* [1978] for vertical scales ~10–20km, and by *Devarajan et al.* [1985] for vertical scales ~6–12km. The similarity of these seasonal variations and the equatorial results in Figure 77 over the 2–10km wavelength range is striking, and adds further weight to a Kelvin–wave interpretation of this equatorial variance. Note, however, Figures 86 and 94 indicate that during the minima in wave activity, alignments are no longer strongly east–west, so that the Kelvin waves are strongly attenuated and gravity waves dominate the variance more at these times.

The long–wavelength Kelvin waves observed by *Hirota* [1978] are believed to provide much of the eastward forcing of the SAO at these heights [*Dunkerton*, 1979]. The similarity of the seasonal activity of these waves (Figure 96) and the smaller–scale waves studied here (Figure 77), combined with the strong attenuation in $\overline{u'^2}+\overline{v'^2}$ observed at upper levels around April–May and October–November, raises a question as to the contribution that these waves might make to the eastward driving of the SAO. Indeed, while early modelling supported the Kelvin–wave forcing mechanism for the eastward SAO phase [*Dunkerton*, 1979], recent modelling by *Hamilton and Mahlman* [1988] has indicated that small–scale gravity waves provide most of this forcing, and large–scale equatorial Kelvin waves contribute very little. Indirect experimental support for this has been provided by analysis of satellite data from this region by *Hitchman and Leovy* [1988]. They concluded that the relative importance of gravity–wave compared to Kelvin–wave forcing increased with altitude. Modelling of the anti–phased mesospheric SAO suggests

that gravity waves are indeed the dominant forcing mechanism at these higher altitudes [*Dunkerton*, 1982*b*].

Figures 86 and 94 show that during periods in April–May and October–November of strong wave attenuation and thus strong wave drag, east–west alignments are not clearly evident, so that gravity waves are at least as energetic as the Kelvin waves. Quantifying possible eastward mean–flow drag from the $\overline{u'^2} + \overline{v'^2}$ results is complicated by the fact that such gravity–wave variance is believed to be dominated by low–frequency waves[2], whereas high–frequency waves are more important for the momentum fluxes $\overline{u'w'}$ and $\overline{v'w'}$, and thus in driving mean–flow accelerations [*Reid*, 1984; *Reid and Vincent*, 1987*a*; *Fritts and Vincent*, 1987]. Furthermore, momentum flux is a partially–cancelling quantity, so that wave propagation azimuths must also be considered in any calculation. While indirect methods can be employed to estimate the wave drag [see, e.g., *Eckermann and Vincent*, 1989], this is beyond the intended scope of this preliminary analysis of the results. These suggestive trends merit further analysis in any followup investigations.

"Mid–Latitude" Wave Characteristics

At around 25–35°N, superimposed upon a basic annual cycle is a strong upper–level burst in $\overline{u'^2} + \overline{v'^2}$ around August (Figure 77), a result not found in the earlier analysis of *Hirota* [1984]. The mean winds during August are westward but are progressively weakening (see Figure 97), therefore favouring the transmission of wave energy through the statosphere due to decreased critical–level filtering. However, weak mean winds also occur around April–May, yet here a peak in variance is only weakly observed at best (it is more prominent around 20°N), which makes intepretation of this August peak difficult.

Within the 20–40km height interval, this August peak is far weaker, which discounts it being produced by stronger wave sources at this time. One possible clue is provided by the alignment data in Figure 85. Recall from earlier chapters that the maximum permitted gravity–wave amplitude is given approximately by the saturation threshold $\mid c - \bar{U}\cos\phi \mid$. During winter the winds are strongly eastward, yet alignments at 40–60km are strongly meridional, so that $\phi \sim 90°$. This implies small values of $\mid c - \bar{U}\cos\phi \mid$ if values of c are mostly small. When the winds weaken around April and October, $\mid c - \bar{U}\cos\phi \mid$ will also be small regardless of the wave orientation. However, during June–August the winds are strongly westward, yet the upper–level alignments are not strongly meridional. As the zonally–propagating waves at this time must have phase speeds c which are eastward or only weakly westward, large values of $\mid c - \bar{U}\cos\phi \mid$ arise, and thus larger $\overline{u'^2} + \overline{v'^2}$ values are permitted.

[2]Recall from section 3.3.3 that $\overline{u'^2} + \overline{v'^2}$ is thought to be governed by an $\omega^{-5/3}$ power spectrum.

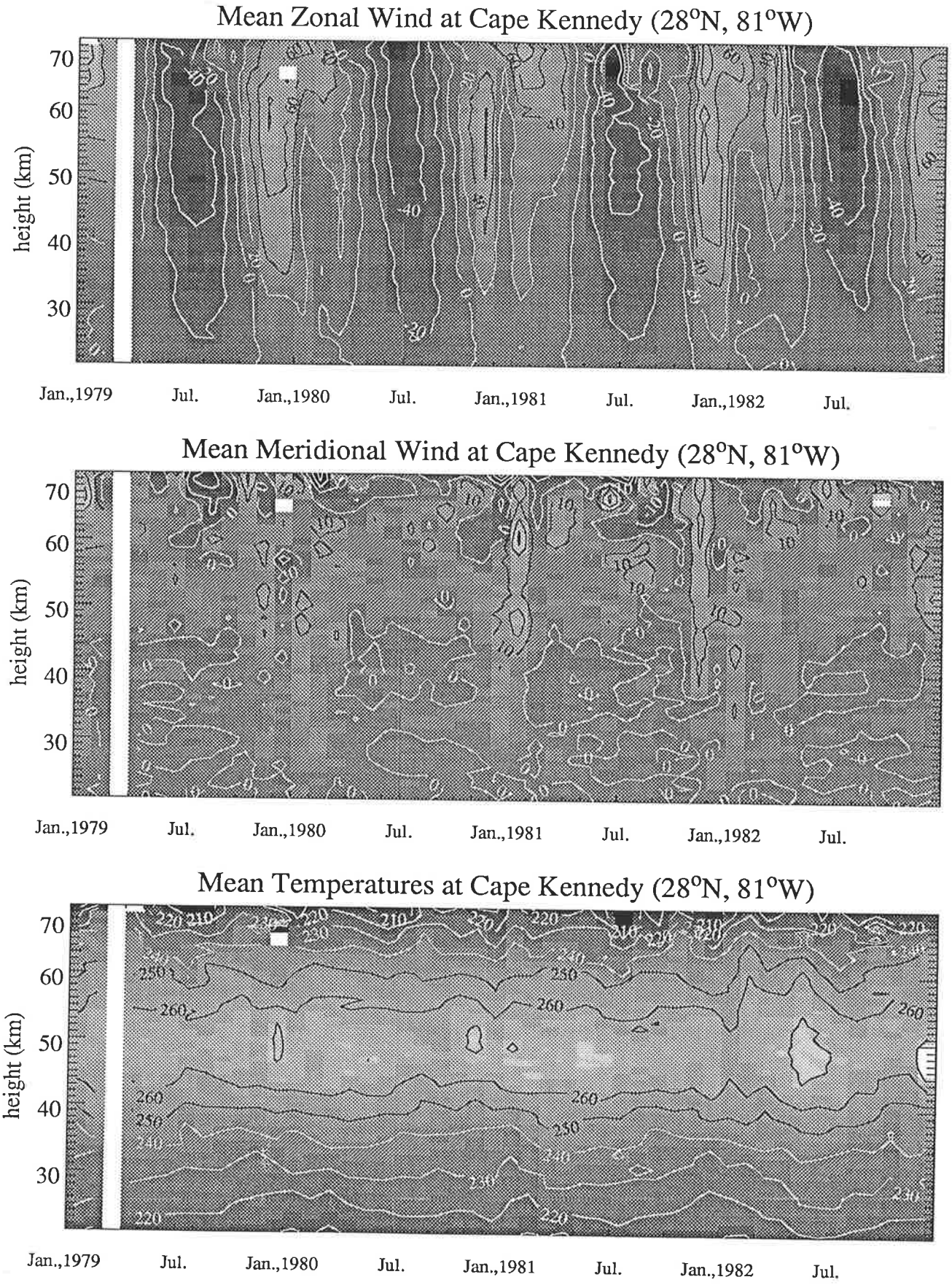

Figure 97: As for Figure 90, but at Cape Kennedy from 1979 through 1982.

There are problems with this explanation. Firstly, it is only valid if ground–based phase speeds c are small, such as might arise if orography was the dominant wave source. This is speculative. Additionally, while the normalized cycles are similar, mean wave amplitudes in Figure 77 vary widely amongst the sites, but the above argument tends to predict similar saturation limits at all sites. While these site–to–site differences may arise in part from varying responses of the falling sensor to these fluctuations [*Eckermann and Vincent*, 1989], the discrepansies are so large that they must indicate real geographical variations in gravity–wave activity. *Nastrom et al.* [1987] and *Jasperson et al.* [1990] noted much larger low–level wave activity over rough terrain in the western United States compared to that over the central—eastern U.S. and oceanic regions, which agrees broadly with the mid– and upper–stratospheric data in Figure 77 (i.e. Barking Sands, Point Mugu, White Sands, and Wallops Island), although strong activity is also noted here south of the western U.S. at Cape Kennedy and Coolidge Field.

Site–to–site differences in the relative temperature variances, while evident in Figure 78, are generally smaller than those in Figure 77. According to (78), the larger values in winter are consistent with the larger wintertime ω values inferred earlier from the clockwise–rotation data in Figure 80, since $f/\omega \sim 0$. The August peak is also observed in the relative temperature variances, albeit more weakly. This seasonal variation of $\overline{\hat{T}'^2}$ is very similar to the seasonal variations of relative–density variance detected in the 33–57km height range by *Shibata et al.* [1986] with a lidar at Fukuoka, Japan (34°N, 130°E). the variations at the Japanese rocket station of Ryori are also similar at 20–40km, but more annual from 40–60km; limited data and questionable wintertime results from this site at upper levels cast some uncertainty as to the reliability of the 40–60km data here. Lidar observations of individual gravity waves have also been conducted at Urbana, Illinois (40°N, 88°W) by *Gardner et al.* [1989], but the data in this study were a little too sparse to confidently identify seasonal variations in the wave activity.

Strongly meridional wave alignments are evident in the wintertime data around 30°N in Figure 85 and 94. Very similar winter alignments were also detected at 30°S by *Eckermann and Vincent* [1989], who analyzed rocket data from 30–60km over Woomera, in central Australia. This tends to suggest that this effect arises from phenomena which are common to both hemispheres during winter. Strong eastward flow occurs in both hemispheres at upper–stratospheric heights during winter (Figure 97; see *Phillips and Vincent* [1989] for mean winds over Woomera), and will filter out most of the eastward propagating waves through critical–level interactions, which could then produce the observed excess of meridionally–aligned waves. Consistent with this hypothesis, *Eckermann and Vincent* [1989] demonstrated that the meridional bias in their wave data intensified with height; this is also clearly observed in the Northern Hemisphere (Figure 85), so that these observations further support the critical–level filtering hypothesis. *Eckermann*

and Vincent [1989] also observed that the alignments at 30°S were more zonal in summer, whereas here we find weakly meridional alignments at this time.

"High–Latitude" Wave Characteristics

The clearest features of the "high–latitude" wave field are the strong annual cycles in $\overline{u'^2} + \overline{v'^2}$ and $\overline{\hat{T}'^2}$, which peak in winter and minimize in summer (Figure 77 and 78). Indeed, a similar annual component is observed at virtually every site, but it is strongest at high latitudes. Such winter–summer contrast was noted in early studies of rocket fluctuations in the mesosphere at Wallops Island by *Theon et al.* [1967]. At high–latitudes the wintertime wave amplitudes are extremely large; at Primrose Lake $\overline{u'^2} + \overline{v'^2}$ nears $200 m^2\ s^{-2}$ and $\overline{\hat{T}'^2}$ is around $(1.5\%)^2$. Strong planetary–wave activity also occurs in the winter stratosphere [*Andrews et al.*, 1987], so that this region appears to be very dynamic at these times. The processes responsible for these variations are analyzed in depth in the following chapter.

At Primrose Lake, the upper–level alignments in winter are predominately north–south (see Figure 84). Strong eastward winds occur in winter at this site, and thus the meridional bias is consistent with the critical–level filtering hypothesis used to explain similar features at mid–latitudes. During September–November, however, strong meridional orientation is observed in both height ranges at Primrose Lake and Fort Churchill. This must arise either from directional sources, or from critical–level filtering below $20km$. At Thule, the alignments are nearly isotropic at 20–$40km$, and weakly zonal at 40–$60km$. The mean winds here are rather weak in all months, and become highly geostrophic in the winter months (see Figure 98). The decreased critical–level filtering that these weaker winds produce is consistent with the more isotropic nature of the wave alignments in Figure 84.

6.3.8 Conclusions

In conclusion, it appears that the reduction and analysis of vertical–spatial variations of rocket–derived atmospheric winds and temperatures between 20 and $60km$ in altitude has provided reliable and important new information on the characteristics of gravity waves and equatorial Kelvin waves in this region of the atmosphere.

Systematic differences amongst different latitude belts were detected, as a function of season within an upper and lower height interval, in the wave amplitudes and propagation directions. The clearest features are as follows: (1) The equatorial variance is dominated by short–wavelength Kelvin waves, which exhibit QBO–modulation at 20–$40km$ and SAO–modulation at 40–$60km$; (2) Large increases in mid–latitude wave activity occur around August, and an excess of waves aligned north–south occurs at

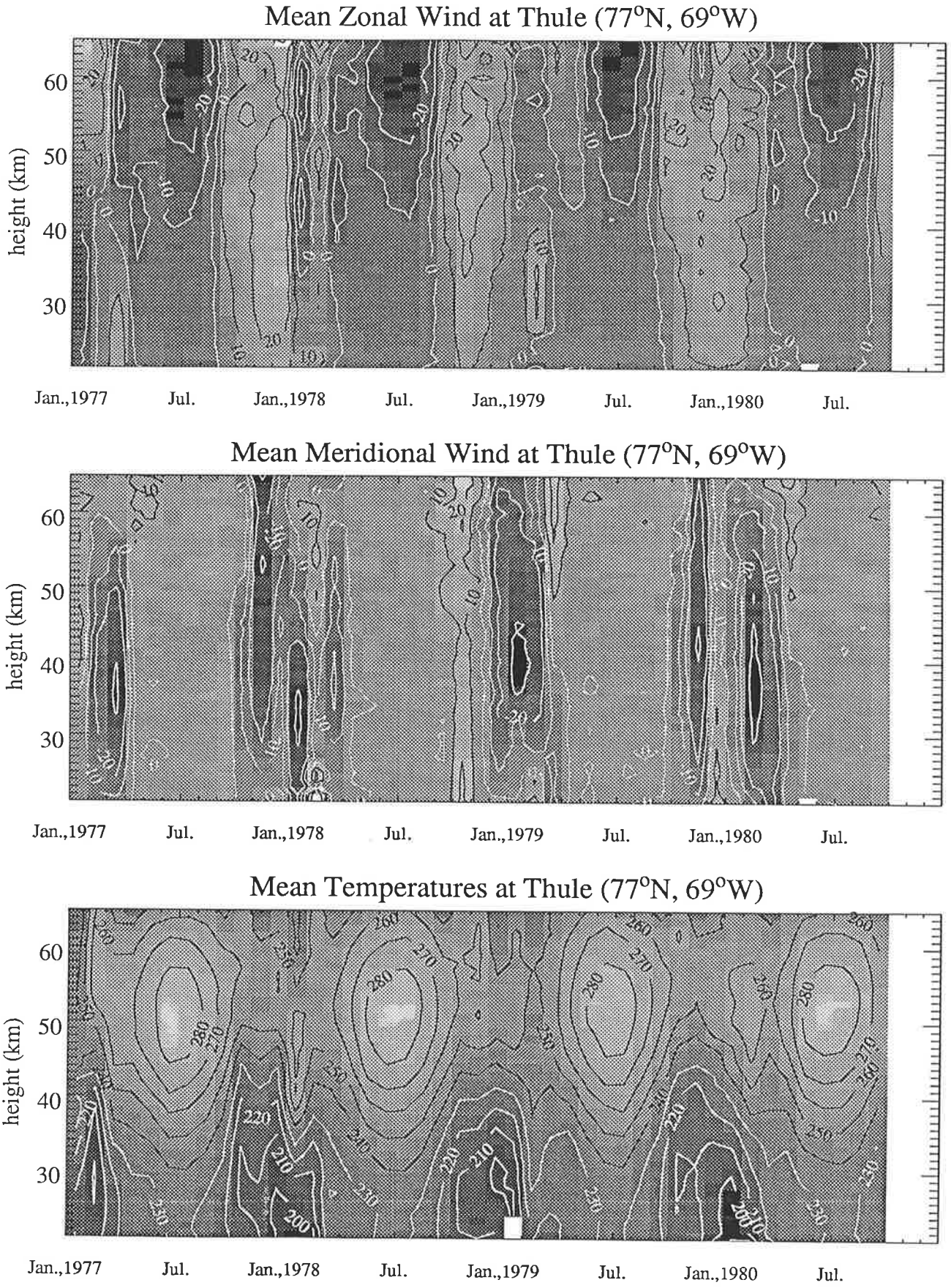

Figure 98: As for Figure 90, but at Thule.

upper levels in winter due to critical–level filtering; (3) At high–latitudes, the wave variance has a strong annual variation, which peaks in winter and minimizes during summer.

Other features of the observations are common to all the sites. The relative temperature fluctuations do not grow significantly with height, but rather than indicating wave dissipation, this seems to result from the decrease in atmospheric stability on approaching the stratopause. The majority of the wave energy propagates upwards from below $20km$. During winter, there seems to be a dearth of inertia gravity waves, whereas at the equinoxes such low frequency waves are more prevalent. Finally, the variances at all but the equatorial sites have an annual component which peaks during winter.

Finally, some possible wider local implications of these observations were discussed. Most importantly, however, these data provide perhaps the most detailed picture yet of the geographical and seasonal nature of the atmospheric gravity wave motions which emerge from the upper stratosphere to enter the mesosphere, where the dissipation of this wave energy determines both the mean and fluctuating structure (see section 1.4.3).

Chapter 7

Modelling of Observed Gravity–Wave Activity

7.1 Chapter Theme

The previous chapter provided experimental data on the basic gravity–wave morphology of the upper stratosphere. Indeed, other observational studies in the troposphere and lower stratosphere [*Massman*, 1981; *Nastrom et al.*, 1987; *Kitamura and Hirota*, 1989; *Fukao et al.*, 1989*c*; *Jasperson et al.*, 1990], the upper stratosphere [*Hirota*, 1984; *Hirota and Niki*, 1985; *Shibata et al.*, 1986; *Eckermann and Vincent*, 1989; *Gardner et al.*, 1989] and mesosphere [*Frezal et al.*, 1981; *Meek et al.*, 1985*b*; *Balsley and Garello*, 1985; *Smith and Lyjak*, 1985; *Yamamoto et al.*, 1986; *Vincent and Fritts*, 1987; *Gardner and Voelz*, 1987; *Shine*, 1989] have provided similar data on the basic seasonal and geographical characteristics of atmospheric gravity waves. Many of these features, however, have yet to be explained convincingly, if at all.

In section 7.2, attention is focussed on the strong seasonal and latitudinal variations in gravity–wave amplitudes which have been found in most observations of the middle atmosphere (see Chapter 6). The mechanisms which produce the distinct seasonal variations in wave activity have yet to be identified unambiguously. For example, high–latitude observations (see, e.g., Figure 77) seem to agree with the findings of *Lindzen* [1981], who demonstrated that a more rapid decrease in atmospheric density with height during winter produced larger wave amplitudes at these times than in summer. More recently, however, variations at mesospheric heights have been explained in terms of saturated waves adjusting in amplitude to the local saturation threshold $\mid \bar{U} - c \mid$ as the background wind profile $\bar{U}$ changes with

height and/or time [see, e.g. *Meek et al.*, 1985*b*; *Vincent and Fritts*, 1987; *Fritts and Vincent*, 1987]. Other workers have viewed the variations as evidence of seasonal variations in the wave–energy produced at the source regions in the lower atmosphere [see, e.g. *Rind et al.*, 1988]. If this last interpretation is correct, these data provide valuable climatological information about gravity–wave sources, which are poorly understood at present. Section 7.2 attempts to systematically determine which, if any, of the three aforementioned mechanisms is most consistent with the observations, most particularly the observations detailed in Chapter 6.

Finally, results of the entire modelling effort are brought together in section 7.4, where they are succinctly summarized and assessed.

7.2 Variations in Wave Activity

7.2.1 Introduction

As mentioned in the preamble, three mechanisms have been associated with the seasonal variability of gravity–wave amplitudes in the middle atmosphere; wave–amplitude saturation, unsaturated wave–amplitude growth with altitude, and wave–source processes. Yet the relative importance of these processes seems to vary from measurement to measurement. Much of this apparent uncertainty is resolved when the processes are considered in terms of their effect on the model vertical wavenumber spectrum for gravity waves, $F_u(m)$, given by (29).

Changes in the variance, as governed by this spectrum, are determined by the changes in m_*, yet m_* also separates saturated ($m > m_*$) and unsaturated ($m < m_*$) gravity waves. The value of m_* decreases exponentially with altitude according to (31), and gives typical values for $2\pi/m_*$ of around $1km$ in the troposphere, $5km$ in the stratosphere, and $20km$ in the mesosphere [*Smith et al.*, 1987]. Consequently, in the mesosphere the majority of the resolved wave field is saturated, and so one would anticipate that wave saturation effects would drive the seasonal variability at these heights. The mesospheric data bear this out [see, e.g., *Meek et al.*, 1985*b*; *Vincent and Fritts*, 1987; *Gardner and Voelz*, 1987]. In the lower atmosphere, however, most of the resolved wave field is unsaturated, but because the waves have not propagated very far vertically, one would anticipate that most of the seasonal variability is source related, which again is largely confirmed by the observations [*Kitamura and Hirota*, 1989; *Fukao et al.*, 1989*c*].

Using these same arguments, however, one can see that the situation in the upper stratosphere is not as clear. Since $2\pi/m_* \approx 5km$ here, both saturated and unsaturated waves will contribute to the

variance. Furthermore, the waves will have propagated some distance vertically, so that both exponential wave–amplitude growth $e^{z/2H_\rho}$ and variations in the wave energy produced at lower–atmospheric sources may well be significant. In accord with this, interpretations of measurements of upper–stratospheric wave activity have touched on all three mechanisms [*Hirota*, 1984; *Hirota and Niki*, 1985; *Shibata et al.*, 1986, 1988; *Hass and Meyer*, 1987; *Rind et al.*, 1988; *Eckermann and Vincent*, 1989; *Gardner et al.*, 1989]. We therefore attempt objective analysis of these various mechanisms, to assess their relative impact on various measurements of upper–stratospheric gravity–wave activity.

7.2.2 Analysis

Hereafter we consider the horizontal–velocity fluctuations u'. The three aforementioned mechanisms act on u' by changing certain terms in the saturated and unsaturated wave–amplitude relations (27) and (28), respectively; wave–amplitude growth with height is controlled via the term $m^{1/2}e^{z/2H_\rho}$, wave–amplitude saturation is determined by the term $\mid \bar{U} - c \mid$, and source effects involve variations in the source–level amplitude u_0 (see Chapter 3). We shall consider not only the $\overline{u'^2}$ measurements[1] from Chapter 6, but also the earlier $(u_{zz})_{rms}$ measurements of *Hirota* [1984], which were reanalyzed in Chapter 6. There it was argued that $(u_{zz})_{rms}$ values are heavily weighted to the saturated waves, whereas $\overline{u'^2}$ is determined more by unsaturated wave–activity. Yet the seasonal variations in each parameter are surprisingly similar considering that they should be determined by different processes (see Figures 75 and 77).

We shall now derive some simple relationships for these processes, which ignore all but the most basic effects. Since source variations are quasi–random, we shall ignore variations in u_0 and consider only wave–amplitude growth with height and wave–amplitude saturation. To keep things as simple as possible, we shall also ignore time and/or height variations in the background wind $\bar{U}$. The following proportionalities result for unsaturated and saturated wave activity, based on the basic formulae (27) and (28) from Chapter 3;

$$\overline{u'^2_{unsat}}(z) \quad \alpha \quad \frac{N(z)}{N_0} e^{\int dz/H_\rho(z)}, \tag{82}$$

$$\overline{u'^2_{sat}}(z) \quad = \quad \text{constant}, \tag{83}$$

$$u^{unsat}_{zz}(z) = \left(\frac{d^2u'}{dz^2}\right)_{unsat} = -m^2 u'_{unsat}(z) \quad \alpha \quad \frac{N^{5/2}(z)}{N_0^{1/2}} e^{\int dz/2H_\rho(z)}, \tag{84}$$

$$u^{sat}_{zz}(z) = \left(\frac{d^2u}{dz^2}\right)_{sat} = -m^2 u'_{sat}(z) \quad \alpha \quad N^2(z). \tag{85}$$

Notice that these simplified relations are independent of individual wave parameters, and so are valid over the entire gravity wave spectrum (to the level of the approximation). To examine this theoretical

[1] here we use the shortened term $\overline{u'^2}$ in referring to the total horizontal variance $\overline{u'^2} + \overline{v'^2}$

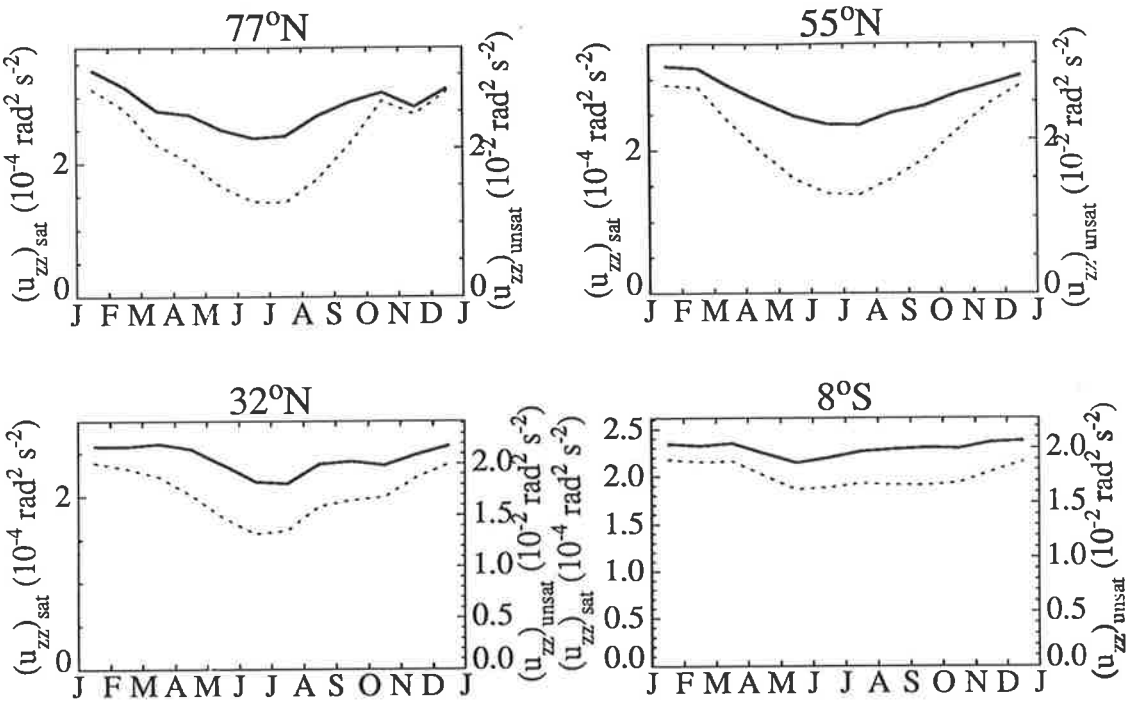

Figure 99: Simulated seasonal cycles in u_{zz}, where the solid line is for the saturated term $u_{zz}^{unsat}(z)$ and the dotted line shows the unsaturated variations. Both terms are evaluated at a height of $60km$, and at latitudes corresponding to the observations of *Hirota* [1984] in Figure 75.

dependence, we use the zonal-mean reference temperatures of *Groves* [1985, 1987]. In evaluating the unsaturated growth terms (82) and (84), the quantity $e^{\int dz/H_\rho}$ was computed by numerically evaluating the integral by accumulative summation in $1km$ steps, from $z_0 = 0$ up to $z = 60km$, using the approximation

$$H_\rho(z) \approx \frac{H(z)}{1 + dH(z)/dz}, \tag{86}$$

where $H(z)$ is the pressure scale height. The $N(z)$ term was evaluated at $60km$, and N_0 was evaluated at $1km$.

7.2.3 Seasonal Variations

The simulated seasonal cycles in $(u_{zz})_{rms}$ for both saturated and unsaturated activity are shown in Figure 99. The saturated variations are shown by the more prominent solid curve, because these should be most relevant in determining the measured variations (see section 6.3.3 and Figure 76). These variations were computed at latitudes corresponding to the observational data of *Hirota* [1984] in Figure 75.

The observed annual variations at 77°N (Thule) and 55°N (Primrose Lake) in Figure 75 are reproduced in Figure 99. Furthermore, the small equinoctial maxima at 32°N (White Sands) are also modelled, although the simulations produce an annual component which is weaker than that observed in Figure 75. The modelled cycle at 8°S does not correspond as well with the Ascension Island results in Figure

75. It was shown in Chapter 6 that the observed semiannual variations near the equator probably result from semiannual transmission of short–wavelength Kelvin waves by the equatorial SAO of the upper–stratospheric zonal wind. Therefore, it is not surprising that this simulation, which incorporates no mean–wind variability, cannot reproduce the observed structure.

One should note that the theoretical estimates presented in Figure 99 are only valid for a measurement of the wave activity at a height of $60km$, whereas, according to the defining formula (72), the $(u_{zz})_{rms}$ results of *Hirota* [1984] are averaged over the 20–65 km height range. It is difficult to incorporate this height–averaging into these theoretical metrics, because m_* also varies with height, so that the relative importance of the saturated and unsaturated wave cycles varies continuously with height. Moreover, the exact m_* variation must be obtained from the observations, which defeats the purpose of the modelling. However, as $2\pi/m_* \approx 10km$ at the uppermost levels near $60km$, the saturated cycles dominate u_{zz} at upper heights, whereas the unsaturated activity has more effect at low altitudes where $2\pi/m_*$ is much smaller. The similarity of both simulated cycles in Figure 99 suggests that the properly combined measure will give much the same seasonal structure.

Figure 100 plots the simulated seasonal variations in $\overline{u'^2}$. Only the unsaturated variations are displayed; the saturated theory predicts uniformly acyclic seasonal behaviour. The two "non–saturated" mechanisms (i.e. wave–amplitude growth with altitude and source effects) should be the appropriate processes in controlling $\overline{u'^2}$ at these heights (see Chapter 6). Here too, the strong high–latitude annual cycle is well reproduced in the simulations, both in phase and in the depth of the variation. Futhermore, the progressive weakening of the annual cycle as one moves equatorward also agrees very well with the observations in Figure 77.

At the equator the simulated variations are weakly semiannual, whereas the data are more strongly semiannual, again due to the modulation of Kelvin–wave activity by the SAO in the background flow. However, note that the variations in the lower height regime in Figure 77 are somewhat acyclic, as simulated here. It is also worth noting that the upper–level meridional–velocity activity found by *Hirota* [1978] was also rather acyclic and flat in nature. Since Kelvin waves oscillate zonally, the meridional oscillations should then be dominated by gravity wave motions, since mixed Rossby–gravity waves are attenuated in the lower stratosphere. Thus, some aspects of the equatorial data seem consistent with the simulated structure

Some key features are not simulated by these simplified calculations. The most noticeable of these is the strong peak in August detected at around 30°N–35°N in Figure 77. Indeed, a second equinoctial peak intensifies around the vernal equinox at lower latitudes, and it is not reproduced either. These

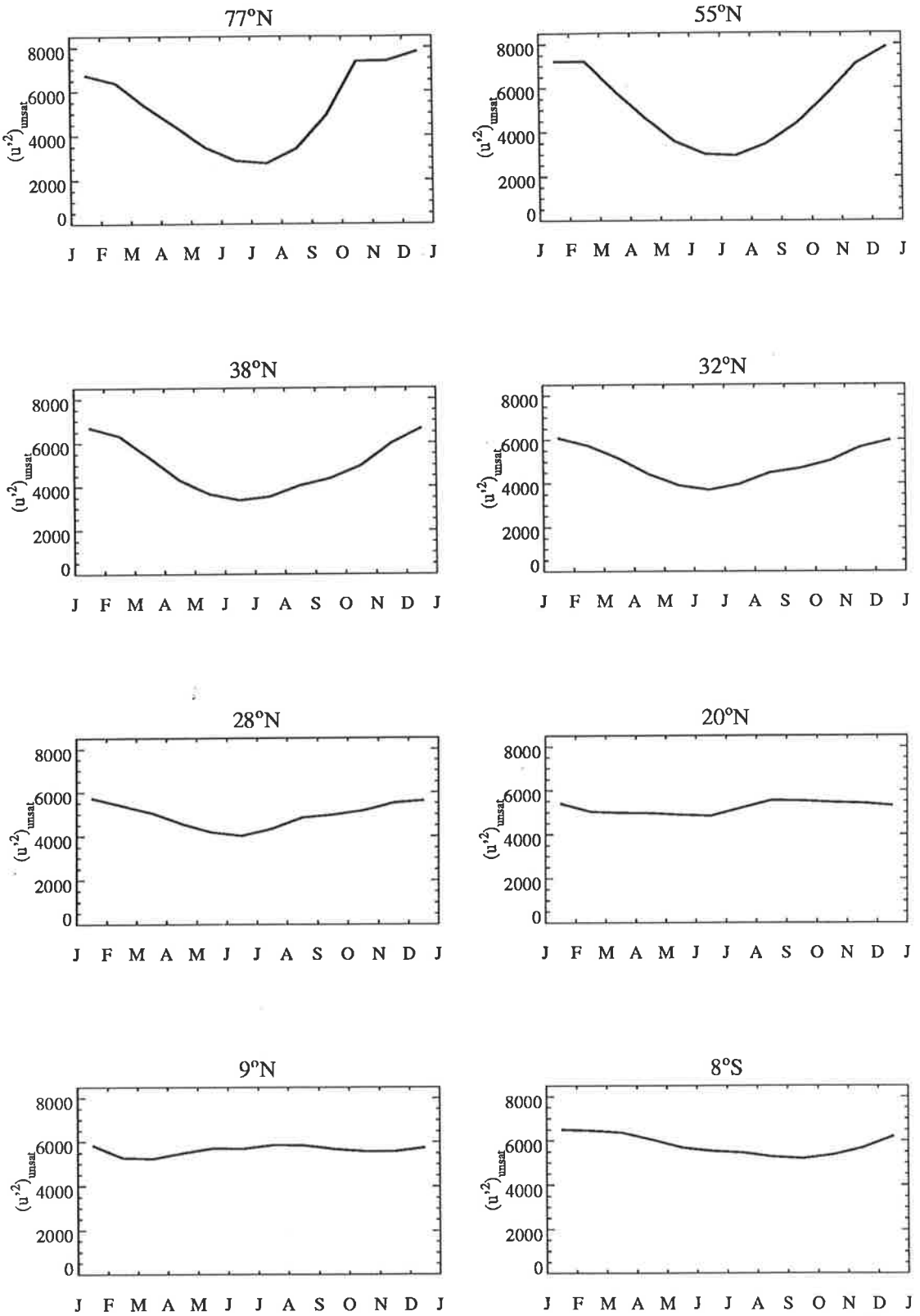

Figure 100: Simulated seasonal cycles in $\overline{u'^2}$, using the exponential amplitude–growth parameterization evaluated at $60km$ for a range of latitudes corresponding to the measurements in Figure 77.

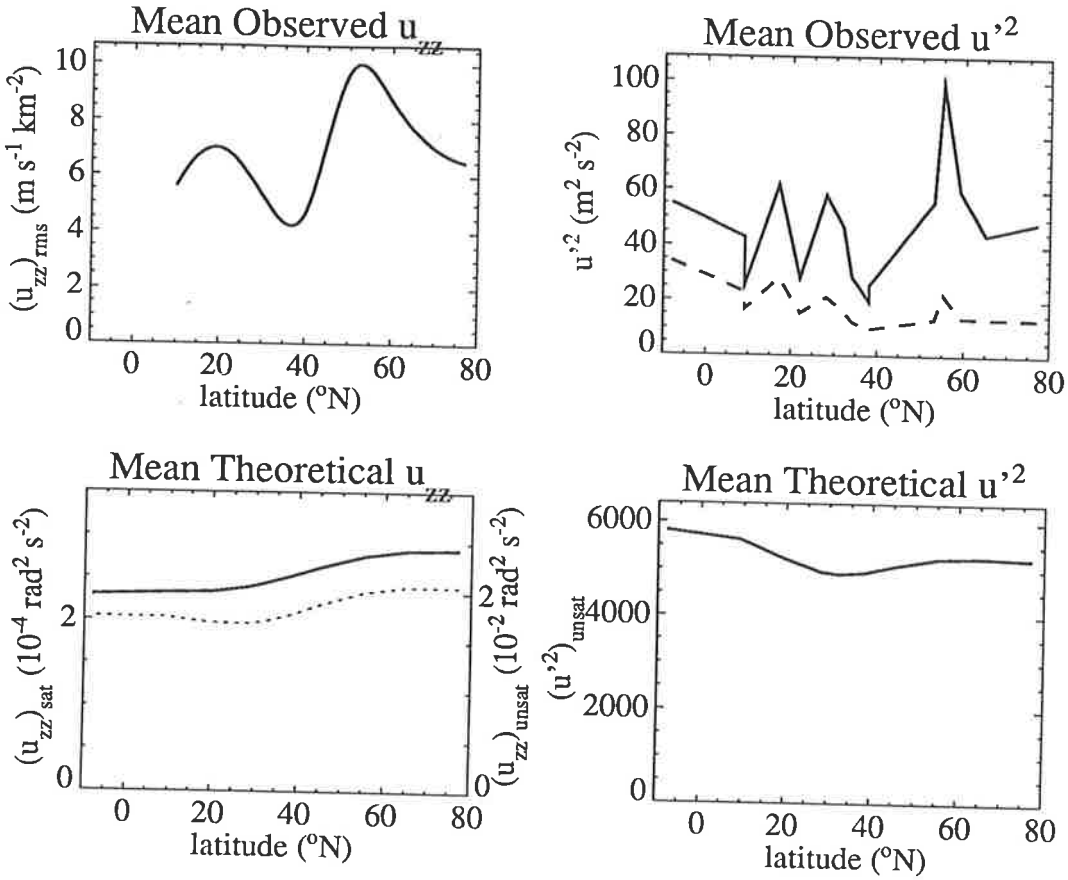

Figure 101: The top graphs show mean values of $(u_{zz})_{rms}$ (adapted from Figure 8 of *Hirota* [1984]) and $\overline{u'^2}$ over two height ranges of 20–40km (dashed curve) and 40–60km (solid curve) from Chapter 6. The data are plotted as a function of observing latitude. Adjacent bottom panels show the corresponding modelled variations.

discrepansies indicate that the features must arise from effects which were ignored in these calculations, such as source effects and/or mean–wind variations. Source effects will tend to produce the same variations at 20–40km and 40–60km, and some of these features, such as the variability in the mean amplitudes between sites in the United States, appear to have this quality (this is investigated further in the following section). Features produced by the local wind structure (e.g., critical level filtering, variable saturation amplitudes) will produce differring structure within the two height ranges. The upper–level structure at the equator certainly fits this criterion, as does the enhanced upper–level equinoctial structure around 30°N.

7.2.4 Latitudinal Variations

The top plots in Figure 101 show annual–mean values of u_{zz}, as measured by *Hirota* [1984], and $\overline{u'^2}$, resulting from the analysis in Chapter 6, plotted as a function of latitude. Simulated variations, based on (82), (84), and (85) evaluated using the model temperatures of *Groves* [1985, 1987], are shown in the

two bottom diagrams. It is immediately apparent that the precise latitudinal distribution of the mean wave activity is not reproduced by the theory for either $(u_{zz})_{rms}$ or $\overline{u'^2}$. However, on closer inspection, one can observe that the ambient variations seem to follow the simulated curves quite well (especially for $\overline{u'^2}$), with strong peaks at around 20°N and 55°N producing the major departures.

Again, the observed variations in u_{zz} and $\overline{u'^2}$, at both 20–40km and 40–60km, are all similar, as was found for the seasonal variations. This is more difficult to resolve in this case, however, because the simulated $(u_{zz})_{sat}$ does not reproduce the observed structure in $(u_{zz})_{rms}$, as it did for the seasonal variations. There are two different explanations which are consistent with the observations.

The first explanation is that the structure may arise from variations in the sensor response to these wind fluctuations at different site (see Chapter 6 and references therein). In this case, the latitudinal differences would be purely an instrumental artifact. This postulate was largely rejected after some consideration in Chapter 6, yet the possibility cannot be entirely discounted.

The second, more likely, possibility is that these peaks arise from latitudinal variations in the intensity of low–level wave–energy production by sources. Recall that an effective test as to whether a feature might be source driven was that the variations at 20–40km and 40–60km should be similar, which is clearly the case here. Source effects were associated earlier with the term u_0, but in terms of the vertical–wavenumber spectrum (29), the effects manifest themselves in a latitudinal variations in m_* at a given height. This will then produce the latitudinal changes in both u_{zz} and $\overline{u'^2}$ when the spectrum is integrated, producing similar variations in both parameters, as occurs in Figure 101.

If this latter interpretation is correct, then one should note that source effects were, for the most part, only secondary in explaining the seasonal variations in wave activity. This then suggests that the dominant gravity–wave source mechanism has an intensity which is rather variable with location, but somewhat invariant in time. Wave production by flow over surface topography would seem to satisfy this criterion very well, as orographic features are spatially varying, but temporally constant. A recent GCM simulation of gravity–wave production and propagation in the middle atmosphere by *Rind et al.* [1988] indeed suggested that mountain waves are the dominant source of gravity–wave momentum flux for the middle atmosphere in the Northern Hemisphere [*Rind et al.*, 1988]. Correlations between rough underlying terrain and increased gravity–wave variance in the lower atmosphere have been reported by *Nastrom et al.* [1987] and *Jasperson et al.* [1990]. Similar correlations were noted amongst the sites studied in chapter 6.

A complete summary of the modelling results from this and the following section is given at the end of this chapter in section 7.4.

7.3 A Numerical Study of Global Gravity–Wave Propagation through the Zonally–Averaged Middle Atmosphere

7.3.1 Introduction

The simple theoretical assessment of seasonal and latitudinal variations in the gravity–wave activity of the upper stratosphere in the previous section proved particularly successful in determining some of the processes which are are important in producing the observed structure. Nevertheless, some features were not reproduced, due to the omission of many important variables such as the mean wind $\bar{U}$ and ground–based gravity–wave phase speeds c. Furthermore, the analysis assumed that the waves propagated straight upwards, whereas inertia gravity waves, which are believed to produce the bulk of the variance at these heights, propagate obliquely (indeed, quasi–horizontally) up through the atmosphere. Consequently, the next logical step is to enact a model which incorporates some of these omitted effects.

Yet gravity–wave amplitudes are not the only wave parameters to have been experimentally measured. For example, measurements of the phase speeds, wavelengths, periods, and amplitudes of single waves in various regions of the atmosphere have been collated, and show some interesting, but as yet unexplained, distributions and interrelationships [see, e.g., *Meek et al.*, 1985*a*; *Reid*, 1986, 1989; *Gardner and Voelz*, 1987; *Manson and Meek*, 1988; *Gardner et al.*, 1989]. Additionally, measurements have been made of the major wave–propagation directions [*Vincent and Fritts*, 1987; *Ebel et al.*, 1987; *Manson and Meek*, 1988; *Eckermann and Vincent*, 1989; see also Chapter 6], which reveal that the waves propagate within a restricted range of azimuths, and this azimuthal distribution varies appreciably with season and location. Anisotropy in azimuthal wave–propagation is known to arise due to critical–level filtering of the wave spectrum as it propagates up through the zonal–wind structure of the intervening atmosphere [*Houghton*, 1978; *Lindzen*, 1981]. However, detailed measurement of azimuthal wave propagation has revealed wave alignments which seem to be more localized than would be expected by critical–level filtering alone [*Vincent and Fritts*, 1987; *Ebel et al.*, 1987; *Manson and Meek*, 1988; *Eckermann and Vincent*, 1989]. It has been suggested that these observations can only be explained fully if there is anisotropic azimuthal launching of waves at their source levels [e.g. *Ebel et al.*, 1987].

In addition to source and critical–level effects, the process of horizontal wave *refraction* is potentially just as important in producing the observed wave propagation azimuths, yet it has received limited attention to date. Spatial variation of the background atmospheric medium causes gravity wave trajectories to change not only in the vertical, as is well–known [*Hines*, 1960], but also produces horizontal refraction

which can significantly modify the azimuthal direction of wave propagation. *Dunkerton and Butchart* [1984] examined the propagation of "intermediate" frequency waves (i.e. $f^2 \ll \omega^2 \ll N^2$) through the stratosphere during a sudden warming. They found that horizontal refraction was a small effect in their simulations. In a subsequent study, however, *Dunkerton* [1984] showed that inertia gravity waves in the winter stratosphere of the Northern Hemisphere can experience considerable horizontal refraction, due mainly to latitudinal shear in the zonal-wind structure.

Despite these promising initial results, the amplitude of these refracted waves was not studied in detail. More detailed subsequent studies of wave propagation by *Schoeberl and Strobel* [1984] and *Schoeberl* [1985] suggested that such refracted waves experience considerable dissipation. This occurs because the amount of horizontal refraction only becomes significant when the vertical group velocity of the wave becomes small, and so the ray takes a long time to propagate vertically. A long vertical transit time, however, means that the wave amplitude becomes more attenuated by infra-red radiative cooling, which produces an exponential decay of the wave's temperature perturbations with time. Using a vertical-wavenumber-dependent radiative-damping scheme described by *Schoeberl et al.* [1983], *Schoeberl et al.* [1983] and *Schoeberl and Strobel* [1984] showed that this damping is so intense that if the intrinsic phase speed of the wave $\mid \mathbf{c} - \bar{\mathbf{u}} \mid \leq 20m\ s^{-1}$ at any stage of its vertical propagation, the wave is so strongly attenuated by radiative cooling that it does not attain saturation amplitude in the mesosphere. This would include virtually all waves which experience any significant horizontal refraction. Furthermore, waves with small vertical group velocities become unstable and saturate at smaller amplitudes than waves with larger group velocities [*Fritts*, 1984; *Fritts and Rastogi*, 1985], so that, once again, refracted waves are attenuated to a greater degree than waves which propagate upwards more rapidly.

Given these findings, a refractive explanation of wave propagation directions seems unlikely. However, *Fels* [1984] demonstrated that the vertical-scale-dependent radiative-cooling rates used by *Schoeberl et al.* [1983] considerably overestimate the attenuation. *Schoeberl et al.* [1983] derived a damping rate proportional to m^2, where m is the vertical wavenumber, whereas *Fels* [1982] found rates proportional to $m^{1/2}$ and m^0 at large m for infra-red cooling by carbon dioxide and ozone, respectively. The two CO_2 schemes are compared in Figure 102, and clearly the discrepansies become very large at large vertical wavenumbers. Such large vertical-wavenumber gravity waves have small vertical group velocities, and thus may undergo apprcciablc horizontal refraction. Therefore one must conclude that the radiative attenuation of horizontally-refracted gravity waves has been significantly overestimated in previous studies. Moreover, the fact that waves undergoing horizontal refraction have smaller saturation amplitudes does not preclude these waves having significant amplitudes higher in the atmosphere. Indeed, the initital

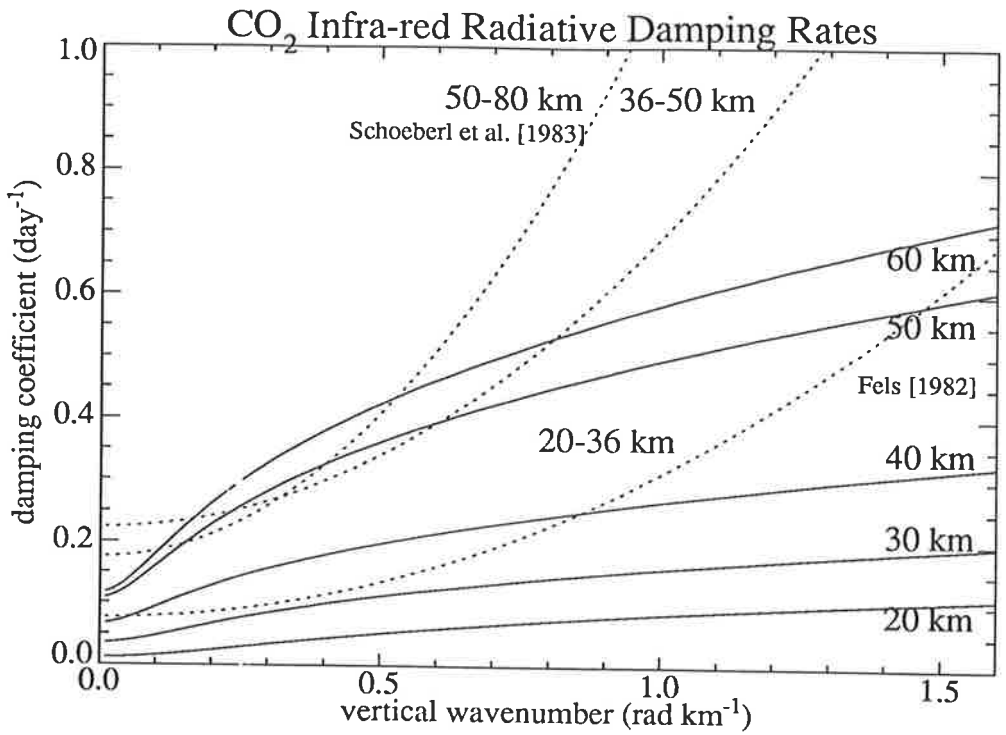

Figure 102: Graph of the vertical scale–dependent CO_2 infra–red radiative damping rates (e^{-1} decay times) computed by *Fels* [1982] (solid curves) and *Schoeberl et al.* [1983] (dotted curves) at different heights in the middle atmosphere. The scheme of *Schoeberl et al.* [1983] is only valid for $0 \leq m \leq 0.2km^{-1}$, and note the large overestimates it gives at large vertical wavenumbers. The *Fels* results were computed using mean temperatures at 35°S in June from *Groves* [1985, 1987].

simulations of *Dunkerton* [1984] showed that most of the wave refraction occurred in the lower stratosphere. Hence, although the wave may have a small saturated amplitude in this region, it can still attain a significant amplitude by the time it reaches the mesosphere, as demonstrated by *Lindzen* [1985].

These objections alone would seem enough to prompt a second look at wave refraction. However, there are other factors favouring wave refraction as a possible explanation of the observations. *Dunkerton* [1984] showed that horizontal refraction was most pronounced for low–frequency inertia gravity waves of large horizontal scale. Observations and theory have revealed that such waves are the largest amplitude motions in the gravity–wave energy spectrum (see section 3.3.3 and references therein), and the experimental wave–alignment measurements detailed earlier are weighted to the largest–amplitude motions in the data. The results of *Dunkerton* [1984] also revealed focussing of refracted wave motions from widely separated source regions into restricted regions of the upper stratosphere. Such focussing effects would also lead to these waves dominating the fluctuations in observational data. Finally, the latitudinal shear in the zonal–wind structure of the Northern Hemisphere winter stratosphere refracts waves meridionally [*Dunkerton*, 1984], and meridional alignments are also a common feature of the observational results [*Vincent and Fritts*, 1987; *Eckermann and Vincent*, 1989; see also chapter 6].

The aim of this study is to cast further light on the physical processes which produce these features in the observations. This is undertaken with the aid of a ray–tracing model of gravity–wave propagation through realistic wind and temperatures in the middle atmosphere.

7.3.2 Theory

As with any wave–propagation phenomenon, the effects can be investigated using ray–tracing techniques. Lucid developments of the ray–tracing equations for gravity–wave motions in a background flow are given by *Lighthill* [1978] and *Jones* [1969]. Defining $\mathbf{x} = (x, y, z) = x_i$ (i = 1,2,3) as the spatial vector (in conventional Cartesian coordinates), $\mathbf{k} = (k, l, m) = k_i$ as the total wavenumber vector, $\bar{\mathbf{u}} = (\bar{u}, \bar{v}, 0) = \bar{u}_i$ as the mean horizontal–wind vector, and $\mathbf{c} = (c_x, c_y, 0) = c_i$ as the ground–based horizontal phase speed vector of the wave (which is always parallel to the horizontal component of $\mathbf{k}$), then the gravity wave ray tracing equations have the following form [see, e.g., *Lighthill*, 1978]

$$\frac{dx_i}{dt} = \bar{u}_i + \frac{\partial \omega}{\partial k_i} \quad (i = 1, 2, 3), \tag{87}$$

$$\frac{dk_i}{dt} = \sum_{j=1}^{3} \left(-k_j \frac{\partial \bar{u}_j}{\partial x_i} \right) - \frac{\partial \omega}{\partial x_i} \quad (i = 1, 2, 3), \tag{88}$$

where

d/dt is the temporal rate of change along the ray,

ω $= \mathbf{k}.(\mathbf{c} - \bar{\mathbf{u}}) = \Omega - \mathbf{k}.\bar{\mathbf{u}}$ is the intrinsic wave frequency, and

Ω $= \mathbf{k}.\mathbf{c}$ is the ground–based wave frequency.

Equation (87) governs the velocity of the gravity–wave packet along its ray path, and consists of a simple vector sum of the mean wind velocity ($\bar{u}_i$), which merely advects the packet, and the group velocity of the wave ($\partial\omega/\partial k_i$). Equation (88) describes the *refraction* of the wave due to changes in the background atmospheric medium through which the wave propagates. This includes refraction due to a spatially–varying background flow ($\sum_{j=1}^{3} -k_j \ \partial\bar{u}_j/\partial x_i$) and spatially–varying fluid characteristics which affect the wave through its dispersion relation ($\partial\omega/\partial x_i$).

Using these ray–tracing equations, one can show that $d\Omega/dt = 0$ [*Lighthill*, 1978], so that

$$\Omega = \mathbf{k}.\mathbf{c} = kc_x + lc_y = \text{constant along a ray.} \tag{89}$$

This is the same frequency invariance which arises in optics when one considers the propagation of light through refracting media.

Subsequent sections will focus on large–scale low–frequency gravity wave motions. The simplified dispersion relation appropriate for such waves is

$$\omega^2 = f^2 + \frac{N^2\left(k^2+l^2\right)}{m^2}, \tag{90}$$

where f is the Coriolis parameter or inertial frequency and N is the Brunt-Väisäla frequency, such that $f^2 < \omega^2 < N^2$.

Using (90), the ray–tracing equations (87) and (88) become, for horizontally–constant N [e.g., *Dunkerton*, 1984];

$$\frac{dx}{dt} = \bar{u} + \frac{kN^2}{\omega m^2}, \tag{91}$$

$$\frac{dy}{dt} = \bar{v} + \frac{lN^2}{\omega m^2}, \tag{92}$$

$$\frac{dz}{dt} = -\frac{N^2\left(k^2+l^2\right)}{\omega m^3}, \tag{93}$$

$$\frac{dk}{dt} = -k\frac{\partial \bar{u}}{\partial x} - l\frac{\partial \bar{v}}{\partial x}, \tag{94}$$

$$\frac{dl}{dt} = -k\frac{\partial \bar{u}}{\partial y} - l\frac{\partial \bar{v}}{\partial y} - \frac{f}{\omega}\frac{df}{dy}, \tag{95}$$

$$\frac{dm}{dt} = -k\frac{\partial \bar{u}}{\partial z} - l\frac{\partial \bar{v}}{\partial z} - \frac{\omega^2 - f^2}{\omega N}\frac{dN}{dz}, \tag{96}$$

Since m can be calculated directly from the dispersion relation (90), the refraction equation (96) is not necessary. However, separate determinations of m using both equations served as a useful consistency check when these ray–tracing equations were computed in tracing gravity–wave propagation paths.

The amplitude of a propagating wave packet is governed by the wave action conservation equation [*Bretherton and Garrett*, 1968; *Andrews and McIntyre*, 1978], which has the following form for non–transient, unsaturated wave amplitudes (see chapter 2);

$$\sum_{j=1}^{3} \frac{\partial}{\partial x_j}\left(A\frac{dx_j}{dt}\right) = 0, \tag{97}$$

where $A = E/\omega$ is the wave action density, and E is the wave–energy density.

Using the divergence theorem and (97), this can be simplified by considering only vertical variability thus [see, e.g., *Lighthill*, 1978];

$$A\frac{\partial \omega}{\partial m} = \text{constant along a ray.} \tag{98}$$

This equation states that the vertical wave–action flux is conserved along a ray, and is analagous to the WKB solution for the unsaturated gravity–wave amplitude (27) [*Lindzen*, 1981; *Schoeberl*, 1985].

Attempts were made at incorporating latitudinal variability into the action equation by expressing the action equation in ray–tracing form

$$\frac{dA}{dt} = -A\left(\frac{d\hat{c_{gy}}}{dy} + \frac{d\hat{c_{gz}}}{dz}\right), \tag{99}$$

and forward-stepping it in time, as for (91)-(95), where $c_{\hat{gy}} = dy/dt$ and $c_{\hat{gz}} = dz/dt$. However, $dc_{\hat{gy}}/dy$ becomes singular whenever $l = 0$. This can be crudely explained by noting that when $l = 0$, $c_{\hat{gy}}$ equals zero, and so the latitudinal displacement dy also equals zero, hence the singularity. This also occurs in the vertical when m nears zero, and corresponds to the wave reaching a critical level; however, no such clear physical interpretation exists for this latitudinal singularity. Indeed, it seems likely that the effect might be purely computational, since if one were to rotate the coordinate axes through, say, 45°, it is difficult to see that the singularity can persist, since a component of the zonal displacement dx and zonal wavenumber k is resolved on each axis. Indeed, it appears that this type of method was used by *Brasseur et al.* [1990] in solving (99) for Rossby wave propagation through the middle atmosphere. Yet if this interpretation is correct and one does need to continually monitor and rotate the coordinate axes to ensure that this numerical singularity never arose, this would involve a considerable upgrading of the model algorithm. Due to the uncertainties, in this initial study we consider only the vertical variations, and leave consideration of the latitudinal effects for subsequent study.

7.3.3 Numerical Ray Tracing Model

To investigate gravity-wave propagation and refraction within a realistic background atmosphere, a numerical ray-tracing model was developed. An updated version of the zonal-mean reference atmosphere model of *Groves* [1985, 1987] was used to specify a realistic background atmosphere in any given month over most of the earth. The great advantage that the *Groves* [1985, 1987] model has for ray-tracing purposes is that, for a given month, the entire zonal-mean pressure scale-height structure of the atmosphere, $H(\theta, z)$, is represented by a continuous polynomial of the following form

$$H^{-1}(\theta, z) = \sum_{n=1}^{11} \sum_{s=1}^{9} C_{n,s} (sin\theta)^{s-1} \zeta^{n-1}, \tag{100}$$

where

θ is the latitude (negative in the Southern Hemisphere),

$\zeta = (z - 40)/40$ is a normalized altitude,

z is the true altitude (in km), and

$C_{n,s}$ are the polynomial coefficients that model the atmospheric structure.

From this structure, one can derive similar analytical, artificially-continuous relations for temperature $T(\theta, z)$ and geostrophic zonal-wind $\bar{u}(\theta, z)$, and all their spatial derivatives. If a discretely-sampled reference atmosphere was used, one would get sudden jumps in background parameters, which would

make accurate tracing of ray paths difficult. The continuous polynomial representation of *Groves* [1985, 1987], on the other hand, avoids such discontinuities, and so is ideal for ray–tracing simulations.

However, one disadvantage of the *Groves* [1985, 1987] model is that geostrophic winds cannot be determined equatorward of $\pm 10^{\circ}$ in latitude or poleward of $\pm 80^{\circ}$ in latitude. Rays which travel into these ranges cannot be traced further and the trace must be terminated, so that cross–polar and cross-equatorial propagation is not simulated. Furthermore, questions exist as to the accuracy of these geostrophic winds in the Northern Hemisphere winter stratosphere [*Elson*, 1986; *Boville*, 1987]. Indeed, inspection of the mean–wind plots in chapter 6 show that ageostrophic winds certainly occur in the winter stratosphere. Additionally, strong planetary–wave activity occurs at these times [*Hirota et al.*, 1983; *Plumb*, 1989], which the zonal–mean atmospheric model does not represent.

Within this background structure, the model launches a wave from a specified starting location (ϕ_0, θ_0, z_0) over the globe, with predefined values of its total horizontal wavenumber $K_0^{tot} = (k_0^2 + l_0^2)^{1/2}$, total horizontal ground–based phase speed $c_0^{tot} = (c_{x0}^2 + c_{y0}^2)^{1/2}$, and azimuth direction φ_0. If $\omega > 0$, the vertical wavenumber m is set negative so that the wave propagates upwards in energy [*Gossard and Hooke*, 1975]. If, however, $\omega < 0$, one has a situation where the ground–based horizontal phase speed $\mathbf{c}$ and the intrinsic horizontal phase speed $\mathbf{c} - \bar{\mathbf{u}}$ are in opposite directions (see Chapter 5 and Figure 67). and in this situation m must be set positive [see, e.g., *Pitteway and Hines*, 1965]. The ray–tracing equations (91)–(95) are then successively incremented in time with some step interval δt. The vertical wavenumber m is updated at each time increment from the dispersion relation (90), using local values of $N(\theta, z)$ and $f(\theta)$. Latitudinal variations in $N(\theta, z)$, which are ignored in equation (95), produce negligible alterations to ray paths when included using this model atmosphere.

Francis [1972] demonstrated that the ray paths of internal gravity waves are refracted around the Earth, due to the spherically symmetric nature of the Earth's gravitational field, and thus follow its spherical curvature. This means that a "flat earth" coordinate system can be used in tracing gravity wave ray paths, such that the horizontal ray displacements x and y can be interpreted directly as horizontal distances or arclengths around the Earth's surface. As a result, ray displacements at each time step, $\delta x, \delta y$, and δz, were additively accumulated into total polar coordinate displacements (r, θ, ϕ) using the following simple geometrical conversions;

$$\phi_{t+\delta t} = \phi_t + \frac{\delta x}{r_t cos\theta_t}, \tag{101}$$

$$\theta_{t+\delta t} = \theta_t + \frac{\delta y}{r_t}, \tag{102}$$

$$r_{t+\delta t} = r_t + \delta z, \tag{103}$$

such that $r_0 = R_E + z_0$, where R_E is the radius of the earth.

The quantities

$$D = \int \frac{2dt}{\tau(\theta, z)}, \tag{104}$$

$$G = \int \frac{dz}{H_\rho(\theta, z)}, \tag{105}$$

are similarly updated at each time step by accumulative summation. The term $\tau(\theta, z)$ is the local exponential decay time of the temperature perturbations due to infra-red radiative cooling, and is calculated using the vertical-scale-dependent analytical parameterizations for carbon dioxide and ozone of *Fels* [1982] at the local background temperature $T(\theta, z)$. More complex parameterizations were available which incorporate wave-frequency dependence as well [*Zhu and Holton*, 1986], but were not used as they are not as easily implemented and do not differ greatly from the results of *Fels* [1982]. As *Fels'* parameterizations do not extend below $20km$ in altitude, radiative damping is not applied in this region, but as the damping in this region is considerably weaker than in the 20-60 km height range, this is not a serious omission. The term $H_\rho(\theta, z)$ is the local density scale height, and is calculated from the pressure scale height using equation (86). Equation (105) describes the growth of wave variance due to the decrease of atmospheric density with height. The combined altitude growth and radiative attenuation at any point on the ray path is given by the instantaneous value of e^{-D+G}.

Stability of the wave is checked at each time step by analyzing the peak horizontal-velocity amplitude of the wave parallel to its direction of motion, which we shall denote here by U'. The simple scheme of *Fritts and Rastogi* [1985] is used, where the saturated peak amplitude of the wave U'_{sat} is given by

$$U'_{sat} = a \frac{N(\theta, z)}{m}, \tag{106}$$

$$a = \frac{(\gamma^2 + 4\gamma)^{1/2} - \gamma}{2},$$

$$\gamma = 4(\omega^2/f^2 - 1),$$

If the wave amplitude U' exceeds U'_{sat} at any time, it is scaled back to this saturation value, and the vertical flux of wave action (98) is recalculated accordingly.

Critical levels are accounted for in two ways. Firstly, following *Schoeberl* [1985], if the vertical group speed $\mid dz/dt \mid < 1cm\ s^{-1}$, the wave is considered to have "stalled" at a critical level, and the trace is terminated. Secondly, if the wave amplitude is attenuated to one tenth of its starting amplitude, the ray is considered to have dissipated at a critical level, and again the trace is stopped.

If the ray reaches an altitude of $60km$, the trace is stopped, and the final wave displacement and wavenumber vector are calculated. The final horizontal-velocity amplitude U'_f of the wave is calculated

from the vertical flux of wave action, possibly rescaled by saturation and taking into account the altitude growth e^G and radiative attenuation e^{-D} of U'^2. $U_f'^2$ is then multiplied by $1+(f/\omega)^2$, which accounts for the increase in wave kinetic energy at the expense of its potential energy at near-inertial frequencies [see, e.g., *Dunkerton*, 1984]; see also equation (20).

7.3.4 Single Wave Simulations

In this section, results of tracing individual gravity waves through the zonal–mean atmosphere are presented. In these examples, one successively launches a given gravity wave from a range of equispaced latitudes, and the ray paths that result are then plotted, following *Dunkerton* [1984]. This enables comparison with the model results of *Dunkerton* [1984], and also helps illustrate some of the important physical effects which arise, and which may be important in the real atmosphere.

Dunkerton [1984] traced gravity–wave ray paths through the zonally–averaged stratosphere of the Northern Hemisphere during January (winter). Figure 103 shows the three–dimensional ray–paths of a gravity wave with an initial horizontal wavelength $2\pi/K_0^{tot}$ of $400km$ and a ground–based phase speed $c_0^{tot} = 25m\ s^{-1}$ directed westward ($\varphi_0 = 180°$), which is launched progressively in 2° latitude steps from a height of $10km$ in Northern Hemisphere during January with a horizontal–velocity amplitude of $0.5m\ s^{-1}$. The latitude–height zonal/geostrophic wind contours are plotted on the left of the diagram, and latitude–height projections of the ray paths are plotted with dotted lines on the adjacent latitude–height plane, to allow comparison with similar wind and ray path plots presented by *Dunkerton* [1984]. The final (ϕ,θ) positions of the gravity waves at $60km$ are joined with a dotted line, which is projected to the surface, where at each of these points a wave vector is plotted whose direction indicates the final horizontal wavevector direction of the wave[2], and whose length is proportional to the final horizontal–velocity amplitude of the wave.

The latitude–height ray–path structure in Figure 103 is similar to that obtained by *Dunkerton* [1984]. While all the waves were launched with zonal (westward) propagation at $10km$, those waves at low latitudes have been refracted poleward by the strong latitudinal shear in the zonal wind, according to (95), and are almost meridionally aligned at $60km$. Note, however, that the amplitudes of these refracted waves are not strongly attenuated relative to the other waves; indeed, r.m.s. wave amplitudes $(\overline{u'^2}+\overline{v'^2})^{1/2}$ at $60km$ vary fairly smoothly from $\sim 14.7m\ s^{-1}$ at 76°N to around $18.4m\ s^{-1}$ at 20°N.

[2] One should be aware that these ray paths and wave–vector directions are distorted somewhat because a given longitudinal displacement corresponds to a different absolute displacement distance at different latitudes, due to sphericity. On these rectangular plots, this tends to dilate the zonal variations at high latitudes relative to similar variations at low latitudes, since zonal displacements are plotted in degrees of longitude. The wave vector length, however, is corrected for this effect.

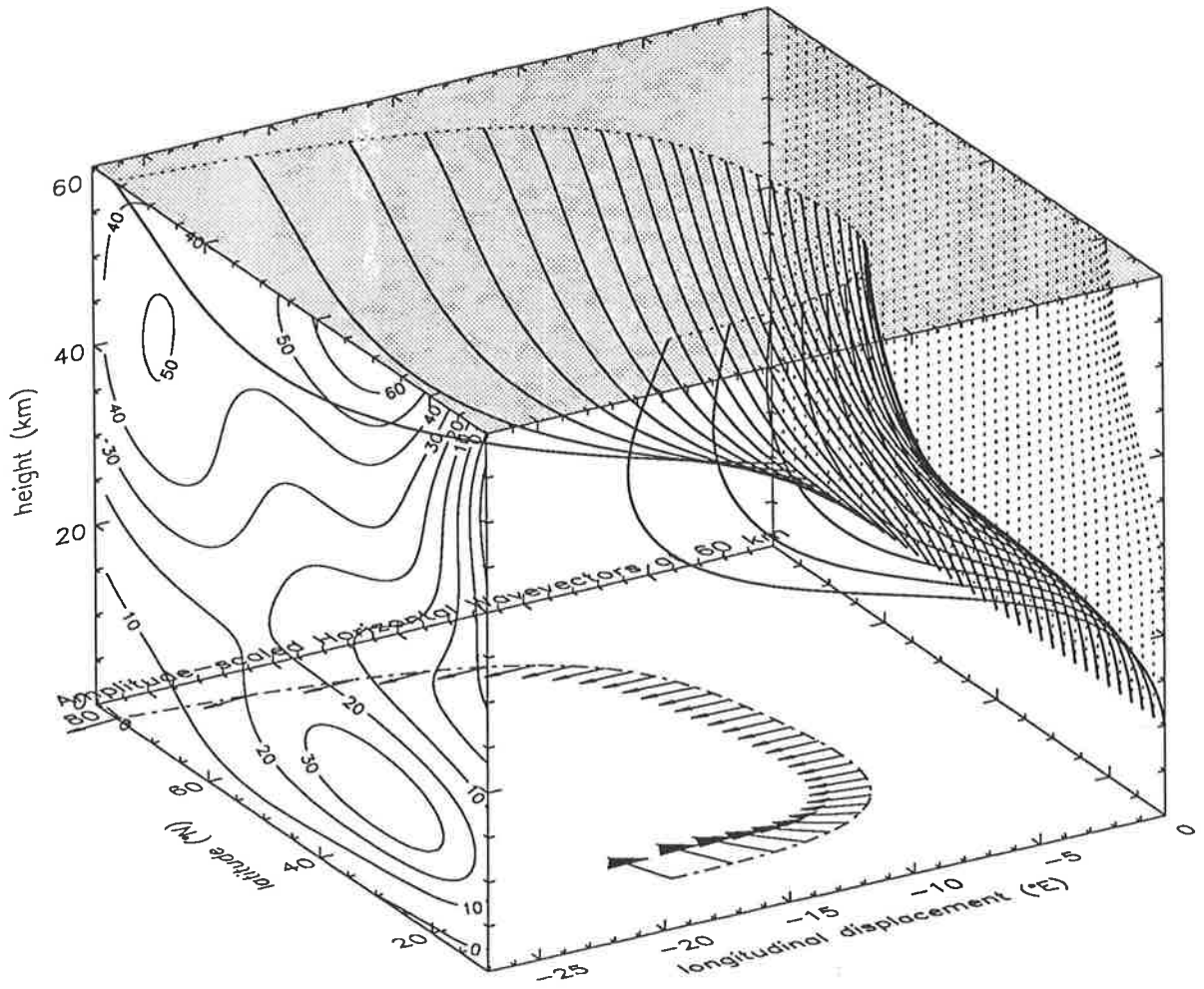

Figure 103: Three-dimensional gravity-wave ray paths through the zonal-mean middle atmosphere of the Northern Hemisphere during January, with the longitude, latitude, and altitude directions indicated on the plot axes. Zonal-wind contours are plotted on the left-side latitude-height plane, where the contour labels are in $m\ s^{-1}$, and positive values indicate eastward winds. On the opposing latitude-height plane the projections of these ray paths are plotted with dotted curves. The final longitude and latitude of these rays at $60km$ are connected with a dotted curve, which is projected to ground level, where at each point the final horizontal wave-vector directions are plotted with lengths proportional to their final horizontal-velocity amplitude.

However, choosing $c_0^{tot} = 0$ produces ray paths which reach low-level critical levels at the highest and lowest latitudes; the first few ray paths at these end-latitudes which do penetrate to $60km$ all overlay one another at upper levels, thus forming *caustics* which violate the slowly-varying ray-tracing formulation, giving unreliable results [see, e.g., *Dunkerton*, 1984]. However, the amplitudes of these waves are very small, since the formation of caustics in this model is invariably associated with waves which are near a critical level (ω near f), and such waves become unstable at very small amplitudes according to (106). Thus, unreliable ray-tracing at or near caustics does not affect any combined results, because these waves have negligible amplitude.

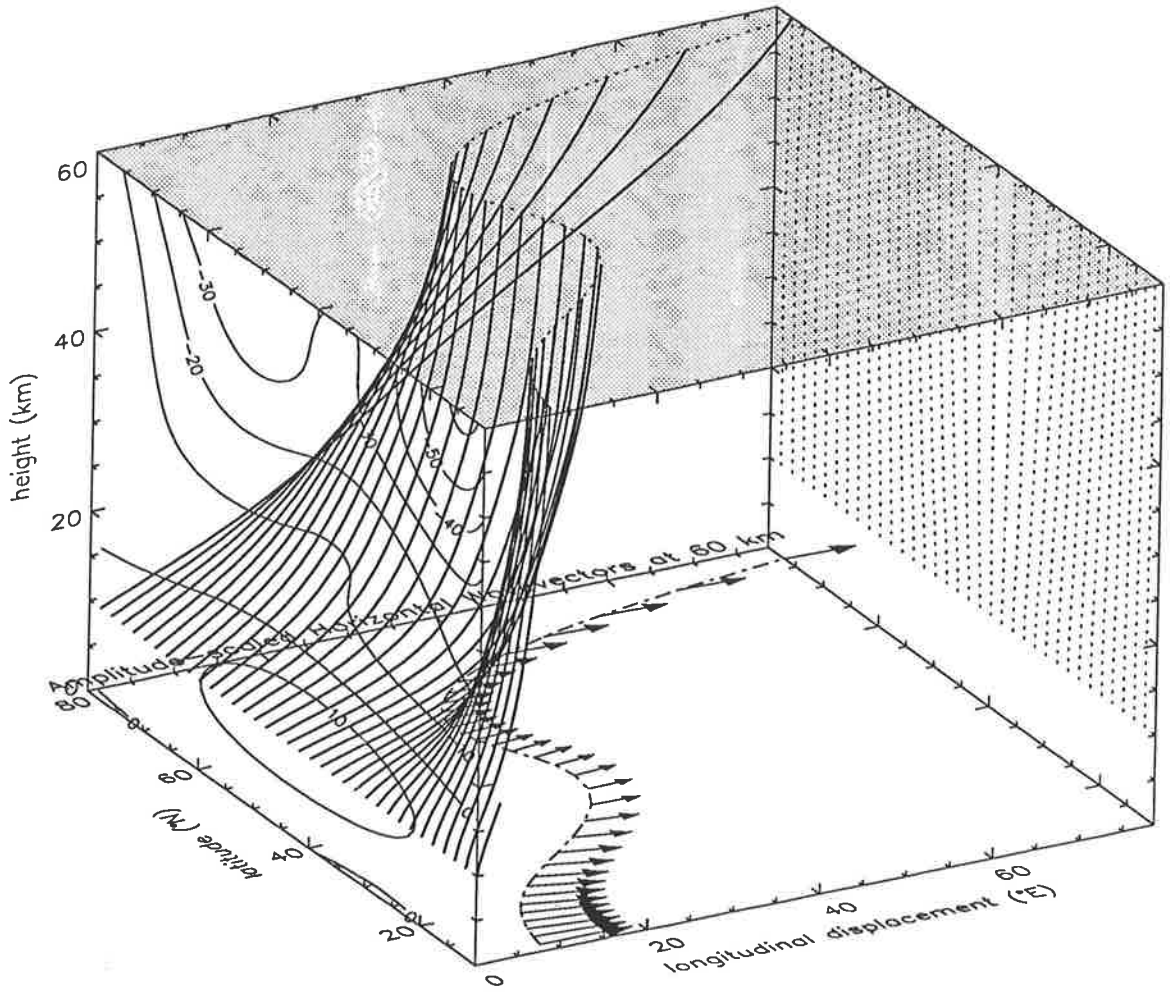

Figure 104: As for Figure 103, but for a gravity wave, with initial parameters $K_0^{tot} = 2\pi\ (400km)^{-1}$, $c_0^{tot} = 30m\ s^{-1}$, and $\varphi_0 = 0°$, propagating through the zonally–averaged middle atmosphere of the Northern Hemisphere during June.

While this example gives a good initial picture of the global propagation of such waves, intense planetary–wave activity occurs in the stratosphere during winter, which produces longitudinal zonal–wind gradients $\partial\bar{u}/\partial x$ which also affect ray paths [*Dunkerton and Butchart*, 1984; *Dunkerton*, 1984; *Schoeberl*, 1985]. The zonally–averaged atmosphere is a better representation of the actual atmosphere during summer, when planetary waves are excluded by critical–level filtering. Figure 104 plots ray paths in the Northern Hemisphere during June, for a gravity wave for which $K_0^{tot} = 2\pi(400km)^{-1}$, $c_0^{tot} = 30m\ s^{-1}$, and $\varphi_0 = 0°$ (eastward). Note that the refraction effects here are smaller, due to smaller lateral wind shears. Similar results arise in summer (January) in the Southern Hemisphere.

Furthermore, planetary–wave amplitudes are also weak during mid–winter in the Southern Hemisphere [*Hirota et al.*, 1983; *Plumb*, 1989], so that here too the zonally–averaged atmosphere serves as a good approximation to the full three–dimensional structure. Figure 105 plots ray paths in the Southern Hemi-

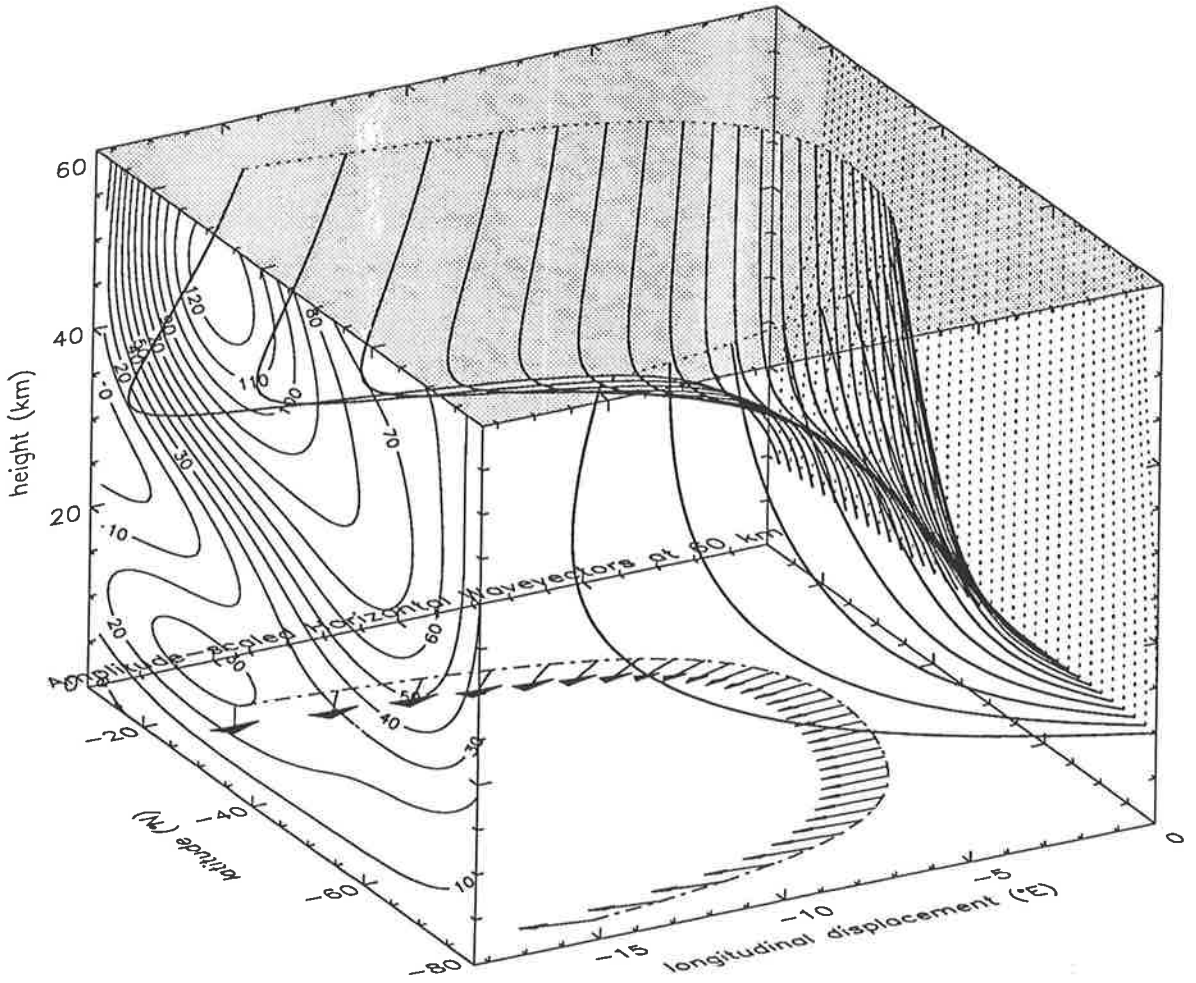

Figure 105: As for Figure 103, but for a gravity wave, with initial parameters $K_0^{tot} = 2\pi\ (400km)^{-1}$, $c_0^{tot} = 15m\ s^{-1}$, and $\varphi_0 = 180°$, propagating through the zonally–averaged middle atmosphere of the Southern Hemisphere during June.

sphere during June for a gravity wave with initial parameters of $K_0^{tot} = 2\pi(400km)^{-1}$, $c_0^{tot} = 15m\ s^{-1}$, and $\varphi_0 = 180°$ (i.e. westward). The low–latitude latitudinal shear in the zonal wind, noted in Figure 103 in the Northern winter, is even stronger in the Southern Hemisphere during winter and produces strong refractive focussing of waves at low latitudes in towards the core of the stratospheric zonal–wind jet. Again, the amplitudes of these waves are similar to those of less–refracted waves at other latitudes.

Analysis of the Refraction Process

Some analysis of these results will prove useful here. Firstly, note from (94) that the zonal component k of the total wavenumber stays constant since there are no zonal variations, and l increases/decreases according to (95), so that the total horizontal wavenumber $K^{tot} = (k^2 + l^2)^{1/2}$ varies in magnitude. This is an important effect, because K^{tot} is generally treated as an invariant for gravity waves. However, it

is the ground-based wave frequency Ω that is a constant, where $\Omega = K^{tot}c^{tot}$, according to (89). This immediately indicates that the ground-based horizontal phase speed c^{tot} varies inveresly with K^{tot} so that Ω remains constant.

The changes of K^{tot} and c^{tot} due to refraction are particularly important, as these parameters are believed by many workers to remain relatively constant as the waves propagate upwards from the lower atmosphere through the middle atmosphere. One also requires knowledge of representative values of K^{tot} and c^{tot} produced by low-level sources to model wave-induced mean-flow accelerations at mesospheric heights [see, e.g., *Holton*, 1982, 1983]. However, phase speeds of gravity waves generated in the troposphere are similar to the mean-wind speeds at the source region [*Gossard and Hooke*, 1975; *Atkinson*, 1981; *Reid*, 1989], which rarely exceed 30–40$m\ s^{-1}$, yet in the middle atmosphere a broad range of phase-speeds arise, many of which exceed[3] 100$m\ s^{-1}$, as well as a broad range of horizontal wavelengths [*Reid*, 1986, 1989; *Reid and Vincent*, 1987*b*; *Meek and Manson*, 1988].

Complex numerical simulations of dissipation and saturation of transient gravity waves [*Grimshaw*, 1975; *Fritts and Dunkerton*, 1984] have shown that c^{tot} can be increased by a complex interaction between the dissipating wave and the mean flow which was labelled "self acceleration", and could be important in altering the phase-velocity distribution of the wave field. Similarly, geostrophic adjustment of the mean flow to wave forcing can also change the horizontal-wavelength and phase-speed distribution of the wave field [*Zhu and Holton*, 1987]. However, these processes alter c^{tot} during and after the wave has saturated, whereas "refractive acceleration" is a natural consequence of wave propagation, and can occur before the wave breaks. When the wave does eventually dissipate, it will accelerate the mean flow towards the direction and phase speed that the wave has aquired on reaching this breaking altitude. As such, this refraction process is potentially very important.

7.3.5 Many-Ray Climatological Simulation

Following these promising initial results, and to further investigate climatological trends in global gravity-wave activity and propagation, a detailed multi-wave simulation was undertaken. Rays were individually traced in 1° latitude steps at starting latitudes θ_0 from 10° to 80° in both hemispheres. Simulations were performed for all months of the year using the *Groves* [1985, 1987] reference atmosphere model. The details of this multi-wave model simulation will now be described.

A crude wave "source spectrum"[4] was simulated by choosing a range of different initial horizontal

[3] some of these large values may be trace speeds which arise from only resolving a component of the motion
[4] it is not a true spectrum because the waves do not mutually interact

wavelengths $(\lambda_x^{tot})_0 = 2\pi/K_0^{tot}$, ground-based horizontal phase speeds c_0^{tot}, and wave azimuths φ_0. The following initial ray parameters were adopted,

$$\begin{aligned} (\lambda_x^{tot})_0 &= 200, 400, 800km \\ c_0^{tot} &= 0, 5, 15, 35m\ s^{-1} \\ \varphi_0 &= 0°, 45°, 90°, 135°, 180°, 215°, 270°, 315° \end{aligned}$$

which gives a total of 96 different rays in the "spectrum". The choice of these parameters was based on the premise that only those "source effects" for which there is some experimental support should be built into the model.

Available measurements of ground-based wave phase velocities in the lower atmosphere reveal values similar in magnitude to typical mean wind speeds [see, e.g., *Gossard and Hooke*, 1975; *Atkinson*, 1981; *Reid*, 1989]. There also appears to be strong evidence from modelling and observations that mountains are one of the more intense sources of gravity-wave variance [see, e.g., *Miyahara et al.*, 1986; *Nastrom et al.*, 1987; *Rind et al.*, 1988; *Jasperson et al.*, 1990], which produce waves with phase speeds near zero. We therefore choose phase velocities of 0, 5, 15, and $35m\ s^{-1}$, which is similar to the Gaussian phase speed distributions adopted in some previous models [see, e.g., *Matsuno*, 1982].

In choosing horizontal wavelengths, the best guide comes from airborne studies of horizontal wavenumber spectra, which show that the small wavenumbers (large wavelengths) possess the largest variance (see section 3.3.3 and references therein). However, as discussed in section 3.3.3, it is inclear just how much of this variance is due to gravity waves, as quasi-two-dimensional turbulence may also contribute significantly to the variance. Nevertheless, theory predicts a similarly shaped spectrum of gravity waves [see, e.g., *VanZandt*, 1982, 1985], and similar spectral measurements in the mesosphere, where a gravity-wave interpretation is accepted, also have the same "red" nature [*Fritts et al.*, 1989; *Kwon et al.*, 1990]. The lower-atmospheric spectra also show that horizontal wavelengths ~1000-3000 km are in an enstrophy-cascading regime of geostrophic turbulence [see, e.g., *Nastrom and Gage*, 1985], so that horizontal gravity wave scales > 1000 km are probably unlikely. On this evidence, we choose wavelengths of 200, 400, and 800 km, large scales which should be the most important as far as the variance is concerned. These values are within the range of measured values in the lower-atmosphere as collated by *Reid* [1989].

It is clear that most of the wave energy in the middle atmosphere originates from the troposphere [see, e.g., *Thompson*, 1978; *Fritts and Chou*, 1987; *Kitamura and Hirota*, 1989], but tropospheric studies reveal wave production occurs at a range of heights in the troposphere (see results in section 4.3 and references therein). Therefore we assume a tropospheric "oven" wherein the waves are produced, and all

eventually emerge at the tropopause "lid" to propagate into the middle atmosphere. Consequently, each ray was launched at an altitude $z_0 = 10km$, which is meant to coincide very roughly with the tropopause. This emergent "spectrum" is taken to be azimuthally isotropic, since there is no firm evidence to suggest that these emergent tropospheric gravity waves have any preferred propagation directions. Furthermore, evidence of low–level seasonal and geographical variations in the wave activity is sketchy at best, and so all rays were launched with the same starting amplitude U_0' of 0.5 $m\ s^{-1}$, which is of the order of mean observed amplitudes at this height [see, e.g., *Fritts et al.*, 1988*a*; *VanZandt et al.*, 1990; see also section 4.3].

This same "source spectrum" was used at all latitudes and in all months of the year. Note that there is no seasonal, geographical, or "intra–spectral" variability in wave amplitudes or wave azimuths built into the model, so that any such variability that subsequently arises cannot be a source effect, but rather arises from propagation through the middle atmosphere.

As the background atmosphere used has no zonal variability, there was no need to launch waves at different longitudes. However, to maintain a uniform number density of launched waves over the earth's surface area, ray counts needed to be weighted according to $\cos\theta_0$, in order to account for the reduction in circumference of circles of longitude as one moves to more poleward latitudes. Therefore, for a given ray i, its "sphericity weight" W^i was defined as

$$W^i = \frac{\cos\theta^i_{z=10km}}{\cos\theta^i_{z=60km}}, \tag{107}$$

and were used to calculate weighted means.

7.3.6 Wave Amplitudes at $60km$

Seasonal and Latitudinal Variations

Figure 106 shows shaded contours of mean wave activity at $60km$ as a function of month and latitude. The activity hereafter is characterized by the r.m.s. horizontal–velocity amplitude of the wave, taking into acccount the elliptical polarization which arises as ω nears f. Averaging was performed within 5° latitude bins for each month. The weighted ray counts $\overline{C}$ in a given month and latitude interval were calculated according to

$$\overline{C} = \sum_{i=1}^{N} W^i U'^i_{z=30km}, \tag{108}$$

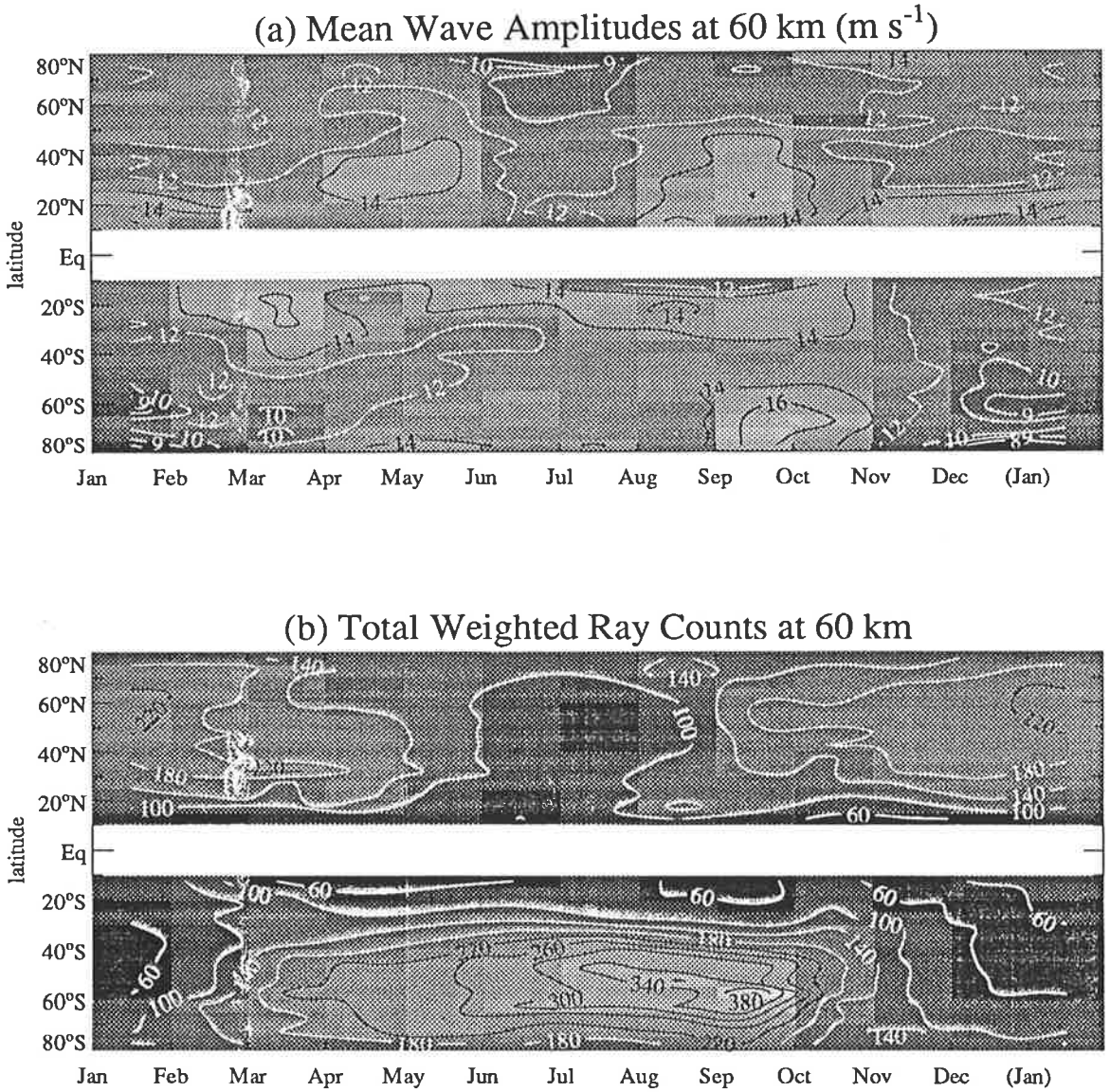

Figure 106: Latitude–time contour plots of (a) the sphericity–weighted mean wave amplitudes, and (b) total sphericity–weighted ray counts, both at a height of $60km$. Amplitude contour labels are in $m\ s^{-1}$.

and final results in Figure 106 were divided by $15m\ s^{-1}$ to normalize the weighting effect of the wave amplitude. Mean wave amplitudes $\overline{U'}$ were computed as a weighted mean

$$\overline{U'} = \frac{\overline{C}}{\sum_{i=1}^{N} W^i}. \tag{109}$$

Several seasonal trends are apparent in Figure 106*a*. Mean wave amplitudes show an annual cycle in the high–latitude Northern Hemisphere, with a summer minimum and winter maximum, as was simulated using simpler methods in section 7.2. An annual cycle also arises at high latitudes in the Southern Hemisphere, again producing a minimum during summer, but a maximum around September (spring). These annual cycles grow weaker as one moves equatorward. At around 20°–45°N and 25°–40°S, the

annual cycle disappears and a clear semiannual cycle arises, with equinoctial maxima and solticial minima. Recall that equinoctial maxima also arose in the observations in chapter 6, but were not simulated by the simple theory of section 7.2.

The total ray numbers in Figure 106*b* are more uniformly and strongly annual. Again there is a winter maximum and summer minimum in the Northern Hemisphere, and a summer minimum and early spring maximum in the high-latitude Southern Hemisphere. This early spring maximum changes into a winter maximum on progressing from high to mid latitudes in the Southern Hemisphere. The most intense maxima and deepest minima occur at 50°–60° latitude in both hemispheres. However, the Southern Hemisphere maxima are much larger than those in the Northern Hemisphere. Weak equinoctial peaks also occur around 30°N. At low latitudes in both hemispheres, the annual cycle decays, and weak equinoctial peaks also occur around 30°N. At the lowest latitudes, a teranuual variation arises, which resembles the low-latitude seasonal variations measured at Barking Sands and Coolidge Field in Chapter 6.

Relationship with other Wave Parameters

Scatter plots of the wave amplitudes at $60km$ versus various wave parameters are shown in Figure 107 for the months May–August in the Southern Hemisphere. A clear feature is these diagrams is the $m^{1/2}$ variation at low wavenumbers and m^{-1} variation at large wavenumbers, according to (27) and (28), and incorporated in a spectral representation (29). This arises despite the use here of more sophisticated formulae governing both unsaturated and saturated wave amplitudes. These results are very similar in form to plots of observational results by *Gardner and Voelz* [1987] and *Gardner et al.* [1989]. Furthermore, the break in these variations, corresponding to m_* in (29), occurs at $\sim 2\pi(7-10km)^{-1}$, which is close to theoretical spectral predictions [*Smith et al.*, 1987]. One can also observe diminished amplitude for the longer-propagating waves, due to radiative and saturative damping, and the spreading of the initially discrete K^{tot} distribution due to latitudinal refraction, without significant dimunition in amplitude.

7.3.7 Refraction Effects

Figure 108 shows plots which characterize the refraction effects in the Southern Hemisphere during winter. The top-left panel is a scatter plot of $\lambda_x^{tot} = 2\pi/K^{tot}$ versus c^{tot} at $60km$. The diamond-shaped symbols show the 9 discrete values which existed at the source level of $10km$ (the $c = 0$ waves are excluded because they are out of range). The spreading, due to refraction, of these initial values occurs along straight lines because $\Omega = K^{tot}c^{tot}$ is a constant, so that λ_x^{tot} is always proportional to c^{tot} by the same constant. The

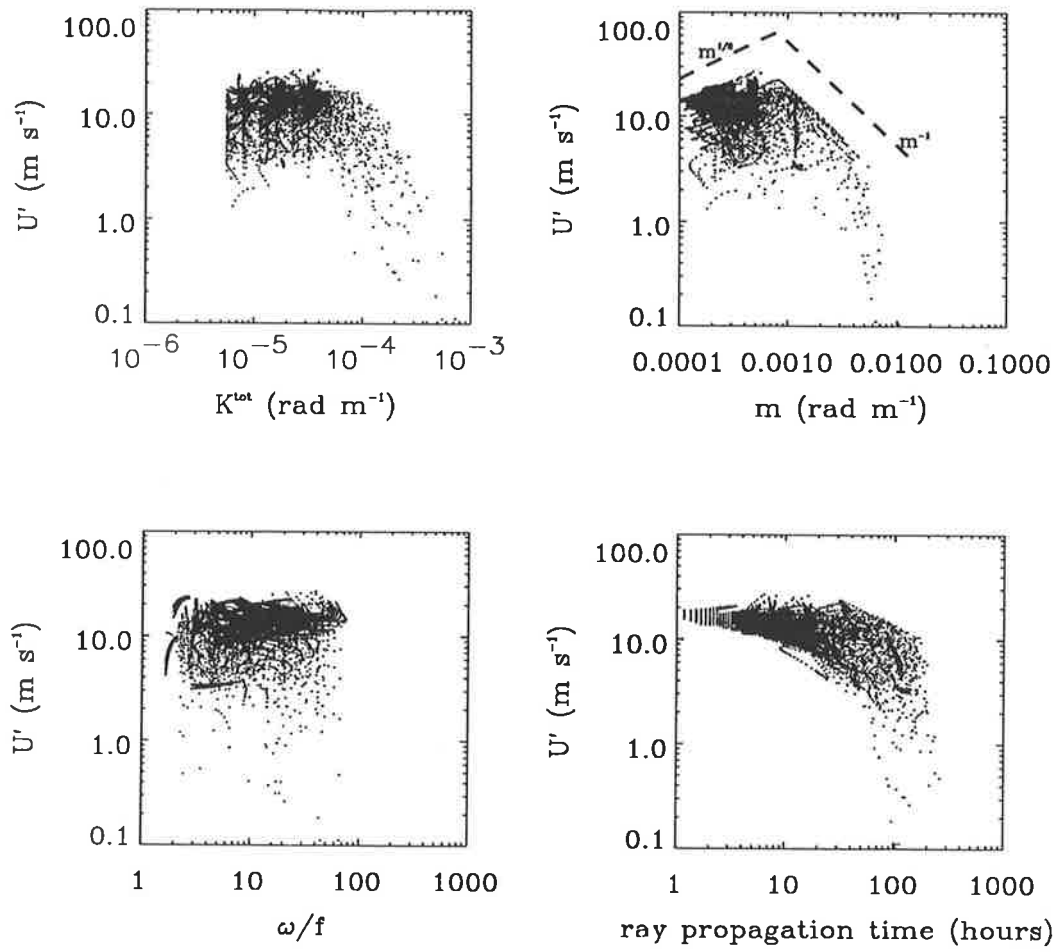

Figure 107: Plots of wave amplitudes at $60km$ versus K^{tot}, m, ω/f, and the total time it took the wave to propagate to $60km$. The data come from the Southern Hemisphere during May–August.

top–right plot shows the amplitudes of the rays versus c^{tot} at $60km$, and reveals again that rays which have undergone refractive acceleration/deceleration are not strongly attenuated in amplitude.

The bottom two plots show the distribution of these c^{tot} and λ_x^{tot} values at $60km$. The $c^{tot} = 0$ waves were excluded from the phase–speed results, since this zero value is not changed by refraction effects, whereas these stationary waves were included in compiling the λ_x^{tot} histograms since λ_x^{tot} values change for both stationary and nonstationary waves alike. The spreading of the initially–discrete c^{tot} and λ_x^{tot} distributions is clear in these diagrams. What is more evident, however, is the strong modification to the λ_x^{tot} distribution during propagation through the middle atmosphere, such that most of the long $800km$ wavelengths have been removed, presumably through critical–level filtering, and the wavelength distribution is dominated by the shortest horizontal–scale ($200km$) waves. A similar excess of short horizontal–scale waves has been found when measurements made at mesospheric heights have been collated [*Meek et al.*, 1985*a*; *Reid and Vincent*, 1987*b*; *Manson and Meek*, 1988], although questions exist

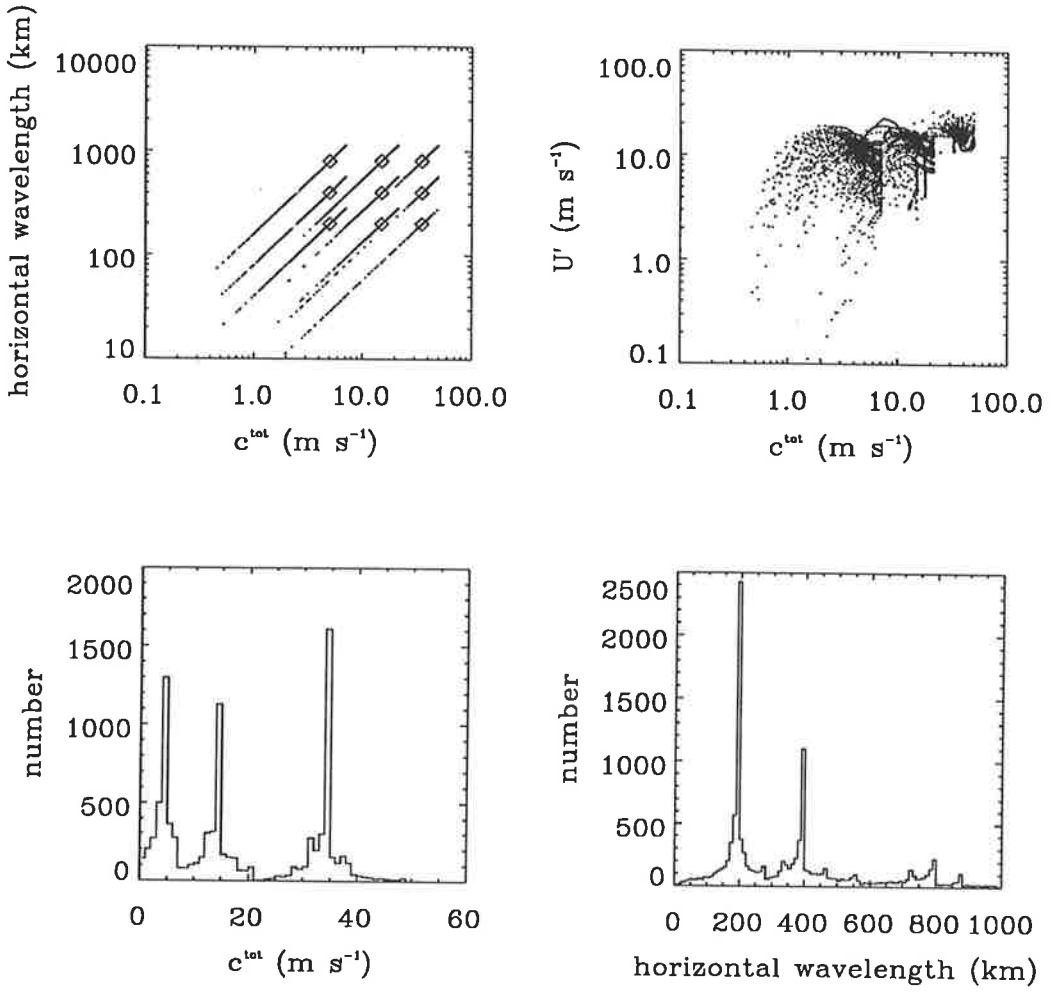

Figure 108: Four plots, using data from the Southern Hemisphere during May–August, which characterize the effects of refraction on c^{tot} and λ_x^{tot} at $60km$ in altitude. The top–left panel plots these two quantities together as a scatter plot, and another scatter plot is provided on the top–right for wave amplitude versus c^{tot}. The bottom two plots provide histograms of the number of occurrences of c^{tot} and λ_x^{tot} values at $60km$.

as to possible observational biases inherent in some of these measurements [*I.M. Reid and R.A. Vincent*, private communication, 1990].

Figure 109 shows similar results from summer in the Northern Hemisphere. One can see that the spreading is smaller during summer due to the smaller latitudinal shears, as inferred in section 7.3.4. Note, however, that not only are the larger λ_x^{tot} values removed, but also most of the smaller c^{tot} waves have been filtered out by critical–level interactions.

7.3.8 Azimuthal Directionality

To investigate the azimuthal propagation directions of the waves, the mean weighted ray count C was evaluated vectorially according to the individual propagation azimuths $\varphi_i = \arctan(l_i/k_i)$ of each ray; we shall denote this phasor $\vec{C}$. The mean phasors $\vec{C}$ are plotted in latitude–height form in Figure 110,

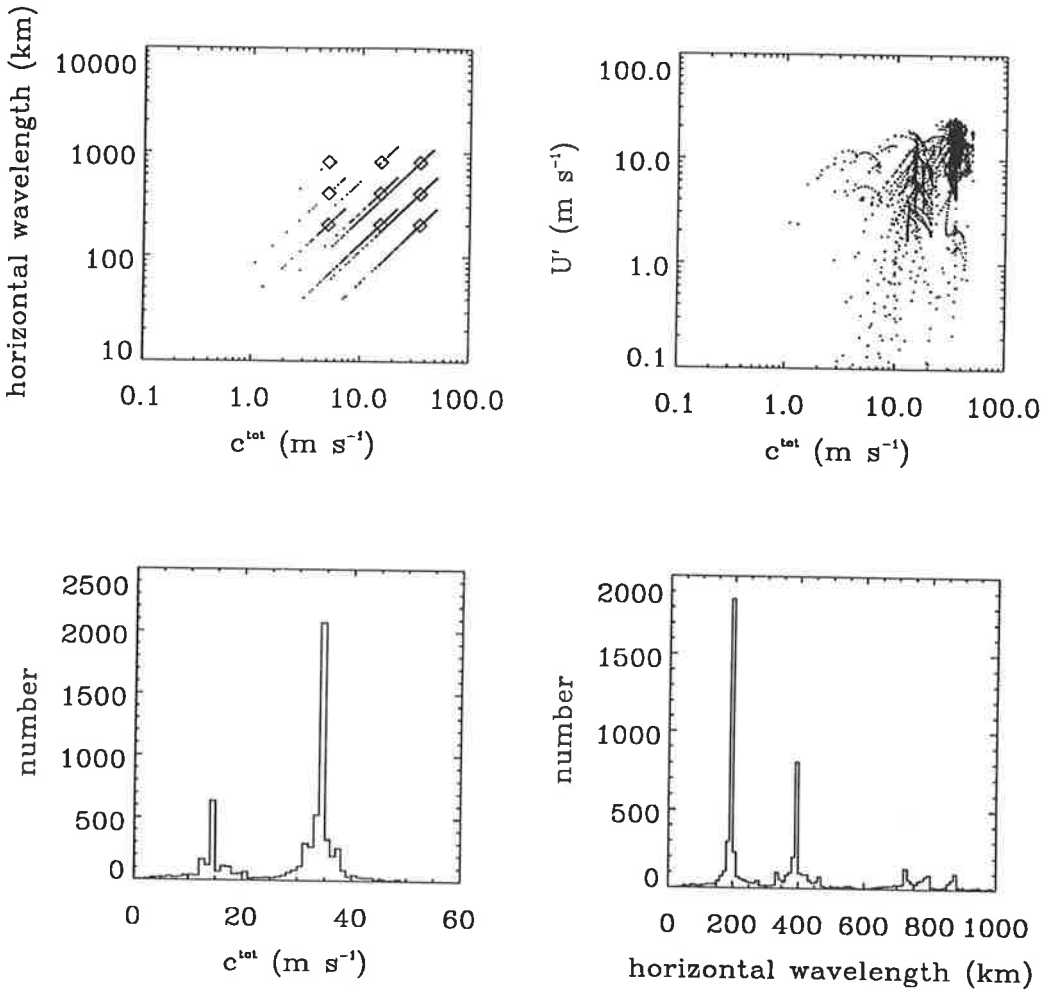

Figure 109: As for Figure 108, but using data from the Northern Hemisphere during May–August.

much like the $\overline{C}$ values in Figure 106; indeed, similar seasonal cycles to those in Figure 106 occur in the length of these vectors, despite the vectorial cancellation which can occur.

The most striking feature of Figure 110 is the strong annual cycle in phasor directions, which arises from critical–level filtering of the azimuthally isotropic wave field at $10km$ by the zonal–wind structure of the middle atmosphere from 10–$60km$ in height. At mid– to high–latitudes in both hemispheres, the phasors are westwardly aligned not only during winter, but also in spring and autumn. This "westward phase" is longest at all latitudes, lasting about 7–8 months at low latitudes and 9–10 months at high latitudes. Furthermore, eastward wave alignments during summer are weak at mid–latitudes and non–existent at high latitudes. Only at the more equatorial latitudes does a clear eastward phase in wave directions arise.

It is also apparent in Figure 110 that a significant meridional component to the mean wave propagation arises in the simulation. During the westward phase (centred around winter) an excess in poleward propagating waves arises at all but the lowest latitudes in the both hemispheres. During the eastward

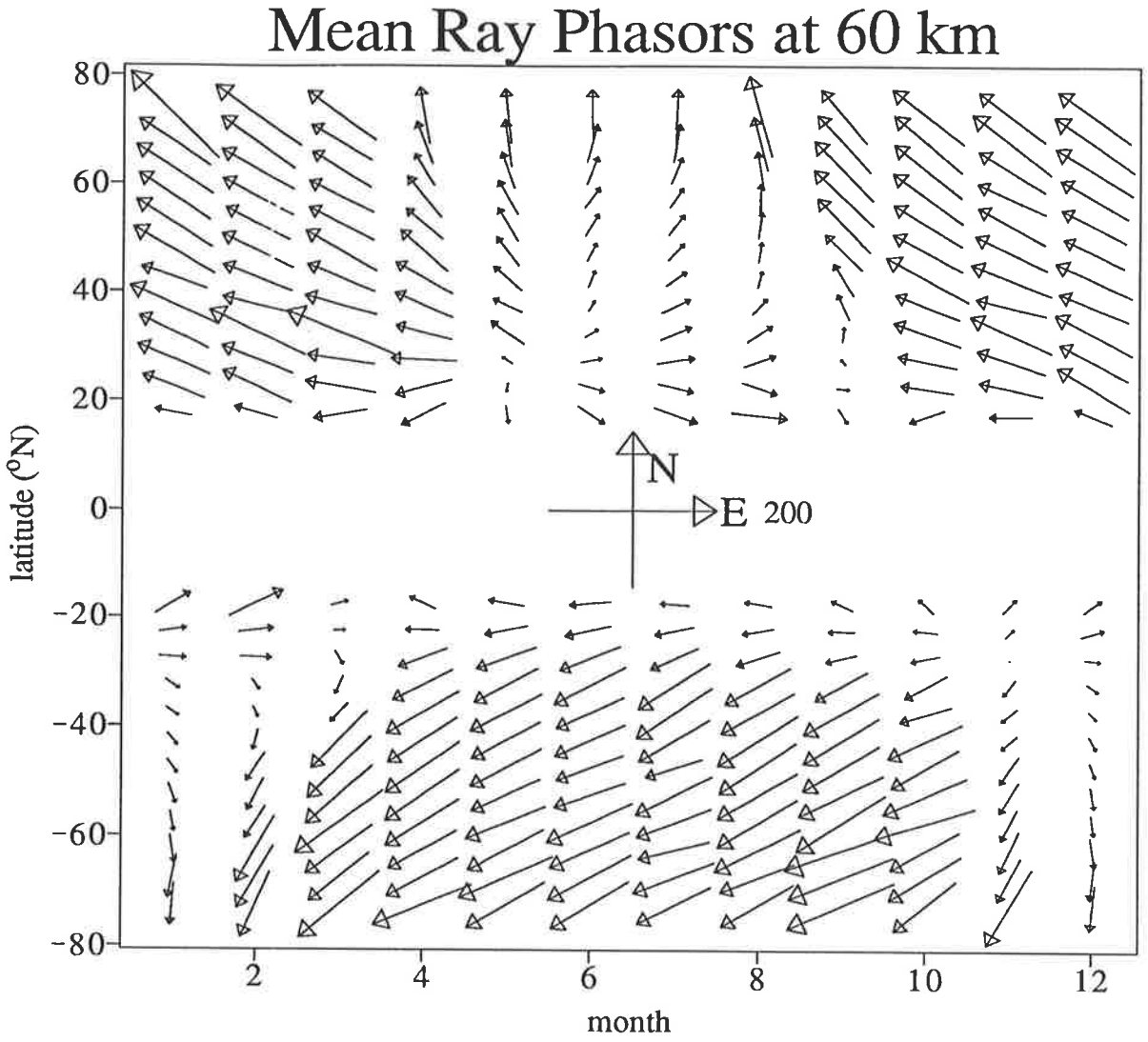

Figure 110: Mean phasors of the weighted ray counts, $\vec{C}$, evaluated at $60km$ in height as a function of latitude and month of the year, with the direction of each vector being the mean propagation direction of the wave field. Each phasor is evaluated over a 5° latitude interval. The length of the reference vectors in the centre of the plot is $\mid \vec{C} \mid = 200$. The phasor directions can be interpreted directly from the reference directions, so that the mean phasor direction at 60°S in June is about 25° south of west.

phase (summer), a clear trend in meridional propagation directions also occurs in both hemispheres. At latitudes < 30°, equatorward propagation is favoured, and becomes more distinct with decreasing latitude. At latitudes > 30°, however, poleward propagation is preferred, and becomes more pronounced as one progresses to polar latitudes. Thus, in summer, the model simulates "nodes" in the meridional gravity-wave propagation at 30° latitude.

The $\vec{C}$ results in Figure 110 are not directly comparable with measured calculations of wave alignments, such as those presented in Figures 84–86 in chapter 6 and by *Eckermann and Vincent* [1989]. This can be seen by the following example. If in winter there were more meridionally-propagating waves

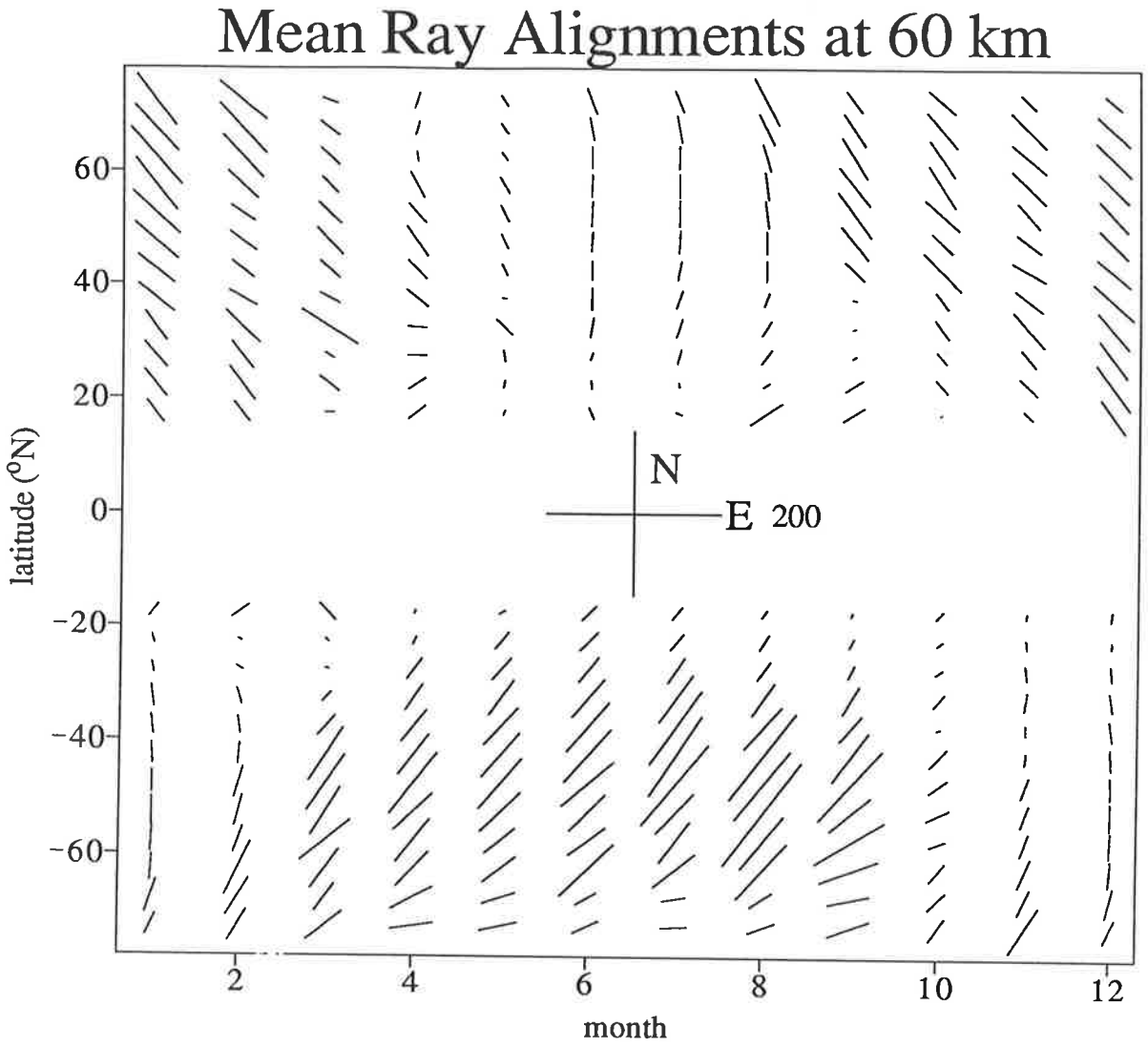

Figure 111: As for Figure 110, but the alignments of weighted counts $\tilde{C}$.

than westward propagating waves, yet there were equal amounts of northward and southward propagating waves, calculations would give a westward mean phasor but an essentially meridional alignment calculation. Consequently, the quantity $\tilde{C}$ was calculated, much in the manner of $\vec{C}$, except that the propagation azimuth φ_i was scaled such that antipropagating waves were assigned the same angle, giving angles in the range 0°–180°; for example, if $\varphi_i = 45°$ (north–east) or 225° (south–west), the alignment angle was set to 45° in both cases. This quantity $\tilde{C}$ should be more comparable with the observed wave alignments.

Figure 111 plots the results of these $\tilde{C}$ calculations. The alignments generally have a greater meridional component than the phasors in Figure 110. This indicates that some cancellation of northward and southward propagating waves occurs when the mean phasor is calculated. Indeed, the alignments are more meridional than zonal at all but the most southern latitudes during winter.

Figure 112 plots polar histograms of propagation azimuths in the Northern Hemisphere during the winter months. It can be seen that the angular spectra are reasonably evenly distributed about the mean phasor direction, but this mean phasor direction is not westward but has a significant northward component. Thus, the concept of a wave drag which is purely westward during winter and purely eastward in summer is not supported by these model results. The result is not definitive, however, because it is high–frequency gravity waves with short horizontal wavelengths which produce the bulk of the momentum–flux convergence in the upper–middle atmosphere [*Reid*, 1986; *Reid and Vincent*, 1987*b*, *Fritts and Vincent*, 1987], so that these longer–wavelength results are not necessarily indicative of the characterisitcs of the wave momentum flux. However, one should recall that most of the long horizontal wavelengths have been removed from the model wave field, leaving a shorter–wavelength spectrum at $60km$ (Figures 108–109). Furthermore, momentum–flux measurements in the mesosphere appear to support the idea that the flux and its convergence is generally non–zonal [*Reid*, 1984, 1986; *Reid and Vincent*, 1987*b*, *Fritts and Vincent*, 1987].

The original aim of this modelling was to cast light on the morphology of wave amplitudes in the middle atmosphere, and not the momentum flux. Nevertheless, the promising model results presented here suggest the approach is worth continuing, and study of the momentum flux is one logical next step. Such study would be easily facilitated by the inclusion of additional smaller horizontal wavelengths (say $50km$ and $100km$) and an upgrade of the model equations so that the dispersion relation was valid when ω nears N, which will undoubtedly arise should such short wavelengths be included.

7.4 Summary and Evaluation of the Modelling

Observed seasonal variations in gravity–wave activity in the middle atmosphere have been analyzed as to their cause. Wave–amplitude growth with altitude and wave saturation were first modelled using simplified theoretical formulae in section 7.2, which omitted source effects, ground–based phase-speed distributions, and mean–wind variability. These formulae were evaluated using the zonal–mean temperature structure presented by *Groves* [1985, 1987], so that zonal variations in temperature are also omitted. The simulated structures were compared with observations, and these comparisons enabled some definite conclusions to be drawn.

Seasonal variations of a wave–activity index computed by *Hirota* [1984] were well reproduced at all but the equatorial sites by the simulated saturated measure. This reaffirms arguments in Chapter 6 that these measurements are heavily weighted towards those waves with short vertical wavelengths, which are mostly

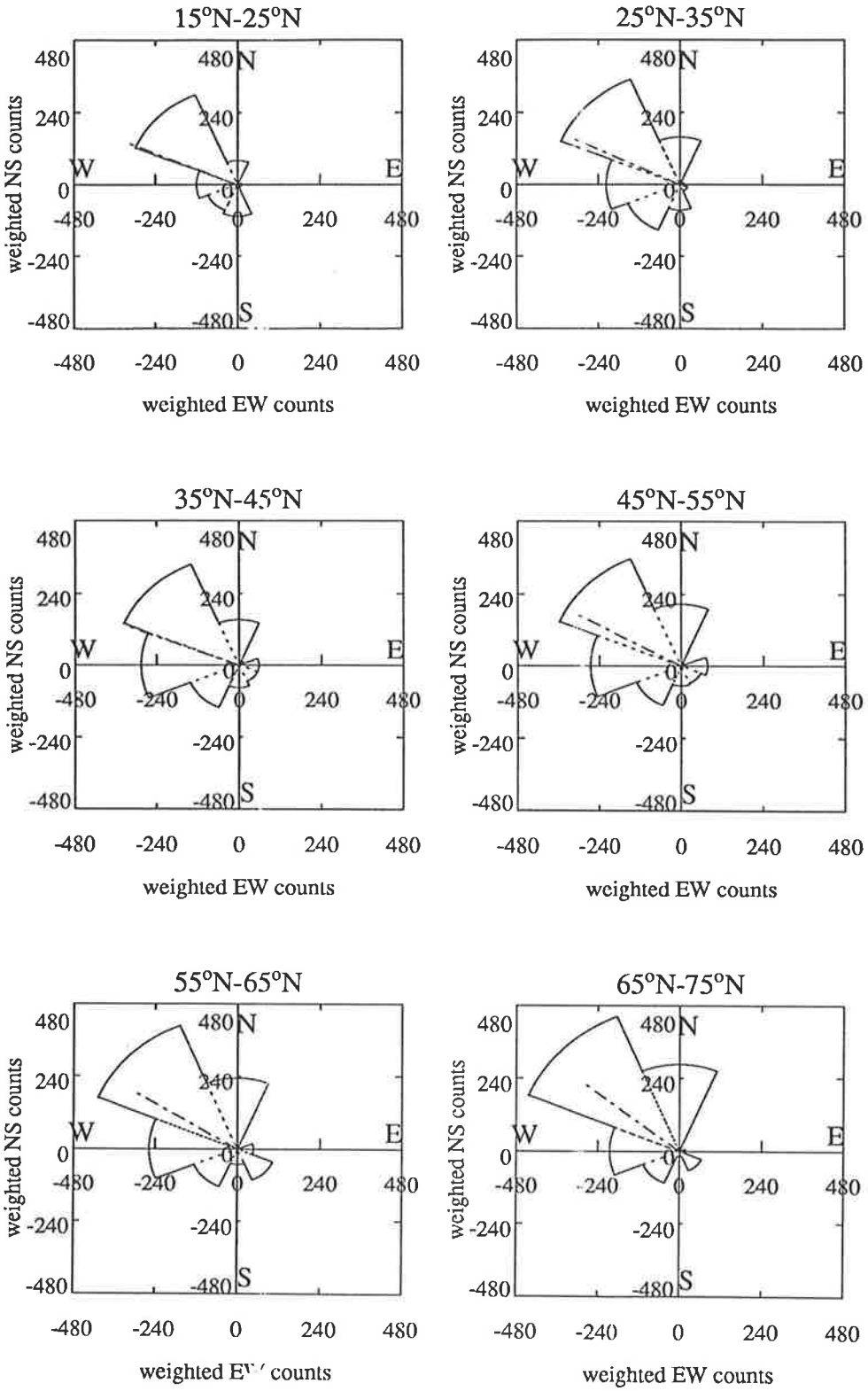

Figure 112: Polar histograms of the weighted ray counts $\overline{C}$ within different azimuth ranges in the Northern Hemisphere during winter (December–February). The thick broken line indicates the mean phasor direction $\vec{C}$. Note that the values of $\overline{C}$ are larger here due to the use of three months of data and 10° latitude bins.

saturated. Therefore, it seems clear that the seasonal variations of *Hirota* [1984] are not indicative of seasonal variations in unsaturated wave activity influenced by exponential amplitude growth with altitude and/or low–level sources, as has been the interpretation placed on these results in some studies [see, e.g., *Rind et al.*, 1988].

Some features of the seasonal cycles in the horizontal–velocity variance $\overline{u'^2}$ were well modelled by the simulated unsaturated measure derived for this variance, confirming that $\overline{u'^2}$ is determined more by unsaturated wave activity (see Chapter 6). In particular, the observed annual variation in wave activity, peaking in winter and minimizing in summer, is reproduced, both in phase and in the depth of the variation, by this modelling. Furthermore, the modelled annual variation is strong at high latitudes, and weakens on moving equatorward, as observed. One can therefore conclude that this annual variation in wave activity is produced by an annual variation in the vertical atmospheric density structure, which arises from the annual variation in atmospheric temperature which modulates the density scale height H_ρ. It is important to note that no annual variation in the wave–energy produced by low–level sources is required to reproduce this feature.

There are, however, some significant differences in the observed and simulated seasonal variability. The enhanced semiannual variability at equatorial sites and upper–level equinoctial peaks around 20°N–35°N do not arise in the simulations. These features must therefore arise from processes not incorporated by the modelling, such as mean–wind variations and/or source effects, as was concluded using different arguments in Chapter 6.

While the broad latitudinal change in the mean wave activity is also evident in the simulated structure, there are strong peaks at North American sites around 20°N–30°N and 55°N which are not reproduced. While some of this structure may be instrumental, the observed structure is consistent with geographical variations in the mean wave energy produced by low–level sources. If the variation is due to sources, the analysis indicates that the "source variable" varies considerably with location, but is more invariant in time, which is consistent with orography being the dominant wave source mechanism in and around North America. Similar conclusions have been drawn in some other theoretical and observational studies.

The modelling effort was extended in section 7.3 to address some of the unresolved questions from the initial theoretical study. A simple numerical model was developed which simulated wave propagation through the middle atmosphere, and produced a number of important findings which will now be briefly summarized and assessed.

The annual variation in high–latitide r.m.s. horizontal–velocity amplitudes is reproduced by the simulation. Furthermore, equinoctial maxima at around 30° and terannual variability at lower latitudes

which was measured in chapter 6, but which could not be reproduced using simple theory in section 7.2, is better, although by no means accurately, simulated using this model. The variation of the horizontal-velocity amplitudes at $60km$ with vertical wavenumber m agrees well with current theoretical ideas and observational results.

The tracing of single waves through the zonally-averaged middle atmosphere showed that latitudinal refraction could be appreciable during winter, but less so in summer, particularly at latitudes around $\pm 20°$–$40°$. Such refraction tended to rotate zonally-aligned waves to near meridional directions, a process which seemed consistent with the strong meridional alignments observed in chapter 6 in winter at northern latitudes and by *Eckermann and Vincent* [1989] at a southern latitude site in this range. Global simulations with many rays showed that the winter alignments have a strong meridional component. However, the simulated alignments were strong most of the time, and particularly around $\pm 35°$–$60°$ in summer, yet such clear features are not evident in the observations in chapter 6 nor in the findings of *Eckermann and Vincent* [1989], but do arise in the mesospheric results of *Vincent and Fritts* [1987].

The latitudinal refraction highlighted a potentially important process which was referred to as "refractive acceleration", where ground-based horizontal phase speeds c^{tot} change in proportion to the variations in the total horizontal wavelength λ_x^{tot} induced by the refraction. This process causes speading of initially discrete distributions of c^{tot} and λ_x^{tot}. Many-wave simulations indicated that the largest λ_x^{tot} values were filtered from the spectrum during propagation, as were small c^{tot} values during summer. The simulated preponderance of small horizontal scales in the upper middle atmosphere is supported by observations.

The initial results afforded by this modelling have been encouraging, and have better highlighted the actual gravity-wave dynamics responsible for features in many measurements, such as the observations presented in previous chapters. Consequently, further development of the method seems justified. Many improvements can be made. Foremost of these, perhaps, is an upgrade of the model equations to deal with intrinsic frequencies which approach N, so that shorter horizontal wavelengths, which are important for the momentum flux, can be incorporated. A better background atmosphere model should also be used, certainly one that covers all latitudes so that cross-equatorial and cross-polar propagation can be incorporated, and perhaps a model which incorporates zonal variability. Incorporation of latitudinal variability into the wave-action equation should also be studied as to its feasibility. A long-term goal would be to carry out such ray tracing in an interactive model, where wave saturation and radiative damping can influence the mean flow, and where mutual interactions amongst many waves are also incorporated within the ray-tracing formalism [see, e.g., *Jacobs and Cox*, 1987].

Appendix A

Relationship between Stokes Parameters and Other Spectral Formulae

In this thesis, the so-called Stokes parameters [see, e.g , *Kraus*, 1966] of a wave are extensively used to investigate the nature of the gravity wave field in the atmosphere. In particular, *Eckermann and Vincent* [1989] have presented formulae for calculating these parameters in the Fourier domain. Here it is shown that these formulae are also closely associated with some better-known spectral relations which are used in more general applications. The purpose of this appendix is to show that if one is spectrally analyzing motions which one knows are wavelike, then several well-known spectral formulae, which are often calculated routinely anyway, correspond in a simple way to the Stokes parameters of this wave field, and therefore have a fundamental physical meaning.

A.1 Stokes Parameters in the Fourier Domain

A lucid derivation and explanation of the Stokes parameters of any general wave motion is given by *Kraus* [1966], and their usefulness in determining the characteristics of atmospheric gravity waves has been highlighted by *Vincent and Fritts* [1987] and *Eckermann and Vincent* [1989]. These parameters uniquely characterize any wave motion by quantifying the total amount of wave variance, the axial anisotropy of this variance, the amount of linear polarization, and the amount of circular polarization. I

shall denote these quantities by I, D, P and Q, respectively.

Consider the case where one analyzes gravity wave velocity fluctuations in the zonal (u') and meridional (v') directions over some height interval, as in the analysis of data from rocket profiles. I shall represent the Fourier transforms of these velocity fluctuations over this height range as $U_R(m) + iU_I(m)$ for the zonal fluctuations, and $V_R(m) + iV_I(m)$ for the meridional fluctuations, where m is the vertical wavenumber. *Eckermann and Vincent* [1989] derived the following formulae for evaluating the Stokes parameters in the Fourier domain

$$\begin{aligned} I &= A\left(\overline{U_R^2(m)} + \overline{U_I^2(m)} + \overline{V_R^2(m)} + \overline{V_I^2(m)}\right) \\ D &= A\left(\overline{U_R^2(m)} + \overline{U_I^2(m)} - \overline{V_R^2(m)} - \overline{V_I^2(m)}\right) \\ P &= 2A\left(\overline{U_R(m)V_R(m)} + \overline{U_I(m)V_I(m)}\right) \\ Q &= 2A\left(\overline{U_R(m)V_I(m)} - \overline{U_I(m)V_R(m)}\right) \end{aligned}$$

The overbars denote averages over all desired profiles so as to remove the effects of incoherent motions (sometimes this is either inappropriate or impossible), and A is a constant which shall hereafter be taken to equal 1.

It is immediately apparent that I and D in the Fourier domain are simply the sum and difference, respectively, of the zonal and meridional power spectra (sometimes referred to as the "autospectra" since they are the Fourier transform of the autocorrelation function). One might also recognize the formula for P as the cross spectrum, and the formula for Q as the quadrature spectrum, between the zonal and meridional oscillations [see, e.g., *Jenkins and Watts*, 1968].

Consequently, the four Stokes parameters are expressed in the Fourier domain in terms of four other better-known spectral quantities; the power spectrum of u', the power spectrum of v', the cross spectrum between u' and v', and the quadrature spectrum between u' and v'.

Clearly, then, these basic spectral quantities have direct physical significance when calculated for a data series containing wave motions. Dynamical atmospheric data containing gravity wave motions is one such example.

A.2 Stokes Parameters and the Rotary Spectrum

Using the same notation as before, the rotary amplitude spectrum $R(m)$ is defined as the Fourier transform of the complex vector $u'(z) + iv'(z)$. Detailed explanations of the usefulness of the rotary spectrum in various problems have been given by *Gonella* [1972] and *Hayashi* [1979]. The rotary spectrum has

been successfully applied to gravity wave oscillations in the ocean [see, e.g., *Fofonoff*, 1969; *Leaman and Sanford*, 1975] and atmosphere [see, e.g., *Thompson*, 1978; *Vincent*, 1984; *Hass and Meyer*, 1987; *Eckermann and Vincent*, 1989] to provide information on preferred senses of gravity wave ellipse rotation in the horizontal, which in turn specifies whether wave energy is propagating upwards or downwards [see, e.g., *Vincent*, 1984].

In calculating the rotary power spectrum, the total power spectrum $U_R^2(m)+U_I^2(m)+V_R^2(m)+V_I^2(m)$ is split up into a sum of a circular clockwise ($CW(m)$) and anticlockwise ($ACW(m)$) rotating component. These components are given by

$$\begin{aligned} CW(m) &= \frac{R^*(-m)R(-m)}{2} \\ ACW(m) &= \frac{R^*(m)R(m)}{2} \end{aligned}$$

where asterisks denote complex conjugation.

Although the rotary spectrum is calculated by a more indirect spectral technique than are the Stokes parameters, the fact that they both quantify the total spectral power and the amount and sense of the circular wave polarization suggests that they must be interrelated.

In fact, it is possible to derive from the basic definition of the rotary spectrum corresponding expressions in terms of Stokes parameters. The derivation is straightforward, but rather long, and so will not be reproduced here. In fact, expressions for the rotary spectrum in terms of the individual power spectra of u' and v', and the cross and quadrature spectra of u' and v', have been given by *Gonella* [1972], and since their correspondence to the Stokes parameters has been given, the derivation is essentially analagous.

The final result is that the rotary spectrum is related to the Stokes parameters in the following simple way

$$\begin{aligned} CW(m) &= \frac{I-Q}{2} \\ ACW(m) &= \frac{I+Q}{2} \end{aligned}$$

Therefore, the rotary spectrum can be calculated directly from the expressions of *Eckermann and Vincent* [1989] for Stokes parameters in the Fourier domain. This affords a considerable saving of analysis time. Rather than band passing raw data using Fast Fourier Transform (FFT) methods, and then retransforming $u' + iv'$, as one does in conventional rotary spectral analysis [see, e.g., *Vincent*, 1984], the rotary spectrum can be calculated directly from the Stokes parameters of the raw spectrum. In other words, calculating the rotary spectrum directly from I and Q involves just one FFT, rather than an FFT, an inverse FFT, and finally another FFT as in conventional rotary spectral analysis.

The rotary power spectrum is the most basic quantity one can derive in rotary spectral analysis. There are many other related and potentially useful quantities one can also calculate from the rotary spectrum [see, e.g., *Gonella*, 1972; *Hayashi*, 1979]. Nevertheless, all of these quantities too can be calculated directly from the Stokes parameters formulae of *Eckermann and Vincent* [1989], with a similar considerable saving of computing time.

Appendix B

Digitization Noise and its Spectral Shape

The rocket data used in Chapter 6 are digitized to the nearest metre per second in velocity and to the nearest degree Kelvin for temperature, which clearly impacts on the resolution of the small-scale fluctuating motions evident in such data. These effects may be significant when the data are spectrally analyzed.

We shall consider first the horizontal velocity fluctuations u'. If we represent the digitizating increment by δu ($= 1\ m\ s^{-1}$), the conventional wisdom is that an additional "noise" variance of $\delta u^2/12$ is produced, and this extra "noise" variance has a white (i.e. flat) spectrum [see, e.g., *Kristensen and Kirkegaard*, 1987]. While the former conclusion is easily derived, *Kristensen and Kirkegaard* [1987] investigated the spectral characteristics of digitization noise is depth, for the case of spectral analysis of time series of inertial range turbulence. They found that a white spectrum of digitization noise usually resulted, but if the digitization noise variance was larger than the signal, or if the time series was sampled faster than the so-called "Taylor microscale"[1], then the noise spectrum was no longer white, and most of the noise power was concentrated at the very lowest and very highest frequencies.

These findings are not directly applicable to the spectral analysis of rocket profiles of gravity wave fluctuations with altitude. However, the requirement that the signal variance be larger than the noise variance is clearly met for the horizontal velocities, as measured variances are around 10–100 $m^2 s^{-2}$ (see Figure 77), whereas the noise variance $\delta u^2/12 = 1/12 m^2 s^{-2}$. The second criterion is unique to turbulence, and not applicable to these wave dynamics. Therefore, a white spectrum of digitization noise

[1] the time it takes the autocovariance function to fall to zero

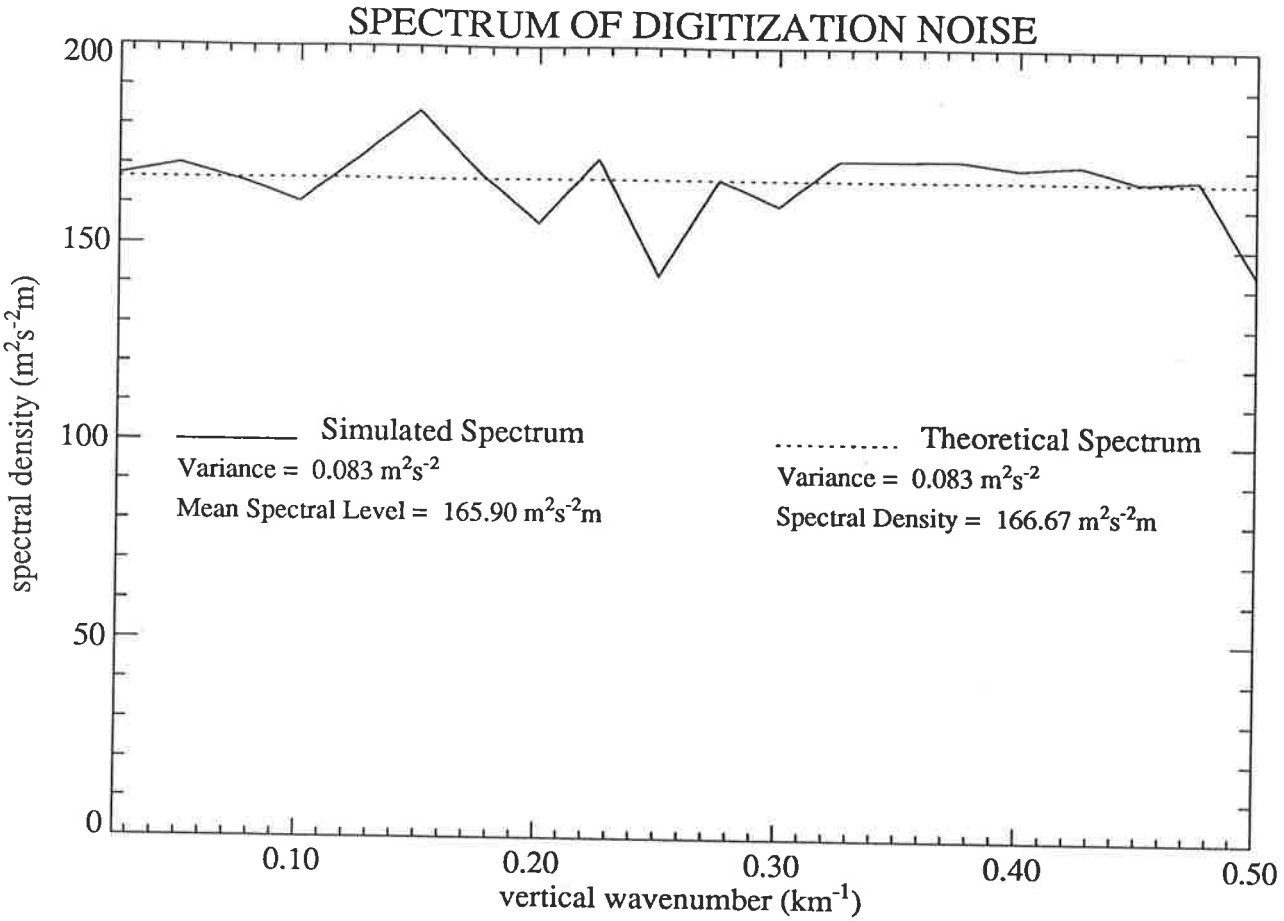

Figure 113: Spectrum of digitization noise obtained from numerical simulations (solid line) and the theoretical prodiction of *Kristensen and Kirkegaard* [1987] (dotted line).

appears most likely.

Simulations very similar to those detailed in sections 3.3.2–3.3.3 were performed to test this tentative inference. For each simulation, two identical altitude profiles of randomly phased gravity wave fluctuations were synthesized from the gravity wave spectrum (29) using $m_* = 3km^{-1}$ and $N = 0.02rad\ s^{-1}$. The wind values in one of these profiles was digitized to the nearest metre per second. Both profiles were Fourier transformed, and power spectra computed, and the noise spectrum then was obtained my simply subtracting the digitized and "undigitized" spectrum.

Figure 113 shows the resulting mean spectrum of digitization noise obtained from 300000 independent simulations. The theoretical spectral level is overlayed with a dotted curve. Close agreement is evident. This well–predicted noise spectrum can be removed from the computed spectra, thus eliminating its effects on intrinsic spectral shapes.

Appendix C

Computing Potential Temperature from Radiosonde Temperatures

Radiosonde temperatures from Adelaide Airport come plotted on aerological diagrams, with unequal spacing in altitude between successive data points. These data were digitized, and potential temperatures, ignoring humidity effects, were evaluated using the following algorithm.

The potential temperature $\Theta(z)$ at some height z is defined as the temperature a parcel of air at this height would attain if it were abiabatically compressed to a nominal sea–level pressure of $p_0 = 10^5 Pa$.

$$\Theta(z) = T(z)\left(\frac{p_0}{p(z)}\right)^{R/C_p}, \tag{110}$$

where $T(z)$ is the temperature and $p(z)$ is the pressure at height z, R is the ideal gas constant, and C_p is the specific heat of air at constant pressure. Since hydrostatic balance in the vertical means $p(z') = p_0 e^{-\int_0^{z'} z/H(z)}$, where $H(z)$ is the pressure scale height at height z, then rearranging this equation produces

$$\Theta(z') = T(z')e^{g/C_p \int_0^{z'} dz/T(z)}, \tag{111}$$

where g is the gravitational acceleration.

With the radiosonde data, we have a series of unevenly spaced heights $z_0, z_1, z_2, ..., z_n$ and corresponding temperature measurements at these heights $T_0, T_1, T_2, ..., T_n$. Using (111) and assuming that the vertical temperature gradient is linear between successive points, the potential temperature $\Theta(z_k)$ at a height z_k, where $0 \leq k \leq n$, is given by the following analytical expression

$$\Theta(z_k) = \prod_{i=0}^{k} \left(\frac{T_{i+1}}{T_i}\right)^{(z_{i+1}-z_i)g/(T_{i+1}-T_i)/C_p}. \tag{112}$$

The advantage of this algorithm is that it analytically assumes a linear variation of $T(z)$ between successive points z_i and z_{i+1}, which is a usually a good approximation in the troposphere, especially when the separation between successive points is small.

When plotting isentropes, one needs to evaluate the altitude where a specified value of Θ occurs. Equation (112) is not easily solved for z analytically, but is easily solved numerically.

Appendix D

Determining the "Height–averaged" Gravity–wave Spectrum

A so–called "height–averaged" spectrum was derived in Chapter 6 as equation (77). To specify its particular form in any given observational situation, the parameters $m_*(z_1)$ and H_E must be determined, and can be evaluated self–consistently from observational data as follows.

It is a straightforward task to evaluate and plot the mean horizontal velocity variances produced by these gravity wave motions as a function of height [see, e.g., *Hirota and Niki*, 1985; *Hass and Meyer*, 1987; *Eckermann and Vincent*, 1989]. Yet a theoretical estimate of these values at various height is given by integrating the original gravity wave spectrum over the resolved wavenumber range, say between m_1 and m_2. A general analytical expression for this integral was derived in section 3.3.2 as equation (30). This experssion means that, by evaluating N, $\overline{u'^2(z)}$, m_2 and m_1 from the data, an $m_*(z)$ value can then be calculated self–consistently from (30). By doing this at an upper and a lower height, then, from the change in m_*, the parameter H_E can be estimated using formula (31) in section 3.3.2. All the parameters are now specified, and so the height-averaged spectrum appropriate for the data in this height range can then be evaluated and plotted.

An example of such a calculation is given here, and the results are used in Chapter 6 to plot this spectrum. Earlier calculations using meteorological rocket data by *Hirota and Niki* [1985] show that horizontal velocity variances produced by gravity waves in the upper stratosphere are typically around $10m^2\ s^{-2}$ at a height of $30km$, and around $60m^2\ s^{-2}$ at $60km$. Using a representative value of $N \sim 0.02rad\ s^{-1}$ and values of $m_1 = 2\pi(15km)^{-1}$ and $m_1 = 2\pi(2km)^{-1}$ appropriate to the wavenumber band

analyzed by *Hirota and Niki* [1985], then putting these numbers into (30) and solving this equation for the only unknown parameter m_* gives $m_*(z = 30km) \sim 2\pi(2.7km)^{-1}$ and $m_*(z = 60km) \sim 2\pi(7.1km)^{-1}$. Putting these two values into equation (31) then gives a value of $H_E \sim 16.7km$.

Appendix E

Falling sphere observations of anisotropic gravity wave motions in the upper stratosphere over Australia

This is a reprint of a paper by S.D. Eckermann and R.A. Vincent, published in *Pure Appl. Geophys.*, *130*, 509–532, 1989.

Stephen D. Eckermann and Robert A. Vincent (1989) Falling sphere observations of anisotropic gravity wave motions in the upper stratosphere over Australia.
Pure and Applied Geophysics, v. 130 (2/3), pp. 509-532, June 1989

Appendix F

Effect of superposition on measurements of atmospheric gravity waves: A cautionary note and some reinterpretations

This is a reprint of a paper by S.D. Eckermann and W.K. Hocking, published in *J. Geophys. Res.*, *94*, 6333–6339, 1989.

Effect of Superposition on Measurements of Atmospheric Gravity Waves: A Cautionary Note and Some Reinterpretations

STEPHEN D. ECKERMANN AND WAYNE K. HOCKING

Department of Physics and Mathematical Physics, University of Adelaide, Adelaide, South Australia

AS APPEARED IN J. GEOPHYS. RES., 94, 6333–6339, 1989

Recent studies of gravity waves in the upper stratosphere have produced some interesting, but as yet unexplained, results. The observation and analysis of apparently "monochromatic" waves is not at first sight consistent with the current conception that the wave motions at these heights are due to a spectrum of superposed waves with a wide range of frequencies. Recent studies have suggested that regardless of season or location, inertia gravity waves with intrinsic frequencies around 3 times the inertial frequency appear to dominate the wave field. We address these issues using both digital simulation and analytical analysis, first showing how seemingly "monochromatic" waves can arise naturally from a broad spectrum of waves. Critical reappraisal of the analysis technique used to infer the peak in wave activity near 3 times the inertial frequency shows that this result is not definitive. This peak is demonstrated to be a statistical manifestation of wave superposition. These results in fact indicate azimuthal directionality in wave propagation, an important measurement of a little-known quantity. Strong directionality in winter and at the equator is revealed. The equatorial results suggest a deficiency in inertia gravity waves and a preponderance of Kelvin wave and/or mixed Rossby-gravity wave motions.

INTRODUCTION

Present knowledge of the characteristics of atmospheric gravity waves in the height interval between 30 and 60 km is fragmentary, with rockets and lidars being the only significant sources of information. Despite this, studies have revealed distinct local, seasonal, and latitudinal features in the wave field [e.g., *Hirota*, 1984; *Hirota and Niki*, 1985; *Shibata et al.*, 1986; *Hass and Meyer*, 1987; *Eckermann and Vincent*, 1989]. However, few explanations of these important observations have been put forward.

We focus here on some puzzling findings of gravity wave intrinsic frequency estimates made at these heights [*Hirota and Niki*, 1985]. The results indicated that quasi-monochromatic inertia gravity waves dominate in this region. Distributions of intrinsic frequencies peaked sharply at around 3 times the inertial frequency, essentially independent of latitude or season. This is at odds with recent theories of a broad spectrum of atmospheric gravity waves [e.g., *VanZandt*, 1982]. Other studies in the lower stratosphere have revealed that apparently monochromatic inertia gravity waves can often be observed [e.g., *Cadet and Teitelbaum*, 1979; *Maekawa et al.*, 1984; *Cot and Barat*, 1986]. Yet, if the spectrum of waves does indeed have a peak at 3 times the inertial frequency in the lower stratosphere, it seems difficult to imagine how this could be maintained into the upper stratosphere, where strong mean wind shears should substantially alter wave intrinsic frequencies and hence the position of this peak. If the peak found by *Hirota and Niki* [1985] is real, then the results seem to indicate that some "in situ" wave generation or enhancement process acts on a global scale, which selectively produces this peak in intrinsic frequency; alternatively, there may be shortcomings in the analysis technique advanced by *Hirota and Niki* [1985].

We have reexamined the measurement technique used to infer these results. After careful inspection, we conclude that the results are biased by wave superposition and do not reflect the true situation. Furthermore, we show that the results are rather an indicator of the azimuthal directionality in wave propagation. These assertions are supported by both computer simulations and derived analytical formulae. We conclude by comparing our new interpretations of the physical significance of the measurements with a recent general circulation model simulation of wave production and propagation in the middle atmosphere. We begin, however, by illustrating how analysis of individual wave events can be potentially hazardous and the results misleading, assuming that a broad spectrum of superposed gravity waves exists in the atmosphere.

Paper number 88JD03916
0148-0227/89/88JD-03916$05.00

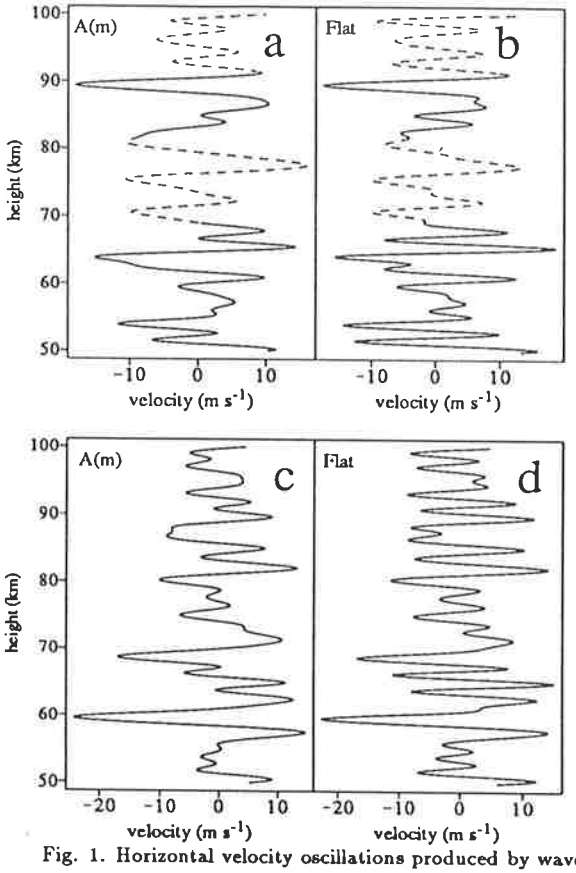

Fig. 1. Horizontal velocity oscillations produced by waves with random phases and governed in amplitude by a power spectral density $P(m)$ in the 2- to 10-km vertical wavelength interval (containing 20 waves), and zero power spectral density outside this band. This models experimental rocket profiles [e.g., *Hirota*, 1984]. $P(\mathrm{m}) = A(m) = E\ (1 + [m/m_*]^3)^{-1}$ ($m_* = 2\pi/(5\ \mathrm{km})$) was used in Figures 1*a* and 1c, and $P(m) = E'$ (flat) was used in Figures 1*b* and 1*d*, with E and E' scaled so that the variance was 100 $\mathrm{m^2\ s^{-2}}$ in each case. The same phases were used in Figures 1*a* and 1*b* and in Figures 1c and 1*d*. "Monochromatic" oscillations are highlighted by dashed curves. The height scale is arbitrary.

"Monochromatic" Wave Events

Extended atmospheric observations have revealed a spectrum of waves in the atmosphere [e.g., *VanZandt*, 1982; *Dewan et al.*, 1984]. How, then, can one reconcile this with frequent "observations" of, and indeed analysis of, quasi-monochromatic waves [e.g., *Hirota and Niki*, 1985; *Devarajan et al.*, 1985; *Cot and Barat*, 1986]?

A simulation was performed to investigate this. An analytical vertical wave number power spectral density $A(m) = E(1 + [m/m^*]^3)^{-1}$, which best models observed spectra [*VanZandt*, 1985; *Smith et al.*, 1987], was adopted. Wave fields were then synthesized digitally from $A(m)$, using a simple Fourier transform technique described by *Owens* [1978] and *Hocking* [1987]. However, in this example a random phase was introduced between the real and imaginary components of each harmonic in Fourier space, and the transformed amplitude spectrum was Hermitian, in order to ensure a real wave field, with all the waves coaligned. In this way a series of differently superposed single-wave profiles were produced, while the energy distribution as a function of wave number in every profile was the same.

On inspecting these profiles, occasionally "monochromatic" wavelike oscillations arise merely by fortuitous superposition amongst a wave ensemble (Figure 1*a*). Indeed, even a flat spectrum with equal power spectral density over a range of wave numbers produces similar "monochromatic" events (Figure 1*b*), indicating that the occurrence of such events is independent of the spectral form. Typical wave profiles, which show no "monochromatic" events, are shown in Figures 1c and 1*d*.

Interpretation of oscillations in single atmospheric profiles as "monochromatic waves" must be considered dangerous in light of these findings. It is not clear whether it is valid to analyze a wave of this type by treating it as a monochromatic wave. It is possible that the oscillation arises because all the other Fourier components fortuitously sum to zero over this range, leaving one true wave, but caution should certainly be exercised in analysis. The dangers in subjective analysis of wind data have previously been illustrated by *Hines* [1966]. For example, it is well known that two superposing waves of wave numbers m_1 and m_2 and constant amplitude will produce a "beating" wave of wave number $(m_1 + m_2)/2$ and an amplitude envelope of wave number $(m_1 - m_2)/2$. Analysis of this beating pattern as a monochromatic event would clearly give erroneous wave number and amplitude information. Notice that the "monochromatic" oscillation between 70 and 80 km in Figure 1*a* seems to grow with height somewhat, even though no growth with height is incorporated in the simulation, and so it must be, to some extent, a "beating" or coherence length effect. Superposition effects like this might explain why gravity waves often only appear to exist over one or two time cycles and only retain coherence over a few kilometers in the vertical [e.g., *Harper and Woodman*, 1977; *Miller et al.*, 1978].

One should not interpret these arguments as a refutation of all observations of monochromatic waves. The atmospheric gravity wave spectrum has enormous variability over small time scales, and individual large-amplitude waves certainly arise [e.g., *Balsley et al.*, 1983, *Cot and Barat*, 1986]. Instead, these results should encourage efforts to verify the coherence of such waves before subjecting them to an in-depth analysis. If this is not done, superposition effects may lead one to infer individual wave amplitudes and wavelengths which are incorrect. Since measured wave parameters are often used to trace waves back through the atmosphere to their source and wave amplitude variation with height is used to investigate wave saturation effects, then clearly a potential for erroneous inferences exists. An example of the dangers in analyzing generally polychromatic

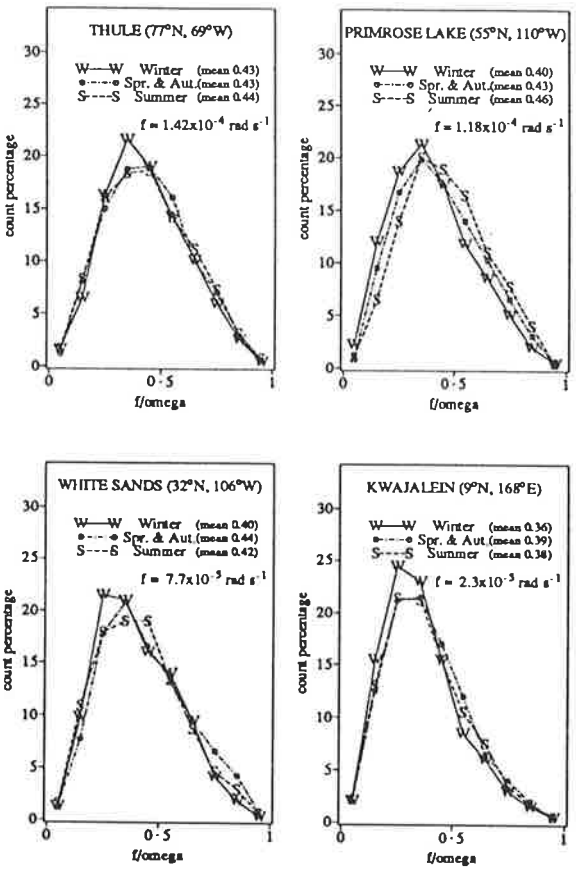

Fig. 2. Histograms of f/ω for gravity waves between 30 and 60 km from four different rocket stations, using all available data [after *Hirota and Niki*, 1985].

wave motions will now be presented.

Inferences About f/ω

The horizontal wind velocity perturbations of a small amplitude gravity wave of intrinsic frequency ω, propagating in an unsheared, inviscid atmosphere with Coriolis parameter f, are governed by the following polarization relation [*Gossard and Hooke*, 1975]

$$V' = -i\frac{f}{\omega}U' \qquad (1)$$

where U' and V' are the velocity components parallel with, and transverse to, the direction of horizontal propagation, respectively.

The formula implies an elliptically polarized wave motion in the horizontal with a frequency dependent ellipse axial ratio. *Hirota and Niki* [1985] (hereafter referred to as HN) realized that by measuring $|V'/U'|$, it was possible to determine f/ω and hence the intrinsic wave frequency ω. This is a potentially powerful way of measuring this important wave parameter, since ground-based measurements of wave frequencies (e.g., radars, lidars) are contaminated by the Doppler-shifting effects of the background winds.

Since in an experiment it is usual to measure the zonal (u') and meridional (v') oscillations, (1) must be expressed with respect to these coordinate axes, and so depends on u', v', and the wave propagation azimuth direction θ. Rather than infer θ, HN computed the ellipse vector length $r = (u'^2+v'^2)^{1/2}$, reasoning that the ratio of the maximum and minimum ellipse vectors defines the ellipse axial ratio and hence f/ω. Local maxima and minima of the wave motion were located from this quantity, and inner and outer "r" envelopes of the wave motion determined by interpolation. The ratio of the inner to outer envelope at each height was then taken to be a measure of f/ω.

Results from many meteorological rocket stations were collated into histograms and are reproduced in Figure 2. HN found that, virtually regardless of season or location, a most probable value of $f/\omega \approx 0.3$ results, and there is little probability of finding values of f/ω near 0 or 1. Only a slight but distinct decrease in peak value with decreasing latitude is evident. This result is despite the fact that changes in latitude alter the inertial frequency f and that the strong variation of the upper stratospheric background wind with altitude, latitude, and season must also change ω.

We propose that the distributions are an artifact of the method of analysis, as discussed in the next section.

Explanation Of Observations

Clearly, the HN analysis is perfectly valid for a single wave (assuming background wind shears are not significant). However, a spectrum of gravity waves exists in the atmosphere which, as has already been shown, will produce important superposition effects. Therefore a random superposition of waves exists generally, and individual wave ellipses will be severely distorted by the remaining oscillations (e.g., Figure 1 of HN). As r_{min}/r_{max} must, by definition, lie between 0 and 1, one must ask whether the observed ratio of ~0.3 might result rather from the data's distribution. For example, even if the wave spectrum were composed entirely of high-frequency waves, there is no reason why wave superposition could not produce r_{min}/r_{max} ratios anywhere in the range 0–1.

To examine this possibility, a simple simulation was performed. Independent zonal and meridional real oscillations due to many linearly polarized waves with random phase and amplitude were synthesized, as in Figure 1. This independence means that the vector length $(u'^2+v'^2)^{1/2}$ has two degrees of freedom. These data are statistically equivalent to an azimuthally isotropic wave field, which has two degrees of freedom in vector length as a result of the independence of the polar coordinates (r,ϕ). These simulated profiles were then analyzed using the HN technique. The dashed curves in Figure 3 are the distributions of r, r_{min}, r_{max} and r_{min}/r_{max} produced in a typical simulation. Notice especially the similarity in form of the simulated r_{min}/r_{max} distribution (Figure 3e) and the experimental f/ω distributions in Figure 2. The peak at $f/\omega \sim 0.3$ should be particu-

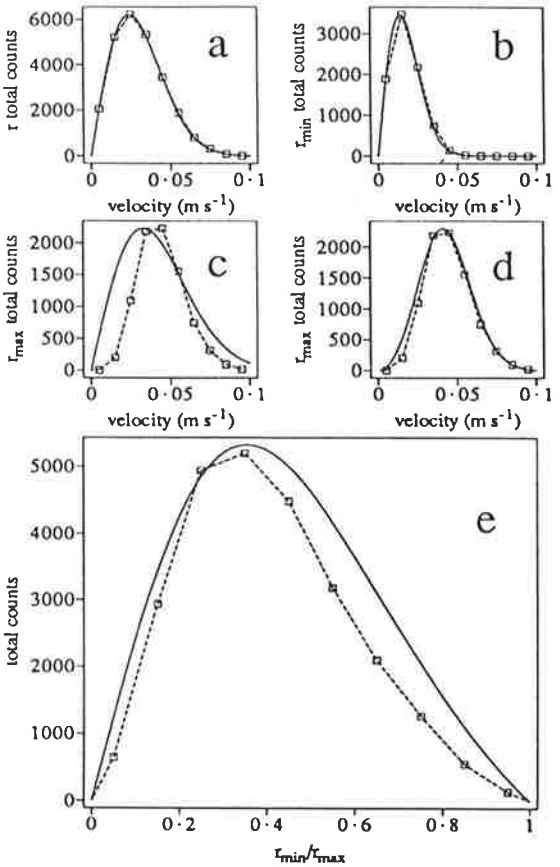

Fig. 3. Simulated (dashed curve) and analytical (solid curve) distributions of (*a*) r; (*b*) r_{min}; (*c*) and (*d*) r_{max}; and (*e*) r_{min}/r_{max}, where $r = (u'^2 + v'^2)^{1/2}$. See text for further details.

larly noted.

One can also demonstrate analytically that the peak near 0.3 is spurious. It is well known that a random superposition of phasors produces a resultant phasor whose vector length is Rayleigh distributed [e.g., *Beckmann*, 1962]. So, for a random superposition of gravity waves, u' and v' will have a Normal distribution, $r^2 = (u'^2+v'^2)$ will have a χ^2 distribution with ν equal to two degrees of freedom, denoted $p_\chi^\nu(r'^2)$, and r will have a corresponding Rayleigh distribution, denoted $p_R^\nu(r')$ (Figure 3*a*).

$$p_R^\nu(r') = \frac{2r'}{2^{\nu/2}\Gamma(\nu/2)} r'^{(\nu-2)} e^{-r'^2/2} = 2r'\, p_\chi^\nu(r'^2) \quad (2)$$

where $r' = r/\sigma$, and $\Gamma(x)$ is the gamma function.

Since f/ω is inferred from r_{min}/r_{max}, it is the latter quantity one must consider. Let us initially assume that like r, r_{min} and r_{max} are Rayleigh distributed with mean square values σ_{min}^2 and σ_{max}^2. The ratio $(r_{min}/r_{max})^2$ will then have an F distribution, with (ν_1=2,ν_2=2) degrees of freedom [*Johnson and Kotz*, 1970], denoted $p_F^{\nu_1,\nu_2}(t)$.

$$p_F^{\nu_1,\nu_2}(t) = \frac{1}{B(\nu_1/2,\nu_2/2)} \frac{t^{(\nu_1-2)/2}}{(1+t)^{(\nu_1+\nu_2)/2}} \quad (3)$$

where $t = (r_{min}/r_{max})^2(\sigma_{max}/\sigma_{min})^2$, and $B(x,y)$ is the beta function.

Figures 3*b* and 3*c* overlay simulated distributions of r_{min} and r_{max}, respectively, with Rayleigh distributions (using σ^2 values evaluated in the simulation). The simulated and analytical curves agree well for r_{min} but poorly for r_{max}. This poor agreement for r_{max} is not surprising, because one must expect this distribution to be offset to the right somewhat. Indeed, apart from an x axis shift, the simulated r_{min} and r_{max} distributions are similar in form and so the r_{max} distribution is better described by a noncentral Rayleigh distribution, denoted $p_R^{\nu,\lambda}(r)$, where λ is the square of some (constant) offset from zero along the x axis [*Johnson and Kotz*, 1970].

$$p_R^{\nu,\lambda}(r') = 2r' \sum_{j=0}^{\infty} \left(\frac{(\lambda/2)^j}{j!} \right) e^{-(\lambda/2)} \left[p_\chi^{\nu+2j}(r'^2) \right] \quad (4)$$

This formula holds for a constant offset λ, whereas in this application the offset itself has a probability distribution (Figure 3*b*). Despite this, on fitting (4) to the simulated r_{max} distributions, one obtains close agreement (Figure 3*d*). Consequently, the ratio $(r_{min}/r_{max})^2$ should then have a noncentral F distribution, with (ν_1=2,ν_2=2) degrees of freedom [*Johnson and Kotz*, 1970], denoted $p_F^{\nu_1,\nu_2,\lambda}(t)$.

$$p_F^{\nu_1,\nu_2,\lambda}(t) = \sum_{j=0}^{\infty} \left(\frac{(\lambda/2)^j}{j!} \right) e^{-(\lambda/2)} \left[p_F^{\nu_1,\nu_2+2j}(t) \right] \quad (5)$$

Using conservation of probability (i.e., $P(A^2)\, d(A^2) = P(A)\, dA$), one then finds that the ratio $\epsilon = r_{min}/r_{max}$ is distributed as $Q(\epsilon)$, where

$$Q(\epsilon) = 2\epsilon\, p_F^{\nu_1,\nu_2,\lambda}\left[\epsilon^2 \left(\sigma_{max}^2/\sigma_{min}^2\right)\right] \quad (6)$$

Calculations of r_{min}/r_{max} necessarily lie between 0 and 1. So the distribution value produced at $\epsilon = \epsilon^*$ will be proportional to $Q(\epsilon^*) + Q(1/\epsilon^*)$, since a value of ϵ greater than 1 will be treated as its reciprocal in the analysis. Since $P(1/A) = -A^2[P(A)]$, we finally derive the form of the f/ω distribution, $P(f/\omega)$, where K is a normalization constant.

$$P(f/\omega) = K\left(1 - (f/\omega)^2\right) Q(f/\omega) \quad (7)$$

Figure 3*e* overlays both the simulated f/ω distribution (from analysis of simulated data) and the analytical distribution (7), using λ, σ_{min}^2, and σ_{max}^2 values from the distributions in Figures 3*b* and 3*d*. Notice the similarity in shape amongst the simulated, analytical, and experimental (Figure 2) distributions.

Thus it is clear that the shape of the curves derived by HN and the peak at $f/\omega \sim 0.3$ are not necessarily indicative of the major gravity waves. Indeed, the same shape would even arise if the atmospheric gravity wave spectrum comprised only linearly polarized waves, and waves with $f/\omega \sim 0.3$ did not exist! While it may be

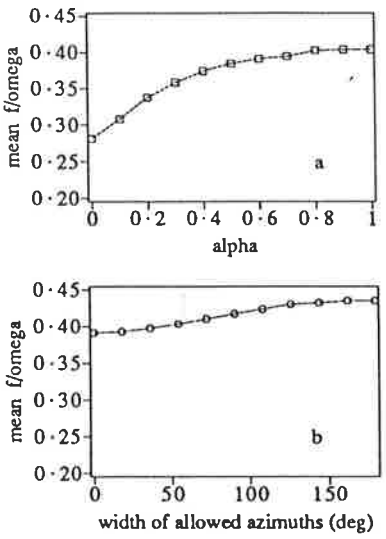

Fig. 4. Graphs of the change in the mean ratio $<f/\omega> = <r_{min}/r_{max}>$ with increased horizontal directionality, (*a*) using attenuation α of random meridional oscillations and (*b*) a numerical model in which gravity waves have a restricted width of allowed azimuths equal to $\beta(180°)$. See text for details of the model used in Figure 4*b*.

that some of the profiles analyzed by HN provided information on monochromatic oscillations, it seems clear that the combined results in Figure 2 are a statistical manifestation of a generally superposed wave field.

Mathematical Implications

The illustrated sole dependence of these f/ω distributions on the statistical parameters λ, σ^2_{min}, and σ^2_{max} has important implications. In particular, any horizontal anisotropy in wave propagation directions would effectively reduce the degrees of freedom ν_1 and ν_2, which in turn alters σ^2_{min} and σ^2_{max} and produces a change in shape of the distributions.

To investigate this possibility, two simulations were performed. In the first, independent zonal and meridional oscillations were produced in the manner previously outlined. A variable attenuation factor α was applied to the meridional components of oscillation, so that the degrees of freedom were effectively reduced, and the HN analysis was then performed. Since the unattenuated profiles are statistically equivalent to an azimuthally isotropic wave field, this process is equivalent to making the wave azimuth distribution progressively more anisotropic. From the resulting distributions, a mean value $<f/\omega> = \int(f/\omega)P(f/\omega)\ d(f/\omega)$ was evaluated. A mean value rather than the peak value was used to allow more accurate comparison with the distributions in Figure 2. Figure 4*a* plots the change in $<f/\omega>$ with attenuation α.

This simulation assumes that all the waves are linearly polarized along the direction of propagation. In fact, a secondary oscillation orthogonal to the direction of propagation is predicted by (1). Consequently, a more physically realistic simulation was performed using a gravity wave computer model. In this model a grid was set up in vertical wave number and intrinsic frequency space, and each point on the grid was defined an individual wave, except that the wave azimuth was, at this stage, undefined. Wave amplitudes were assigned by analytically integrating the two-dimensional wave spectrum [*VanZandt*, 1985; *Smith et al.*, 1987] over a rectangle centered on the relevant grid point and with dimensions equal to the grid spacing. Each wave was given a random starting phase and was allowed to propagate in time and space. All of the waves propagated energy upwards ($m < 0$), consistent with observations [e.g., HN; *Eckermann and Vincent*, 1989]. An isothermal 250 K atmosphere with no mean wind was used in this study. To investigate isotropy effects, each wave was also assigned a random azimuth direction between 0° and $\beta(180°)$, where β was between 0 and 1. In this way, azimuthal wave propagation had a "box car" polar diagram of width $\beta(180°)$. Resulting wave fields were analyzed using the HN method and $<f/\omega>$ values obtained as in the first simulation. The change in $<f/\omega>$ as a function of $\beta(180°)$ is shown in Figure 4*b* and may be compared with the mean f/ω values in Figure 2.

Using this gravity wave model, each simulated profile was also stored and analyzed for its direction of wave vector rotation, using the change in the ellipse vector phase angle with height, as described by HN. Using this technique, HN found appreciable anisotropy in the direction of wave vector rotation, consistent with the majority of the wave energy propagating from lower altitudes. Despite extensive superposition, we find, using the gravity wave model, that 65–70% of the rotations are clockwise in the mid-latitude northern hemisphere for a azimuthally isotropic field of 128 waves, consistent with the HN results. If one either decreases the number of waves (i.e., if one reduces the superposition) or if one introduces some azimuthal directionality, this clockwise percentage increases further. An example of the variation with azimuthal directionality is shown in Figure 5.

Physical Implications

Inspection of (5)–(7) reveals that the distributions depend only on the parameters λ, σ^2_{min}, and σ^2_{max}. Hence inferences of dominant wave frequencies from such results are not sustainable. Rather, the values are a measure of the horizontal localization in direction of the oscillations (Figure 4). With this new perspective, Figure 2 implies greater directionality in azimuthal wave propagation with decreasing northern latitude. It also reveals more alignment during winter than in the other seasons, which is consistent with increased critical level filtering by the strong wintertime zonal wind jets.

Some tentative corroboration for these inferences of

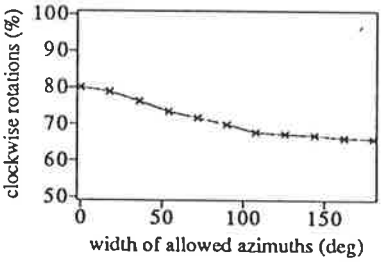

Fig. 5. Variation in the percentage of clockwise wave vector rotations (northern hemisphere) with azimuthal directionality for an ensemble of 128 waves produced by a numerical gravity wave model, as in Figure 4*b*.

wave directionality comes from a global gravity wave simulation using the Geophysical Fluid Dynamics Laboratory (GFDL) "SKYHI" general circulation model [*Miyahara et al.*, 1986]. All of the rocket stations in the HN study lie within a relatively narrow longitude interval, with eight of the 12 lying between 60° and 120°W. In this longitude zone, *Miyahara et al.* [1986] found a strong stratospheric $u'\Omega'$ flux, with Ω' equal to vertical pressure velocity, a pressure weighted vertical velocity expressed in log-pressure coordinates [*Miyahara et al.*, 1986], peaking at -2 x 10^{-5} m s^{-1} mbar s^{-1} at latitudes around 50°-60°N. At the equatorial locations of the HN study (Kwajalein and Ascension Island), a strongly positive $u'\Omega'$ flux of 4 x 10^{-5} m s^{-1} mbar s^{-1} was produced in the stratosphere, twice as large as the peak at 50°N. However, an earlier study by *Hirota* [1984] revealed that wave amplitudes around 50°N greatly exceed those at either Kwajalein or Ascension Island. This can only mean one of two things. Either the wave field at the tropical stations is far more directional than at the mid-latitude stations, which is precisely the result that we inferred earlier, or a much larger $v'\Omega'$ flux occurs at 50°N than at the equatorial sites. Unfortunately, meridional stress terms are not presented by *Miyahara et al.* [1986], nor in a more recent simulation with the Goddard Institute for Space Studies (GISS) model by *Rind et al.* [1988]. Mesospheric measurements from Saskatoon (52°N, 107°W) do suggest some preference for a north-south alignment during winter [*Manson and Meek*, 1988]. However, Figure 17 of *Miyahara et al.* [1986] shows more sign of meridional wave propagation at the equatorial stations than at the mid-latitude stations. Similarly, the wintertime scatter plots of *Hirota* [1984] show more indication of a preferred meridional alignment at Kwajalein (9°N, 168°E) than at Thule (77°N, 69°W). This tends to favor our interpretation of greater equatorial directionality, though clearly only direct measurement can confirm this.

Furthermore, we note from Figure 2 that the oscillations at Kwajalein exhibit even more directional localization than is allowed for in Figure 4*b*. So not only is the wave field here very directional, but there is less energy in the V' oscillations than theoretically predicted for a representative model spectrum of gravity waves. This means from (1) that, rather than a predominance, there is a relative dearth of inertia gravity waves at this location. This means that there is a low-frequency dip in the equatorial gravity wave intrinsic frequency spectrum, so that, in the end, the HN results have told us something about the intrinsic frequency of gravity waves. This result seems to be consistent with other observations that Kelvin wave and mixed Rossby-gravity wave motions are prevalent in the equatorial stratosphere [e.g., *Wallace*, 1973; *Hirota*, 1978; *Devarajan et al.*, 1985], since these fundamentally different types of waves are physically constrained to discrete horizontal directions, as opposed to simple gravity waves, giving rise to a very directional wave field. However, there is strong theoretical and observational evidence to suggest that mixed Rossby-gravity waves only occur in the lower stratosphere [e.g., *Hirota*, 1980], which favors an interpretation in terms of Kelvin waves alone.

Some experimental support for these assertions comes from the fact that the clockwise energy percentages calculated by HN at the equatorial stations (~65%) are significantly less than those at more northward latitudes (~80–90%). This implies either an azimuthally isotropic equatorial wave field (Figure 5), which contradicts our earlier inferences, or a lack of equatorial inertia gravity wave energy compared to that at more northward latitudes. Notice also that the 80–90% clockwise rotation found by HN at the nonequatorial sites indicates that superposition in the real atmosphere is less severe than in the 128-wave simulation used to produce Figure 5, as one might reasonably expect.

Our reanalysis of f/ω distributions can tell us nothing about directions of propagation, only the degree of directionality. At the tropical locations, *Miyahara et al.* [1986] found distinct indications of meridional gravity wave propagation from the low-latitude southern troposphere into the low to mid-latitude northern stratosphere, produced by the filtering action of easterly planetary wave winds. The study of *Miyahara et al.* [1986] simulated only short time intervals in December, January, and February. The invariance with season of the f/ω distributions at Kwajalein suggests that similarly directional gravity wave propagation may occur all the year round, although Kelvin wave and mixed Rossby-gravity wave motions must also be considered.

Further investigations into the horizontal propagation directions of stratospheric gravity waves are clearly needed, in order to compare with the three-dimensional wave propagation being found in global simulations. *Eckermann and Vincent* [1989] inferred highly directional south–eastward wave propagation during summer. General circulation model simulations during the southern summer [*Miyahara et al.*, 1986] also pro-

duce distinct south-eastward wave propagation from the equatorial troposphere into the middle atmosphere above Australia. Since these simulations have so far only produced climatologies of the $u'\Omega'$ stress term (a partially cancelling quantity), more detailed knowledge of horizontal wave directionality will also be needed in order to make more meaningful comparisons amongst these results and the mean u'^2 and T'^2 values that are most easily calculated in observational studies.

Conclusions

Wave superposition can lead to, and has led to, erroneous inferences concerning the occurrence of seemingly "monochromatic" gravity waves in the atmosphere. The need for caution in analyzing such events has been noted. In particular, we have addressed some recent measurements of wind structure made by rocket-borne techniques, which were analyzed in order to determine gravity wave intrinsic frequencies. We have shown that the analysis method, based on single wave assumptions, does not in fact supply information about intrinsic frequencies because of superposition effects, but it can, however, be reinterpreted to give information about the azimuthal directionality in wave propagation. A reanalysis reveals more wave directionality in winter than in other seasons at all latitudes and a highly directional wave field at the tropics. The equatorial directionality exceeds theoretical predictions for gravity waves and suggests a dearth of inertia gravity waves at the tropics, with Kelvin wave and mixed Rossby-gravity wave motions being more prevalent.

Acknowledgments. We thank R. A. Vincent, B. H. Briggs, I. Hirota, and two anonymous referees for constructive comments. We also thank Laurence Campbell for the use of his plotting software. SDE is supported by a Commonwealth of Australia Postgraduate Scholarship.

References

Balsley, B. B., W. L. Ecklund, and D. C. Fritts, VHF echoes from the high latitude mesosphere and lower thermosphere: Observations and interpretations, *J. Atmos. Sci.*, *40*, 2451–2466, 1983.

Beckmann, P., Statistical distribution of the amplitude and phase of a multiply scattered field, *J. Res. Natl. Bur. Stand., Sect. D*, *66*, 231–240, 1962.

Cadet, D., and H. Teitelbaum, Observational evidence of internal inertia-gravity waves in the tropical stratosphere, *J. Atmos. Sci.*, *35*, 892–907, 1979.

Cot, C., and J. Barat, Wave-turbulence interaction in the stratosphere, *J. Geophys. Res.*, *91*, 2749–2756, 1986.

Dewan, E. M., N. Grossbard, A. F. Quesada, and R. E. Good, Spectral analysis of 10-m resolution scalar velocity profiles in the stratosphere, *Geophys. Res. Lett.*, *11*, 80–83, 1984. (Correction, *Geophys. Res. Lett.*, *11*, 624, 1984.)

Devarajan, M., C. A. Reddy and C. Raghava Reddy, Rocket observations of Kelvin waves in the upper stratosphere over India, *J. Atmos. Sci.*, *42*, 1873–1879, 1985.

Eckermann, S. D., and R. A. Vincent, Falling sphere observations of anisotropic gravity wave motions in the upper stratosphere over Australia, *Pure Appl. Geophys.*, *130*, 509–532, 1989.

Gossard, E. E., and W. H. Hooke, *Waves in the Atmosphere*, 456 pp., Elsevier Science, New York, 1975.

Harper, R. M., and R. F. Woodman, Preliminary multiheight radar observations of waves and winds in the mesosphere over Jicamarca, *J. Atmos. Terr. Phys.*, *39*, 959–963, 1977.

Hass, H., and W. Meyer, Gravity wave fields above Andøya, *J. Atmos. Terr. Phys.*, *49*, 705–721, 1987.

Hines, C. O., On the analysis and interpretation of winds observed at heights of 85 to 135 kilometers: A rebuttal, *J. Geophys. Res.*, *71*, 1461–1475, 1966.

Hirota, I., Equatorial waves in the upper stratosphere and mesosphere in relation to the semiannual oscillation of the zonal wind, *J. Atmos. Sci.*, *35*, 714–722, 1978.

Hirota, I., Observational evidence of the semiannual oscillation in the tropical middle atmosphere: A review, *Pure Appl. Geophys.*, *118*, 217–238, 1980.

Hirota, I., Climatology of gravity waves in the middle atmosphere, *J. Atmos. Terr. Phys.*, *46*, 767–773, 1984.

Hirota, I., and T. Niki, A statistical study of inertia gravity waves in the stratosphere, *J. Meteorol. Soc. Jpn.*, *63*, 1055–1066, 1985.

Hocking, W. K., Reduction of the effects of non-stationarity in studies of amplitude statistics of radio wave backscatter, *J. Atmos. Terr. Phys.*, *49*, 1119–1131, 1987.

Johnson, N. I., and S. Kotz, *Continuous Univariate Distributions*, vol. 2, 306 pp., Houghton Mifflin, New York, 1970.

Maekawa, Y., S. Fukao, T. Sato, S. Kato, and R. F. Woodman, Internal inertia gravity waves in the tropical lower stratosphere observed by the Arecibo radar, *J. Atmos. Sci.*, *41*, 2359–2367, 1984.

Manson, A. H., and C. E. Meek, Gravity wave propagation characteristics (60–120 km) as determined by the Saskatoon MF radar (Gravnet) system: 1983–1985 at 52°N, 107°W, *J. Atmos. Sci.*, *45*, 932–946, 1988.

Miller, K. L., S. A. Bowhill, K. P. Gibbs, and I. D. Countryman, First measurements of mesospheric vertical velocities by VHF radar at temperate latitudes, *Geophys. Res. Lett.*, *5*, 939–942, 1978.

Miyahara, S., Y. Hayashi, and J. D. Mahlmann, Interactions between gravity waves and planetary-scale flow simulated by the GFDL "SKYHI" general circulation model, *J. Atmos. Sci.*, *43*, 1844–1861, 1986.

Owens, A. J., An algorithm for generating fluctuations having any arbitrary power spectrum, *J. Geophys. Res.*, *83*, 1673–1675, 1978.

Rind, D., R. Suozzo, N. K. Balachandran, A. Lacis, and G. Russell, The GISS global climate-middle atmosphere model, I; Model structure and climatology, *J. Atmos. Sci.*, *45*, 329–370, 1988.

Shibata, T., T. Fukuda, and M. Maeda, Density fluctuations in the middle atmosphere over Fukuoka observed by an XeF Rayleigh lidar, *Geophys. Res. Lett.*, *13*, 1121–1124, 1986.

Smith, S. A., D. C. Fritts and T. E. VanZandt, Evidence of a saturated spectrum of atmospheric gravity waves, *J. Atmos. Sci.*, *44*, 1404–1410, 1987.

VanZandt, T. E., A universal spectrum of buoyancy waves in the atmosphere, *Geophys. Res. Lett.*, *9*, 575–578, 1982.

VanZandt, T. E., A model for gravity wave spectra observed by Doppler sounding systems, *Radio Sci.*, *20*, 1323–1330, 1985.

Wallace, J. M., General circulation of the tropical lower stratosphere, *Rev. Geophys.*, *11*, 191–222, 1973.

S .D. Eckermann and W. K. Hocking, Department of Physics and Mathematical Physics, University of Adelaide, Adelaide,
South Australia 5001, Australia.

(Received June 21, 1988;
revised September 28, 1988;
accepted October 17, 1988.)

Appendix G

Effects of nonstationarity on spectral analysis of mesoscale motions in the atmosphere

This is a preprint of a paper by S.D. Eckermann, which has been accepted for publication in *J. Geophys. Res.*, 1990.

Effects of Nonstationarity on Spectral Analysis of Mesoscale Motions in the Atmosphere

STEPHEN D. ECKERMANN[1]

Department of Physics and Mathematical Physics, University of Adelaide, Adelaide, South Australia

Computation of the power spectra of mesoscale atmospheric motions from experimental data has become a way of addressing a number of important dynamical questions. These include whether gravity waves or quasi two–dimensional turbulence (also interpreted as vortical modes) are the more energetic mesoscale fluctuations, and whether the atmospheric gravity wave spectrum is convectively saturated. Yet the variance of these small-scale atmospheric motions varies appreciably in space and time, and so spectra computed from such nonstationary data will generally differ from the stationary shape. A model of the vertical wave number spectrum of horizontal velocity fluctuations produced by saturated gravity wave motions has been developed, and it predicts that the spectral form varies considerably with altitude. The effects on spectral computations of this inherent nonstationarity are examined in depth. It is found that this altitude nonstationarity gives rise to computed spectra of the form m^{-t}, where t lies between the nominal unsaturated and saturated values of 0 and 3 respectively. Many spectral measurements which do not compare favorably with the original model spectrum have this shape, and on inspection appear likely to suffer appreciably from nonstationarity, while other measurements which better compare with the model spectrum appear to do so because the nonstationarity was minimized in these measurements. Simulations involving observed examples of the temporal nonstationarity of time–fluctuating motions reveal that computed frequency spectra are not significantly altered in shape. However, gravity wave and vortical mode theories both provide models of the ground–based frequency spectrum, and both theories predict that these spectra are also nonstationary if the background wind speed varies with time, due to Doppler–shifting effects. Representative simulations of the problem reveal that limited distortions to the gravity wave spectrum arise, but that the vortical mode spectrum can be modified significantly; on occasions its shape is altered to one more like that of the gravity wave model spectra. This may be a candidate for explaining why a number of studies comparing measured frequency spectra with model predictions, in order to ascertain whether gravity waves or vortical modes (or both) produce this fluctuating variance, have produced conflicting conclusions. Because of this possibility, a more stationary measure, termed the "polarization ratio", is derived and presented as an additional independent means of evaluating whether gravity waves or vortical modes are responsible for the horizontal velocity fluctuations measured by ground–based sensors.

1. INTRODUCTION

Computation of power spectra has become standard in the analysis of mesoscale motions within the atmosphere and ocean. In the atmosphere, advances in ground-based remote sensing techniques have facilitated spectral investigations of velocity, temperature and density fluctuations over a wide spatial and temporal range. Many such measurements have been made at different times of the year and at different locations, and they have revealed reproducible shapes and similar intensities [e.g., *Balsley and Carter*, 1982; *Vincent*, 1984; *Meek et al.*, 1985; *Fritts and Chou*, 1987; *Fritts et al.*, 1988; *Shibata et al.*, 1988; *Fritts et al.*, 1990; *Kwon et al.*, 1990]. Much theoretical effort has been directed towards understanding the dynamics which give rise to these observed spectra, and two different processes have been proposed.

VanZandt [1982] suggested that the spectra are produced by internal gravity wave motions. Following the successful analysis of similar oceanic spectra by *Garrett and Munk* [1972, 1975], *VanZandt* [1982] presented empirical analytical relations which best modelled the observed spectra while ensuring consistency with the dispersion relation for gravity waves. This approach has been continued and updated by *Sidi et al.* [1988]. On the other hand, *Gage and Nastrom* [1985, 1986] have argued that quasi two-dimensional turbulence, or the vortical mode of motion as it is now often interpreted [e.g., *Müller et al.*, 1988; *Gage and Nastrom*, 1988], is responsible for these spectra and the associated mesoscale

variance.

Both theories predict the spectral shapes which should be observed if either process is the more dominant in energy [e.g., *Gage*, 1979; *VanZandt*, 1982; *Scheffler and Liu*, 1986; *Dewan and Good*, 1986; *Fritts and VanZandt*, 1987; *Smith et al.*, 1987; *Gage and Nastrom*, 1988]. Despite this, comparisons of spectral measurements with the predictions of each theory have been equivocal. While it now seems generally accepted that gravity wave motions are responsible for the vertical velocity frequency spectra measured in light wind conditions [e.g., *Ecklund et al.*, 1986], in stronger wind conditions and in the horizontal there is enough ambiguity in the comparisons that neither process can yet be accepted as dominant or dismissed as inconsistent with observations. This superficially suggests that both types of motion coexist, as postulated by *Lilly* [1983], but that the relative and absolute contributions to the total mesoscale variance are variable, or nonstationary.

Analysis of the spectra in terms of gravity waves has generally been more successful, and so this interpretation has gained wider acceptance. However, the physical processes that act on the gravity wave field to produce the observed spectral shape and intensity have yet to be agreed upon. The ability of non-linear interactions amongst a wave ensemble to produce and maintain the oceanic spectrum has been extensively investigated (see the review of *Müller et al.* [1986]). In the atmosphere, however, wave amplitude saturation due to convective instability is now thought to be responsible for much of the spectral structure, although other mechanisms have also been considered (see reviews by *Fritts* [1984, 1989], and *Dunkerton* [1989]). *Dewan and Good* [1986] and *Smith et al.* [1987] have used a linear gravity wave saturation hypothesis to derive a theoretical vertical wave number spectrum for horizontal velocity fluctuations in the atmosphere. This theory, if correct, could have important applications in parameterizing the effects on the background flow of a full spectrum of dissipating gravity waves [e.g., *Fritts*, 1989; *VanZandt and Fritts*, 1989].

Spectra computed from measurements have been used to test this idea too, and again the degree of correspondence with the theory has been variable. While the model spectrum agrees very well with some measurements [*Dewan et al.*, 1984; *Fritts and Chou*, 1987; *Fritts et al.*, 1988], there are other experimentally determined vertical wave number spectra where the agreement is less marked, and so these spectra appear to deviate somewhat from the model [e.g., *Vincent*, 1984; *Hass and Meyer*, 1987; *Maekawa et al.*, 1987; *Shibata et al.*, 1988; *Eckermann and Vincent*, 1989].

While dynamical theories which can explain the observed atmospheric spectra have been actively pursued, possible sources of contamination that might affect such spectral measurements have not been investigated in depth. Nevertheless many such sources have been identified in measurements, such as the sampling and digitization used in recording the data [e.g., *Kristensen and Kirkegaard*, 1987; *Moore et al.*, 1988; *Kaimal et al.*, 1989], and many different instrumental effects [e.g., *Miller*, 1969; *Fukao et al.*, 1988*a*, *b*; *May et al.*, 1988; *Sidi et al.*, 1988; *Eckermann and Vincent*, 1989]. In addition, the motion spectra themselves vary in response to environmental factors, such as background wind speed [e.g., *Ecklund et al.*, 1986; *Scheffler and Liu*, 1986; *Fritts and VanZandt*, 1987] and atmospheric stability [e.g., *Smith et al.*, 1987; *VanZandt and Fritts*, 1989].

Whatever the actual dynamics are, it is clear from obser-

vations that the resulting mesoscale variance often changes appreciably on both short and long time scales [e.g., *Hirota*, 1984; *Meek et al.*, 1985; *Vincent and Fritts*, 1987; *Fritts and Chou*, 1987; *Cornish*, 1988; *Fukao et al.*, 1989; *Fritts*, 1989]. The variance also increases systematically with altitude [e.g., *Balsley and Carter*, 1982; *Hirota and Niki*, 1985; *Balsley and Garello*, 1985] and exhibits appreciable geographic variability [e.g., *Hirota*, 1984; *Gage and Nastrom*, 1986; *Nastrom et al.*, 1987; *Fritts et al.*, 1989]. This means that spatial and temporal series of experimentally sampled data, from which spectra are computed, must indeed be nonstationary; that is, the variance, and hence the spectral form, is not the same at all points in the data series. Although "nonstationarity" is usually associated with time series analysis, it will be used hereafter to describe the variability evident in both spatial and temporal data series.

It is well known that nonstationarity can change the spectral shape when data are Fourier transformed, yet the possible effects on spectral computations of nonstationary characteristics evident in mesoscale motion data have not been adequately addressed. Since the shape and intensity of measured spectra are now being used to evaluate theories about the nature of these fluctuating dynamics, investigation of possible nonstationary distortion of computed spectra is warranted.

To address these issues, the specific problem of nonstationarity with altitude of the model vertical wave number spectrum of *Smith et al.* [1987] is first considered in section 2. The insights gained here are then applied in section 3 to the general problem of spectral analysis of mesoscale motions in the frequency and horizontal wave number domain. In section 4, a fractional measure, which remains stationary even when the variance is nonstationary, is developed and presented as being potentially useful in experimentally evaluating whether gravity waves or vortical modes are the more energetic fluctuations in generally nonstationary data.

2. Altitude Nonstationarity of the Vertical Wave Number Spectrum

To investigate the general problem of spectral nonstationarity, we shall first consider a specific one; the change of form with altitude of the model vertical wave number spectrum proposed by *Smith et al.* [1987]. This is done for two main reasons. The first is that the height variation of this spectrum has a regular exponential form, and so is amenable to analysis. Secondly, the wave saturation theory used to derive the model spectrum of *Smith et al.* [1987] is important in its own right, and requires experimental corroboration. Therefore, any contamination of the spectral measurements which might affect the comparisons needs to be investigated.

2.1. *Background Theory*

Consider a gravity wave, produced at ground level with a peak horizontal velocity amplitude u_0' and vertical wave number m_0, which propagates upwards and zonally into the middle atmosphere. Assuming the wave has neither a very low nor very high intrinsic frequency, then on propagating to some altitude z, the peak wave amplitude $u'_{\rm peak}(z)$ is given approximately by the expression [*Lindzen*, 1981; *Schoeberl*, 1985]

$$u'_{\rm peak}(z) = u_0' \left(\frac{m}{m_0}\right)^{1/2} e^{z/2H_\rho} \qquad (1)$$

where m is the vertical wave number and H_ρ is the density scale height.

A wave therefore grows in amplitude exponentially as it propagates vertically into the less–dense upper atmosphere. The wave amplitude may eventually become so large that it produces a vertical temperature gradient which exceeds the adiabatic lapse rate of the background atmosphere, and so the wave becomes convectively unstable. This occurs when [e.g., *Fritts*, 1984]

$$u'_{\rm peak}(z) \geq \mid \bar{U} - c \mid \approx N/m \qquad (2)$$

where $\bar{U}$ is the background horizontal wind speed, c is the ground-based horizontal phase speed, and N is the Brunt-Väisälä frequency.

Saturation theory, in its simplest form [e.g., *Lindzen*, 1981; *Fritts*, 1984, 1989; *Dunkerton*, 1989], predicts that the wave does not overturn and dissipate completely at this altitude. Instead, only sufficient turbulent diffusion is generated to maintain the wave amplitude $u'_{\rm peak}(z)$ at the instability threshold N/m. *Dewan and Good* [1986] argued that this implies a saturated vertical wave number power spectrum of u' fluctuations, designated hereafter $F_u(m)$, proportional to N^2/m^3. *Smith et al.* [1987] extended this single wave theory to include a general superposition of both saturated and unsaturated waves. They arrived at the following quasi-empirical expression for the power spectrum:

$$F_u(m) = \frac{N^2}{6m_*^3} \frac{1}{[1 + (m/m_*)^3]} \qquad (3)$$

This model spectrum is illustrated in Figure 1. The waves which have wave numbers greater than m_* are saturated and produce an m^{-3} spectrum, whereas waves with wave numbers less than m_* are unsaturated, produce a flat spectrum, and grow in amplitude approximately as $e^{z/2H_\rho}$. Hence there is a convenient partitioning of the saturated and unsaturated waves in the vertical wave number domain. The analytical function (3), however, is to some extent arbitrary. The formula itself was originally used by *Desaubies* [1976] to model the oceanic wave spectrum. It was later adopted by *VanZandt* [1985] and *Smith et al.* [1987] for the atmospheric spectrum because it most closely represents the observed spectral shape of the transition region between the saturated and unsaturated spectrum, which theory currently makes no prediction about. Nevertheless, different analytical formulae can be, and have been, used [e.g., *VanZandt*, 1982; *Sidi et al.*, 1988; *VanZandt and Fritts*, 1989].

The flat nature of the unsaturated spectrum is also somewhat arbitrary, and is chosen again because it corresponds with the observations. *Fukao et al.* [1989] showed that the wave amplitude variation (1) implies a flat unsaturated spectrum for a constant u'_0, just as (2) implies an m^{-3} spectrum. However, *VanZandt and Fritts* [1989] argued that the unsaturated portion of the spectrum should have a positive spectral index, so that the vertical flux of wave action remains finite. In any case, in the real atmosphere source transience will always make this part of the spectrum rather variable in form, and so any functional fit of the unsaturated spectrum can never be adequate for every measurement.

The variance of the wave field $\overline{u'^2}$ is found, according to Rayleigh's theorem [*Bracewell*, 1978], by integrating this spectrum.

$$\overline{u'^2(z)} = \int_{m_1}^{m_2} \frac{N^2}{6m_*^3(z)} \frac{1}{1 + [m/m_*(z)]^3} dm$$

$$= \frac{N^2}{6m_*^2(z)}\left[\frac{1}{6}\ln\left(\frac{(\mu+1)^2}{\mu^2-\mu+1}\right)+ \frac{1}{\sqrt{3}}\arctan\left(\frac{2\mu-1}{\sqrt{3}}\right)\right]_{m_1}^{m_2} \quad (4)$$

where $\mu = m/m_*(z)$ and where m_1 and m_2 define the wave number range. On integrating over all wave numbers ($m_1 = 0$ to $m_2 = \infty$), one finds $\overline{u'^2} \approx N^2/5{m_*}^2$. This total wave variance is assumed to grow with height as e^{z/H_E}, where $H_E > H_\rho$ due to the nongrowth with height of the saturated waves. This in turn implies

$$m_*(z) \approx m_*(z_0)e^{-(z-z_0)/2H_E} \quad (5)$$

indicating that, with increasing altitude, a greater fraction of the wave field ($m > m_*$) becomes saturated. As most of the variance is concentrated around m_* [e.g., *Smith et al.*, 1987], this also implies that the vertical wavelength of the most energetic waves in the spectrum increases with height.

This model spectrum, however, is unusual, in so far as it holds only at a given height, since m_* is height dependent. Yet the very process of obtaining a vertical wave number spectrum involves transforming data over a prescribed height range. Clearly then, if one were to compute a vertical wave number spectrum from data over a large altitude range, one would expect this change in spectral form with height (see Figure 1) to produce a resultant spectrum somewhat different to (3). The effect has been considered for a single wave propagating in the sodium layer by *Gardner and Voelz* [1985, 1987] and within the neutral atmosphere by *Gardner et al.* [1989]. A detailed consideration of the problem in a general sense will be attempted here for a full spectrum of waves. Before introducing a model used to accurately simulate the full effects, however, a brief outline of the problem will be given.

2.2. *Formulation of the Problem*

Let $v'(z)$ be a height profile of wave fluctuations which are governed by the model spectrum (3) as evaluated at one height z_1 (so that $v'(z)$ is stationary), and let $V(m)$ be its Fourier transform, where $V(m)$ is generally complex. Now we define a more realistic wave profile $p'(z)$ which grows in amplitude with height as $a(z)$, such that $p'(z) = a(z)v'(z)$. If the Fourier transform of $a(z)$ is $A(m)$, then it is well known that the Fourier transform of $p'(z)$, designated $P(m)$, is given by the convolution of $A(m)$ with $V(m)$ [e.g., *Bracewell*, 1978], here denoted $A(m) \otimes V(m)$. Thus the measured spectrum $|P(m)|^2$ will generally be different to the model spectrum $|V(m)|^2$ given by (3).

Consider first a case where $m_* \to \infty$, so that all the constituent waves are unsaturated and grow in amplitude with height as $a(z) = e^{z/2H_\rho}$. The Fourier transform $A(m)$ of this exponential growth over an altitude range $z_s = z_2 - z_1$ (where z_2 and z_1 are the upper and lower height limits of the measurement, respectively) is

$$A(m) = \frac{2}{(1/2H_\rho)^2+m^2}\left\{\left[\frac{1}{2H_\rho}\sinh\left(\frac{z_s}{4H_\rho}\right)\cos\left(\frac{mz_s}{2}\right)+m\cosh\left(\frac{z_s}{4H_\rho}\right)\sin\left(\frac{mz_s}{2}\right)\right]+ i\left[m\sinh\left(\frac{z_s}{4H_\rho}\right)\cos\left(\frac{mz_s}{2}\right)-\right.$$

$$\frac{1}{2H_\rho}\cosh\left(\frac{z_s}{4H_\rho}\right)\sin\left(\frac{mz_s}{2}\right)\Bigg]\Bigg\} \qquad (6)$$

$$A(m) = A_R(m) + iA_I(m)$$

Figure 2*a* plots $A_R(m)$ and $A_I(m)$ as dotted and dashed lines, respectively, using representative values of $z_s = 40$ km [*Hass and Meyer*, 1987; *Eckermann and Vincent*, 1989] and $H_\rho = 7$ km. $|A(m)|$ is overlayed with a solid curve.

Since $A_R(m)$ and $A_I(m)$ have a modulated sinusoidal nature, the convolved spectrum $P(m) = A(m) \otimes V(m)$ must depend on the instantaneous phases amongst the constituent waves in the spectrum $V(m)$. Such phases are indeterminate, and so for one spectral measurement, the exact form of the measured power spectrum $|P(m)|^2$ cannot be predicted. However, since no preferred phase scheme for the wave spectrum $V(m)$ should occur, the averaged effect of this convolution will be dictated largely by the forms of $|A(m)|$ and $|V(m)|$. The intrinsic spectral amplitude at a wave number m_i, $|V(m_i)|$, should therefore be spread on average through wave number space according to $|A(m - m_i)|$. Figure 2*b* illustrates how $|A(m)|$ evolves as the scale height H_ρ changes. When $H_\rho \gg z_s$, the wave growth $a(z)$ is negligible, the profile is stationary, and $|A(m)|$ produces the $\sin(m)/m$ spectral spreading which characterizes truncated data [e.g., *Kaimal et al.*, 1989]. Dashed lines in Figure 2*b* mark the points which are sampled using a fast Fourier transform (FFT) algorithm. This $\sin(m)/m$ shape appears as a delta function using digital Fourier techniques, and so no further spreading occurs, as one would expect for a stationary process. As the scale height H_ρ decreases and exponential growth over the height range z_s becomes more pronounced, however, these $|A(m)|$ curves assume a broad Lorentzian shape, which will produce spreading of the stationary spectral power $|V(m)|^2$.

Since $|A(m - m_i)|$ spreads energy equally either side of m_i, the flat unsaturated part of the spectrum should ideally be unaltered in shape after convolution with $|A(m)|$. However, as the computational realization of this convolution is incomplete at the end points of the spectrum (the amplitude can be spread in one direction but cannot be spread in the other direction), then this must in practice result in some reduction of spectral power at the smallest wave numbers.

The effect on the saturated part of the spectrum, however, should be more pronounced. Even though $|A(m)|$ produces a symmetrical spreading of spectral power, the "red" m^{-3} nature of $|V(m)|^2$ at saturated wave numbers must result in more spectral power being spread to higher wave numbers than that spread to lower wave numbers, and will produce an actual fall-off in spectral power more gradual than m^{-3}.

The effects on the spectrum of the exponential growth of a single wave have been considered by *Gardner and Voelz* [1985, 1987] and *Gardner et al.* [1989], and similar convolution effects to those anticipated here do indeed arise. In the sodium layer, due to a highly nonlinear response, a single wave is characterized by a "notch" in the spectrum between two peaks [*Gardner and Voelz*, 1985]. Any exponential wave growth with height results in spectral power being spread from the peaks to fill in this "notch" region. Indeed, *Gardner and Voelz* [1985, 1987] have used the observed difference in height between the "notch" and peaks (i.e., how much the "notch" has been "filled in") to measure the amplitude growth with height of individual waves. Within the neutral atmosphere, the relative density response of a monochromatic wave gives rise to a main peak with side lobes in the density fluctuation spectrum [*Gardner et al.*, 1989]. Here

again, wave growth with height causes spreading which fills in the gaps between successive peaks.

2.3. *Numerical Simulation of the Problem*

If $a(z)$ indeed had a well-defined functional form of the type $e^{z/2H_\rho}$ for all wave numbers m, the growth could be mathematically incorporated into the model spectrum, as in the single wave derivations of *Gardner and Voelz* [1985, 1987] and *Gardner et al.* [1989]. However, in most measurements the growth profile of the gravity waves is a function of both height and wave number, designated $\hat{a}(z,m)$. This arises because some wave numbers in the profile are saturated at all heights, others are unsaturated but grow with height to eventually saturate at some altitude, while still others are unsaturated at all heights. This makes mathematical analysis of the problem infeasible, and so the best way to gauge the effect of the growth $\hat{a}(z,m)$ on the spectrum is by numerical simulation. A model used to carry this out will now be described.

At a starting height z_1, $K/2$ individual waves of wave number m_i were defined. Their initial wave variances $\overline{u'^2(z_1,m_i)} = u'^2_{\text{peak}}(z_1,m_i)/2$ $(i = 1,...,K/2)$ were calculated by integrating under the model spectrum (3) over a wave number interval which was centred on $m_i = i(\Delta m)$ and had a width $\Delta m = 2\pi/(K\delta z)$, where δz was the height resolution. This integral was evaluated using the exact analytical expression (4). The fully superposed wave field $p'(z)$ of K sampled points was then synthesized up to a height z_K using the superposition relation

$$p'(z) = \sum_{j=1}^{K} \sum_{i=1}^{K/2} u'_{\text{peak}}(z_j,m_i) \sin(m_i z_j + \varphi_i) \qquad (7)$$

where the peak amplitude $u'_{\text{peak}}(z_j,m_i)$ was recalculated at each height z_j using (4). This must be done because the spectrum, and hence the wave variance, changes with height according to its m_* dependence in (5). This results in the same wave growth with height and wave number $\hat{a}(z,m)$ that is incorporated in the model spectrum (3). The wave phases φ_i were set randomly between 0° and 360°. The data were then Fourier transformed using an FFT algorithm, and the power spectrum calculated.

This entire process was carried out 2000 times in the example presented here to produce one phase-averaged mean power spectrum. It is plotted as the solid curve in Figure 3*a*, and will be referred to as the nonstationary spectrum. In this simulation, values of $z_K - z_1 = 44.8$ km, $K = 256$, $N = 0.02$ rad s^{-1}, $H_E = 10$ km, and $m_*(z_1) = (1\text{ km})^{-1}$ were used. The original model spectrum (3), evaluated using a value of m_* which gives a near fit to the nonstationary spectrum, is also plotted for comparison with a dashed line.

Clearly the nonstationary spectrum exhibits a more gradual transition in slope than the model spectrum (3). The addition of power at the largest wave numbers, as anticipated in section 2.2, is particularly significant, and in this example gives rise to a constant power law form of $m^{-2.5}$ at the saturated wave numbers, as opposed to the stationary m^{-3} shape. Figure 4 enlarges the region between 1 and 15 km, which approximates the smallest and largest resolvable vertical wavelengths, respectively, of various rocket [e.g., *Hirota*, 1984; *Eckermann and Vincent*, 1989], lidar [e.g., *Shibata et al.*, 1988; *Gardner et al.*, 1989], and radar [e.g., *Vincent*, 1984; *Maekawa et al.*, 1987] observations of the middle atmosphere. Note the more gradual transition in slope of

the nonstationary spectrum as compared to the model spectrum.

One should be a little wary in comparing the results in Figure 3 too closely with actual spectral measurements. As mentioned in section 2, the model spectrum (3) is a quasi-empirical relation, and may not depict the true local spectrum. In fact, being based to some extent on observations, (3) must really be a nonstationary version of the local spectrum, arising from the effects that nonstationarity with height must have on even the most high resolution spectral measurements. Since a principal effect of the altitude nonstationarity is to make the transition from the saturated to unsaturated spectral regimes more gradual (see Figure 4), it suggests that the break point in the local spectrum may be sharper than in the present model. As (3) is therefore already somewhat broadened, these simulations probably overestimates the spreading effects a little. If a better form of the local spectrum is found, similar nonstationarity simulations should be more correctly applied to it rather than the current model.

There are other experimental effects in addition to nonstationarity with height that must be considered. For example, spectral aliasing may be important. To investigate this, the same simulation was repeated with the original $K/2$ unaliased waves, plus a further $K/2$ aliased waves, all of which are governed by the model spectrum (3). The results are shown in Figure 3*b*. Comparing Figures 3*a* and 3*b*, one can see that aliasing produces further enhancement of spectral power at the largest saturated wave numbers.

There are many other experimental and environmental factors that may also produce spectral contamination. However, while one can sometimes eliminate the effects of these processes with judicious correction techniques, distortion due to the inherent nonstationarity of the spectrum with height is an experimentally intractable problem.

2.4. *Comparison with Observations*

Figures 3 and 4 show that a major effect of nonstationarity in height is the production of a somewhat constant power law form of m^{-t} over a significant wave number range, where $0 < t < 3$. Many measured wave number spectra that do not correspond very well with the model spectrum of *Smith et al.* [1987] have such a shape, and are also taken over a large altitude and moderate wave number range, similar to Figure 4 [e.g., *Vincent*, 1984; *Maekawa et al.*, 1987; *Hass and Meyer*, 1987; *Shibata et al.*, 1988; *Eckermann and Vincent*, 1989]. Furthermore, intercomparisons of various spectral studies in the upper stratosphere [e.g., *Hass and Meyer*, 1987; *Eckermann and Vincent*, 1989] and mesosphere [e.g., *Vincent*, 1984; *Maekawa et al.*, 1987] measured over similar wave number ranges revealed a spectral index $t \approx 1$–2 in the stratosphere, but $t \approx 2$–3 at mesospheric altitudes. *Eckermann and Vincent* [1989] demonstrated explicitly that t grows with height by comparing spectral calculations at an upper and lower height range. This is consistent with the findings presented here, since a greater fraction of the waves at higher altitudes are saturated/stationary, according to (5), and so the shift in the spectral index away from the saturated value of t=3 toward the unsaturated t=0 should be less severe in the mesosphere than in the stratosphere.

One must now ask why some other measured spectra do indeed agree very well with the original model spectrum [*Dewan et al.*, 1984; *Fritts and Chou*, 1987; *Fritts et al.*, 1988]. The study of *Dewan et al.* [1984] used stratospheric smoke-

trail data over a small height range, with a vertical resolution of 10 m. Similarly, *Fritts and Chou* [1987] analyzed ST radar data between 9 and 19 km with a resolution of 300 m, and *Fritts et al.* [1988] analyzed high resolution balloon and radar data over several small altitude ranges. In all cases, the spectra were taken over short time spans. Therefore in each study any effects of nonstationarity in both height and time were minimized. The high vertical resolution in each data set also means that a significant fraction of the resolved wave field at large wave numbers was always saturated, and therefore stationary, as can be seen in Figure 1.

2.5. *"Universal" Spectra*

This spectral nonstationarity impacts on the so-called "universal spectrum" of gravity waves. The idea of spectral universality first arose from long-term averaging of observed oceanic and atmospheric spectra [e.g., *Garrett and Munk*, 1972, 1975; *VanZandt*, 1982], and so the "universal spectrum" was a relation that was only applicable to long-term spectral averages. With the ensuing theoretical development of the gravity wave vertical wave number spectrum [e.g., *Dewan and Good*, 1986; *Smith et al.*, 1987], and appreciation of the nonstationarity of this spectrum, comparisons with the new model are now best done in the atmosphere using data with good height and time resolution, but taken over a restricted height range.

With this new perspective, the initial universal vertical wave number spectrum put forward by *VanZandt* [1982] can be viewed as the mean result of altitude (and possibly temporal) nonstationarity of the local wave spectrum. The universal spectral index of t=2.4, initially found by *VanZandt* [1982] to best fit the measured spectra from the lower atmosphere, is likely the long-term end result of the distortion of a largely saturated spectrum of gravity waves by spectral nonstationarity. The $m^{-2.5}$ shape of the simulated nonstationary spectrum in Figure 3*a* should be especially noted. Other theoretical studies addressing Doppler shifting of gravity wave energy [*Scheffler and Liu*, 1986; *Fritts and VanZandt*, 1987] have also altered the perspective on spectral universality in the frequency domain. The atmospheric gravity wave spectrum in fact can be rather variable, and ideas of long-term universality of gravity wave spectra, which initially motivated their study, have now been superseded by the resulting advances in theoretical understanding of these spectra.

The analytical spectral formula $F'(m)$ adopted by *VanZandt* [1982] is the same relation that *Garrett and Munk* [1975] used in their spectral parameterization of the oceanic wave field, and has the form

$$F'(m) = \frac{E}{m_*} \frac{t-1}{(1+m/m_*)^t} \tag{8}$$

where E is the total energy. Although *VanZandt* [1982] used $t = 2.4$, the spectrum is plotted in Figure 5 using $t = 3$ for ease of comparison with the model of *Smith et al.* [1987]. The model saturated spectrum (3) and the nonstationary spectrum from Figure 3*a* are replotted in Figure 5 as well. Notice in Figure 5 that (8) incorporates a more gradual transition between saturated and unsaturated spectral shapes than the transition region of the model spectrum of *Smith et al.* [1987]. The nonstationary spectrum also exhibits a more gradual transition than the model spectrum, and any temporal nonstationarity may produce further broadening. Thus spectral nonstationarity drives the spectrum towards

a shape more like that of the Garrett-Munk relation (8) used by *VanZandt* [1982]. This adds weight to the assertion that the original universal spectral parameterizations may be viewed as the long-term results of nonstationarity in both height and time of the local gravity wave spectrum.

3. Nonstationarity of Other Spectra

In addition to vertical wave number spectra, one can also compute horizontal wave number spectra and ground–based frequency spectra of mesoscale motions in the atmosphere. However, there are several factors which make the analysis of these spectra less straightforward than vertical wave number spectral analysis.

First, the altitude variability of the vertical wave number spectrum has a well–defined form. No such systematic nonstationarity arises in the study of horizontal wave number or frequency spectra. Quasi–random changes occur in these cases, and so an all–encompassing simulation of the problem is impossible. Consequently, only representative simulations of some observed examples of nonstationarity will be attempted here.

Second, the exact dynamics and the intrinsic spectral shapes are not well known for these spectra. While a gravity wave interpretation of mesoscale motion spectra was assumed in section 2, *Gage* [1979], *Lilly* [1983], and *Gage and Nastrom* [1985, 1986] have argued instead that quasi two-dimensional turbulence is responsible for the fluctuation spectra. More recently, *Gage and Nastrom* [1988] and *Müller et al.* [1988] have associated this quasi two-dimensional turbulence with the vortical mode of motion. Quasi two–dimensional turbulence currently makes no predictions about the vertical wave number spectrum, and so only the gravity wave model can be tested in this case, although *Weinstock* [1985] argued that the m^{-3} spectrum is also consistent with an extended buoyancy subrange of three–dimensional turbulence. For horizontal wave number and frequency spectra, however, the gravity wave and vortical mode theories both make predictions, and to date, spectral measurements have been unable to conclusively verify or disprove either theory. As a result, consideration of both theories is required when studying these spectra.

3.1. *Theory*

A third wave solution to the fluid equations arises in a three–dimensional formulation, in addition to to the gravity wave and acoustic wave solutions [e.g., *Dong and Yeh*, 1988]. It has only recently been considered in the atmospheric context, and has come to be known as the "vortical mode". It is termed "vortical" because it possesses a vertical component of potential vorticity, unlike gravity waves [*Müller et al.*, 1988]. The vortical mode has no intrinsic frequency, and its velocity oscillations are constrained to the horizontal plane. As a result, this "wave" does not propagate, unlike gravity and acoustic waves, hence the preferred nomenclature "mode."

The horizontal velocity oscillations produced by a single high–frequency gravity wave and a single vortical mode are depicted in Figure 6*a*. Notice that with respect to the horizontal wave vector k_h, the horizontal velocity fluctuations are longitudinal for gravity waves, and transverse for the vortical mode (the absolute k_h direction of the vortical mode is really $\pm 180°$ uncertain, since it is nonpropagating). When two orthogonally aligned vortical modes superpose, they produce rotational structure in the horizontal [*Dong and Yeh*, 1988], whereas similarly superposed gravity

waves produce irrotational, divergent structure (see Figure 6*b*). Whereas this vortical mode structure is "frozen" in the background flow, the gravity wave structure will vary continously due to wave propagation.

Quasi two-dimensional turbulence, on the other hand, has been known of since the theoretical study of *Kraichnan* [1967]. A review of the theory is given by *Kraichnan and Montgomery* [1980], and more recent numerical and experimental investigations have been reviewed in an oceanic context by *Hopfinger* [1987]. The theory predicts that production occurs at small scales, and that progressively larger stratified motions arise from strong nonlinear interactions amongst the horizontally stratified eddies. Such interactions have been observed and studied in the laboratory [e.g., *Hopfinger*, 1987] and the entire process is known as "reverse cascading," since conventional three-dimensional turbulence cascades to smaller scales. A resulting $k^{-5/3}$ horizontal wave number energy spectrum is predicted, and *Gage* [1979] argued that the same $k^{-5/3}$ turbulence spectrum exists in the atmosphere at horizontal scales between ~10–500 km. This argument has been further developed by *Lilly* [1983] and *Gage and Nastrom* [1985, 1986, 1988].

While usually assumed, the equivalence between vortical modes and quasi two-dimensional turbulence is not clearly established at present. Although both theories predict a horizontally stratified, eddylike structure, an important interpretative difference is that the vortical mode solution is wavelike. While the eddylike structure that a superposition of vortical modes produces may appear rather random, it is certainly not turbulent in the strict sense. A likely explanation is that vortical mode nonlinearities have been omitted, such as the coupling of vortical modes with each other or with other waves. For example, *Dong and Yeh* [1988] and *Yeh and Dong* [1989] have shown that vortical modes grow in amplitude through nonresonant wave–wave interactions with large amplitude gravity waves. Yet *Yeh and Dong* [1989] proposed that the resultantly excited vortical modes cascade not into larger scale structures, but into smaller scale structures which are eventually dissipated by viscosity. This cascade process clearly differs from the "reverse cascade" that occurs for two–dimensional turbulence. Nevertheless, in the subsequent discussion equivalence between vortical modes and quasi two-dimensional turbulence will be assumed.

3.2. *Spectral Theory and Observations*

Both the gravity wave and two-dimensional turbulence theories make definite spectral predictions. The spectral theory of gravity waves is most clearly developed through the saturated vertical wave number spectrum (3) of *Smith et al.* [1987]. Quasi two–dimensional turbulence, however, currently makes no predictions as to the form of the vertical wave number spectrum.

The most direct spectral prediction that quasi two-dimensional turbulence theory provides is a horizontal wave number spectrum of horizontal velocities, $\mathcal{F}_u(k)$, proportional to $k^{-5/3}$ [*Gage*, 1979]. Using the vertical wave number spectrum (3), a simplified dispersion relation, and assuming spectral separability, gravity wave theory predicts that $\mathcal{F}_u(k)$ should have the same shape as the vertical wave number spectrum (3), giving a k^{-3} spectrum for $k > k_*$, and a flat spectrum for $k < k_*$, where k_* performs the same function as m_* in (3) [e.g., *VanZandt*, 1985]. Thus it would appear that measurements of horizontal wave number spectra

should enable discrimination between the two theories.

Nastrom and Gage [1985] calculated mean horizontal wave number spectra of horizontal velocities, using data from a large number of commercial aircraft flights. They found that the final mean spectrum had a $k^{-5/3}$ shape at wave numbers less than ~500 km, which *Gage and Nastrom* [1986] interpreted as direct evidence of quasi two-dimensional turbulence at atmospheric mesoscales. Subsequent measurements by *Nastrom et al.* [1987], *Fritts et al.* [1989], and *Kwon et al.* [1990] also found spectral shapes of the form k^{-p}, with p ~1–2. However, all of these latter studies found some spectral behavior which agreed with gravity wave theory, and *Fritts et al.* [1989] argued that nonseparability of the gravity wave spectra may result in a gravity wave horizontal wave number spectrum different from the predicted k^{-3}, and more like the shape observed. Evidence for such spectral nonseparability was presented by *Fritts and Chou* [1987]. Hence the dynamics responsible for these spectra are still under debate.

The spectral measurement that is predicted best by both theories is the frequency spectrum of horizontal velocities measured by a ground-based sensor, hereafter denoted $E_u(\Omega)$. For gravity waves, all the constituent waves of the spectrum have their own intrinsic wave frequency ω, and so, in a frame moving with the mean atmospheric motion $\bar{U}$, an intrinsic frequency spectrum exists, which is believed to have the form $\omega^{-5/3}$. However, at the ground these intrinsic frequencies are Doppler shifted by the mean motion of the atmosphere $\bar{U}$, producing a ground–based frequency Ω given by

$$\Omega = \omega + k\bar{U}\cos\phi \tag{9}$$

where ϕ is the azimuthal difference between the wave propagation direction and the wind speed direction [e.g., *Scheffler and Liu*, 1986; *Fritts and VanZandt*, 1987]. Thus the ground–based frequency spectrum for gravity waves, $E_u^{GW}(\Omega)$, can differ considerably from its intrinsic frequency spectrum. *Scheffler and Liu* [1986] and *Fritts and VanZandt* [1987] modeled how $E_u^{GW}(\Omega)$ evolved as background wind speeds varied, and the results of the latter study are shown in Figure 7*a* for equal amounts of up– and down–shifting of wave frequencies, and where $\beta = \bar{U}m_*/N$ conveniently quantifies the degree of Doppler shifting by the mean wind $\bar{U}$. Note that an ω^{-2} rather than an $\omega^{-5/3}$ intrinsic frequency spectrum was used by *Fritts and VanZandt* [1987] for analytical convenience.

For quasi two-dimensional turbulence, a simple Taylor transformation is used to predict the frequency spectrum $E_u^{VM}(\Omega)$ measured at the ground as the "frozen–in" turbulence structure is advected by the mean wind over the ground–based field of view, producing an $\Omega^{-5/3}$ spectrum [e.g., *Gage*, 1979; *Gage and Nastrom*, 1988]. Using a vortical mode interpretation, this transformation is better understood in terms of a Doppler shifting of the zero intrinsic frequency of the vortical modes to nonzero ground-based values, according to (9) [see also *Vincent and Eckermann*, 1990]. The variation of $E_u^{VM}(\Omega)$ with wind speed, as calculated by *Gage and Nastrom* [1988], is shown in Figure 7*b*. The vortical mode spectrum preserves its $\Omega^{-5/3}$ shape in all wind conditions, whereas the gravity wave spectrum becomes "flatter" as the wind speed increases. Consequently, investigating the behavior of measured ground-based frequency spectra with wind speed should indicate which theory, if either, fits the observations better, thus providing information on the nature of these fluctuating dynamics.

Early experimental studies averaged spectral calculations from all heights and times to produce a mean spectrum. While some such studies revealed an $\Omega^{-5/3}$ shape [e.g., *Balsley and Carter*, 1982; *Larsen et al.*, 1982], other studies revealed more variable shapes and spectral indices [e.g., *Vincent*, 1984; *Meek et al.*, 1985; *Balsley and Garello*, 1985; *Fukao et al.*, 1985; *Fritts and Chou*, 1987; *Fritts et al.*, 1990]. *Gage and Nastrom* [1988] compared the spectral models in Figure 7 with computed frequency spectra from ground-based radar data. They found that neither theory fitted the observations very closely, but that the two-dimensional turbulence model gave a better fit. On the other hand, while *Fritts et al.* [1990] also found variable agreement with the models, they concluded that their observations were more consistent with gravity waves. Therefore, here too the comparisons give equivocal findings as to whether the gravity wave or vortical mode theory is more consistent with observations.

3.3. *Spectral Nonstationarity due to Doppler Shifting*

It can be seen from Figure 7 that both the gravity wave and vortical mode theories predict that the ground–based frequency spectrum $E_u(\Omega)$ is nonstationary when the background wind $\bar{U}$ changes. Significant mean wind variability often occurs in the lower atmosphere due to meteorological phenomena [e.g., *Fukao et al.*, 1989; *Vincent and Eckermann*, 1990], and in the middle atmosphere due to large amplitude planetary waves and tides [e.g., *Andrews et al.*, 1987], which must give rise to nonstationary spectral shapes.

In the case of the vortical mode spectrum, this mean wind variability gives rise to nonstationary frequencies, according to (9), rather than nonstationary variance. Put another way, the variations in spectral shape detailed in Figure 7*b* are due to nonstationarity of the horizontal axis variable (frequency), as opposed to the variations in the vertical axis variable that occurred in the studies of nonstationary variance in section 2.3. Indeed, the gravity wave vertical wave number spectrum $F_u(m)$ of *Smith et al.* [1987] should also suffer from nonstationary wave numbers because the vertical wave number m varies with $\bar{U}$, but as their model was presented as being applicable in all wind conditions, such effects must be implicitly incorporated into their spectrum.

At first glance, one might expect that the variability of the gravity wave spectrum due to Doppler shifting in Figure 7*a* must also arise from nonstationary frequencies according to (9). In fact, this is not the case. While for vortical modes, ω is a constant (zero) and Ω varies with the mean wind $\bar{U}$, for gravity waves the opposite is true; the intrinsic frequency ω varies with $\bar{U}$, and the ground–based frequency Ω is a constant. So for gravity waves, the frequency Ω is stationary, and the variability of $E_u^{GW}(\Omega)$ is a problem of nonstationary variance within a given frequency band.

Therefore two rather different simulations were performed to investigate the effects of mean wind variability on computation of the frequency spectra $E_u^{GW}(\Omega)$ and $E_u^{VM}(\Omega)$. In the gravity wave case, simulations very similar to those detailed in section 2.3 were undertaken. Temporal fluctuations $q'(t)$ were synthesized using the superposition relation (7) adapted for time series analysis as follows

$$q'(t) = \sum_{j=1}^{K} \sum_{i=1}^{K/2} u'_{\text{peak}}(t_j, \Omega_i) \sin(\Omega_i t_j + \varphi_i) \qquad (10)$$

where again peak amplitudes $u'_{\text{peak}}(t_j, \Omega_i)$ had to be recal-

culated at each time t_j, because variations in $\beta = \bar{U} m_* / N$ change the spectral shape according to analytical relations derived by *Fritts and VanZandt* [1987] (see Figure 7*a*). Phases φ_i were chosen randomly, and 600 profiles were Fourier transformed in every simulation to obtain a final phase–averaged mean spectrum.

Results for three different time variations in β, which is proportional to $\bar{U}$, are shown in Figure 8. The Gaussian β profile roughly models strong, transient intensifications of the mean wind which have been observed in the lower atmosphere [e.g., *Fukao et al.*, 1989; *Vincent and Eckermann*, 1990]. The sinusoidal profile crudely models the effects of a planetary wave or tide, which are important in the middle atmosphere [e.g., *Andrews et al.*, 1987]. Although these large variations in β imply a highly nonstationary spectral shape (see Figure 7), the results of these simulations reveal that the final nonstationary spectrum is well–fitted in each case by the stationary Doppler–shifted spectrum of *Fritts and VanZandt* [1987] evaluated using the mean value of β over the time interval, denoted $\overline{\beta}$. Thus the "Doppler nonstationarity" of $E_u^{GW}(\Omega)$ appears to have limited impact on comparisons of this model spectrum with observed spectra. Aliasing also produces only small distortions to the spectral shape in these examples.

More complex modelling was required to simulate the variability of the vortical mode spectrum $E_u^{VM}(\Omega)$, as frequency variability must be incorporated here. To achieve this, 1024 "waves" were defined by integrating the $k^{-5/3}$ horizontal wave number spectrum proposed by *Gage* [1979] in 1024 successive harmonic wave number steps. The largest wavelength was chosen to be $\lambda_x^{max} = 1024$ km, so that the smallest resulting wavelength was $\lambda_x^{min} = \lambda_x^{max}/1024 = 1$ km. The mean wind $\bar{U}$ was allowed to vary only between $\bar{U}_{min} = 5$ m s^{-1} and $\bar{U}_{max} = 40$ m s^{-1}. Since the period $\tau = \lambda_x / \bar{U}$, then as the wind varies between $\bar{U}_{min}$ and $\bar{U}_{max}$, the smallest fluctuating period $\tau_{min} = \lambda_x^{min}/\bar{U}$ ranges from $\lambda_x^{min}/\bar{U}_{max} =$ 25 s to $\lambda_x^{min}/\bar{U}_{min} = 200$ s. Similarly the maximum wave period $\tau_{max} = \lambda_x^{max}/\bar{U}$ varies between ~7.11 and 56.89 hours. Thus the period interval between 200 s and 7.11 hours is always "full" of wave frequencies, and so temporal fluctuations were digitally synthesized from the wave number data using a Nyquist frequency of 100 s and a total data length of ~7.11 hours, which corresponds to 256 data points. Since periods greater and smaller than these values also arise, the data were somewhat aliased, and mean values arose which had to be removed before Fourier transformation. A total of 2000 randomly phased profiles were analyzed to give one phase–averaged mean nonstationary spectrum.

Figure 9 shows the temporal variations in $\bar{U}$ used in the simulations, which are similar to those used in the gravity wave simulations in Figure 8. The graphs on the right show three spectra in each case; a simulated nonstationary spectrum, a simulated spectrum evaluated using a constant value of $\bar{U} = 20$ m s^{-1} (i.e., an aliased stationary spectrum), and the theoretical $\Omega^{-5/3}$ spectral shape.

Several spectral features in Figure 9 bear highlighting. First, the simulated stationary and nonstationary spectra decrease more gradually with frequency than $\Omega^{-5/3}$, which is in part due to the addition of spectral power at the highest frequencies by aliased fluctuations. The nonstationary spectra have a least squares power law form around $\Omega^{-1.4}$ in each case. When one computes the spectral indices over the frequency band Ω =0.00004–0.002 Hz, which excludes the highest frequencies which are contaminated by aliased

fluctuations, the simulated stationary spectrum assumes an $\Omega^{-5/3}$ shape, whereas the nonstationary spectrum still has a "bluer" shape around $\Omega^{-1.6}$. This implies that the gradual spectral roll-off with frequency of the nonstationary spectrum is due in part to aliasing, but also in part to frequency nonstationarity.

Another feature is a flattening of the nonstationary spectrum in examples 1 and 3 at the lowest frequencies, yet this does not arise in the simulated stationary spectrum in either case. Therefore, this must be a product of the nonstationarity. This flattening makes the computed spectra in these cases appear more like the model gravity wave spectral shapes at low frequencies in Figure 7*a*. The finding of absolute values of the nonstationary spectral index $< 5/3$ (i.e., $\sim$1.4) is also superficially more consistent with the behaviour of the Doppler-shifted gravity wave spectra in Figure 7*a* rather than the vortical mode model spectra in Figure 7*b*, despite this being a nonstationary vortical mode spectrum.

Figure 10 shows results from further simulations where the wind was allowed to vary between 3 and 48 m s^{-1}. This gives rise to a period range between 333 s and 5.93 hours which is always "full" of wave frequencies, and so fluctuations were synthesized from the previous horizontal wave number data, using a Nyquist frequency of 167 s and a total data length of $\sim$5.93 hours, which produced 128 data points. The frequency nonstationarity is greater in these examples due to the larger temporal excursions in $\bar{U}$. The results show that the computed absolute values of the spectral indices of the nonstationary spectra are smaller than in Figure 9, and that the spectral flattening at the lowest frequencies persists.

3.4. *Nonstationary Variance*

Notwithstanding the nonstationarity of frequency spectra due to Doppler shifting, observed time series of mesoscale motions also exhibit large, transient bursts in variance above the ambient level. Examples from the lower atmosphere are strong increases in wave/turbulence activity associated with meteorological events [e.g., *Fritts and Chou*, 1987; *Fukao et al.*, 1989; *Vincent and Eckermann*, 1990]. Transient bursts in the fluctuating variance are recorded commonly in the middle atmosphere as well [e.g., *Vincent and Reid*, 1983; *Vincent and Fritts*, 1987].

To investigate the effect such nonstationarity might have on computed frequency spectra, Monte Carlo simulations similar to those described in sections 2.3 and 3.3 were performed for a stationary spectrum of the form $\Omega^{-5/3}$, which closely fits the two spectral models $E_u^{GW}(\Omega)$ and $E_u^{VM}(\Omega)$. Fluctuations were synthesized from this spectrum as in (7) and (10), and were then modulated by a Gaussian "burst" function, which approximates some observed increases in variance [e.g., *Fritts and Chou*, 1987]. Various modulation profiles, and the modified spectra they produce, are shown in Figure 11. The results show that the computed spectral indices are reasonably robust to the applied nonstationarity in these examples, differing by no more than 3% from the stationary value of -5/3.

3.5. *Horizontal Wave Number Spectra*

The simulations detailed in this section also have some impact on computations of horizontal wave number spectra. For example, Figure 11 can be quite validly applied to horizontal wave number spectra, as a similarly shaped $k^{-5/3}$ spectrum occurs [*Nastrom and Gage*, 1985]. Furthermore, large bursts in variance with horizontal flight distance are

also encountered in such measurements. For instance, *Nastrom et al.* [1987] found that the mesoscale velocity variance for flight segments over rough terrain was ~2–5 times greater than that over flat terrain or oceans, and they showed explicitly that the horizontal wave number spectra over each type of terrain differed significantly. Similar variability with flight distance was reported by *Fritts et al.* [1989].

Problems involving nonstationary horizontal wave numbers arise too, similar to the frequency nonstationarity which arises in the vortical mode frequency spectrum. An airborne sensor moving horizontally with velocity V, and measuring a fluctuation moving with respect to the ground with a speed C, will record the horizontal wavelength of this fluctuation to be λ_x', which differs from its intrinsic horizontal scale, λ_x, according to the Doppler–shifting formula

$$\lambda_x' = \lambda_x \left(1 + \frac{C}{V}\right) \tag{11}$$

For gravity waves, C is the ground–based horizontal phase speed of the wave, and for vortical modes $C = \bar{U}$, as vortical modes are merely advected by the background flow. *Kwon et al.* [1990] investigated how the horizontal motion of airborne sensors can produce artificial Doppler shifts in the horizontal wavelengths of measured fluctuations, and presented experimental examples of varying spectral shapes produced by such effects.

4. "Stationary" Analysis of Mesoscale Motions

Simulations in the previous section have indicated how observed variability of mesoscale variance can complicate spectral analysis of these fluctuating motions. While nonstationary variances appear to produce limited distortion, nonstationary frequencies arising in the ground–based frequency spectrum of vortical modes produce a spectral change with frequency more gradual than $\Omega^{-5/3}$, and in some cases producing rather flat shapes at the lowest frequencies, both of which are more consistent with a gravity wave interpretation (see Figure 7).

Comparison of experimental spectra with model spectra is currently used widely to provide information about the fundamental dynamics (gravity waves or vortical modes), yet a number of such studies have produced equivocal findings to date. While this may indicate that both gravity waves and vortical modes usually coexist with approximately equal variance, the aforementioned spectral distortions due to nonstationarity can also produce similar uncertainty. There is no easy way to compensate for nonstationary distortion. One can circumvent the problem by spectrally analyzing only those data segments where the spectra should theoretically be quasi–stationary [*Fritts and Chou*, 1987], but the amount of available data may then be very small, whereupon the uncertainties in the computed spectral shape will be large. For nonstationary data, it would be better to be able to calculate a more stationary quantity, which produces distinctly different results in the presence of either gravity waves or vortical modes.

4.1. *The Polarization Ratio*

In time series analysis of horizontal velocity data from ground-based sensors, we define the ratio R of the fluctuating horizontal velocity variance parallel ($\overline{u_p'^2}$) and transverse

$(\overline{u_t'^2})$ to the direction of the mean wind.

$$R = \frac{\overline{u_p'^2}}{\overline{u_t'^2}} \tag{12}$$

Being a ratio of horizontal variance components, nonstationarity of the total variance does not affect its value (i.e., it is stationary to variance changes). Furthermore, at middle to high ground-based frequencies, we shall show that the ground–based spectral theories of gravity waves and vortical modes (Figure 7) can still be used to predict distinctly different R values if one or the other dynamical process is the more energetic.

The gravity wave model spectra depicted in Figure 7*a* show that, at middle to high ground–based frequencies, the Doppler–shifted frequency spectrum is more intense than the intrinsic (unshifted) frequency spectrum [*Scheffler and Liu*, 1986; *Fritts and VanZandt*, 1987]. Since waves with k_h parallel to the mean wind direction are strongly Doppler shifted, whereas waves with k_h orthogonal to the wind direction experience no such shift, according to (9), it implies an enhancement in the observed high frequency variance of those waves aligned with the mean wind direction relative to those aligned transverse to it. The effect becomes more pronounced as background wind speeds increase (see Figure 7*a*).

The observed frequency Ω induced by a vortical mode is also given by the Doppler–shift formula (9), which, since $\omega = 0$ in this case, takes the form $k\bar{U}\cos\phi$, where ϕ is the difference in azimuth between the vortical mode alignment and the mean wind direction. For any given value of Ω and $\bar{U}$, $k\cos\phi$ will be the same for all the modes which contribute to the variance at this observed frequency. However, those modes where k is smallest produce the greatest contribution to this variance, due to the $k^{-5/3}$ wave number spectrum [*Gage*, 1979]. Therefore, since $k\cos\phi$ is constant, these smallest wave number modes must also have $\phi \sim 0°$, which implies that they are aligned with the background wind direction.

Thus both theories predict enhancements in the measured variance of those motions with k_h coaligned with the background wind direction. However, the different horizontal polarization of the gravity wave and the vortical mode results in distinctly different trends in the ratio R in each case. Since the horizontal fluctuations of a gravity wave oscillate parallel with k_h (Figure 6*a*), the enhanced gravity waves should therefore produce values of $R > 1$ on average (i.e., $\overline{u_p'^2} > \overline{u_t'^2}$). The value of R should increase as the mean wind speed increases, because the enhancement in variance of the Doppler–shifted wave spectrum increases with $\bar{U}$ (see Figure 7*a*). It should be noted, however, that the model Doppler–shifted spectra in Figure 7a assume equal amounts of up– and down–shifting of wave frequencies. While this variance enhancement persists for a wide variety of different up– and down–shifting amounts, in extreme cases where almost every wave in the spectrum is down–shifted in frequency, these enhancements in variance may not occur [*Fritts and VanZandt*, 1987].

One other complicating factor is that, at the very lowest frequencies, a gravity wave become elliptically polarized, aquiring a transverse component v'_{peak} of f/ω times its longitudinal component u'_{peak}, where f is the inertial frequency. Note, however, that v'_{peak} is always smaller than u'_{peak}, and that v'_{peak} attenuates rapidly with frequency. The individ-

ual variances $\overline{u'^2}$ and $\overline{v'^2}$ over the entire intrinsic frequency spectrum are given by

$$\overline{u'^2} = \int_f^N W\omega^{-5/3}d\omega = \frac{3W}{2f^{2/3}}\left[1-(f/N)^{2/3}\right] \quad (13)$$

$$\overline{v'^2} = \overline{\left(\frac{f}{\omega}\right)^2 u'^2} = \int_f^N Wf^2\omega^{-11/3}d\omega$$

$$= \frac{3W}{8f^{2/3}}\left[1-(f/N)^{8/3}\right] \quad (14)$$

where W is a constant.

For a realistic value of $N \sim 100f$, the terms in square parentheses in (13) and (14) are both near one, so that equating (13) and (14) gives

$$\frac{\overline{u'^2}}{\overline{v'^2}} \approx \frac{3/2}{3/8} = 4 \quad (15)$$

This illustrates that, over the entire spectrum, the longitudinal fluctuations produce 80% of the variance. Within high observed frequency bands, this percentage will be even higher. Therefore these transverse gravity wave fluctuations are of insufficient amplitude to alter the general trends in R produced by the longitudinal gravity wave fluctuations (i.e., $R > 1$).

The vortical mode, unlike a gravity wave, oscillates at right angles to its wavevector k_h (Figure 6*a*). Therefore, even though those fluctuations with k_h in the direction of $\bar{U}$ are enhanced in variance, just as for gravity waves, the transverse polarization of the vortical mode means that values of $R < 1$ must arise in the presence of such a spectrum (i.e. $\overline{u_t'^2} > \overline{u_p'^2}$).

These trends in R can be qualitatively visualized by inspecting the simple superposition structure in Figure 6*b*. On moving in either the x or y direction in these diagrams and observing the variation of the wind vectors, one can see that the gravity wave structure produces fluctuations in the direction of movement ($R > 1$), whereas the vortical mode structure fluctuates transverse to the movement ($R < 1$). Therefore, notwithstanding the strong enhancement in the variance within high frequency bands of those gravity waves aligned with the mean wind direction predicted in Figure 7*a*, values of $R > 1$ still arise due to the horizontal polarization of the wave.

Equivalence between vortical modes and quasi two-dimensional turbulence has been assumed to now. However, some discrepansies between the two theories were highlighted earlier, and one or the other process may be the more relevant to consider. Therefore it is worth determining whether two–dimensional turbulence theory can also be used to predict a trend in R, and whether it is comparable with the vortical mode prediction of $R < 1$.

Gage [1979] has adapted the well–developed theory of inertial range three–dimensional turbulence to this postulated two–dimensional inertial range turbulence. Longitudinal and transverse Eulerian (ground–based) structure functions were defined by *Gage* [1979] as follows

$$D_{\text{long}}(r) = A_{\text{long}}\epsilon^{2/3}r^{2/3} \quad (16)$$

$$D_{\text{tran}}(r) = A_{\text{tran}}\epsilon^{2/3}r^{2/3} \quad (17)$$

where $A_{\text{long}}, A_{\text{tran}}$ are constants, ϵ is the eddy dissipation rate per unit mass, and r is the spatial separation.

Using analogous derivations to those advanced in the

three–dimensional theory, *Gage* [1979] then argued that $A_{\text{long}} \sim 1.75$, and

$$A_{\text{tran}} = \frac{5}{3} A_{\text{long}} \tag{18}$$

In the same way, longitudinal and transverse horizontal wave number spectra can also be defined, using the $k^{-5/3}$ two–dimensional turbulence spectrum proposed by *Gage* [1979], as follows

$$E_{\text{long}}(k) = B_{\text{long}} \epsilon^{2/3} k^{-5/3} \tag{19}$$

$$E_{\text{tran}}(k) = B_{\text{tran}} \epsilon^{2/3} k^{-5/3} \tag{20}$$

The structure function constants ($A_{\text{long}}, A_{\text{tran}}$) are related to the spectral constants ($B_{\text{long}}, B_{\text{tran}}$) by a multiplicative constant [e.g., *Tatarski*, 1961], so that (18) also implies

$$B_{\text{tran}} = \frac{5}{3} B_{\text{long}} \tag{21}$$

Assuming now that a mean wind $\bar{U}$ advects this "frozen–in" two–dimensional turbulence spectrum over a ground–based observer, then ground–based frequency spectra are given by a simple Taylor transformation ($\Omega = k\bar{U}$) of the horizontal wave number spectra (19) and (20) [e.g., *Gage and Nastrom*, 1988], producing

$$F_{\text{long}}(\Omega) = \frac{B_{\text{long}} \epsilon^{2/3} (\Omega/\bar{U})^{-5/3}}{\bar{U}} \tag{22}$$

$$F_{\text{tran}}(\Omega) = \frac{B_{\text{tran}} \epsilon^{2/3} (\Omega/\bar{U})^{-5/3}}{\bar{U}} \tag{23}$$

One can now see that u'_p fluctuations are governed by the $F_{\text{long}}(\Omega)$ spectrum, and u'_t fluctuations are governed by $F_{\text{tran}}(\Omega)$, so that, using (21)–(23), one can theoretically evaluate R as follows

$$R = \frac{\overline{u'^2_p}}{\overline{u'^2_t}}$$

$$R = \frac{\int_{\Omega_1}^{\Omega_2} F_{\text{long}}(\Omega) d\Omega}{\int_{\Omega_1}^{\Omega_2} F_{\text{tran}}(\Omega) d\Omega}$$

$$R = \frac{\int_{\Omega_1}^{\Omega_2} B_{\text{long}} \epsilon^{2/3} \Omega^{-5/3} \bar{U}^{2/3} d\Omega}{\int_{\Omega_1}^{\Omega_2} 5/3 B_{\text{long}} \epsilon^{2/3} \Omega^{-5/3} \bar{U}^{2/3} d\Omega}$$

$$R = 3/5 \tag{24}$$

Hence the vortical mode and quasi two-dimensional turbulence theories both predict R values less than unity. The final results are summarized here: gravity waves, $R > 1$ (R increases with $\bar{U}$); vortical modes and quasi two-dimensional turbulence, $R < 1$ ($R = 3/5$ for two–dimensional turbulence).

This ratio R affords several practical advantages over spectral analysis in evaluation of the gravity wave/vortical mode question. First, R remains stationary even when the fluctuating variance is nonstationary, unlike spectra. R can vary, however, when "Doppler nonstationarity" occurs due to mean wind variability, yet these varying values are always >1 for gravity waves and <1 for vortical modes, thus still enabling differentiation between each dynamical process. Simulations in the previous section indicated that such differentiation may not always be possible when spectrally analyzing the motion field. R is also a less-derived

computation, using the measured fluctuations of horizontal wind velocities directly, whereas spectra must be numerically computed after aquiring the wind data, introducing possible distortion of the spectra during such computations. Yet the well–developed gravity wave and vortical mode spectral theories can still be used to derive theoretical R ratios. Finally, this additional method of evaluating the mesoscale motion field is useful because it provides an independent check of inferences provided by other means (e.g., spectral analysis).

In a companion study, *Vincent and Eckermann* [1990] apply this polarization ratio R to time series of radar-derived horizontal wind velocities from the troposphere, and compare their experimental findings with the above predictions of the gravity wave and vortical mode theories. They find that R becomes distinctly greater than unity as the mean wind speed increases, and on this basis conclude that gravity wave motions appear to be the more energetic mesoscale process in this case. Further theoretical and experimental studies are needed to better quantify the principally qualitative trends in R initially derived in this study.

5. Conclusions

The nonstationarity nature of mesoscale atmospheric motions can distort the computed spectra of these motions, thus complicating interpretation based upon such spectra. The inherent nonstationarity with altitude of the saturated vertical wave number spectrum of gravity waves proposed by *Smith et al.* [1987] gives rise to experimentally calculated spectra which differ significantly in shape from the model spectrum. The principal changes are a broadening of the transition region from saturated to unsaturated spectral shapes, and an enhancement of spectral power at saturated wave numbers. Both effects combine to give a horizontal velocity power spectrum of the form m^{-t} over a broad range of wave numbers, where t lies between the nominal unsaturated value of $t = 0$ and the saturated value of $t = 3$. These effects can explain the apparently anomalous nature of many spectral measurements, while not precluding the close agreement to the model spectrum found in other measurements.

More random nonstationarity is encountered in the computation of horizontal wave number spectra and ground–based frequency spectra of mesoscale atmospheric fluctuations, While nonstationary variance appears to produce small changes to the stationary spectral shapes, the frequency nonstationarity arising from the advection of a field of vortical modes over a ground–based sensor by a time–varying mean flow can produce distortions to computed ground–based frequency spectra which drive the shape away from the stationary $\Omega^{-5/3}$ shape, and, in some cases, more towards the shape predicted by the competing gravity wave model. Such modifications to spectral shapes due to nonstationarity may well explain, at least in part, the widely varying conclusions of various experimental spectral evaluations of the gravity wave and vortical mode descriptions of these fluctuating motions.

In light of this possibility, the more stationary "polarization ratio" R was developed for time series analysis of ground-based atmospheric measurements of horizontal velocity. This ratio is stationary even when the mesoscale variance is nonstationary, and assumes a distinctly different value if the either gravity waves or vortical modes dominate the variance. This statistic may provide a useful independent means of checking conclusions about the fundamental

nature of these mesoscale dynamics made using conventional spectral inspection or other means.

Acknowledgments. I thank particularly W.K. Hocking for stimulating discussions about vortical modes and turbulence. I also thank W.K. Hocking, I.M. Reid, B.H. Briggs, T.E. VanZandt, and R.A. Vincent for comments on earlier drafts of the manuscript, Laurie Campbell for the use of his plotting software, and two referees for helpful review comments. Finally, I acknowledge the financial support of a Commonwealth of Australia Postgraduate Research Scholarship during 1987–1989, and an Australian Postgraduate Priority Research Award during 1990.

References

Andrews, D.G., J.R. Holton, and C.B. Leovy, *Middle Atmosphere Dynamics*, Academic, San Diego, Calif., 489 pp., 1987.

Balsley, B.B., and D.A. Carter, The spectrum of atmospheric velocity fluctuations at 8 and 86 km, *Geophys. Res. Lett.*, *9*, 465–468, 1982.

Balsley, B.B., and R. Garello, The kinetic energy density in the troposphere, stratosphere and mesosphere: A preliminary study using the Poker Flat radar in Alaska, *Radio Sci.*, *20*, 1355–1362, 1985.

Bracewell, R.N., *The Fourier Transform and Its Applications*, 2nd ed., pp. 112–113, McGraw-Hill, New York, 1978.

Cornish, C.R., Observations of vertical velocities in the tropical upper troposphere and lower stratosphere using the Arecibo 430-MHz radar, *J. Geophys. Res.*, *93*, 9419–9431, 1988.

Desaubies, Y.J.F., Analytical representation of internal wave spectra, *J. Phys. Oceanogr.*, *6*, 976–981, 1976.

Dewan, E.M., and R.E. Good, Saturation and the "universal" spectrum for vertical profiles of horizontal scalar winds in the atmosphere, *J. Geophys. Res.*, *91*, 2742–2748, 1986.

Dewan, E.M., N. Grossbard, A.F. Quesada, and R.E. Good, Spectral analysis of 10-m resolution scalar velocity profiles in the stratosphere, *Geophys. Res. Lett.*, *11*, 80–83, 1984. (Correction, *Geophys. Res. Lett.*, *11*, 624, 1984.)

Dong, B., and K.C. Yeh, Resonant and nonresonant wave-wave interactions in an isothermal atmosphere, *J. Geophys. Res.*, *93*, 3729–3744, 1988.

Dunkerton, T.J., Theory of internal gravity wave saturation, *Pure Appl. Geophys.*, *130*, 373–397, 1989.

Eckermann, S.D., and R.A. Vincent, Falling sphere observations of anisotropic gravity wave motions in the upper stratosphere over Australia, *Pure Appl. Geophys.*, *130*, 509–532, 1989.

Ecklund, W.L., K.S. Gage, G.D. Nastrom, and B.B. Balsley, A preliminary climatology of the spectrum of vertical velocity observed by clear-air Doppler radar, *J. Clim. Appl. Meteorol.*, *25*, 885–892, 1986.

Fritts, D.C., Gravity wave saturation in the middle atmosphere: A review of theory and observations, *Rev. Geophys.*, *22*, 275–308, 1984.

Fritts, D.C., A review of gravity wave saturation processes, effects, and variability in the middle atmosphere, *Pure Appl. Geophys.*, *130*, 343–372, 1989.

Fritts, D.C., and H.-G. Chou, An investigation of the vertical wavenumber and frequency spectra of gravity wave motions in the lower stratosphere, *J. Atmos. Sci. 44*, 3610–3624, 1987.

Fritts, D.C., and T.E. VanZandt, Effects of Doppler shifting on the frequency spectra of atmospheric gravity waves, *J. Geophys. Res.*, *92*, 9723–9732, 1987.

Fritts, D.C., T. Tsuda, T. Sato, S. Fukao, and S. Kato, Observational evidence of a saturated gravity wave spectrum in the troposphere and lower stratosphere, *J. Atmos. Sci.*, *45*, 1741–1759, 1988.

Fritts, D.C., R.C. Blanchard, and L. Coy, Gravity wave structure between 60 and 90 km inferred from Space Shuttle reentry data, *J. Atmos. Sci.*, *46*, 423–434, 1989.

Fritts, D.C., T. Tsuda, T.E. VanZandt, S.A. Smith, T. Sato, S. Fukao, and S. Kato, Studies of velocity fluctations in the lower atmosphere using the MU radar. Part II: Momentum fluxes and energy densities, *J. Atmos. Sci.*, *47*, 51–66, 1990.

Fukao, S., Y. Maekawa, T. Sato, and S. Kato, Fine structure of mesospheric wind fluctuations observed by the Arecibo UHF Doppler radar, *J. Geophys. Res.*, *90*, 7547–7556, 1985.

Fukao, S., T. Sato, P.T. May, T. Tsuda, S. Kato, M. Inaba, and I. Kimura, A systematic error in MST/ST radar wind measurement induced by a finite range volume effect, 1, Observational

results, *Radio Sci.*, *23*, 59–73, 1988*a*.

Fukao, S., M. Inaba, I. Kimura, P.T. May, T. Sato, T. Tsuda, and S. Kato, A systematic error in MST/ST radar wind measurement induced by a finite range volume effect, 2, Numerical considerations, *Radio Sci.*, *23*, 74–82, 1988*b*.

Fukao, S., M.D. Yamanaka, H. Matsumoto, T. Sato, T. Tsuda, and S. Kato, Wind fluctuations near a cold vortex-tropopause funnel system observed by the MU radar, *Pure Appl. Geophys.*, *130*, 463–479, 1989.

Gage, K.S., Evidence for $k^{-5/3}$ law inertial range in mesoscale two-dimensional turbulence, *J. Atmos. Sci.*, *36*, 1950–1954, 1979.

Gage, K.S., and G.D. Nastrom, On the spectrum of atmospheric velocity fluctuations seen by MST/ST radars and their interpretation, *Radio Sci.*, *20*, 1339–1347, 1985.

Gage, K.S., and G.D. Nastrom, Theoretical interpretation of atmospheric wavenumber spectra of wind and temperature observed by commercial aircraft during GASP, *J. Atmos. Sci.*, *43*, 729–740, 1986.

Gage, K.S., and G.D. Nastrom, Further discussion of the dynamical processes that contribute to the spectrum of mesoscale atmospheric motions, paper presented at the Eighth Symposium on Turbulence and Diffusion, Am. Meteorol. Soc., San Diego, Calif., 1988.

Gardner, C.S., and D.G. Voelz, Lidar measurements of gravity wave saturation effects in the sodium layer, *Geophys. Res. Lett.*, *12*, 765–768, 1985.

Gardner, C.S., and D.G. Voelz, Lidar studies of the nighttime sodium layer over Urbana, Illinois, 2, Gravity waves, *J. Geophys. Res.*, *92*, 4673–4694, 1987.

Gardner, C.S., M.S. Miller, and C.H. Liu, Rayleigh lidar observations of gravity wave activity in the upper stratosphere at Urbana, Illinois, *J. Atmos. Sci.*, *46*, 1838–1854, 1989.

Garrett, C.J.R., and W.H. Munk, Space-time scales of internal waves, *Geophys. Astrophys. Fluid Dyn.*, *3*, 225–235, 1972.

Garrett, C.J.R., and W.H. Munk, Space-time scales of internal waves: a progress report, *J. Geophys. Res.*, *80*, 291–297, 1975.

Hass, H., and W. Meyer, Gravity wave field above Andøya, *J. Atmos. Terr. Phys.*, *49*, 705–721, 1987.

Hirota, I., Climatology of gravity waves in the middle atmosphere, *J. Atmos. Terr. Phys.*, *46*, 767–773, 1984.

Hirota, I., and T. Niki, A statistical study of inertia-gravity waves in the middle atmosphere, *J. Meteorol. Soc. Jpn.*, *63*, 1055–1066, 1985.

Hopfinger, E.J., Turbulence in stratified fluids: a review, *J. Geophys. Res.*, *92*, 5287–5303, 1987.

Kaimal, J.C., S.F. Clifford, and R.J. Lataitis, Effect of finite sampling on atmospheric spectra, *Boundary Layer Meteorol.*, *47*, 337–347, 1989.

Kraichnan, R.H., Inertial range in two-dimensional turbulence, *Phys. Fluids*, *10*, 1417–1423, 1967.

Kraichnan, R.H., and D. Montgomery, Two–dimensional turbulence, *Rep. Prog. Phys.*, *43*, 547–619, 1980.

Kristensen, L., and P. Kirkegaard, Digitization noise in power spectral analysis, *J. Atmos. Oceanic Technol.*, *4*, 328–335, 1987.

Kwon, K.H., D.C. Senft, and C.S. Gardner, Airborne sodium lidar observations of horizontal wave number spectra of mesopause density and wind perturbations, *J. Geophys. Res.*, in press, 1990.

Larsen, M.F., M.C. Kelley, and K.S. Gage, Turbulence spectra in the upper troposphere and lower stratosphere at periods between 2 hrs and 40 days, *J. Atmos. Sci.*, *39*, 1035–1041, 1982.

Lilly, D.K., Stratified turbulence and the mesoscale variability of the atmosphere, *J. Atmos. Sci.*, *40*, 749–761, 1983.

Lindzen, R.S., Turbulence and stress owing to gravity wave and tidal breakdown, *J. Geophys. Res.*, *86*, 9707–9714, 1981.

Maekawa, Y., S. Fukao, I. Hirota, M.P. Sulzer, and S. Kato, Some further results on long term mesospheric and lower thermospheric wind observations by the Arecibo UHF radar, *J. Atmos. Terr. Phys.*, *49*, 63–71, 1987.

May, P.T., S. Fukao, T. Tsuda, T. Sato, and S. Kato, The effect of thin scattering layers on the determination of wind by Doppler radars, *Radio Sci.*, *23*, 83–94, 1988.

Meek, C.E., I.M. Reid, and A.H. Manson, Observations of mesospheric wind velocities, 2, Cross sections of power spectral density for 48–8 h, 8–1 h, 1h–10min over 60–110 km for 1981, *Radio Sci.*, *20*, 1383–1402, 1985.

Miller, A.J., Response characteristics of meteorological rocket wind reduction techniques, *J. Geophys. Res.*, *74*, 6853–6858, 1969.

Moore, M.I., P.J. Thomson, and T.G.L. Shirtcliffe, Spectral analysis of ocean profiles from unequally spaced data, *J. Geophys. Res.*, *93*, 655–664, 1988.

Müller, P., G. Holloway, F. Henyey and N. Pomphrey, Non-linear interactions among internal gravity waves, *Rev. Geophys.*, *24*, 493–536, 1986.

Müller, P., R. Lien, and R. Williams, Estimates of potential vorticity at small scales in the ocean, *J. Phys. Oceanogr.*, *18*, 401–416, 1988.

Nastrom, G.D., and K.S. Gage, A climatology of atmospheric wavenumber spectra of wind and temperature observed by commercial aircraft, *J. Atmos. Sci.*, *42*, 950–960, 1985.

Nastrom, G.D., D.C. Fritts, and K.S. Gage, An investigation of terrain effects on the mesoscale spectrum of atmospheric motions, *J. Atmos. Sci.*, *44*, 3087–3096, 1987.

Scheffler, A.O., and C.H. Liu, The effects of Doppler shift on gravity wave spectra observed by MST radar, *J. Atmos. Terr. Phys.*, *48*, 1225–1231, 1986.

Schoeberl, M.R., A ray tracing model of gravity wave propagation and breakdown in the middle atmosphere, *J. Geophys. Res.*, *90*, 7999–8010, 1985.

Shibata, T., S. Ichimori, T. Narikiyo, and M. Maeda, Spectral analysis of vertical temperature profiles in the upper stratosphere and the lower mesosphere, *J. Meteorol. Soc. Jpn.*, *66*, 1001–1005, 1988.

Sidi, C., J. Lefrere, F. Dalaudier, and J. Barat, An improved atmospheric buoyancy wave spectrum model, *J. Geophys. Res.*, *93*, 774–790, 1988.

Smith, S.A., D.C. Fritts and T.E. VanZandt, Evidence of a saturated spectrum of atmospheric gravity waves, *J. Atmos. Sci.*, *44*, 1404–1410, 1987.

Tatarski, V.I., *Wave Propagation in a Turbulent Medium*, McGraw–Hill, New York, 1961.

VanZandt, T.E., A universal spectrum of buoyancy waves in the atmosphere, *Geophys. Res. Lett.*, *9*, 575–578, 1982.

VanZandt, T.E., A model for gravity wave spectra observed by Doppler sounding systems, *Radio Sci.*, *20*, 1323–1330, 1985.

VanZandt, T.E., and D.C. Fritts, A theory of enhanced saturation of the gravity wave spectrum due to increases in atmospheric stability, *Pure Appl. Geophys.*, *130*, 399–420, 1989.

Vincent, R.A., Gravity-wave motions in the mesosphere, *J. Atmos. Terr. Phys.*, *46*, 119–128, 1984.

Vincent, R.A., and S.D. Eckermann, VHF radar observations of mesoscale motions in the troposphere: Evidence of gravity wave Doppler shifting, *Radio Sci.*, in press, 1990.

Vincent, R.A., and D.C. Fritts, A climatology of gravity wave motions in the mesopause region at Adelaide, Australia, *J. Atmos. Sci.*, *44*, 748–760, 1987.

Vincent, R.A., and I.M. Reid, HF Doppler measurements of mesospheric gravity wave momentum fluxes, *J. Atmos. Sci.*, *40*, 1321–1333, 1983.

Weinstock, J., Theoretical gravity wave spectrum: Strong and weak wave interactions, *Radio Sci.*, *20*, 1295–1300, 1985.

Yeh, K.C., and B. Dong, The nonlinear interaction of a gravity wave with the vortical modes, *J. Atmos. Terr. Phys.*, *51*, 54–50, 1989.

S. D. Eckermann, Department of Atmospheric, Oceanic, and Planetary Physics, Hooke Institute, Clarendon Laboratory, Oxford University, Parks Road, Oxford, OX1 3PU, England.

(Received December 23, 1988;
revised March 28, 1990;
accepted May 14, 1990.)

Paper number 90JD01216.
0148-0227/90/90JD-01216$05.00

Paper number 90JD01216.

Fig. 1. The model vertical wave number power spectrum of horizontal velocity fluctuations produced by gravity waves, due to *Smith et al.* [1987], evaluated using $m_* = (2\text{ km})^{-1}$, $(5\text{ km})^{-1}$, and $(10\text{ km})^{-1}$. These values of m_* are typical of the lower, middle, and upper stratosphere, respectively. Note the variation of the spectrum with $m_*(z)$.

Fig. 2. The top panel shows the Fourier transform $A(m) = A_R(m) + iA_I(m)$ of the exponential wave amplitude growth with height $e^{z/2H_\rho}$, using representative values of $z_s = 40$ km and $H_\rho = 7$ km. The bottom panel details the change in $|A(m)/A(0)|$ with H_ρ. The dashed lines show the points where these curves are sampled when using a fast Fourier transform algorithm.

Fig. 3. Phase–averaged nonstationary spectra resulting from (*a*) unaliased and (*b*) aliased numerical simulations performed 2000 times in each case and averaged. The stationary model spectrum is also plotted for comparison. The simulation used a total height range $z_K - z_1 = 44.8$ km, $K = 256$, $N = 0.02$ rad s^{-1}, $H_E = 10$ km, and $m_*(z_1) = (1\text{ km})^{-1}$. See text for details about the numerical model used here. A least squares determination of the nonstationary spectral index in the 0.0002–0.0028 m^{-1} wave number range is also provided.

Fig. 4. An enlargement of the vertical wavelength region ~1–15 km from Figure 3. Such a wavelength range is typical of many spectra computed from experimental data from the middle atmosphere. Aliasing at the largest wave numbers is not included.

Fig. 5. Plot of the model saturated spectrum of *Smith et al.* [1987], the nonstationary realization of this spectrum from Figure 4*a*, and the "universal" spectral formula adopted by *VanZandt* [1982].

Fig. 6. (*a*) The horizontal velocity oscillations of a single gravity wave and vortical mode. The dotted vector represents the horizontal wave vector k_h. (*b*) Instantaneous horizontal velocity vectors produced by the superposition of two orthogonally aligned gravity waves and vortical modes; x and y are displacements normalized by the wavelengths λ_x and λ_y, respectively, and $\lambda_x = \lambda_y$ in these examples.

Fig. 7. Theoretical ground-based frequency spectra for (*a*) gravity waves and (*b*) vortical modes in different background wind conditions. The gravity wave model parameter $\beta = \bar{U}m_*/N$ parameterizes the degree of Doppler shifting, and at a given height is proportional to the mean wind $\bar{U}$. These gravity wave spectra are computed for equal amounts up– and down–shifting of frequencies [see *Fritts and VanZandt*, 1987], and plotted frequency labels $\hat{\Omega}$ are normalized by the inertial frequency f. The vortical mode spectrum here is based on a Taylor–transformed $k^{-5/3}$ horizontal wave number spectrum. One should also note that the vortical mode frequency spectrum for $\bar{U} = 0$ is a delta function at zero frequency (since vortical modes have no intrinsic frequency).

Fig. 8. The three panels on the left show various time variations in the gravity wave Doppler–shifting parameter $\beta = \bar{U}m_*/N$. The dotted line shows the mean value $\overline{\beta}$ over the time interval. The corresponding plots on the right show the resulting nonstationary gravity wave frequency spectra that these variations in Doppler–shifting produce. The aliased spectrum has been displaced vertically by 0.3 of a decade. These spectra are also compared to the stationary Doppler–shifted spectrum evaluated for $\beta = \overline{\beta}$ (dotted line), as one would usually do when comparing computed and model spectra. Equal up– and down–shifting of energy, and a value of $\hat{N} = N/f = 9.18$, were used in each example.

Fig. 9. The three panels on the left show various time variations in the background wind speed $\bar{U}$, and the dotted line shows the mean value evaluated over the whole time interval. The solid curves on the right show the resulting nonstationary vortical mode frequency spectra that these variations in wind speed give rise to. The dashed line shows the simulated results for a stationary wind speed of 20 m s^{-1}. Both of these spectra are aliased. The theoretical $\Omega^{-5/3}$ is also plotted as a dotted curve for reference. Least squares determinations of the spectral indices of the simulated spectra are given in each case over the whole spectrum, and over the band Ω = 0.00004–0.002 Hz, which excludes the highest frequencies.

Fig. 10. As for Figure 9, but for mean wind variability between 3 and 48 m s^{-1} rather than between 5 and 40 m s^{-1}. There are 128 points in the time series in these examples rather than 256 in the examples in Figure 9. The band over which spectral indices were fitted was Ω = 0.000025–0.00065 Hz.

Fig. 11. The panels on the left show various time variations in the fluctuating variance. The corresponding plots on the right show the stationary $\Omega^{-5/3}$ spectrum (dotted curve) and the simulated nonstationary spectrum (solid curve). Each simulated spectrum is an average of 2000 individual spectra from randomly phased time series. A least squares determination of the nonstationary spectral index is given in each case.

Fig. 1. The model vertical wave number power spectrum of horizontal velocity fluctuations produced by gravity waves, due to *Smith et al.* [1987], evaluated using $m_* = (2\text{ km})^{-1}$, $(5\text{ km})^{-1}$, and $(10\text{ km})^{-1}$. These values of m_* are typical of the lower, middle, and upper stratosphere, respectively. Note the variation of the spectrum with $m_*(z)$.

Fig. 2. The top panel shows the Fourier transform $A(m) = A_R(m) + iA_I(m)$ of the exponential wave amplitude growth with height $e^{z/2H_\rho}$, using representative values of z_s = 40 km and H_ρ = 7 km. The bottom panel details the change in $|A(m)/A(0)|$ with H_ρ. The dashed lines show the points where these curves are sampled when using a fast Fourier transform algorithm.

Fig. 3. Phase–averaged nonstationary spectra resulting from (*a*) unaliased and (*b*) aliased numerical simulations performed 2000 times in each case and averaged. The stationary model spectrum is also plotted for comparison. The simulation used a total height range $z_K - z_1$ = 44.8 km, K = 256, N = 0.02 rad s^{-1}, H_E = 10 km, and $m_*(z_1) = (1\text{ km})^{-1}$. See text for details about the numerical model used here. A least squares determination of the nonstationary spectral index in the 0.0002–0.0028 m^{-1} wave number range is also provided.

Fig. 4. An enlargement of the vertical wavelength region ~1–15 km from Figure 3. Such a wavelength range is typical of many spectra computed from experimental data from the middle atmosphere. Aliasing at the largest wave numbers is not included.

Fig. 5. Plot of the model saturated spectrum of *Smith et al.* [1987], the nonstationary realization of this spectrum from Figure 3*a*, and the "universal" spectral formula adopted by *VanZandt* [1982].

Fig. 6. (*a*) The horizontal velocity oscillations of a single gravity wave and vortical mode. The dotted vector represents the horizontal wave vector k_h. (*b*) Instantaneous horizontal velocity vectors produced by the superposition of two orthogonally aligned gravity waves and vortical modes; x and y are displacements normalized by the wavelengths λ_x and λ_y, respectively, and $\lambda_x = \lambda_y$ in these examples.

Fig. 7. Theoretical ground-based frequency spectra for (*a*) gravity waves and (*b*) vortical modes in different background wind conditions. The gravity wave model parameter $\beta = \bar{U}m_*/N$ parameterizes the degree of Doppler shifting, and at a given height is proportional to the mean wind $\bar{U}$. These gravity wave spectra are computed for equal amounts up– and down–shifting of frequencies [see *Fritts and VanZandt*, 1987], and plotted frequency labels $\hat{\Omega}$ are normalized by the inertial frequency f. The vortical mode spectrum here is based on a Taylor–transformed $k^{-5/3}$ horizontal wave number spectrum. One should also note that the vortical mode frequency spectrum for $\bar{U} = 0$ is a delta function at zero frequency (since vortical modes have no intrinsic frequency).

Fig. 8. The three panels on the left show various time variations in the gravity wave Doppler–shifting parameter $\beta = \bar{U}m_*/N$. The dotted line shows the mean value $\overline{\beta}$ over the time interval. The corresponding plots on the right show the resulting nonstationary gravity wave frequency spectra that these variations in Doppler–shifting produce. The aliased spectrum has been displaced vertically by 0.3 of a decade. These spectra are also compared to the stationary Doppler–shifted spectrum evaluated for $\beta = \overline{\beta}$ (dotted line), as one would usually do when comparing computed and model spectra. Equal up– and down–shifting of energy, and a value of $\hat{N} = N/f = 9.18$, were used in each example.

Fig. 9. The three panels on the left show various time variations in the background wind speed $\bar{U}$, and the dotted line shows the mean value evaluated over the whole time interval. The solid curves on the right show the resulting nonstationary vortical mode frequency spectra that these variations in wind speed give rise to. The dashed line shows the simulated results for a stationary wind speed of 20 m s^{-1}. Both of these spectra are aliased. The theoretical $\Omega^{-5/3}$ is also plotted as a dotted curve for reference. Least squares determinations of the spectral indices of the simulated spectra are given in each case over the whole spectrum, and over the band Ω = 0.00004–0.002 Hz, which excludes the highest frequencies.

Fig. 10. As for Figure 9, but for mean wind variability between 3 and 48 m s^{-1} rather than between 5 and 40 m s^{-1}. There are 128 points in the time series in these examples rather than 256 in the examples in Figure 9. The band over which spectral indices were fitted was Ω = 0.000025–0.00065 Hz.

Fig. 11. The panels on the left show various time variations in the fluctuating variance. The corresponding plots on the right show the stationary $\Omega^{-5/3}$ spectrum (dotted curve) and the simulated nonstationary spectrum (solid curve). Each simulated spectrum is an average of 2000 individual spectra from randomly phased time series. A least squares determination of the nonstationary spectral index is given in each case.

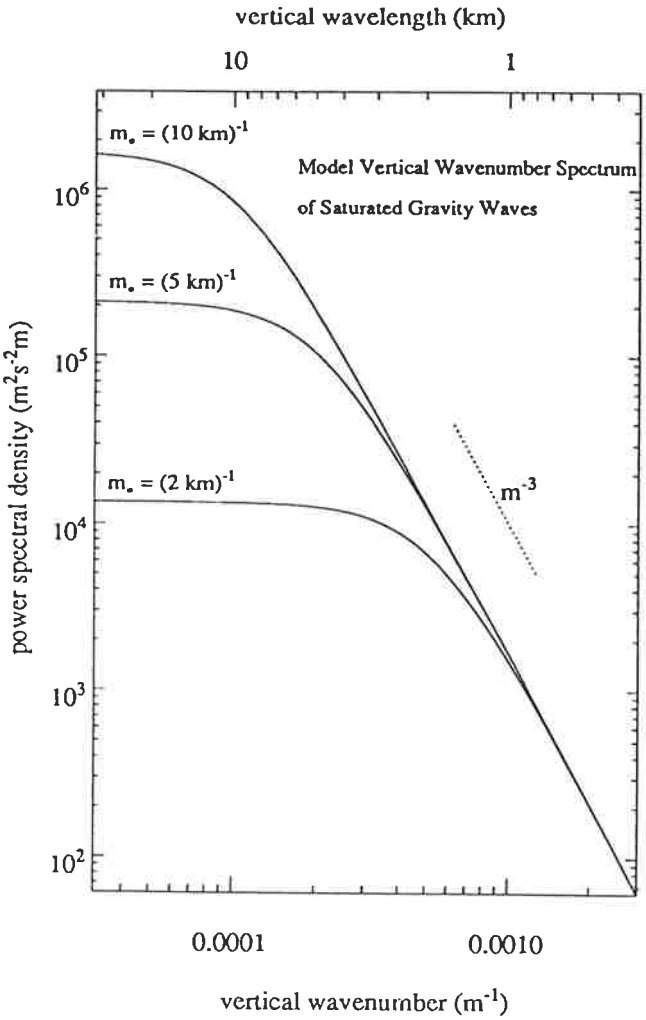
vertical wavelength (km)
10
1
$m_* = (10\ km)^{-1}$
Model Vertical Wavenumber Spectrum
of Saturated Gravity Waves
$m_* = (5\ km)^{-1}$
$m_* = (2\ km)^{-1}$
m^{-3}
power spectral density ($m^2s^{-2}m$)
10^6
10^5
10^4
10^3
10^2
0.0001
0.0010
vertical wavenumber (m^{-1})

Fig. 1

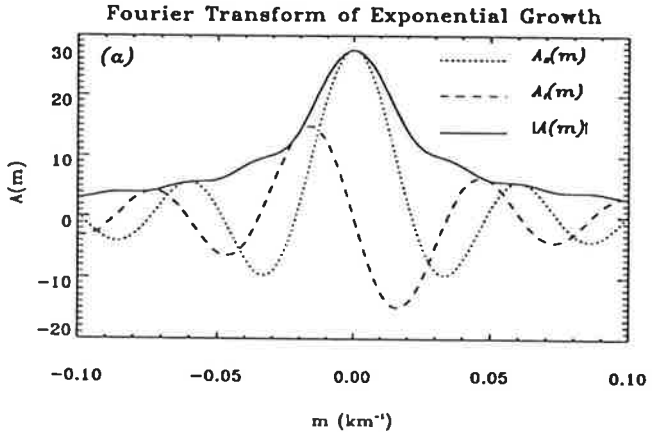
Fourier Transform of Exponential Growth
(a)
A(m)
m (km⁻¹)

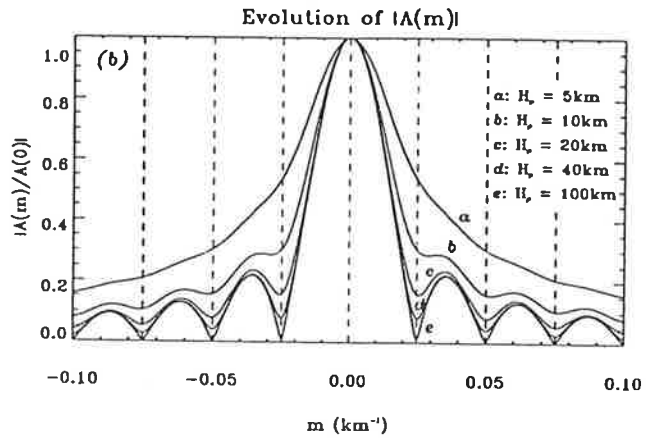
Evolution of |A(m)|
(b)
|A(m)/A(0)|
m (km⁻¹)
a: H = 5km
b: H = 10km
c: H = 20km
d: H = 40km
e: H = 100km

Fig. 2

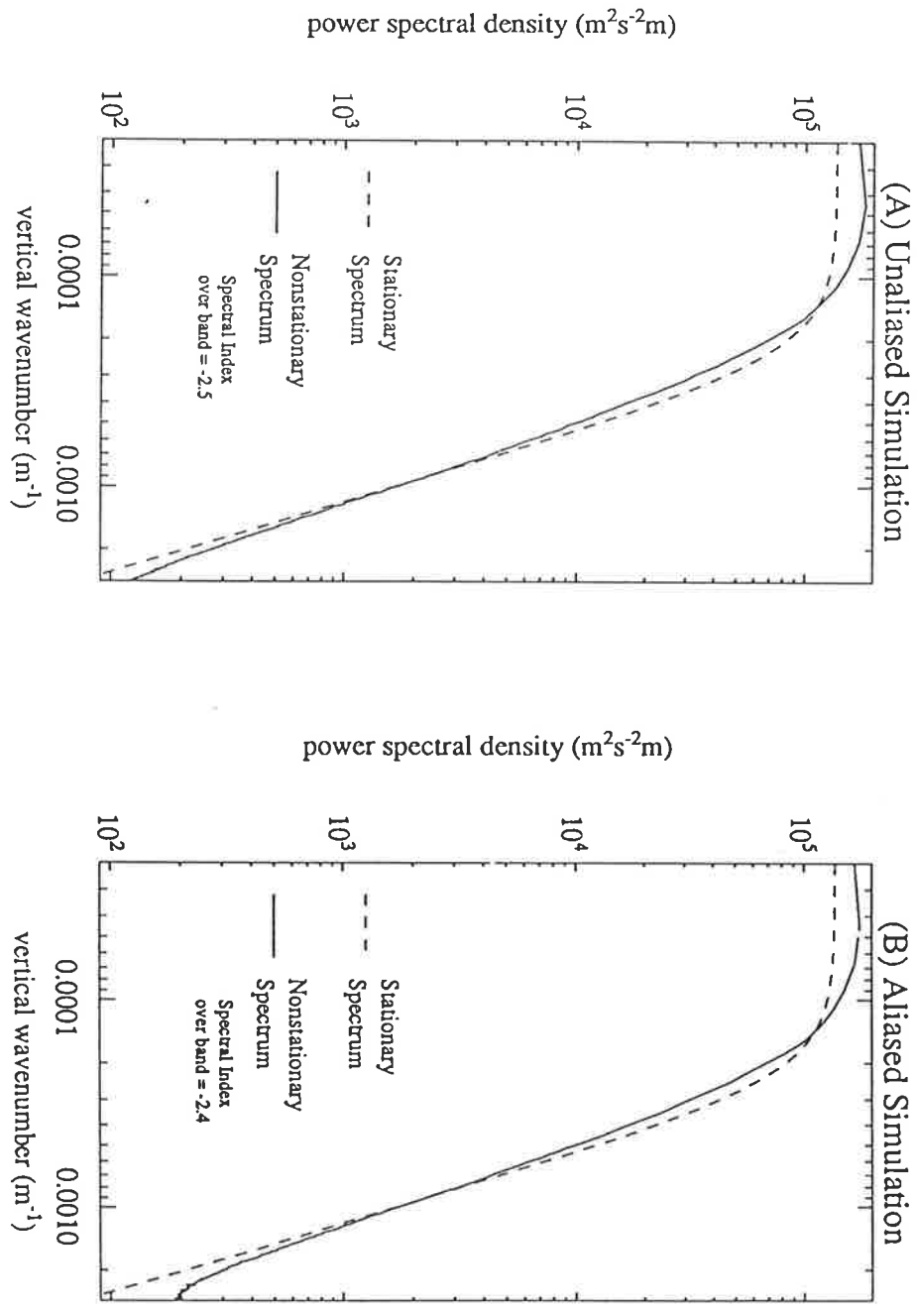
power spectral density ($m^2s^{-2}m$)
10^2
10^3
10^4
10^5
(A) Unaliased Simulation
Stationary Spectrum
Nonstationary Spectrum
Spectral Index over band = -2.5
0.0001
0.0010
vertical wavenumber (m^{-1})
power spectral density ($m^2s^{-2}m$)
10^2
10^3
10^4
10^5
(B) Aliased Simulation
Stationary Spectrum
Nonstationary Spectrum
Spectral Index over band = -2.4
0.0001
0.0010
vertical wavenumber (m^{-1})

Fig. 3

Fig

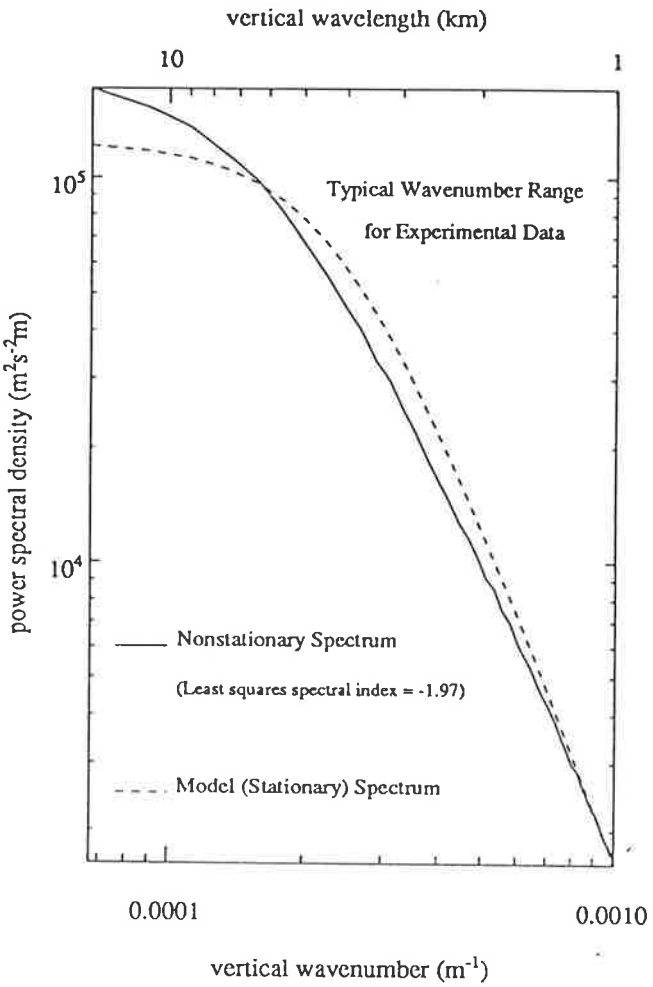
vertical wavelength (km)
10
1
10^5
10^4
power spectral density ($m^2s^{-2}m$)
Typical Wavenumber Range
for Experimental Data
Nonstationary Spectrum
(Least squares spectral index = -1.97)
Model (Stationary) Spectrum
0.0001
0.0010
vertical wavenumber (m^{-1})

Fig. 4

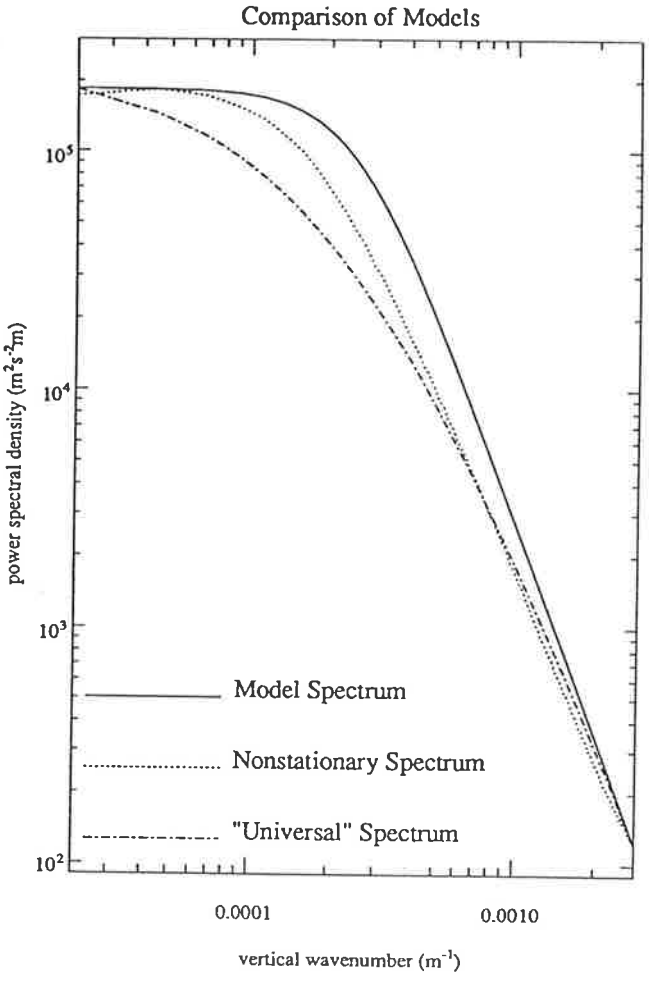
Comparison of Models
power spectral density (m²s⁻²m)
10⁵
10⁴
10³
10²
Model Spectrum
Nonstationary Spectrum
"Universal" Spectrum
0.0001
0.0010
vertical wavenumber (m⁻¹)

Fig. 5

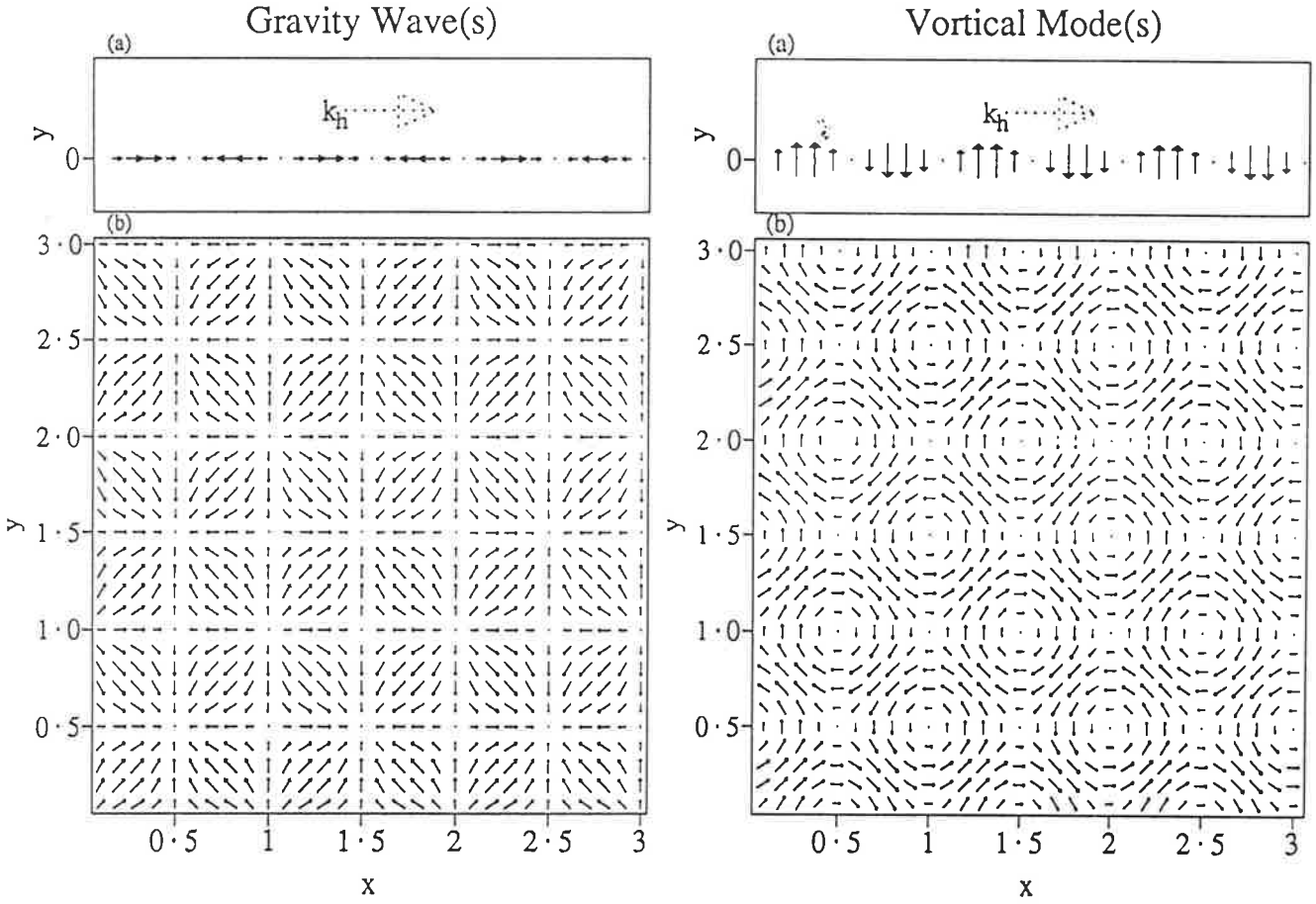
Gravity Wave(s)
Vortical Mode(s)
(a)
(b)
k_h
y
x
0
0·5
1
1·5
2
2·5
3
3·0
2·5
2·0
1·5
1·0
0·5

Fig. 6

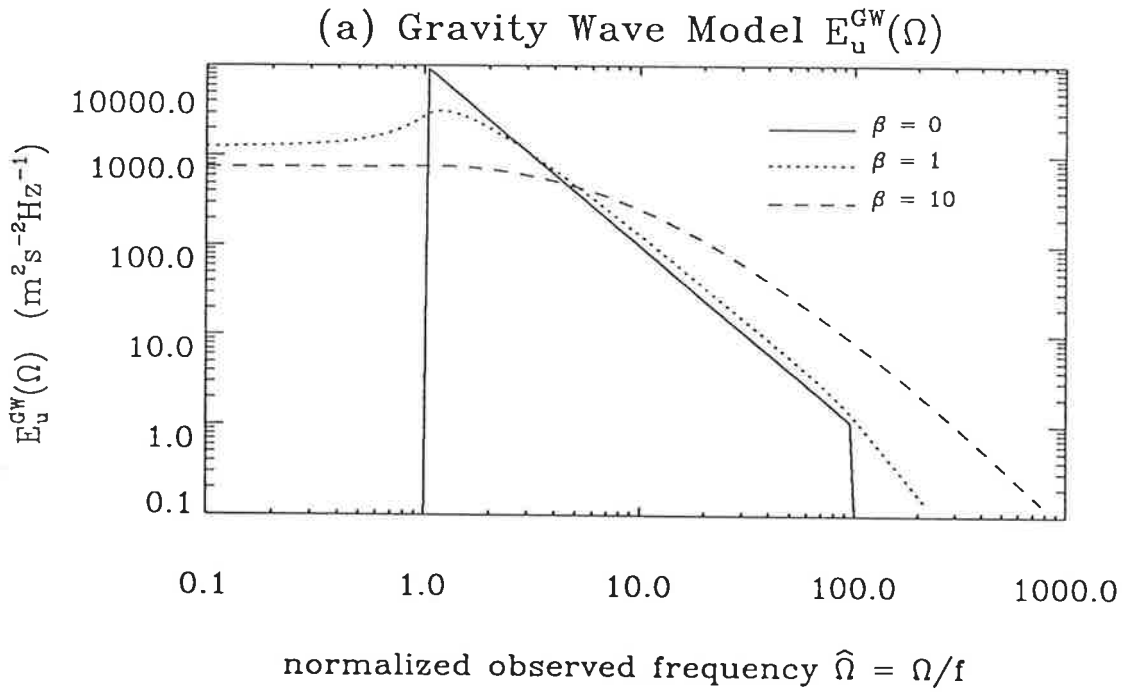
(a) Gravity Wave Model $E_u^{GW}(\Omega)$
$E_u^{GW}(\Omega)$ $(m^2 s^{-2} Hz^{-1})$
10000.0
1000.0
100.0
10.0
1.0
0.1
β = 0
β = 1
β = 10
0.1
1.0
10.0
100.0
1000.0
normalized observed frequency $\hat{\Omega} = \Omega/f$

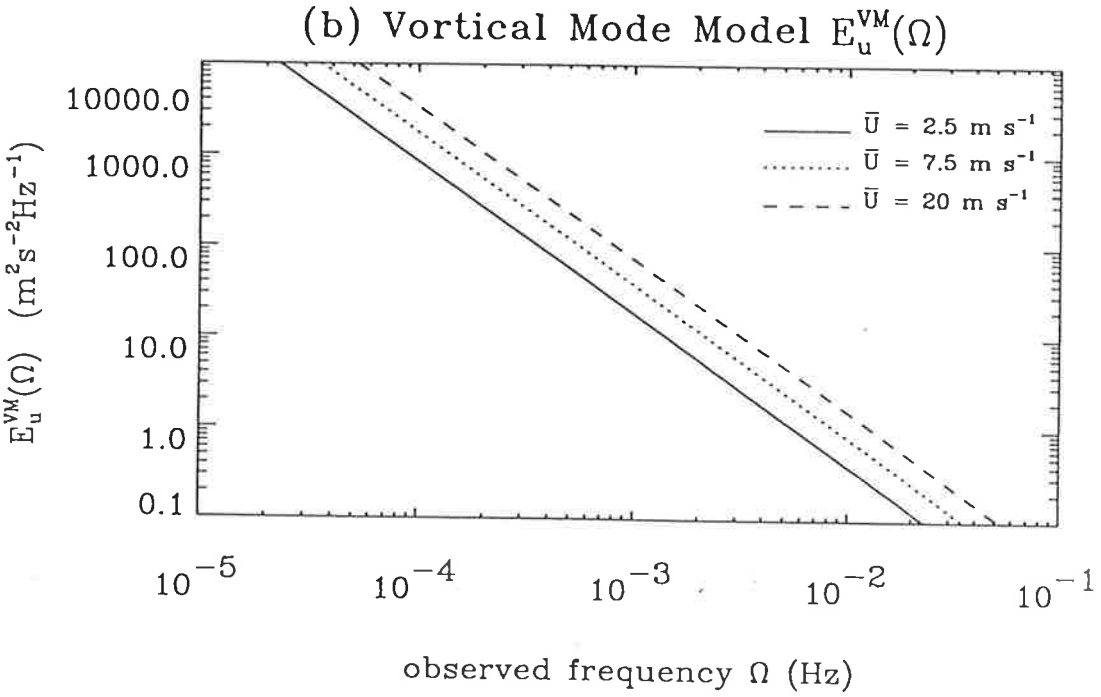
(b) Vortical Mode Model $E_u^{VM}(\Omega)$
$E_u^{VM}(\Omega)$ $(m^2 s^{-2} Hz^{-1})$
10000.0
1000.0
100.0
10.0
1.0
0.1
$\bar{U}$ = 2.5 m s^{-1}
$\bar{U}$ = 7.5 m s^{-1}
$\bar{U}$ = 20 m s^{-1}
10^{-5}
10^{-4}
10^{-3}
10^{-2}
10^{-1}
observed frequency Ω (Hz)

Fig. 7

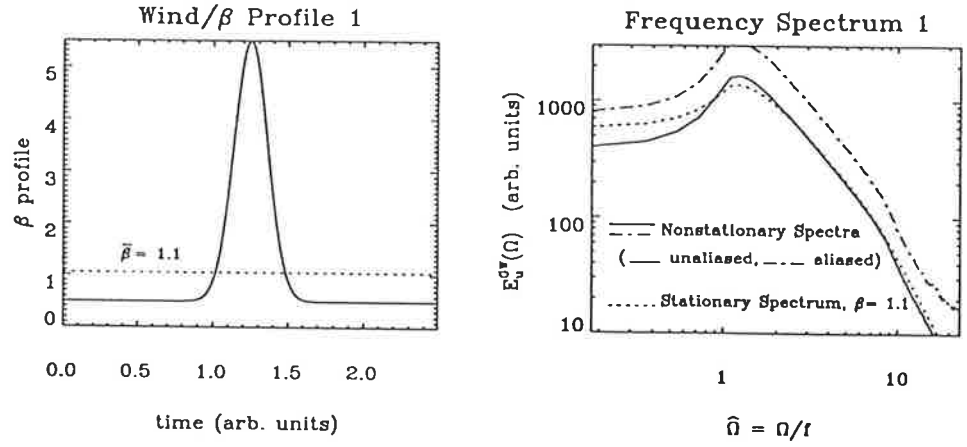
Wind/β Profile 1
β profile
$\bar{\beta}$ = 1.1
time (arb. units)
Frequency Spectrum 1
$E_u^{\sigma_T}(\Omega)$ (arb. units)
Nonstationary Spectra
(unaliased, aliased)
Stationary Spectrum, β = 1.1
$\hat{\Omega} = \Omega/f$

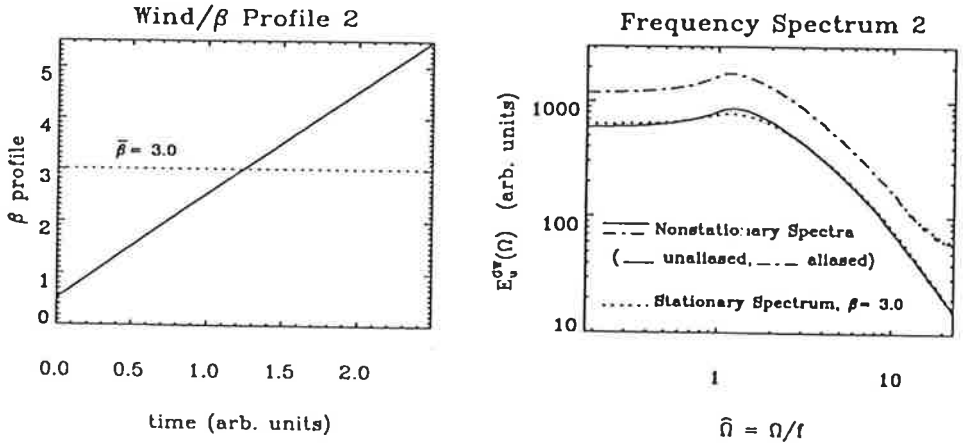
Wind/β Profile 2
β profile
$\bar{\beta}$ = 3.0
time (arb. units)
Frequency Spectrum 2
$E_u^{\sigma_T}(\Omega)$ (arb. units)
Nonstationary Spectra
(unaliased, aliased)
Stationary Spectrum, β = 3.0
$\hat{\Omega} = \Omega/f$

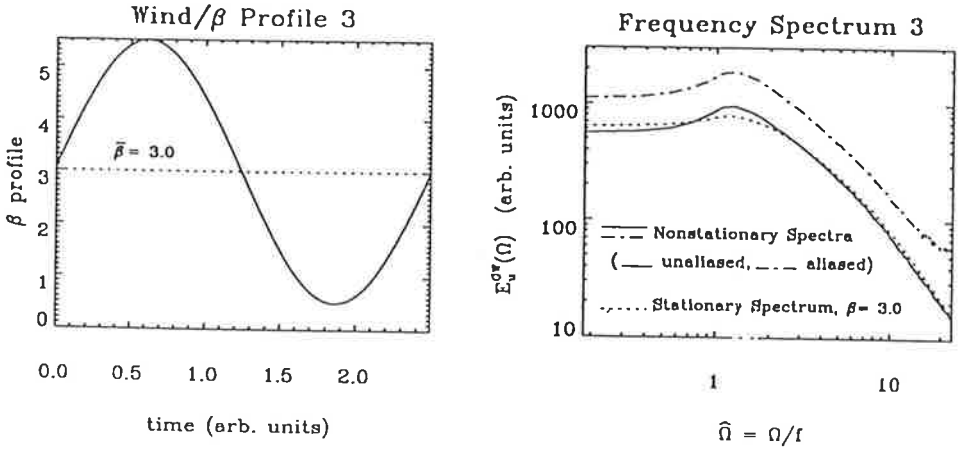
Wind/β Profile 3
β profile
$\bar{\beta}$ = 3.0
time (arb. units)
Frequency Spectrum 3
$E_u^{\sigma_T}(\Omega)$ (arb. units)
Nonstationary Spectra
(unaliased, aliased)
Stationary Spectrum, β = 3.0
$\hat{\Omega} = \Omega/f$

Fig. 8

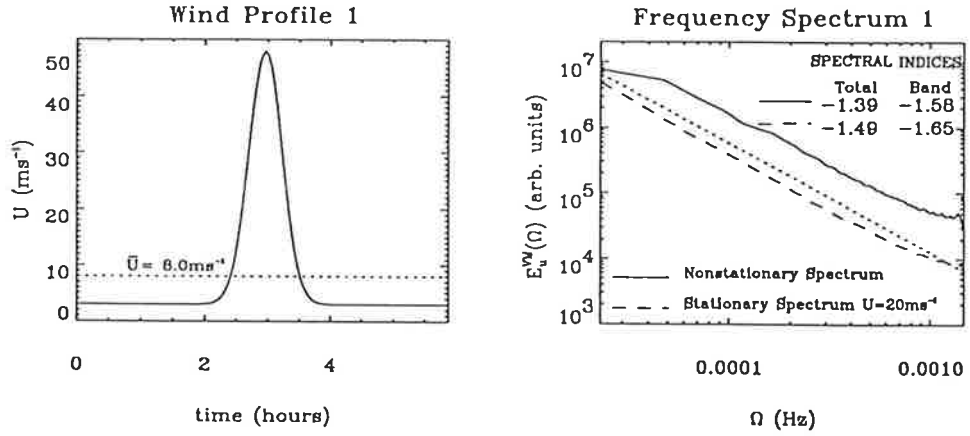
Wind Profile 1
U (ms⁻¹)
50
40
30
20
10
0
Ū = 8.0ms⁻¹
0
2
4
time (hours)
Frequency Spectrum 1
SPECTRAL INDICES
Total Band
−1.39 −1.58
−1.49 −1.65
Nonstationary Spectrum
Stationary Spectrum U=20ms⁻¹
$E_u^W(\Omega)$ (arb. units)
10^7
10^6
10^5
10^4
10^3
0.0001
0.0010
Ω (Hz)

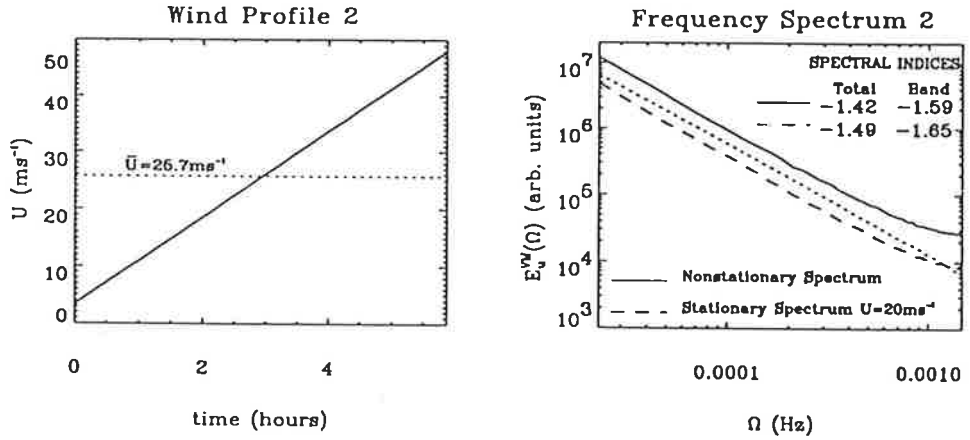
Wind Profile 2
U (ms⁻¹)
50
40
30
20
10
0
Ū=25.7ms⁻¹
0
2
4
time (hours)
Frequency Spectrum 2
SPECTRAL INDICES
Total Band
−1.42 −1.59
−1.49 −1.65
Nonstationary Spectrum
Stationary Spectrum U=20ms⁻¹
$E_u^W(\Omega)$ (arb. units)
10^7
10^6
10^5
10^4
10^3
0.0001
0.0010
Ω (Hz)

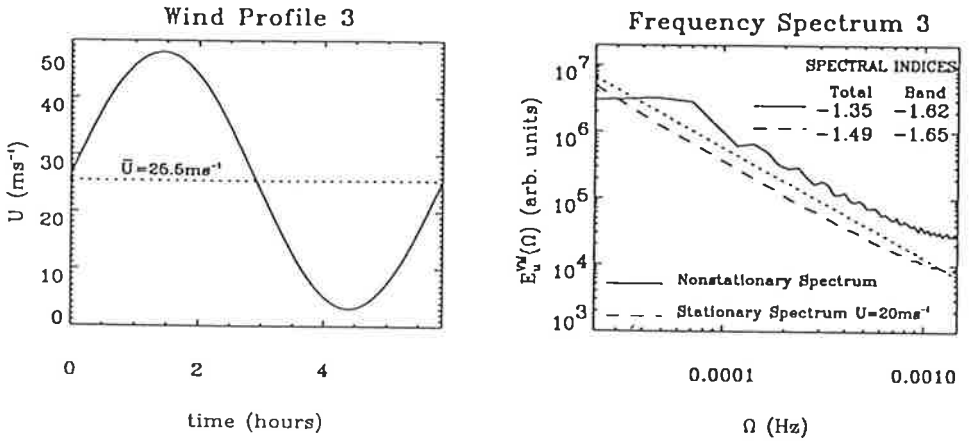
Wind Profile 3
U (ms⁻¹)
50
40
30
20
10
0
Ū=25.6ms⁻¹
0
2
4
time (hours)
Frequency Spectrum 3
SPECTRAL INDICES
Total Band
−1.35 −1.62
−1.49 −1.65
Nonstationary Spectrum
Stationary Spectrum U=20ms⁻¹
$E_u^W(\Omega)$ (arb. units)
10^7
10^6
10^5
10^4
10^3
0.0001
0.0010
Ω (Hz)

Fig. 9

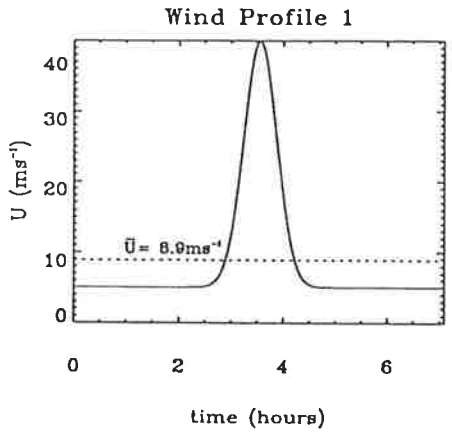
Wind Profile 1
U (ms⁻¹)
Ū= 8.9ms⁻¹
time (hours)

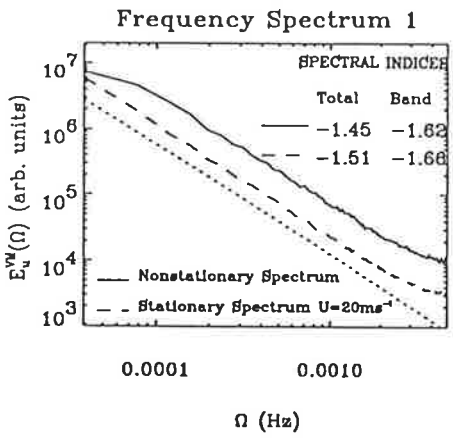
Frequency Spectrum 1
SPECTRAL INDICES
Total Band
−1.45 −1.62
−1.51 −1.66
Nonstationary Spectrum
Stationary Spectrum U=20ms⁻¹
Ω (Hz)

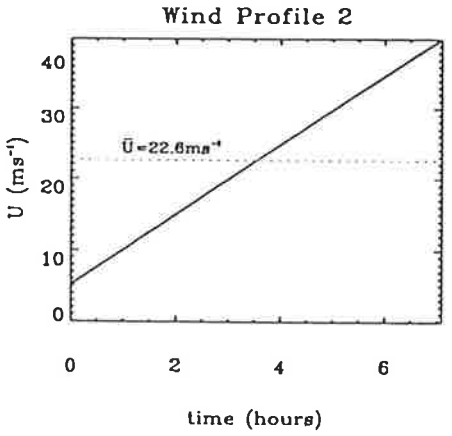
Wind Profile 2
U (ms⁻¹)
Ū=22.6ms⁻¹
time (hours)

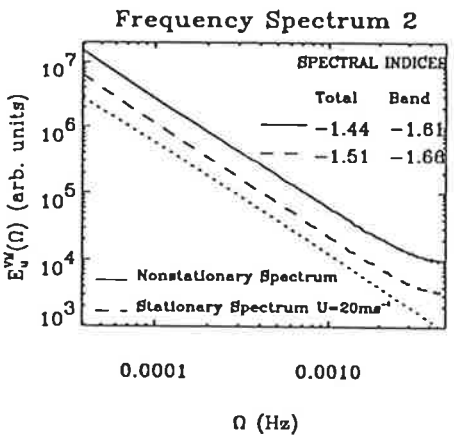
Frequency Spectrum 2
SPECTRAL INDICES
Total Band
−1.44 −1.61
−1.51 −1.66
Nonstationary Spectrum
Stationary Spectrum U=20ms⁻¹
Ω (Hz)

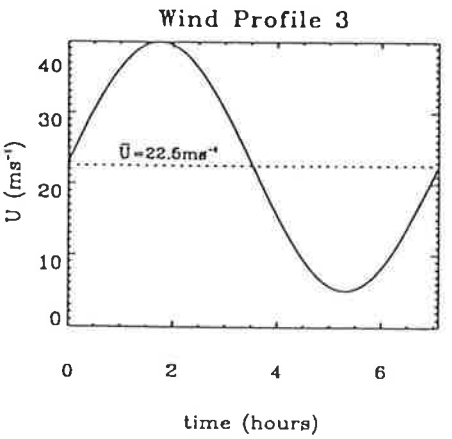
Wind Profile 3
U (ms⁻¹)
Ū=22.5ms⁻¹
time (hours)

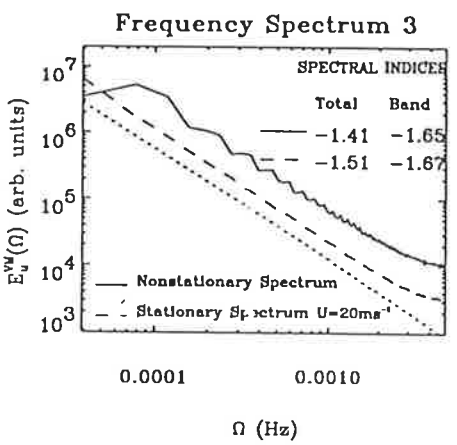
Frequency Spectrum 3
SPECTRAL INDICES
Total Band
−1.41 −1.65
−1.51 −1.67
Nonstationary Spectrum
Stationary Spectrum U=20ms⁻¹
Ω (Hz)

Fig. 10

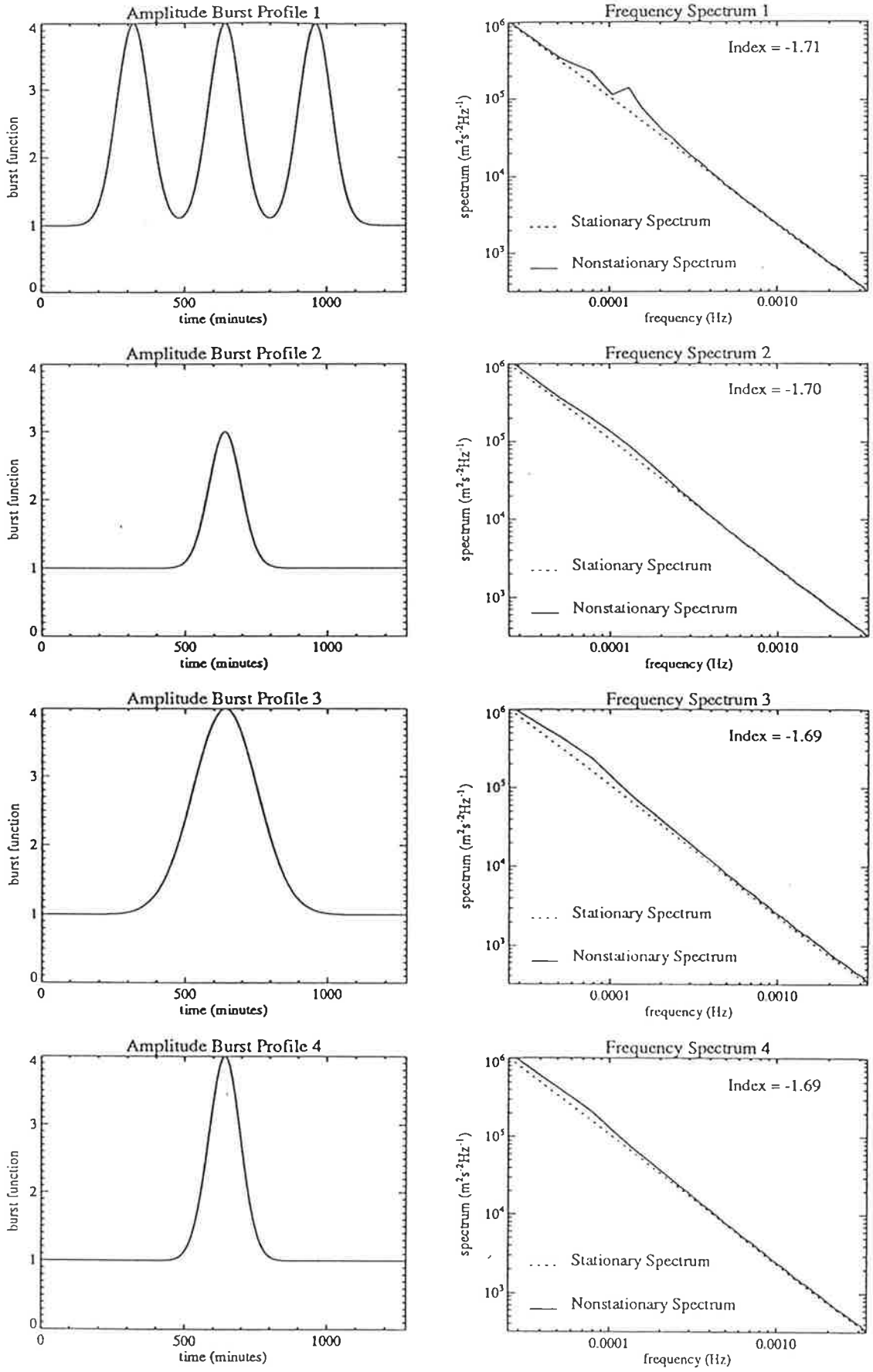
Amplitude Burst Profile 1
burst function
time (minutes)
Frequency Spectrum 1
Index = -1.71
spectrum (m²s⁻²Hz⁻¹)
frequency (Hz)
Stationary Spectrum
Nonstationary Spectrum
Amplitude Burst Profile 2
Frequency Spectrum 2
Index = -1.70
Amplitude Burst Profile 3
Frequency Spectrum 3
Index = -1.69
Amplitude Burst Profile 4
Frequency Spectrum 4
Index = -1.69

Fig. 11

Appendix H

VHF radar observations of mesoscale motions in the troposphere: Evidence of gravity wave Doppler shifting

This is a preprint of a paper by R.A. Vincent and S.D. Eckermann, which has been accepted for publication in *Radio Sci.*, 1990.

VHF radar observations of mesoscale motions in the troposphere: Evidence for gravity wave Doppler shifting

R. A. Vincent and S. D. Eckermann

Department of Physics and Mathematical Physics, University of Adelaide, Australia

(Received June 6, 1989; revised October 23, 1989; accepted November 6, 1989.)

A VHF radar at Adelaide (35°S, 138°E) has been used to study small-scale horizontal velocity fluctuations in the troposphere. The measurements have been analyzed in the frequency domain and show that the motions are often "polarized," such that they show a preference to be aligned along the direction of the mean background wind. This azimuthal anisotropy is especially apparent at high observed frequencies and becomes more pronounced as the wind speed increases. The cause of the polarization is analyzed in terms of both the gravity wave and vortical mode explanations of the mesoscale wind fluctuations. It is shown that the observed behavior is very consistent with the predicted effects of Doppler shifting on a spectrum of atmospheric gravity waves by non zero background winds. The results, however, are inconsistent with the predicted behavior of a spectrum of vortical modes advected past a ground-based observer. It is concluded that internal gravity wave motions dominate the energy of the tropospheric mesoscale wind field in these observations. These findings have a number of implications for studies which use ground-based techniques to study gravity wave wind fluctuations in the frequency domain because Doppler shifting of wave energy can produce significant biases, especially if narrow frequency bands are used. This problem and possible solutions are discussed.

1. INTRODUCTION

Ground-based radars have proved powerful tools for the study of mesoscale wind motions in the middle atmosphere and in particular of motions produced by atmospheric gravity waves. Through studies of wave motions, radars have been used to investigate not only particular wave parameters [e.g., Meek et al., 1985; Reid and Vincent, 1987] but also the statistical properties of the wave field in both the wave number and frequency domains [e.g., Balsley and Carter, 1982; Larsen et al., 1982; Vincent, 1984; Balsley and Garello, 1985; Fukao et al., 1985; Fritts and Chou, 1987; Franke et al., 1988]. Spectral studies using data produced by both radar and other techniques have proved especially useful as a way of summarizing the average properties of the wave field. An

interesting and important feature is that the spectra computed from observations made at widely differing locations often show great similarity in spectral slope and, to a lesser extent, in magnitude.

There are many similarities between the wave number and frequency spectra of motion fields observed in the ocean and atmosphere. VanZandt [1982, 1985] adapted the oceanic gravity wave spectral model originally developed by Garrett and Munk [1972] to the atmospheric situation and showed that the spectra are consistent with the gravity wave dispersion relation. An updated spectral model has been proposed by Sidi et al. [1988]. While the initial spectral models were somewhat empirical in nature, recent theoretical developments have shown that the shape of the vertical wave number spectrum is determined by gravity wave saturation processes [Dewan and Good, 1986; Smith et al., 1987]. The development of this approach has now reached the stage where it is possible to make predictions about how the spectrum of gravity waves is modified by changes in the environment through which the waves propagate. For example, VanZandt and Fritts [1989] have analyzed the consequences of changes in the spectral distribution of waves caused by an encounter between upward propagating gravity waves and a region of rapid increase in atmospheric stability.

An alternative model invoking stratified or quasi-two-dimensional turbulence, also often referred to as the vortical mode, has been proposed to explain the spectral distribution of horizontal wind motions. Vortical modes, so-called because, unlike gravity waves, they possess a vertical component of vorticity [Müller et al., 1988], result in horizontally stratified eddies which are "frozen" in the background flow. At large horizontal scales the turbulence is called geostrophic turbulence because the motions are in geostrophic and hydrostatic balance. At these scales, greater than about 500 - 1000 km, the turbulent energy is thought to follow a k^{-3} enstrophy cascade, where k is the horizontal wave number. At scales less than about 500 km down to scales about 1 - 10 km, the spectral index of the horizontal wave number spectrum becomes -5/3 and turbulence in this range is referred to as stratified turbulence [e.g., Gage, 1979;

Lilly, 1983; Gage and Nastrom, 1986, 1988]. Energy is presumed to be injected at small scales and to reverse-cascade through non linear processes to larger scales.

In the formulation of Müller et al. [1988] and Dong and Yeh [1988] the vortical mode is treated as an atmospheric wave motion similar to gravity and acoustic waves. Recently, Dong and Yeh [1988] discussed how vortical modes may grow by nonresonant wave-wave interactions with gravity waves. It was not clear how often this process might occur because the threshold amplitude for an interaction between a gravity wave and two vortical modes appeared to exceed that required for convective breakdown of gravity waves [e.g. Dong and Yeh, 1988; Fritts, 1989]. Yeh and Dong [1989] have demonstrated, however, that the effect of the Earth's rotation acts to relax the threshold effect, thus making the interaction more likely. Yeh and Dong [1989] propose that the energy spectrum of vortical modes is controlled via non linear cascading to small scales with energy being ultimately dissipated by viscosity.

The equivalence between stratified turbulence and vortical modes is somewhat ambiguous, yet the terms are sometimes used interchangeably to describe the same geophysical process [e.g., Müller et al., 1988; Gage and Nastrom, 1988; Dunkerton, 1989]. An ambiguity arises because of the wave nature of the vortical mode which seems inconsistent with the inherently nonlinear nature of turbulence. Nevertheless, many of the effects of vortical modes, such as rotation, appear turbulentlike [e.g., Dewan, 1985]. Here we assume that vortical modes and stratified or two-dimensional turbulence are equivalent, so that the horizontal wave number spectrum is presumed to follow a $k^{-5/3}$ relation [e.g., Gage, 1979]. This enables us to make use of the insights into the structure of the vortical mode presented by Dong and Yeh [1988] and Müller et al. [1988] in order to assess its importance to the mesoscale energetics of the lower atmosphere.

Of particular importance to radar studies is the need to describe how the frequency spectra respond to changes in the background winds in the atmosphere. If the motions are primarily due to gravity waves, then the observed frequency distribution of the energy of atmospheric

motions, as measured by a ground-based radar, is not necessarily the same as the distribution of energy of the wave field in the atmosphere. It is the spectral distribution as a function of the intrinsic frequency, ω' (the frequency in a reference frame moving with the wind), which is relevant, not the distribution as a function of the frequency, ω, as observed by a radar. For a single wave the equation relating the observed and intrinsic frequencies is

$$\omega = \omega' + k_h.\bar{U} = \omega' + k_h\bar{U}\cos\theta \quad (1)$$

where k_h is the horizontal wave number vector, $\bar{U}$ is the mean wind vector, k_h and $\bar{U}$ are their respective magnitudes, and θ is the angle between k_h and $\bar{U}$. The $k.\bar{U}$ contribution to (1) may be thought of as a Doppler-shifting term, which obviously has its greatest effect if the wave is propagating either parallel or antiparallel to the wind. Waves which have horizontal phase speeds (ω/k) small compared with $\bar{U}$ will suffer a larger relative Doppler shift than waves with high phase speeds.

Although little is yet known about the actual phase speed distribution of atmospheric gravity waves, it is probable that many waves have velocities which are comparable in magnitude with the background wind velocity [e.g., Gossard and Hooke, 1975]. In this situation, Doppler-shifting effects can produce significant differences between observed and model intrinsic frequency spectra. The general problem has been recognized for some time, and studies by Scheffler and Liu [1986] have shown how Doppler shifting can affect radar measurements of gravity wave spectra. The problem has also been addressed by Fritts and VanZandt [1987] (hereinafter referred to as FV87) who used a simpler analytic approach to show that Doppler shifting can cause major effects on the observed frequency spectra of both horizontal and vertical motions. They showed how the frequency spectra are modified as the velocity of the background flow increases.

Gage and Nastrom [1988] have discussed how the spectra of horizontal motions caused by two-dimensional turbulence or vortical modes will be modified by changes in the background wind speed. The vortical

mode has no intrinsic frequency spectrum but, as the eddylike structures are advected past a ground-based observer by the prevailing wind, a ground-based frequency spectrum will be produced, just as in (1) with ω' equal to zero.

The predictions of FV87 and Gage and Nastrom [1988] became of direct interest to us when we started to examine observations of short-period horizontal wind motions in the troposphere using a Stratosphere-troposphere (ST) radar operating at VHF (54.1 MHz) at a site near Adelaide. These particular investigations were part of a larger study of the mesoscale dynamics associated with the passage of cold fronts and were directed toward determining the degree of possible gravity wave generation caused by frontal activity. In the course of these studies we found that irregular wind motions with periods of a few hours or less often show a high degree of azimuthal anisotropy such that the motions exhibit a preferential alignment along the direction of the background wind; this effect becomes stronger as the background wind speed increases. Although both gravity waves and two-dimensional turbulence may contribute to the mesoscale wind field, we show that this phenomenon is better explained in terms of Doppler shifting of gravity wave energy as described by FV87.

The experimental situation and data analysis techniques are described in section 2. The mean winds and variations in the mesoscale motions are discussed in sections 3 and 4, respectively. The results are evaluated in terms of the gravity wave and turbulence models in section 5, and the implications for these and other ground-based wind studies in the middle atmosphere are discussed in section 6.

2. DATA ANALYSIS

The data discussed in this paper were acquired during the course of a study of the dynamics of the troposphere during the passage of cold fronts across southern Australia. The wind measurements were made with an ST radar which is located on the coastal plain some 40 km north of Adelaide (35°S, 138°E). The site is flat, and the nearest hills are situated about 40 to 50 km to the east. The radar, which operates

at a frequency of 54.1 MHz, is designed to use either the spaced antenna or the Doppler beam-swinging methods for wind measurement. In this study the spaced antenna method was used exclusively.

Details of the radar configuration and operation are given by Vincent et al. [1987], but the salient features are briefly described here. The transmitting antenna is of the coaxial-colinear type and is 16 λ square, so that it has a theoretical half-power half-width of 1.6°. In these experiments it was phased to transmit vertically. Three smaller yagi arrays arranged in the form of an equilateral triangle with a basic spacing of 50 m were used for reception. A solid-state transmitter was used with a pulse repetition frequency (PRF) of 8192 Hz. Coherent integration over 4096 received pulses was used, so that the sampling interval was 0.5 s. With a pulse length of 7 μs the mean power was about 300 W, and, with this relatively low power, echoes were received from the troposphere and the lowest part of the stratosphere only. The echoes were sampled every 500 m in the height range between 2 and 12 km.

Data were acquired for about 2 min and then analyzed in real time before the next measurements were made. Since the analysis took a total of about 2 min for the 20 heights sampled, this meant that the winds were measured every 4 min. Horizontal wind velocities were computed by the so-called full correlation analysis method applied to the complex echo amplitudes after correction for noise [Briggs, 1984; Vincent et al., 1987; May, 1988]. There is excellent agreement between the radar wind velocities and winds measured by balloon-borne radiosondes launched from nearby Adelaide Airport [Vincent et al., 1987]. Vertical wind velocities were deduced from the Doppler shifts of the echoes using the phase of the complex autocorrelation functions. The resulting wind data were then stored on disk for subsequent off-line analysis. The latter commenced with an editing procedure designed to remove spurious points or outliers. Various editing techniques have been proposed [e.g., Bemra et al., 1986] and, after some testing, we adopted a procedure which progressively removed outliers in a series of repeated steps at each height of observation, as follows: (1) The mean wind velocity vector was computed from data in a time window of 2-hour duration. (2) The

individual wind value in that block which showed the largest deviation in vector magnitude from the mean was then discarded. (3) Steps (1) and (2) were repeated four times before moving on to the next 2-hour block.

This method typically removed about 10% of the data, and while it probably removed some good data points, it succeeded in removing most outliers. For further reliability and to reduce aliasing by high-frequency motions, the next step was to form 15-min-average values for the zonal (u), meridional (v), and vertical (w) velocity components at each height. Because of the horizontal displacement of the transmitting and receiving antennas, it was necessary to correct the vertical velocities for possible contamination by the horizontal winds (see Vincent et al. [1987] for further details). Any short gaps in the 15-min averages were then filled by interpolation using a cubic spline procedure. This was done to ensure that sharp transitions did not contaminate the spectrum during filtering of the data used to study the short-period motions (see below), but interpolated values were not used in any subsequent calculations.

3. MEAN WINDS

Wind observations were made on a continuous basis for periods extending up to a month in duration, with passages of cold fronts usually occurring every 5 to 10 days. In this study a total of about 30 days data were used. Figures 1a, 2a, and 3a all show the sequence of the mean horizontal wind variations which occurred during the passage of frontal systems in August and November 1988. The plots are in the form of wind vectors which are formed from averages taken in this case over 4-hour intervals and show the magnitude and direction toward which the wind is directed. The u and v components are positive in the eastward and northward directions, respectively. The time evolution of the wind field during the passage of the fronts on August 22, August 26, November 14, and November 20/21 is typical of that observed during the passage of moist wintertime and early-summer fronts [Vincent et al. 1987; May et al. 1990]. Ahead of the front the winds are strong (~20–40 m s^{-1}) and directed

toward the southeast. After the frontal passage they swing round to become essentially northward.

Gaps in the data are evident for lengthy periods at heights above 8 km. There are two reasons for these breaks in the data. First, the temperature lapse rates in the height region immediately below the tropopause, which was at an altitude near 10 km during these measurements, were often very close to the dry adiabatic lapse rate, particularly at times immediately prior to the frontal passage. Even in the presence of strong turbulence there would be only small fluctuations in the radio refractive index and hence weak radar backscatter. Second, the galactic center, which is a strong source of noise at VHF, passes close to the zenith for several hours each day. The strong increase in background noise coupled with weak scatter often resulted in poor signal-to-noise ratios for echoes near the tropopause, and the data were usually rejected.

4. MESOSCALE WIND MOTIONS

The temporal variations of motions associated with mesoscale phenomena were studied by numerically filtering time series of the zonal and meridional wind components. The time series of 15-min-average wind values were bandpass filtered to produce the perturbation wind components, u', v', and w', in three different bands which covered the period ranges 8 to 24 hours, 2 to 8 hours and 30 min to 2 hours, respectively. Hereafter these ranges are referred to as the "long-," "medium-," and "short-"period bands. The variances of the wind components were computed for each band. Examination of the sum of the horizontal variances $\overline{u_T'^2} = (\overline{u'^2} + \overline{v'^2})$, which is proportional to kinetic energy per unit mass, indicated that the energies varied strongly with time. Peak values of $\overline{u_T'^2}$ were found in time intervals extending over several hours, and were up to 10–100 times stronger than the normal or background values. The large bursts in energy usually appeared ahead of a front, and seemed to coincide with regions of strong vertical velocities associated with convection. The bursts appeared to be associated with gravity waves generated either by the convective processes or by

regions of strong wind shear located near the tropopause. It is not our purpose here to discuss the possible wave sources, but to consider the azimuthal or directional anisotropy which was evident in the horizontal motions when such quantities as the ratios of the component variances ($\overline{u'^2}/\overline{v'^2}$) were formed.

An objective way of measuring the degree of anisotropy or polarization of wave energy in a statistical sense is the use of the so-called Stokes parameters, a method which has been applied to studies of wave motions in the mesosphere [Vincent and Fritts, 1987] and stratosphere [Eckermann and Vincent, 1989]. The method makes use of the following quantities, calculated for a suitable frequency band:

$$I = (\overline{u'^2} + \overline{v'^2}) \qquad (2)$$

$$D = (\overline{u'^2} - \overline{v'^2}) \qquad (3)$$

$$P = 2\,\overline{u'v'\cos\delta} \qquad (4)$$

$$Q = 2\,\overline{u'v'\sin\delta} \qquad (5)$$

I is the sum of the zonal and meridional velocity variances, D their difference, P and Q the inphase and quadrature covariances, and δ is the phase difference between the u' and v' components. For high frequency motions ($\omega \gg f$) the u' and v' motions are essentially inphase ($\delta \sim 0°$) and Q should be negligible. The inertial frequency, f, is 8.34×10^{-5} rad s^{-1} at Adelaide, which corresponds to a period of 20.9 hours, so Q is probably small for intrinsic wave periods less than ~2 hours, since these periods are much smaller than the inertial period, although the effects of Doppler shifting of frequencies must be born in mind.

From the above parameters it is possible to calculate the degree of polarization, defined as

$$d = (D^2 + P^2 + Q^2)^{\frac{1}{2}} / I \qquad (6)$$

which reduces to $d = (D^2 + P^2)^{\frac{1}{2}}/I$ in the high-frequency limit. This factor gives an estimate of the ratio of the polarized to unpolarized motions, so that d = 1

signifies a totally polarized field, and d = 0 denotes a random wave field. The mean azimuthal orientation or alignment, ϕ, of the polarized motions is given by

$$\phi = \tfrac{1}{2} \arctan(P/D) \qquad (7)$$

Figures 1b, 2b, and 3b show plots of the state of polarization of wind motions in the 30-min to 2-hour period range. Results have been averaged over the same 4-hour intervals as were used for the mean wind vectors shown in Figures 1a, 2a, and 3a. The polarization is represented by a line whose length is proportional to the degree of polarization, d, and whose rotation counterclockwise from east denotes the alignment, ϕ. These lines are, of course, not vectors since we do not have any information about the absolute directions of propagation of any waves which may cause the perturbation wind field to be polarized. Close inspection of the wind vector and polarization-plot pairs reveals that there is usually a strong correlation between the alignments and the direction of the mean wind vectors, such that perturbation motions are aligned along the direction of the mean wind. This tendency is especially strong during periods of high wind speed, particularly when the wind is steady in strength and direction for several hours.

In order to quantify this apparent relation between alignment and wind we grouped the alignment data into three background wind speed ranges of 0-5 m s^{-1}, 5-10 m s^{-1}, and greater than 10 m s^{-1}, corresponding to low-, medium-, and high-wind conditions, respectively. For each wind range the angular differences between the alignments and wind vectors were then calculated and grouped in 10° intervals in the range 0-90°. Figure 4 shows histograms of the number of observations in each interval as a function of mean wind speed for all three period bands, for all observations. To simplify the comparisons, the data for both the short- and medium-period bands were averaged in 8-hour segments, and the long-period band data were averaged in 24-hour segments.

For motions in the short-period band at low wind speeds ($\bar{U} \sim 2.5$ m s^{-1}) it is evident that the angular differences are reasonably evenly spread, although there

is evidence for perturbation wind motions to be aligned within a range of angles at 45 - 90° to the mean wind, i.e., approximately transverse to the wind. As the wind speed increases, however, the histograms become more strongly clustered in the range 0-20°, so that there is a strong polarization parallel to the mean wind.

Similar histograms for motions in the medium and long bands are also shown in Figure 4. There are, of course, fewer intervals for analysis in the long-period (8-24 hour) range, as the results are for 24-hour intervals only. For the medium-period range the results are similar to the short-period range with the angular difference changing from approximately 90° at low-wind speeds to 0° at high speeds. However, in this case the change is more gradual as a function of increasing $\bar{U}$ than is the situation for the short-period motions. In complete contrast, for the long-period motions there is a much stronger tendency for the perturbations to become aligned transverse (~90°) to the wind for speeds between 5 and 10 m s^{-1} and even in high-wind conditions the histogram shows that the angular differences are rather evenly spread, with a tendency to group in ranges near 30°, as opposed to the strong clustering near 0° evident for the higher frequency motions.

Care must be taken in attributing all motions in the low-frequency range to phenomena such as waves or turbulence because, particularly during the passage of fronts, the mean wind itself changes systematically in magnitude and direction on time scales of about a day (see Figures 1a, 2a, and 3a). During the filtering process these systematic changes themselves will produce Fourier components which contribute to the variance at long periods.

5. INTERPRETATION OF THE DATA

An analysis of the perturbation motions in the troposphere caused by mesoscale phenomena shows that the motions are often anisotropic. The Stokes parameters approach, which utilizes the variances of the wind components and their correlations, has been used to quantify the degree of anisotropy or polarization of the winds. Especially for motions with

periods of 8 hours or less, there is an increasing tendency for the motions to be aligned along the mean wind direction as the wind velocity increases. This result is particularly marked in the case of short-period motions. An immediate question is whether the polarization effect is an artifact of the spaced antenna wind measuring technique used in the observations.

There are three reasons that suggest that the effect is not caused by the observational technique. First, the receiving antennas are arranged at the vertices of an equilateral triangle [Vincent et al. 1987] precisely in order to reduce possible biases in the measurement of wind direction. Second, estimates of the random errors intrinsic to spaced antenna wind measurements, based on the theory of May [1988], show that the errors should be equally distributed between the wind components parallel and transverse to the mean wind vector. Third, the effects of random errors are also considerably reduced by the extensive averaging that was carried out, firstly into 15-min means, and then by averaging the band-passed data in 4-, 8-, and 24-hour time blocks. If the fluctuations were due to random errors, the degrees of polarization, d, would be zero after such extensive averaging. It is clear from Figures 1b, 2b, and 3b that typical values of d are between 50 and 100%.

We conclude that the observed anisotropies are manifestations of atmospheric mesoscale phenomena which are influenced by the strength of the prevailing wind. As noted in section 1, both atmospheric gravity wave and two-dimensional turbulence/vortical mode models have been proposed to explain the spectral distribution of mesoscale motions in the atmosphere. To date, most comparisons have concentrated on the shape and intensity of the spectra predicted by either theory. S.D. Eckermann (Effects of nonstationarity on spectral analysis of mesoscale motions in the atmosphere, submitted to Journal of Geophysical Research, 1989) (hereinafter referred to as Eckermann, submitted manuscript, 1989) has argued, however, that because of the transience of mesoscale variance in the atmosphere, the resulting distortion of spectra by this and other nonstationary effects (e.g., Doppler shifting) has often made it difficult to differentiate between

the two theories. Eckermann (submitted manuscript, 1989) suggested that the ratio of the variances of the fluctuating wind components parallel ($\overline{u_p'^2}$) to and transverse ($\overline{u_t'^2}$) to the mean wind might be a more useful measure in evaluating which theory is applicable, because, unlike spectral calculations, this ratio is not affected by variations in wave intensity due to source transience. Nevertheless, the two spectral theories can still be tested using this ratio, since each variance in a given frequency range can be found by integrating beneath the relevant spectrum.

To explain this, let the variance ratio, R, be defined as

$$R = (\overline{u_p'^2})/(\overline{u_t'^2}) \qquad (8)$$

In order to test the two models we need to examine how R responds to changes in the background wind speed for the various frequency intervals. Figure 5 shows log(R) plotted as a function of wind speed for all available data. For the short- and medium-period bands, each point represents an 8-hour average, while for the long-period band each point represents a mean over one day. The solid line in each plot indicates a least squares fit of a sixth-order polynomial to log(R); it is meant to be used only as a qualitative guide to trends evident in the data. The bars give the standard errors. These plots show more quantitatively what is evident from inspection of Figure 4. Except at low wind speeds ($\bar{U} < 5$ m s^{-1}), R is always greater than unity for the shorter period bands and increases steadily as $\bar{U}$ increases, to values of R ~ 2 - 10. For the long-period motions, however, R is less than unity for $\bar{U}$ less than about 15 m s^{-1} indicating that transverse motions predominate. Only at larger wind speeds does u_p' exceed u_t'.

Before examining in detail how gravity waves and vortical modes respond to changing background winds it is helpful to visualize the different nature of the horizontal wind motions associated with gravity waves and vortical modes, and how they differently affect radar observations. Wind vectors for both types of wave are plotted in the horizontal plane in Figure 6. Figure 6a shows how the horizontal wind component of a gravity wave is longitudinally polarized along the

horizontal wave vector, k_h. The superposition of two otherwise similar waves propagating at right angles produces the wind field illustrated in Figure 6b. The main feature is the divergent but irrotational nature of the perturbation motions. In contrast, because the horizontal motions of vortical modes are transverse to k_h (Figure 6c), the motions are rotational but nondivergent as is evident when two, otherwise similar, modes aligned orthogonally to each other are superposed (Figure 6d). Another important difference is that, in the absence of a background wind, a ground-based radar would detect the harmonically varying gravity wave motions but would only determine a constant wind in the case of the vortical modes.

5.1. The gravity wave model

The effects of Doppler shifting on gravity wave frequency spectra are most easily demonstrated by following the approach of FV87. For the purpose of illustration, they considered the case of a two-dimensional spectrum of waves which propagate either with or against the mean flow direction. As equation (1) shows, waves which propagate perpendicular to the flow will not be Doppler shifted. Figure 7a, which follows Figure 4a of FV87, shows frequency spectra of horizontal wind motions for three values of β, where β is the wind speed, $\bar{U}$, normalized by the so-called characteristic intrinsic horizontal phase speed of the wave field, c_*. The characteristic phase speed is, in turn, more conveniently put in terms of the characteristic vertical wave number, m_*, so that $\beta = \bar{U}/(N/m_*)$, where N is the Brunt-Väisälä frequency [FV87]. The solid line in Figure 7a is the model intrinsic frequency spectrum (no wind or $\beta = 0$) which has a ω^{-2} shape. The other curves, for $\beta = 1$ and 10, respectively, show that as the wind speed increases, the spectrum still peaks near the inertial frequency f but there is reduction in the spectral density, $E_{gw}(\omega)$, at these low frequencies, and a corresponding increase in $E_{gw}(\omega)$ at higher frequencies due to the preferential Doppler shifting of energy to higher observed frequencies.

As we are interested in the change in variance of the horizontal motions, a better estimate of the change in energy in a given frequency band can be obtained by replotting the frequency spectra in energy content form, $\omega E_{gw}(\omega)$ [VanZandt, 1985], as shown in Figure 8. The vertical lines indicate approximately the boundaries of the frequency intervals used in this study. The variance of the horizontal motions in any given interval for a particular value of $\bar{U}$ is directly proportional to the area under the appropriate curve in Figure 8. The shift of energy or variance to higher frequencies as β or $\bar{U}$ increases is especially apparent in these spectra; indeed, for $\beta = 5$ the spectral peak has shifted to observed periods of about 6-7 hours, and at $\beta = 10$ the curve peaks at a 2-hour observed period.

Under high-wind conditions ($\beta \sim 5$-10) we estimate that for the short-period band the variance due to gravity waves with a strong component of motion parallel to the mean flow will be a factor ~2-3 times greater than that for the zero wind situation. Since the variance due to waves which are propagating at right angles to the horizontal flow will be unaffected by Doppler shifting (i.e., β=0), R will be significantly greater than unity for large $\bar{U}$, as is observed in Figure 5. In the 2 - 8 hour band there is a smaller increase in $\overline{u_p'^2}$ for $\beta = 10$.

For the long-period band it is more difficult to predict how R changes as $\bar{U}$ increases. Figure 8 shows that there is a net decrease in the parallel wind component as β increases which would suggest that R should be less than unity, as observed in light-wind conditions in Figure 5. However, the horizontal motions of quasi-inertial oscillations are elliptically polarized, which means that there will be a decrease in the contribution to u_t' from parallel propagating waves. Waves propagating transverse to $\bar{U}$ will still contribute to u_p'. Another complicating factor is the probable contamination caused by systematic changes in the mean wind caused by frontal passages contributing to the variances.

Care must be used when interpreting the results shown in Figures 7a and 8. First, for ease of calculation, FV87 used a spectral model in which the energy density varied as ω^{-2}, rather than the

usually accepted $\omega^{-5/3}$. However, use of a more realistic spectral slope is unlikely to change the overall conclusions. Second, we do not know the appropriate value for c_*, the characteristic horizontal phase speed. Estimates of m_* can be made from vertical wave number spectra [e.g., Smith et al., 1987], but we have insufficient height resolution to enable us to do this with the present data. Observations in the northern hemisphere give values in the range $(m_*)^{-1} \sim 1 - 3$ km in the troposphere and lower stratosphere [Smith et al., 1987; Fritts and Chou, 1987; Fritts et al., 1988], which suggests that $c_* = N/m_* \sim 1.5 - 5$ m s^{-1} using a value of $N \sim 0.01$ rad s^{-1} appropriate to the troposphere. Characteristic phase speeds of this magnitude imply that values of β greater than about 10 are quite feasible during the passage of fronts when wind speeds up to and exceeding 30 m s^{-1} can be maintained for many hours (see Figures 1a, 2a, and 3a). Such values of β would easily produce the observed changes in R seen in Figure 5.

Doppler shifting of the gravity wave spectra also produces a shift of energy for the vertical motions. The net effect is to produce a net decrease in energy at observed frequencies less than the Brunt-Väisälä frequency, N, and an increase for frequencies greater than N [see FV87]. At the frequencies we are concerned with here the predicted effect is to increase the ratio of horizontal to vertical energies as $\bar{U}$ increases [see FV87, Figure 5], especially in the short- to medium-period bands. Figure 9 shows scatter plots of $\log(\overline{u_T'^2}/\overline{w'^2})$ against $\bar{U}$ for the three period bands, where $\overline{u_T'^2} = (\overline{u'^2} + \overline{v'^2})$ is the total variance of the horizontal motions. It is clear that the ratio increases in the manner predicted, with the mean ratio for the short-period band increasing by greater than an order of magnitude as the wind speed increases from near zero to over 30 m s^{-1}. Inspection of Figure 6 in FV87 suggests that there would be an increase of about a factor of 10 as β increases from 0 to 10. Considering the approximations inherent in their calculations there is extremely good agreement between our results and their predictions.

5.2. Vortical mode model

The wave-associated flows produced by vortical modes in the short wavelength limit are transverse to the wave normal and contained in the horizontal plane (see Figure 6c). As discussed in section 1, vortical modes have zero intrinsic frequency ($\omega'=0$), but a wind of velocity $\bar{U}$ causes a Doppler shift to give an observed frequency of $\omega = k.\bar{U}$. Gage and Nastrom [1988] used the Taylor transformation to determine the frequency spectrum, $E_{vm}(\omega)$, of vortical modes as a known horizontal wave number field is advected past. The frequency spectrum is

$$E_{vm}(\omega) = F_v(k)/\bar{U} = F_v(\omega/\bar{U})/\bar{U} \qquad (9)$$

where results from instrumented aircraft (Global Atmospheric Sampling Program) were used to give a model spatial wave number spectrum of $F_v(k)$ proportional to $k^{-5/3}$. It should be noted that equation (9) is probably incomplete in that a more extensive analysis shows that a better spectrum would have the functional form $F_v(\omega/\bar{U}\cos\theta)/(\bar{U}\cos\theta)$ if the k_h spectrum is isotropic and different forms again if the k_h spectrum is anisotropic (K. C. Yeh, private communication, 1989). Certainly, all theory to date has assumed an isotropic k_h spectrum of vortical modes, and so, without further information on the angular distribution of k_h, we take (9) as adequate for our purposes.

Figure 7b illustrates the Doppler shifted spectrum predicted by Gage and Nastrom [1988] plotted for different wind speeds. Comparison with Figure 7a shows that the shape of the vortical mode spectrum is preserved as $\bar{U}$ increases, unlike the Doppler-shifted gravity wave spectrum, and that the energy density at a given observed frequency increases as $\bar{U}$ increases.

An assumption which seems implicit in the estimates of Gage and Nastrom [1988] is that the energy is isotropically distributed as a function of the observed frequency. However, when the geometry of oscillations associated with vortical modes is considered, it can be shown that as the structures are advected past, a ground-based observer will detect time-varying motions which are essentially

transverse to the mean flow. For simplicity, consider the background wind $\bar{U}$ directed eastward and a single vortical mode with horizontal wave number $k_h = (k_x, k_y)$ aligned at an angle θ to the flow. This vortical mode has an associated horizontal motion, $v = (u', v') = A_k(-k_y, k_x)$, where A_k is a complex amplitude [Müller et al., 1988]. These motions are orthogonal to k. From (1), it is apparent that the ground-based frequency is $\omega - k_x\bar{U} - k_h\bar{U}\cos\theta$. Hence only those modes with wave numbers closely aligned with the mean flow produce significant ground-based frequencies, whereas a mode with a meridionally directed wave number will have not only a zero intrinsic frequency, but also zero observed frequency. Doppler shifting therefore causes a bias in the frequency domain to modes whose wave vectors are coaligned with the mean flow, and such modes will produce mostly transverse (u_t') fluctuations.

Furthermore, the $k^{-5/3}$ wave number spectrum postulated by Gage [1979] also favors the observation of vortical modes with k_h parallel to $\bar{U}$. At a given observed frequency ω, all vortical modes must have the same wave vector component, ($k\cos\theta$) parallel to $\bar{U}$, but their components perpendicular to $\bar{U}$ (of magnitude $k\sin\theta$) will generally be different. Because of the "red" nature of the $k^{-5/3}$ spectrum, those modes with $k\sin\theta \sim 0$ must have the largest variance, since their total wave number is smallest, and will hence dominate the variance in the frequency spectrum.

On these grounds we argue that vortical modes with wave vectors closely aligned with the mean flow will have the largest amplitude in the observed frequency domain, but it is these particular modes which have their oscillations directed transverse to $\bar{U}$. Hence it is expected that the variance transverse to the mean wind (u_t') will be greater than the parallel component, and so $R < 1$ is predicted for vortical modes, a result which should become more pronounced as the wind speed increases. Since this contradicts our observations (Figure 5), we conclude that vortical modes do not contribute significantly to the motion field in the troposphere at Adelaide.

6. DISCUSSION

We have used wind measurements made with the Adelaide VHF ST radar to show that horizontal wind motions associated with mesoscale phenomena in the troposphere often appear azimuthally anisotropic. The anisotropy manifests itself as a tendency for the motions to become increasingly aligned along the direction of the background wind as its strength increases. The effect is especially evident in motions with observed periods in the 30-min to 2-hour range.

The results have been interpreted in terms of the effects of Doppler shifting produced by a nonzero mean wind, $\bar{U}$, on model spectra of atmospheric gravity waves and vortical modes. In both of these models, Doppler shifting produces a net shift of energy to higher observed frequencies for waves which have a component of the horizontal wave number parallel or antiparallel to $\bar{U}$. Oscillations which propagate at right angles to $\bar{U}$ are unaffected. However, the resulting ratio (R) of energy for motions parallel to and perpendicular to $\bar{U}$ is different for the two models. This disparity arises because of the different polarization of the perturbation motions associated with gravity waves and vortical modes. For both wave types the motions are polarized orthogonal to the wave normal, k, but for gravity waves the horizontal components of the motion are aligned along k_h, the horizontal component of k, whereas the motions for vortical modes lie in the horizontal plane and are perpendicular to k (compare Figures 6a and 6c). Consequently, the gravity wave model predicts an enhancement of R greater than unity as $\bar{U}$ increases, as observed in Figure 5, whereas the vortical mode model predicts a decrease in R, with values less than unity as $\bar{U}$ increases.

We therefore conclude that our observations are consistent with the hypothesis that, in the lower atmosphere, gravity waves are responsible for the bulk of the variance in the mesoscale wind field and that vortical modes or two-dimensional turbulence are not significant in terms of energy. The contribution that vortical modes might make to shear and potential vorticity in the atmosphere has yet to be explored, although it appears they may play a significant role in the ocean [Müller et al., 1988]. Our

conclusion is in accord with that of Fritts and Chou [1987] and Fritts et al. [1988] who, respectively, spectrally analyzed Mesosphere-stratosphere-troposphere (MST) radar winds measured at Poker Flat, Alaska, and Kyoto, Japan. Additional support for the gravity wave model comes from our comparison of the ratio of the horizontal to vertical energy, which exhibits an increase as $\bar{U}$ increases, in line with the predictions of FV87.

These findings have some implications for studies which use ground-based radar wind measurements to investigate azimuthal anisotropies of gravity wave motions in the middle atmosphere, especially if the observations are confined to a narrow observed frequency range. Vincent and Fritts [1987] and Ebel et al. [1987], for example, have reported significant anisotropies in wave motions within given observed frequency bands in the mesosphere and have interpreted their results in terms of the directional filtering effects acting on a spectrum of waves propagating up through the middle atmosphere. However, Doppler shifting, acting on a spectrum of waves whose horizontal phase speed distribution is azimuthally isotropic, can produce differences in the observed frequency spectra as the effects are most pronounced for those waves which are propagating either with or against the mean wind, an effect not anticipated in these earlier studies. The situation is particularly acute for high observed frequencies, and the effect will be more important if c_* is small compared with $\bar{U}$, which is equivalent to m_*^{-1} small compared with $\bar{U}/N$.

Although values of m_*^{-1} are not well known, Smith et al. [1987] suggest values ~ 5 and 20 km in the stratosphere and mesosphere, respectively. With $N \sim 0.02$ rad s^{-1} these values correspond to c_* ~16 m s^{-1} in the stratosphere and ~60–70 m s^{-1} in the mesosphere. Doppler shifting effects are therefore likely to be very important in the stratosphere where, at the solstices, mean wind speeds of up to 100 m s^{-1} are possible. The higher values of c_* in the mesosphere and the smaller mean winds in that region mean that Doppler shifting effects are probably less severe. Mean winds ~ 70 m s^{-1} correspond to values of $\beta \sim 1$ which produce only small changes in the spectrum of horizontal motions (e.g., see Figure 8), and so the findings of Vincent and Fritts

[1987] and Ebel et al. [1987] are not appreciably contaminated by Doppler shifting. Nevertheless, it is possible that the semiannual variation in the magnitude of the mean zonal wind in the lower mesosphere could accentuate the semi-annual variation of gravity wave amplitudes which has been observed in this region [e.g., Vincent and Fritts, 1987; Ebel et al., 1987]. The fact, however, that the semiannual variation in gravity wave activity is still apparent in the mesosphere at Adelaide after the variances have been integrated over the whole frequency spectrum [Vincent and Fritts, 1987] shows that it must be a real phenomenon at this location.

It is often necessary to examine the gravity wave motions in a number of frequency bands in order, for example, to determine the influence of possible wave sources. The results from this paper suggest, however, that caution should be exercised when variations of gravity wave amplitudes are investigated with ground-based sensors so that the possible influence of Doppler shifting is taken into account. Our observations support the conclusions of Fritts and VanZandt [1987] that particular care should be taken at high observed frequencies where Doppler-shifting effects can be pronounced. Integration of the variances over the whole observed frequency spectrum should be used wherever possible. Finally, it should be noted that studies which use the vertical spatial structure of the wave motions to investigate azimuthal anisotropies [e.g., Eckermann and Vincent, 1989] will not be influenced by Doppler shifting because the vertical wave number is itself an intrinsic wave parameter.

7. SUMMARY AND CONCLUSIONS

We have presented observations of mesoscale horizontal wind motions in the lower atmosphere over Adelaide, Australia, and show that the fluctuating motions are often closely aligned to the background wind direction. This alignment becomes more pronounced as the strength of the background wind speed increases, especially at high observed frequencies. In order to explain this phenomenon we consider how the gravity wave and vortical

mode (two-dimensional turbulence) models of mesoscale motions respond to changes in the background flow. Both models predict that Doppler-shifting effects will cause increasing energy to be measured at high observed frequencies as the magnitude of the background wind increases. However, because the horizontal wind components of gravity waves and vortical modes are polarized differently relative to their horizontal wave number vector, the partition of energy between motions parallel and transverse to the mean wind direction is different. For gravity waves, Doppler shifting causes the fluctuations parallel to the mean wind to be enhanced relative to the transverse oscillations, whereas for vortical modes the opposite is the case. Doppler shifting of gravity wave energy would therefore result in an apparent alignment of the wave fluctuation with the mean flow, as is observed. We therefore conclude that our observations are in better accord with the predictions of Doppler shifting of gravity wave energy and that gravity wave motions dominate the mesoscale energetics of the lower atmosphere. The implications of this study for other ground-based radar measurements of gravity wave parameters are discussed, and it is pointed out that Doppler shifting may significantly bias the results unless the effects are properly accounted for.

Acknowledgments. We thank B. H. Briggs, W. K. Hocking, I. M. Reid, and K. C. Yeh for their critical reviews of early drafts of this paper and for their many helpful comments and L. Campbell for the use of his plotting software. This work was supported by the Australian Research Council. One of us (S.D.E) is the recipient of a Commonwealth Research Postgraduate Award.

REFERENCES

Balsley, B. B., and D. A. Carter, The spectrum of atmospheric velocity fluctuations at 8 and 86 km, Geophys. Res. Lett., 9, 465-468, 1982.

Balsley, B. B., and R. Garello, The kinetic energy density in the troposphere, stratosphere and mesosphere: A preliminary study using the Poker Flat radar in Alaska, Radio Sci., 20, 1355-1362, 1985.

Bemra, R. S., P. K. Rastogi, and B. B. Balsley, A study of gravity-wave spectra in the troposphere and stratosphere at 5-min to 5-day periods with the Poker Flat MST radar, in Handbook for MAP, vol 20, pp 216-224, SCOSTEP Secr., Univ. of Ill., Urbana, 1986.

Briggs, B. H., The analysis of spaced sensor records by correlation techniques, in Handbook for MAP, vol. 13, pp 166-186, SCOSTEP Secr., Univ. of Ill., Urbana, 1984.

Dewan, E. M., On the nature of atmospheric waves and turbulence, Radio Sci., 20, 1301-1307, 1985.

Dewan, E. M., and R. E. Good, Saturation and the "universal" spectrum for velocity profiles of horizontal scalar winds in the atmosphere, J. Geophys. Res., 91, 2742-2748, 1986.

Dong, B., and K. C. Yeh, Resonant and nonresonant wave-wave interactions in an isothermal atmosphere, J. Geophys. Res., 93, 3729-3744, 1988.

Dunkerton, T. J., Theory of internal gravity wave saturation, Pure Appl. Geophys., 130, 373-397, 1989.

Ebel, A., A. H. Manson, and C. E. Meek, Short period fluctuations of the horizontal wind measured in the upper middle atmosphere and possible relationships to internal gravity waves, J. Atmos. Terr. Phys., 49, 385-401, 1987.

Eckermann, S. D., and R. A. Vincent, Falling sphere observations of anisotropic gravity wave motions in the upper stratosphere over Australia, Pure Appl. Geophys., 130, 510-532, 1989.

Franke, S. J., C. H. Liu, I. J. Fu, R. Rüster, P. Czechowsky, and G. Schmidt, Multibeam radar observations of winds in the mesosphere, J. Geophys. Res., 93, 15965-15971, 1988.

Fritts, D. C., A review of gravity wave saturation processes, effects, and variability in the middle atmosphere, Pure Appl. Geophys., 130, 343-371, 1989.

Fritts, D. C., and H. Chou, An investigation of the vertical wave number and frequency spectra of gravity wave motions in the lower stratosphere, J. Atmos. Sci., 44, 3610-3624, 1987.

Fritts, D. C., and T. E. VanZandt, Effects of Doppler shifting on frequency spectra of atmospheric gravity waves, J. Geophys. Res., 92, 9723-9732, 1987.

Fritts, D.C., T. Tsuda, T. Sato, S. Fukao, and S. Kato, Observational evidence of a saturated gravity wave spectrum in the troposphere and lower stratosphere, J. Atmos. Sci., 45, 1741-1758, 1988.

Fukao, S., Y. Maekawa, T. Sato, and S. Kato, Fine structure in mesospheric wind fluctuations observed at Arecibo by the Arecibo UHF Doppler radar, J. Geophys. Res., 90, 7547-7556, 1985.

Gage, K. S., Evidence for a $k^{-5/3}$ law inertial range in mesoscale two-dimensional turbulence, J. Atmos. Sci., 36, 1950-1954, 1979.

Gage, K. S., and G. D. Nastrom, Theoretical interpretation of atmospheric wave number spectra of wind and temperature observed by commercial aircraft during GASP, J. Atmos. Sci., 43, 729-740, 1986.

Gage, K. S., and G. D. Nastrom, Further discussion of the dynamical processes that contribute to the spectrum of mesoscale atmospheric motions, in Eighth Symposium on Turbulence and Diffusion, pp. 217-220, American Meteorological Society, Boston, Mass., 1988.

Garrett, C. J. R., and W. H. Munk, Space-time scales of internal waves, Geophys. Astrophys. Fluid Dyn., 3, 225-235, 1972.

Gossard, E. E., and W. H. Hooke, Waves in the Atmosphere, Developments in Atmospheric Science, vol. II 456 pp. Elsevier, New York, 1975.

Larsen, M. F., M. C. Kelly, and K. S. Gage, Turbulence spectra in the upper troposphere and lower stratosphere at periods of between 2 hours and 40 days, J. Atmos. Sci., 39, 1035-1041, 1982.

Lilly, D. K., Stratified turbulence and the mesoscale variability of the atmosphere, J. Atmos. Sci., 40, 749-761, 1983.

May, P. T., Statistical errors in the determination of wind velocities by the spaced antenna technique, J. Atmos. Terr. Phys., 50, 21-32, 1988.

May, P. T., K. J. Wilson, and B. F. Ryan, VHF radar studies of cold fronts passing across Southern Australia, Beitraege f. Atmos. Physik, (in press), 1990.

Meek, C. E., I. M. Reid, and A. H. Manson, Observations of mesospheric wind velocities, 1. Gravity wave horizontal scales and phase velocities from spaced wind observations, Radio Sci., 20, 1363-1382, 1985.

Müller, P, R. Lien, and R. Williams, Estimates of potential vorticity at small scales in the ocean, J. Phys. Oceanogr., 18, 401-416, 1988.

Reid, I. M., and R. A. Vincent, Measurements of the horizontal scales and phase velocities of short period mesospheric gravity waves at Adelaide, Australia, J. Atmos. Terr. Phys., 49, 1033-1048, 1987.

Scheffler, A. O., and C. H. Liu, The effects of Doppler shift on the gravity wave spectra observed by MST radar, J. Atmos. Terr. Phys., 48, 1225-1231, 1986.

Sidi, C., J. Lefrere, F. Dalaudier, and J. Barat, An improved atmospheric buoyancy wave spectrum model, J. Geophys. Res., 93, 774-790, 1988.

Smith, S. A., D. C. Fritts, and T. E. VanZandt, Evidence for a saturated spectrum of atmospheric gravity waves, J. Atmos. Sci., 44, 1404-1410, 1987.

VanZandt, T. E., A universal spectrum of buoyancy waves in the atmosphere, Geophys. Res. Lett., 9, 575-578, 1982.

VanZandt, T. E., A model for gravity wave spectra observed by Doppler sounding systems, Radio Sci., 20, 1323-1330, 1985.

VanZandt, T. E., and D. C. Fritts, A theory of enhanced saturation of the gravity wave spectrum due to increases in atmospheric stability, Pure Appl. Geophys., 130, 400-420, 1989.

Vincent, R. A., Gravity wave motions in the mesosphere, J. Atmos. Terr. Phys., 46, 119-128, 1984.

Vincent, R. A., and D. C. Fritts, A morphology of gravity waves in the mesosphere and lower thermosphere over Adelaide, Australia, J. Atmos. Sci., 44, 748-760, 1987.

Vincent, R. A., P. T. May, W. K. Hocking, W. G. Elford, B. H. Candy, and B. H. Briggs, First results with the Adelaide VHF radar: spaced antenna studies of tropospheric winds, J. Atmos. Terr. Phys., 49, 353-366, 1987.

Yeh, K. C., and B. Dong, The non-linear interaction of a gravity wave with the vortical modes, J. Atmos. Terr. Phys., 51, 45-50, 1989.

R. A. Vincent, and S. D. Eckermann, Department of Physics and Mathematical Physics, University of Adelaide, GPO Box 498, Adelaide, Australia 5001.

Paper number 89RS03481.
0048-6604/90/89RS-03481$08.00

Fig. 1. (a) Height-time cross sections of the horizontal winds observed in the troposphere at Adelaide in the period August 19 to 30, 1988. The wind vectors are plotted every 4 hours. (b) Height-time cross sections of the alignment of mesoscale motions in the period August 19 to 30, 1988. Each line represents the degree of polarization and alignment (see text) of motions in the period range 0.5 - 2 hours averaged over a 4-hour interval.

Fig. 2. As for Figure 1 but for the period November 10 to 18, 1988.

Fig. 3. As for Figure 1 but for the period November 18 to 25, 1988.

Fig. 4. Histograms of the difference between the direction of the mean wind ($\bar{U}$) and the alignment of mesoscale motions plotted for mean wind speeds of 0-5, 5-10, and >10 m s^{-1}. 0° implies parallel alignment, and 90° means transverse alignment. For motions in the 0.5 - 2 hour and 2 - 8 hour period bands the data are for all heights of observation averaged over 8-hour intervals. For the 8 - 24 hour period band the data are averaged over 24-hour intervals.

Fig. 5. Plots of the log(R) versus mean wind speed, where R is the ratio of the variances of mesoscale motions parallel to and transverse to the mean wind. Each point represents an 8-hour average for the 0.5-2 hour and 2-8 hour period bands and 24-hour averages for the 8-24 hour band. The solid line is a least squares sixth-order polynomial fit to the data, and the bars show the associated standard errors.

Fig. 6. Vectors representing the horizontal wind oscillations of (a) a single gravity wave of horizontal wave number k_h, (b) two orthogonally aligned gravity waves, (c) a single vortical mode, and (d) two orthogonally aligned vortical modes. The horizontal and vertical coordinates are in units of wavelength.

Fig. 7. Model observed frequency spectra (a) for horizontal gravity wave motions [after Fritts and VanZandt, 1987] and (b) for vortical modes [after Gage and Nastrom, 1988].

Fig. 8. Model gravity wave spectra of horizontal motions plotted in energy-content form, $\omega E_{gw}(\omega)$.

Fig. 9. Scatterplots of $\log(\overline{u_T'^2}/\overline{w'^2})$ as a function of wind speed. Each point in the 0.5–2 hour and 2–8 hour bands represents an 8-hour average, and the points in the 8–24 hour band are 24-hour averages. The solid line is a least squares sixth-order polynomial fit to the data, and the bars show the standard error.

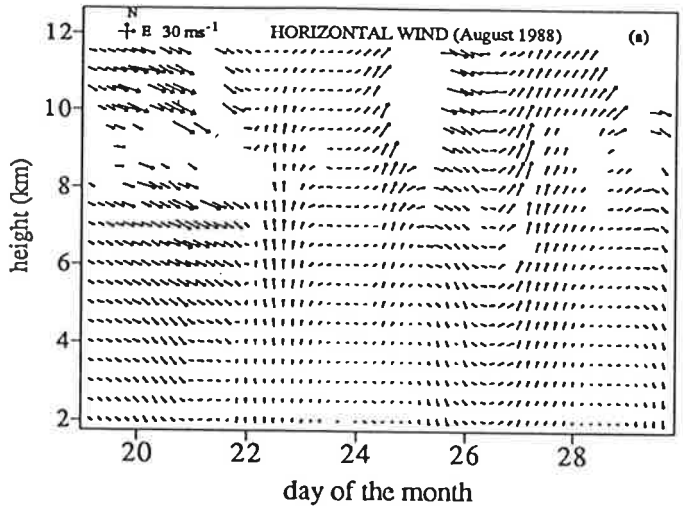
N
E 30 ms-1
HORIZONTAL WIND (August 1988)
(a)
height (km)
12
10
8
6
4
2
20
22
24
26
28
day of the month

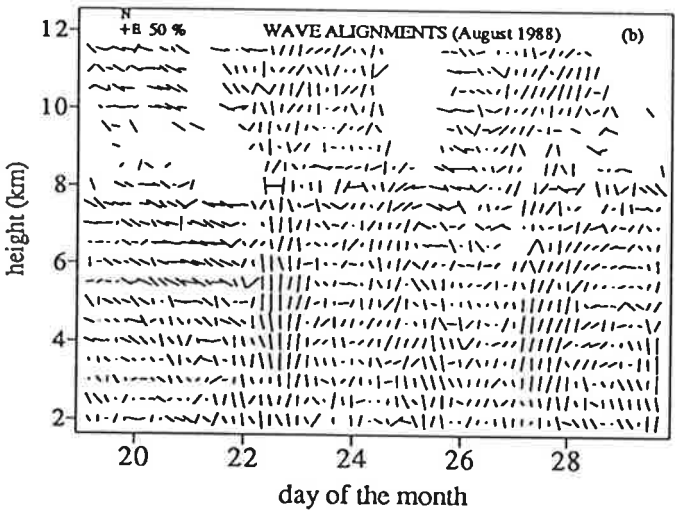
N
E 50 %
WAVE ALIGNMENTS (August 1988)
(b)
height (km)
12
10
8
6
4
2
20
22
24
26
28
day of the month

Fig. 1

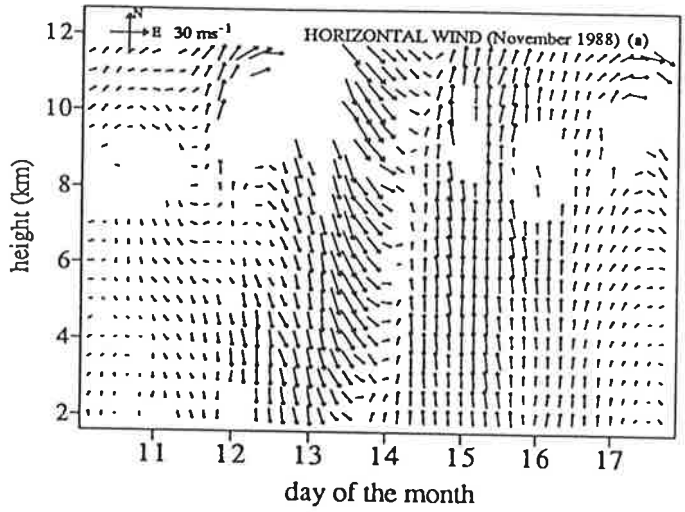
N
E 30 ms⁻¹
HORIZONTAL WIND (November 1988) (a)
height (km)
12
10
8
6
4
2
11
12
13
14
15
16
17
day of the month

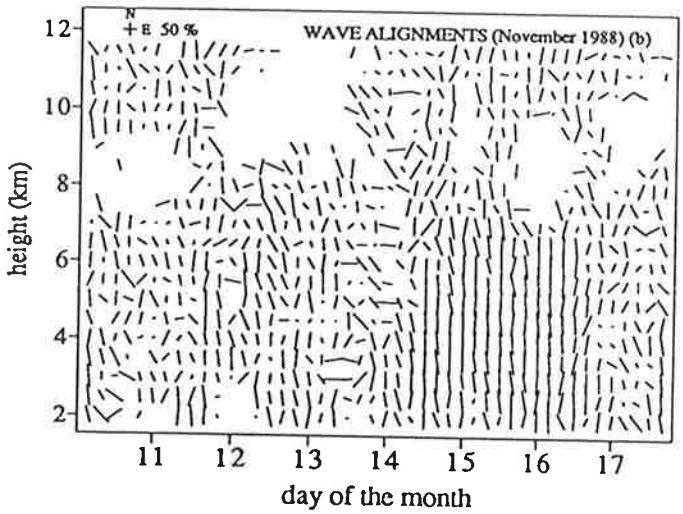
N
E 50 %
WAVE ALIGNMENTS (November 1988) (b)
height (km)
12
10
8
6
4
2
11
12
13
14
15
16
17
day of the month

Fig. 2

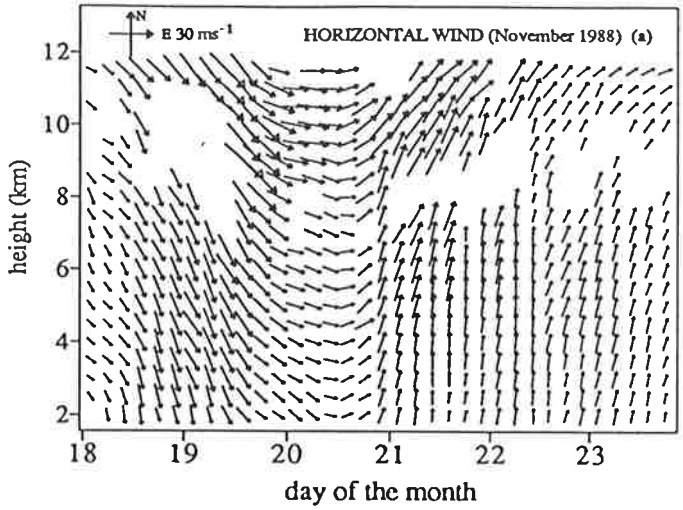
N
E 30 ms⁻¹
HORIZONTAL WIND (November 1988) (a)
height (km)
12
10
8
6
4
2
18
19
20
21
22
23
day of the month

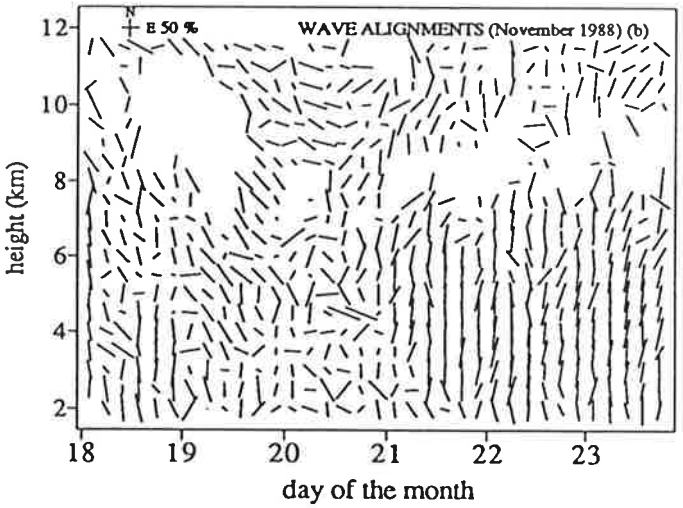
N
E 50 %
WAVE ALIGNMENTS (November 1988) (b)
height (km)
12
10
8
6
4
2
18
19
20
21
22
23
day of the month

Fig. 3

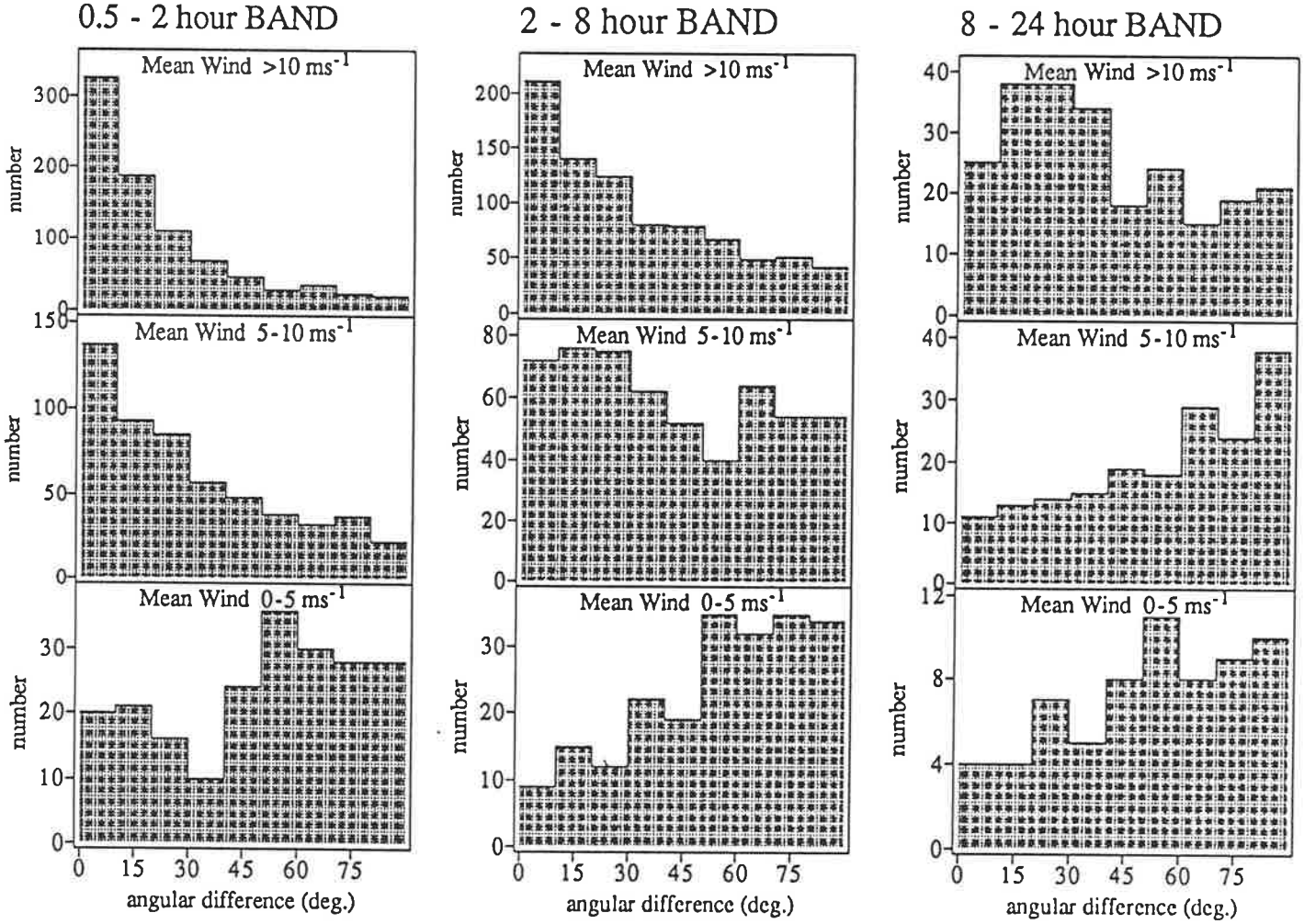
0.5 - 2 hour BAND
2 - 8 hour BAND
8 - 24 hour BAND
Mean Wind >10 ms-1
Mean Wind 5-10 ms-1
Mean Wind 0-5 ms-1
number
angular difference (deg.)
0 15 30 45 60 75

Fig. 4

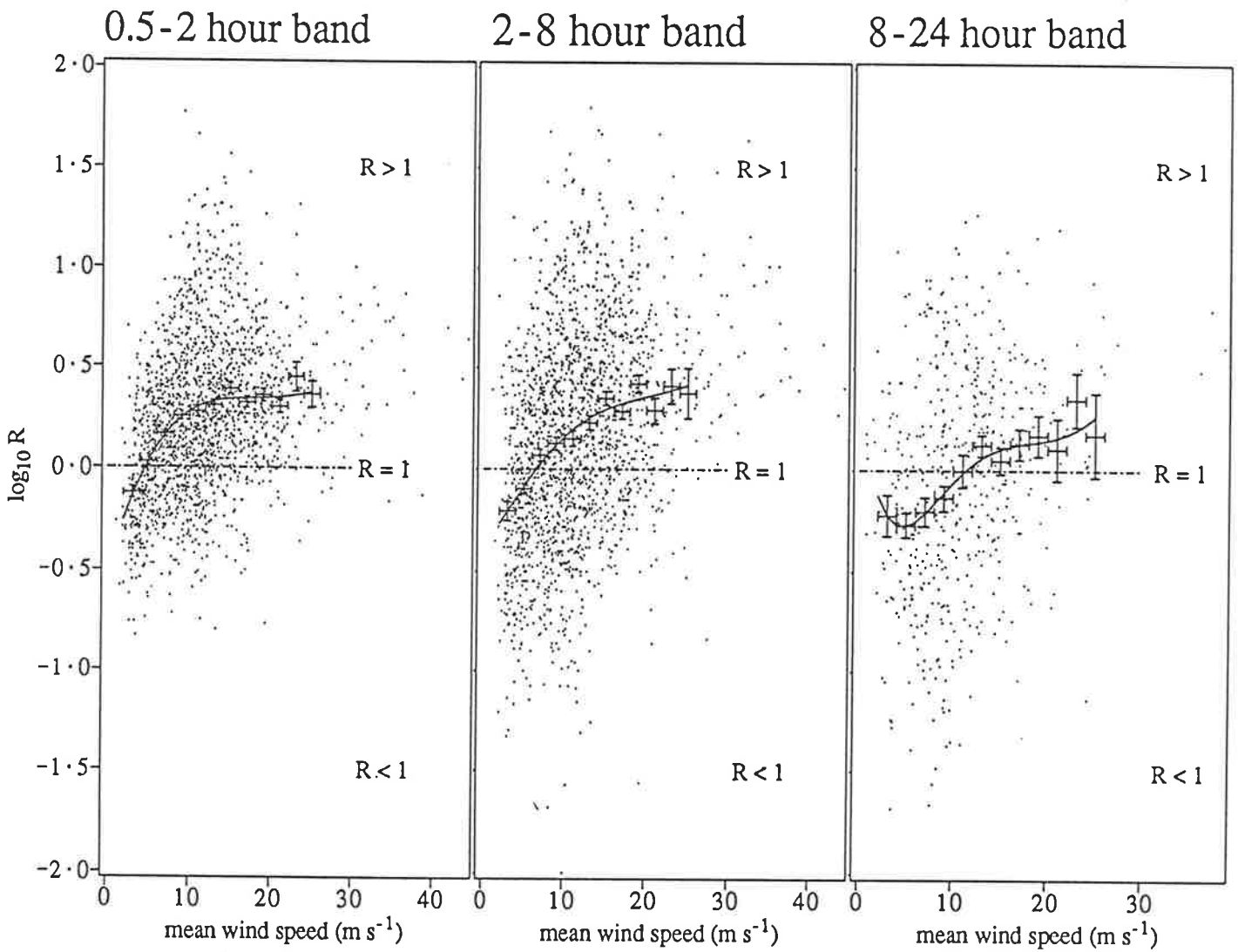
0.5-2 hour band
2-8 hour band
8-24 hour band
2·0
1·5
1·0
0·5
0·0
-0·5
-1·0
-1·5
-2·0
log10 R
R > 1
R = 1
R < 1
0
10
20
30
40
mean wind speed (m s-1)

Fig. 5

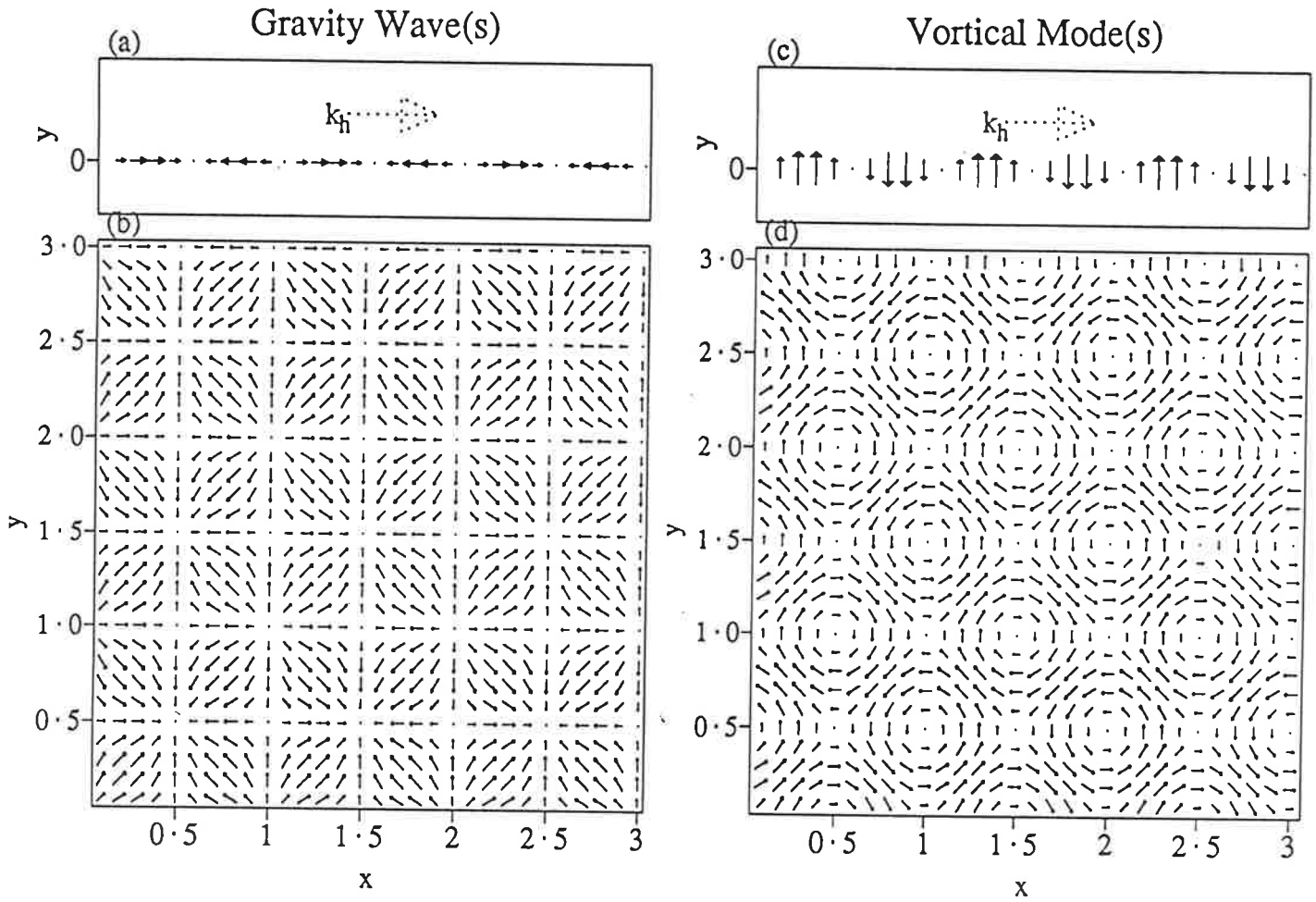

Fig. 6

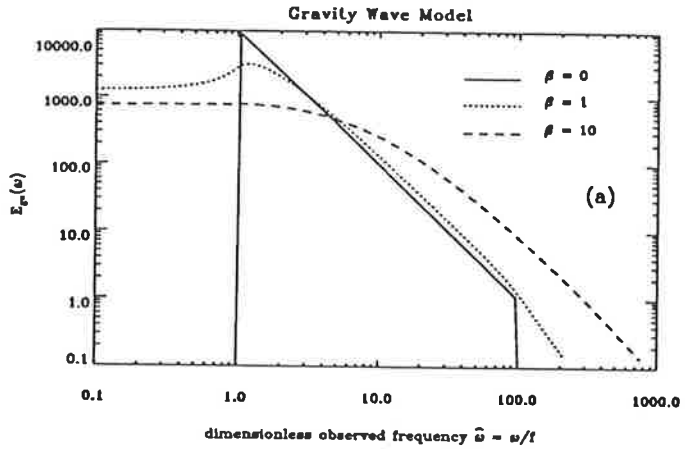
Gravity Wave Model
10000.0
1000.0
100.0
10.0
1.0
0.1
0.1
1.0
10.0
100.0
1000.0
β = 0
β = 1
β = 10
(a)
dimensionless observed frequency ω̂ = ω/f

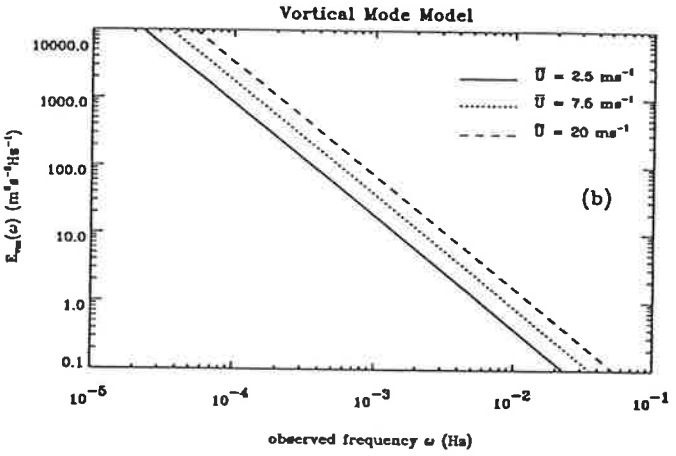
Vortical Mode Model
10000.0
1000.0
100.0
10.0
1.0
0.1
10⁻⁵
10⁻⁴
10⁻³
10⁻²
10⁻¹
Ū = 2.5 ms⁻¹
Ū = 7.5 ms⁻¹
Ū = 20 ms⁻¹
(b)
observed frequency ω (Hz)

Fig. 7

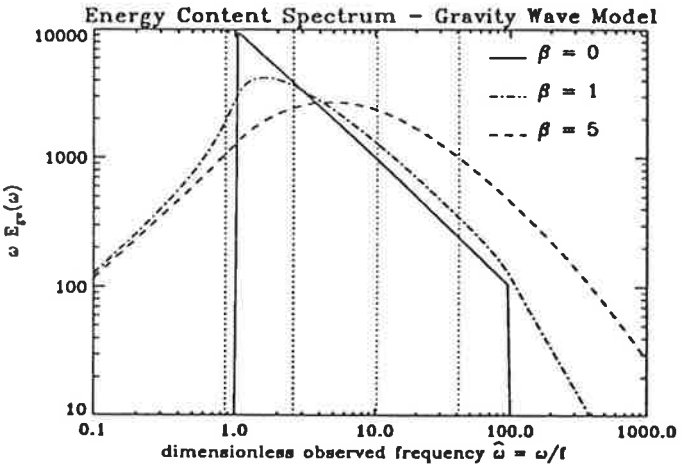
Energy Content Spectrum – Gravity Wave Model
10000
1000
100
10
0.1
1.0
10.0
100.0
1000.0
β = 0
β = 1
β = 5
ω E_pe(ω)
dimensionless observed frequency ω̂ = ω/f

Fig. 8

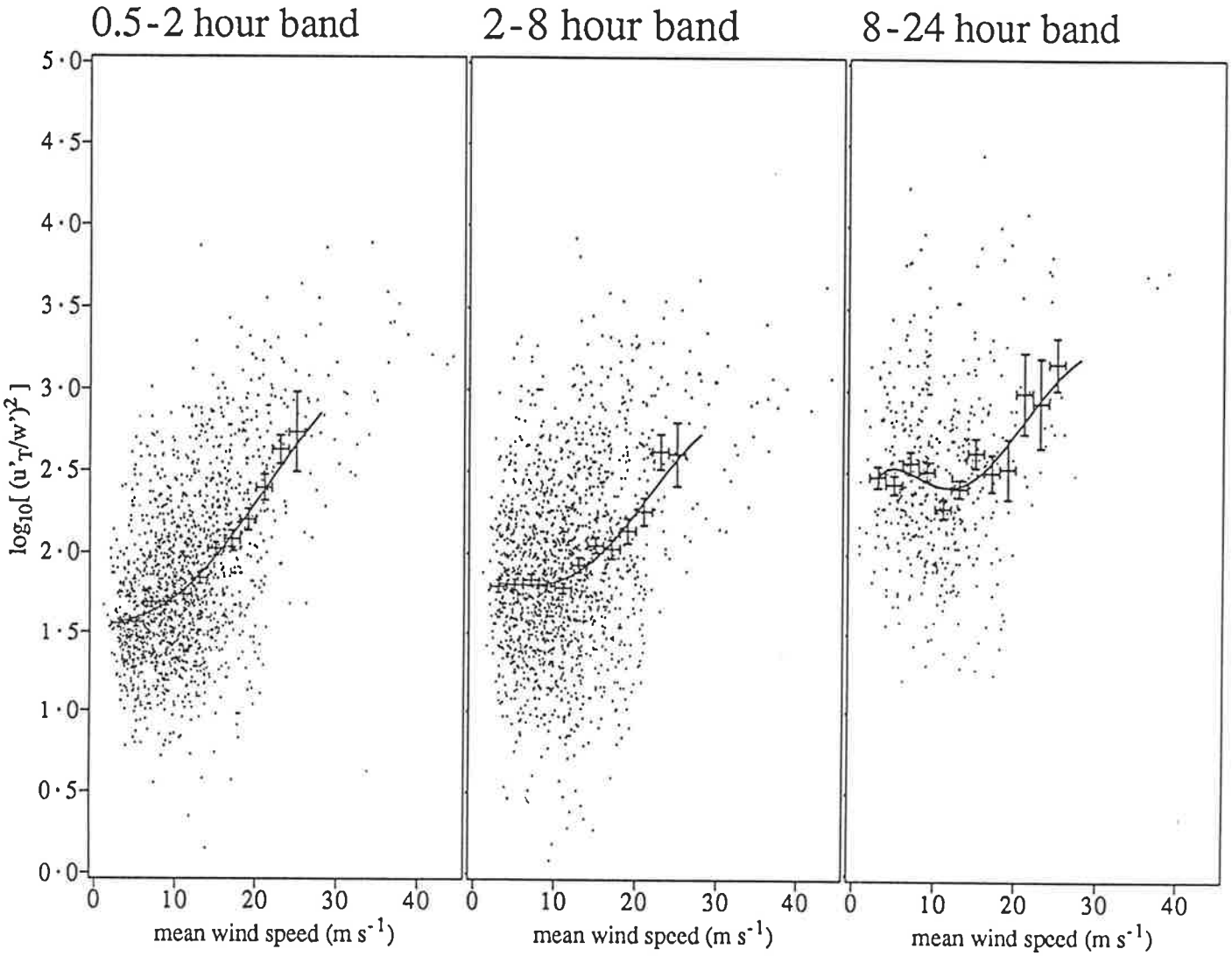
0.5-2 hour band
2-8 hour band
8-24 hour band
log10[(u'τ/w'ζ'2]
5·0
4·5
4·0
3·5
3·0
2·5
2·0
1·5
1·0
0·5
0·0
0
10
20
30
40
mean wind speed (m s-1)

Fig. 9

References

Alfvén, H., *Cosmical electrodynamics*, Clarendon, Oxford, 245pp, 1950.

Andrews, D.G., and B.J. Hoskins, Energy spectra predicted by semigeostrophic theories of frontogenesis, *J. Atmos. Sci.*, *35*, 509–512, 1978.

Andrews, D.G., and M.E. McIntyre, Planetary waves in horizontal and vertical shear: the generalized Eliassen–Palm relation and the mean zonal acceleration, *J. Atmos. Sci.*, *33*, 2031–2048, 1976.

Andrews, D.G., and M.E. McIntyre, On wave–action and its relatives, *J. Fluid Mech.*, *89*, 647–664, 1978.

Andrews, D.G., The influence of atmospheric waves on the general circulation of the middle atmosphere, *Phil. Trans. R. Soc. Lond.*, *323A*, 693–705, 1987.

Andrews, D.G., J.R. Holton, and C.B. Leovy, *Middle atmosphere dynamics*, Academic, San Diego, Calif., 489pp, 1987.

Angell, J.K, and J. Korshover, Quasi–biennial and long term fluctuations in total ozone, *Mon. Wea. Rev.*, *101*, 426–443, 1973.

Atkinson, B.W., *Meso–scale atmospheric circulations*, 288pp, Academic, London, 1981.

Avery, S.K., and B.B. Balsley, Gravity wave momentum flux measurements in the lower and upper atmosphere using the Poker Flat, Alaska MST radar, *J. Geophys. Res.*, (in press), 1990.

Bacmeister, J.T., M.R. Schoeberl, L.R. Lait, P.A. Newman, and B. Gary, ER–2 mountain wave encounter over Antarctica: evidence for blocking, *Geophys. Res. Lett.*, *17*, 81–84, 1990.

Baines, P.G., What's interesting and different about Australian meteorology? – A brief review, *News. Aust. Meteor. Oceanogr. Soc.*, *3*, 22–32, 1990.

Balachandran, N.K., Gravity waves from thunderstorms, *Mon. Wea. Rev.*, *108*, 804–816, 1980.

Balaji, V., and T.L. Clark, Scale selection in locally forced convection fields and the initiation of deep cumulus, *J. Atmos. Sci.*, *45*, 3188–3211, 1988.

Ball, S.M., *Upper atmospheric tides and gravity waves at mid– and low–latitudes*, Ph.D. Thesis, University of Adelaide, Australia, 322pp, 1981.

Balsley, B.B., and D.A. Carter, The spectrum of atmospheric velocity fluctuations at 8 and 86 km, *Geophys. Res. Lett.*, *9*, 465–468, 1982.

Balsley, B.B., and K.S. Gage, The MST radar technique: Potential for middle atmospheric studies, *Pure Appl. Geophys.*, *118*, 452–493, 1980.

Balsley, B.B., and R. Garello, The kinetic energy density in the troposphere, stratosphere and mesosphere: A preliminary study using the Poker Flat radar in Alaska, *Radio Sci.*, *20*, 1355–1362, 1985.

Balsley, B.B., and A.C. Riddle, Monthly mean values of the mesospheric wind field over Poker Flat, Alaska, *J. Atmos. Sci.*, *41*, 2368–2375, 1984.

Balsley, B. B., W. L. Ecklund, and D. C. Fritts, VHF echoes from the high latitude mesosphere and lower thermosphere: Observations and interpretations, *J. Atmos. Sci.*, *40*, 2451–2466, 1983.

Barnett, J.J., and M. Corney, Middle atmosphere reference model derived from satellite data, *Handbook for MAP*, *16*, 47–85, 1985.

Bates, D.R., The green light of the night sky, *Planet. Space Sci.*, *29*, 1061–1067, 1981.

Beckmann, P., Statistical distribution of the amplitude and phase of a multiply scattered field, *J. Res. Natl. Bur. Stand., Sect. D, 66*, 231–240, 1962.

Belmont, A.D., and D.G. Dartt, Semiannual variation in zonal wind from 20 to 65 kilometers at 80°N–10°S, *J. Geophys. Res.*, *78*, 6373–6376, 1973.

Bemra, R.S., P.K. Rastogi, and B.B. Balsley, A study of gravity–wave spectra in the troposphere and stratosphere at 5-min to 5-day periods with the Poker Flat MST radar, in *Handbook for MAP*, *20*, 216–224, SCOSTEP Secr., Univ. of Ill., Urbana, 1986.

Berson, F.A., and M.H. Lamond, Radar observations of wave perturbations in a low–level wind surge, *Aust. Met. Mag.*, *18*, 74–93, 1970.

Bevilacqua, R.M., W.J. Wilson, W.B. Ricketts, P.R. Sch vartz, and R.J. Howard, Possible seasonal variability of mesospheric water vapour, *Geophys. Res. Lett.*, *12*, 397–400, 1985.

Bevilacqua, R.M., W.J. Wilson, and P.R. Schwartz, Measurements of mesospheric water vapour in 1984 and 1985: Results and implications for middle atmospheric transport, *J. Geophys. Res.*, *92*, 6679–6690, 1987.

Bevilacqua, R.M., J.J. Olivero, and C.L. Croskey, Mesospheric water vapour measurements from Penn State: Monthly mean observations (1984–1987), *J. Geophys. Res.*, *94*, 12807–12818, 1989.

Bevilacqua, R.M., D.F. Strobel, M.E. Summers, J.J. Olivero, and M. Allen, The seasonal variation of water vapour and ozone in the upper mesosphere: Implications for vertical transport and ozone photochemistry, *J. Geophys. Res.*, *95*, 883–893, 1990.

Bjarnason, G.G., S. Solomon, and R.R. Garcia, Tidal influences on vertical diffusion and diurnal variability of ozone in the mesosphere, *J. Geophys. Res.*, *92*, 5609–5620, 1987.

Blamont, J.E., and collaborators, Implications of the VEGA balloon results for Venus atmospheric dynamics, *Science*, *231*, 1422–1425, 1986.

Blumen, W., Geostrophic adjustment, *Rev. Geophys.*, *10* 485–528, 1972.

Boer, G.J., Earth–atmosphere exchange of angular momentum simulated in a general circulation model and implications for the length of a day, *J. Geophys. Res.*, *95*, 5511–5531, 1990.

Boer, G.J., N.A. McFarlane, R. Laprise, J.D. Henderson, and J.-P. Blanchet, The Canadian climate centre spectral atmospheric general circulation model, *Atmos. Ocean*, *22*, 397–429, 1984.

Bosart, L.F., and J.P. Cussen Jr., Gravity wave phenomena accompanying east coast cyclogenesis, *Mon. Wea. Rev.*, *101*, 446–454, 1973.

Bosart, L.F., and F. Sanders, Mesoscale structure in the megalopolitan snowstorm of 11–12 February 1983. Part III: A large amplitude gravity wave, *J. Atmos. Sci.*, *43*, 924–939, 1986.

Bosart, L.F., and A. Seimon, A case study of an unusually intense atmospheric gravity wave, *Mon. Wea. Rev.*, *116*, 1857–1886, 1988.

Boville, B.A., The validity of the geostrophic approximation in the winter stratosphere and troposphere, *J. Atmos. Sci.*, *44*, 443–457, 1987.

Bowman, K.P., Global patterns of the quasi–biennial oscillation in total ozone, *J. Atmos. Sci.*, *46*, 3328–3343, 1989.

Brace, L.H., R.C. Elphic, S.A. Curtis, and C.T. Russell, Wave structure in the Venus ionosphere downstream of the terminator, *Geophys. Res. Lett.*, *10*, 1116–1119, 1983.

Bracewell, R.N., *The Fourier transform and its applications*, 2nd ed., McGraw–Hill, New York, p 112–113, 1978.

Brasseur, G., and S. Solomon, *Aeronomy of the middle atmosphere*, 2nd ed., Reidel, Dordrecht, Holland, 452pp., 1984.

Brasseur, G., M.H. Hitchman, S. Walters, M. Dymek, E. Falise, and M. Pirre, An interactive chemical dynamical radiative two–dimensional model of the middle atmosphere, *J. Geophys. Res.*, *95*, 5639–5655, 1990.

Bretherton, F.P., Momentum transport by gravity waves, *Q. J. R. Meteor. Soc.*, *95*, 213–243, 1969*a*.

Bretherton, F.P., On the mean motion induced by internal gravity waves, *J. Fluid Mech.*, *36*, 785–803, 1969*b*.

Bretherton, F.P., and C.J.R. Garrett, Wavetrains in inhomogeneous moving media, *Proc. Roy. Soc.*, *302A*, 529–554, 1968.

Briggs, B.H., The analysis of spaced sensor records by correlation techniques, in *Handbook for MAP*, *13*, 166–186, SCOSTEP Secr., Univ. of Ill., Urbana, 1984.

Briggs, G.A., and C.B. Leovy, Mariner 9 observations of the Mars north polar hood, *Bull. Amer. Meteorol. Soc.*, *55*, 278–296, 1974.

Briscoe, M.G., Internal waves in the ocean, *Rev. Geophys. Space Phys.*, *13*, 591–598, 1975.

Brown, P.R.A., Aircraft measurements of mountain waves and their associated momentum flux over the British Isles, *Q. J. R. Meteor. Soc.*, *109*, 849–865, 1983.

Brunk, I.W., The pressure pulsation of 11 April 1944, *J. Meteor.*, *6*, 181–187, 1949.

Brunskill, J., The Helm wind, *Q. J. R. Meteor. Soc.*, *10*, 267–275, 1884.

Cadet, D., and H. Teitelbaum, Observational evidence of internal inertia–gravity waves in the tropical stratosphere, *J. Atmos. Sci.*, *36*, 892–907, 1979.

Chanin, M.-L., and A. Hauchercorne, Lidar observation of gravity and tidal waves in the stratosphere and mesosphere, *J. Geophys. Res.*, *86*, 9715–9721, 1981.

Chao, W.C., and M.R. Schoeberl, On the linear approximation of gravity wave saturation in the mesosphere, *J. Atmos. Sci.*, *41*, 1893–1898, 1984.

Charney, J.G., Geostrophic turbulence, *J. Atmos. Sci.*, *28*, 1087–1095, 1971.

Chimonas, G., F. Einaudi, and D.P. Lalas, A wave theory for the onset and initial growth of condensation in the atmosphere, *J. Atmos. Sci.*, *37*, 827–845, 1980.

Christie, D.R., Long nonlinear waves in the lower atmosphere, *J. Atmos. Sci.*, *46*, 1462–1491, 1989.

Christie, D.R., and K.J. Muirhead, Solitary waves: A low–level wind shear hazard to aviation, *Int. J. Aviat. Safety*, *1*, 169–190, 1983.

Clancy, R.T., and D.W. Rusch, Climatology and trends of mesospheric (58–90 km) temperature trends based upon 1982–1986 SME limb scattering profiles, *J Geophys. Res.*, *94*, 3377–3393, 1989.

Clarke, R.H., Pressure oscillations and fallout downdraughts, *Q. J. R. Meteor. Soc.*, *88*, 459–469, 1962.

Clarke, R.H., On the mortality of morning glories, *Aust. Met. Mag.*, *37*, 167–172, 1989.

Cogger, L.L., R.D. Elphinstone, and J.S. Murphree, Temporal and latitudinal 5577Å airglow variations, *Can. J. Phys.*, *59*, 1296–1307, 1981.

Colegrove, F.D., W.B. Hanson, and F.S. Johnson, Eddy diffusion and oxygen transport in the lower thermosphere, *J. Geophys. Res.*, *70*, 4931–4941, 1965.

Cornish, C.R., Observations of vertical velocities in the tropical upper troposphere and lower stratosphere using the Arecibo 430-MHz radar, *J. Geophys. Res.*, *93*, 9419–9431, 1988.

Cot, C., and J. Barat, Wave–turbulence interaction in the stratosphere, *J. Geophys. Res.*, *91*, 2749–2756, 1986.

Coy, L., D.C. Fritts, and J. Weinstock, The Stokes drift due to vertically propagating internal gravity waves in a compressible atmosphere, *J. Atmos. Sci.*, *43*, 2636–2643, 1986.

Craig, R.L., and W.G. Elford, Observations of the quasi 2-day wave near $90km$ altitude at Adelaide (35S), *J. Atmos. Terr. Phys.*, *43*, 1051–1056, 1981.

Crane, R.K., Space–time structure of rain rate fields, *J. Geophys. Res.*, *95*, 2011–2020, 1990.

Crook, N.A., Trapping of low–level internal gravity waves, *J. Atmos. Sci.*, *45*, 1533–1541, 1988.

Currie, R.G., and S. Hameed, Evidence of quasi–biennial oscillations in a general circulation model, *Geophys. Res. Lett.*, *15*, 649–652, 1988.

Curry, M.J., and R.C. Murty, Thunderstorm–generated gravity waves, *J. Atmos. Sci.*, *31*, 1402–1408, 1974.

Czechowsky, P., I.M. Reid, R. Rüster, and G. Schmidt, VHF radar echoes observed in the summer and winter polar mesosphere over Andøya, Norway, *J. Geophys. Res.*, *94*, 5199–5217, 1989.

Defant, A., *Physical oceanography*, Vol. 2, Permagon, New York, 598pp, 1961.

Delisi, D.P., and T.J. Dunkerton, Equatorial semiannual oscillation in zonally averaged temperature observed by the Nimbus 7 SAMS and LIMS, *J. Geophys. Res.*, *93*, 3899–3904, 1988.

Desaubies, Y.J.F., Analytical representation of internal wave spectra, *J. Phys. Oceanogr.*, *6*, 976–981, 1976.

Desaubies, Y., and W.K. Smith, Statistics of Richardson number and instability in oceanic internal waves, *J. Phys. Oceanogr.*, *12*, 1245–1259, 1982.

Devarajan, M., C.A. Reddy, and C. Raghava Reddi, Rocket observations of Kelvin waves in the upper stratosphere over India, *J. Atmos. Sci.*, *42*, 1873–1879, 1985.

Dewan, E.M., and R.E. Good, Saturation and the "universal" spectrum for vertical profiles of horizontal scalar winds in the atmosphere, *J. Geophys. Res.*, *91*, 2742–2748, 1986.

Dewan, E. M., N. Grossbard, A. F. Quesada, and R. E. Good, Spectral analysis of 10-m resolution scalar velocity profiles in the stratosphere, *Geophys. Res. Lett.*, *11*, 80–83, 1984. (correction, *Geophys. Res. Lett.*, *11*, 624, 1984.)

Dong, B., and K.C. Yeh, Resonant and nonresonant wave-wave interactions in an isothermal atmosphere, *J. Geophys. Res.*, *93*, 3729–3744, 1988.

Duffy, D.G., Geostrophic adjustment in a baroclinic atmosphere, *J. Atmos. Sci.*, *47*, 457–473, 1990.

Dunkerton, T.J., On the mean meridional mass motions in the stratosphere and mesosphere, *J. Atmos. Sci.*, *35*. 2325–2333, 1978.

Dunkerton, T.J., On the role of Kelvin waves in the westerly phase of the semiannual zonal wind oscillation, *J. Atmos. Sci.*, *36*, 32–41, 1979.

Dunkerton, T.J., Wave transience in a compressible atmosphere. Part II: Transient equatorial waves in the quasi–biennial oscillation, *J. Atmos. Sci.*, *38*, 298–307, 1981.

Dunkerton, T.J., Shear zone asymmetry in the observed and simulated quasi–biennial oscillation, *J. Atmos. Sci.*, *39*, 461–469, 1982*a*.

Dunkerton, T.J., Theory of the mesopause semiannual oscillation, *J. Atmos. Sci.*, *39*, 2681–2690, 1982*b*.

Dunkerton, T.J., Inertia–gravity waves in the stratosphere, *J. Atmos. Sci.*, *41*, 3396–3404, 1984.

Dunkerton, T.J., Theory of internal gravity wave saturation, *Pure Appl. Geophys.*, *130*, 373–397, 1989.

Dunkerton, T.J., and N. Butchart, Propagation and selective transmission of internal gravity waves in a sudden warming, *J. Atmos. Sci.*, *41*, 1443–1460, 1984.

Dunkerton, T.J., and D.P. Delisi, Climatology of the equatorial lower stratosphere, *J. Atmos. Sci.*, *42*, 376–396, 1985.

Dunkerton, T.J., D.P. Delisi, and M.P. Baldwin, Distribution of major stratospheric warmings in relation to the quasi–biennial oscillation, *Geophys. Res. Lett.*, *15*, 136–139, 1988.

Ebel, A., A.H. Manson, and C.E. Meek, Short period fluctuations of the horizontal wind measured in the upper middle atmosphere and possible relationships to internal gravity waves, *J. Atmos. Terr. Phys.*, *49*, 385–401, 1987.

Eckermann, S.D., *Parameterization of VHF Yagi antennae by radio astronomy*, Honours Project Report, University of Adelaide, Australia, 1986.

Eckermann, S.D., Effects of nonstationarity on spectral analysis of mesoscale motions in the atmosphere, *J. Geophys. Res.*, (in press), 1990.

Eckermann, S.D., and W.K. Hocking, Effect of superposition on measurements of atmospheric gravity waves: A cautionary note and some reinterpretations, *J. Geophys. Res.*, *94*, 6333–6339, 1989.

Eckermann, S.D., and R.A. Vincent, Falling sphere observations of anisotropic gravity wave motions in the upper stratosphere over Australia, *Pure Appl. Geophys.*, *130*, 509–532, 1989.

Ecklund, W.L., K.S. Gage, G.D. Nastrom, and B.B. Balsley, A preliminary climatology of the spectrum of vertical velocity observed by clear-air Doppler radar, *J. Clim. Appl. Meteorol.*, *25*, 885–892, 1986.

Einaudi, F., and D.P. Lalas, Wave–induced instabilities in an atmosphere near saturation, *J. Atmos. Sci.*, *32*, 536–547, 1975.

Einaudi, F., W.L. Clark, D. Fua, J.L. Green, and T.E VanZandt, Gravity waves and convection in Colorado during July 1983, *J. Atmos. Sci.*, *44*, 1534-1553, 1987.

Einaudi, G., and Y. Mok, Alfvén wave dissipation in the solar atmosphere, *Astrophys. J.*, *319*, 520–527, 1987.

Eliassen, A., and E. Palm, On the transfer of energy in stationary mountain waves, *Geofys. Publ., 22(3)*, 1–23, 1961.

Elson, L.S., Ageostrophic motions in the stratosphere from satellite observations, *J. Atmos. Sci., 43*, 408–418, 1986.

Erickson, C.O., and L.F. Whitney, Gravity waves following severe thunderstorms, *Mon. Wea. Rev., 101*, 708–711, 1973.

Fels, S.B., A parameterization of scale–dependent radiative damping rates in the middle atmosphere, *J. Atmos. Sci., 39*, 1141–1152, 1982.

Fels, S.B., The radiative damping of short vertical scale waves in the mesosphere, *J. Atmos. Sci., 41*, 1755–1764, 1984.

Ferguson, H.L., Mathematical and synoptic aspects of a small–scale wave disturbance over the lower Great Lakes area, *J. Appl. Meteor., 6*, 523–529, 1967.

Flatté, S.M., R. Dashen, W.H. Munk, K.M. Watson, and F. Zachariasen, *Sound transmsiion through a fluctuating occan*, Cambridge Univ. Press, 256pp, 1979.

Fleer, H.E., *Monsoon dynamics*, editors J. Lighthill and R.P. Pearce, Cambridge Univ. Press, 5–18, 1981.

Fofonoff, N.P., Spectral characteristics of internal waves in the ocean, *Deep Sea Res., 16* (suppl.), 59–71, 1969.

Francis, S.H., Propagation of internal acoustic–gravity waves around a spherical earth, *J. Geophys. Res., 77*, 4221–4226, 1972.

Franke, S.J., C.H. Liu, I.J. Fu, R. Rüster, P. Czechowsky, and G. Schmidt, Multibeam radar observations of winds in the mesosphere, *J. Geophys. Res., 93*, 15965–15971, 1988.

Frezal M.E., M. Glass, J.L. Fellous and M. Massebeuf, Simultaneous meteor observations at Monpazier (France, 44°N) and Punta Borinquen (Puerto Rico, 18°N), III, The latitudinal variations of the energy of gravity waves (2–8 h) in the high mesosphere, *J. Atmos. Terr. Phys., 43*, 543–547, 1981.

Fritts, D.C., Gravity wave saturation in the middle atmosphere: A review of theory and observations, *Rev. Geophys., 22*, 275–308, 1984.

Fritts, D.C., A review of gravity wave saturation processes, effects, and variability in the middle atmosphere, *Pure Appl. Geophys., 130*, 343–372, 1989.

Fritts, D.C., and H.-G. Chou, An investigation of the vertical wavenumber and frequency spectra of gravity wave motions in the lower stratosphere, *J. Atmos. Sci. 44*, 3610–3624, 1987.

Fritts, D.C., and T.J. Dunkerton, A quasi–linear study of gravity wave saturation and self–acceleration, *J. Atmos. Sci., 41*, 3272–3289, 1984.

Fritts, D.C., and P.K. Rastogi, Convective and dynamical instabilities due to gravity wave motions in the lower and middle atmosphere, *Radio Sci.*, *20*, 1247-1277, 1985.

Fritts, D.C., and T.E. VanZandt, Effects of Doppler shifting on the frequency spectra of atmospheric gravity waves, *J. Geophys. Res.*, *92*, 9723–9732, 1987.

Fritts, D.C., and R.A. Vincent, Mesospheric momentum flux studies at Adelaide, Australia: Observations and a gravity wave/tidal interaction model, *J. Atmos. Sci.*, *44*, 605–619, 1987.

Fritts, D.C., and L. Yuan, Measurments of momentum fluxes near the summer mesopause at Poker Flat, Alaska, *J. Atmos. Sci.*, *46*, 2569–2579, 1989.

Fritts, D.C., B.B. Balsley, and W.L. Ecklund, VHF echoes from the arctic mesosphere and lower thermosphere, part II: Interpretations, in *Dynamics of the Middle Atmosphere*, edited by J.R. Holton and T. Matsuno, Terra, Tokyo, 97–115, 1984.

Fritts, D.C., T. Tsuda, T. Sato, S. Fukao, and S. Kato, Observational evidence of a saturated gravity wave spectrum in the troposphere and lower stratosphere, *J. Atmos. Sci.*, *45*, 1741–1759, 1988*a*.

Fritts, D.C., S.A. Smith, B.B. Balsley, and C.R. Philbrick, Evidence of gravity wave saturation and local turbulence production in the summer mesosphere and lower thermosphere during the STATE experiment, *J. Geophys. Res.*, *93*, 7015–7025, 1988*b*.

Fritts, D.C., R.C. Blanchard, and L. Coy, Gravity wave structure between 60 and 90 km inferred from Space Shuttle reentry data, *J. Atmos. Sci.*, *46*, 423–434, 1989.

Fritts, D.C., T. Tsuda, T.E. VanZandt, S.A. Smith, T. Sato, S. Fukao, and S. Kato, Studies of velocity fluctuations in the lower atmosphere using the MU radar. Part II: Momentum fluxes and energy densities, *J. Atmos. Sci.*, *47*, 51–66, 1990.

Fukao, S., T. Sato, S. Kato, R.M. Harper, and W.E. Gordon, Mesospheric winds and waves over Jicamarca on May 23–24, 1974, *J. Geophys. Res.*, *84*, 4379–4386, 1979.

Fukao, S., Y. Maekawa, T. Sato, and S. Kato, Fine structure of mesospheric wind fluctuations observed by the Arecibo UHF Doppler radar, *J. Geophys. Res.*, *90*, 7547–7556, 1985.

Fukao, S., T. Sato, P.T. May, T. Tsuda, S. Kato, M. Inaba, and I. Kimura, A systematic error in MST/ST radar wind measurement induced by a finite range volume effect, 1, Observational results, *Radio Sci.*, *23*, 59–73, 1988*a*.

Fukao, S., M. Inaba, I. Kimura, P.T. May, T. Sato, T. Tsuda, and S. Kato, A systematic error in MST/ST radar wind measurement induced by a finite range vo ume effect, 2, Numerical considerations, *Radio Sci.*, *23*, 74–82, 1988*b*.

Fukao, S., T. Sato, T. Tsuda, S. Kato, M. Inaba, and I. Kimura, VHF Doppler radar determination of the momentum flux in the upper troposphere and lower stratosphere: Comparison between the three- and four–beam methods, *J. Atmos. Oceanic Technol.*, *5*, 57–69, 1988*c*.

Fukao, S., M.D. Yamanaka, H. Matsumoto, T. Sato, T. Tsuda, and S. Kato, Wind fluctuations near a cold vortex-tropopause funnel system observed by the MU radar, *Pure Appl. Geophys.*, *130*, 463–479, 1989*a*.

Fukao, S., T. Tsuda, T. Sato, and S. Kato, Equatorial radar system, in *Handbook for MAP*, *27*, 427–438, SCOSTEP Secr., Univ. of Ill., Urbana, 1989*b*.

Fukao, S., T. Tsuda, T. Sato, M. Yamamoto, and S. Kato, Wind and waves in the middle atmosphere observed with the MU radar, in *Handbook for MAP*, *27*, 427–438, SCOSTEP Secr., Univ. of Ill., Urbana, 1989*c*.

Fukuyama, K., Airglow variations and dynamics in the lower thermosphere and upper mesosphere, 1, Diurnal variation and its seasonal dependency, *J. Atmos. Terr. Phys.*, *38*, 1279–1287, 1976.

Fukuyama, K., Airglow variations and dynamics in the lower thermosphere and upper mesosphere, 2, Seasonal and long term variations, *J. Atmos. Terr. Phys.*, *39*, 1–14, 1977.

Fulton, R., D.S. Zrnić, and R.J. Doviak, Initiation of a solitary wave family in the demise of a nocturnal thunderstorm density current, *J. Atmos. Sci.*, *47*, 319- 337, 1990.

Gage, K.S., Evidence for $k^{-5/3}$ law inertial range in mesoscale two-dimensional turbulence, *J. Atmos. Sci.*, *36*, 1950–1954, 1979.

Gage, K.S., and G.D. Nastrom, On the spectrum of atmospheric velocity fluctuations seen by MST/ST radars and their interpretation, *Radio Sci.*, *20*, 1339–1347, 1985.

Gage, K.S., and G.D. Nastrom, Theoretical interpretation of atmospheric wavenumber spectra of wind and temperature observed by commercial aircraft during GASP, *J. Atmos. Sci.*, *43*, 729–740, 1986.

Gage, K.S., and G.D. Nastrom, Further discussion of the dynamical processes that contribute to the spectrum of mesoscale atmospheric motions, paper presented at the Eighth Symposium on Turbulence and Diffusion, Am. Meteorol. Soc., San Diego, Calif., (preprint vol. p217–220), 1988.

Gall, R.L., R.T. Williams, and T.L. Clark, On the minimum scale of surface fronts, *J. Atmos. Sci.*, *44*, 2562–2574, 1987.

Gall, R.L., R.T. Williams, and T.L. Clark, Gravity waves generated during frontogenesis, *J. Atmos. Sci.*, *45*, 2204–2219, 1988.

Garcia, R.R., and S. Solomon, The effect of breaking gravity waves on the dynamics and chemical composition of the mesosphere and lower thermosphere, *J. Geophys. Res.*, *90*, 3850–3868, 1985.

Garcia, R.R., and S. Solomon, A possible relationship between interannual variability in Antarctic ozone and the quasi–biennial oscillation, *Geophys. Res. Lett.*, *14*, 848–851, 1987.

Gardner, C.S., and D.G. Voelz, Lidar measurements of gravity wave saturation effects in the sodium layer, *Geophys. Res. Lett.*, *12*, 765–768, 1985.

Gardner, C.S., and D.G. Voelz, Lidar studies of the nighttime sodium layer over Urbana, Illinois, 2, Gravity waves, *J. Geophys. Res.*, *92*, 4673–4694, 1987.

Gardner, C.S., M.S. Miller, and C.H. Liu, Rayleigh lidar observations of gravity wave activity in the upper stratosphere at Urbana, Illinois, *J. Atmos. Sci.*, *46*, 1838–1854, 1989.

Garner, S.T., Fully Lagrangian numerical solutions of unbalanced frontogenesis and frontal collapse, *J. Atmos. Sci.*, *46*, 717–739, 1989*a*.

Garner, S.T., Comments on "On a theory of the evolution of surface cold fronts", *J. Atmos. Sci.*, *46*, 1872–1873, 1989*b*.

Garratt, J.R., and W.L. Physick, Low–level wind response to mesoscale pressure systems, *Bound. Layer Meteor.*, *27*, 69–87, 1983.

Garratt, J.R., and W.L. Physick, Numerical study of atmospheric gravity currents. I: Simulations and observations of cold fronts, *Contrib. Atmos. Phys.*, *59*, 282–300, 1986.

Garratt, J.R., W.L. Physick, R.K. Smith, and A.J. Troup The Australian summertime cool change. Part II: Mesoscale aspects, *Mon. Wea. Rev.*, *113*, 202–223, 1985.

Garrett, C.J.R., and W.H. Munk, Space-time scales of internal waves, *Geophys. Astrophys. Fluid Dyn.*, *3*, 225–235, 1972.

Garrett, C.J.R., and W.H. Munk, Space-time scales of internal waves: a progress report, *J. Geophys. Res.*, *80*, 291–297, 1975.

Garrett, C.J.R., and W.H. Munk, Internal waves in the ocean, *Ann. Rev. Fluid Mech.*, *11*, 339–369, 1979.

Gary, B.L., Observational results using the microwave temperature profiler during the Airborne Antarctic Ozone Experiment, *J. Geophys. Res.*, *94*, 11223–11231, 1989.

Geller, M.A., M.-F. Wu, and M.E. Gelman, Troposphere–stratosphere (surface–55 km) monthly winter general circulation statistics for the northern hemisphere–four year averages, *J. Atmos. Sci.*, *40*, 1334–1352, 1983.

Gierasch P.J., Waves in the atmosphere of Venus, *Nature*, *328*, 510–512, 1987.

Gifford, F.A., The shape of large tropospheric clouds, or "very like a whale", *Bull. Am. Met. Soc.*, *70*, 468–475, 1989.

Gill, A.E., *Atmosphere–ocean dynamics*, Academic Press, New York, 488pp., 1982.

Gonella, J., A rotary-component method for analysing meteorological and oceanographic vector time series, *Deep Sea Res.*, *19*, 833–846, 1972.

Gossard, E.E., Vertical flux of energy into the lower ionosphere from internal gravity waves generated in the troposphere, *J. Geophys. Res.*, *67*, 745–757, 1962.

Gossard, E.E., and W.H. Hooke, *Waves in the atmosphere*, Elsevier, New York, 456pp., 1975.

Grard, R., and collaborators, Observations of waves and plasma in the environment of comet Halley, *Nature*, *321*, 290–291, 1986.

Gray, L., and J. Pyle, A two–dimensional model of the quasi–biennial oscillation of ozone, *J. Atmos. Sci.*, *46*, 203–220, 1989.

Grimshaw, R., Nonlinear internal gravity waves and their interaction with the mean wind, *J. Atmos. Sci.*, *32*, 1779–1793, 1975.

Groves, G.V., A global reference atmosphere from 18 to 80 km, Air Force Geophysics Laboratory, Hanscom A.F.B., Massachusetts, U.S.A., Report No. AFGL–TR–85–0129, 1985.

Groves, G.V., Modelling of atmospheric structure 70–130km, Air Force Geophysics Laboratory, Hanscom A.F.B., Massachusetts, U.S.A., Report No. AFGL–TR–87–0226, 1987.

Hamilton, K., The vertical structure of the quasi–biennial oscillation: Observations and theory, *Atmosphere–Ocean*, *19*, 236–250, 1981.

Hamilton, K., Mean wind evolution through the quasi–biennial cycle in the tropical lower stratosphere, *J. Atmos. Sci.*, *41*, 2113–2125, 1984.

Hamilton, K., Interhemispheric asymmetry and annual synchronization of the ozone quasi–biennial oscillation, *J. Atmos. Sci.*, *46*, 1019–1025, 1989.

Hamilton, K., and J.D. Mahlman, General circulation model simulation of the semiannual oscillation of the tropical middle atmosphere, *J. Atmos. Sci.*, *45*, 3212–3235, 1988.

Harper, R. M., and R. F. Woodman, Preliminary multiheight radar observations of waves and winds in the mesosphere over Jicamarca, *J. Atmos. Terr. Phys* , *39*, 959–963, 1977.

Hasebe, F., Interannual variations of global total ozone revealed from Nimbus 4 BUV and ground–based observations, *J. Geophys. Res.*, *88*, 6819–6834, 1983.

Hass, H., and W. Meyer, Gravity wave fields above Andøya, *J. Atmos. Terr. Phys.*, *49*, 705–721, 1987.

Hasselmann, K., Feynman diagrams and interaction rules for wave–wave scattering processes, *Rev. Geophys. Space Phys.*, *4*, 1-32, 1966.

Hauchecorne, A., M.L. Chanin, and R. Wilson, Mesospheric temperature inversion and gravity wave breaking, *Geophys. Res. Lett.*, *14*, 933–936, 1987.

Hayashi, Y., Space-time spectral analysis of rotary vector series, *J. Atmos. Sci.*, *36*, 757–766, 1979.

Hernandez, G.J., and S.M. Silverman, A re–examination of Lord Rayleigh's data on the airglow 5577$\mathring{A}$ (OI) emission, *Planet. Space Sci.*, *12*, 97–112, 1964.

Hines, C.O., Internal gravity waves at ionospheric heights, *Can. J. Phys.*, *38*, 1441–1481, 1960 (see also correction, *Can. J. Phys.*, *42*, 1425–1427, 1964).

Hines, C.O., Minimum vertical scale sizes in the wind structure above 100 kilometers, *J. Geophys. Res.*, *69*, 2847–2848, 1964.

Hines, C. O., On the analysis and interpretation of winds observed at heights of 85 to 135 kilometers: A rebuttal, *J. Geophys. Res.*, *71*, 1461–1475, 1966.

Hines, C.O., The earlier days of gravity waves revisited, *Pure Appl. Geophys.*, *130*, 151–170, 1989.

Hinson, D.P., and G.L. Tyler, Internal gravity waves in Titan's atmosphere observed by Voyager radio occultation, *Icarus*, *54*, 337–352, 1983.

Hirota, I., Equatorial waves in the upper stratosphere and mesosphere in relation to the semiannual oscillation of the zonal wind, *J. Atmos. Sci.*, *35*, 714–722, 1978.

Hirota, I., Kelvin waves in the equatorial middle atmosphere observed by the Nimbus 5 SCR, *J. Atmos. Sci.*, *36*, 217–222, 1979.

Hirota, I., Observational evidence of the semiannual oscillation in the tropical middle atmosphere – A review, *Pure Appl. Geophys.*, *118*, 217–238, 1980.

Hirota, I., Climatology of gravity waves in the middle atmosphere, *J. Atmos. Terr. Phys.*, *46*, 767–773, 1984.

Hirota, I., and T. Niki, A statistical study of inertia–gravity waves in the middle atmosphere, *J. Meteor. Soc. Japan*, *63*, 1055–1066, 1985.

Hirota, I., and T. Niki, Inertial gravity waves in the troposphere and stratosphere observed by the MU radar, *J. Meteor. Soc. Japan*, *64*, 995–999, 1986.

Hirota, I., T. Hirooka, and M. Shiotani, Upper stratospheric circulation in the two hemispheres observed by satellites, *Q. J. R. Meteor. Soc.*, *109*, 443–454, 1983.

Hitchman, M.H., and C.B Leovy, Estimation of the Kelvin wave contribution to the semiannual oscillation, *J. Atmos. Sci.*, *45*, 1462–1475, 1988.

Hitchman, M.H., J.C. Gille, C.D. Rodgers, and G. Brasseur, The separated polar winter stratopause: A gravity–wave driven climatological feature, *J. Atmos. Sci.*, *46*, 410–422, 1989.

Hocking, W.K., *Investigations of the movement and structure of D-region ionospheric irregularities*, Ph.D. Thesis, University of Adelaide, Adelaide, Australia, 1981.

Hocking, W.K., Reduction of the effects of non-stationarity in studies of amplitude statistics of radio wave backscatter, *J. Atmos. Terr. Phys.*, *49*, 1119–1131, 1987*a*.

Hocking, W.K., Turbulence in the region 80–120 km, *Adv. Space Res.*, *7*, (10)171–(10)181, 1987*b*.

Hocking, W.K., Two years of continuous measurements of turbulence parameters in the upper mesosphere and lower thermosphere made with a 2–MHz radar, *J. Geophys. Res.*, *93*, 2475–2491, 1988.

Hocking, W.K., Seasonal variation of turbulence intensities in the upper mesosphere and lower thermosphere measured by radar techniques, in *Handbook for MAP*, *27*, 427–438, SCOSTEP Secr., Univ. of Ill., Urbana, 1989.

Holloway, G., and P. Müller, Topographic stress in the oceans, *Eos*, *71*, 343–344, 1990.

Holton, J.R., *The dynamic meteorology of the stratosphere and mesosphere*, Meteorol. Monogr. No. 37, Am. Meteor. Soc., Boston, Massachusetts, 216pp, 1975.

Holton, J.R., The role of gravity wave–induced drag and diffusion in the momentum budget of the mesosphere, *J. Atmos. Sci.*, *39*, 791–799, 1982.

Holton, J.R., The influence of gravity wave breaking on the general circulation of the middle atmosphere, *J. Atmos. Sci.*, *40*, 2497–2507, 1983.

Holton, J.R., The production of temporal variability in trace constituent concentrations, *Transport Processes in the Mesosphere*, (G. Visconti and R. Garcia editors), D. Reidel, Dordrecht, 313–326, 1987.

Holton, J.R., Influence of the annual cycle in meridional transport on the quasi–biennial oscillation in total ozone, *J. Atmos. Sci.*, *46*, 1434–1439, 1989.

Holton, J.R., and R.S. Lindzen, An updated theory for the quasi-biennial cycle of the tropical stratosphere, *J. Atmos. Sci.*, *29*, 1076–1080, 1972.

Holton, J.R., and M.R. Schoeberl, The role of gravity wave generated advection and diffusion in transport of tracers in the mesosphere, *J. Geophys. Res.*, *93*, 11075–11082, 1988.

Holton, J.R., and H.-C. Tan, The influence of the equatorial quasi–biennial oscillation on the global circulation at 50 mb, *J. Atmos. Sci.*, *37*, 2200–2208, 1980.

Holton, J.R., and H.-C. Tan, The quasi–biennial oscillation in the Northern Hemisphere lower stratosphere, *J. Meteor. Soc. Japan*, *60*, 140–148, 1982.

Holton, J.R., and W.M. Wehrbein, A numerical model of the zonal mean circulation of the middle atmosphere, *Pure Appl. Geophys.*, *118*, 284–306, 1980.

Holton, J.R., and X. Zhu, A further study of gravity wave induced drag and diffusion in the mesosphere, *J. Atmos. Sci.*, *41*, 2653–2662, 1984.

Hopfinger, E.J., Turbulence in stratified fluids: a review, *J. Geophys. Res.*, *92*, 5287–5303, 1987.

Hopkins, R.H., Evidence of polar–tropical coupling in the upper stratospheric zonal wind anomalies, *J. Atmos. Sci.*, *32*, 712–719, 1975.

Houghton, J.T., The stratosphere and mesosphere, *Q. J. R. Meteor. Soc.*, *104*, 1–29, 1978.

Hyson, P., Windfinding data from radar tracking of high altitude sensors, *Q. J. R. Meteor. Soc.*, *94*, 592–597, 1968.

Ingersoll, A.P., D. Crisp, and A.W. Grossman, Estimates of convective heat fluxes and gravity wave amplitudes in the Venus middle cloud layer from VEGA balloon measurements, *Adv. Space Res.*, *7*, No 12, 343–349, 1987.

Ionson, J.A., Resonant absorption of alfvénic surface waves and the heating of solar coronal loops, *Astrophys. J.*, *226*, 650–655, 1978.

Jacobs, D.C., and C.S. Cox, Internal wave stress–shear correlations: A choice of reference frames, *Geophys. Res. Lett.*, *14*, 25–28, 1987.

Jasperson, W.H., G.D. Nastrom, and D.C. Fritts, Further study of terrain effects on the mesoscale spectrum of atmospheric motions, *J. Atmos. Sci.*, *47*, 979–987, 1990.

Jenkins, G.M., and D.G. Watts, *Spectral analysis and its applications*, 525 pp., Holden-Day, San Fransisco, 1968.

Johnson, N.I., and S. Kotz, *Continuous univariate distributions*, vol. 2, 306 pp., Houghton Mifflin, New York, 1970.

Jones, W.L., Ray tracing for internal gravity waves, *J. Geophys. Res.*, *74*, 2028–2033, 1969.

Kaimal, J.C., S.F. Clifford, and R.J. Lataitis, Effect of finite sampling on atmospheric spectra, *Boundary Layer Meteorol.*, *47*, 337–347, 1989.

Kamykowski, D., Possible interactions between phytoplankton and semidiurnal internal tides, *J. Mar. Res.*, *32*, 67–89, 1974.

Kasprzak, W.T., A.E. Hedin, H.G. Mayr, and H.B. Niemann, Wavelike perturbations observed in the neutral thermosphere of Venus, *J. Geophys. Res.*, *93*, 11237–11245, 1988.

Kays, M., and R.O. Olsen, Rocket temperature and wind sensors for synoptic observations, *Bull. Am. Met. Soc.*, *9*, 676–682, 1967.

Keyser, D., and M.J. Pecnick, A two–dimensional primitive equation model of frontogenesis forced by confluence and horizontal shear, *J. Atmos. Sci.*, *42*, 1259–1282, 1985.

Kinoshita, J., Neptune, *Scientific Am., 261(5)*, 60–69, 1989.

Kitamura, Y., and I. Hirota, Small–scale disturbances in the lower stratosphere revealed by daily rawin sonde observations, *J. Meteor. Soc. Jap., 67*, 817–831, 1989.

Koch, S.E., and J. McCarthy, The evolution of an Oklahoma dryline. Part II: Boundary–layer forcing of mesoconvective systems, *J. Atmos. Sci., 39*, 237–257, 1982.

Koch, S.E., and P.B. Dorian, A mesoscale gravity wave event observed during CCOPE. Part III: Wave environment and probable source mechanisms, *Mon. Wea. Rev., 116*, 2570–2592, 1988.

Kochanski, A., Atmospheric motions from sodium cloud drifts, *J. Geophys. Res., 69*, 3651–3662, 1964.

Kraichnan, R.H., Inertial range in two-dimensional turbulence, *Phys. Fluids, 10*, 1417–1423, 1967.

Kraichnan, R.H., and D, Montgomery, Two–dimensional turbulence, *Rep. Prog. Phys., 43*, 547–619, 1980.

Kraus, J.D., *Radioastronomy*, McGraw–Hill, New York, 1966.

Kristensen, L., and P. Kirkegaard, Digitization noise in power spectral analysis, *J. Atmos. Oceanic Technol., 4*, 328–335, 1987.

Kuettner, J., Moazagotl and föhnwelle, *Beitr. Phys. Freien Atmos., 25*, 79–114, 1939*a*.

Kuettner, J., Zur entstehung der föhnwelle, *Beitr. Phys. Freien Atmos., 25*, 251–299, 1939*b*.

Kuettner, J.P, P.A. Hillebrand, and T.L. Clark, Convection waves: Observations of gravity wave systems over convectively active boundary layers, *Q. J. R. Meteor. Soc., 113*, 445-467, 1987.

Kwon, K.H., D.C. Senft, and C.S. Gardner, Airborne sodium lidar observations of horizontal wave number spectra of mesopause density and wind perturbations, *J. Geophys. Res.*, (in press), 1990.

Labitzke, K., Stratospheric–mesospheric midwinter disturbances: A summary of observed characteristics, *J. Geophys. Res., 86*, 9665–9678, 1981.

Labitzke, K., and H. van Loon, Recent work correlating the 11–year solar cycle with atmospheric elements grouped according to the phase of the quasi–biennial oscillation, *Space Sci. Rev., 31*, 239–258, 1989.

Lait, L.R., M.R. Schoeberl, and P.A. Newman, Quasi–biennial modulation of the Antarctic ozone depletion, *J. Geophys. Res., 94*, 11559–11571, 1989.

Landsberg, H.E., Biennial pulses in the atmosphere, *Beitr. Phys. Atmos., 35*, 184–194, 1962.

Larsen, M.F., M.C. Kelley, and K.S. Gage, Turbulence spectra in the upper troposphere and lower stratosphere at periods between 2 hrs and 40 days, *J. Atmos. Sci., 39*, 1035–1041, 1982*a*.

Larsen, M.F., W.E. Swartz, and R.F. Woodmann, Gravi y–wave generation by thunderstorms observed with a vertically pointing 430 MHz radar, *Geophys. Res. Lett., 9*, 571–574, 1982*b*.

Leaman, K.D., and T.B. Sanford, Vertical energy propagation of inertial waves: A vector spectral analysis of velocity profiles, *J. Geophys. Res.*, *80*, 1975–1978, 1975.

Leovy, C.B., Simple models of thermally driven mesospheric circulation, *J. Atmos. Sci.*, *21*, 327–341, 1964.

Leovy, C.B., The atmosphere of Mars, *Sci. Am.*, *237*, 34–43, 1977.

Leovy, C.B., The general circulation of Mars: Models and observations, *Adv. Geophys.*, *28A*, 327–346, 1985.

Leovy, C.B., and R.W. Zurek, Thermal tides and Martian dust storms: Direct evidence for coupling, *J. Geophys. Res.*, *84*, 2956–2968, 1981.

Levy, G., and C.S. Bretherton, On a theory of the evolution of surface cold fronts, *J. Atmos. Sci.*, *44*, 3413–3418, 1987.

Levy, G., and C.S. Bretherton, Reply to comments on "On a theory of the evolution of surface cold fronts", *J. Atmos. Sci.*, *46*, 1874–1875, 1989.

Ley, B.E., and W.R. Peltier, Wave generation and frontal collapse, *J. Atmos. Sci.*, *35*, 3–17, 1978.

Ley, B.E., and W.R. Peltier, Propagating mesoscale cloud bands, *J. Atmos. Sci.*, *38*, 1206–1219, 1981.

Lighthill, Sir M.J., *Waves in Fluids*, Cambridge University Press, New York, 1978.

Lilly, D.K., Wave momentum flux - a GARP problem, *Bull. Amer. Meteor. Soc.*, *53*, 17–23, 1972.

Lilly, D.K., A severe downslope windstorm and aircraft turbulence event induced by a mountain wave, *J. Atmos. Sci.*, *35*, 59–77, 1978.

Lilly, D.K., Stratified turbulence and the mesoscale variability of the atmosphere, *J. Atmos. Sci.*, *40*, 749–761, 1983.

Lilly, D.K., and P.J. Kennedy, Observations of a stationary mountain wave and its associated momentum flux and energy dissipation, *J. Atmos. Sci.*, *30*, 1135–1152, 1973.

Lilly, D.K., and P.F. Lester, Waves and turbulence in the stratosphere, *J. Atmos. Sci.*, *31*, 800–812, 1974.

Lilly, D.K., and E.J. Zipser, The Front Range windstorm of 11 January 1972: A meteorological narrative, *Weatherwise*, *25*, 56–63, 1972.

Lin, Y.–H., and R.C. Goff, A study of a mesoscale solitary wave in the atmosphere originating near a region of deep convection, *J. Atmos. Sci.*, *45*, 194–205, 1988.

Lindzen, R.S., Wave–mean flow interactions in the upper atmosphere, *Bound. Layer Meteorol.*, *4*, 327–343, 1973.

Lindzen, R.S., Turbulence and stress owing to gravity wave and tidal breakdown, *J. Geophys. Res.*, *86*, 9707–9714, 1981.

Lindzen, R.S., Multiple gravity wave breaking levels, *J. Atmos. Sci.*, *42*, 301–305, 1985.

Lindzen R.S., Supersaturation of vertically propagating internal gravity waves, *J. Atmos. Sci.*, *45*, 705-711, 1988.

Lindzen, R.S., and J.R. Holton, A theory of the quasi–biennial oscillation, *J. Atmos. Sci.*, *25*, 1095–1107, 1968.

Lindzen, R.S., and C.Y. Tsay, Wave structure of the tropical stratosphere over the Marshall Islands area during 1 April–1 July 1958, *J. Atmos. Sci.*, *32*, 2008–2021, 1975.

Ling, X.-D., and J. London, The quasi–biennial oscillation of ozone in the tropical middle stratosphere, *J. Atmos. Sci.*, *43*, 3122–3137, 1986.

Long, R.R., Some aspects of the flow of stratified fluids, III. Continuous density gradients, *Tellus*, *7*, 341–357, 1955.

McAfee, J.R., B.B. Balsley, and K.S. Gage, Momentum flux measurements over mountains: Problems associated with the symmetrical two–beam radar technique, *J. Atmos. Oceanic Technol.*, *6*, 500–508, 1989.

McFarlane, N.A., The effect of orographically excited gravity wave drag on the general circulation of the lower stratosphere and troposphere, *J. Atmos. Sci.*, *44*, 1775–1800, 1987.

McIntyre, M.E., Dynamics and tracer transport in the middle atmosphere: An overview of some recent developments, *Transport Processes in the Mesosphere*, (G. Visconti and R. Garcia editors), D. Reidel, Dordrecht, 267–296, 1987.

McIntyre, M.E., On dynamics and transport near the polar mesopause in summer, *J. Geophys. Res.*, *94*, 14617–14628, 1989.

Maekawa, Y., S. Fukao, T. Sato, S. Kato, and R.F. Woodman, Internal inertia–gravity waves in the tropical lower stratosphere observed by the Arecibo radar, *J. Atmos. Sci.*, *41*, 2359–2367, 1984.

Maekawa, Y., S. Fukao, I. Hirota, M.P. Sulzer, and S. Kato, Some further results on long term mesospheric and lower thermospheric wind observations by the Arecibo UHF radar, *J. Atmos. Terr. Phys.*, *49*, 63–71, 1987.

Mahlmann, J.D., and L.J. Umscheid, Dynamics of the middle atmosphere: Successes and problems of the GFDL "SKYHI" general circulation model, in *Dynamics of the Middle Atmosphere*, (ed. J.R. Holton and T. Matsuno), Terrapub, Tokyo, 501–525, 1984.

Manley, G., The Helm wind of Crossfell, 1937–1939, *Q. J. R. Meteor. Soc.*, *71*, 197–220, 1945.

Manney, G.L., and J.L. Stanford, Wave number spectra from temperature–humidity infrared radiometer 6.7–μm water vapour data, *J. Geophys. Res.*, *95*, 909–913, 1990.

Manson, A.H., J.B. Gregory, and D.G. Stephenson, Winds and wave motions (70–100 km) as measured by a partial reflection radiowave system, *J. Atmos. Terr. Phys.*, *35*, 2055–2067, 1973.

Manson, A.H., J.B. Gregory, and D.G. Stephenson, Winds and wave motions to 110 km at mid–latitudes, I, Partial reflection radiowave soundings, 1972–1973, *J. Atmos. Sci.*, *31*, 2207, 1974.

Manson, A.H., J.B. Gregory, and D.G. Stephenson, Winds and wave motions to 110 km at mid–latitudes, IV, Coupling between internal gravity waves and the mean flow, *J. Atmos. Sci.*, *32*, 1682, 1975.

Manson, A. H., and C. E. Meek, Gravity wave propagation characteristics (60–120 km) as determined by the Saskatoon MF radar (Gravnet) system: 1983–1985 at 52°N, 107°W, *J. Atmos. Sci.*, *45*, 932–946, 1988.

Mardia, K.V., Statistics of directional data, Academic Press, London, 1972.

Maruyama, T., Large–scale disturbances in the equatorial lower stratosphere, *J. Meteor. Soc. Japan*, *45*, 391–408, 1967.

Maruyama, T., Long–term behaviour of Kelvin waves and mixed Rossby–gravity waves, *J. Meteor. Soc. Japan*, *47*, 245–254, 1969.

Massman, W.J., An investigation of gravity waves on a global scale using TWERLE data, *J. Geophys. Res.*, *86*, 4072–4082, 1981.

Matsumoto, S., and T. Akiyama, Some characteristic features of the heavy rainfalls observed over western Japan on 9 July 1967. Part 1: Mesoscale structures and short period pulsation, *J. Meteor. Soc. Japan*, *47*, 255–266, 1969.

Matsuno, T., Quasi–geostrophic motions in the equatorial area, *J. Meteor. Soc. Japan*, *44*, 25–43, 1966.

Matsuno, T., A quasi one–dimensional model of the middle atmosphere circulation interacting with internal gravity waves, *J. Meteor. Soc. Japan*, *60*, 215-226, 1982.

May, P.T., *VHF radar observations of the troposphere*, Ph.D. Thesis, University of Adelaide, Australia, 1986.

May, P.T., Statistical errors in the determination of wind velocities by the spaced antenna technique, *J. Atmos. Terr. Phys.*, *50*, 21–32, 1988.

May, P.T., S. Fukao, T. Tsuda, T. Sato, and S. Kato, The effect of thin scattering layers on the determination of wind by Doppler radars, *Radio Sci.*, *23*, 83–94, 1988.

May, P.T., K.J. Wilson, and B.F. Ryan, VHF radar studies of cold fronts passing across Southern Australia, *Beitraege f. Atmos. Physik*, (in press), 1990

Mayr, H.G., I. Harris, W.T. Kasprzak, M. Dube, and F. Varosi, Gravity waves in the upper atmosphere of Venus, *J. Geophys. Res.*, *93*, 11247–11262, 1988.

Meek, C.E., I.M. Reid, and A.H. Manson, Observations of mesospheric wind velocities, 1, Gravity wave horizontal scales and phase velocities from spaced wind observations, *Radio Sci.*, *20*, 1363–1382, 1985*a*.

Meek, C.E., I.M. Reid, and A.H. Manson, Observations of mesospheric wind velocities, 2, Cross sections of power spectral density for 48–8 h, 8–1 h, 1h–10min over 60–110 km for 1981, *Radio Sci.*, *20*, 1383–1402, 1985*b*.

Meek, C.E., and A.H. Manson, Vertical motions in the upper middle atmosphere from the Saskatoon (52°N, 107°W) M.F. radar, *J. Atmos. Sci.*, *46*, 849–858, 1989.

Meyer, W.D., A diagnostic numerical study of the semi–annual variation of the zonal wind in the tropical stratosphere and mesosphere, *J. Atmos. Sci.*, *27*, 820–830, 1970.

Miller, A.J., Response characteristics of meteorological rocket wind reduction techniques, *J. Geophys. Res.*, *74*, 6853–6858, 1969.

Miller, A.J., H.M. Woolf, and F.G. Finger, Small–scale wind and temperature structure as evidenced by meteorological rocket systems, *J. App. Meteorol.*, *7*, 390–399, 1968.

Miller, D.A., and F. Sanders, Mesoscale conditions for the severe convection of 3 April 1974 in the east–central United States, *J. Atmos. Sci.*, *37*, 1041-1055, 1980.

Miller, K.L., S.A. Bowhill, K.P. Gibbs, and I.D. Countryman, First measurements of mesospheric vertical velocities by VHF radar at temperate latitudes, *Geophys. Res. Lett.*, *5*, 939–942, 1978.

Miyahara, S., Y. Hayashi, and J.D. Mahlmann, Interactions between gravity waves and planetary–scale flow simulated by the GFDL "SKYHI" general circulation model, *J. Atmos. Sci.*, *43*, 1844–1861, 1986.

Moore, M.I., P.J. Thomson, and T.G.L. Shirtcliffe, Spectral analysis of ocean profiles from unequally spaced data, *J. Geophys. Res.*, *93*, 655–664, 1988.

Müller, P., G. Holloway, F.S. Henyey, and N. Pomphrey, Nonlinear interactions among internal gravity waves, *Rev. Geophys.*, *24*, 493–536, 1986.

Müller, P., R. Lien, and R. Williams, Estimates of potential vorticity at small scales in the ocean, *J. Phys. Oceanogr.*, *18*, 401–416, 1988.

Munk, W.H., A survey of internal waves and small–scale processes, in *Evolution of Physical Oceanography*, editors B.A. Warren and C. Wunsch, MIT Press, Cambridge, Mass., 264–291, 1981.

Muraoka, Y., K. Kawahira, T. Sato, T. Tsuda, S. Fuka›, and S. Kato, Characteristics of mesospheric internal gravity waves observed by MU radar, *Geophys. Res. Lett.*, *14*, 1154–1157, 1987.

Nastrom, G.D., B.B. Balsley, and D.A. Carter, Mean meridional winds in the mid– and high–latitude summer mesosphere, *Geophys. Res. Lett.*, *9*, 139–142, 1982.

Nastrom, G.D., and K.S. Gage, A climatology of atmospheric wavenumber spectra of wind and temperature observed by commercial aircraft, *J. Atmos. Sci.*, *42*, 950–960, 1985.

Nastrom, G.D., W.H. Jasperson, and K.S. Gage, Horizontal spectra of atmospheric tracers measured during the Global Atmospheric Sampling Program, *J. Geophys. Res.*, *91*, 13201–13209, 1986.

Nastrom, G.D., D.C. Fritts, and K.S. Gage, An investigation of terrain effects on the mesoscale spectrum of atmospheric motions, *J. Atmos. Sci.*, *44*, 3087–3096, 1987.

Naujokat, B., An update of the observed quasi–biennial oscillation of the stratospheric winds over the tropics, *J. Atmos. Sci.*, *43*, 1873–1877, 1986.

Newell, R.E., J.R. Mahoney, and R.W. Lenhard Jr., A pilot study of small–scale wind variations in the stratosphere and mesosphere, *Q. J. R. Meteor. Soc.*, *92*, 41–54, 1966 (corrigenda *94*, 603, 1968).

Oltmans, S.J., and J. London, The quasi–biennial oscillation in atmospheric ozone, *J. Geophys. Res.*, *87*, 8981–8989, 1982.

Orlanski, I., and B.B. Ross, The evolution of an observed cold front. Part II: Mesoscale dynamics, *J. Atmos. Sci.*, *41*, 1669–1703.

Ostrovsky, L.A., and Yu. A. Stepanyants, Do internal solitions exist in the ocean?, *Rev. Geophys.*, *27*, 293–310, 1989.

Owens, A.J., An algorithm for generating fluctuations having any arbitrary power spectrum, *J. Geophys. Res.*, *83*, 1673–1675, 1978.

Palmer, T.N., G.J. Shutts, and R. Swinbank, Alleviation of a systematic westerly bias in general circulation and numerical weather prediction models through an orographic gravity wave drag parameterization, *Q. J. R. Meteor. Soc.*, *112*, 1001–1040, 1986.

Pecnick, M.J., and J.A. Young, Mechanics of a strong sub–synoptic gravity wave deduced from satellite and surface observations. *J. Atmos. Sci.*, *41*, 1850–1862, 1984.

Phillips, A., and R.A. Vincent, Radar observations of prevailing winds and waves in the southern hemisphere mesosphere and lower thermosphere, *Pure Appl. Geophys.*, *130*, 303–318, 1989.

Phillips, O.M., *The dynamics of the upper ocean*, 2nd ed., Cambridge Univ. Press, 336pp., 1977.

Pickersgill, A.O., and G.E. Hunt, The formation of Martian lee waves generated by a crater, *J. Geophys. Res.*, *84*, 8317–8331, 1979.

Pirraglia, J.A., Martian atmospheric lee waves, *Icarus*, *27*, 517–530, 1976.

Pitteway, M.L.V., and C.O. Hines, The reflection and ducting of atmospheric acoustic–gravity waves, *Can. J. Phys.*, *43*, 2222–2243, 1965.

Plumb, R.A., The interaction of two internal waves with the mean flow: implications for the theory of the quasi–biennial oscillation, *J. Atmos. Sci.*, *34*, 1847–1858, 1977.

Plumb, R.A., The quasi–biennial oscillation, in *Proceedings of the U.S.-Japan Seminar on Dynamics of the Middle Atmosphere*, edited by J.R. Holton and T. Matsuno, pp 45–64, Terrapub, Tokyo, 1984.

Plumb, R.A., On the seasonal cycle of stratospheric planetary waves, *Pure Appl. Geophys.*, *130*, 233–242, 1989.

Plumb, R.A., and R.C. Bell, A model of the quasi–biennial oscillation on an equatorial beta–plane, *Q. J. R. Meteor. Soc.*, *108*, 335–352, 1982.

Plumb, R.A., and A.D. McEwan, The instability of a forced standing wave in a viscous stratified fluid: a laboratory analogue of the quasi–biennial oscillation, *J. Atmos. Sci.*, *35*, 1827–1839, 1978.

Plumb, R.A., D.G. Andrews, M.A. Geller, W.L Grose, A. O'Neill, M. Salby, and R.A. Vincent, Dynamical processes, *Atmospheric Ozone 1985, Assessment of our Understanding of the Processes Controlling its Present Distribution and Change*, WMO Global Ozone Research and Monitoring Project, Report No. 16, *1*, 241–347, 1986.

Poole, L.R., S. Solomon, M.P. McCormick, and M.C. Pitts, The interannual variability of polar stratospheric clouds and related parameters in Antarctica during September and October, *Geophys. Res. Lett.*, *16*, 1157–1160, 1989.

Queney, P., The problem of airflow over mountains: a summary of theoretical studies, *Bull. Am. Meteorol. Soc.*, *29*, 16–26, 1948.

Ramanathan, K.R., Bi–annual variation of atmospheric ozone over the tropics, *Q. J. R. Meteor. Soc.*, *89*, 540–542, 1963.

Rastogi, P.K., and S.A. Bowhill, Gravity waves in the equatorial mesosphere, *J. Atmos. Terr. Phys.*, *38*, 51–60, 1976.

Rayleigh, The light of the night sky: Its intensity variations when analyzed by colour filters, *Proc. R. Soc. London, Ser. A*, *106*, 117–137, 1924.

Rayleigh, The light of the night sky: Analysis of the intensity variations at three stations, *Proc. R. Soc. London, Ser. A*, *151*, 22–55, 1935.

Reed, R.J., The quasi–biennial oscillation of the atmosphere between 30 and 50 km over Ascension Island, *J. Atmos. Sci.*, *22*, 331-333, 1965.

Reed, R.J., Zonal wind behaviour in the equatorial stratosphere and lower mesosphere, *J. Geophys. Res.*, *71*, 4223-4333, 1966.

Reed, R.J., W.J. Campbell, L.A. Rasmussen, and D.G. Rogers, Evidence of downward-propagating annual wind reversal in the equatorial stratosphere, *J. Geophys. Res.*, *66*, 813–818, 1961.

Reeder, M.J., and R.K. Smith, A study of frontal dynamics with application to the Australian summertime "cool change", *J. Atmos. Sci.*, *44*, 687–705, 1987

Reeder, M.J., and R.K. Smith, On air motion trajectories in cold fronts, *J. Atmos. Sci.*, *45*, 4005–4007, 1988.

Reid, I.M., *Radar studies of atmospheric gravity waves*, Ph.D. Thesis, University of Adelaide, Adelaide, Australia, 1984.

Reid, I.M., Gravity wave motions in the upper middle atmosphere (60–110 km), *J. Atmos. Terr. Phys.*, *48*, 1057–1072, 1986.

Reid, I.M., Observations of gravity wave scales, fluxes, and saturation during MAP, in *Handbook for MAP*, *27*, 427–438, SCOSTEP Secr., Univ. of Ill., Urbana, 1989.

Reid, I.M., and R.A. Vincent, Measurements of mesospheric gravity wave momentum fluxes and mean flow accelerations at Adelaide, Australia, *J. Atmos. Terr. Phys.*, *49*, 443–460, 1987*a*.

Reid, I.M., and R.A. Vincent, Measurements of the horizontal scales and phase velocities of short period mesospheric gravity waves at Adelaide, Australia, *J. Atmos. Terr. Phys.*, *49*, 1033–1048, 1987*b*.

Reid, I.M., R. Rüster, P. Czechowsky, and G. Schmidt, VHF radar measurements of momentum flux in the summer polar mesosphere over Andenes (69°N, 16°E), Norway, *Geophys. Res. Lett.*, *11*, 1263–1266, 1988.

Rind, D., R. Suozzo, N.K. Balachandran, A. Lacis, and G. Russell, The GISS global climate–middle atmosphere model, I; Model structure and climatology, *J. Atmos. Sci.*, *45*, 329–370, 1988.

Roberts, J., *Internal gravity waves in the ocean*, Dekker, New York, 274pp, 1975.

Robinson, W.A., The application of the quasi-geostrophic Eliassen–Palm flux to the analysis of stratospheric data, *J. Atmos. Sci.*, *43*, 1017–1023, 1986.

Ryan, B.F., K.J. Wilson, J.R. Garratt, and R.K. Smith, Cold Fronts Research Programme: Progress, future plans, and research directions, *Bull. Am. Met. Soc.*, *66*, 1116–1122, 1985.

Ryan, B.F., and K.J. Wilson, The Australian summertime cool change. Part III: Subsynoptic and mesoscale model, *Mon Wea. Rev.*, *113*, 224–240, 1985.

Salawitch, R.J., S.C. Wolfy, and M.B. McElroy, Influence of polar stratospheric clouds on the depletion of Antarctic ozone, *Geophys. Res. Lett.*, *15*, 871–874, 1988.

Salby, M.L., D.L. Hartmann, P.L. Bailey, and J.C. Gille, Evidence for equatorial Kelvin modes in Nimbus-7 LIMS, *J. Atmos. Sci.. 41*, 220–235, 1984.

Salby, M.L., and R.R. Garcia, Dynamical perturbations to the ozone layer, *Physics Today, 43(3)*, 38–46, 1990.

Sanderson, B.G., and A. Okubo, Diffusion by internal waves, *J. Geophys. Res., 93*, 3570–3582, 1988.

Sato, K., An inertial gravity wave associated with a synoptic-scale pressure trough observed by the MU radar, *J. Meteor. Soc. Japan, 67*, 325–334, 1989.

Sawyer, J.S., The introduction of the effects of topography into methods of numerical forecasting, *Q. J. R. Meteor. Soc., 85*, 231–243, 1959.

Sawyer, J.S., Quasi-periodic wind variations with height in the lower stratosphere, *Q. J. R. Meteor. Soc., 87*, 24–33, 1961.

Scheffler, A.O., and C.H. Liu, The effects of Doppler shift on gravity wave spectra observed by MST radar, *J. Atmos. Terr. Phys., 48*, 1225–1231, 1986.

Schmidlin, F.J., Temperature inversions near 75 km, *Geophys. Res. Lett., 3*, 173–176, 1976.

Schmidlin, F.J., Repeatability and measurement uncertainty of the United States meteorological rocketsonde, *J. Geophys. Res., 86*, 9599–9603, 1981.

Schoeberl, M.R., A ray tracing model of gravity wave propagation and breakdown in the middle atmosphere, *J. Geophys. Res., 90*, 7999–8010, 1985.

Schoeberl, M.R., and D.F. Strobel, The zonally averaged circulation of the middle atmosphere, *J. Atmos. Sci., 35*, 577–591, 1978.

Schoeberl, M.R., and D.F. Strobel, Nonzonal gravity wave breaking in the winter stratosphere, in *Proceedings of the U.S.-Japan Seminar on Dynamics of the Middle Atmosphere*, edited by J.R. Holton and T. Matsuno, pp 45–64, Terrapub, Tokyo, 1984.

Schoeberl, M.R., D.F. Strobel, and J.P. Apruzese, A numerical model of gravity wave breaking and stress in the middle atmosphere, *J. Geophys. Res., 88*, 5249- 5259, 1983.

Schubert, G., and J.A. Whitehead, Moving flame experiment with liquid mercury: possible implications for the Venus atmosphere, *Science, 163*, 71–72, 1969.

Schubert, G., and R.L. Walterscheid, Propagation of small-scale acoustic-gravity waves in the Venus atmosphere, *J. Atmos. Sci., 41*, 1202–1213, 1984.

Scinocca, J.F., and W.R. Peltier, Pulsating downslope windstorms, *J. Atmos. Sci., 46*, 2885–2914, 1989.

Scorer, R.S., Theory of waves in the lee of mountains, *Q. J. R. Meteor. Soc., 75*, 41–56, 1949.

Shapiro, M.A., and P.J. Kennedy, Aircraft measurements of wave motions within frontal zone systems, *Mon. Wea. Rev.*, *103*, 1050–1054, 1975.

Sharma, A.S., P.J. Cargill, and K. Papadopoulos, Resonance absorption of Alfvén waves at comet–solar wind interaction regions, *Geophys. Res. Lett.*, *15*, 740-743, 1988.

Shibata, T., T. Fukuda, and M. Maeda, Density fluctuations in the middle atmosphere over Fukuoka observed by an XeF Rayleigh lidar, *Geophys. Res. Lett.*, *13*, 1121–1124, 1986.

Shibata, T., S. Ichimori, T. Narikiyo, and M. Maeda, Spectral analysis of vertical temperature profiles in the upper stratosphere and the lower mesosphere, *J. Meteorol. Soc. Japan*, *66*, 1001–1005, 1988.

Shine, K., Sources and sinks of zonal momentum in the middle atmosphere diagnosed using the diabatic circulation, *Q. J. R. Meteor. Soc.*, *115*, 265–292, 1989.

Sidi, C., J. Lefrere, F. Dalaudier, and J. Barat, An improved atmospheric buoyancy wave spectrum model, *J. Geophys. Res.*, *93*, 774–790, 1988.

Sidi, C., and F. Dalaudier, Temperature and heat flux spectra in the turbulent buoyancy subrange, *Pure Appl. Geophys.*, *130*, 547–569, 1989.

Smith, A.K., and L.V. Lyjak, An observational estimate of gravity wave drag from the momentum balance in the middle atmosphere, *J. Geophys. Res.*, *90*, 2233-2241, 1985.

Smith, R.B., A measurement of mountain drag, *J. Atmos. Sci.*, *9*, 1644–1654, 1978.

Smith, R.B., The influence of mountains on the atmosphere, *Adv. Geophys.*, *21*, 87–230, 1979.

Smith, R.B., Hydrostatic airflow over mountains, *Adv. Geophys.*, *31*, 1–38, 1989.

Smith, R.K., B.F. Ryan, A.J. Troup, and K.J. Wilson, Cold fronts research: The Australian summertime "cool change", *Bull. Am. Met. Soc.*, *63*, 1028–1034, 1982.

Smith, R.K., Travelling waves and bores in the lower atmosphere: The "morning glory" and related phenomena, *Earth-Sci. Rev.*, *25*, 267–290, 1988.

Smith, R.K., and M.J. Reeder, On the movement and low -level structure of cold fronts, *Mon. Wea. Rev.*, *116*, 1927–1944, 1988.

Smith, S.A., D.C. Fritts and T.E. VanZandt, Evidence of a saturated spectrum of atmospheric gravity waves, *J. Atmos. Sci.*, *44*, 1404–1410, 1987.

Stern, M.E., The moving flame experiment, *Tellus*, *11*, 175–179, 1959.

Stobie, J.G., F. Einaudi, and L.W. Uccellini, A case study of gravity waves–convective storms interaction: 9 May 1979, *J. Atmos. Sci.*, *40*, 2804–2830, 1983.

Strobel, D.F., M.E. Summers, R.M., Bevilacqua, M.T. DeLand, and M. Allen, Vertical constituent transport in the mesosphere, *J. Geophys. Res.*, *92*, 6691–6698, 1987.

Strobel, D.F., Constraints on gravity wave induced diffusion in the middle atmosphere, *Pure Appl. Geophys.*, *130*, 533–546, 1989.

Tanaka, H., A slowly varying model of the lower stratospheric zonal wind minimum induced by mesoscale mountain wave breakdown, *J. Atmos. Sci.*, *43*, 1881–1892, 1986.

Tanaka, H., and N. Yoshizawa, A slowly varying model of the quasi–biennial oscillation involving effects of transience, self–acceleration and saturation of equatorial waves, *J. Atmos. Sci.*, *44*, 1427–1436, 1987.

Tatarski, V.I., *Wave propagation in a turbulent medium*, McGraw–Hill, New York, 285pp., 1961.

Testud, J., G. Breger, P. Amayenc, M. Chong, B. Nutten, and A. Souvaget, A Doppler radar observation of a cold front: Three–dimensional air circulation, related precipitation system and associated wavelike motions, *J. Atmos. Sci.*, *37*, 78–98, 1980.

Theon, J.S., W. Nordberg, L.B. Katchen, and J.J. Horvath, Some observations on the thermal behaviour of the mesosphere, *J. Atmos. Sci.*, *24*, 428–438, 1967.

Thomas, R.J., C.A. Barth, and S. Solomon, Seasonal variations of ozone in the upper mesosphere and gravity waves, *Geophys. Res. Lett.*, *11*, 673–676, 1984*a*.

Thomas, R.J., C.A. Barth, D.W. Rusch, and R.W. Sanders, Solar Mesosphere Explorer near–infrared spectrometer, *J. Geophys. Res.*, *89*, 9569–9580, 1984*b*.

Thompson, R.O.R.Y., Observation of inertial waves in the stratosphere, *Q. J. R. Meteor. Soc.*, *104*, 691–698, 1978.

Tillman, J.E., Mars global atmospheric oscillations: Annually synchronized, transient normal–mode oscillations and the triggering of global dust storms, *J. Geophys. Res.*, *93*, 9433–9451, 1988.

Toon, O.B., R.P. Turco, J. Jordan, J. Goodman, and G.Ferry, Physical processes in polar stratospheric ice clouds, *J. Geophys. Res.*, *94*, 11359–11380, 1989.

Trenberth, K.E., A quasi–biennial standing wave in the Southern Hemisphere and interrelations with sea–surface temperature, *Q. J. R. Meteor. Soc.*, *101*, 55–74, 1975.

Trenberth, K.E., Atmospheric quasi–biennial oscillations, *Mon. Wea. Rev.*, *108*, 1370–1377, 1980.

Tsurutani, B.T., and E.J. Smith, Hydromagnetic waves and instabilities associated with cometary ion pickup: ICE observations, *Geophys. Res. Lett.*, *13*, 263–266, 1986.

Tyson, P.D., *Climate change and variability in Southern Africa*, Oxford Univ. Press, 319pp, 1986.

Uccellini, L.W., A case study of apparent gravity wave initiation of severe convective storms, *Mon. Wea. Rev.*, *103*, 497–513, 1975.

Uccellini, L.W., and S.E. Koch, The synoptic setting and possible energy sources for mesoscale wave disturbances, *Mon. Wea. Rev.*, *115*, 721–729, 1987.

VanHoven, G., Energetics and dynamics of solar activity, *Eos*, *70*, 593 & 606–607, 1989.

VanZandt, T.E., A universal spectrum of buoyancy waves in the atmosphere, *Geophys. Res. Lett.*, *9*, 575–578, 1982.

VanZandt, T.E., A model for gravity wave spectra observed by Doppler sounding systems, *Radio Sci.*, *20*, 1323–1330, 1985.

VanZandt, T.E., and D.C. Fritts, A theory of enhanced saturation of the gravity wave spectrum due to increases in atmospheric stability, *Pure Appl. Geophys.*, *130*, 399–420, 1989.

VanZandt, T.E., S.A. Smith, T. Tsuda, D.C. Fritts, T. Sato, S. Fukao, and S. Kato, Studies of velocity fluctuations in the lower atmosphere using the MU radar. Part I: Azimuthal anisotropy, *J. Atmos. Sci.*, *47*, 39–50, 1990.

Veryard, R.G., and R.A. Ebdon, Fluctuations in lower stratospheric winds, *Meteor. Mag.*, *90*, 125–143, 1961.

Vincent, R.A., Gravity-wave motions in the mesosphere, *J. Atmos. Terr. Phys.*, *46*, 119–128, 1984.

Vincent, R.A., Planetary and gravity waves in the mesosphere and lower thermosphere, *Adv. Space Res.*, *7(10)*, 163–169, 1987.

Vincent, R.A., and S.M. Ball, Tides and gravity waves in the mesosphere at low– and mid–latitudes, *J. Atmos. Terr. Phys.*, *39*, 965–970, 1977.

Vincent, R.A., and S.D. Eckermann, VHF radar observations of mesoscale motions in the troposphere: Evidence of gravity wave Doppler shifting, *Radio Sci.*, (in press), 1990.

Vincent, R.A., and D.C. Fritts, A climatology of gravity wave motions in the mesopause region at Adelaide, Australia, *J. Atmos. Sci.*, *44*, 748–760, 1987

Vincent, R.A., and I.M. Reid, HF Doppler measurements of mesospheric gravity wave momentum fluxes, *J. Atmos. Sci.*, *40*, 1321–1333, 1983.

Vincent, R.A., and T.J. Stubbs, A study of motions in the winter mesosphere using the partial reflection drift technique, *Planet. Space Sci.*, *25*, 441–455, 1977.

Vincent, R.A., P.T. May, W.K. Hocking, W.G. Elford, B.H. Candy, and B.H. Briggs, First results with the Adelaide VHF radar: spaced antenna studies of tropospheric winds, *J. Atmos. Terr. Phys.*, *49*, 353–366, 1987.

Vincent, R.A., T. Tsuda, and S. Kato, A comparitive study of mesospheric solar tides observed at Adelaide and Kyoto, *J. Geophys. Res.*, *93*, 699–708, 1988.

vonZahn, U., and W. Meyer, Mesopause temperatures in polar summer, *J. Geophys. Res.*, *94*, 14647–14651, 1989.

Wahr, J.M., The Earth's rotation, *Ann. Rev. Earth Planet. Sci.*, *16*, 231–249, 1988.

Wallace, J.M., General circulation of the tropical lower stratosphere, *Rev. Geophys. Space Phys.*, *11*, 191–222, 1973.

Wallace, J.M., and J.R. Holton, A diagnostic numerical model of the quasi–biennial oscillation, *J. Atmos. Sci.*, *25*, 280–292, 1968.

Wallace, J.M., and V.E. Kousky. Observational evidence of Kelvin waves in the tropical stratosphere, *J. Atmos. Sci.*, *25*, 900–907, 1968.

Walterscheid, R.L., and W.K. Hocking, Stokes diffusion by atmospheric internal gravity waves, *J. Atmos. Sci.*, (in press), 1990.

Walterscheid, R.L., and G. Schubert, Nonlinear evolution of an upward propagating gravity wave: Overturning, convection, transience, and turbulence, *J. Atmos. Sci.*, *47*, 101–125, 1990.

Wang, D.–Y., and D.C. Fritts, Evidence of gravity wave–tidal interaction observed near the summer mesopause at Poker Flat, *J. Atmos. Sci.*, (in press), 1990.

Weinstein, A.I., E.R. Reiter, and J.R. Scoggins, Mesoscale structure of 11–20 *km* winds, *J. Appl. Meteor.*, *5*, 49–57, 1966.

Weinstock, J., On the theory of turbulence in the buoyancy subrange of stably stratified flows, *J. Atmos. Sci.*, *35*, 634–649, 1978.

Weinstock, J., Theoretical gravity wave spectrum: Strong and weak wave interactions, *Radio Sci.*, *20*, 1295–1300, 1985.

Weinstock, J., Time–averaged transport coefficients in photochemical modelling: A conjecture, *J. Geophys. Res.*, *94*, 14703–14704, 1989.

Whitaker, W.A., Heating of the solar corona by gravity waves, *Astrophys. J.*, *137*, 914–930, 1963.

Witt, G., Height, structure, and displacements of noctilucent clouds, *Tellus*, *14*, 1–18, 1962.

Woodrum, A., and C.G. Justus, Measurement of the irregular winds in the altitude region near 100 kilometers, *J. Geophys. Res.*, *73*, 7535–7537, 1968.

Wright, P.B., Precursors of the southern oscillation, *J. Climatol.*, *6*, 17–30, 1985.

Wu, Y.–F., and H.–U. Widdel, Observational evidence of a saturated gravity wave spectrum in the mesosphere, *J. Atmos. Sci.*, *51*, 991–996, 1989.

Wu, Y.–F., and H.–U. Widdel, Spectral analysis of atmospheric velocity fluctuations in the mesosphere, *J. Atmos. Sci.*, *52*, 23–33, 1990.

Yamamoto, M., T. Tsuda and S. Kato, Gravity waves observed by the Kyoto meteor radar in 1983-1985, *J. Atmos. Terr. Phys.*, *48*, 597–603, 1986.

Yamamoto, M., T. Tsuda, S. Kato, T. Sato, and S. Fukao, A saturated inertia gravity wave in the mesosphere observed by The Middle and Upper Atmosphere Radar, *J. Geophys. Res.*, *92*, 11993–11999, 1987.

Yamamoto, M., T. Sato, T. Tsuda, S. Fukao, and S. Kato, Full–correlation analysis of turbulent scattering layers in the mesosphere observed by the MU radar, *Pure Appl. Geophys.*, *130*, 605–616, 1989.

Yamanaka, M.D., Picture of the global field of "quasi–monochromatic" internal gravity waves observed by stratospheric balloons and MST radars, *Adv. Space. Res.*, *10(10)*, 185–188, 1990.

Yamanaka, M.D., S. Fukao, H. Matsumoto, T. Sato, T. Tsuda, and S. Kato, Internal gravity wave selection in the upper troposphere and lower stratosphere observed by the MU radar, *Pure Appl. Geophys.*, *130*, 481–495, 1989.

Yanai, M., and T. Maruyama, Stratospheric wave disturbances propagating over the equatorial Pacific, *J. Meteor. Soc. Japan*, *44*, 291–294, 1966.

Yeh, K.C., and B. Dong, The nonlinear interaction of a gravity wave with the vortical modes, *J. Atmos. Terr. Phys.*, *51*, 45–50, 1989.

Yeh, K.C., and C.H. Liu, The instability of atmospheric gravity waves through wave–wave interactions, *J. Geophys. Res.*, *86*, 9722–9728, 1981.

Young, R.E., R.L. Walterscheid, G. Schubert, A. Seiff, V.M. Linkin, and A.N. Lipatov, Characteristics of gravity waves generated by surface topography on Venus: comparison with the VEGA balloon results, *J. Atmos. Sci.*, *44*, 2628–2639, 1987.

Zhu, X., and J.R. Holton, Photochemical damping of inertio–gravity waves, *J. Atmos. Sci.*, *43*, 2578–2584, 1986.

Zhu, X., and J.R. Holton, Mean fields induced by local gravity–wave forcing in the middle atmosphere, *J. Atmos. Sci.*, *44*, 620–630, 1987.

Zurek, R.W., Free and forced modes in the Martian atmosphere, *J. Geophys. Res.*, *93*, 9452–9462, 1988.